Alma Mater Studiorum – Università di Bologna

DOTTORATO DI RICERCA IN

FISICA

Ciclo XXV

Settore Concorsuale di afferenza: 02/A1

Settore Scientifico disciplinare: FIS/04

The AMS-02 Experiment and the Dark Matter Search

Presentata da:
Dott. Nicolò Masi

Coordinatore Dottorato
Prof. Fabio Ortolani

Relatore
Prof. Andrea Contin

Esame finale anno 2013

Index

Chapter 1 Introduction 4

Chapter 2 Dark Matter Theory Unveiled: Why it's needed and how it works 5

2.1 **Local evidences** **6**
  2.1.1 Galactic Rotation Curves 7
  2.1.2 Velocity dispersions of dwarf spheroidal galaxies 9
  2.1.3 Milky Way warp due to dark satellite galaxies 9
  2.1.4 Planck Galactic haze 10

2.2 **Cosmic evidences** **11**
  2.2.1 Dynamics of Galaxy Clusters 11
  2.2.2 Velocity dispersions of spiral galaxy satellites 15
  2.2.3 X-Ray Cluster Emission 15
  2.2.4 Gravitational Lensing 16
  2.2.5 DM Skeleton between galaxies 18

2.3 **Cosmological hints** **18**
  2.3.1 Einstein Cosmology 19
  2.3.2 Particle Cosmological Production 21
  2.3.3 CMB Acoustic Peaks 26
  2.3.4 Baryonic Oscillation, Structure Formation and Evolution 28

2.4 **Non-particle DM theories: a brief criticism** **30**
  2.4.1 MOND 30
  2.4.2 MOG and Non-Local Gravity 33

Chapter 3 Phenomenology: a Dark Matter Search Program 38

3.1 **Dark Matter Halo** **38**

3.2 **Cosmic Rays Physics** **41**
  3.2.1 CR Propagation 41
  3.2.2 DM Indirect detection 52

3.3 **PAMELA, FERMI: a starting point** **53**
3.3.1 The positron-antiproton anomaly 54
3.3.2 Dark Matter Mass and Annihilation cross section 59

3.4 **Hadronic Signals:** **66**
3.4.1 Antiprotons 66
3.4.2 Antideuterons 69
3.4.3 Fluxes Uncertainties 74

3.5 **Dark Matter Candidates and AMS-02** **77**
3.5.1 Neutralino 77
3.5.2 Little Higgs Particle 83
3.5.3 Scalar Singlet 85
3.5.4 Primordial Black Holes 85
3.5.5 Kaluza-Klein particle 87
3.5.6 Axions and other particles 90
3.5.7 AMS-02 fluxes estimates 92

3.6 **A synthetic scheme: the uptodate DM candidates landscape** **95**
3.6.1 LHC input 95
3.6.2 Favored and ill-favored candidates 100

3.7 **Alternatives** **105**
3.7.1 Modified Fluxes: IBEX and anisotropic propagation 105
3.7.2 Astrophysical primary fluxes 108

3.8 **The Final Recipe: a DM search guideline** **112**
3.8.1 Scattering Cross Section 112
3.8.2 Particle Dark Matter ID: conclusions 118
3.8.3 Open Questions 120

Chapter 4 The detector: AMS-02, the TOF and the Data Acquisition **121**

4.1 **The magnet and the tracker** **129**
4.2 **The TRD** **134**
4.3 **The ECAL and the Star Tracker** **135**
4.4 **The RICH** **137**
4.5 **The ACC, the DAQ and the Trigger** **137**
4.6 **The Time of Flight in details** **144**
4.6.1 Electronics 146

4.6.2 How it works 158
4.6.3 TOF performances and optimizations 166

4.7 **AMS-02 Chronology** **174**
4.8 **On the ISS: Data Acquisition** **177**
4.9 **The Payload Operation Control Center** **181**

Chapter 5 The Analysis: Event Selection and Cut Stability **194**

5.1 **Events Selection** **194**
5.1.1 Background description 194
5.1.2 Variables definition 195
5.1.2 Integrity, Cleaning and Physical Cuts on Events Variables 197
5.1.2.1 Data Integrity Cuts 197
5.1.2.2 Cleaning Cuts 200
5.1.2.3 Particle Identification Cuts 210
5.1.2.4 Discriminators Maps 217
5.1.2.5 Charge confusion 223

5.2 **Data analysis as a function of time** **226**
5.3 **Positron fraction stability** **233**

Chapter 6 Conclusions **237**

Appendix **238**

Bibliography **242**

Chapter 1

Introduction

The Standard Model (SM) is a successful theory of particle physics. It has passed every laboratory test to date. However, this is not the end of the story. First of all, Higgs mass needs to be stabilized, new particle sectors should be added and the model enlarged to take into account several internal open questions.

Dark matter (DM) could solve part of these quests and it also seems to make up 80% of the matter in our Universe. Analyzing the nature of DM and its search opportunities with a space detector, like AMS-02, is the reason of this thesis.

Already in the thirties, Zwicky observed that the velocities of galaxies in the Coma cluster far exceeded the velocities expected based on the gravitational potential of the luminous matter. He postulated the existence of a non-luminous matter that made up the remaining mass of the cluster. Since then, numerous other studies have pointed to the existence of dark matter, both on cosmic and cosmological scale; also separate measurements of the baryon density show that this cannot be baryons. While a host of astrophysical measurements have precisely determined the amount of dark matter in our Universe, its identity is not known yet. At present, one could imagine that the dark matter is a Weakly Interacting Massive Particle (WIMP), an axion, or something more exotic and complex.

The focus of the examination will be on WIMP dark matter candidates and on the hunt with primary hadronic and leptonic cosmic rays spectra, which come from DM self-annihilation. AMS-02 space searches look at antiparticle spectra: primary antiparticle fluxes can easily overcome secondary ones, whereas particle fluxes would be mixed with astrophysical background and not clearly separable.

The aim of chapter 2 is to demonstrate that nowadays DM is, at the same time, a necessity and almost a certainty, dealing with recent observations and offering a criticism of alternative "modified gravity" theories.

In chapter 3 a clear-headed analysis of the uptodate DM theories landscape is presented, in order to establish a modern guideline for space born DM experiments: starting from phenomenological cross checks, experimental constraints and simplicity criteria, the conclusions are quite stringent, depicting a very *narrow* and bound scenario for dark matter models and dark matter properties.

Chapter 4 makes a detailed presentation of the AMS-02 detector, zooming on The Time-of-Flight subdetector, which has been developed and built in our Bologna INFN Laboratories.

In chapter 5 an experimental analysis of AMS-02 data is shown, which illustrates AMS measurement potentiality, through a great particle discrimination capability: in particular, the study is finalized to demonstrate that the experiment is very stable in time and offers a unique opportunity to measure antiparticle to particle ratios and to corroborate or disqualify DM candidates.

Chapter 2

Dark Matter Theory Unveiled: Why it's needed and how it works

The combination of many observations, including galactic rotation curves, gravitational lensing, the cosmic microwave background (CMB), and primordial light element abundances, cannot be explained without extending the Standard Model of particle physics. The simplest extensions involve dark matter, composed of a new particle that may annihilate or decay to Standard Model particles detectable far from their source. Astroparticle experiments seek to discover the particle nature of DM and determine its properties indirectly through the detection of cosmic ray (CR), gamma ray and neutrino signatures. Such work is complementary to direct and accelerator-based searches. Accelerators may detect new candidate particles but cannot ascertain whether they form the DM. Direct and indirect detection experiments rely on different unknown properties of particle DM, so it is important to pursue both. DM searches with astroparticle data have the potential to determine the astrophysical distribution of the DM particles, which is not possible with the other methods.

In this chapter a general overview of DM signatures is given; however, the subject has a large literature and it's impossible to cover it in entirety here.

The approximate distribution of DM in our Universe can be deduced from its gravitational effects, but its nature and microphysical properties are still unknown. There are constraints on the properties of DM particle candidates that strongly favor or rule out various models. Non-gravitational interactions between DM and Standard Model particles are highly constrained by the lack of observations of particle DM. This strongly disfavors DM that is electrically charged or interacts by the strong nuclear force. In addition, DM must clump gravitationally to form galaxies. This requires DM to be "cold", that is non-relativistic at the time of structure formation, or possibly "warm". In fact "hot" DM, that is relativistic during structure formation, cannot explain the ensemble of data. Within these constraints, the theoretically best-motivated candidates for a DM particle are a weakly interacting massive particle (WIMP) or an axion. The axion was originally postulated as a solution to the strong CP problem (Peccei & Quinn, 1977; Wilczek, 1978; Weinberg, 1978): the reviews by Kolb and Turner et al. [1] and Kuster et al. [2] diffusely discuss axion DM and cosmology.

Typically WIMPs are considered to be thermal relics left over from the Early Universe. The interactions of WIMPs with Standard Model particles kept them in thermal equilibrium at the high temperatures that existed at that time. As the Universe expanded the rate of these interactions, formation and annihilation, eventually became too low, and the WIMP abundance froze out. Thereafter their total number in the Universe no longer changed significantly. Therefore, the abundance today is inversely proportional to the WIMP self-annihilation cross section. The fractional abundance, relative to the critical density, is

$$\Omega_{\mathrm{WIMP}} \approx \frac{0.1}{h^2}\left(\frac{3\times10^{-26}\,\mathrm{cm}^3\,\mathrm{s}^{-1}}{\langle\sigma v\rangle}\right) \tag{2.1}$$

where $\langle\sigma v\rangle$ is the DM annihilation cross section times the relative velocity of two WIMPs averaged over their velocity distribution, and $0.1/h^2$ is the approximate observed abundance of DM (see formula 2.39). Note that this depends on the DM annihilation cross section and fundamental constants but not on a DM particle mass.

Therefore, to reproduce the observed DM density of our Universe, a WIMP of any mass must have an annihilation cross section of

$$\langle \sigma v \rangle \approx 3 \times 10^{-26}\, \mathrm{cm}^3\, \mathrm{s}^{-1} \tag{2.2}$$

Because this is a typical value expected for a particle with mass near the weak scale [O(100 GeV)], or with interactions suppressed by that scale, there is a strong motivation to consider DM models in which the candidate particle interacts with a weak force and has a mass around the weak scale (100 GeV – 1 TeV). The fact that the observed abundance of DM points to new physics at the weak scale, completely independent of particle physics motivations for new physics at the same scale, is the so-called WIMP miracle [3].

The only real bound on a thermal relic DM particle is that it should be heavier than 1 keV so that it is cold instead of hot. On the other hand DM particles have been usually assumed to be relatively "light", meaning lighter than a few hundred TeV. This limit is a consequence of the existence of a maximum annihilation cross section for a particle of a given mass, m_{DM}, set by the so-called *unitarity bound*. Griest and Kamionkowski [4] applied this bound and the constraint on the relic density to infer an upper limit on the dark matter particle mass: $m_{DM} \lesssim 340$ TeV (from now on natural units are used for masses and momenta, to streamline the text). Nowadays, using the WMAP constraint, this bound can be made about three times stronger: $m_{DM} \lesssim 120$ TeV.

So it's possible to identify so far some well spread paradigms [3, 88], or "theoretical prejudice", for this type of unknown matter:

1. DM is dark, i. e. it has a zero electromagnetic cross section;
2. DM cannot be seen in an accelerator through its annihilation products;
3. DM particles are thermal relics: this would imply, without new physics contributions, that m_{DM} should be less than 1 TeV;
4. DM annihilates in pairs into Standard Model particles;
5. DM is a stable and "simple" particle, not affected by Standard Model-like anomalies and violations.

These assumptions can be proved only to the combine effort of astronomy, space and laboratory experiments. Through its astrophysical and cosmological gravitational behavior in galaxies, cluster of galaxies and Big Bang radiation a blind glimpse of this tricky matter is obtained. These observations can put some constraints on DM interaction properties and quantum characteristics.

But first it's fundamental to convince ourselves that DM really exists.

2.1 Local evidences: some examples

For local evidences galactic scale evidences are referred to, including the well-known rotation curves problem and peculiar properties of our Galaxy, or strange evidences and phenomena in small galaxies [7, 34]. Obviously, also anomalous cosmic rays fluxes could be considered a local galactic evidence of new dark physics. We don't deal with it here because this will be the topic of the third chapter.

2.1.1 Galactic Rotation Curves

Spiral galaxies are stable gravitationally bound systems in which visible matter is composed of stars and interstellar gas. Most of the observable matter is in a relatively thin disc, where stars and gas rotate around the galactic center on nearly circular orbits. If the circular velocity at radius r is v in a galaxy with mass $M(r)$ inside r, the condition for stability is that the centrifugal acceleration v/r should equal the gravitational pull $GM(r)/r^2$, and the radial dependence of v would then be expected to follow Kepler's law

$$v(r) = \sqrt{\frac{GM(r)}{r}} \tag{2.3}$$

where $M(r) = 4\pi \int \rho(r) r^2 dr$.

The surprising result from measurements of galaxy-rotation curves is that the velocity does not follow this $1/\sqrt{\mathrm{r}}$ law, but stays constant after attaining a maximum at about 5 kpc. The most obvious solution to this is that the galaxies are embedded in extensive, diffuse haloes of dark matter. If the enclosed mass inside the radius r, $M(r)$, is proportional to r it follows that $v(r)$ remains constant. The rotation curve of most galaxies can be fitted by the superposition of contributions from the stellar and gaseous disks, the luminous components, both modeled by thin exponential disks, sometimes a bulge, and the dark halo, described in first approximation by a quasi-isothermal sphere. The inner part is difficult to model because the density of stars is high, rendering observations of individual star velocities difficult. Thus the fits are not unique, the relative contributions of disk and dark matter is model-dependent, and it is not even sure whether galactic disks do contain dark matter [324].

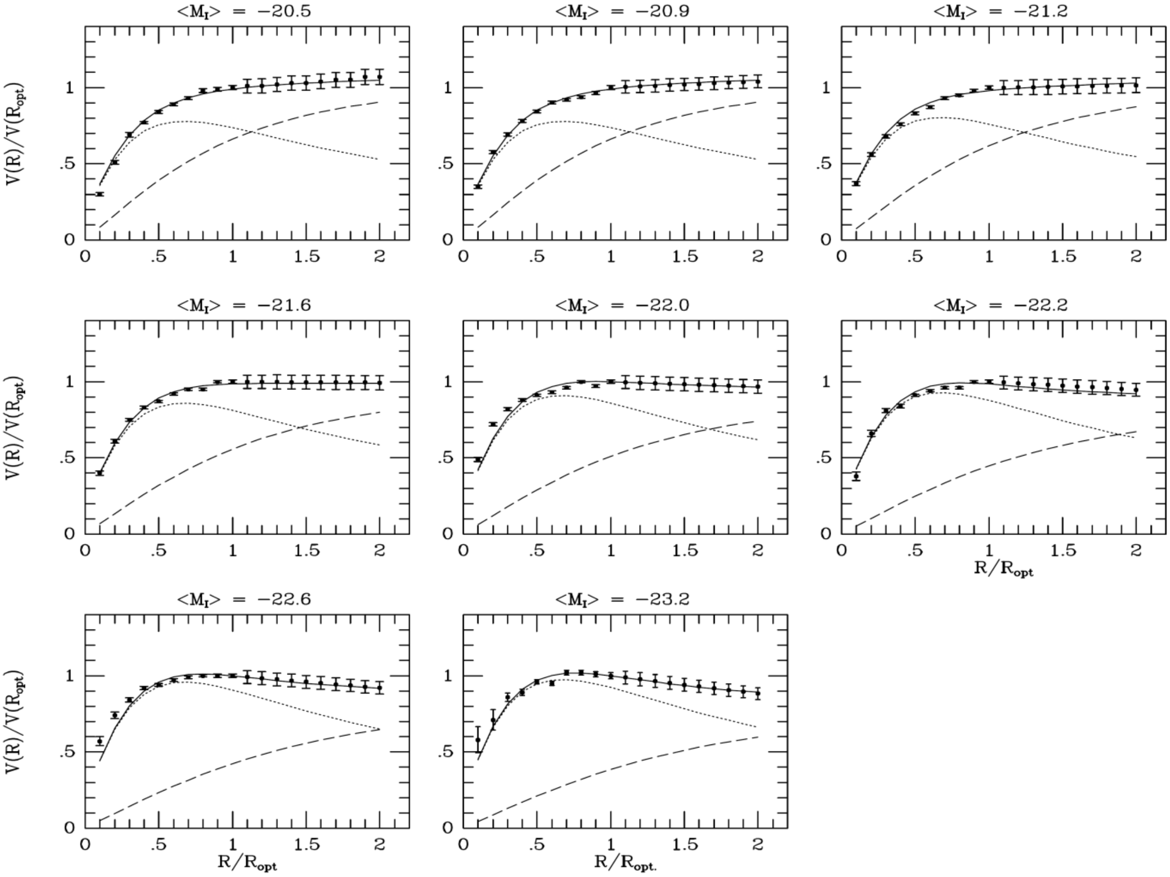

Figure 1 - The rotation curves fitted for eleven well-measured galaxies are shown [5]. One notes that, at very small radii, the dark halo component is indeed much smaller than the luminous disk

component. At large radii, however, the need for a halo of dark matter is obvious. On galactic scales, the contribution of dark matter generally dominates the total mass [138].

Our Galaxy is complicated because of what appears to be a density dip at 9 kpc and a small dip at 3 kpc, as it's depicted in Fig. 2 [6]. To fit the measured rotation curve one needs at least three contributing components: a central bulge, the star disk + gas, and a dark matter halo. For small radii there is a choice of empirical rotation curves, and no dark matter component appears to be needed until radii beyond 15 kpc.

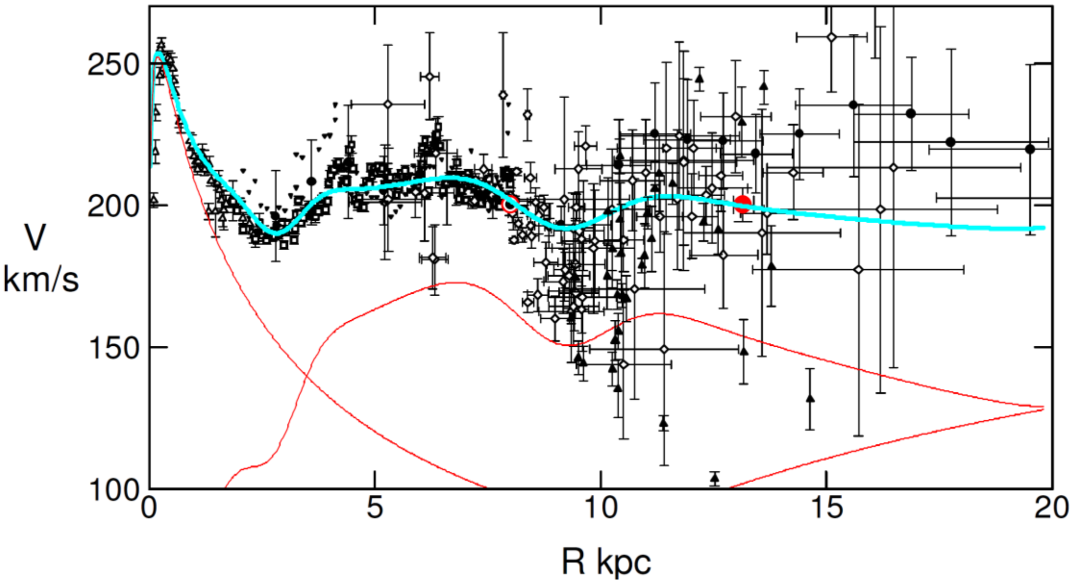

Figure 2 - Decomposition of the rotation curve of the Milky Way into the components bulge, stellar disk + interstellar gas, dark matter halo (the red curves from left to right) [6].

Mass autocorrelation functions

Some authors use abundance matching arguments to derive an accurate relation between galaxy stellar mass and dark matter halo mass. They combine a stellar mass function based on spectroscopic observations with a precise halo/subhalo mass function obtained from simulations. By comparing the galaxy autocorrelation function with the total mass autocorrelation function, as averaged over the Local Supercluster (LSC) volume, one concludes that a large amount of matter in the LSC is dark [36].

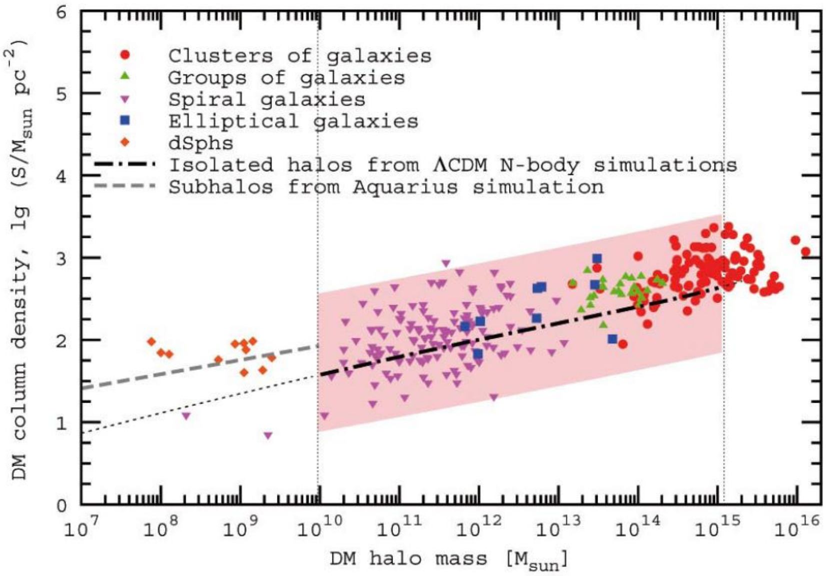

Figure 3 - DM column density vs. dark matter halo mass in solar units [7].

Boyarsky et al. [8] find a *universal relation between DM column density and DM halo mass*, satisfied by matter distributions at all observable scales, in halo sizes from 10^8 to 10^{16} solar masses, as shown in Fig. 3. Such a universal property is very difficult to explain without dark matter.

2.1.2 Velocity dispersions of dwarf spheroidal galaxies

In few words, peculiar velocity dispersion of small galaxies implies mass–to–light ratios larger than those observed in our "local" neighborhood. While the profiles of individual dwarfs show scatter, there is no doubt about the overall dark matter content. Important examples are the studies in [9, 10, 11], in which the authors analyze the stellar velocity dispersion profiles for seven Milky Way dwarf spheroidal (dSph) satellite galaxies. They have measured 8394 line-of-sight velocities (±2.5 km s^{-1}) for 6804 stars from high-resolution spectra obtained at the Magellan and MMT telescopes, combining these new data with previously published velocities to obtain the largest available kinematic samples, which include more than 5500 dSph members. All the measured dSphs have stellar velocity dispersion of order 10 km s^{-1}, which remains approximately constant with distance from the dSph center, out to and in some cases beyond the radius at which the mean surface brightness falls to the background level. Assuming dSphs reside within dark matter halos characterized by a NFW density profile (see formula 3.1), they obtain reasonable fits to the empirical velocity dispersion profiles.

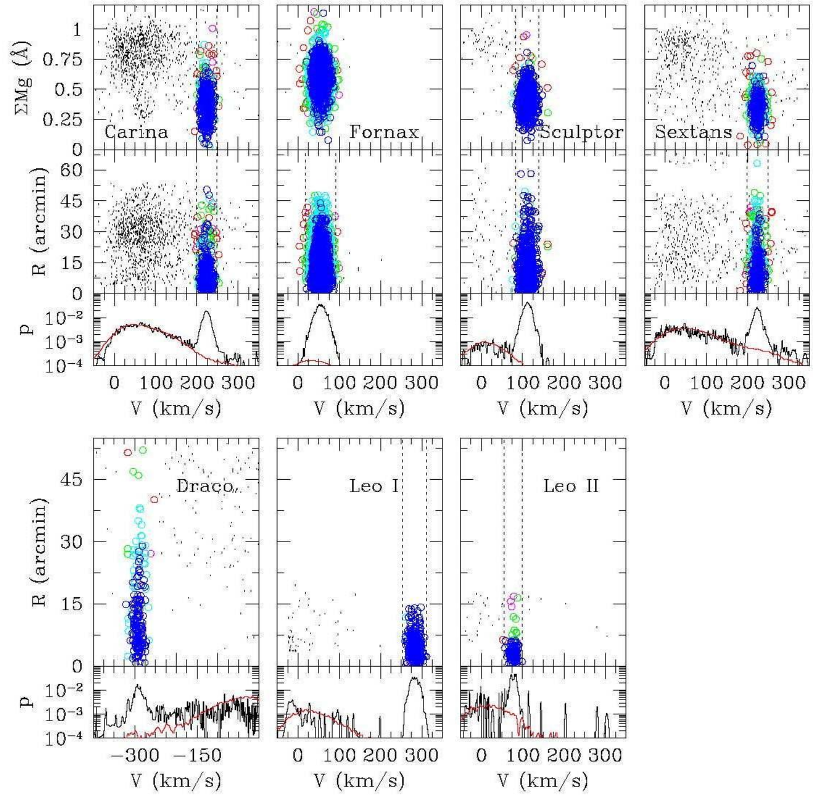

Figure 4 – Some dSph velocity dispersion relations [10].

2.1.3 Milky Way warp and dark galaxies

Milky Way like a long play record

Magellanic Cloud origin for the warp of the Milky Way can explain several quantitative features of the outer HI layer recently identified by Levine, Blitz, Chakrabarti et al. (2006-2011). They construct a model similar to that of Weinberg (1998), that produces distortions in the dark matter halo, and they calculate the combined effect of these dark-halo distortions and the direct tidal forcing by the Magellanic Clouds on the disk warp in the linear regime [12, 13, 14, 15]. The interactions of the dark matter halo with the disk, i. e. resonances between the orbit of the Clouds and the disk, account for the large amplitudes observed for the vertical m = 0, 1, 2 harmonics. The disk is shown to be very dynamic, constantly changing its shape as the Clouds proceed along their orbit.

But Magellanic Clouds don’t explain the entire problem. With the Sloan Digital Sky Survey a lot of low-brightness satellites galaxies have been discovered, but not enough to account the whole dynamical Milky Way warp: there should be tens of almost dark galaxies. This is not impossible because it’s already known that they might exist, from the great 2005-2008 observations of VIRGOHI-21. For example, there is evidence that in the Universe there are 10 to 100 times fewer small galaxies than permitted by what the dark matter theory of galaxy formation predicts. This is known as “the dwarf galaxy problem”. There were observed to be around 38 dwarf galaxies in the Local Group, and only around 11 orbiting the Milky Way, yet cosmological dark matter simulations predicted hundreds Milky Way dwarf satellites.

This problem has potential solutions: the smaller halos do exist but only a few of them end up becoming visible because they have not been able to attract enough baryonic matter to create a visible dwarf galaxy. In support of this, Keck observations in 2007 of eight newly discovered ultra-faint Milky Way dwarf satellites showed that six were around 99.9% dark matter (with a mass to light ratio of about 1000).

The strange case of VIRGOHI-21

Analysis of its internal motion indicates that it may contain a large amount of dark matter, as much as a small galaxy [16]. Since VIRGOHI21 apparently contains no stars, this would make it a dark galaxy. VIRGOHI21 was detected through radio telescope observations of its neutral hydrogen 21 cm emissions. The detected hydrogen has a mass of about 100 million solar masses and is about 50 million light-years away. By analyzing the Doppler shift of the emissions, astronomers determined that the gas has a high velocity-profile width; that is, different parts of the cloud are moving at high speed relative to other parts. Follow-up Hubble space telescope deep observations of the region have detected very few stars (a few hundred).

Accurate Swift XRT observations were performed on April 22 and April 26, 2008 for a total exposure time of 9.2 ks [17]. This is the first pointed X-ray observation of VIRGOHI 21 and no photons were detected from this source.

If the high velocity-profile width of VIRGOHI21 is interpreted as rotation, it is far too fast to be consistent with the gravity of the detected hydrogen. Rather, it implies the presence of a dark matter halo with tens of billions of solar masses. Given the very small number of stars detected, this implies a mass-to-light ratio of about 500, far greater than that of a normal galaxy. The large gravity of the dark matter halo in this interpretation explains the perturbed nature of the nearby spiral galaxy NGC 4254 and the bridge of neutral hydrogen extending between the two entities.

So VIRGOHI21 would be the first discovery of the dark galaxies anticipated by simulations of dark-matter theories. Although other dark-galaxy candidates have previously been observed, follow-up observations indicated that these were either very faint ordinary galaxies or tidal tails. VIRGOHI21 is considered the best current candidate for a dark galaxy.

2.1.4 Planck Galactic haze

In 2012, the full-sky observations from Planck permit to identify and characterize the emission from the Galactic “haze” at microwave wavelengths [12]. The haze is a distinct component of

diffuse Galactic emission, roughly centered on the Galactic Center, and extends to |b| ∼ 35◦ in Galactic latitude and |l| ∼ 15◦ in longitude. By combining the Planck data with observations from the Wilkinson Microwave Anisotropy Probe, they have been able to determine the spectrum of this emission to high accuracy. The derived spectrum is consistent with power-law emission with a spectral index of −2.55 ± 0.05, thus excluding free-free emission as the source and instead favoring hard-spectrum synchrotron radiation from an electron population with a spectrum (number density per energy) $dN/dE \propto E^{-2.1}$. At Galactic latitudes |b| < 30◦, the microwave haze morphology is consistent with that of the Fermi gamma-ray "haze" or "bubbles," indicating a multi-wavelength view of a distinct component of our Galaxy.
So, this newest data from the Planck mission reveals unusual radiation from our own Galaxy: a unique emission of radio radiation from the center of our Galaxy originated by leptons circulating at high energies around the lines of the magnetic field in the center of the Galaxy, and there are quite strong indications that it could come from dark matter. In fact, from theoretical predictions, the concentration of dark matter particles around the center of galaxies is very high, they can collide there and in the collision electrons and positrons are formed. These electrons and positrons start to rotate around the magnetic field at the Galactic center and, in doing so, produce this very unusual synchrotron radiation. Otherwise, they have discovered absolutely new (and unknown in physics) mechanism of acceleration of particles in the Galactic Center.

2.2 Cosmic evidences: Different Methods

With comic scale evidences virial systems formed by many galaxies are addressed, which may give us important information about DM abundance and properties, thanks to the collective dynamics of these cluster, catastrophic events and intracluster medium [177].

2.2.1 Dynamics of Galaxy Clusters

Virially bound systems
Stars move in galaxies and galaxies in clusters along their orbits; the orbital velocities are balanced by the total gravity of the system. In the simplest dynamical framework one treats clusters of galaxies as statistically steady, spherical, self-gravitating systems of N objects of average mass m and average orbital velocity v. The total kinetic energy E of such a system is then

$$E = \frac{1}{2} N m v^2 \ . \tag{2.4}$$

If the average separation is r, the potential energy of N(N − 1)/2 pairings is

$$U = -\frac{1}{2} N(N-1) \frac{Gm^2}{r} \ . \tag{2.5}$$

The virial theorem states that for such a system $E = -U/2$.
The total dynamic mass M can then be estimated from *v*, and *r* from the cluster volume

$$M = Nm = \frac{2rv^2}{G} \ . \tag{2.6}$$

This is only a classical first order approximation that must be enlarged.

The Coma cluster and the AC 114 cluster

Historically, the first possible indication of dark matter was found by Fritz Zwicky in 1933. While measuring radial velocities of member galaxies in the Coma cluster (that contains some 1000 galaxies), and the cluster radius from the volume they occupy, Zwicky was the first to use the virial theorem to infer the existence of unseen matter. He was able to infer the average mass of galaxies within the cluster, and obtained a value about 160 times greater than expected from their luminosity (a value revised today), and proposed that most of the missing matter was dark. His suggestion was not taken seriously at first by the astronomical community. Clearly, there was no candidate for the dark matter because gas radiating X-rays and dust radiating in the infrared could not yet be observed, and non-baryonic matter was unthinkable. Only some forty years later when studies of motions of stars within galaxies also implied the presence of a large halo of unseen matter extending beyond the visible stars, dark matter became a serious possibility.

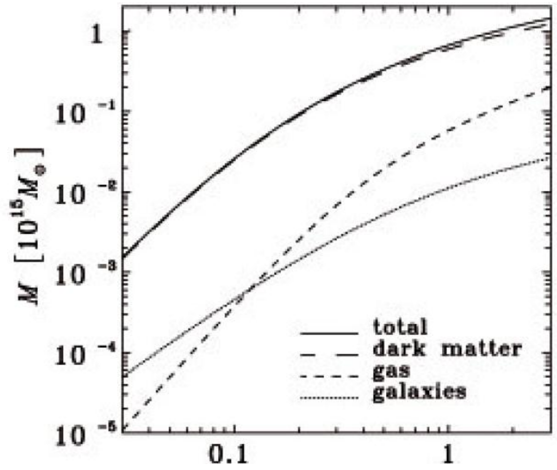

Figure 5 - Density profile of matter components enclosed within a given radius *r* in the Coma cluster versus r/r_{virial}, fitted with a centrally finite DM profile which is almost flat. In the outskirts of galaxy clusters the virial radius roughly separates bound galaxies from galaxies which may either be infalling or unbound. The virial radius r_{virial} is conventionally defined as the radius within which the mean density is 200 times the background density [19].

Luminous stars represent a very small fraction of a cluster mass; in addition there is a baryonic, hot intracluster medium (ICM) visible in the X-ray spectrum. Rich clusters typically have more mass in hot gas than in stars; in the largest virial systems like the Coma the composition is about 85% dark matter, 14% ICM, and only 1% stars (see Fig. 5).

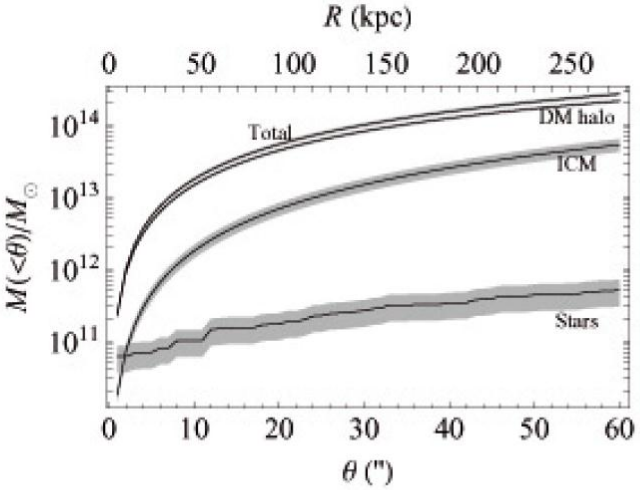

Figure 6 - Density profile of matter components in the cluster AC 114, enclosed within a given projected radius [20].

Dark matter is usually dissected from baryons in lensing analyses by first fitting the lensing features to obtain a map of the total matter distribution and then subtracting the gas mass fraction as inferred from X-ray observations [20]. The total mass map can then be obtained with parametric models in which the contribution from cluster-sized DM haloes can be considered together with the main galactic DM haloes. Mass in stars and stellar remnants is estimated converting galaxy luminosity to mass assuming suitable stellar mass to light ratios.
The results of such an analysis of the dynamically active cluster AC 114 is shown in Fig. 6.

The Local Group and the dark energy virial correction

The Local Group is a very small virial system, dominated by two large galaxies, the M31 or Andromeda galaxy, and the Milky Way. The M31 exhibits blueshift, falling in towards us.
Evidently, our Galaxy and M31, as well as all the minor galaxies in the Local Group, form a bound system which is oscillating.
In this virial system the two large galaxies dominate the dynamics, so that it is not meaningful to define, as for the Coma, an average pairwise separation between galaxies, an average mass or an average orbital velocity. The total kinetic energy E is still given by the sum over all the group members, and the potential energy U by the sum over all the galaxy pairs, but here the pair formed by the M31 and the Milky Way dominates, and the pairings of the small members with each other are negligible.
An interesting recent claim is, that the mass estimate of the Local Group is also affected by the accelerated expansion, the “dark energy”. It has been demonstrated [21] the potential energy U is reduced in the force field of dark energy, so that the virial theorem for N masses m_i with baryocentric radius vectors r_i takes the form

$$E = -\frac{1}{2}U + U_2 \ , \tag{2.7}$$

where U is defined as in Eq. (2.5), and

$$U_2 = -\frac{4\pi\rho_v}{3} \sum m_i \mathrm{r}_i^2 \tag{2.8}$$

is a correction which reduces the potential energy due to the background dark energy density ρ_v.
In the Local Group this correction to the mass appears to be quite substantial, of the order of 30% ÷ 50%. The dynamical mass of the local group comes out to be 3.2−3.7 10^{12} solar masses whereas the total visible mass of the Galaxy + M31 is only 2 10^{11} solar masses. Thus there is a large amount of dark matter.

Merging Galaxies

A fundamental direct empirical proof of the existence of dark matter is furnished by observations of *1E0657-558*, the *Bullet Cluster*, a unique cluster merger [22]. Due to the collision of two clusters, the dissipationless stellar component and the fluid-like X-ray emitting plasma are spatially segregated. The gravitational potential observed by weak and strong lensing (see section 2.2.4) does not trace the plasma distribution which is the dominant baryonic mass component, but rather approximately traces the distribution of galaxies (Fig. 7). The center of the total mass is offset from the center of the baryonic mass peaks, proving that the majority of the matter in the system is unseen. In front of the smaller “bullet” cluster which has traversed the larger one, a bow shock is evident in the X-rays.

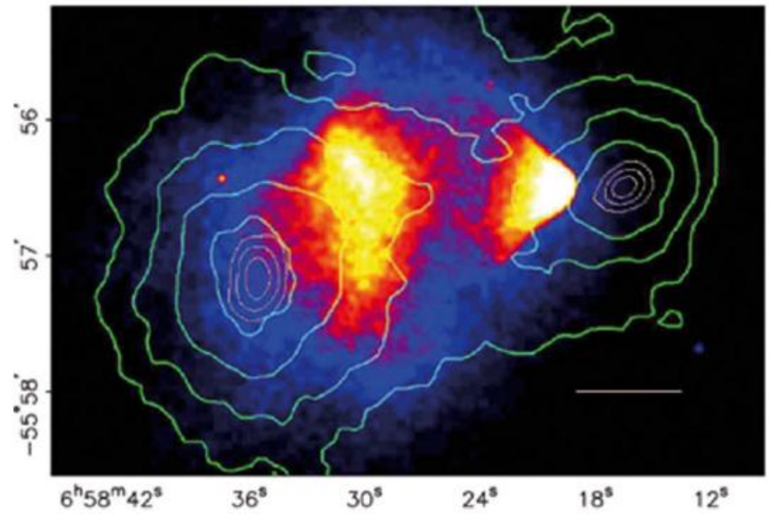

Figure 7 - The merging cluster 1E0657-558. On the right is the smaller “bullet” cluster which has traversed the larger cluster. The colors indicate the X-ray temperature of the plasma: blue is coolest and white is hottest. The green contours are the weak lensing reconstruction of the gravitational potential of the cluster [22].

In theories without dark matter, such as Modified Newtonian Dynamics (MOND), discussed in 2.4.1, the lensing would be expected to follow the baryonic matter, i.e. the X-ray gas. However, the lensing is strongest in two separated regions near (possibly coincident with) the visible galaxies. This provides support for the idea that most of the mass in the cluster pair is in the form of collisionless dark matter.

Other merging systems with similar characteristics have been seen, although with lower spatial resolution and less clear-cut cluster geometry. In Fig.8 the post-merging galaxy cluster *MACS J0025.4-1222* is shown, also called “the Baby Bullet”, at redshift z = 0.586.

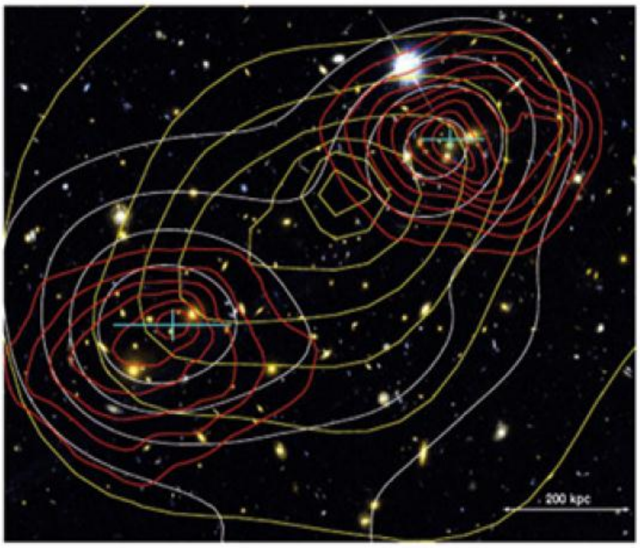

Figure 8 - The color composite of the cluster MACS J0025.4.1222. Overlaid in red contours is the surface mass density from the combined weak and strong lensing mass reconstruction. The X-ray brightness contours (also linearly spaced) are overlaid in yellow and the I-band light is overlaid in white. The measured peak position and error bars for the total mass are given as a cyan cross [23].

Other promising under study merging systems are *A1758*, *Abell 2146* and *2744* and “*El Gordo*”, the fat cluster of galaxies *ACT-CL J0102-4915*.

2.2.2 Velocity dispersions of spiral galaxy satellites

The velocity dispersions of spiral galaxy satellites suggest the existence of huge dark halos around spiral galaxies, similar to our own, extending at galactocentric radii ≳ 200 kpc, i.e. well behind the optical disc. This applies in particular to the Milky Way, where both dwarf galaxy satellites and globular clusters probe the outer rotation curve [3].

Dwarf galaxies represent the dominant population, by number, of the present-day Universe. The summed optical luminosity of all dwarfs may rival that of the giant, high-surface brightness galaxies. If low-luminosity galaxies are universally dominated by dark matter they could account for a large fraction of the mass of galaxy clusters, and perhaps of the entire Universe. The dwarf ultra−low surface brightness galaxies of the Local Group offer the best opportunity to study these “dark” dynamics [9, 35].

2.2.3 X-Ray Cluster Emission

The mass of a cluster can be determined via several methods, including application of the virial theorem to the observed distribution of radial velocities, by gravitational lensing, and by studying the profile of X–ray emission that traces the distribution of hot emitting gas in rich clusters [3, 7].

Consider the equation of hydrostatic equilibrium for a system with spherical symmetry

$$\frac{1}{\rho}\frac{dP}{dr} = -a(r) \tag{2.9}$$

where P, ρ, and *a(r)* are, respectively, the pressure, the density, and the gravitational acceleration of the gas, at radius r. For an ideal gas, this can be rewritten in terms of the temperature T and the average molecular weight, μ ≈ 0.6, in different ways:

$$\frac{GM(r)}{r^2} = -\frac{k_B T}{\mu m_p}\left[\frac{d\log\rho}{dr} + \frac{d\log T}{dr}\right] \tag{2.10}$$

or

$$\frac{d\log\rho}{d\log r} + \frac{d\log T}{d\log r} = -\frac{r}{T}\left(\frac{\mu m_p}{k}\right) a(r)\ , \tag{2.11}$$

where m_p is the proton mass. The temperature of clusters is roughly constant outside of their cores and the density profile of the observed gas at large radii roughly follows a power–law with an index between −2 and −1.5. Then the temperature should obey the relation

$$kT \approx (1.3 - 1.8)\mathrm{keV}\left(\frac{M_r}{10^{14}M_\odot}\right)\left(\frac{1\mathrm{Mpc}}{r}\right) \tag{2.12}$$

for the baryonic mass of a typical cluster, where M_r is the mass enclosed within the radius r. The disparity between the temperature obtained with the previous formula and the corresponding observed temperature, T ≈ 10 keV, when M_r is identified with the baryonic mass, suggests the existence of a substantial amount of dark matter in clusters.

The fraction of baryons inside a cluster, crucial to disentangle the contributions of ordinary (visible) and dark matter, can also be inferred through the so–called **Sunyaev-Zel’dovich effect** by which the cosmic microwave background gets spectrally distorted through Compton scattering on hot electrons [3].

2.2.4 Gravitational Lensing

Following Einstein's theory of General Relativity, light propagates along geodesics which deviate from straight lines when passing near intense gravitational fields. The distortion of the images of background objects due to the gravitational mass of a cluster can be used to infer the shape of the potential well and thus the mass of the cluster. There are three classes of gravitational lensing:

1. **Microlensing**: where no distortion in shape can be seen but the amount of light received from a background object changes in time. The lensing object may be stars in the Milky Way in one typical case, with the background source being stars in a remote galaxy, or, in another case, an even more distant quasar. The effect is small, such that even a galaxy with a mass more than 100 billion times that of the Sun will produce multiple images separated by only a few arcseconds. Galaxy clusters can produce separations of several arcminutes. In both cases the galaxies and sources are quite distant, many hundreds of megaparsecs away from our Galaxy.
2. **Weak lensing**: where the distortions are small and can only be detected by analyzing large numbers of sources to find coherent distortions of only a few percent. The lensing shows up statistically as a preferred stretching of the background objects perpendicular to the direction to the center of the lens. By measuring the shapes and orientations of large numbers of distant galaxies, their orientations can be averaged to measure the shear of the lensing field in any region. This, in turn, can be used to reconstruct the mass distribution in the area: in particular, the background distribution of dark matter can be reconstructed.

Background galaxies would be ideal tracers of distortions if they were intrinsically circular, because lensing transforms circular sources into ellipses. Any measured ellipticity would then directly reflect the action of the gravitational tidal field of the interposed lensing matter, and the statistical properties of the distortions would reflect the properties of the matter distribution. But many galaxies are actually intrinsically elliptical, and the ellipses are randomly oriented. This introduces noise into the inference of the tidal field from observed ellipticities. A useful feature in the sky is a fine-grained pattern of faint and distant blue galaxies appearing as a "wall paper". This makes statistical weak-lensing studies possible, because it allows the detection of the coherent distortions imprinted by gravitational lensing on the images of the galaxy population. Thus weak lensing has become an important technique to map non-luminous matter [24].

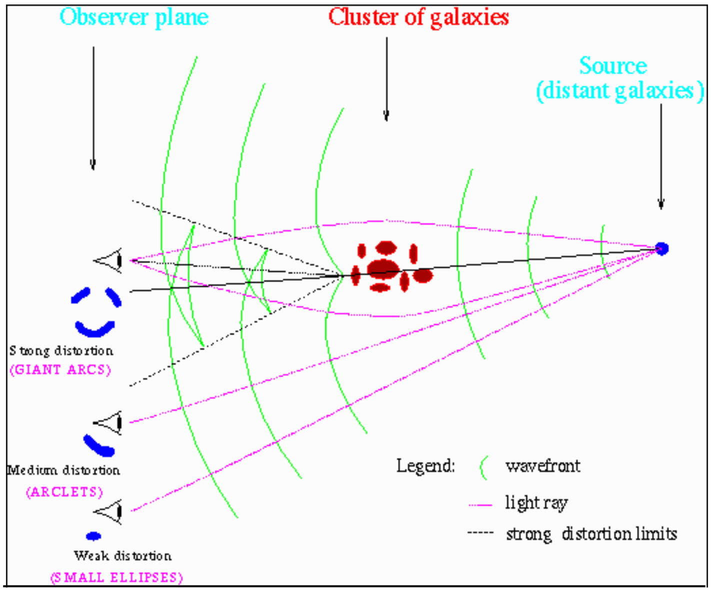

Figure 9 – Schematic wave fronts and light rays in the presence of a cluster perturbation: strong distortions, medium distortions, weak distortions.

A reconstruction of the largest and most detailed weak lensing survey ever undertaken with the Hubble Space Telescope is shown in Fig. 10. This map covers a large enough area to see extended filamentary structures.

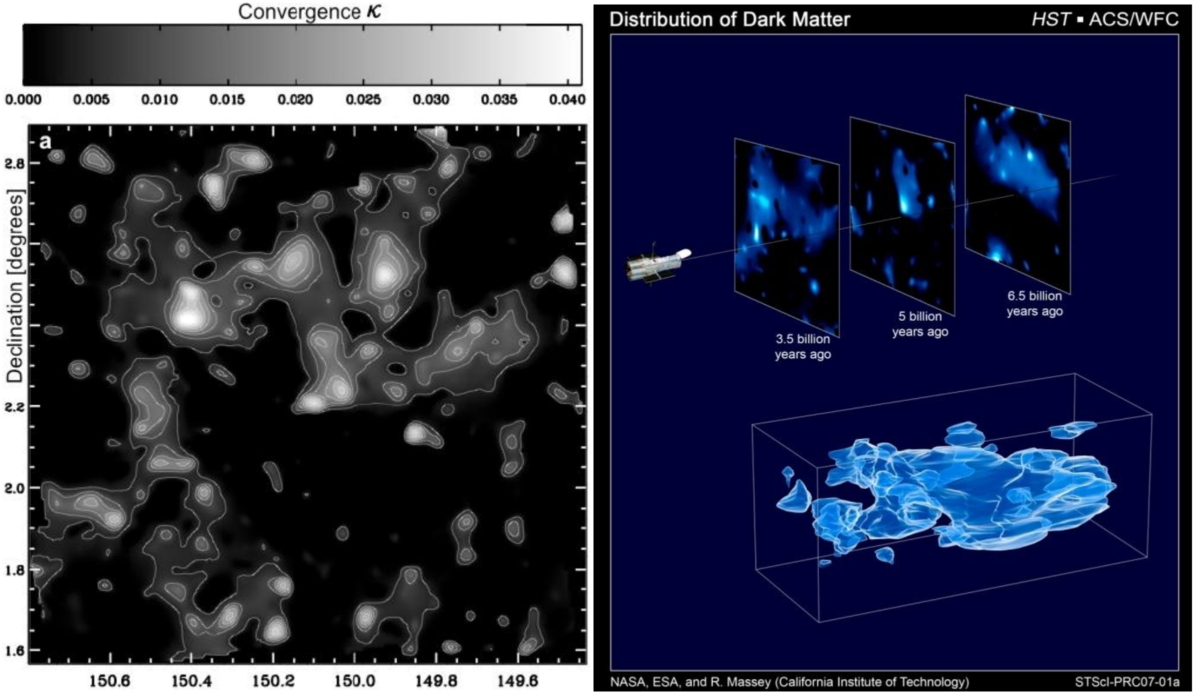

Figure 10 – a) Map of the dark matter distribution in the 2-square degree COSMOS (Cosmic Evolution Survey) field: the linear gray scale on top shows the gravitational lensing magnification κ, which is proportional to the projected mass along the line of sight [25]. Contours begin at 0.4% and are spaced by 0.5%; b) COSMOS 3D DM distribution from 3.5 to 6.5 billion years ago.

3**. Strong lensing**: where there are easily visible distortions such as the formation of Einstein rings, arcs, and multiple images. The angle of deflection is:

$$\theta = \frac{4GM}{rc^2} \qquad (2.13)$$

In Strong lensing the photons move along geodesics in a strong gravitational potential which distorts space as well as time, causing larger deflection angles and requiring the full theory of GR. The images in the observer plane can then become quite complicated because there may be more than one null geodesic connecting source and observer; it may not even be possible to find a unique mapping onto the source plane (Fig.9) .

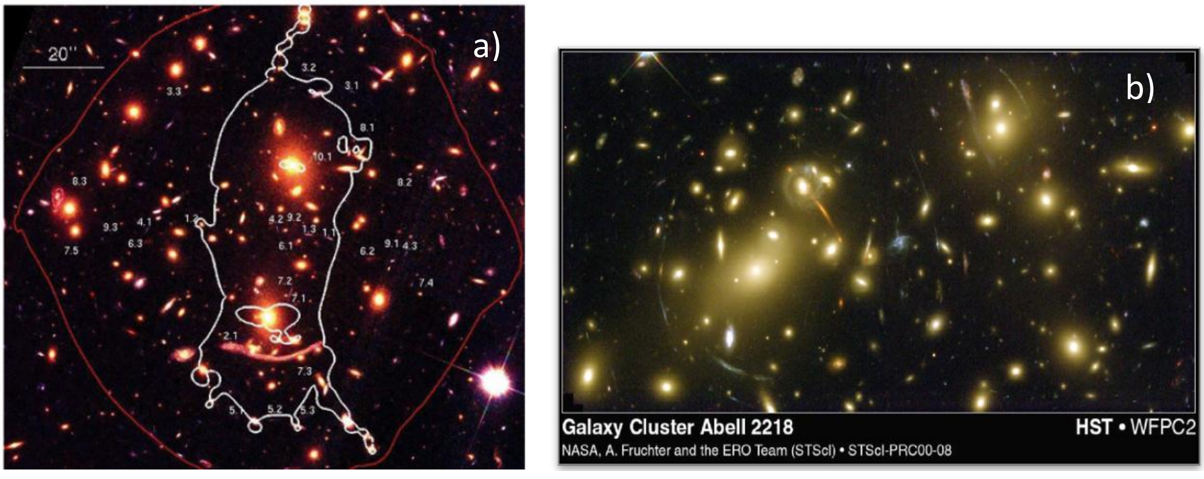

Figure 11 - a) Strong lensing analysis of the galaxy cluster *Abell 370* (z=0.375) shown with the locations of the identified multiple systems within the critical line at z=1.2 in white (the redshift for

the majority of the multiple images). The red line delimits the region of multiple images for very high redshift sources (here assuming z = 6) [26]; b) great optical view of the strong lensing in the *Abell 2218* galaxy cluster.

2.2.5 DM Skeleton between galaxies

A recent result puts in light the concordance between observations and cold-dark-matter cosmological model predictions: galaxy clusters occur at the intersection of large-scale structure filaments. The thread-like structure of this "cosmic web" has been traced by galaxy redshift surveys for decades. More recently, the warm–hot intergalactic medium (a sparse plasma with temperatures of 10^5 Kelvin to 10^7 Kelvin) residing in low-redshift filaments has been observed in emission and absorption.
In this study [27] it's reported the detection of a dark-matter filament connecting the two main components of the *Abell 222/223* supercluster system from its weak gravitational lensing signal, both in a non-parametric mass reconstruction and in parametric model fits (Fig. 12). This filament is coincident with an overdensity of galaxies and diffuse soft-X-ray emission, and contributes a mass comparable to that of an additional galaxy cluster to the total mass of the supercluster. By combining this result with X-ray observations, an upper limit of 0.09 on the hot gas fraction can be placed (the mass of X-ray-emitting gas divided by the total mass) in the filament.

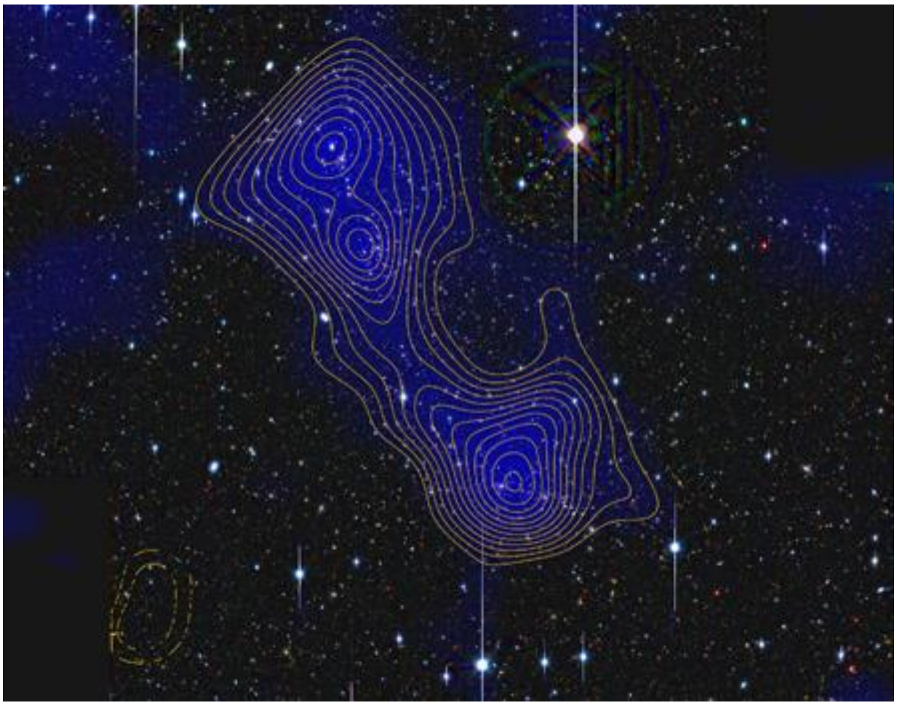

Figure 12 - Contour lines outline an invisible dark matter filament connecting the galaxy clusters Abell 222 (bottom) and Abell 223 (top) in the night sky. The cosmic thread revealed itself by distorting light coming from distant galaxies [27].

2.3 Cosmological hints

If dark matter is needed at an astrophysical level, it's also necessary to summon it to construct a "good" Big bang, to account for Universe densities and hierarchically assemble large scale objects, such as galaxies and galaxy clusters, from dust and radiation.

2.3.1 Einstein Cosmology

Standard Cosmology

Although the exact definition of the Standard cosmological model evolves with time, following the progress of experiments in measuring the cosmological parameters, most cosmologists agree on a fundamental picture, the so-called Big Bang scenario, which describes the Universe as a system evolving from a highly compressed state existing around 13,7 billion of years ago [3, 28, 29].

This is an extremely sophisticated model, allowing us to explain in a satisfactory way the thermal history, relic background radiation, abundance of elements, large scale structure and many other properties of the Universe. Nevertheless, it's clear that our understanding is still only partial.

To "build" a cosmological model, in a modern sense, three fundamental ingredients are needed:

- Einstein equations, relating the geometry of the Universe with its matter and energy content;
- metrics, describing the symmetries of the problem;
- Equation of state, specifying the physical properties of the matter and energy content.

The Einstein field equation can be derived almost from first principles, assuming that: 1) the equation is invariant under general coordinate transformations, 2) the equation tends to Newton's law in the limit of weak fields, and 3) the equation is of second differential order and linear in second derivatives:

$$R_{\mu\nu} - \frac{1}{2} g_{\mu\nu} R = -\frac{8\pi G_N}{c^4} T_{\mu\nu} + \Lambda g_{\mu\nu}, \qquad (2.14)$$

where $R_{\mu\nu}$ and R are, respectively, the Ricci tensor and scalar obtained by contraction of the Riemann curvature tensor. $g_{\mu\nu}$ is the metric tensor, G_N is Newton's constant, $T_{\mu\nu}$ is the energy-momentum tensor, and Λ is the so–called cosmological constant.

Ignoring for a moment the term involving the cosmological constant, the equation is easily understood: the geometry of the Universe, described by the terms on the left-hand-side, is determined by its energy content, described by the energy-momentum tensor on the right-hand-side. This is the well-known relationship between the matter content and geometry of the Universe, which is the key concept of General Relativity.

The addition of the cosmological constant term, initially introduced by Einstein to obtain a stationary solution for the Universe and subsequently abandoned when the expansion of the Universe was discovered, represents a "vacuum energy" associated with space-time itself, rather than its matter content, and is a source of gravitational field even in the absence of matter. The contribution of such "vacuum energy" to the total energy of the Universe can be important, if one believes recent analyses of type *Ia* supernovae and parameter estimates from the cosmic microwave background.

To solve the Einstein equations one has to specify the symmetries of the problem. Usually one assumes the properties of statistical homogeneity and isotropy of the Universe, which greatly simplifies the mathematical analysis. Such properties, made for mathematical convenience, are confirmed by many observations. In particular, observations of the Cosmic Microwave Background (CMB) have shown remarkable isotropy (once the dipole component, interpreted as due to the Earth motion with respect to the CMB frame, and the contribution from the galactic plane were subtracted). Isotropy alone, if combined with the Copernican principle, or "mediocrity" principle, would imply homogeneity. Nevertheless, direct evidence of homogeneity comes from galaxy surveys, suggesting a homogeneous distribution at scales in excess of ~ 100 Mpc. More specifically, spheres with diameters larger than ~ 100 Mpc centered in any place of the Universe should contain, roughly, the same amount of matter.

The properties of isotropy and homogeneity imply a specific form of the metric: the line element can in fact be expressed as

$$ds^2 = -c^2\mathrm{d}t^2 + a(t)^2\left(\frac{\mathrm{d}r^2}{1-kr^2} + r^2\mathrm{d}\Omega^2\right), \tag{2.15}$$

where a(t) is the so-called scale factor and the constant k, describing the spatial curvature, can take the values k = −1, 0, +1. For the simplest case, k = 0, the spatial part of the equation reduces to the metric of ordinary (flat) Euclidean space.

The Einstein equations can be solved with this metric, one of its components leading to the Friedmann equation

$$\left(\frac{\dot{a}}{a}\right)^2 + \frac{k}{a^2} = \frac{8\pi G_N}{3}\rho_{tot}, \tag{2.16}$$

where ρ_{tot} is the total average energy density of the universe. It is common to introduce the Hubble parameter

$$H(t) = \frac{\dot{a}(t)}{a(t)} \quad . \tag{2.17}$$

A recent estimate of the present value of the Hubble parameter, H_0 (also referred to as the Hubble constant) is $H_0 = 74.3 \pm 2.1$ km s^{-1} Mpc^{-1} (Freedman et al., 2012). We see from equation (2.16) that the universe is flat (k = 0) when the energy density equals the critical density, ρ_c:

$$\rho_c \equiv \frac{3H^2}{8\pi G_N} \quad . \tag{2.18}$$

In what follows, the abundance of a substance in the Universe (matter, radiation or vacuum energy) will be expressed in units of ρ_c. The quantity Ω_i of a substance of species *i* and density ρ_i is defined as

$$\Omega_i \equiv \frac{\rho_i}{\rho_c} \quad . \tag{2.19}$$

It is also customary to define

$$\Omega = \sum_i \Omega_i \equiv \sum_i \frac{\rho_i}{\rho_c}, \tag{2.20}$$

in terms of which the Friedmann equation (2.16) can be written

$$\Omega - 1 = \frac{k}{H^2a^2} \quad . \tag{2.21}$$

The sign of *k* is therefore determined by whether is greater than, equal to, or less than one (see Table 1). The various *i* evolve with time differently, depending on the equation of state of the component. A general expression for the expansion rate is

$$\frac{H^2(z)}{H_0^2} = \Big[\Omega_X (1+z)^{3(1+\alpha_X)} + \Omega_K (1+z)^2 \\ + \Omega_M (1+z)^3 + \Omega_R (1+z)^4\Big] \tag{2.22}$$

where *M* and *R* are labels for matter and radiation, $\Omega_K = \frac{-k}{a_0^2 H_0^2}$ and *X* refers to a generic substance with equation of state $p_X = \alpha_X \rho_X$ (in particular, for the cosmological constant, $\alpha_X = -1$); *z* is the redshift. These are the basis for the standard cosmology ΛCDM (Lamba-Cold Dark Matter) model.

$\rho < \rho_c$	$\Omega < 1$	$k = -1$	open
$\rho = \rho_c$	$\Omega = 1$	$k = 0$	flat
$\rho > \rho_c$	$\Omega > 1$	$k = 1$	closed

Table 1 - Classification of cosmological models based on the value of the average density, ρ, in terms of the critical density, ρ_c.

2.3.2 Particle Cosmological Production

In a hot Universe which is filled with particles interacting with each other, these all are in thermal equilibrium at some epoch. However, as Universe cools and expands some of these may go out of thermal equilibrium and eventually decouple. The equilibrium criterion is that the mean free path $l_{m.f.p.}$ is smaller than the distance these particles travel since the beginning, i.e.

$$l_{m.f.p.} < v\, t\ . \tag{2.23}$$

If this holds, then particles will interact with the cosmic soup and there is no way of escaping. The mean free path is defined by $l_{m.f.p.} \equiv 1/(n\sigma)$, where σ is the interaction cross section of the particles under consideration and *n* their density. Since the expansion rate is inversely proportional to time $H \sim 1/t$, the equilibrium criterion can be expressed as

$$\varGamma > H, \quad (\,\varGamma \equiv \frac{1}{v\, n\, \sigma}\,)\ . \tag{2.24}$$

If $\varGamma > H$ at some epoch and $\varGamma < H$ at later times, then there is a temperature T_D for which $\varGamma = H$. T_D is called the decoupling or freeze-out temperature. For $T \leq T_D$ these particles do not interact any longer with the cosmic soup and they expand freely. Their total number, after decoupling, remains constant and thus their density decreases with the cube of the cosmic scale factor $n \sim 1/a^3$.

A notable example of this situation are neutrinos. They decoupled when the Universe was as hot as ten million Kelvin degrees and their relics today account for a small fraction of the total energy of the Universe. Neutrinos interact only weakly and they are nearly massless. For temperatures below the muon mass, that is $kT < m_\mu$, the active degrees of freedom in the hot Universe are the photons, the neutrinos and their antiparticles, the electrons and the positrons. For $T \leq T_D$ the neutrinos and their antiparticles decouple and they do not interact any longer with electrons and positrons. They can be conceived, as being in an isolated bath at temperature T_v which equals to the photons temperature at the moment of decoupling. Since they do not interact any longer with the rest of the particles, their total number is locked.

In the same way, various models of particle physics predict the existence of Weakly Interacting Massive Particles that have decoupled long ago and their densities at the present epoch may account for the “missing mass” or Dark Matter of the Universe. The relic abundance of a dark matter particle can be calculated using the transport Boltzmann equation.

Calculating DM Relic Abundances: The Boltzmann Transport Equation

The number density of a decoupled particle can be calculated by use of the Boltzmann transport equation. Let us assume for definiteness that the DM particle under consideration is the neutralino $\tilde{\chi}$, the LSP (Lightest Supersymmetric Particle), although the discussion can be generalized to other sort of self-annihilating particles as well. In order to know its relic abundance and compare it with the current data its density today should be computed assuming that at some epoch $\tilde{\chi}$ s were in thermal equilibrium with the cosmic soup. Their density decreases because of annihilation only since they are the LSP s and hence stable. If the $\tilde{\chi}$ density at a time *t* is *n*(*t*) then it satisfies the following equation known as *Boltzmann transport equation* [29, 49]

$$\frac{dn}{dt} = -3\,\frac{\dot{a}}{a}\,n - \langle v\,\sigma\rangle\,(\,n^2 - n_{eq}^2\,)\,. \tag{2.25}$$

where σ is the cross section of the annihilated $\tilde{\chi}$ s, and *v* is their relative velocity. The thermal average $\langle v\sigma\rangle$ is defined in the usual manner as any other thermodynamic quantity.

The first term on the r.h.s. of (2.25) is easy to understand. It expresses the fact that the density changes because of the expansion. Momentarily ignoring the interactions of the $\tilde{\chi}$ s with the rest of the particles, their total number remains constant. Therefore $n\,a^3$ = const, from which it follows, by taking the derivative with respect the time, that the density rate is given by the first term on the r.h.s. of (2.25). However the $\tilde{\chi}$ s do interact and their number decreases because of pair annihilation. In fact LSP's are stable Majorana particles and it is possible to be annihilated by pairs to Standard Model particles. Their number is therefore reduced until the freezing-out temperature below which they do not interact any further with the remaining particles and their total number is locked.

Therefore, their density decreases as $dn/dt = -n\Gamma_{ann}$, where the annihilation rate Γ_{ann} is given by $\Gamma_{ann} = v\,\sigma\,n$. This explains the second term on the r.h.s. of (2.28). However the $\tilde{\chi}$ s do not only annihilate but are also produced through the inverse process. The last term expresses exactly this fact. Note that when $\tilde{\chi}$ s were in thermal equilibrium with the rest of the particles and the environment was hot enough, the annihilated products had enough energy to produce back the $\tilde{\chi}$ s at equal rates. During this period $n = n_{eq}$ and the last two terms cancel each other, as they should. Thus the picture is the following: the $\tilde{\chi}$ s are in thermal and chemical equilibrium at early times. During this period $\Gamma >> H$ and $n = n_{eq} \propto T^3$.

However, as the temperature drops and eventually passes $k\,T \sim m_{\tilde{\chi}}$ the $\tilde{\chi}$ s annihilate but their products do not have enough thermal energy to produce back the annihilated $\tilde{\chi}$ s. The $\tilde{\chi}$ s are in thermal but not in chemical equilibrium any more. In addition, their density drops exponentially exp $(-\,m_{\tilde{\chi}}/kT\,)$ following the Boltzmann distribution law and $\Gamma \equiv nv\sigma$ decreases, so that eventually at a temperature T_f , the freeze-out temperature, Γ equals to the expansion rate *H*. Below this temperature, $\Gamma < H$ and the $\tilde{\chi}$ s are out of thermal equilibrium. They decouple not interacting any longer with the cosmic soup and they expand freely. Their total number is locked to a constant value and their density changes because of the expansion. Actually for $T < T_{\tilde{\chi}}$ their density is much larger than the equilibrium density $n >> n_{eq}$ and since $\Gamma >> H$, the first term dominates, so that $n{\cdot}a^3$ is indeed a constant.

Concerning the cross section thermal average, in general for two annihilating particles 1, 2, under the assumption that they obey Boltzmann statistics, which is valid for $T \le m_{1,2}$, one find [29]

$$\langle v\sigma_{12}\rangle = \frac{\int_{(m_1+m_2)^2}^{\infty} ds\, K_1(\sqrt{s}/T)\, p_{cm}\, W(s)}{2\, m_1^2\, m_2^2\, T\, K_2(m_1/T)\, K_2(m_2/T)} \tag{2.26}$$

where p_{cm} is the magnitude of the momentum of each incoming particle in their CM frame and $K_{1,2}$ are Bessel functions. The quantity $W(s)$ within the integral is related to the total cross section $\sigma(s)$ through $\sigma = 4p_{cm}\sqrt{s}W(s)/\lambda(s, m_1^2, m_2^2)$. The initial condition in solving Boltzmann's equation should lie in this regime and at a point above the decoupling temperature. This is perfectly legitimate for the case of neutralinos since their decoupling temperature is well below $m_{\tilde{\chi}}$, around $T_f \sim m_{\tilde{\chi}}/20$. This is another paradigm for neutralino-like dark matter obtained via thermal production. It can be noted that, if the neutralino-like particle is heavy enough, for example $m_{\tilde{\chi}} \gtrsim 2\, TeV$, this temperature could be compared to the weak scale (see chapter 3.3.2).

This expression can be considerably simplified if one follows a non-relativistic treatment, expanding the cross section in powers of their relative velocity v,

$$v\,\sigma \;=\; a \;+\; \frac{b}{6}\,v^2 \;. \tag{2.27}$$

With this approximation the LSP s annihilation thermal average is

$$\langle v\,\sigma\rangle \;=\; a \;+\; (b - \frac{3}{2}\,a)\,\frac{kT}{m_{\tilde{\chi}}} \;. \tag{2.28}$$

The goal is to solve (2.25), in order to know the density at today's temperature $T_0 \simeq 2.7\ K$, provided that $n = n_{eq}$ long before decoupling time. By defining the yield $Y \equiv n/s$, where s is the entropy density, and using a new variable $x = T/m_{\tilde{\chi}}$, one arrives at a simpler looking equation, i. e. a Boltzmann equation in the yield

$$\frac{dY}{dx} \;=\; m_{\tilde{\chi}}\,\langle v\,\sigma\rangle \left(\frac{45 G_N}{\pi}\;g\right)^{-1/2} (\;h + \frac{x}{3}\,\frac{dh}{dx}\;)\,(\;Y^2 \;-\; Y_{eq}^2\;) \tag{2.29}$$

The function h that appears in this equation counts the effective entropy degrees of freedom related to the entropy density through $s = \frac{2\pi^2}{45}h(T)(k_B T)^3$. Another compact form is

$$s\dot{Y} = -\langle\sigma v\rangle s^2 \left(Y^2 - Y^{eq2}\right) \tag{2.30}$$

The prefactor of $Y^2 - Y_{eq}^2$ is usually a large number, due to the appearance of the gravitational constant $G_N^{-1/2}$ in (2.29), and this can be exploited in using numerical approximations reminiscent of the WKB in quantum mechanics [29]. One can solve this to find Y today, which is very close to $Y_0 = Y(0)$, and from this the matter density of dark matter candidate. The latter is

$$\varrho_{\tilde{\chi}} \;=\; n_{\tilde{\chi}}\,m_{\tilde{\chi}} \;=\; m_{\tilde{\chi}}\;s_0 Y_0 \;=\; \frac{2\pi^2}{45}\;m_{\tilde{\chi}}\;h_{eff}^0\;Y_0\;T_\gamma^3 \tag{2.31}$$

where $s_0 = 2889.2\ cm^{-3}$ is the present entropy density and h_{eff}^0 is today's value for the effective entropy degrees of freedom, which is $h_{eff}^0 \simeq 3.919$. The relic density is then

$$\Omega_{\tilde{\chi}}\,h_0{}^2 \;=\; h_0{}^2\,\frac{\varrho_{\tilde{\chi}}}{\varrho_c} \;=\; 0.6827 \times 10^8\;\frac{m_{\tilde{\chi}}}{GeV}\;h_{eff}^0 Y_0 \left(\frac{T_\gamma}{T_0}\right)^3 \;. \tag{2.32}$$

In writing (2.32) the relation $\rho_c = 8.1 \times 10^{-47}\, h_0^2\, GeV^4$ is used. We have also expressed the dependence on temperature through the ratio T_γ/T_0 by using a reference temperature $T_0 = 2.7\ K$. The CMB temperature has been determined by measurements of the CMB to be $T_\gamma = 2.752 \pm 0.001\ K$.

As said, the required value of Y_0 can be found by solving (2.30) numerically, with the boundary condition that $Y \rightarrow Y_{eq}$ at temperatures well above the freezeout temperature. There are good packages in the literature, like DarkSUSY and microOMEGAs [29, 30], which can be used to handle numerically the Boltzmann equation and find the DM relic density.

From these computations is also possible to put an upper bound to the dark matter mass, as a function of the relic density and of the freezing function $x_f = T_f/m_{\tilde{\chi}}$, through the relation $m_{\tilde{\chi}} \leq \sqrt{\Omega_{\tilde{\chi}} h^2/\left(1.7 \cdot 10^{-6}\sqrt{x_f}\right)}$, for a Majorana fermion or a boson [4]. With today WMAP constraints on $\Omega_{\tilde{\chi}} h^2$ and assuming $x_f \sim 20$, the bound becomes $m_{\tilde{\chi}} \leq 120\, TeV$.

Approximate Solutions to Boltzmann Equation

Approximate solutions can be found under the assumption that $Y \ll Y_{eq}$ below the freezing point $x_f = T_f/m_{\tilde{\chi}}$ while $Y \simeq Y_{eq}$ above it. Omitting then the Y_{eq} term in (2.29), which is valid for x between x_f and $x_0 \simeq 0$, and putting $x=x_f$ in (2.29) an equation for x_f is derived

$$x_f^{-1} = \ln \left[\, 0.03824\, g_s \frac{M_{Planck}\, m_{\tilde{\chi}}}{\sqrt{g^*}} \langle v\, \sigma \rangle \; c(c+2)\, x_f^{1/2} \,\right] , \tag{2.33}$$

which can be solved numerically to obtain x_f. In this, $g*$ stands for the effective energy degrees of freedom at the freeze-out temperature $g* = g(x_f)$, and the derivative term dh/dx in (2.29) has been ignored in this approximation; g_s are the spin degrees of freedom and $c(c+2)$ is approximately equal to one: it is empirically found that very good approximation for the freeze-out point temperature is obtained with values $c \simeq 1/2$. As already said, the freeze out temperature for a WIMP is close to $T_f \sim m_{\tilde{\chi}}/20$. Now that x_f has been determined one can integrate (2.29) from x_f to zero, under the same assumptions, to obtain $Y(0)$ and from this the relic abundance. The solution for $Y(0)$ entails to a density

$$\varrho_{\tilde{\chi}} = \left(\frac{4\pi^3}{45} \right)^{1/2} \left(\frac{T_{\tilde{\chi}}}{T_\gamma} \right)^3 \frac{T_\gamma^3}{M_{Planck}} \frac{\sqrt{g^*}}{J} \, . \tag{2.34}$$

The quantity J is given by the integral of the thermal cross section $J \equiv \int_0^{x_f} \langle v\sigma \rangle dx$. In this expression the neutralino's temperature appears explicitly, that is different from that of photons. In fact, it is found [29] that, due to the decoupling of both neutralinos and neutrinos, $\left(T_{\tilde{\chi}}/T_\gamma\right)^3 = 4/11 \cdot g(T_\nu)/g(T_f) = 3.91/g(T_f)$, with T_ν the neutrino decoupling temperature and T_f that of $\tilde{\chi}$s. Using this and (2.33), for the dark matter relic density $\Omega_{\tilde{\chi}} = \rho_{\tilde{\chi}}/\rho_c$ the following result is obtained

$$\Omega_{\tilde{\chi}}\, {h_0}^2 = \frac{1.066 \times 10^9\; GeV^{-1}}{M_{Planck}\, \sqrt{g^*}\; J} \, , \tag{2.35}$$

which is the expression quoted in many articles. The quantity J, which has already been defined, is given in GeV^{-2} units. Note that the relic density is roughly inverse proportional to the total cross section. This means that the larger the cross section the smaller the relic density is and vice versa.

To have an estimate of the predicted relic density for the case of a neutralino LSP the approximations $J \approx x_f \langle \sigma v \rangle_f$ and $\langle \sigma v \rangle \sim \alpha/m_{\tilde{\chi}}^2$ are used, where α is a typical electroweak coupling. Since x_f is of the order of ~ 0.1 and $g*$ is $\simeq 100$ for WIMP masses in the range 20 GeV – 1 TeV , the relic density (2.35) turns out to be the same in formula (2.1):

$$\Omega_{\rm WIMP} \approx \frac{0.1}{h^2} \left(\frac{3 \times 10^{-26}\, {\rm cm}^3\, {\rm s}^{-1}}{\langle \sigma v \rangle} \right) \tag{2.36}$$

That means dark matter density parameter for thermal production of the order of 0.2. Therefore it follows that relic densities of the right order of magnitude can naturally arise in supersymmetric theories if one interprets the Dark Matter as due to a stable neutralino.

Co-annihilations

All discussion so far concerned cases in which the stable WIMP is not degenerate in mass with other heavier species with m_i that can decay to it. Therefore there is an epoch where the Universe is filled by SM particles and the LSPs, whose density decreases because of pair annihilations when the temperature starts passing the point where SM particles do not have enough energy to produce back LSPs. However it may happen: in fact, when $\delta m_i \equiv m_i - m_{\tilde{\chi}} \sim T_f$ these particles are thermally accessible and this implies that they are as abundant as the relic species. This drastically affects the calculation of the LSP relic density. Actually, in the most popular supersymmetric schemes and many other DM models (Little Higgs, Scalar Multiplet, KK theory, Minimal DM), advocating the existence of good CDM candidates, there are regions having this characteristic so it is worth discussing this case.

Since all nearly degenerate particles with the LSP will eventually decay to it, the relevant quantity to calculate for the relic abundance of the LSP is the density $n = \sum_i n_i$. n_i is the density of the particle *i* and the sum runs from *i* = 1, ...*N*. With *i* = 1 the LSP is labeled, and with *i* = 2, ...*N* the rest of the particles that are almost degenerate in mass with it. The Boltzmann transport equation is generalized to

$$\frac{dn}{dt} = -3\,\frac{\dot{a}}{a}\,n - \sum_{i,j}^{N} \langle v_{ij}\,\sigma_{ij} \rangle \,\left(n_i n_j - n_i^{eq} n_j^{eq} \right) . \tag{2.37}$$

Since the criterion for which particles coannihilate with the LSP is roughly given by $\delta m \sim T_f$ and $T_f \sim m_{\tilde{\chi}}/20$, the particles participating in the co-annihilation process are those for which the mass differences are $\delta m_i \simeq 5\%\, m_{\tilde{\chi}}$. Their equilibrium densities are given by $n_i^{eq} = g_i \frac{T}{2\pi} m_i^2 K_2(m_i/T)$, where g_i denotes the spin degrees of freedom. Approximating $n_i/n \simeq n_i^{eq}/n^{eq}$, (2.37) can be cast in the following form

$$\frac{dn}{dt} = -3\,\frac{\dot{a}}{a}\,n - \sum_{i,j}^{N} \langle v\,\sigma_{eff} \rangle \,\left(n^2 - n_{eq}^2 \right) \tag{2.38}$$

where the effective thermal average appearing in this equation is a generalization given by

$$\langle v\sigma_{eff} \rangle = \sum_{i}^{N} \frac{n_i^{eq}\, n_j^{eq}}{n_{eq}^2} \,\langle v_{ij}\sigma_{ij} \rangle \tag{2.39}$$

This can be written as a single integral generalizing the previous result

$$\langle v\sigma_{eff} \rangle = \frac{\int_2^{\infty} da\; K_1(a/x) \sum_{i,j} \lambda(a^2, b_i^2, b_j^2)\; g_i g_j\; \sigma_{ij}(a)}{4x\,\left(\sum_i g_i b_i^2 K_2(b_i/x) \right)^2} , \tag{2.40}$$

where $b_i \equiv m_i/m_{\tilde{\chi}}$. Seeking for an approximate solution, as was done in the no co-annihilation case, then the freeze-out point is

$$x_f^{-1} = \ln \left[\, 0.03824\, g_{eff}\, \frac{M_{Planck}\; m_{\tilde{\chi}}}{\sqrt{g^*}} \;\langle v\,\sigma_{eff} \rangle\; c(c+2)\; x_f^{1/2} \,\right] \tag{2.41}$$

In this g_{eff} is defined as

$$g_{eff} \equiv \sum_i g_i \left(1 + \Delta_i \right)^{3/2} \exp\left(-\Delta_i / x_f\right) \tag{2.42}$$

where $\Delta_i \equiv (m_i - m_{\tilde{\chi}})/ m_{\tilde{\chi}}$. As for the relic abundance, the solution is given by (2.34) with the quantity J defined now as $J \equiv \int_0^{x_f} \langle v\sigma_{eff} \rangle dx$. In calculating this, the fact that all nearly degenerate particles with the LSP will eventually decay has been used. In supersymmetric models the relevant co-annihilation channels are between neutralinos, charginos and sfermions.

It must be mentioned that, for example, the cosmological bound on the LSP neutralino mass is immediately pushed to 600 *GeV* from about 200 *GeV* in the stau co-annihilation region, and to 1.5 *TeV* in the chargino co-annihilation, increasing upper bounds and weakening the prospects of discovering supersymmetry in high energy accelerators [29, 31].

2.3.3 CMB Acoustic Peaks

The observations discussed do not allow us to determine the total amount of dark matter in the Universe. This information can be extracted from the analysis of the Cosmic Microwave Background. The existence of background radiation originating from the propagation of photons in the Early Universe (once they decoupled from matter) was predicted by George Gamow and his collaborators in 1948 and inadvertently discovered by Arno Penzias and Robert Wilson in 1965. After many decades of experimental effort, the CMB is known to be isotropic at the 10^{-5} level and to follow with extraordinary precision the spectrum of a black body corresponding to a temperature T = 2.726 K (Fig. 13).

The observed temperature anisotropies in the sky are usually expanded as [3, 7, 28, 47]

$$\frac{\delta T}{T}(\theta, \phi) = \sum_{\ell=2}^{+\infty} \sum_{m=-\ell}^{+\ell} a_{\ell m} Y_{\ell m}(\theta, \phi) \tag{2.43}$$

where $Y_{\ell m}(\theta, \phi)$ are spherical harmonics. The variance C_ℓ of $a_{\ell m}$ is given by

$$C_\ell \equiv < |a_{\ell m}|^2 > \equiv \frac{1}{2\ell + 1} \sum_{m=-\ell}^{\ell} |a_{\ell m}|^2. \tag{2.44}$$

If the temperature fluctuations are assumed to be Gaussian, as appears to be the case, all of the information contained in CMB maps can be compressed into the power spectrum, essentially giving the behavior of C_ℓ as a function of ℓ. Usually plotted is $\ell(\ell + 1)C_\ell/2\pi$ versus ℓ (see Figs. 14).

The methodology for extracting information from CMB anisotropy maps is simple, at least in principle. Starting from a cosmological model with a fixed number of parameters (usually 6 or 7), the best-fit parameters are determined from the peak of an N-dimensional likelihood surface.

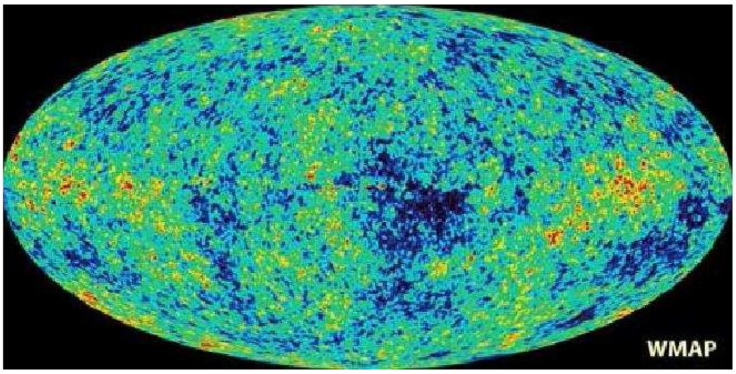

Figure 13 - CMB temperature fluctuations from WMAP. Image from http://map.gsfc.nasa.gov/.

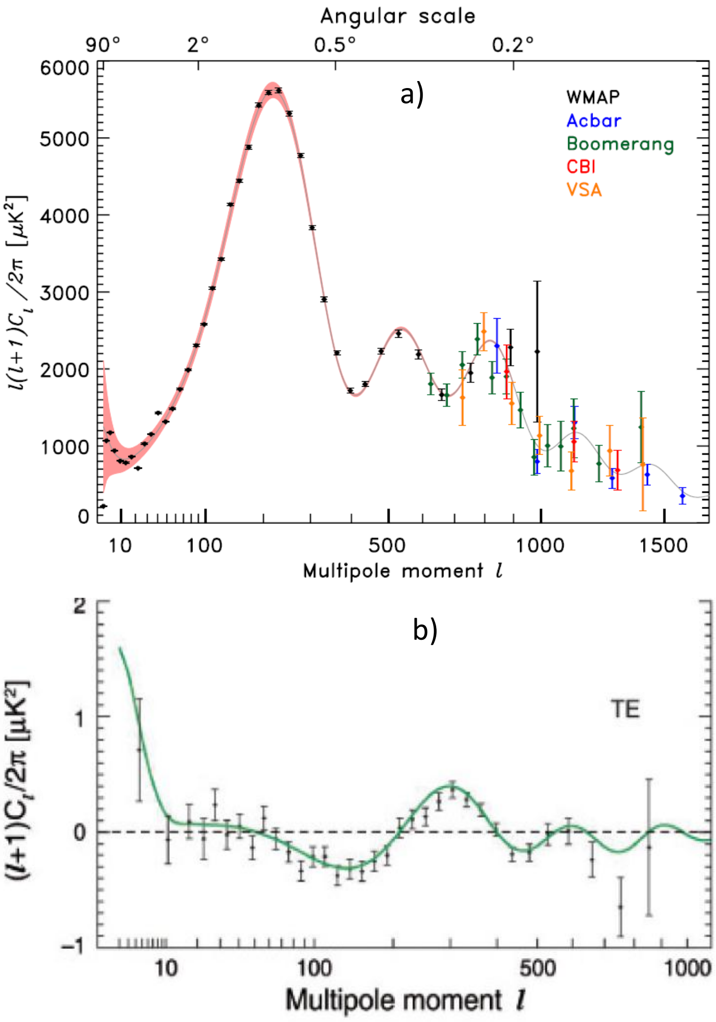

Figure 14 - a) The observed power spectrum of CMB anisotropies [136] in terms of radiation temperature from different experiments. b) Temperature-polarization correlations from WMAP.

The first big peak in Figure 14a corresponds to the Universe curvature; the second one represents the Baryon density, and the third to the Matter density, that can be easily related to the power spectrum.

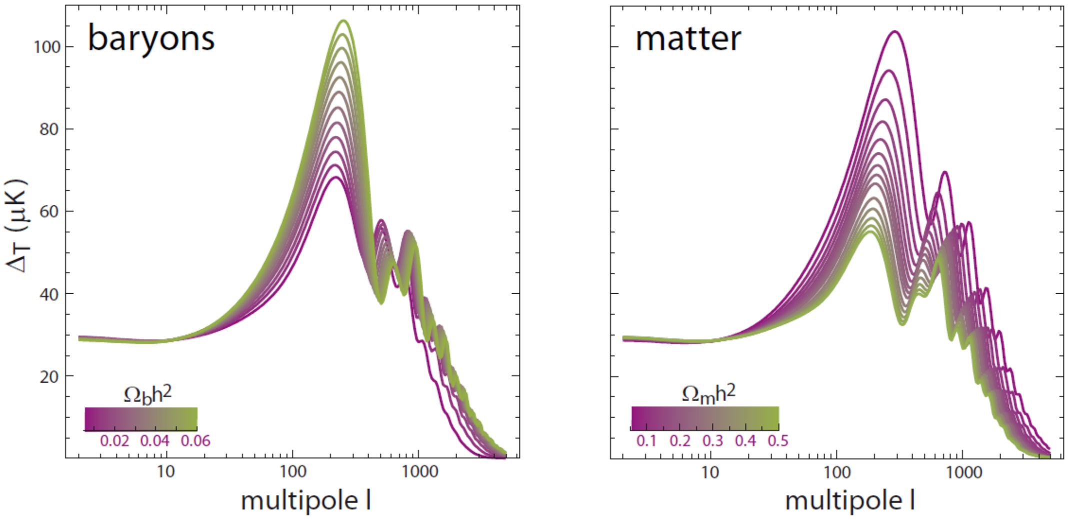

Figure 15 – Temperature fluctuation of CMB spectrum obtained modulating the baryons and the matter density.

From the analysis of the WMAP, taking into account data from CMB experiments studying smaller scales (with respect to WMAP), such as ACBAR and CBI, and astronomical measurements of the power spectrum from large scale structure and the Lyman α forest, the constraints become [3, 28]:

$$\Omega_B h^2=0.022\pm0.002,\ \ \Omega_m h^2=0.135\pm0.009 \tag{2.45}$$

and using a proper value for h^2, almost equal to 0.5 [136],

$$\Omega_B=0.04\pm0.01\ ,\ \Omega_m=0.27\pm0.04 \tag{2.46}$$

2.3.4 Baryonic Oscillation, Structure Formation and Evolution

A cornerstone of cosmology is the Copernican principle, that implies matter in the Universe is distributed homogeneously on the largest scales of superclusters, separated by voids. On smaller scales inhomogeneities are observed in the forms of galaxies, galaxy groups, and clusters.

The common approach to this situation is to turn to non-relativistic hydrodynamics and treat matter in the Universe as an adiabatic, viscous, non-static fluid, in which random fluctuations around the mean density appear, manifested by compressions in some regions and rarefactions in other. The origin of these density fluctuations was the tight coupling established before decoupling between radiation and charged matter density, causing them to oscillate in phase. So, baryon acoustic oscillations (BAO) refers to regular, periodic fluctuations in the density of the visible baryonic matter of the universe, caused by acoustic waves which existed in the early universe. In the same way that supernova experiments provide a "standard candle" for astronomical observations, BAO matter clustering provides a "standard ruler" for length scale in cosmology. The length of this standard ruler (~ 490 million light years in today's universe) can be measured by looking at the large scale structure of matter using astronomical surveys.

In the primordial fluid of our Universe three effects are competing: gravitational attraction, density dilution due to the Hubble flow, and radiation pressure felt by charged particles only. Inflationary models predict that the primordial mass density fluctuations should be adiabatic, Gaussian, and exhibit the same scale invariance as the CMB fluctuations. Therefore the baryonic acoustic oscillations can be treated similarly to CMB (Fig. 16).

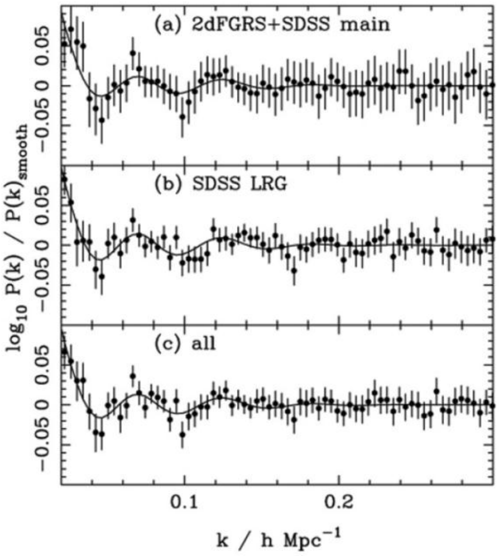

Figure 16 - BAO in power spectra calculated from (a) the combined SDSS and 2dFGRS main galaxies, (b) the SDSS DR5 LRG sample, and (c) the combination of these two samples (solid symbols with 1σ errors) [32].

Consider a single wave originating from this overdense region in the center of the primordial plasma. This region contains dark matter, baryons and photons. The pressure results in a spherical sound wave of both baryons and photons moving with a speed slightly over half the speed of light outwards from the overdensity. The dark matter only interacts gravitationally and so it stays at the center of the sound wave, the origin of the overdensity. Before decoupling, the photons and baryons move outwards together. After decoupling the photons are no longer interacting with the baryonic matter so they diffuse away. This relieves the pressure on the system, leaving a shell of baryonic matter at a fixed radius. This radius is often referred to as the sound horizon. Without the photo-baryon pressure driving the system outwards, the only remaining force on the baryons is gravitational. Therefore, the baryons and dark matter (still at the center of the perturbation) form a configuration which includes overdensities of matter both at the original site of the anisotropy and in a shell at the sound horizon [32, 33].

The scale of BAO depends on $\Omega_m$and on the Hubble constant. But in the ratio Ω_b/Ω_m the h dependence cancels out, so one can also quantify the amount of dark matter on very large scales: $\Omega_b/\Omega_m = 0.18 \pm 0.04$.

Now, an important argument arises: whether the galaxies could have formed from primordial density fluctuations in a purely baryonic medium. It has been stressed that the fluctuations in CMB and BAO maintain adiabaticity. So the amplitude of the primordial baryon density fluctuations would have needed to be very large in order to form the observed number of galaxies. But then the amplitude of the CMB fluctuations would also have been very large, leading to intolerably large CMB anisotropies today. Thus galaxy formation in purely baryonic scenario is ruled out by this argument alone. One concludes that the galaxies could only have been formed in the presence of gravitating dark matter which started to fluctuate early, unhindered by radiation pressure.

In the ΛCDM paradigm, the nonlinear growth of dark matter structure is a well-posed problem, where both the initial conditions and the evolution equations are known.

The Aquarius Project is a Virgo Consortium program to carry out high-resolution dark matter simulations of Milky-Way-sized halos in the standard cosmology (Fig. 17). This project seeks clues to the formation of galaxies and to the nature of the dark matter by designing strategies for exploring the formation of our Galaxy and its luminous and dark satellites.

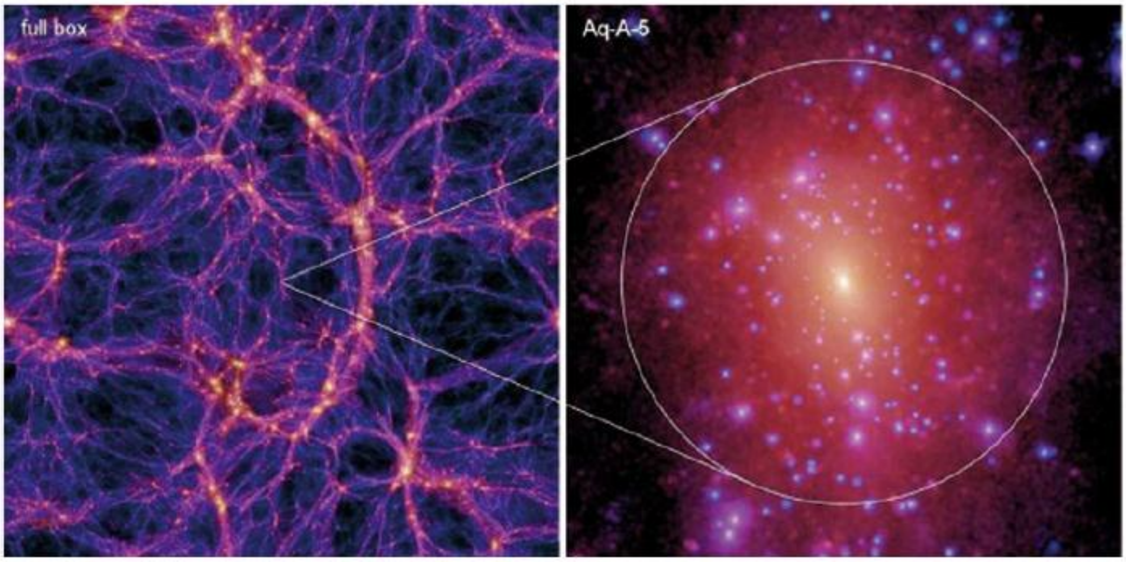

Figure 17 - The left panel shows the projected dark matter density at z = 0 in a slice of thickness 13.7 Mpc through the full box (137 Mpc on a side) of the 9003 parent simulation [33]. The right panel show this halo resimulated at a different numerical resolution. The image brightness is

proportional to the logarithm of the squared dark matter density projected along the line-of-sight. The circles mark *r50*, the radius within which the mean density is 50 times the background density.

The galaxies population on scales from 50 kpc to the size of the observable Universe has been predicted by hierarchical ΛCDM scenarios, and compared directly with a wide array of observations: so far, it has passed these tests successfully, particularly those that consider the large-scale matter distribution, and has led to the discovery of a universal internal structure for dark matter halos. The observed structure of galaxies, clusters and superclusters, as illustrated in Fig. 17, could not have formed in a baryonic medium devoid of dark matter.

2. 4 Non-particle DM theories: a brief criticism

It must be admitted that there's also another chance: it's assumed to know the exact form of gravitational force at all scales, but it's wrong. Something changes at galactic and/or cosmological scale and distort our knowledge, modifying Newton's and Einstein's paradigms and originating non-particle dark matter scenarios. These theories are difficult to prove, and so far there are many observations, not completely conclusive, against them. For a criterion of simplicity it would be important if these models had a mechanism inside to account for both dark matter and dark energy, strengthening gravitational force on the galactic scale and introducing antigravitative phenomena on cosmological scale.

2.4.1 MOND

Modified Newtonian dynamics (MOND) is a hypothesis that proposes a modification of Newton's law of gravity to explain the galaxy rotation problem [37, 38]. When the uniform velocity of rotation of galaxies was first observed, it was unexpected because Newtonian theory of gravity predicts that objects that are farther out will have lower velocities.

MOND was proposed by Mordehai Milgrom in 1983 as a way to model this observed uniform velocity data, in contrast with dark matter theories. Milgrom noted that Newton's law for gravitational force has been verified only where gravitational acceleration is large, and suggested that for extremely small accelerations the theory may not hold. MOND theory posits that acceleration is not linearly proportional to gravitational force at small values.

Actually, Milgrom provided several interpretations of his proposal, one being a modification of Newton's second law of motion. However, this proposed interpretation is inconsistent with conservation of momentum, requiring some unconventional physical assumptions to regain plausibility. A second interpretation, as a modification of the law of gravity, requires that the acceleration due to gravitational force not depend simply upon the mass m, but upon the form $m/\mu(a/a_0)$, where μ is some function approaching the value one for large arguments and a/a_0 for small arguments, a is the acceleration caused by gravity and a_0 is a natural constant, $a_0 \approx 10^{-10}$ m/s^2. The centripetal accelerations of stars and gas clouds at the outskirts of spiral galaxies tend to be below a_0. This interpretation is also inconsistent with momentum conservation; but this can be repaired by substituting a Lagrangian-based theory known as AQUAL, developed by Milgrom himself and Jacob Bekenstein [39].

A third interpretation views MOND simply as a description of the behavior of the dark matter in a galaxy; this leads to the conclusion that the dark matter must be tightly correlated with the visible matter in accordance with a fixed law, at least for stable galaxies.

The exact form of μ is unspecified, only its behavior when the argument a/a_0 is small or large. As Milgrom proved in his original paper, the form of μ does not change most of the consequences of the theory, such as the flattening of the rotation curve.

In the everyday world, a is much greater than a_0 for all physical effects, therefore $\mu(a/a_0) = 1$ and $F=ma$ as usual. Consequently, the change in Newton's law of gravity is negligible and Newton could not have seen it.

Predicted rotation curve

Far away from the center of a galaxy, the gravitational acceleration a star undergoes is predicted by MOND to be roughly:

$$\mu\left(\frac{a}{a_0}\right)a = \frac{GM}{r^2} \tag{2.47}$$

with G the gravitation constant, M the mass of the galaxy, and r the distance between the center and the star.

Assuming that, at this large distance r, a is smaller than a_0, $\mu\left(\frac{a}{a_0}\right) = \frac{a}{a_0}$. This gives:

$$\frac{GM}{r^2} = \frac{a^2}{a_0} \tag{2.48 a}$$

Therefore:

$$a = \frac{\sqrt{GMa_0}}{r} \tag{2.48 b}$$

Since the equation that relates the velocity to the acceleration for a circular orbit is $a = \frac{v^2}{r}$, one has:

$$a = \frac{v^2}{r} = \frac{\sqrt{GMa_0}}{r} \tag{2.49 a}$$

and then:

$$v = \sqrt[4]{GMa_0} \tag{2.49 b}$$

Consequently, the velocity of stars on a circular orbit far from the center is a constant and does not depend on the distance *r*: the rotation curve is flat.

The proportion between the "flat" rotation velocity to the observed mass derived here is matching the observed relation between "flat" velocity to luminosity, known as the Tully-Fisher relation.

At the same time, there is a clear relationship between the velocity and the constant a_0. The equation $v = (GMa_0)^{1/4}$ allows one to calculate a_0 from the observed v and M. Milgrom found $a_0 = 1.2\times10^{-10}\ \mathrm{ms}^{-2}$. As expected, this quantity is far smaller than any acceleration typically found in solar system-scale interactions.

To explain the meaning of this constant, Milgrom said : "... It is roughly the acceleration that will take an object from rest to the speed of light in the lifetime of the universe. It is also of the order of the recently discovered acceleration of the universe."

Some recent attempts have been done to give a Lagrangian representation of MOND, through nonlocal metric formulation of Milgrom's idea [37], trying to reproduce the Tully-Fisher dispersion relation and weak lensing effects at the same time:

$$\mathcal{L}_{\mathrm{MOND}} = \frac{9a_0^2}{32\pi G}\, y^2 e^{-y} \sqrt{-g} \tag{2.50}$$

where g is the determinant of the metric tensor and the unique MOND variable is y. Added to the Einstein-Hilbert usual term, this suffices to reproduce the MOND dynamics and enough weak lensing at large distances, while predicting fully negligible deviations from General Relativity at small distances, vanishing when a_0 goes to zero. The theory introduces non-local operators and the y function is promoted to a new scalar field. This type of MOND model creates a bridge to the MOG theories (see 2.4.2).

Consistency with the observations

According to the Modified Newtonian Dynamics theory, every physical process that involves small accelerations due to gravity will have an outcome different from that predicted by the simple law $F=ma$. Therefore, astronomers need to look for all such processes and verify that MOND remains compatible with observations, that is, within the limit of the uncertainties on the data. There is, however, a complication overlooked up to this point but that strongly affects the compatibility between MOND and the observed world: in a system considered as isolated, for example a single satellite orbiting a planet, the effect of MOND results in an increased velocity beyond a given range (actually, below a given acceleration, but for circular orbits it is the same thing), that depends on the mass of both the planet and the satellite. However, if the same system is actually orbiting a star, the planet and the satellite will be accelerated in the star's gravitational field. For the satellite, the sum of the two fields could yield acceleration greater than a_0, and the orbit would not be the same as that in an isolated system.

For this reason, the typical acceleration of any physical process is not the only parameter astronomers must consider. Also critical is the process's environment, which is all external forces that are usually neglected.

This affects MOND's application to experimental observation and empirical data because all experiments done on Earth or its neighborhood are subject to the Sun's gravitational field, and this field is so strong that all objects in the Solar system undergo an acceleration greater than a_0. This explains why the flattening of galaxies' rotation curve, or the MOND effect, had not been detected until the early 1980s, when astronomers first gathered empirical data on the rotation of galaxies.

So far, MOND has remained valid, because astrophysical uncertainties are too large to conclude in favor of or against it. Indeed, conditions for conducting an experiment that could confirm or disprove MOND may only be possible outside the Solar system [3, 28]. A couple of near-to-Earth tests of MOND have been proposed though: one involves flying the LISA Pathfinder spacecraft through the Earth-Sun saddlepoint; another involves using a precisely controlled spinning disk to cancel out the acceleration effects of Earth's orbit around the Sun, and Sun's orbit around the Galaxy.

An exception to MOND is prediction of the speeds of galaxies that gyrate around the center of a galaxy cluster. Our Galaxy is part of the Virgo supercluster. MOND predicts a rate of rotation of these galaxies about their center, and temperature distributions, that are contrary to observation.

Computer simulations show that MOND is generally very precise at predicting individual galaxy rotation curves, of all kinds of galaxies: spirals, ellipticals, dwarfs, etc. However, MOND and MOND-like theories are not so good at predicting galactic cluster-scale, or cosmological scale structures [38].

Lee Smolin and co-workers have tried unsuccessfully to obtain a theoretical basis for MOND from quantum gravity. His conclusion is "MOND is a tantalizing mystery, but not one that can be resolved now." (from *"The Trouble with Physics: The Rise of String Theory, the Fall of a Science, and What Comes Next"*, 2011).

Studies of the aforementioned Bullet Cluster (August 2006), that consists of two colliding clusters of galaxies, provide the best evidence for the existence of DM: at a statistical significance of 8σ, it was found that the spatial offset of the center of the total mass from the center of the baryonic mass peaks cannot be explained with an alteration of the gravitational force law. It provides evidence against some of the more popular versions of MOND.

In addition, an important 2011 study observing the gravity-induced redshift of galactic clusters found results that strongly supported General Relativity: MOND can fit the determined redshifts slightly worse than does General Relativity with dark halos [39].

2.4.2 MOG and Non-Local Gravity

Besides MOND, other notable theories that try to explain the mystery of the rotational curves, under the name of Modified Gravity (MOG), are Nonsymmetric Gravitational Theory proposed by John Moffat [40, 41, 42], Conformal Gravity by Philip Mannheim and Non-Local Gravity by Barvinski and Arkani-Hamed.

With **MOG** several theories which introduce new cosmological fields are addressed, starting from a tensor generalization of Einstein Gravitational Theory. In General Relativity, the gravitational field is characterized by a symmetric rank-2 tensor, the metric tensor. The possibility of generalizing the metric tensor has been considered by many, including Einstein and others. A general (nonsymmetric) tensor can always be decomposed into a symmetric and an antisymmetric part. As the electromagnetic field is characterized by an antisymmetric rank-2 tensor, there is an obvious possibility for a unified theory: a nonsymmetric tensor composed of a symmetric part representing gravity, and an antisymmetric part that represents electromagnetism. Research in this direction ultimately proved fruitless and the desired classical unified field theory was not found.

In 1979, Moffat made the observation that the antisymmetric part of the generalized metric tensor need not necessarily represent electromagnetism; it may represent a new, hypothetical force. Later, in 1995, Moffat noted that the field corresponding with the antisymmetric part need not be massless, like the electromagnetic (or gravitational) fields.

The uptodate Modified Gravity (MOG) is a fully relativistic theory of gravitation that is derived from a relativistic action principle involving scalar, tensor, and vector fields. MOG has evolved as a result of investigations of Nonsymmetric Gravity Theory (NGT) and, most recently, it has taken the form of Scalar-Tensor-Vector Gravity (STVG), that includes Einstein-Hilbert action and extend it using new fields actions and new constants above the Newtonian one [43].

It starts with the Einstein-Hilbert Lagrangian:

$$\mathcal{L}_G = -\frac{1}{16\pi G}\left(R + 2\Lambda\right)\sqrt{-g}, \qquad (2.51)$$

where R is the trace of the Ricci tensor, G is the gravitational constant, g is the determinant of the metric tensor $g_{\mu\nu}$, while Λ is the cosmological constant.

Then the Maxwell-Proca Lagrangian for the STVG vector field ϕ_μ is introduced:

$$\mathcal{L}_\phi = -\frac{1}{4\pi}\omega\left[\frac{1}{4}B^{\mu\nu}B_{\mu\nu} - \frac{1}{2}\mu^2\phi_\mu\phi^\mu + V_\phi(\phi)\right]\sqrt{-g}, \qquad (2.52)$$

where $B_{\mu\nu} = \partial_\mu \phi_\nu - \partial_\nu \phi_\mu$, μ is the mass of the vector field, ω characterizes the strength of the coupling between the fifth force and matter, and V_ϕ is a self-interaction potential.

The three constants of the theory, G, μ and ω, are promoted to scalar fields by introducing associated kinetic and potential terms in the Lagrangian density:

$$\mathcal{L}_S = -\frac{1}{G}\left[\frac{1}{2}g^{\mu\nu}\left(\frac{\nabla_\mu G \nabla_\nu G}{G^2} + \frac{\nabla_\mu \mu \nabla_\nu \mu}{\mu^2} - \nabla_\mu \omega \nabla_\nu \omega\right) + \frac{V_G(G)}{G^2} + \frac{V_\mu(\mu)}{\mu^2} + V_\omega(\omega)\right]\sqrt{-g}, \tag{2.53}$$

where ∇_μ denotes covariant differentiation with respect to the metric $g_{\mu\nu}$, while V_G, V_μ, and V_ω are the self-interaction potentials associated with the scalar fields. The STVG action integral takes the form [47]

$$S = \int (\mathcal{L}_G + \mathcal{L}_\phi + \mathcal{L}_S + \mathcal{L}_M)\, d^4x, \tag{2.54}$$

where $\mathcal{L}_M$ is the ordinary matter Lagrangian density.

So, Einstein gravity coupled to massive fields leads to an acceleration law that modifies the Newtonian law of attraction between particles with a Yukawa-like term [42], generating a running of the effective gravitational coupling G and an increase of it at large galactic distances:

$$a_{\text{MOG}} = -\frac{G_N M}{r^2}(1 + \alpha(1 - (1 + \mu r)e^{-\mu r})) \tag{2.55}$$

where the model predicted values for the constants are $\alpha \simeq 0.03$ and $\mu \simeq (160\, pc)^{-1}$.

On the other hand, at shorter distances, gravity is counteracted by a repulsive fifth force due to the vector field.

This theory has been applied successfully to a range of astronomical, astrophysical, and cosmological phenomena. On the scale of the solar system, the theory predicts no deviation from the results of Newton and Einstein. This is also true for star clusters containing no more than a maximum of a few million solar masses. The theory accounts for the rotation curves of spiral galaxies, correctly reproducing the Tully-Fisher law. Furthermore STVG is in good agreement with the mass profiles of galaxy clusters; also the gravitational lensing of clusters of galaxies can be explained without exotic dark matter [40, 41]. It can also account for key cosmological observations, with an effective effective G = G(t) running with time, including:

- The acoustic peaks in the cosmic microwave background radiation;
- The accelerating expansion of the universe that is apparent from type Ia supernova observations;
- The matter power spectrum of the universe that is observed in the form of galaxy-galaxy correlations.

Conformal gravity is a generic name for gravity theories which are invariant under conformal transformations in the Riemannian geometry sense; more accurately, they are invariant under Weyl transformations $g_{ab} \to \Omega^2(x) g_{ab}$, where g_{ab} is the metric tensor and $\Omega(x)$ is a function on space-time.

The simplest theory in this category has the square of the Weyl tensor as the Lagrangian [44]

$$\mathcal{S} = \int \mathrm{d}^4x \sqrt{-g}\, C_{abcd} C^{abcd}, \tag{2.56}$$

where C_{abcd} is the Weyl tensor. This is to be contrasted with the usual Einstein–Hilbert action where the Lagrangian is just the Ricci scalar. The equation of motion upon varying the metric is called the *Bach equation*,

$$2\nabla_a\nabla_d C^{a}{}_{bc}{}^{d} + C^{a}{}_{bc}{}^{d}R_{ad} = 0, \tag{2.57}$$

where R_{ab} is the Ricci tensor. Conformally flat metrics are solutions of this equation.

Since these theories lead to fourth order equations for the fluctuations around a fixed background, they are not manifestly unitary. It has therefore been generally believed that they could not be consistently quantized.

So Conformal gravity is an example of a 4-derivative theory. This means that each term in the wave equation can contain up to 4 derivatives. There are pros and cons of 4-derivative theories. The pros are that the quantized version of the theory is more convergent and renormalizable. The cons are that there may be issues with causality. A simpler example of a 4-derivative wave equation is the scalar 4-derivative wave equation:

$$\Box^2\Phi = 0 \tag{2.58}$$

The solution for this is, in a central field of force, is:

$$\Phi(r) = 1 - 2m/r + ar + br^2 \tag{2.59}$$

The first two terms are the same as a normal wave equation. Since this equation is a simpler approximation to conformal gravity then *m* corresponds to mass of the central source. The last two terms are unique to 4-derivative wave equations. It has been suggested to assign small values to them to account for the galactic acceleration constant, i. e. dark matter effect, and the dark energy constant. The solution equivalent to the Schwarzschild solution in General Relativity for a spherical source for conformal gravity has a metric with:

$$\phi(r) = g^{00} = (1 - 6bc)^{\frac{1}{2}} - \frac{2b}{r} + cr + \frac{d}{3}r^2 \tag{2.60}$$

to show the difference between General Relativity [44, 47]. *6bc* is very small so can be ignored. The problem is that now *c* is the total mass-energy of the source, *b* is the integral of density times distance to source squared. So this is a completely different potential to General Relativity and not just a small modification.

The main issue with conformal gravity theories, as well as any theory with higher derivatives, is the typical presence of ghosts, which point to instabilities of the quantum version of the theory [44].

Non-local gravity

String-inspired non-local field theory models have gained popularity in recent years. These theories often present novel cosmological features and has been used to obtain at the same time inflation, dark energy and dark matter. Like most other higher derivative models, these field theories are better behaved in the UV as compared to the usual renormalizable models, the quantum theory, in fact, is finite and provides deviations in scattering cross sections which may be detectable in particle physics experiments.

The main idea of these theories is to make the effective Newton constant depend on the frequency and wavelength, in such a way that for sources that are uniform in both space and time, such as the vacuum energy, the effective Newton constant is tiny, shutting off their gravitational effects. Analogs in electromagnetism are frequency-dependent dielectrics and highpass filters.

To explain this physics from a consistent quantum effective field theory is not the purpose of this discussion. Indeed, the modifications of the Einstein-Hilbert action are non-local and acausal, and are hard to imagine coming from conventional field theories.

Einstein gravity is modified at the level of classical equations of motion, implementing the physical idea of "the Newton constant as a high-pass filter", while retaining all the usual successes of General Relativity. This can be accomplished with extremely simple non-local modifications of the equations of motion [45-48].

A first example of a modified Einstein equation that incorporates the abovementioned properties takes the form

$$M_{\rm Pl}^2 \left(1 + \mathcal{F}(L^2\nabla^2)\right) G_{\mu\nu} = T_{\mu\nu} \tag{2.61}$$

where $\mathcal{F}(L^2\nabla^2)$ is the "filter function" with the following properties: $F(\alpha) \to 0$ for $\alpha \gg 1$, and $F(\alpha) \gg 1$ for $\alpha \ll 1$. L is a distance scale at which gravity is modified; it can be infinite, or very large but finite; $\nabla^2 \equiv \nabla_\mu\nabla^\mu \equiv \Box$ denotes the covariant d'Alambertian.

One can think of (2.61) as the Einstein equation with an effective Newton constant $(8\pi G_N^{eff})^{-1} = M_{Pl}^2(1+\mathcal{F})$, where $\mathcal{F}$ is usually proportional to $\Box^{-1}$. It is immediately clear that at least for the case where $T_{\mu\nu}$ is pure vacuum energy density $Eg_{\mu\nu}$, the maximally symmetric solution to these equations of motion can have acceptably small curvature if F(0) is large enough. In other words, for Barvinski's point of view [45], the usual Ricci scalar action is substituted with a scale dependent one:

$$R \;\Rightarrow\; R + R^{\mu\nu}F(\Box)G_{\mu\nu} \tag{2.62}$$

So, in these theories the idea of scale dependent gravitational coupling must be introduced, i. e. a General Relativity running for G_N and its related mass scale [47]. The theory can be implemented adding some dynamically dependent terms.

Many attempts have been done in the past to enlarge Einstein theory, for example adding new scalars constructed with quadratic forms of Ricci scalar, Riemann and Ricci tensors (such as Gauss-Bonnet), or with the more generalized Lovelock's theory, which reduces to the Gauss-Bonnet one at the second order term:

$$\mathcal{L} = \sqrt{-g}\,\left(\alpha_0 + \alpha_1 R + \alpha_2\left(R^2 + R_{\alpha\beta\mu\nu}R^{\alpha\beta\mu\nu} - 4R_{\mu\nu}R^{\mu\nu}\right) + \alpha_3\mathcal{O}(R^3)\right), \tag{2.63}$$

where α_0 correspond to the cosmological constant, α_1 is the Einstein $(16\pi G_N)^{-1}$ term and α_n with $n \geq 2$ are coupling constants of additional terms that represent ultraviolet corrections to Einstein theory. The Gauss-Bonnet Lagrangian derives from the generalized Gauss-Bonnet Theorem. Despite being quadratic in the Riemann tensor, for a four-dimensional space terms containing more than 2 partial derivatives of the metric cancel out, making the Euler–Lagrange equations second order quasilinear partial differential equations in the metric.

In the most exhaustive non-local case [48], higher order terms are introduced for a scale-dependent counterpart of the Gauss-Bonnet theory, which explicitly depend on the covariant d'Alambertian: i.e. some filter functions $\mathcal{F}_n(\Box)$ are used, which define the follow generalized action, with new acausal coupling constant α_n:

$$S = \int d^4x\sqrt{-g}\left(\frac{M_P^2}{2}R + a_1 R\mathcal{F}_1 R + a_2 R_{\mu\nu}\mathcal{F}_2 R^{\mu\nu} + a_3 R_{\mu\nu\alpha\beta}\mathcal{F}_3 R^{\mu\nu\alpha\beta} + \Lambda\right) \tag{2.64}$$

In this case, however, even in 4 dimensions both such new terms, in Ricci and Riemann tensors, are not trivial because of the presence of an operator in the middle, admitting inclusion of higher degrees of curvature tensors with covariant derivatives acting on second and fourth rank tensors.
Two phases could be considered: the $\Box \gg R$ one, for small scale phenomena (galaxy and star systems), and the $\Box \ll R$ regime, for cosmological treatment. From the first regime, attractive DM-like interactions could occur, from the second antigravitative cosmological phenomena.
The computational burden of these theories is clearly very heavy and tedious.

What has been learned from these theoretical attempts to account for all the gravitational anomalies observed in the last 80 years is this:

- MOND is going to be ruled out, because of very problematic accordance with observations.
- Conformal and non-local gravity don't follow a simplicity criterion at all, because they're high-order derivative theories, with ghosts and acausal principia.
- MOG STVG theory seems more strong and predictive, but it also add a fifth force and several bosonic massive fields that act on the space-time dynamics to put things right.
- These theories are not capable to reproduce all the observations discussed in the first three paragraphs (2.1, 2.2, 2.3), especially the cosmological ones, i. e. CMB and BAO physics and structure formations.

So a consistent particle dark matter apparatus is needed.

Chapter 3

Phenomenology: a Dark Matter Search Program

The aim of this chapter is to trace a dark matter aware program to serve as a guideline for AMS-02 (and future multi-purpose space experiment for dark matter research). An uptodate scenario of dark matter search is going to be depicted, through cosmic rays physics and theories beyond the Standard Model, trying to create an operative link with experimental environment.
Below, the fundamental knowledge for a good and well-posed DM research and understanding are described, dealing with: DM halo and CR propagation models (with their uncertainties), PAMELA and FERMI possible dark matter leptonic signatures, expected hadronic signals, to which a special attention will be paid (i. e. antiproton and antideuterons), and AMS-02 good dark matter candidate, showing some alternatives and new phenomena and discovery to think about. LHC and direct experiments results help us in this overall close examination. The conclusions are personal and also quite stringent, but could not be shared by all the experts in the field.

3.1 Dark Matter Halo

The most widely adopted approach to the problem of large-scale structure formation involves the use of N-body simulations. Modern, high resolution simulations make full use of the tremendous increase in computational power over the last few decades. The evolution of structure is often approximated with non–linear gravitational clustering from specified initial conditions of dark matter particles and can be refined by introducing the effects of gas dynamics, chemistry, radiative transfer and other astrophysical processes. The reliability of an N-body simulation is measured by its mass and length resolution. The mass resolution is specified by the mass of the smallest particle considered, being the scale below which fluctuations become negligible. Length resolution is limited by the so-called softening scale, introduced to avoid infinities in the gravitational force when elementary particles collide. Recent N-body simulations suggest the existence of a **universal dark matter profile**, with the same shape for all masses, epochs and input power spectra, which envelops galactic disks [3, 28, 50, 51]. The usual parameterization for a dark matter halo density is

$$\rho(r) = \frac{\rho_s}{(r/R)^{\gamma}[1+(r/R)^{\alpha}]^{(\beta-\gamma)/\alpha}} \tag{3.1}$$

Various authors have ended up with different results for the spectral shape in the innermost regions of galaxies and galaxy clusters. In particular, several groups have failed to reproduce the initial results of Navarro, Frenk and White [53], which find a value for the power–law index in the innermost part of galactic halos of $\gamma = 1$. In Table 1 the values of the parameters (α, β, γ) for some of the most widely used profile models are given, namely the Kravtsov, Moore and modified isothermal profiles. Note that α, β, γ are the astrophysical/gravitational parameters, ρ_s and R are scale parameters which vary from halo to halo.
The spherical universal profile could be rewritten as a function of the Solar System parameters $r_\odot$ and $\rho_\odot$:

$$\rho(r) = \rho_\odot \left(\frac{r_\odot}{r}\right)^{\gamma} \left[\frac{1+(r_\odot/R)^{\alpha}}{1+(r/R)^{\alpha}}\right]^{(\beta-\gamma)/\alpha} \tag{3.2}$$

where $r_{\odot} = 8.5\,kpc$ is the main Sun distance from the Galactic Center and $\rho_{\odot} = 0.3 \div 0.4\,GeV\ cm^{-3}$ the local dark matter density [142]. There are still uncertainties associated with the local density. The local density of dark matter is determined by observing the rotation curves of the Milky Way. This is somewhat difficult to do from our location within the galaxy. Furthermore, rotation curves measure the total mass within an orbit, thus the density distributions of the galactic bulge and disk are needed to accurately calculate the dark matter profile [3, 51].

In addition to the local density, the velocity distribution of dark matter in the local region is needed to accurately calculate direct and indirect detection rates. This is also best inferred from observed rotation curves.

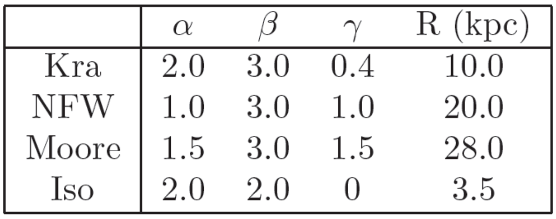

	α	β	γ	R (kpc)
Kra	2.0	3.0	0.4	10.0
NFW	1.0	3.0	1.0	20.0
Moore	1.5	3.0	1.5	28.0
Iso	2.0	2.0	0	3.5

Table 1 - Parameters of some widely used profile models for the dark matter density in galaxies. Values of R can vary from system to system [3, 57].

Although it is definitely clear that the slope of the density profile should increase as one moves from the center of a galaxy to the outer regions, the precise value of the power-law index in the innermost galactic regions is still under debate.

Taylor and Navarro [54] studied the behavior of the phase-space density (defined as the ratio of spatial density to velocity dispersion cubed, ρ/σ^3) as a function of the radius, finding excellent agreement with a power-law extending over several decades in radius. The final result of their analysis is a “critical” profile, following a NFW profile in the outer regions, but with a central slope converging to the value $\gamma_{TN} = 0.75$, instead of $\gamma_{NFW} = 1$. The density profiles do not converge to any specific power-law at small radii. The logarithmic slope of the profile continuously flattens when moving toward the galactic center. The slope at the innermost resolved radius varies between 1 and 1.5, i.e. between the predictions of the NFW and Moore profiles. It is important to keep in mind that predictions made adopting such profiles probably overestimate the density near the Galactic center and should be used cautiously. Recently, Prada et al. [55] have suggested that the effects of *adiabatic compression on the dark matter* profile near the Galactic center could play an important role, possibly enhancing the dark matter density by an order of magnitude in the inner parsecs of the Milky Way.

Two other model have been proposed and they represents modern parameterizations updated to the new astrophysical observations, the Burkert (3.3) and the Einasto (3.4) profiles:

$$\rho(r) = \frac{\rho_s}{(1 + r/R)(1 + (r/R)^2)} \tag{3.3}$$

$$\rho(r) = \rho_s exp\left[-(r/R')^{\frac{1}{n}}\right] \tag{3.4}$$

where R' is a rescaled R factor, function of n, and the new parameter n controls the degree of curvature of the profile and worth $n = 5 \div 8$ for outer component of galaxies and is < 2 for central component [56]; often $1/n = 0.17$ is taken.

Also a *Dark Disk* (not a “halo”) has been proposed to complete the local description of the DM profile (see 3.8.1).

The Case of the Milky Way

One way to probe the nature of matter in our neighborhood is to study microlensing events in the direction of the Galactic Center (GC). In fact, such events can only be due to compact objects, acting as lenses of background sources, and it is commonly believed that dark matter is simply too weakly interacting to clump on small scales [3]. Klypin, Zhao and Somerville (KZS) have found a good agreement between NFW profiles ($\gamma = 1$) and observational data for our Galaxy and M31. But the dark matter profile in the inner region of the Milky Way is more uncertain. Observations of the velocity dispersion of high proper motion stars suggest the existence of a Super Massive Black Hole (SMBH) lying at the center of our Galaxy, with a mass, $M_{SMBH} \approx 2.6 \times 10^6 M_\odot$. It has long been argued that if a SMBH exists at the galactic center, the process of adiabatic accretion of dark matter on it would produce a “spike” in the dark matter density profile [3, 50, 56, 58, 59]. Gondolo and Silk have applied such a process to study the enhancement of the annihilation signal from the galactic center [309]. Considering an initial power-law type profile of index γ, similar to those previously discussed, the corresponding *GC dark matter profile* $\rho'(r)$, after this accretion process is:

$$\rho' = \left[\alpha_\gamma \left(\frac{M}{\rho_D D^3}\right)^{3-\gamma}\right]^{\gamma_{sp}-\gamma} \rho_D \, g(r) \left(\frac{D}{r}\right)^{\gamma_{sp}} \tag{3.5}$$

where $\gamma_{sp} = (9 - 2\gamma)/(4 - \gamma)$, $D = r_\odot \simeq 8.5$ kpc is the solar distance from the Galactic Center and $\rho_D = \rho_\odot \simeq 0.3\, GeV\, cm^{-3}$ is the density in the solar neighborhood. The factors α_γ and *g(r)* cannot be determined analytically. Eq. (3.5) is only valid in a central region of size $R_{sp} = \alpha_\gamma D(M/\rho_D D^3)1/(3-\gamma)$, where the central black hole dominates the gravitational potential [133].

It is easy to understand the basics of adiabatic accretion under the assumptions of circular orbits. Assuming an initial power–law distribution, $\rho \propto r^{-\gamma}$, and a final distribution, $\rho \propto r^{-\gamma_{sp}}$, the equations of conservation of mass and angular momentum can be expressed, respectively, as

$$\rho_i r_i^2 \mathrm{d}r_i = \rho_f r_f^2 \mathrm{d}r_f \tag{3.6}$$

and

$$r_i M_i(r) = r_f M_f(r) \approx r_f M_{BH}, \tag{3.7}$$

which imply, respectively,

$$r_i \propto r_f^{(3-\gamma_{sp})/(3-\gamma)} \tag{3.8}$$

$$r_i \propto r_f^{1/(4-\gamma)} \quad . \tag{3.9}$$

The final distribution will thus have a power–law index

$$\gamma_{sp} = \frac{9-2\gamma}{4-\gamma}, \tag{3.10}$$

which assumes values in the range of 2.25 to 2.5 as γ varies in the interval of 0 to 2.

Taking into account the annihilation of dark matter particles, the density cannot grow to arbitrarily high values, the maximal density being fixed by the value

$$\rho_{core} = \frac{m}{\sigma v \, t_{BH}}, \tag{3.11}$$

where $t_{BH} \approx 10^{10}$ yr is the age of the central black hole. The final profile, resulting from the adiabatic accretion of annihilating dark matter on a massive black hole is

$$\rho_{dm}(r) = \frac{\rho'(r)\rho_{core}}{\rho'(r) + \rho_{core}} \tag{3.12}$$

following a power-law for large values of r, and with a flat core of density, ρ_{core},

$$R_{core} = R_{sp}\left(\frac{\rho(R_{sp})}{\rho_{core}}\right)^{(1/\gamma_{sp})} . \tag{3.13}$$

Finally, the existence of such spikes due to this process would produce a dramatic enhancement of the annihilation radiation from the galactic center. The implications for indirect detection of dark matter particles are obviously relevant and these spikes could enhance the dark matter annihilation products in cosmic rays. Only gamma and neutrino astronomy could trace these particle hints, because of the possibility of directional observations.
New studies similar to Gondolo and Silk's one have being applied on FERMI's data [310], to constraint the GC models.

3.2 Cosmic Rays Physics

3.2.1 CR Propagation

Most of the available information about matter in our Universe, and in our Galaxy in particular, comes indirectly from the collection of the electromagnetic radiation (from meter waves to γ rays) that was emitted or absorbed by this matter. A completely different information is provided by the cosmic ray nuclei, which constitute a genuine sample of galactic matter. Many different nuclei species are observed, in a wide range of energy and with different origins. Some of them come unaltered from the sources (they are called primaries), others (secondaries) come from nuclear reactions between the primaries and the interstellar medium, or from the disintegration of unstable species. Moreover, the trajectories of these nuclei from creation to detection are rather erratic, due to the influence of the galactic magnetic field and it's impossible to follow the direction of an incoming nucleus back to the source.
Cosmic Rays charged particles reach the Earth atmosphere in all directions, after they traveled throughout the Galaxy for several million years. The CR flux detected at Earth is predominantly composed by protons and nuclei ($\sim$ 85% protons, $\sim$ 12% helium and $\sim$ 1% heavier nuclei), while electrons and positrons contribute with $\sim$2% to the total flux [30, 60, 61].

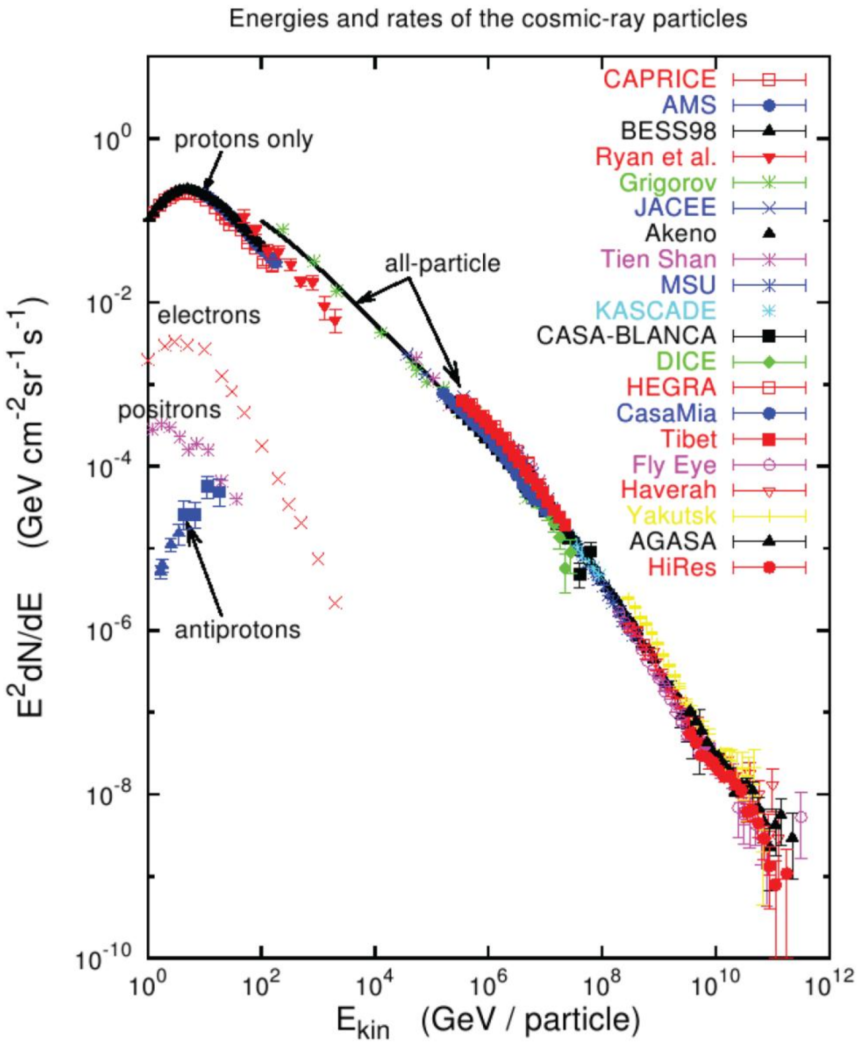

Figure 1 - All particle CR spectrum [62]. The spectrum extends to many orders of magnitude. Measurements from different experiments are shown.

The CR energies span over a wide interval, from eV to 10^{21} eV, whereas the all-species differential fluxes vary significantly: from particle/cm^2/second/MeV up to particle/km^2/century/ZeV respectively. CRs with lowest energy, eV ÷ GeV, are of solar origin and make up the solar wind.

CRs with energy between 10^9 and 10^{18} eV are thought to originate and accelerated in supernova explosions occurring in the Galaxy. In this picture, particle are accelerated by non-thermal mechanisms that lead to the power-law spectrum described in Fig. 1:

$$\Phi = \Phi_0 E^{-\gamma} \tag{3.14}$$

where the spectral index takes the value ~ 2.7. The low energy part of the CR spectrum (E < 10 GeV) is influenced by the solar wind, as discussed later. At energies of the order of 10^{15} eV the CR spectrum has a steeping, the *knee*, characterized by a sudden variation of the all-particle spectral index from 2.7 to 3.1 (Fig. 1), probably due to the galactic pulsar.

At higher energies, the *ankle* is observed at $\sim 10^{18}$ eV, which marks another transition to a flatter spectrum, with $\gamma \sim 2.7$. As the nature and the origin of these structures are still debated, they are thought to be related to the transition between the galactic and the extra-galactic component of the CR flux: they would come from AGN (Active Galactic Nuclei) [30, 60]. In the highest energy region $E \sim 10^{19}$ eV, the Greisen-Zatsepin-Kuzmin (GZK) suppression is expected on the flux, due to inelastic interactions of cosmic rays with the CMB photons.

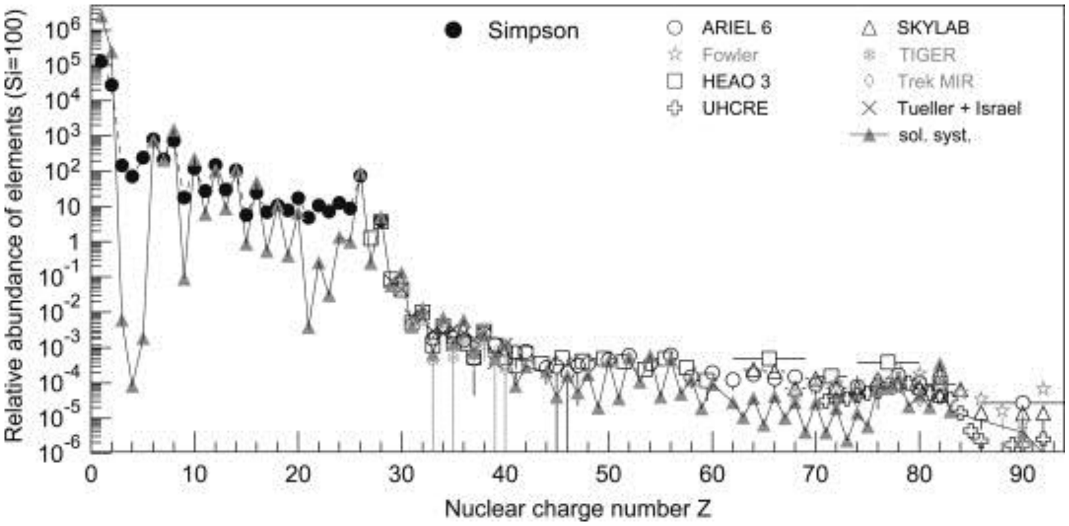

Figure 2 - Relative abundances of the various elements in CRs and in the solar system. The correlation with solar system well confirms a galactic origin for CRs, while the discrepancies in the Li-Be-B and sub-Fe groups indicate spallation properties of CRs in the ISM [62, 63, 64].

CR propagation can be summarized in few words, before studying in deep each phenomenon.
Let's explain a *two dimensional diffusion model*. In order to parameterize the uncertainty in propagation, CR propagation is computed with MIN, MED, and MAX propagation parameters as listed in Table 2.
The diffusion equation [30, 65] for charged cosmic rays, neglecting energy losses, is given by

$$\frac{\partial}{\partial t}\psi(r,z,E) = Q(r,z,E) - 2h\delta(z)\Gamma_{ann}(E)\left(n_H + 4^{\frac{2}{3}}n_{He}\right)\psi(r,z,E) + K(E)\left(\frac{\partial^2}{\partial z^2} + \frac{1}{r}\frac{\partial}{\partial r}r\frac{\partial}{\partial r}\right)\psi(r,z,E) - V_c\frac{\partial}{\partial z}\psi(r,z,E) \tag{3.15}$$

where ψ (r, z,E) is the number density of a cosmic ray species. Steady state solutions are given by setting $\frac{\partial}{\partial t}\psi(r,z,E)$ = 0. Also, the region over which this equation is solved is assumed to be a cylinder with height *L*, which can vary as in Table 2, and a radius fixed at R = 20 kpc. A conservative estimate of the CR flux can be made by assuming that ψ(R, z, E) = ψ(r, ±L, E) = 0 at the boundary. A second boundary condition is given by assuming continuity through the z = 0 plane. Solutions are expressed in terms of a Bessel Series Expansion.

Case	δ	K_0 (kpc^2/Myr	L (kpc)	V_c (km/s)	V_A (km/s)	$\chi^2_{\mathrm{B/C}}$
max	0.46	0.0765	15	5	117.6	39.98
med	0.70	0.0112	4	12	52.9	25.68
min	0.85	0.0016	1	13.5	22.4	39.02

Table 2 – CR propagation parameters for the three set, min, med, max, which correspond to minimum, medium and maximum flux for particles compatible with the B/C ratio [66, 67, 68].

All the parameters may be fixed using CR nuclei ratio, such as B/C and ^{10}Be/^{9}Be ratio (and also Be/B). In fact, from the ratio of unstable/stable nuclei (like ^{10}Be/^{9}Be) one obtains the average residence time of CRs in the Galaxy to be of the order of 10^7 yrs. Particles can be lost either by fragmentation, decay or just leaving the Galaxy to outer space. Since they travel with relativistic speed the long residence time requires that they cannot move rectilinear to outer space, but must be scattering many times without losing too much energy. During their journey CRs may interact with the gas in the Galaxy and produce secondary particles. The ratio of secondary/primary particles, like the B/C ratio is a measure for the amount of traversed matter (grammage) by CRs during their lifetime [30, 69, 70, 71].

So, with light nuclei ratios it's possible to improve the accuracy of GALPROP, DRAGON (Fig. 3) and other propagation programs which numerically solve the cosmic ray propagation [141, 143].

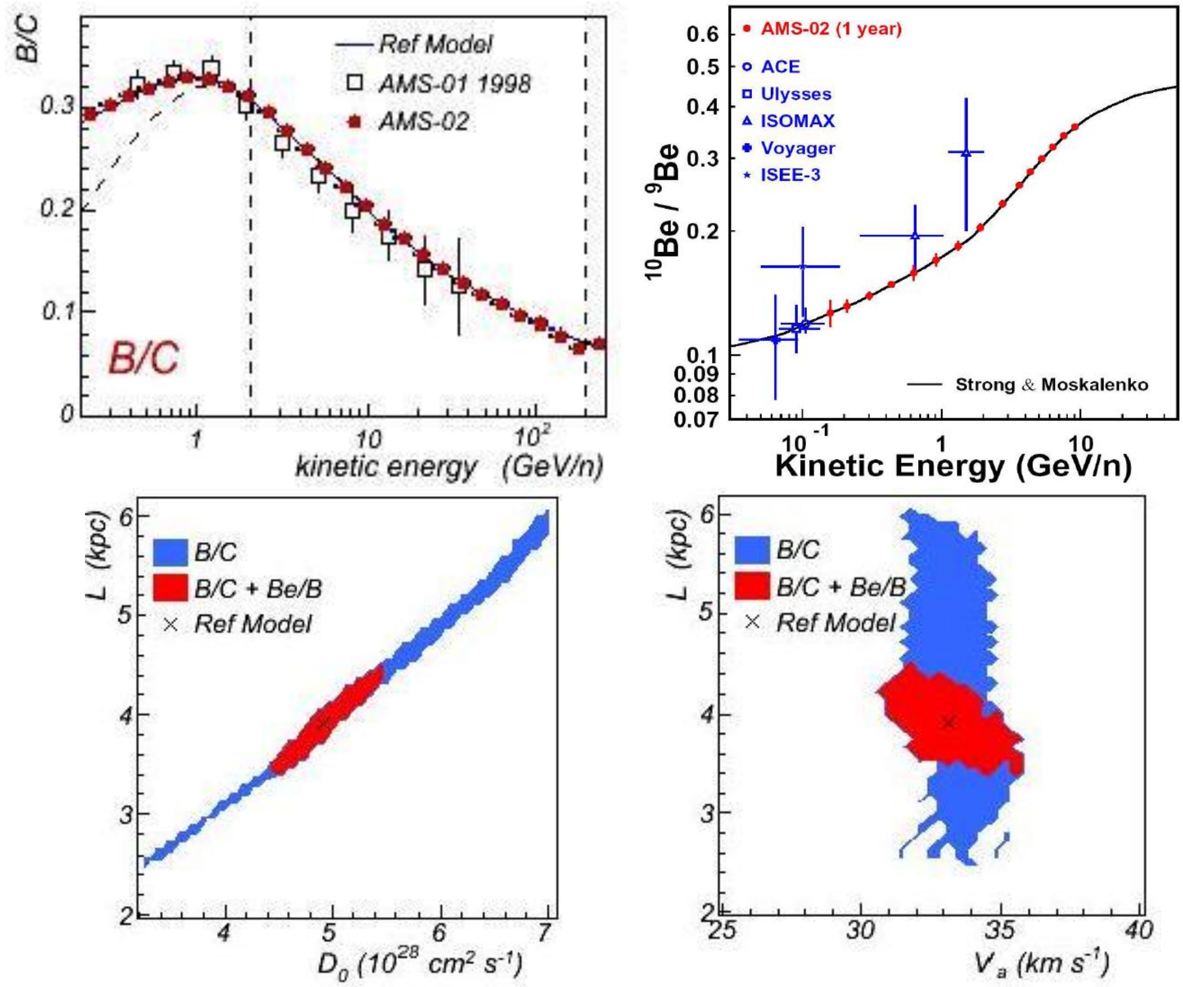

Figure 3 - Expected AMS-02 measurements of B/C (upper left) and ^{10}Be/^{9}Be (upper right) ratio after one year are compared to recent measurements. From B/C the average grammage can be deduced, i. e. the amount of matter traversed by the CR; from ^{10}Be/^{9}Be the average residence time in the Galaxy. In the lower row the expected constraints on the height of the magnetic halo L as a function of the diffusion coefficient D_0 (K_0 in this dissertation, also called D_{xx} in GALPROP) and the Alfvén speed of plasma waves V_a, obtained from the measured B/C and Be/B ratios after one year [69].

It is common to write fluxes in terms of particle kinetic energy (T) rather than energy (E), so this is done in what follows. In (3.14) the function Q(r, z, T) depends on the injection spectrum as

$$Q(r,z,T) = \frac{1}{2}\langle\sigma v\rangle\left(\frac{\rho(r,z)}{m_{DM}}\right)^2\frac{dN}{dT}. \qquad (3.16)$$

The Hydrogen and Helium number density in the galactic disk are: $n_H = 1/\text{cm}^3$ and $n_{He} = 0.07\ n_H$, respectively. Γ_{ann}(T) describes the depletion of nuclei population due to dissociation after scattering from interstellar Hydrogen and Helium, Γ_{ann} (T) = σ(T)v where

$$\sigma(T) = \{ \begin{array}{ll} 661(1 + 0.0115T^{-0.774} - 0.984T^{0.0151})\text{mb} & T < 15.5 \text{ GeV} \\ 36T^{-0.5}\text{mb}, & T \geq 15.5 \text{ GeV} \end{array} \tag{3.17}$$

$$K(T) = K_0(R(T))^{\delta}, \quad R(T) = \frac{(E(T)^2 - m^2)^{\frac{1}{2}}}{|Ze|}, \quad E(T) = T + m$$

with T in units of GeV. *K₀* sets the overall scale for charged particle diffusion and V_C (Table 2) accounts for a “galactic wind” that pulls charged particles out of the disk. K_0 and V_C for different sets of propagation parameters are listed in Table 2. The solution for the number density of CR’s is given by [65, 134, 142]:

$$\psi(R_{\odot}, 0, T) = \sum_i N_i(0, T) J_0(\frac{R_{\odot}}{R}\xi_i) \tag{3.18 a}$$

where

$$N_i(0, T) = e^{\frac{-V_C L}{2K(T)}} \times \frac{y_i(L)}{A_i \sinh{(S_i L/2)}} \tag{3.18 b}$$

with

$$y_i(T) = 2\int_0^L e^{(\frac{V_c}{2K(T)}(L - z'))} \times \sinh{(\frac{S_i}{2}(L - z'))} q_i(z') dz',$$

$$q_i(z) = \frac{2}{J_1^2(\xi_i)} \int_0^1 \rho Q(\rho, z) J_0(\xi_i \rho) d\rho, \quad \rho = \frac{r}{R}, \tag{3.19}$$

$$S_i = \left(\frac{V_C^2}{K^2(T)} + 4\frac{\xi_i^2}{R^2}\right)^{\frac{1}{2}}, \quad A_i = 2h\Gamma_{ann} + V_C + K(T)\coth{(S_i L/2)}$$

where ξ_i are the zeros of Bessel J_0. The cosmic ray flux at the Sun is given by

$$\Phi(R_{\odot}, 0, T) = \frac{v(T)}{4\pi}\psi(R_{\odot}, 0, T). \tag{3.20}$$

Finally, to relate the flux at the Sun’s position to the flux at Earth, the effect of solar modulation must be taken into account. Solar modulation reduces the flux of low energy cosmic ray species. We take into account solar modulation using the Gleeson Axford force field model [30, 65]:

$$\Phi_{\oplus}(T_{\oplus}) = \frac{2mT_{\oplus} + T_{\oplus}^2}{2mT + T^2}\Phi(T), \quad T = T_{\oplus} + e\phi_F. \tag{3.21}$$

When considering whether or not a predicted signal from a primary source is large enough to be significant or not, it is important to understand the astrophysical sources which generate the background, i. e. secondary (and tertiary species), due to protons colliding with interstellar Hydrogen and Helium.

Below, the diffusion model is explained in detail, specifying some features useful for DM fluxes investigation; leptons interactions are treated in 3.7.2.

Spatial diffusion: It has been assumed to be isotropic. Actually, the diffusion coefficient K should be replaced by a tensor, with parallel and transverse components. As regards the first one, there is a strong consensus about a form

$$K_{||}(\mathcal{R}) = K_0\,\beta\,\mathcal{R}^{2-\kappa}\,, \tag{3.22}$$

where κ is the spectral index of the turbulence spectrum, and the normalization K_0 and the spectral index $2-\kappa=\delta$ should ideally be related to the astrophysical properties of the interstellar medium. β is 1 for ultrarelatistic particles. Unfortunately, our knowledge in this field is still demanding, and the value of the two parameters K_0 and δ can only be determined indirectly by the analysis of cosmic ray observations [142].

Geometry: The propagation of cosmic rays ceases to be of diffusive nature beyond some surface where they can freely stream out of the diffusive volume. The density then drops to nearly zero, so that this surface may be considered as an absorbing boundary. The exact shape and dimensions of this boundary are not known, but direct observations of the radio halo of external galaxies suggest that it might radially follow the galactic disc, with a greater thickness. Embedded in this diffusive halo lies the disc containing the stars and the gas . The gas is mostly made of hydrogen (90%), neutral and ionized, and helium (10%) (the heavier nuclei that may be present are of negligible importance). The different components, stars and gas, have different half heights of the order of h ∼ 100 pc; so they all satisfy h ≪ L, so that the disc will be considered as infinitely thin for all practical purposes. Sources and interactions with matter are confined to the thin disc and diffusion which occurs throughout disc and halo with the same strength, is independent of space coordinates. The Solar System is located in the galactic disc (z = 0) and at a Galactocentric distance $R_\odot$ = 8.5 kpc . A schematic view of the galactic model is shown in Fig. 4.

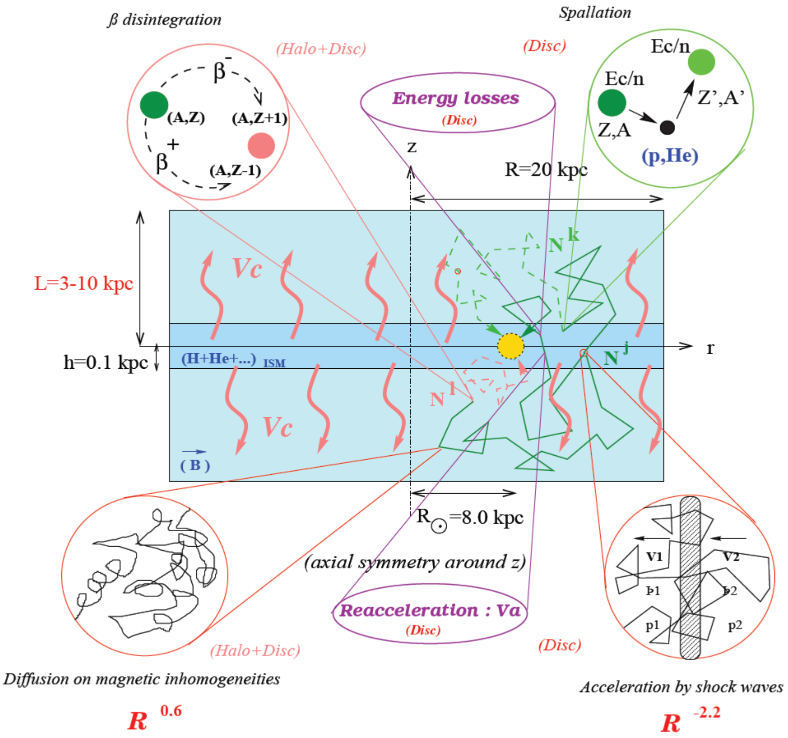

Figure 4 - Schematic view of our Galaxy as well as all propagation steps included in the diffusive model.

Energy losses from interaction with the ISM: There are two types of energy losses which are relevant for nuclei: ionization losses in the ISM neutral matter and Coulomb energy losses in a completely ionized plasma, dominated by scattering off the thermal electrons. The other effects are bremsstrahlung, synchrotron radiation and inverse Compton, which are important for ultrarelativistic leptons (see section 3.7.2). The Coulomb energy loss rate is

$$\left(\frac{dE}{dt}\right)_{\mathrm{Coul}} \approx -4\pi r_e^2 c m_e c^2 Z^2 n_e \ln\Lambda \frac{\beta^2}{x_m^3+\beta^3} \ , \tag{3.23}$$

In these expressions r_e and m_e denote the classical radius and rest mass of the, $\langle n_e \rangle \sim 0.033$ cm^{-3} and $T_e \sim 10^4$ K denote the density and temperature of the interstellar Electrons, Z and M are the charge and mass numbers of the incoming nucleus and lnΛ ~ 40 ÷ 50 is the Coulomb logarithm. The relativistic expression giving the ionization losses is

$$\left(\frac{dE}{dt}\right)_{\mathrm{Ion}} (\beta \geq \beta_0) \approx -\frac{2\pi r_e^2 m_e c^3 Z^2}{\beta} \sum_{\mathrm{s=H,He}} n_s B_s \tag{3.24}$$

where

$$B_s \equiv \ln\left(\frac{2m_e c^2 \beta^2 \gamma^2 Q_{\max}}{I_s^2}\right) - 2\beta^2 \ ; \tag{3.25}$$

$$Q_{\max} \equiv \frac{2m_e c^2 \beta^2 \gamma^2}{1+[2\,\gamma\, m_e/M]} \ ; \tag{3.26}$$

and βc ~ 0.01c is the typical velocity of bound electrons in the hydrogen atom, I_s is the geometrical mean of all the ionization and excitation potentials of the considered atom, (I_H = 19 eV and I_{He} = 44 eV), $M \gg m_e$ is the incident nucleon mass, and n_s is the density of the target atom in the ISM.

Adiabatic losses from convective wind: Among the phenomena affecting the propagation of cosmic rays, the magnitude of those presented here are more subject to debate because of the uncertainty associated to parameters V_c and V_a. It is very likely that the medium responsible for diffusion is moving away from the disc, with a velocity V_c. This is referred to as convective or galactic wind, in analogy with the Solar wind. One of the effects of this galactic wind is to dilute the energy of the particle located in the disc in a larger volume. This adiabatic expansion results in a third type of energy loss, depending on $\nabla \cdot V_c$. It is considered to be perpendicular to the disc plane and to have a constant magnitude throughout the diffusive volume, so that $dV_c/dz = 0$ except at z = 0 where a discontinuity occurs, due to the opposite sign of the wind velocity above and below the galactic plane. In this case, the dilution effect on the energy is given by a term that can be expressed in the same form as ionization and coulomb losses

$$\left(\frac{dE}{dt}\right)_{\mathrm{Adiab}} = -E_k \left(\frac{2m+E_k}{m+E_k}\right) \frac{V_c}{3h} \ . \tag{3.27}$$

E_k stands for the total kinetic energy. It must be emphasized that this term corresponds to a process occurring only in the disc but not in the halo.

Reacceleration: Along with a the spatial diffusion coefficient K, the complete propagation equation also contains the momentum diffusion coefficient K_{pp}; both are related to the diffusive nature of the process. The latter coefficient K_{pp} is related to the velocity of disturbances in the hydrodynamical plasma, called Alfvén velocity. From the quasi-linear theory, it is given [65, 67]

$$K_{pp} = \frac{h_{\rm reac}}{h} \times \frac{4}{3\delta(4-\delta^2)(4-\delta)} {V_a}^2 p^2 / K(E).$$

In this expression, h_{reac} stands for the half-height of the cylinder in which reacceleration occurs. The *Full Propagation Equation* can be rewritten in this way, calling $N_j(E) \equiv d\psi_j/dE$

$$\begin{aligned} -\vec{\nabla}\left[K\vec{\nabla}N^j(E) - \vec{V_c}N^j(E)\right] - \Gamma^j N^j \\ -\frac{(\vec{\nabla}.\vec{V_c})}{3}\frac{\partial}{\partial E}\left[\frac{p^2}{E}N^j(E)\right] = \mathcal{Q}^j(E) + \\ \frac{\partial}{\partial E}\left[-b_{\rm tot}(E)N^j(E) + \beta^2 K_{pp}\frac{\partial N^j(E)}{\partial E}\right] \end{aligned} \tag{3.29}$$

where the following notation has been used for the total energy loss term $b_{tot} = b_{loss} + b_{reac}$, with

$$b_{\rm loss}(E) = \left(\frac{dE}{dt}\right)_{\rm Ion} + \left(\frac{dE}{dt}\right)_{\rm Coul} + \left(\frac{dE}{dt}\right)_{\rm Adiab} \tag{3.30}$$

and the reacceleration drift term defined as

$$b_{\rm reac}(E) = \frac{(1+\beta^2)}{E} K_{pp} \; . \tag{3.31}$$

We also use a compact notation to describe the most general form for a source term

$$\mathcal{Q}^j(E) = q_0 Q^j(E) + \sum_k^{m_k > m_j} \Gamma^{kj} N^k(0) \tag{3.32}$$

which includes primary sources – normalized abundance q_0, spectrum $Q^j(E)$ – but also secondary sources, coming from spallations or radioactive decay of a heavier species. In fact, when a cosmic ray crosses the disc, it may interact with an interstellar hydrogen or helium nucleus and initiate a nuclear reaction, the spallation. The importance of this effect is governed by the corresponding cross sections. The cross section for a given channel is often referred to as the spallation or fragmentation cross section.

Diffusive magnetic halo: Many aspects of cosmic rays propagation call for the existence of an extended magnetic halo. First, clear evidences were obtained from non–thermal radio emission in NGC 4631. Two components of the galactic magnetic field coexist: a regular one (average value about a few µG, parallel to the galactic plane, responsible for confinement) and a stochastic one which is responsible for charged nuclei diffusion (as well as diffusive reacceleration), that has about the same strength. In the last ten years, several studies tried to constrain the halo size using a combination of stable plus radioactive nuclei ratio measurements. They found L ~ 4 kpc [65].
As all the authors used quite different diffusion parameters, with or without wind, reacceleration, and as they took quite different diffusion slopes δ, the trend seems to favor small halos. However, the radial γ-ray distribution in our Galaxy is rather flat, which points towards a large halo. It's possible to propose more complex diffusion models, where some quantities, such as galactic wind, have a spatial dependence.

Solar modulation: The cosmic rays that are detected at Earth atmosphere had to penetrate the Solar cavity, a process by which they lose energy. This phenomenon is called Solar modulation and may be pictured as follows. The Sun emits low energy particles in the form of a fully ionized plasma having $v \sim 400$ km s^{-1}, basically low energy electrons and protons ($E \sim 0.5$ MeV). Once the plasma has left the corona, the dynamic pressure of this wind dominates over the magnetic pressure through most of the solar system, so that the magnetic field lines are driven out by the plasma. The combination of the outflowing particles motion with the Sun's rotation leads to a spiral pattern for the flow. This so-called Solar wind shields the Solar cavity from penetration of low energy CR. The region of space in which the solar wind is dominant is called *heliosphere*. The charged particles that penetrate the heliosphere are diffused and energetically influenced by the expanding solar wind. As this effect involves all the cosmic rays that are detected at Earth (or in near space), it must be taken into account for interpretation of the measured spectra. The energy spectrum of CRs in the solar system is in general modulated for energies up to several GeV/n.

It was first studied by Parker who established the evolution of the flux in the Solar cavity. Analog to the propagation in the Galaxy, it is a diffusion equation in a quite different geometry (spherical). For practical purposes, this equation can be solved numerically, or one can use the force-field approximation [72, 73, 74].

Force-field: Perko provided a useful and compact approximation to the full modulation equation. The final result for a nucleus with charge Z and atomic number A is a mere shift in the total energy

$$E^{\mathrm{TOA}}/A \;=\; E^{\mathrm{IS}}/A \,-\, |Z|\,\phi/A \;. \tag{3.33}$$

Here E^{TOA} and E^{IS} correspond to the top-of-atmosphere (modulated) and interstellar total energy, respectively. The Solar modulation parameter ϕ has the dimension of a rigidity (or an electric potential of the solar wind radial field), and its value varies according to the 11-years Solar cycle, being greater for a period of maximal Solar activity. The equivalent quantity used in (3.33) is $\Phi = |Z|\ \phi/A \simeq 1/2\phi$. Once the momenta at the Earth p^{TOA} and at the boundaries of the heliosphere p^{IS} are determined, the interstellar flux of the considered nucleus is related to the TOA flux according to the simple rule

$$\frac{\Phi^{\mathrm{TOA}}\left(E^{\mathrm{TOA}}\right)}{\Phi^{\mathrm{IS}}\left(E^{\mathrm{IS}}\right)} \;=\; \left\{\frac{p^{\mathrm{TOA}}}{p^{\mathrm{IS}}}\right\}^{2} \;. \tag{3.34}$$

The determination of the modulation parameter ϕ is totally phenomenological and suffers from some uncertainties. It may be interpreted as the characteristic energy loss, per charge unit, of CR particles in the heliosphere. Its value ranges between $\sim$ 300MV (solar minimum) and $\sim$ 1500MV (solar maximum), depending on the solar activity conditions. More refined models includes curvature, gradient and drifts effects. Such models describe the modulation dependence on the charge sign of CR particles and magnetic polarity of the solar wind.

The effect of Solar modulation may be decoupled from the problem of interstellar propagation.

An example of modulated Local Interstellar Spectrum (LIS) is illustrated in Fig. 5.

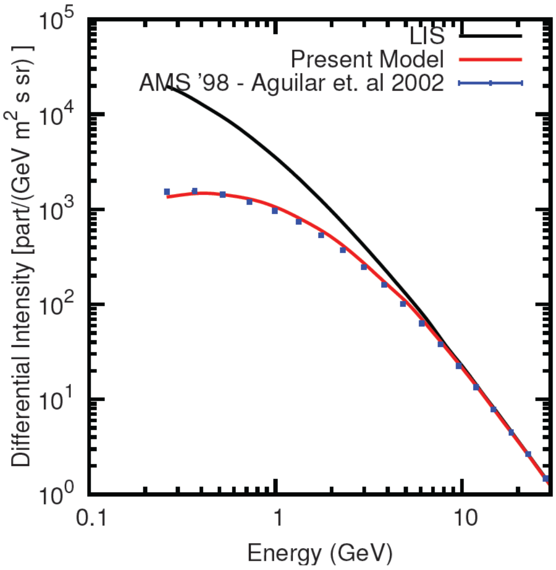

Figure 5 - Interstellar (black) and solar modulated (red) proton spectrum [74]. LIS stands for Local Interstellar spectrum (100 MeV-10 GeV energy range) [390].

Earth Magnetosphere

The last obstacle for cosmic rays before being detected by an Earth orbiting detector is the Earth magnetosphere, that extends its influence on the cosmic radiation modulating the low-energy part of the observed spectra (up to ~15÷20 GV of rigidity).

To first approximation, the geomagnetic field can be represented as an offset and tilted dipole field with moment $M = 8.1 \cdot 10^{25}$ G·cm^3, an inclination of 11° to the axis of Earth rotation and a displacement of about 400 km with respect to the Earth center. Because of the offset, the geomagnetic field, for a fixed altitude from the ground, is characterized by distortion, the highest of which is in the South Atlantic, where the field strength is the weakest. The charged particles penetrate deeper in this region and the radiation becomes stronger. This high radiation phenomenon (Fig.6) is the so called *South Atlantic Anomaly* (SAA).

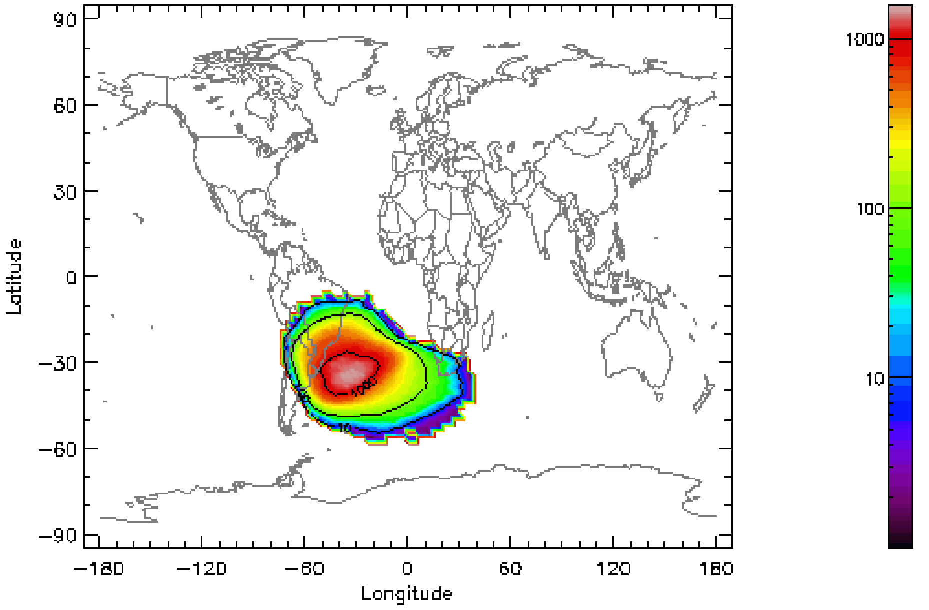

Figure 6 – The SAA (red) projected on the geographic surface with a relative CR particle rate. The SAA is the area where the Earth's inner Van Allen radiation belt comes closest to the Earth's surface dipping down to an altitude of 200km, leading to an increased flux of energetic particles [75, 294]. The SAA magnetic field worth 25000 nT against the normal value of 45000 nT [392].

The most important aspect for CR measurements is the determination of the **geomagnetic cut-off**. Charged particles traversing the magnetic field experience the Lorentz force that produces a curved path for low rigidity particles. Cosmic rays can thus be prevented from reaching a space detector, depending on their rigidity and incoming direction.

For a CR particle directed toward the Earth, the screening is determined by its rigidity, the detector location in the geomagnetic field and its incoming direction. Conversely, for given arrival direction and location, there will exist a minimum value of the particle rigidity R_C for which galactic CRs are allowed to penetrate the magnetosphere and be detected. In the dipole approximation, the rigidity cut-off *RC* was analytically evaluated by Störmer that found the relation [75, 76, 294]:

$$R_c = \frac{M\cos^4\lambda}{R_e^2\left[1+(1\pm\cos^3\lambda\cos\phi\sin\xi)^{\frac{1}{2}}\right]^2} \tag{3.35}$$

where M is the dipole moment. The arrival direction is defined by ξ and ϕ, respectively the polar angle from local zenith and the azimuthal angle counted clock-wise form local magnetic East. The ± sign applies to negatively/positively charged particles. The arrival location is defined by the geomagnetic coordinates (R_e,λ), a commonly used coordinate system relative to the dipole axis. R_e is the distance from the dipole center expressed in Earth radii units, and λ is the latitude along the dipole. These quantities come from the simple dipole field description, where the components of the field are:

$$B_r = -\frac{M}{r^3}2\sin\lambda$$

$$(3.36)$$

$$B_\lambda = \frac{M}{r^3}\cos\lambda$$

and the field lines have the form $r \propto cos^2\lambda$. For vertical incidence (ξ = 0) the azimuthal dependence of the cut-off simply vanished, putting in evidence the cutoff behavior as a function of the geomagnetic latitude:

$$R_{VC} = \frac{M}{4R_e^2}\cos^4\lambda \equiv \frac{M_0}{R_e^2}\cos^4\lambda \tag{3.37}$$

where M_0 = 15 if R_{VC} is measured in GV . The cut-off is maximum at the geomagnetic equator, with a value of approximately 15 GV, and vanishes at the poles. A more precise description of the cut-off can be obtained by replacing the dipole coordinates (GM) with the Corrected GeoMagnetic coordinates (CGM). The method consists in defining an opportune transformation GM ↔ CGM that maps a more realistic geomagnetic field model into the dipole representation.

The most commonly used geomagnetic field model is the DGRF/IGRF one. In this picture, a rather complex magnetic field *B* is treated as the derivative of a scalar potential *V*, $B = -\nabla V$, with *V* expressed by a series of spherical harmonics [76, 294]:

$$V = \bar{R}_E\sum_{n=0}^{\infty}\left(\frac{\bar{R}_E}{r}\right)^{n+1}\sum_{m=0}^{n}P_n^m(cos\theta)(g_n^m\,cos(m\psi)+h_n^m\,sin(m\psi)) \tag{3.38}$$

where $\bar{R}_E$ is the mean Earth radius (6321.2 km), r is the geocentric radius, θ is the geographic colatitude and ψ is the East longitude from Greenwich. $P_n^m(cos\theta)$ are the Legendre polynomial functions, g_n^m and h_n^m are the Gaussian coefficients that specify the geomagnetic field, determined experimentally. The DGRF/IGRF model is widely used in geophysics and contains coefficients up to order 12. The dominant terms in Eq. (3.38) are related to *n* = 1, that leads to the simple dipole field.

By definition, the CGM coordinates (latitude, longitude) of a point in space are computed by tracing the DGRF/IGRF magnetic field line through the specified point to the dipole geomagnetic equator, then returning to the same altitude along the dipole field line and assigning the obtained dipole latitude and longitude as the CGM coordinates to the starting point. At the near-equatorial region, where the magnetic field lines may not reach the dipole equator and where, therefore, the standard definition of CGM coordinates is irrelevant, a different approach based on a B_{min} value along the given magnetic field line can be used. The procedure evaluates also a CGM altitude (the distance from the center of the "effective" magnetic dipole). Using the CGM coordinates allows to use Störmer equations in a more realistic IGRF framework.

3.2.2 DM Indirect detection

Dark Matter annihilation or decay into Standard Model particles produces CRs, photons, and neutrinos. CRs and gamma rays have been measured by many experiments, but the detection of high-energy neutrinos from extraterrestrial sources has so far proved elusive.

The experiments dedicated to the study of charged particle CRs ranged from deep space probes such as: NASA's Advanced Composition Explorer ACE (Stone et al., 1998, for description), to orbiting particle detectors such as PAMELA (Picozza et al., 2007), to massive balloon payloads, e.g. BESS (Shikaze et al., 2007), to enormous ground-based arrays such as the Pierre Auger Observatory (Abraham et al., 2004). Gamma-ray instruments also operate in space, such as EGRET (Thompson et al., 1993) on the Compton Gamma Ray Observatory, the Fermi Large Area Telescope (Fermi-LAT; Atwood et al., 2009), and AGILE (Tavani et al., 2008); and on the ground, e.g. the Imaging Air Cherenkov Telescopes (IACTs), High Energy Stereoscopic System HESS (Hinton, 2004), Major Atmospheric Gamma Imaging Cherenkov telescope (MAGIC; Ferenc et al., 2005), and Very Energetic Radiation Imaging Telescope Array System (VERITAS; Weekes et al., 2002). Meanwhile, IceCube (Halzen & Klein, 2010) is inaugurating the era of neutrino astronomy.

The detectability of a DM signal from annihilation or decay depends on the types of Standard Model particles, their energies and where they are produced [77, 78, 79, 80, 176]. Particle physics describes the source spectrum for Standard Model particle species in terms of a sum over all possible annihilation final states *f*, each with branching fraction $B_{f,s}$:

$$\Phi_s(E) = \frac{1}{4\pi}\frac{\langle\sigma v\rangle}{2M_\chi^2}\sum_f \frac{dN_f}{dE}B_{f,s}\,, \tag{3.39}$$

where E is the secondary particle energy, M_χ is the WIMP mass, and dN_f/dE is the production rate per annihilation of species *f*. Substituting $\langle\sigma v\rangle/2M_\chi^2 \to \Gamma/M_\chi$, where Γ is the annihilation/decay rate, gives the corresponding production spectrum for decaying DM.

DM may annihilate or decay to any of the Standard Model particles: quarks, leptons, or gauge bosons (W, Z, gluon, photon).

For annihilations the final state is often a particle and its antiparticle, though for either annihilations or decays the final state can be more complicated, e.g., three-body. Most of these particles decay rapidly, leaving only the few stable particles and their antiparticles: photons, protons and antiprotons, electrons and positrons and the three flavors of neutrino. Note that it may also be possible to produce a deuterium or anti-deuterium nucleus, which may be detectable with AMS-02 (see 3.4.2).

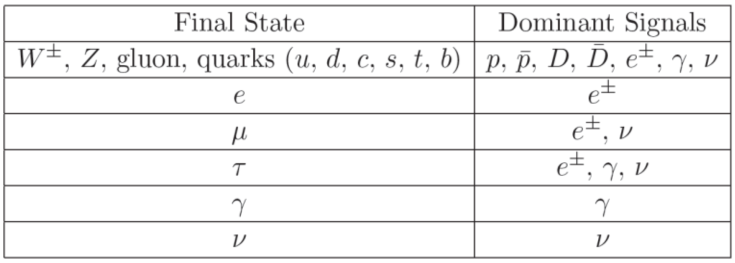

Final State	Dominant Signals
$W^{\pm}$, Z, gluon, quarks (u, d, c, s, t, b)	p, $\bar{p}$, D, $\bar{D}$, $e^{\pm}$, γ, ν
e	$e^{\pm}$
μ	$e^{\pm}$, ν
τ	$e^{\pm}$, γ, ν
γ	γ
ν	ν

Table 3 - The first column shows the possible Standard Model particles that DM could annihilate or decay into. The second column shows the dominant indirect detection signals that arise from these final states.

At a smaller level almost every possible signal can be produced by any final state through loop corrections, final state radiation, and inverse-Compton scattering. Theoretically, each different possible final state can produce a different experimental signature. Even if only two-body final states are counted (particle-antiparticle) this would be 16 possible final states. However, in practice, most of the final states produce similar signatures and are often grouped together when setting experimental limits. So as an approximation it is often sufficient to consider only five types of final states. First, those that contain quarks or the W, Z, or gluon. All these decay through quantum chromodynamical processes, ultimately producing hadrons: $p/\bar{p}$, and pions (also, possibly $d/\bar{d}$). The π^0s decay to gamma rays, while the $\pi^{\pm}$ decays produce $e^{\pm}$.
Second are states with $e^{\pm}$s or $\mu^{\pm}$s, which dominantly produce a hard $e^{\pm}$ spectrum, with the $\mu^{\pm}$ decays also producing ν_e and ν_{μ}. Third, are final states with $\tau^{\pm}$. These produce a softer $e^{\pm}$ spectrum and a strong neutrino signal. In addition, the $\tau^{\pm}$ can decay hadronically to pions (but, never protons) and thus can also produce a strong gamma-ray signal. Fourth, if there is a photon in the final state it produces a strong gamma-ray signal with a hard spectrum and often either a sharp edge, or in the case of a two-body final state, a line in the gamma-ray spectrum. Lastly, states with neutrinos dominantly produce only a hard neutrino spectrum as they do not decay. This is summarized in Table 3. Secondarily, as said, each of these final states can also produce every other type of particle. However, this is at a much smaller level than the dominant production modes [78, 79].
If only a specific model (e.g., a supersymmetric or an extra-dimensional model) is considered, then the experimental limits on DM annihilation or decay can be derived for the particular final states predicted by that model, according to the source equation. When setting general experimental limits it is preferable to express them for a few representative final states, so that they are as model independent as possible.

3.3 PAMELA, FERMI: a starting point

PAMELA is an orbiting detector dedicated to CR measurements that was launched in 2006. It consists of a magnetic spectrometer, an anticoincidence system (to veto particles entering through the sides of the spectrometer), a time-of-fight system, an electromagnetic sampling calorimeter of 16.3 radiation lengths thickness, a showertail-catcher scintillator, and a neutron detector. Its spectrometer can measure the momentum and charge sign of charged CR particles, while the time-of-fight system, calorimeter, and neutron detector serve to identify the particle type. Its acceptance for electrons is small compared to those of ATIC and the Fermi-LAT (see below), but it is able to separate electrons from positrons cleanly up to 270 GeV·c^{-1} momentum by means of the magnetic spectrometer [81].

NASA's **Fermi-LAT**, launched in 2008, is the preeminent gamma-ray telescope in the energy range above ~ 100 MeV. It is a pair-conversion telescope, like its immediate predecessor EGRET and its much smaller contemporary AGILE, launched in 2007. Thirty-six layers of silicon-strip detectors interleaved with tungsten foils pair-convert the gamma rays and track the resulting electrons and positrons. The tracking section is followed by a segmented CsI crystal calorimeter that measures the energy of the electromagnetic shower. A veto-counter system, based on segmented scintillator tiles, helps to tag charged CRs and, together with the detailed event reconstruction in the tracker and calorimeter, reduce that background by at least five orders of magnitude. The tracking resolution is generally limited by multiple scattering of the electrons and positrons in the tungsten foils and other material, giving a point-spread function (PSF) with 68% containment angles for individual photons ranging from a few degrees at 100 MeV down to about 0.1° for energies $\gtrsim$ 10 GeV [79, 82].

The Fermi-LAT has an extraordinarily large field of view of 2.4 sr, thus seeing nearly 20% of the entire sky at any instant. It normally operates pointing outward from the Earth, scanning the sky, and achieves a fairly uniform exposure over 4π·sr by rocking back and forth by 50° toward one orbital pole or the other on successive orbits. Its all-sky view together with its excellent signal-to-noise and large energy range, from ~ 100 MeV to beyond 300 GeV, make it very well suited to searches for DM annihilation in all types of possible sources, point-like or diffuse, Galactic or extragalactic.

The Fermi-LAT is also a very capable CR electron detector. It has no atmospheric overburden and already has an exposure at least 200 times larger (depending on energy) than that of ATIC.

3.3.1 The positron-antiproton anomaly

The PAMELA instrument team has reported measurements of the antiproton spectrum and fraction [83, 84, 85], and the positron fraction [86, 87]. Figure 7a) shows the combined measurements of the CR antiproton fraction as of late 2010, whereas Figure 7b) shows the antiproton spectrum as measured by many experiments up to PAMELA data.

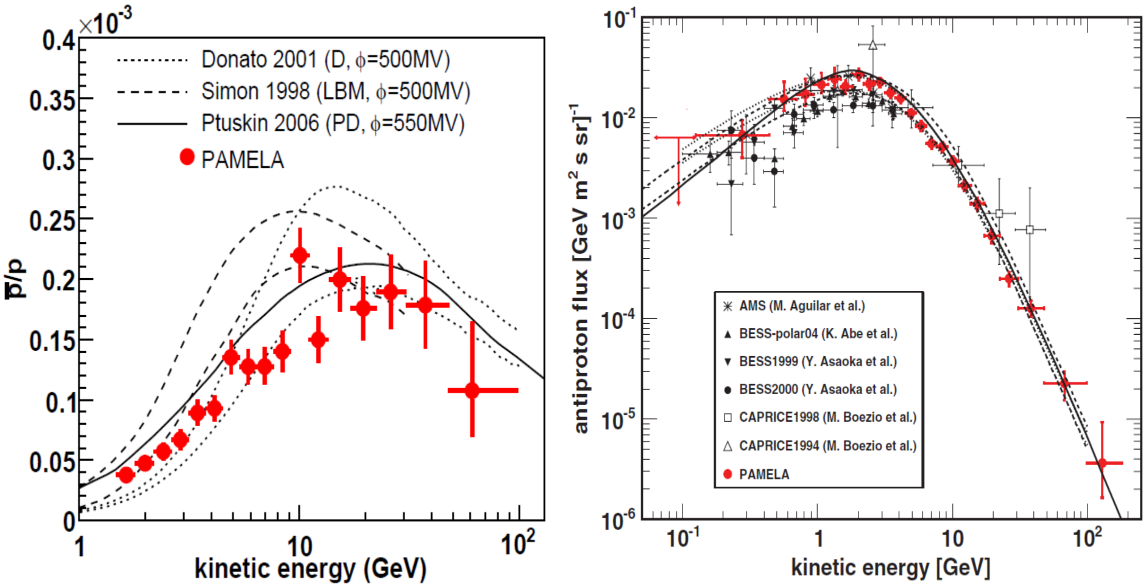

Figure 7 – a) Antiproton on proton flux ratio and b) antiproton flux measured by PAMELA.

For antiprotons, the curves correspond to models with different assumptions for the treatment of CR propagation, uncertainties in the assumed propagation model parameters, and cross section uncertainties for antiproton production, annihilation, and scattering. Experimental data show a perfect secondary spectrum with nonexotic astrophysical origins.

However, the PAMELA positron fraction (i. e. the $e^+/(e^+ + e^-)$ fluxes ratio) rises with increasing energy, opposite to the expected behavior of secondaries produced in the ISM: it is at the level of 5% at 10 GeV and 10% at 100 GeV (Fig.8). In fact, the production spectrum for the secondary positrons and electrons in the ISM follows the parent CR nuclei spectrum, which has the power-law index ~ 2.7. The primary CR electrons produced in, e.g., supernova remnants, outnumber the secondaries by a factor 10 or more, depending on energy. The primary electrons have source spectra typically flatter than the secondary positrons by $\sim 0.3 \div 0.5$ index. While propagation and energy losses further steepen the spectra, these effects are independent of charge sign, so the positron fraction from this process falls with increasing energy proximately as the ratio of the source spectra [87]. CR nuclei interacting with gas in the ISM cannot easily explain a positron fraction that rises with increasing energy.

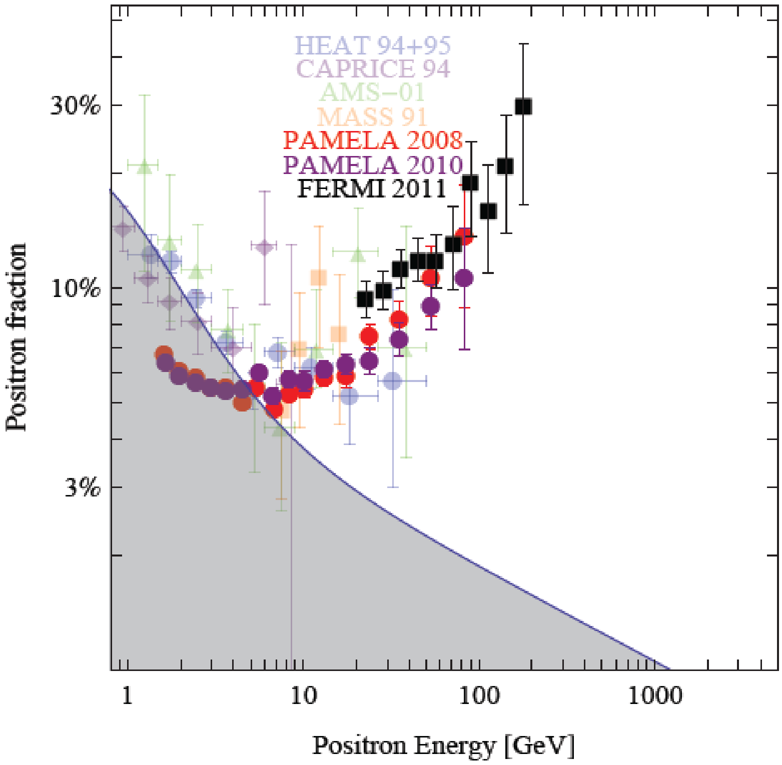

Figure 8 - A compilation of recent and less recent data for positron fraction rays, superimposed on plausible but uncertain astrophysical backgrounds from secondary production [88]. The discrepancy between recent data and the background from 1 GeV to 10÷20 GeV is only due to solar modulation, i. e. the background is plotted for a past solar cycle [390].

The PAMELA's data apparently confirm the results from the earlier HEAT balloon experiment and AMS test flight (although the results of both of those experiments have much larger uncertainties). PAMELA uses its magnetic spectrometer, time-of-fight system (at low energy), calorimeter, and neutron detector for the separation of protons and antiprotons from positrons and electrons. The spectrometer separates the electrons and antiprotons from the positrons and protons (except at the highest energies, where there is some spill-over). The calorimeter is able to separate electromagnetic and hadron-initiated (proton/antiproton) showers very well using information on the longitudinal and lateral shower development. However, early neutral pion production at the

top of the calorimeter by interacting hadrons produces an electromagnetic shower in hadron-initiated events at about the percent level. This makes the separation between true electromagnetic and hadron-initiated events difficult when this occurs because the two look essentially identical in the calorimeter. For the protons and positrons, because the ratio of these particles is large (in favor of the protons) and rises with energy, a slightly larger than expected misidentification of protons could easily lead to a rising positron fraction [79, 89]. The PAMELA collaboration has published details of their analysis, including performance of the particle discrimination [86]. However, some researchers have questioned if sufficient rejection power is obtained by the instrument (Schubnell, 2009) because additional hadron/electromagnetic discrimination systems, like transition radiation detectors, are not used. It would be useful to have the absolute positron spectrum that PAMELA measures to ascertain whether anomalous spectral features also exist in that, but so far it has not been published. These questions will be resolved by follow-up measurements by AMS-02, which is analyzing with unprecedented precision and binning the PAMELA energy range and studying the spectrum fine structure.
Moreover, as it can be seen from Fig. 8, FERMI confirms the PAMELA excess at high energies is larger than the one predicted by models of standard cosmic rays propagation without new primary sources [91].

Furthermore, the positron fraction can be written as

$$f(E) \equiv \frac{1}{1 + (\Phi_{e^-}/\Phi_{e^+})} \tag{3.40}$$

where the fluxes refer to the ones at the top of the atmosphere above 10 GeV (to minimize the charge-dependent solar modulation effects). At the same time, a fit of the PAMELA electron data over the corresponding energy interval provides $\Phi_{e^-} \propto E^{-3.23\pm0.02}$[90]. As a consequence, one could infer an absolute positron spectrum which goes like $\Phi_{e^+} \propto E^{-2.85\pm0.06}$. Now, the proton flux measured by PAMELA itself in the similar energy-range is $\Phi_{e^-} \propto E^{-2.82\pm0.02}$ and it is this hadronic CR spectrum which enters as source for the ISM positron one.
In a pure diffusive propagation framework without dark matter, secondary/primary yields indicate that diffusion alone would steepen the spectrum by about $\delta \simeq 0.4$ [90]. Recent numerical analysis predicts a secondary positron spectrum roughly declining as $\Phi_{e^+} \propto E^{-3.4} \div E^{-3.5}$ in the range of interest, clearly yielding an e^+ fraction inconsistent with the data.

Preliminary works of Drlica-Wagner (2012) of the FERMI-LAT collaboration also show that there's no significant sky anisotropy for e^+ and e^-, which might have been expected from a local source (Fig.9).

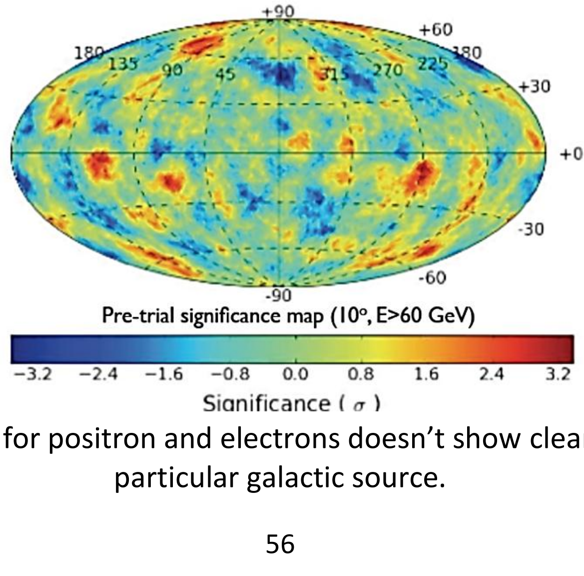

Figure 9 – Correlation map for positron and electrons doesn't show clear anisotropy pointing to a particular galactic source.

In addition, recent measurements of the total lepton spectrum have shown anomalies. Toward the end of 2008 the ATIC collaboration (Chang et al., 2008) announced a surprising result: a bump in the CR electron spectrum in the energy range 300 ÷ 800 GeV, where conventional astrophysical sources are expected to produce a smooth, power-law spectrum. The PPS-BETS experiment [132] detected a similar excess over approximately the same energy range as ATIC [93], although with less statistical significance. See Fig. 10 for the combined measurements of the CR electron spectrum up to the end of 2010. Together with the positron fraction measured by PAMELA, these results stimulated a lot of speculation about the origin of the spectral features.

No discrepancy between AMS-02 and PAMELA are expected in the leptonic channel, except for extremely tiny modulations in the 1 ÷ 10 region, due to not identical, even if similar, solar cycles, for the first two years of AMS activity [“Extreme Space Weather Events", National Geophysical Data Center].

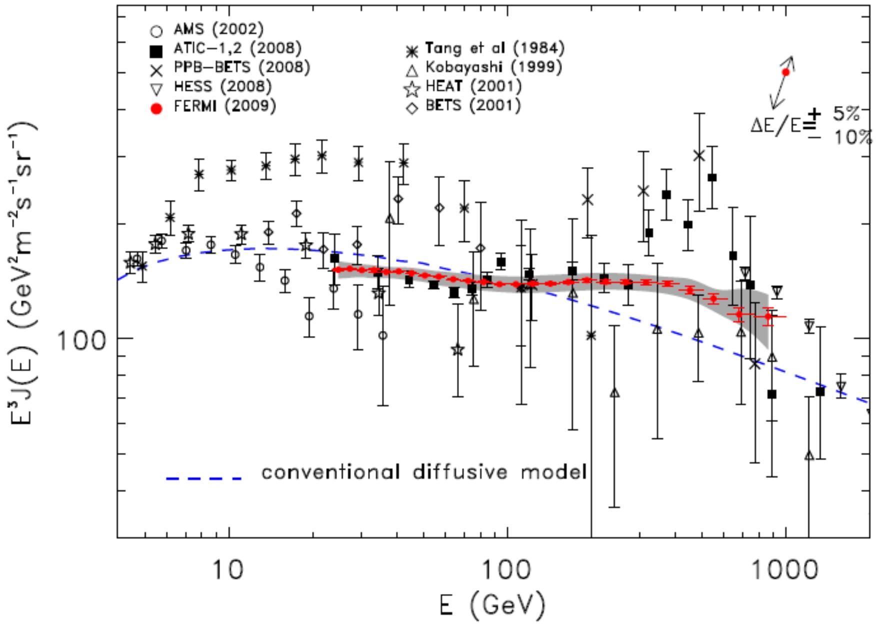

Figure 10 – Total electron plus positron spectrum measured by ATIC, FERMI, HESS and other collaborations [92].

This result is still circumstantial and don’t give us neat information about dark matter, because it’s a total flux. Moreover, as Figure 10 shows, the Fermi-LAT measurement does not show so clearly the anomalous spectral features described by ATIC and PPB-BETS, compatible with a power law. The systematic errors for the Fermi-LAT measurement are shown by the grey band. The dashed line shows the predicted total CR electron and positron spectrum for a diffusive-reacceleration CR propagation model based on CRs and other data measured prior to the Fermi-LAT results. This model was not tuned to the Fermi-LAT measurements and used a CR electron injection spectrum that was a single power law above 100 GeV. So the plot simply illustrates that the data are not well-reproduced by such a simple spectral model [93, 94, 137, 141].

Going back to the positron fraction, the Fermi-LAT and PAMELA data have motivated the construction of DM models to reproduce the apparent features observed by these instruments. Because DM annihilation or decay creates equal amounts of matter and antimatter with a hard spectrum up to the DM particle mass, it can naturally produce a rising positron fraction and has been a widely conjectured explanation of the PAMELA positron data. However, models must also explain several unexpected characteristics of these data, first of all the measured antiproton fraction that does not rise with energy at all. So this tension must be explained and the positron anomaly consistently understood.

Several kinds of non-standard DM models have been developed to fit both the PAMELA and Fermi-LAT data. The Fermi-LAT data provide an upper bound to enhancements in the cross section. These include adding a Sommerfeld enhancement to the cross section due to a hypothetical long-range force, which will be discussed in 3.3.2, a nonthermal production mechanism during the Big Bang (e.g., Nelson & Spitzer, 2010; Fairbairn & Zupan, 2008), or DM decay [95, 96, 97], that implies specious DM theoretical constructions [98, 99].

A different explanation of these CR data could be that the assumptions made estimating the astrophysical background are overly simplified. Any DM signal in CRs exists on a background of particles from astrophysical sources, e.g., supernovae, supernova remnants, pulsars, compact objects in close binary systems, stellar winds, etc. The primary CRs are produced at these sources, eventually escaping to propagate in the ISM of the Galaxy, where their spectra change over tens of millions of years as they lose or gain energy through interactions with the interstellar gas, magnetic fields and turbulence. Their composition also changes as the destruction of primary CR nuclei via spallation on the interstellar gas gives rise to secondary particles, including nuclear isotopes that are rare in nature, antiprotons, and electrons, positrons, and neutrinos from the decays of charged pions, and even modified by the solar wind. So it’s clear that our understanding of CR sources and propagation is limited and uncertainties impact our ability to disentangle DM from astrophysical signals [142] (see 3.7.1 and 3.7.2).

For **modeling CR production from astrophysical sources**, the assumption is usually made that the sources are described by a smoothly varying function of position, and that they have a common characteristic source spectrum. The assumed spatial distribution is typically based on supernova remnant and pulsar survey. That is a cheapish approximation for CR nuclei, which are influenced by selection effects. For CR electrons and positrons the severe radiative losses from interactions with the interstellar gas and magnetic field mean that a source of high-energy electrons must be within ∼ 1 kpc if the detected particles have energies larger than a few hundred GeV. Therefore, assuming a smooth spatial distribution is not correct, and details of the discrete source distribution in the vicinity of the Solar System are important. Also, many authors assume that the ISM is homogeneous, which is incorrect for these particles.

Even at the highest Galactic CR energies (> 100 TeV), where the dominant electron/positron energy losses are IC scattering of the CMB and synchrotron radiation, inhomogeneities in the magnetic field are important. Furthermore, the assumption of a single source spectrum is unrealistic, because there are a variety of production mechanisms for high-energy electrons and positrons: acceleration at shocks and production of secondary electrons/positrons in situ by shock accelerated hadrons, in addition to possible production by DM annihilation or decay.

A more subtle issue is related to the treatment of the inhomogeneous CR lepton source distribution within a particular propagation model [79]. Researchers commonly use the free-space 3-dimensional spherically symmetric analytic diffusion results of Aharonian et al. (1995) to treat the nearby source contribution and then a diffusion model variant (either numerical or analytically solved) with a smooth spatial distribution for the far (> 1 kpc) sources. The problem is that the propagation parameters used to calculate the nearby contribution are obtained from the propagation model used for the far sources. But it may not have the same spatial configuration (2/3-dimensional cylindrical/cartesian), boundary conditions, and/or distributions for ISM components. This inconsistent treatment of the sources and propagation could partially cloud the interpretation of the results.

Given the uncertainties associated with modeling the CR sources, propagation, and so forth, it is possible but not probable that both the PAMELA/FERMI data and the total electron spectrum can be explained by modifying the assumptions usually made when calculating the standard astrophysical background (see 3.7.2). All these astrophysical sources model have a set of fine-tuned parameters that are adjusted to reproduce the observations, depending on the production mechanism intensities, and none of the non-exotic models can be pointed to as the unique solution.

Thus the DM explanations remain the main guide line [88, 91].

All these results can be summarized:

- Data from PAMELA satellite showed a steep increase in the energy spectrum of the positron fraction $e^+/(e^+ + e^-)$ above 10 GeV up to 100 GeV, compatibly with previous hints from HEAT and AMS-01.
- Recently, the positron findings have been confirmed with an independent measurement by the FERMI satellite, and extended to about 200 GeV.
- Data from PAMELA also showed no excess in the $\bar{p}/p$ energy spectrum compared with the predicted background up to 120 GeV.
- The balloon experiments ATIC-2 and PPB-BETS were reporting the presence of a peak in the $e^+ + e^-$ energy spectrum at around 500-800 GeV.
- This sharp feature has been later questioned and superseded by the results of FERMI: while an excess with respect to the expected background is confirmed, the $e^+ + e^-$ spectrum is found to be instead reproduced by a simple power law and a DM decay products mechanism is not necessary.

So it's fundamental to reach a theoretical understanding of this lepton-hadron tension and use AMS-02 data to extend the experimental positron fraction energy range and the antiproton spectrum.

It has to be stressed in advice that the antiproton channel could be more interesting because high energy hadrons are more difficult to produce in astrophysical processes and could give a fundamental hint in favor of dark matter (section 3.7.2).

3.3.2 Dark Matter Mass and Annihilation Cross section

In order to reproduce this tension between leptonic and hadronic results, the properties of the particle dark matter candidate have to be deeply understood, and also under which conditions it's possible to justify experimental observations.

An "excess" in the positron fraction is qualitatively expected in all DM annihilation models; unfortunately, typical "old-style" predictions from WIMP dark matter annihilation fail to reproduce the data in three main aspects [94]:

1. First of all, the peculiar signature for an exotic origin of the signal would rather be a *spectral edge* (more or less sharp, depending on the final state) after an initial rise; this drop back to the expected background at high energies is not observed, neither in the e+ fraction nor reflected as a dip in the $e^+ + e^-$ data.
2. The standard thermal *cross section seems to be surprisingly large*, with a huge annihilation into relatively light final states, compared with typical expectation for a S-wave annihilating thermal relic matching the observed dark matter abundance: i.e. in terms of annihilating

cross sections, $\langle\sigma v\rangle \gg \langle\sigma v\rangle_{S-wave} \approx$ 1 pb. The SUSY low mass neutralino is a Majorana particle and, as such, its (S-wave) annihilation cross section is helicity suppressed by a large factor of $\left(m_f/m_{DM}\right)^2$, where m_f is the fermion final state mass. The scorecard for the neutralino does not look great.

3. Such a large yield of $e^{\pm}$ pairs should imply large yields of high-energy particles in other channels; in particular one expects *anomalies in antiprotons*, then in gamma-rays and possibly neutrinos, while no anomaly has been revealed yet in this respect.

The third problem is a tuning problems, which involves a mere astrophysical constraints net that has to be taken into account to create a correct dark matter scenario. In particular, the fact it hasn't been seen yet an antiproton signal let us exclude the region where $m_{DM} < 150\ GeV$.

The first kind of problem (the spectrum rise and fall) can be overcome by pushing the mass of the DM to values sufficiently higher than the range explored by PAMELA, perhaps to the few TeV scale where the lepton fluxes appears to fall. This fits rather uncomfortably in a theory, such as SUSY, whose typical scale should be close to the mass of the Higgs boson, if naturalness is a valid criterion. Moreover, if no antiproton signal will be detected by AMS-02, **leptophilicness** is to invoke [100, 101], but typical neutralino annihilation channels do not distinguish between leptons and quarks, and often couple to gauge bosons, so a dangerous component of hadrons is generically expected. A leptophilic sector may consist in a Standard Model extension. One way this can happen is if the DM does not annihilate directly to the SM but instead first annihilates to a new unknown state which in turn decays to SM states. If this new state is lighter than the proton, the final state will only contain leptons. Thus, the lack of hadronic final states is determined by the spectrum of new states. There is also instead the possibility that due to a symmetry the new states only have tree-level couplings to leptons but not to gauge bosons or quarks, i. e. there is a dark sector containing a weakly coupled broken U(1)' gauge symmetry, under which only the dark matter state and the leptons are charged [102].

The second problem can be cured introducing a mechanism capable to increase the annihilation cross section and reconcile the very large value of the annihilation rate required to fit the CR excesses (corresponding to $\langle\sigma v\rangle \sim 10^{-23} cm^3/s$) and the smaller value ($\langle\sigma v\rangle \sim 10^{-26} cm^3/s$) individuated by the paradigm of DM production as a thermal relic in the Early Universe. There are three theoretical ways:

- Via an astrophysical **boost factor**: the presence, in today's galactic halo, of DM overdensities predicted by numerical simulations boosts the annihilation rate (proportional to the squared density of DM particles). If the boost could reach a O(10^3) value, this would explain why the rate is much larger today, without modifying the cross section itself. The typical realistic values, however, have been proven to be O(10) at most [103].
- Annihilating via a **resonance** [104]: if the resonance mass is just below twice the DM mass, the annihilation cross section becomes sensitive to the details of the velocity distribution of the DM particles; since (on average) DM particles are slower today than in the Early Universe, many more of them meet the conditions of a Breit-Wigner-like resonant annihilation and therefore the rate is enhanced, if relevant parameters are appropriately fine-tuned. Typically one needs the mass of the resonance to differ by less than 1% from twice the DM mass and the width of the resonance to be of the order of 10^{-5} of its mass, in order to obtain the correct enhancement.

- Thanks to the **Sommerfeld enhancement** [105], a non-perturbative quantum effect which modifies the annihilation cross section in the regime of small relative velocity of the annihilating particles and in presence of an effectively long-range force between them. This is a non-relativistic, non-perturbative enhancement of the plane wave two-body cross section. Indeed, this well-known quantum mechanical effect can occur in DM annihilations if the two annihilating particles exchange an interaction mediated by a force carrier of mass m_ϕ and with a coupling constant $g \approx \sqrt{4\pi\alpha_X}$ such that $\alpha_X m_{DM}/m_\phi \gtrsim 1$, where X denote a single particle dark matter, with $m_\phi/m_{DM} \lesssim 10^{-(2\div3)}$ [106] and $\alpha_X \gtrsim 10^{-2}$. For very heavy DM particles (~ 10 TeV), the exchange of SM weak bosons can mediate the effect, in which case α_X could be just the one of weak interactions and $m_\phi \approx m_Z \approx 100$ GeV. If a new force exists, however, mediated by a scalar particle with mass $m_\phi \approx 1$ GeV and gauge-like coupling strength with DM particles only (with no tree-level couplings to the Standard Model), even DM particles of mass $\lesssim 1$ TeV would enjoy the Sommerfeld enhancement. The enhancement shows an inverse proportionality with the relative velocity of the two particles, and it typically saturates to a maximum value when $v \lesssim 10^{-3}c$.
  It's not known if the **Sommerfeld boson** could give non-tree-level signatures of its existence independent from DM interactions, i. e. if it is "dark" or not. If not, the dark sector ϕ boson could become a *fifth force* with visible impacts [395], unto a hypothetical link between dark matter and dark energy.

Let's focus on this third mechanism, which has a strong theoretical basis, doesn't need fine-tuning and could introduce new physics, due to the interacting boson.
In general, adding the Sommerfeld quantum enhancement [105, 109], the DM annihilation cross section can be rewritten as follow

$$\langle\sigma v\rangle_{ann} \sim a + bv^2 + c\frac{1}{v} \tag{3.41}$$

and the three terms are plotted in Fig. 11 to understand the different effects [95, 105]:

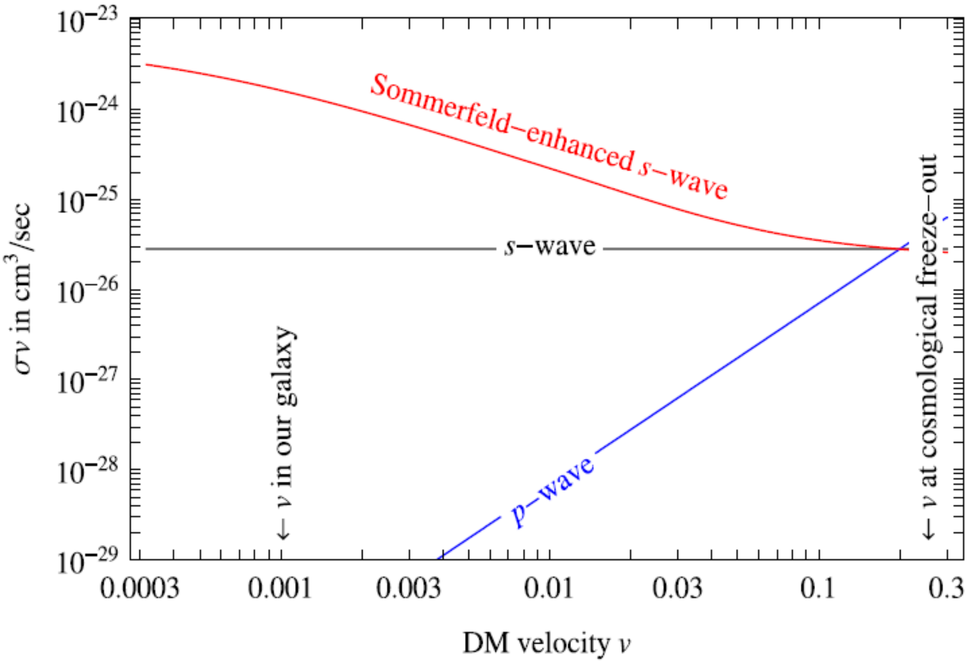

Figure 11 – The three main components of DM annihilation cross section as a function of relative velocity.

As it can be argued, the S-wave is the constant part and corresponds to the usual thermal value. The P-wave is less important and, for low velocity, its contribution disappears. On the other hand the Sommerfeld enhancement increase at low "galactic" velocity and could produce the correct amplification factor, and dark matter freezes out at early times when this effect is negligible. So, the resulting annihilation cross section is $S\langle\sigma v\rangle_{thermal}$, where S is the Sommerfeld factor [107, 109]

$$S = \frac{\pi\alpha_X/(\frac{v}{2})}{1-e^{-\pi\alpha_X/(\frac{v}{2})}} \xrightarrow{\alpha_X \gg v} \frac{2\pi\alpha_X}{v} \tag{3.42}$$

The Sommerfeld factor and the total cross section could be related with DM candidate mass (Fig.12 and Fig. 13).

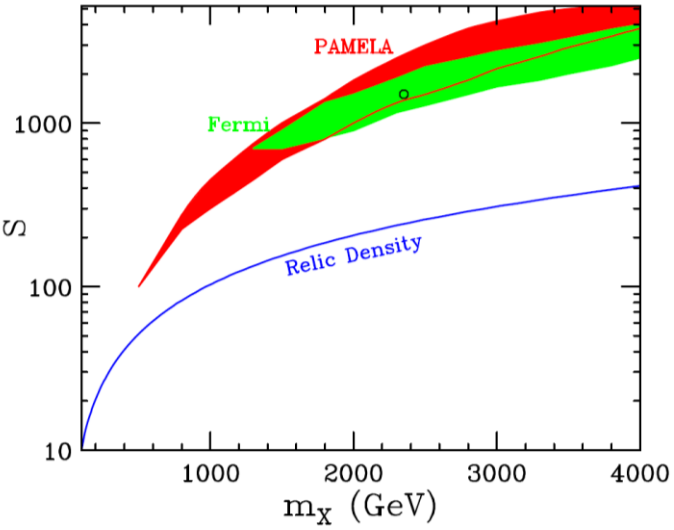

Figure 12 – Sommerfeld enhancement factor as a function of DM mass, with the regions favored by PAMELA (red) and FERMI (green). For a multi-TeV DM the Sommerfeld factor reach the request value of 10^3 [3].

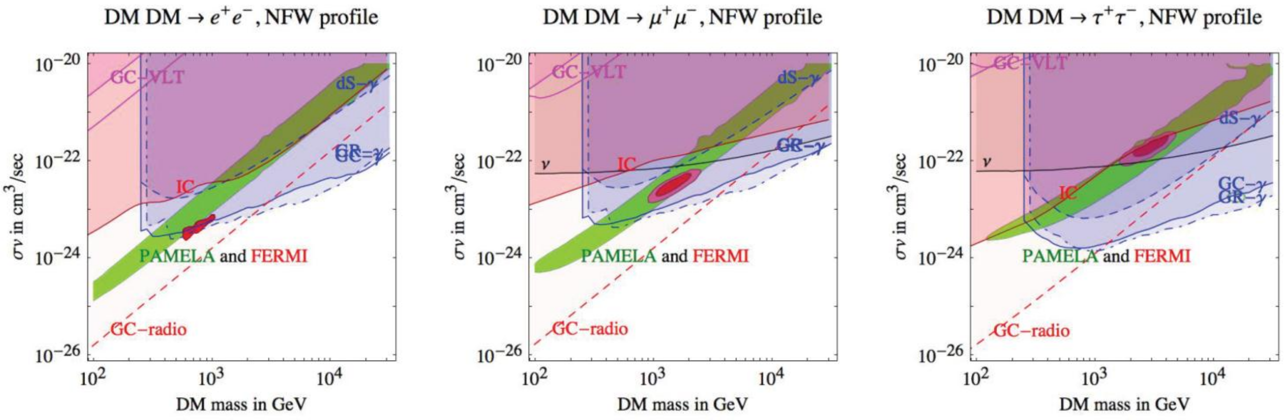

Figure 13 – Comparison between the region favored by PAMELA (green bands) and by PAMELA, FERMI and HESS observations (red ellipses) and other experiments and astrophysical measurements. For a multi-TeV DM the region with $\langle\sigma v\rangle \sim 10^{-23} \div 10^{-22} cm^3/s$ is favored [110].

From a Feynmann diagram point of view, the WIMP interact with the new boson with a multi-box diagram, depicted in Fig. 14, and produce more light leptons than expected.

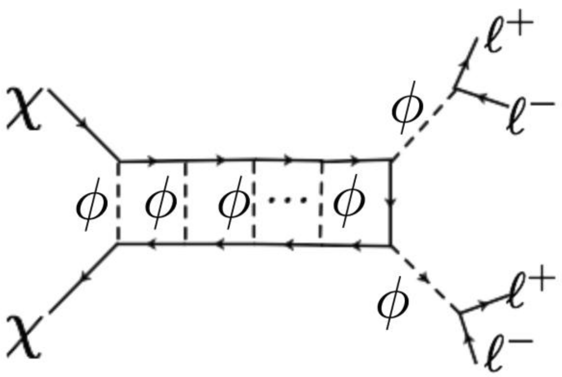

Figure 14 – Feynmann diagram for the Sommerfeld enhancement.

In a certain way, this argument has already been complicated by **cosmological observations**.
The basic physics mechanism is that DM annihilations inject energy and energetic particles in the primordial medium, and therefore affect its evolution. The constraints come essentially from two cosmological probes: Big Bang Nucleosynthesis (BBN) and the Cosmic Microwave Background.
The injection of electromagnetic radiation or high-energy hadrons during or after BBN can have several effects on the newly formed light nuclei, destroying some species and overproducing others, therefore altering their final abundances and spoiling the agreement with observations. The upper bounds for the annihilation cross section found for several models and data samples [111, 112] vary in the range $10^{-23} \div 10^{-21}$ cm^3/sec for a 1 TeV DM mass, depending on the DM annihilation channel and the light element which is used. They lie therefore quite above the value of the thermal cross section and they are also generically not strong enough to significantly constraint the DM interpretation of the charged CRs excesses.
Concerning CMB, the actual physical effect of energy injection around the recombination epoch is that it ionizes the gas and therefore results in an increased amount of free electrons, which survive to lower redshifts and affect the CMB anisotropies. From these studies several interesting constraints come out (Fig.15).

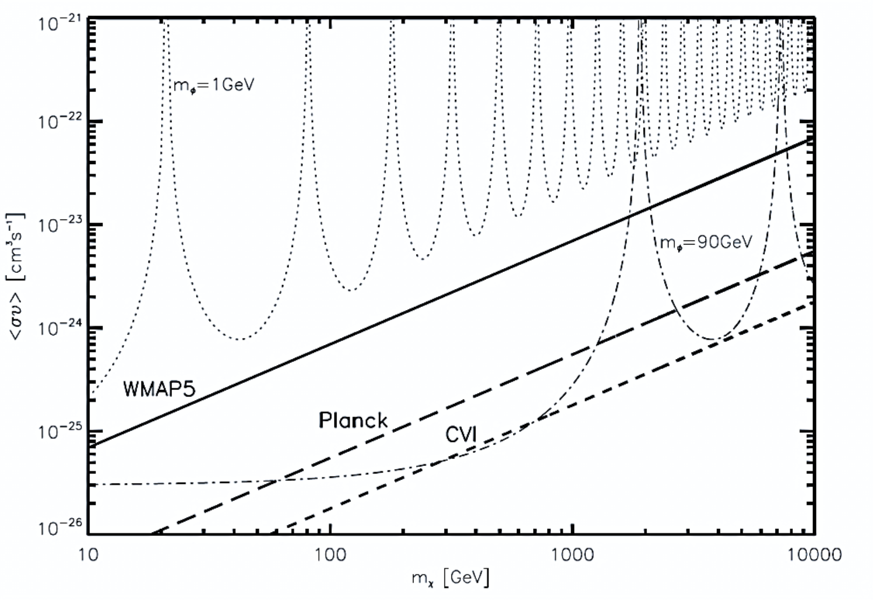

Figure 15 - Constraints on the self-annihilation cross section at recombination. Regions above the solid (/long dashed/short dashed) thick lines are ruled out by WMAP5 [136] (/Planck forecast/Cosmic Variance limited); the thin dotted and dashed-dotted lines are the predictions of

the Sommerfeld enhanced self-annihilation cross sections with force carrying bosons of m_ϕ = 1 GeV and m_ϕ = 90 GeV respectively [113, 114].

You note from Fig. 15 that very light Sommerfeld bosons have already been excluded by cosmological evidences and future experiments will provide great constraints, several order of magnitude more stringent than other astrophysical ones. Two jumps are evident with a 90 GeV scalar mediator, for a ~ 2 TeV and 8 TeV dark matter, which lead to an annihilation cross section of the order of $10^{-23} \div 10^{-21}$ cm^3/s. This is the cosmological upper limit. The position of these enhancement peaks also strongly depends on the splitting between the mass of the dark matter and charged states of the theory particle spectrum ($\delta m_\pm = m_{\chi^\pm} - m_{\chi^0}$ for SUSY), since it controls the transition of the DM state to a particle able to experience the long-range effect of the electromagnetic interaction. The mass splitting should be $100\, MeV < \delta m_\pm < few\, GeV$ for a multi-TeV DM [106, 345] (always below the 5% m_{DM} prescription for primordial coannihilation, as shown in section 2.3.2).

Also **astrophysical observations** give us some constraints about DM annihilation cross section.
For example, the accretion of dark matter (DM) particles on compact stars, such as white dwarfs and neutron stars [302]. They show that in large regions of the DM parameter space, these objects are sensitive probes of the presence of DM, and can be used to set constraints both on the DM density and on the physical properties of DM particles. But these constraints are not stringent.
Another example is a study on the FERMI γ-rays data for galaxies clusters [111, 112, 135]. They analyze 2.8-yr data of 1÷100 GeV photons for clusters of galaxies, collected with the Large Area Telescope onboard the Fermi satellite. By analyzing 49 nearby massive clusters located at high Galactic latitudes, they find no excess gamma-ray emission towards directions of the galaxy clusters. Using flux upper limits, they show that the Fornax cluster provides the most stringent constraints on the dark matter annihilation cross section (Fig.16), which is $10^{-23} \div 10^{-22}\, cm^3/s$, one order of magnitude better than the one from Carina, Sculptor and other dwarf galaxies.

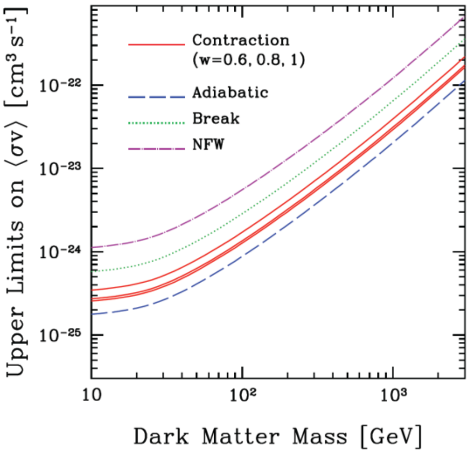

Figure 16 - Cross section upper limits for various contraction models for the NFW initial profile and the b$\bar{\text{b}}$ annihilation channel from the Fornax cluster [112]. See the text for details.

Another way to justify the great annihilating cross section is to consider a mechanism of production of the positrons which does not involve annihilations at all, rather **DM decay**. Unfortunately, the lifetime $\simeq 10^{26}$ s required to fit the data is not predicted in these scenarios, rather obtained a posteriori, although its scale might be justified in GUT models, and the source term for decaying dark matter is linearly proportional to ρ_{DM} and not to ρ_{DM}^2, introducing other astrophysical problems [88, 98, 99, 139, 140]. Furthermore, a symmetry must be broken in order to let DM decay. This is possible in some gravitino scenario and other theories which are today disfavored (see also section 3.6.2).

The first basis of our dark matter research can be put: we're dealing with a **TeV-ish Dark Matter** with an annihilation cross section between $10^{-26} \div 10^{-22}\, cm^3/s$. Furthermore, with $m_{DM} > 10\, TeV$ a cross section $> 10^{-22}\, cm^3/s$ is necessary to reproduce PAMELA's positron/electron data, which are not allowed by cosmological constraints.
Again, as said in chapter 2.3.2, since the cosmological Big Bang model prescribes a DM freeze-out temperature of $T_f \sim m_{DM}/20$, a dark matter with $2\, TeV < m_{DM} < 10\, TeV$ grant a temperature comparable with the electroweak symmetry-breaking one, bringing out dark matter at the same scale and with a possible interconnected mechanism.

Now, the third initial problem can be reformulated: are the great leptonic yield and the associated huge "Sommerfeld-boosted" cross section compatible with the absence of antiprotons?
Many studies have been done to front this matter, first of all the analysis of Donato et al. [91], proposed in Fig. 17.

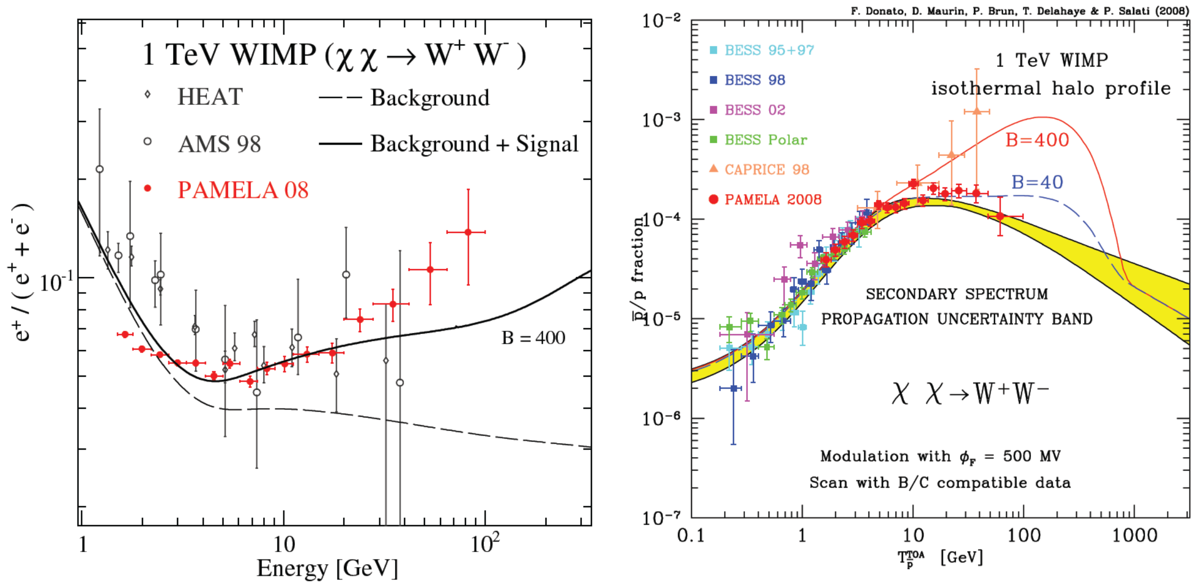

Figure 17 - The case of a 1 TeV LSP annihilating into a W^+W^- pair is featured. In the left panel, the positron signal which this DM species yields has been increased by a factor of 400, hence the solid curve and a marginal agreement with the PAMELA data. Positron fraction data are from HEAT, AMS-01 and PAMELA. If the Sommerfeld effect is invoked to explain such a large enhancement of the annihilation cross section, the same boost applies to antiprotons and leads to an unacceptable distortion of their spectrum as indicated by the red solid line of the right panel [91].

Already at this stage one can see that **it is necessary to give up some usual assumptions** (introduction of chapter 2), either the naturalness of Supersymmetry (invoking multi-TeV DM) and/or DM astrophysics (invoking very large boost factors) and/or that the DM is a thermal relic (invoking some nonthermal DM cosmological production mechanism) and/or invoking new Sommerfeld-like processes.
These things lead to only two possibilities:

- The *dark matter particle is very heavy*, not 1 TeV but a multi-TeV particle which can annihilate both into leptons and hadrons, through quarks, electroweak bosons and the Higgs boson.
- The *dark matter particle is leptophilic* and directly annihilate into leptons pair. In principle leptophilic DM annihilation is viable for any mass value, but several studies show that PAMELA best fits occurs for M $\sim$ 1 TeV dark matter [88, 95, 115].

Even if the second scenario remains valid, it excludes the entire hadronic research with space telescope such as AMS-02. And a robust hadronic signal would be a great evidence of the presence of a particle dark matter, well-motivated by the unsuccessful researches at Tevraton and LHC colliders (see section 3.61).

Accordingly it’s important to decide where to look and which DM hadrons can be seen with AMS-02: antiprotons, deuterons or both.

3.4 Hadronic Signals

3.4.1 Antiprotons

The old antiprotons research was focused on the low energy region of the CR spectrum, i. e. the range between 0.01 GeV and 1 GeV [117, 118, 119, 120]. And no antiproton rising was predicted for kinetic energies greater than 1 GeV [116, 122]: the secondary flux was supposed to be too high, removing the possibility to distinguish a primary dark matter spectrum for each propagation parameters set (MIN, MED, MAX, in Table 2). Today the paradigm has changed and, after PAMELA’s antiproton data, everything moves through a high energy research.

Now the entire range between 1 GeV and 100 ÷ 150 GeV may be called “low-energy”, i. e. the known spectrum, and the high-energy one lies above 100 GeV up to few TeV.

Below in Fig. 18, the AMS-02 expected spectrum for the here called low-energy physics is shown.

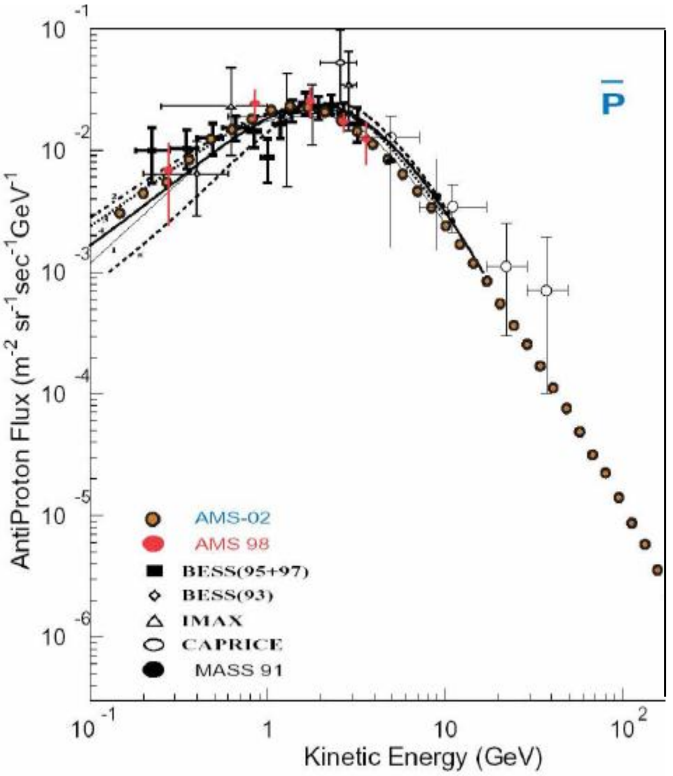

Figure 18 – Simulated AMS-02 antiproton spectrum from 0.1 GeV to 150 GeV, in comparison with several sets of data.

No discrepancy between AMS-02 and PAMELA are expected [125, 126]. What is really interesting is the physics beyond. As said, if DM is pure leptophilic the hadronic scenario is quite “boring”. So it’s challenging to focus on the possibility to see a bump in the spectrum at few hundreds GeV due to a multi-TeV dark particle.

DM with $M = 150$ GeV that annihilates into W^+W^-

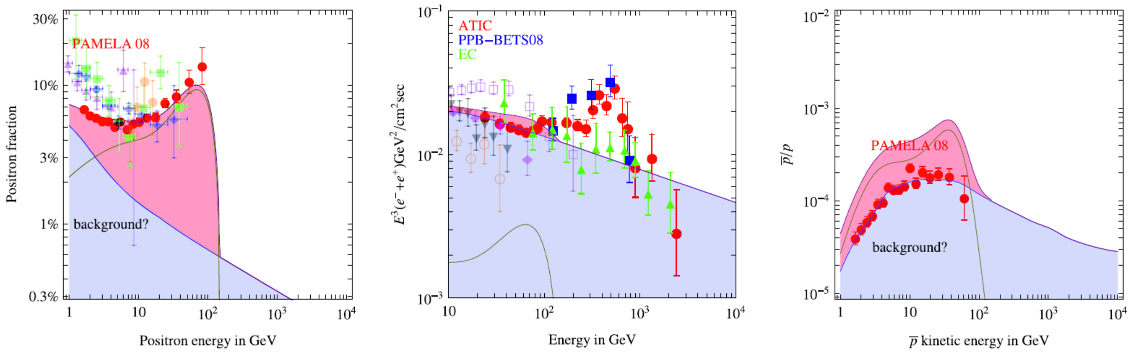

DM with $M = 1$ TeV that annihilates into $\mu^+\mu^-$

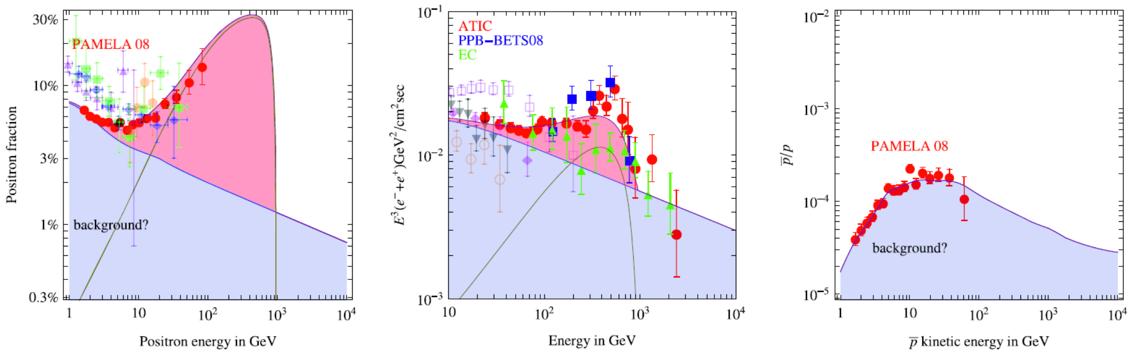

DM with $M = 10$ TeV that annihilates into W^+W^-

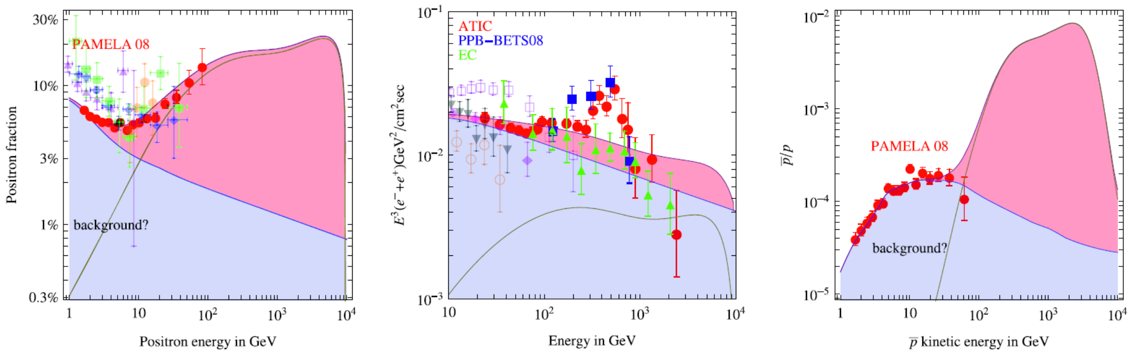

Figure 19 - Three examples of fits of positron fraction data (left), $e^+ + e^-$ (center), $\bar{p}/p$ (right) data, for M = 150 GeV (upper row, excluded by $\bar{p}$), M = 1 TeV (middle row, favored by leptophilic theories), M = 10 TeV (lower row, non leptophilic). Galactic DM profiles and propagation models are varied to provide the best fit [125].

In the first scenario in Fig. 19 a low-mass non-leptophilic DM which decays into electroweak bosons reproduce PAMELA’s positron excess but obviously fail to fit the total leptonic spectrum and the antiproton one. In the second row a 1 TeV leptophilic DM that decays into $\mu^+\mu^-$, as already known, fit all PAMELA’s data. But the most interesting one is the huge case: a 10 TeV non-leptophilic dark matter which decays into W^+W^-. This candidate is successful in reproducing the positron fraction and lifts up the antiproton on proton spectrum around 100 GeV (1÷2 order of magnitude), giving rise to a completely brand new astrophysical scenario. It seems that this case fails to reproduce the total e^+e^- spectrum but this plot should not fool us, since it doesn't show the experimental 2011-2012 FERMI's data which, as discussed previously, smooth the ATIC and BESS observations and perfectly fit with this simulation [126, 127].

So, the *puzzle* can be summarized as follow: there's always a promising electron-positron physics, but there may also be an antiproton new physics for AMS-02 in the kinetic energy between 100 GeV and 10 TeV for dark matter with $m_{DM} \lesssim 10\ TeV$. AMS-02 is able to see the spectra rise but it could miss the fall which, for $m_{DM} \sim 10\ TeV$, starts at 3 TeV for $\bar{p}/p$ and at 6 TeV for the positron fraction [125]; in principle, both the falls are probably detactable for $m_{DM} < 5\ TeV$.

Indeed it has to be stressed that the second scenario calculated in Fig. 19 is not completely correct. In fact, even if leptophilic, dark matter annihilation always produces a tiny amount of hadrons due to second order corrections [128].

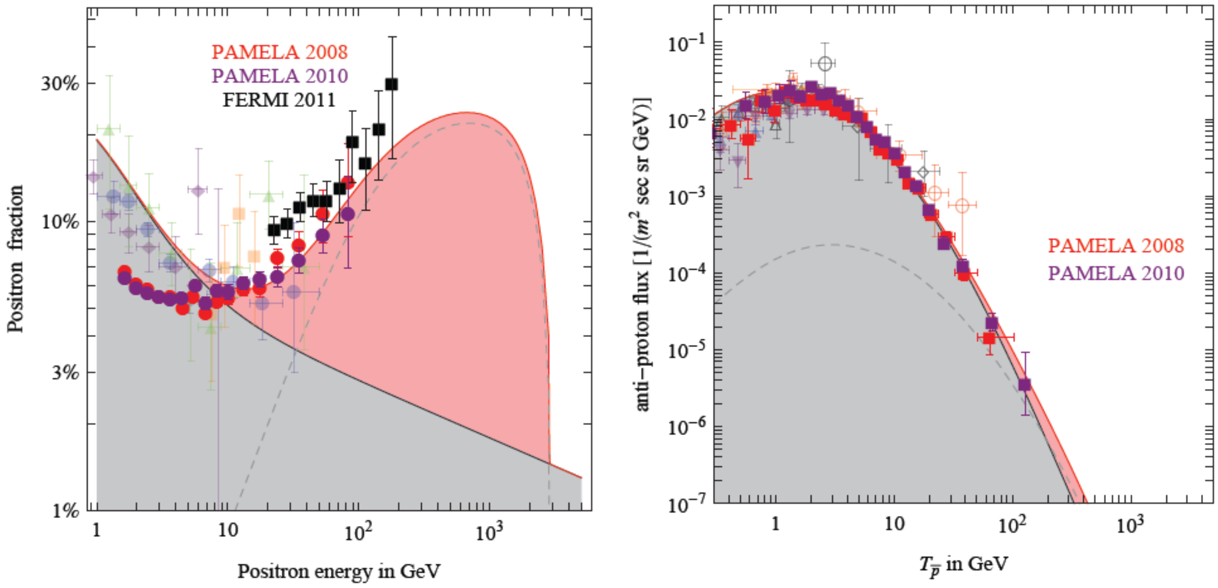

Figure 20 - Charged cosmic ray data interpreted in terms of Dark Matter annihilations for a leptophilic candidate: the flux from the best fit DM candidate (a 3 TeV DM particle annihilating into $\tau^+\tau^-$ with a cross section of $2 \cdot 10^{-22}$ cm^3/sec) is the lower dashed line and is summed to the supposed background, giving the pink flux which fits the data [88, 134].

The appearance of a small but visible flux of antiprotons from a DM DM → $\tau^+\tau^-$ annihilation mode in Fig. 20 (right) may be at first sight surprising. It is due to the fact that these fluxes are computed including electroweak corrections, i.e. the radiation from the initial $\tau^\pm$ of EW gauge bosons ($W^\pm$, Z) which then decay into many other SM particles, including quarks that hadronize into antiprotons. More generally, the importance of such corrections has been appreciated only relatively recently. Without entering in the details, remind that (i) the corrections are particularly relevant for large DM masses (above a TeV); (ii) they can alter significantly the ID fluxes, both in their spectral shape and in their amplitude, affecting especially the low energies portion and (iii) in some cases they can also largely modify the annihilation cross section itself, since they can lift the helicity suppression into light fermions (see section 3.4.3).

It's necessary to reach a great resolution and measurement precision to appreciate this antiproton production [129, 130, 131].

Concluding, with AMS-02 it's possible and desirable to see high energy antiprotons from heavy dark matter candidate and the collaboration team is going to search for them, after positrons.

3.4.2 Antideuterons

Antideuterons obey to the same propagation model described in section 3.2.1 and arrive at the top of atmosphere and may pass through AMS and give a signal. What changes is in the source term (eq. 3.16). In order to calculate the injection spectrum of antideuterons from a particular dark matter model, one needs to know the dark matter mass and annihilation cross section into various final states. The dark matter mass sets the energy scale of the final state, and the composition of the final state determines how that the system hadronizes into (anti-)baryons. This process can be modeled by numerical Monte Carlo, for example PYTHIA. Then one must make a prescription as to how a $\bar{p}$ and a $\bar{n}$ form an antideuteron. Antideuteron production, whether secondary from p + H → $\bar{d}$ + X or primary from dark matter annihilation, requires such a prescription. One prescription is the so-called "Coalescence Model". According to this model in the $\bar{n}$ rest-frame of a $\bar{n}-\bar{p}$ system, if the $\bar{p}$ has kinetic energy less than the antideuteron binding energy, B, then one assumes the two bind to form an antideuteron. This crude model provides a good order of magnitude estimate for the formation of antideuterons. Said more precisely, if $KE_{\bar{p}} \sim B \left(|k_{\bar{p}}| \sim (2m_p B)^{1/2}\right)$ then antideuteron formation is assumed. So the condition that a $\bar{n}$ and $\bar{p}$ in a hadronic final state form an antideuteron is: $|k_{\bar{n}} - \overrightarrow{k_{\bar{p}}}| < (2m_p B)^{1/2} \sim p_0 \sim 30 \div 160\ MeV$. p_0 is referred to as the "coalescence momentum." Typically, when using the coalescence model (Fig. 21) one assumes that the distribution of $\bar{n}$ and $\bar{p}$ with energy $E_{\bar{n},\bar{p}}$ is spherically symmetric and factorizes [144, 145].

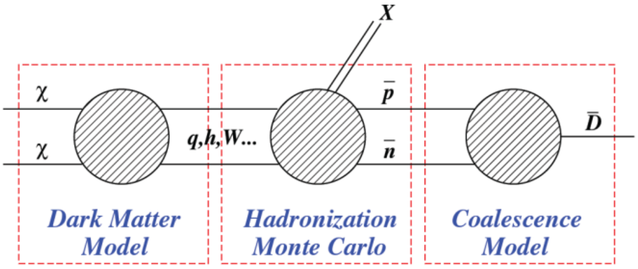

Figure 21 - A conceptual outline of how to compute the antideuteron flux induced by a dark matter particle pair annihilation.

The standard formula for the antideuteron spectrum, obtained under the assumption of spherical symmetry of the events, in terms of the anti-nucleon ($\bar{p}$ plus $\bar{n}$) energy spectrum per annihilation, dN_N/dT, is [145]

$$\frac{dN_{\bar{d}}}{dT_{\bar{d}}} = \frac{p_0^3}{3k_{\bar{d}} m_p} \left(\frac{1}{2}\frac{dN_N}{dT}\right)^2_{T=T_d/2}, \tag{3.43}$$

where the kinetic energies T = E - m are $T_p = T_n = T_d/2$; $m_p = m_n = m_d/2$ and $k_{\bar{d}} = \sqrt{T_{\bar{d}}^2 + 2m_d T_{\bar{d}}}$.

The d̄ flux in the galactic medium around the solar system can be written as

$$\frac{d\Phi_{\bar{d}}}{dT} = \frac{v_{\bar{d}}}{4\pi} f = \frac{v_{\bar{d}}}{4\pi}\frac{\langle\sigma v\rangle}{2}\left(\frac{\rho_\odot}{M}\right)^2 R_d(T)\frac{dN_{\bar{d}}}{dT}, \tag{3.44}$$

fully analogous to the solution for the a generic CR flux. The function $dN_{\bar{d}}/dT$ contains the particle physics input and the function $R_d(T)$ encodes the Milky Way astrophysics (see further Fig.30).

Now, the actual BESS bound for antideuteron flux from primary DM source is [144]

$$\Phi_{\bar{D}} < 0.95 \times 10^{-4}[m^2 \ s \ sr \ \mathrm{GeV}]^{-1} \quad 0.17 \leq T/n \leq 1.15 \tag{3.45}$$

PAMELA is not able to produce an antideuteron spectrum, so BESS is the only landmark available. Here it needs to be understood if there is a factual chance to detect an antideuteron flux with AMS. Let's start from the light dark matter case. For a very light WIMP an appreciable low energy signal in the 0.1 GeV – few GeV window could be detected (see Fig. 22).

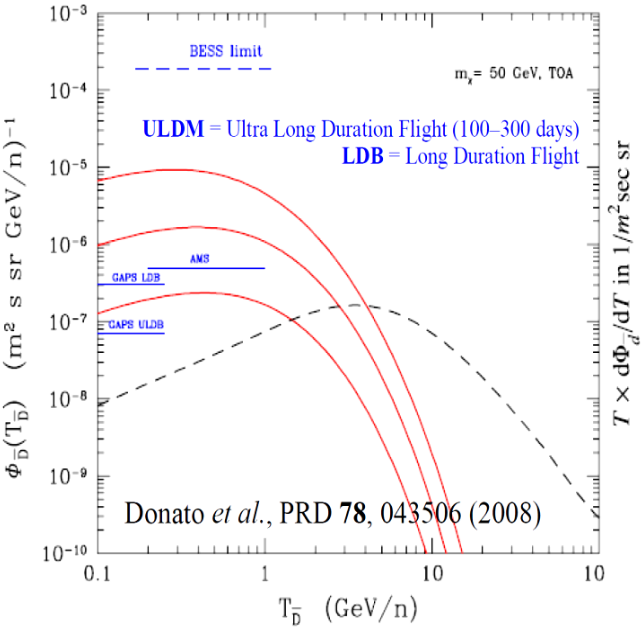

Figure 22 – TOA primary (red solid lines) and secondary (black dashed line) antideuteron fluxes, modulated at solar minimum. The signal is derived for a m_{DM} = 50 GeV WIMP and for the three propagation models MIN MED MAX. The secondary flux is shown for the median propagation model. The upper dashed horizontal line shows the current BESS upper limit [144, 151] on the search for cosmic antideuterons. The three horizontal solid (blue) lines are the estimated sensitivities for (from top to bottom) AMS-02, GAPS [150, 153] on a long (LDB) and ultralong (ULDB) duration balloon flights [147, 148, 149].

Other studies compute the same order of magnitude of sensibility for AMS-02 [144]:

$$\begin{aligned} \Phi_{\bar{D}} &= 2.25 \times 10^{-7}[m^2 \ s \ sr \ \mathrm{GeV}]^{-1} \quad 0.2 \leq T/n \leq 0.8 \ (\mathrm{GeV/n}) \quad \mathrm{AMS-02} \\ \Phi_{\bar{D}} &= 2.25 \times 10^{-7}[m^2 \ s \ sr \ \mathrm{GeV}]^{-1} \quad 2.2 \leq T/n \leq 4.2 \ (\mathrm{GeV/n}) \quad \mathrm{AMS-02} \end{aligned} \tag{3.46}$$

From Fig. 22 it's evident that AMS-02 can detect such a flux for both MED and MAX set of propagation parameters. But it's not our heavy mass scenario: TeV-ish dark matter is needed.
If a thermal annihilation cross section is taken and you look at the high energy range in the Fig. 23 below, the primary flux is overcame by the secondary one. So it's impossible to see any signal.

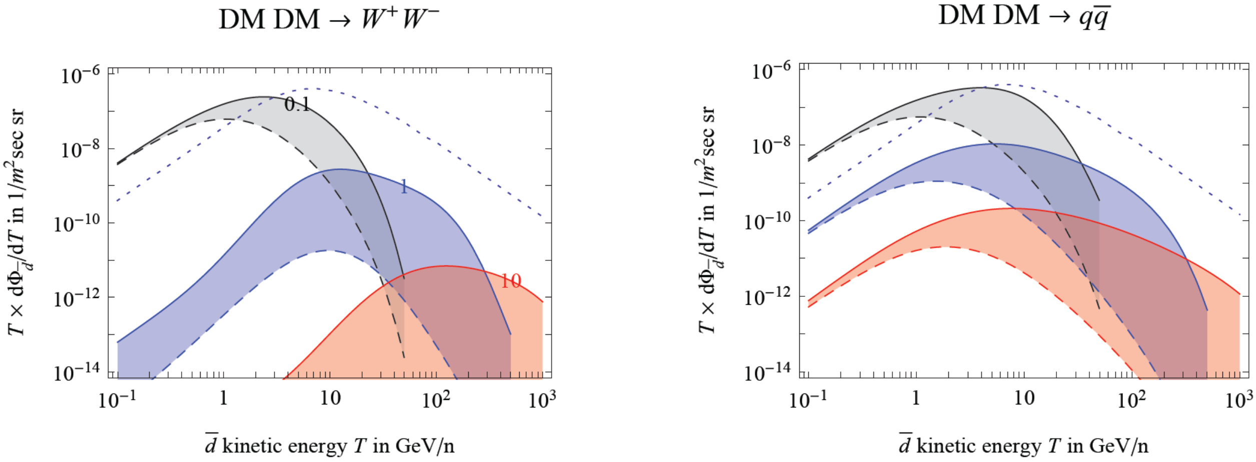

Figure 23 - Assuming $\langle\sigma v\rangle = 3 \cdot 10^{-26} cm^3/s$, the NFW profile, MED propagation and DM masses M = 0.1, 1, 10 TeV, the comparison between the antideuteron flux obtained from the full computation (continuous lines) with the one from the spherical approximation. The dotted line is the expected astrophysical background [145].

But making two assumptions, it's possible to reach a small but distinguishable flux at high energy. The first is that there's a cross section amplification factor – in fact the thermal cross section paradigm is almost broken and we deal with $\langle\sigma v\rangle \sim 10^{-23} cm^3/s$ – which may be parametrized with the dark matter mass and it's proportional to the square mass. Moreover a $m_{DM} \lesssim 10\,TeV$ dark matter is invoked, as it has been explained in detail in 3.3.2. Even if there's the possibility to separate primary fluxes from background (Fig. 24 right), they're too faint to be easily detected by AMS-02: they worth less than $10^{-9}\ (m^2 sr\ s\ GeV/n)^{-1}$.

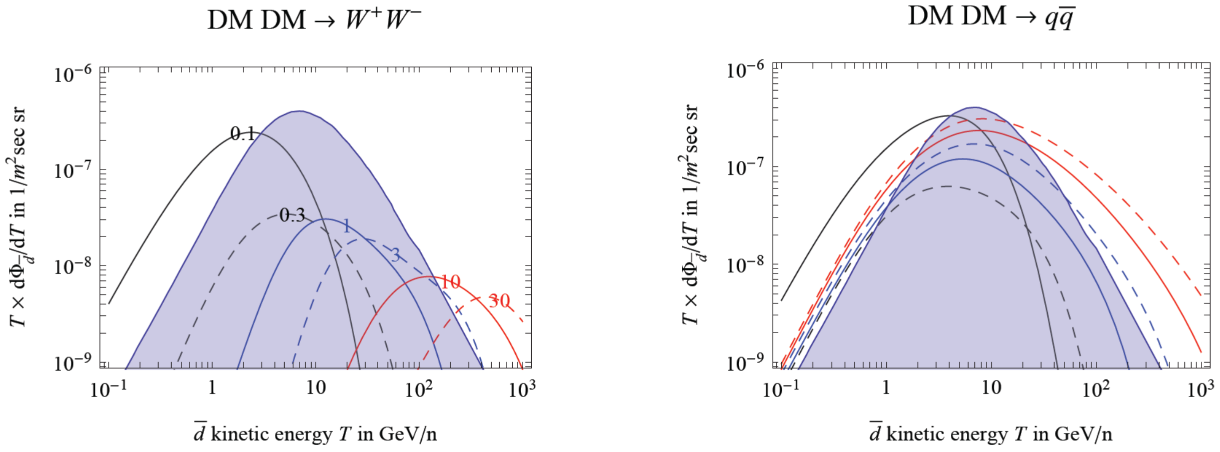

Figure 24 – Antideuteron flux for full computation (non spherical approximation) for DM masses M = 0.1, 1, 10 TeV (black, blue, red continuous curves) and M = 0.3, 3, 30 TeV (black, blue, red dashed curves), DM annihilations into W^+W^- (left) and $q\bar{q}$ (right) with $\langle\sigma v\rangle = 3 \cdot 10^{-26} cm^3/s \times \max(1, M_{DM}/300\ GeV)^2$, the NFW DM profile, MED propagation, solar modulation ϕ_F = 0.5 GV, p_0 = 160 MeV. Shading indicates the expected astrophysical antideuteron background [145].

There is a chance to have a low energy antideuteron flux too, even for heavy dark matter with high annihilation cross section. As it's shown below in Figs. 25 and 26, there are great uncertainties around the flux determination. Predicted fluxes depend on the propagation set choice (Figure 25a), on the halo model (Figure 25b, but only to a small extent), on the solar modulation in the

MeV ÷ few GeV region (Figure 26a), and strongly depend on the coalescence momentum (Figure 26b).

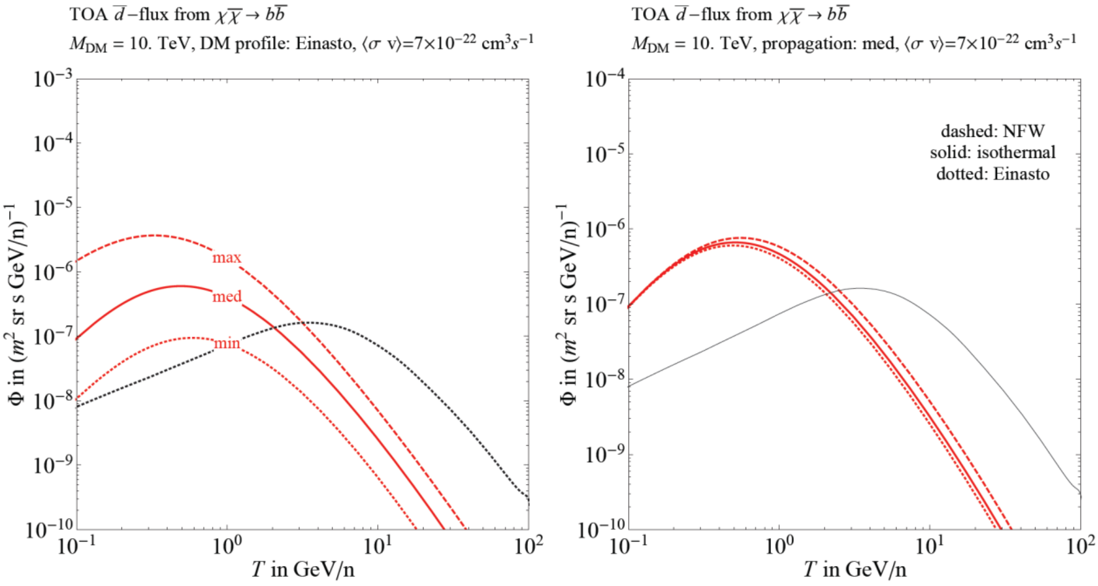

Figure 25 - Left panel a): Propagated "top-of-the-atmosphere (TOA)" antideuteron flux, including solar modulation, from a DM with mass 10 TeV annihilating into $b\bar{b}$, fixing the DM halo profile at Einasto and changing the propagation parameters (min, med, max). Right panel b): Fixing the propagation parameters at med and changing the halo profile (NFW, Isothermal, Einasto) [152].

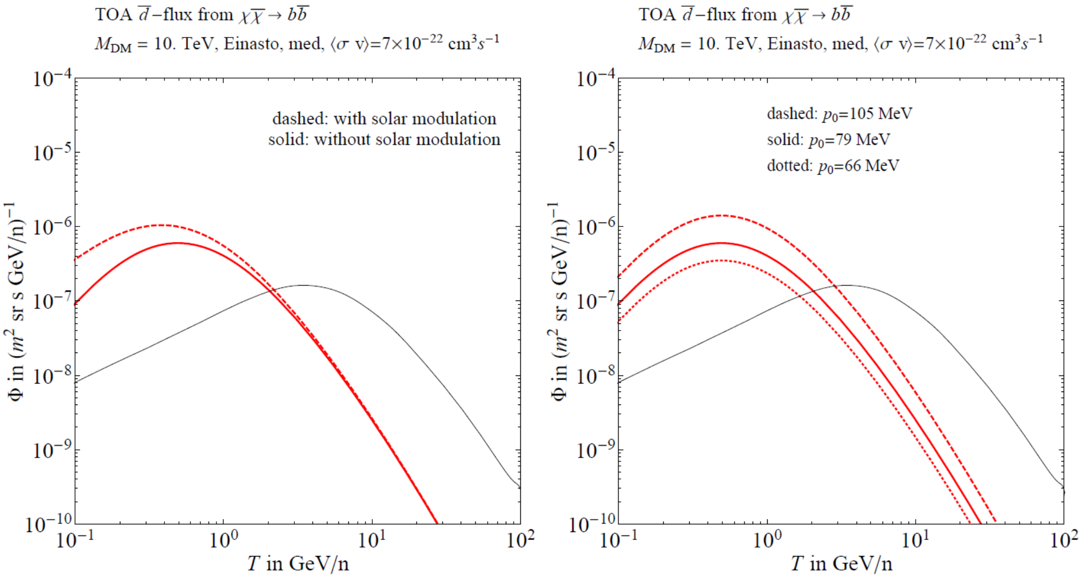

Figure 26 - Left panel a): Propagated antideuteron flux from a DM with mass 10 TeV annihilating into $b\bar{b}$, fixing an Einasto DM profile and med propagation parameters, with and without the solar modulation effect. Right panel b): The same flux (including solar modulation) for different choices of the coalescence momentum p_0 [152].

The propagation model affects deeply the low energy spectrum, with a span of two order of magnitude (the same it's true for antiprotons); at high energies these discrepancies decrease of one order of magnitude (Figs. 25 and 26 right).

So, with a great luck, there's a hope to discover dark matter in the low energy window, for a $M_{DM} < 10\ TeV$ candidate and a good (high rate) favored decay into quarks (and/or gluons), as it's illustrated in Figs. 27 and 28.

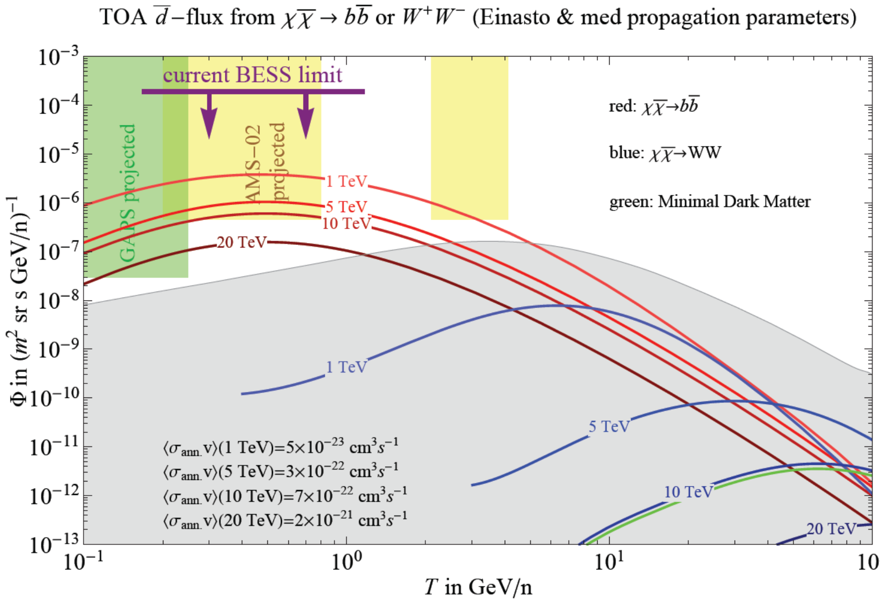

Figure 27 - The final fluxes of anti-deuterons for the different heavy DM candidates and for Minimal Dark Matter compared to the background (gray shaded area) and to expected experiment sensitivities. Here an Einasto DM profile is assumed, med propagation parameters, and included the solar modulation effect [88, 152].

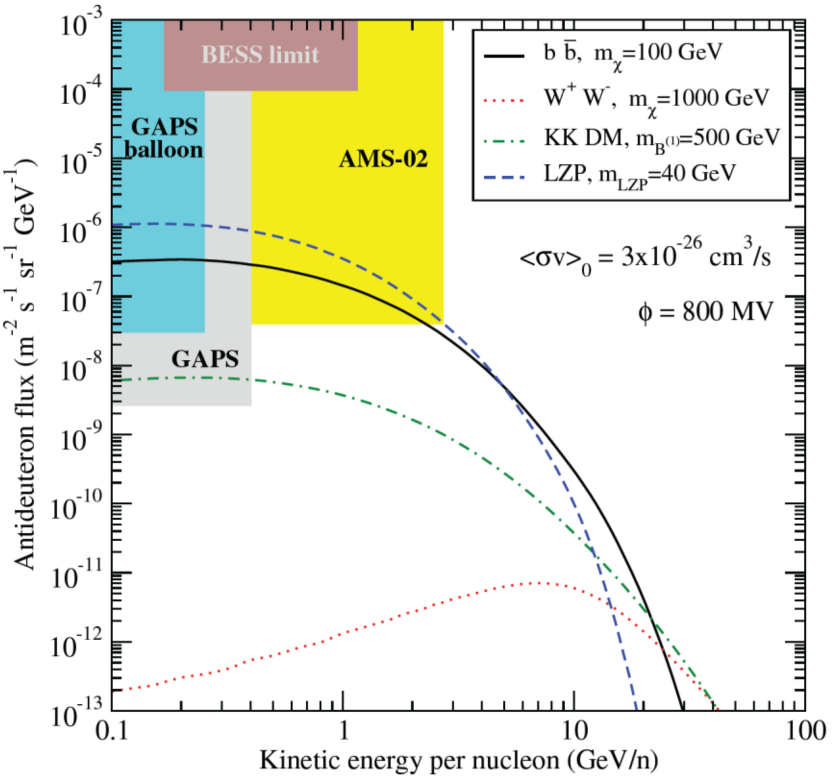

Figure 28 - Differential antideuteron flux from four different WIMP models, as a function of the antideuterons' kinetic energy per nucleon. The solid black line corresponds to a WIMP with mass 100 GeV annihilating with BR = 1 into a $b\bar{b}$ pair, the red dotted line to a 1 TeV WIMP annihilating

with BR = 1 into W^+W^- pairs, the green dot–dashed line to a 500 GeV $B^{(1)}$ (the Kaluza–Klein first excitation of the hypercharge gauge boson), LKP in the UED scenario, while the blue dashed line to a LZP particle pair annihilating dominantly through the Z S-channel resonance, with a mass of 40 GeV. The shaded regions correspond to the sensitivities of various existing and proposed experiments featuring antideuteron searches [146, 162].

As shown in Fig. 28 and Fig. 29, classical lighter candidate (non-Wino neutralino, or light LZP right-handed neutrino) could be clearly detected, but in this case the previous TeV-ish DM analysis has to be dismissed.

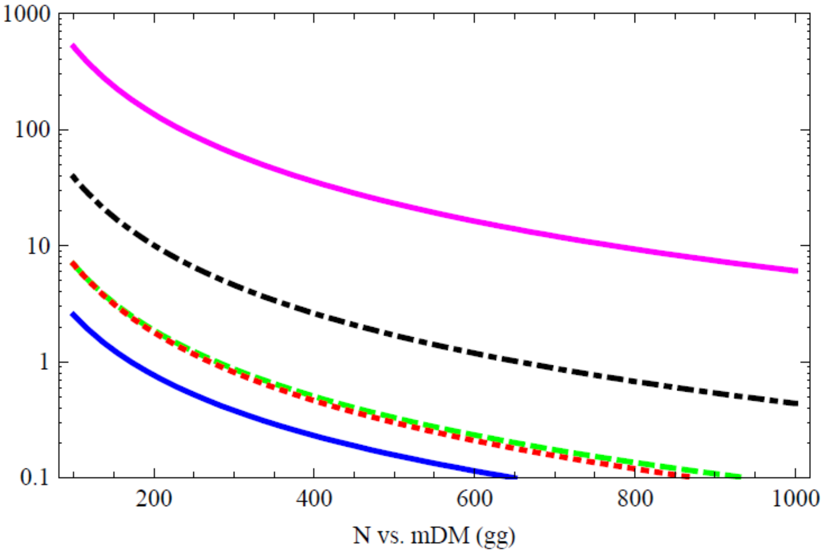

Figure 29 - The expected number of primary antideuterons in one year for the AMS-02 (high) (blue/solid), AMS-02 (low) (green/dashed), GAPS (LDB) (red/dotted), GAPS (ULDB) (black/dot-dashed) and GAPS (SAT) (pink/solid/upper line) experiments for dark matter annihilation into *gg* final state, which give the higher antideuteron yield, and a thermal annihilation cross section. Propagation is done with “MED” parameters [144].

From Fig. 29, for a 300 GeV – 1 TeV particle, AMS-02 sees about 0.1÷1 antideuteron in on year [144, 155, 157, 159].

Finally it’s to stress that measurable antideuteron fluxes, both at 0.1÷1 GeV and > 100 GeV scales, are not in conflict with the antiproton spectra. In fact, at low energy you can have antideuterons but not antiprotons without contradiction.

3.4.3 Fluxes Uncertainties

Before analyzing the dark matter particle candidate, let’s complete the examination of the uncertainties that afflict the CR spectra, in particular the antiproton and the antideuteron ones, to understand the limit of our knowledge.

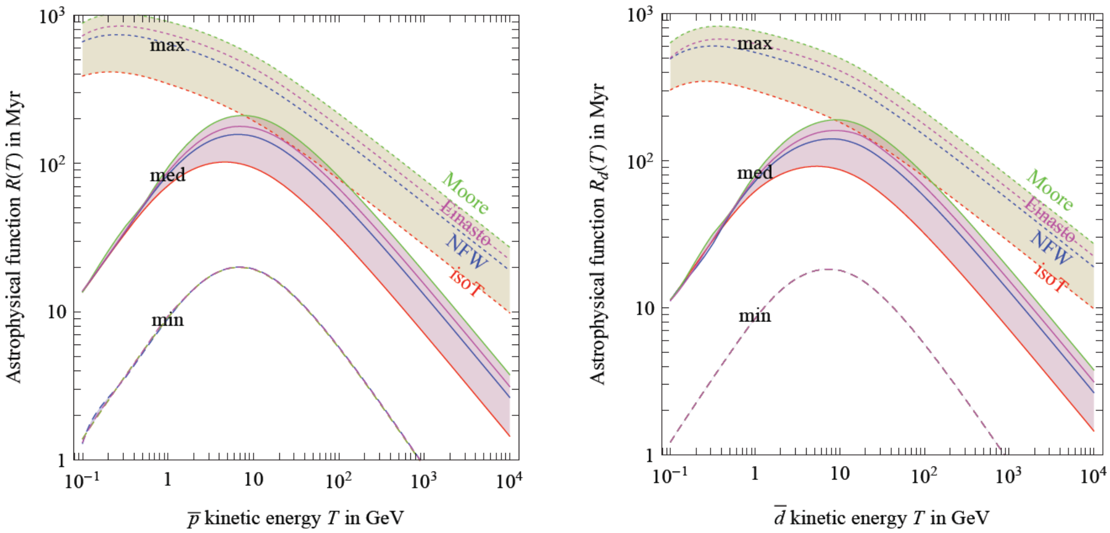

Figure 30 - The $\bar{p}$ (left) and $\bar{d}$ (right) astrophysical functions R(T) of eq. (3.44), computed under different assumptions. In both cases, the dashed (solid) [dotted] bands assumes the min (med) [max] propagation configurations. Each band contains 4 lines, that correspond to the isothermal (red lower lines), NFW (blue middle lines), Einasto (magenta) and Moore (green upper lines) DM density profiles [145].

The astrophysical function for the antiproton and antideuteron primary production in Fig. 30 shows the importance of the **propagation model** over the **DM profile**. For MIN nothing changes, for MED there's a variation > 50% depending on the profile (from the isothermal to the Moore one), from 10 GeV till 10 TeV, for MAX there's a higher uncertainty [147].

So these spectra are intrinsically affected by great uncertainties, especially from the propagation set – about two order of magnitude from MIN to MAX – and then from the DM profile – around a factor 3, roughly speaking, depending on the models in comparison. Whereas the secondary process (spallation) is known better, propagation uncertainties afflict secondary spectra in a less significant way (they don't exceed 25%).

Moreover, overdense regions (spikes) in the Galactic Centre could produce an annihilation enhancement, increasing particle fluxes.

For the case of antideuteron the situation is worst. In fact there's also a great uncertainty coming from the **coalescence momentum**, which represents a third important source of ignorance (Fig. 31).

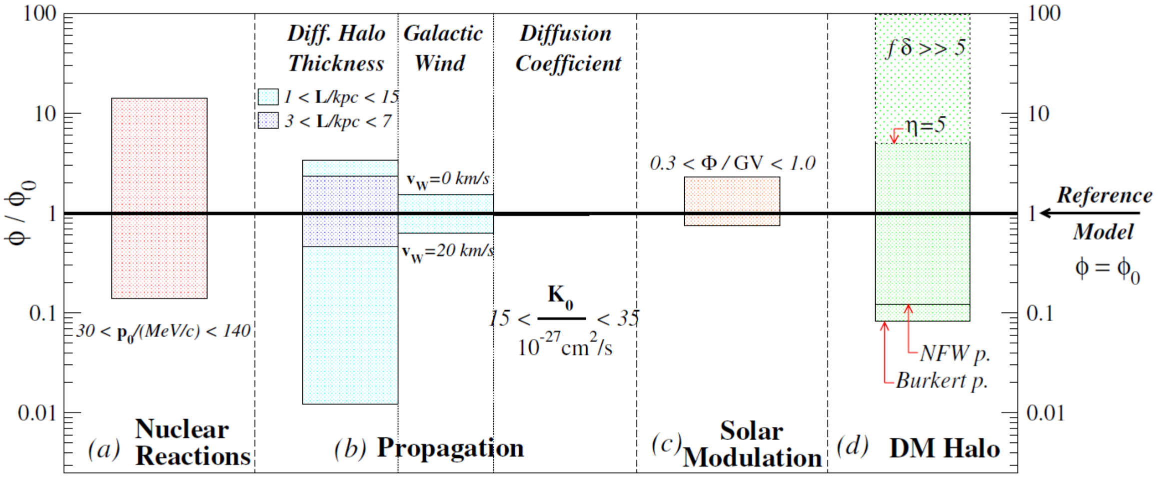

Figure 31 – Overall sources of uncertainties for the antideuteron flux with respect to the reference MIN propagation set [146, 159].

Propagation parameters (diffusive halo thickness, galactic wind, diffusion coefficient, solar modulation and so on), DM profile and coalescence model afflict the spectrum at same time. But, while the $\bar{d}$ spectrum has a quadratic dependence in the density distribution ($\Phi_{\bar{d}} \propto \rho_{DM}^2$), the dependence in the coalescence momentum is $\Phi_{\bar{d}} \propto p_0^3$, therefore quite fundamental [146].

A fourth source of uncertainty, after propagation, density distribution and coalescence momentum, is a particle physics uncertainty, i. e. the **weak bosons emission in the "next to the leading order approximation"**: the inclusion of electroweak radiation eludes LO suppression and opens up a potentially sizeable S-wave contribution to the annihilation cross section, regardless of mass and preferred annihilation channels [164, 165, 166].

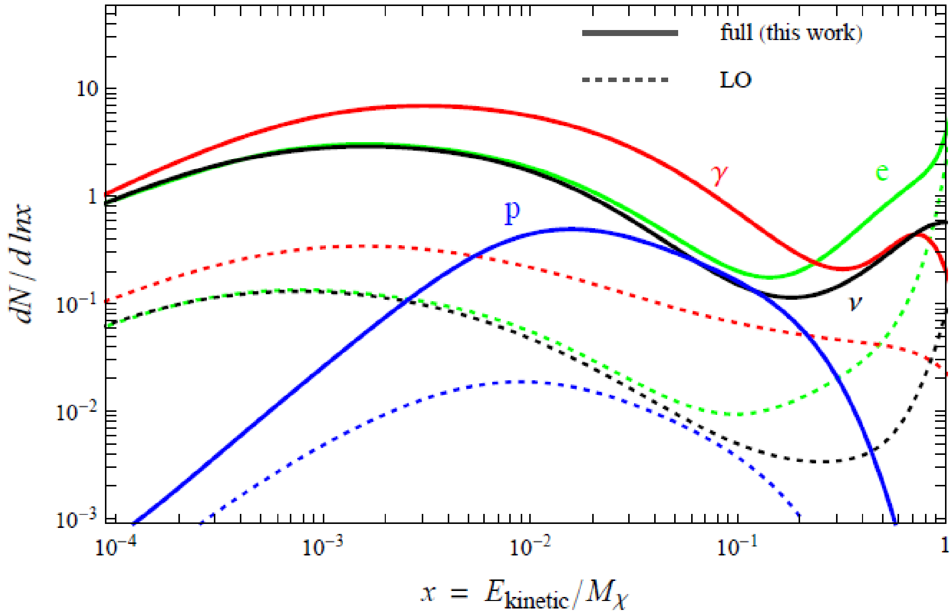

Figure 32 - The spectra from the DM annihilation into light fermions (positrons and electrons or neutrinos channels) with the corresponding weak boson emission corrections, for the case M = 1 TeV. For comparison, the spectra in the LO approximation (dotted).

The NLO radiative corrections in Fig. 32 are truly important and can drastically modify the primary DM spectra, producing an enhancement of at least one order of magnitude for antiprotons and positrons. This is manifestly a great thing, that can provide us a more friendly detection of DM annihilation products. These corrections increase with the dark matter mass, so they should be always consider for heavy DM candidate [166, 167]. As already said, also leptophilic dark matter could produce a tiny antiprotons flux through these processes.

Moreover no one knows if there are **new primary astrophysical high energy phenomena** that could affect our CR spectra, warping and increasing them (see section 3.7.2), and **unknown background.**

A notable new feature is represented by the **"discrepant hardenings" in CR spectra** [169]: recent data from the CREAM balloon-borne experiment seem to confirm earlier suggestions that cosmic ray spectra at few TeV/nucleon are harder than in the 10-100 GeV range, and that helium and heavier nuclei fluxes are harder than the proton flux at corresponding energies. Preliminary data from PAMELA also suggest a hardening, or *fluxes break*, in *p* and *He* spectra at a rigidity of about 250 GV, with a He spectrum having an index ~ 0.1 lower than the proton one over all energies above a few GeV. The ignorance on the origin of the features represents a systematic error in the extraction of astrophysical parameters as well as for background estimates for indirect dark matter searches. Spectral modifications could be appreciable above 100 GeV and could affect antiprotons, (anti)deuterons (and also gammas) at energies close to 1 TeV [170].

There are also some possible modifications of our propagation paradigm (for example anisotropic propagation, see 3.7.1) and new effects only recently introduced in DM distribution halo modeling [3, 88, 112]:

- Baryons could either steepen the DM profile at the center, thanks to adiabatic contraction, or smoothen it due to friction [55].
- There is no assurance about velocity distribution of DM particles in the galactic halos, and if they have irrotational or swirling properties (*Tidal Torque Theories* – Sikivie 2012, Navarro 2007, Brunino 2007).

So our knowledge is limited enough, and we have to deeply think about these uncertainties before assuming to have discovered something: once fixed the propagation model with AMS-02 (3.2.1), flux uncertainties of at least one order of magnitude survive yet.

3.5 Dark Matter Candidates and AMS-02

In this section the main characteristics of the most important and sensible dark matter candidates are reviewed, dealing with pros and cons of each one, without the pretense of an exhaustive argumentation of the single theories.

Technicolor [171, 172, 173] is intentionally excluded from this chapter because of the recent discovery of the Higgs (-like) particle. For each theory it's discussed if it produces a good candidate for AMS and how this candidate can be seen with the Alpha Magnetic Spectrometer.

3.5.1 SUSY particles

The *gauge hierarchy problem* is most elegantly solved by supersymmetry [78, 174, 175, 178]. In supersymmetric extensions of the SM, every SM particle has a new, as-yet-undiscovered partner particle, which has the same quantum numbers and gauge interactions, but differs in spin by 1/2. The introduction of new particles with opposite spin-statistics from the known ones supplements the SM quantum corrections to the Higgs boson mass with opposite sign contributions:

$$\Delta m_h^2 \sim \frac{\lambda^2}{16\pi^2}\int^{\Lambda}\frac{d^4p}{p^2}\bigg|_{\mathrm{SM}} - \frac{\lambda^2}{16\pi^2}\int^{\Lambda}\frac{d^4p}{p^2}\bigg|_{\mathrm{SUSY}} \sim \frac{\lambda^2}{16\pi^2}\left(m_{\mathrm{SUSY}}^2 - m_{\mathrm{SM}}^2\right)\ln\frac{\Lambda}{m_{\mathrm{SUSY}}}\ , \tag{3.47}$$

where m_{SM} and m_{SUSY} are the masses of the SM particles and their superpartners. For $m_{SUSY} \sim m_{weak}$, this is at most an O(1) correction, even for $\Lambda \sim M_{Pl}$. This by itself stabilizes, but does not solve, the gauge hierarchy problem; one must also understand why $m_{SUSY} \sim m_{weak} << M_{Pl}$. There are, however, a number of ways to generate such a hierarchy; given such a mechanism, the relation implies that quantum effects will not destroy the hierarchy, and the gauge hierarchy problem may be considered truly solved.

Not surprisingly, the doubling of the SM particle spectrum has many implications for cosmology. For dark matter, it is natural to begin by listing all the new particles that are electrically neutral. For technical reasons, supersymmetric models require two Higgs bosons.

The neutral supersymmetric particles are then

Spin 3/2 Fermion:	Gravitino $\tilde{G}$
Spin 1/2 Fermions:	$\tilde{B}; \tilde{W}; \tilde{H}_1; \tilde{H}_2 \xrightarrow{yields}$ Neutralinos $\chi_1, \chi_2, \chi_3, \chi_4$
Spin 0 Scalars:	Sneutrinos $\tilde{\nu}_e, \tilde{\nu}_\mu, \tilde{\nu}_\tau$

As indicated, the neutral spin 1/2 fermions mix to form four mass eigenstates, the neutralinos. The lightest of these, $\chi \equiv \chi_1$, is a WIMP dark matter candidate. The **sneutrinos** are not good dark matter candidates, as both their annihilation and scattering cross sections are large, and so they are under-abundant or excluded by null results from direct detection experiments for all masses near m_{weak}. The **gravitino** is not a WIMP, but it is a viable dark matter candidate. The gravitino is the supersymmetric partner of the graviton. If it exists, it is a fermion of spin 3⁄2 and therefore obeys the Rarita-Schwinger equation. This varies greatly between different models of supersymmetry breaking, but if supersymmetry is to solve the hierarchy problem of the Standard Model, the gravitino cannot be more massive than about 1 TeV [31, 78]. It's a strange candidate, the only high spin candidate, which give a lot of cosmological problems and it's not able to produce the correct actual dark matter density of our Universe [179]. It has also a low annihilation cross section and it's a superpartner of an hypothetical particle, the graviton, which could (probably) not exist at all.
The Ockham's razor grandly disqualifies this candidate.

A general supersymmetric extension of the SM contains many unknown parameters. To make progress, it is typical to consider specific models in which simplifying assumptions unify many parameters, and then study to what extent the conclusions may be generalized (see [185–215] for in-depth analysis of SUSY *state of art*).
The canonical model for supersymmetric studies is the Minimal SUSY Model (MSSM), or minimal supergravity, which is minimal in the sense that it includes the minimum number of particles and includes a large number of assumptions that drastically reduces the number of independent model parameters. Minimal Supersymmetric theory is defined by five parameters [31]:

$$m_0, M_{1/2}, A_0, \tan\beta, \mathrm{sign}(\mu) \ . \tag{3.48}$$

The most important parameters are the universal scalar mass m_0 and the universal gaugino mass $M_{1/2}$, both defined at the scale of grand unified theories $m_{GUT} \sim 2 \cdot 10^{16}$ GeV.
The assumption of a universal gaugino mass and the choice of m_{GUT} are supported by the fact that the three SM gauge couplings unify at m_{GUT} in supersymmetric theories. The assumption of scalar mass unification is much more ad hoc, but it does imply highly degenerate squarks and sleptons, which typically satisfies the constraints of the new physics flavor problem. Finally, the parameter A_0 governs the strength of cubic scalar particle interactions, and $\tan\theta$ and $\mathrm{sign}(\mu)$ are parameters that enter the Higgs boson potential: $\tan\theta$ is the ratio of vevs of the two neutral Higgs and μ is the Higgsino mass parameter.
For all but their most extreme values, these last three parameters have much less impact on collider and dark matter phenomenology than m_0 and $M_{1/2}$. One fixed the first three, a SUSY plot can be constructed (Fig. 33).

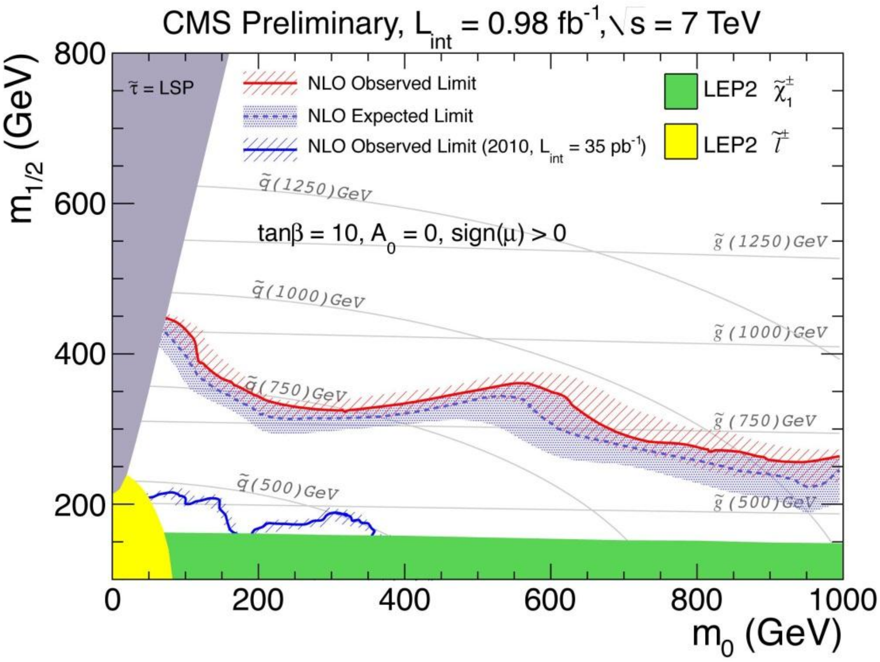

Figure 33 - Exclusion region in the CMSSM (Constrained MSSM) framework using same charge di-leptons. The result of the previous analysis is shown to illustrate the improvement since CMS found no excess in the number of events predicted by the SM. An upper limit of 95% CL has been placed on the non-SM contributions. In the context of CMSSM, the excluded regions in the parameter space exceed those set by the previous experiments such as Tevatron [from CMS website].

In the supersymmetric extension of the Standard Model, baryon number and lepton number are no longer conserved by all of the renormalizable couplings in the theory. Since baryon number and lepton number conservation have been tested very precisely, these couplings need to be very small in order not to be in conflict with experimental data. R-parity is a Z_2 symmetry acting on the MSSM fields that forbids these couplings and can be defined as:

$$P_R = (-1)^{2s+3B+L} \tag{3.49}$$

with spin s, baryon number B, and lepton number L. All Standard Model particles have R-parity of 1 while supersymmetric particles have R-parity -1. With R-parity being preserved, the lightest supersymmetric particle (LSP) cannot decay.

Let’s go back to the neutralino. The exact properties of each neutralino will depend on the details of the mixing and they tend to have masses in a large energy span (100-10000 GeV) and couple to other particles with strengths characteristic of the weak interaction. In this way they are phenomenologically similar to neutrinos. In fact they are Majorana fermions and not directly observable in particle detectors at accelerators.

It may be written as a linear combination of the four major fields (Bino, Wino and Higgsinos) previously written:

$$\chi = \alpha\widetilde{B} + \beta\widetilde{W}^3 + \gamma\widetilde{H_1} + \delta\widetilde{H_2} \tag{3.50}$$

Then a mixing matrix is constructed, complementary to the one of the Higgs sector, which mix the mass and the electroweak/supersymmetric states. In the previous basis the neutralino mass matrix can be expressed as

$$\mathcal{M}_N = \begin{pmatrix} M_1 & 0 & -M_Z \cos\beta \sin\theta_W & M_Z \sin\beta \sin\theta_W \\ 0 & M_2 & M_Z \cos\beta \cos\theta_W & -M_Z \sin\beta \cos\theta_W \\ -M_Z \cos\beta \sin\theta_W & M_Z \cos\beta \cos\theta_W & 0 & -\mu \\ M_Z \sin\beta \sin\theta_W & -M_Z \sin\beta \cos\theta_W & -\mu & 0 \end{pmatrix} \tag{3.51}$$

where θ_W is the Weinberg angle.
If a combined parameter *P* is defined

$$P = \alpha^2 + \beta^2, \tag{3.52}$$

three types of neutralino can be identified, depending on the value of this quantity: for P > 0.9 it's a gaugino, for P < 1 an Higgsino, and for $0.1 \leq P \leq 0.9$ a mixed neutralino. So three are the main SUSY Model, described in the following table.

Model	Bino fraction	Wino fraction	Higgsino fraction
Funnel	>99.6%	< 0.05%	< 0.05%
AMSB	<0.02%	> 98% for $m_\chi > 100$ GeV	> 2% for $m_\chi > 100$ GeV
NUGM	<0.01%	< 0.2%	99.8%

Table 4 - The lightest neutralino composition for the three SUSY models in term of the bino, wino and higgsino fractions [180].

All three models are instances of minimal supersymmetric extensions of the Standard Model [184]. In particular, both the Funnel and Non Universal Gaugino Mass (NUGM) models involve supergravity, although the latter allows for the non universality of the gaugino mass, in term of which all other SUSY particle masses are determined; the Anomaly Mediated Symmetry Breaking (AMSB) model implements a different scheme based on scale anomalies in the so called *hidden sector* of the theory. The three schemes produce neutralino realizations in which one of the components is largely dominant over the other as detailed in Table 4, and are therefore suitable to be used as benchmarks to evaluate the visibility of SUSY signals.
They differ from several points of view:

- The *mass*: Funnel and NUGM are low-mass realization of LSP, with mass in the range 100-1000 GeV. The AMSB Wino neutralino has 300-10000 GeV mass instead.

- The *type of interaction*, i.e. the operators for annihilation (spin-independent scattering and spin-dependent scattering have always the same quantum field theory representation). For example, the interaction operator for Bino neutralino are (see [144] for insights):

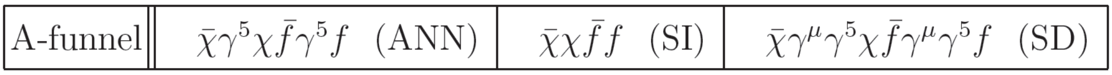

A-funnel	$\bar{\chi}\gamma^5\chi\bar{f}\gamma^5 f$ (ANN)	$\bar{\chi}\chi\bar{f}f$ (SI)	$\bar{\chi}\gamma^\mu\gamma^5\chi\bar{f}\gamma^\mu\gamma^5 f$ (SD)

while for a Wino-like

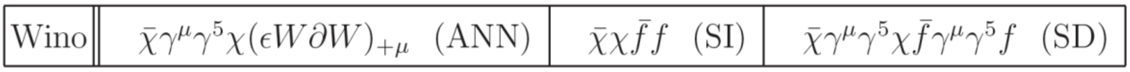

Wino	$\bar{\chi}\gamma^\mu\gamma^5\chi(\epsilon W\partial W)_{+\mu}$ (ANN)	$\bar{\chi}\chi\bar{f}f$ (SI)	$\bar{\chi}\gamma^\mu\gamma^5\chi\bar{f}\gamma^\mu\gamma^5 f$ (SD)

and for a mixed state (mostly Bino)

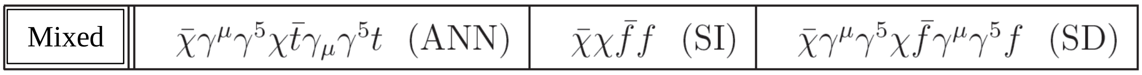

Mixed	$\bar{\chi}\gamma^\mu\gamma^5\chi\bar{t}\gamma_\mu\gamma^5 t$ (ANN)	$\bar{\chi}\chi\bar{f}f$ (SI)	$\bar{\chi}\gamma^\mu\gamma^5\chi\bar{f}\gamma^\mu\gamma^5 f$ (SD)

where γs are usual Dirac matrices, *f* stands for a generic fermion coupling, *W* for the electroweak boson and *t* for the quark top.

- The *annihilation cross section*, i.e. different importance of the S/P-wave in the annihilation computation. In general, low-mass neutralino theories have the S-wave annihilation channel helicity suppressed for light fermions, while high-mass neutralinos have no suppression in this channel.

So there are more suitable and less suitable scenarios for AMS-02.

After defining a discrimination parameter I_ϕ, function of the chi square value required to discriminate DM signal from background at a given confidence value and of the experimental setup (acceptance and exposure time), a discrimination power for AMS-02 is determined, depending on the SUSY neutralino candidate. The result, as it is inferable from Figure 34, is that the AMSB Wino MSSM is the most suitable for AMS-02, both in antiproton and positron channel.
And this is a great thing, because the heavy Wino model is the only one compatible with the previous research depicted scenario.

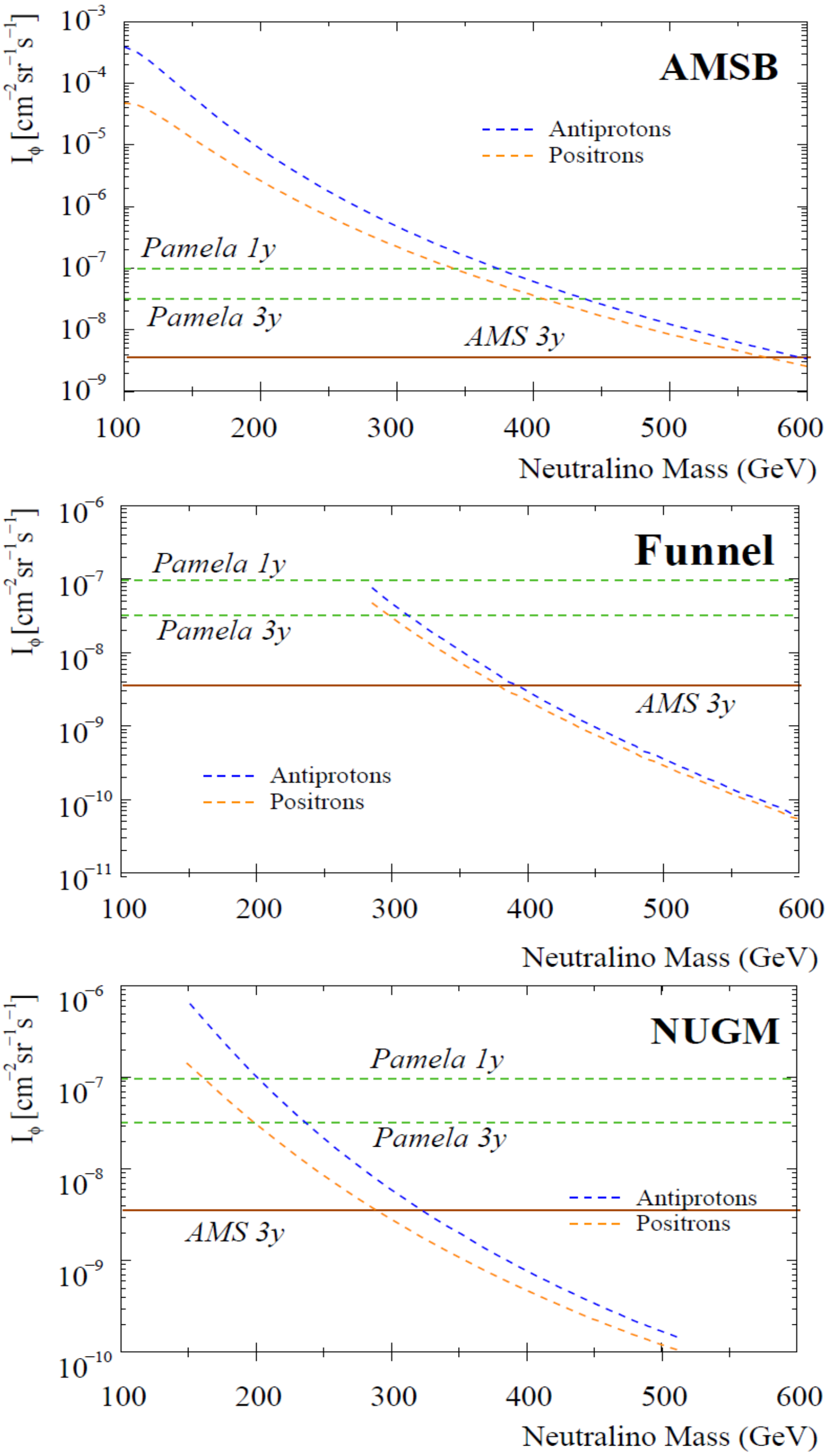

Figure 34 - In these plots, the I_ϕ parameter is reported as a function of the neutralino mass in each of the discussed SUSY scenarios for both the anti-proton (dashed curve) and positron (dotdashed curve) signals. The pairs of horizontal dashed lines represent the estimates of $I_\phi^{95\%}$ for the PAMELA satellite after an operating time of one and three years, assuming for the average acceptance the value of the geometrical one. The estimate for the 95% C.L. discrimination parameter of AMS in three years of data taking (with superconductive magnet) is shown as a solid horizontal line [180].

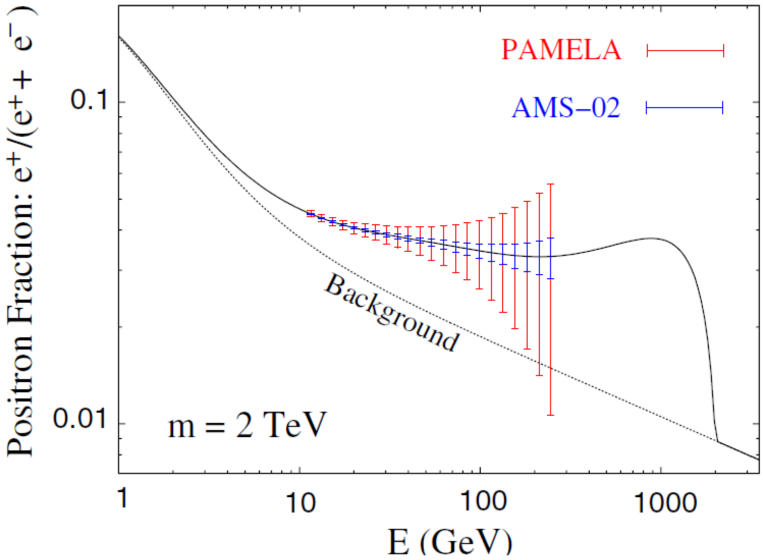

Figure 35 – Positron fraction from a heavy Wino neutralino [107, 181, 182].

A 2 TeV Wino could be easily detected by AMS-02 (Fig. 35), with a great resolution, much better than PAMELA's one.

3.5.2 Little Higgs Particle

As an alternative mechanism (to Supersymmetry) to stabilize the weak scale, the so-called "Little Higgs" model, has been proposed and developed. In these models, the Standard Model Higgs is a pseudo-Goldstone boson with its mass protected by approximate nonlinear global symmetries.
Although the idea was first suggested in the 1970s, a viable model was only constructed by Nima Arkani-Hamed, Andy Cohen, and Howard Georgi in the spring of 2001. The idea was explored further by Nima Arkani-Hamed, Andy Cohen, Thomas Gregoire and Jay Wacker in the spring of 2002. Also in 2002, several other papers appeared that refined the ideas of little Higgs theories.
Little Higgs theories were an outgrowth of dimensional deconstruction [216]. In these theories, the gauge group has the form of a direct product of several copies of the same factor, for example SU(3) × SU(3). Each SU(3) factor may be visualized as the SU(2) group living at a particular point along an additional dimension of space. Consequently, many virtues of extra-dimensional theories may be reproduced even though the little Higgs theory is 3+1-dimensional. In the Minimal Moose model these symmetries acquires a clear physical attribute: they're a chiral symmetry $SU(3)_L \times SU(3)_R$ and a collective spontaneous symmetry breaking produces the vector subgroup from which the Standard Model descends [216, 217, 218].
The main idea behind the Little Higgs models is that the one-loop contribution to the tachyonic Higgs boson mass coming from the top quark cancels. The other one-loop contributions are small enough that they don't really matter; the top Yukawa coupling is huge (because related to its mass) and all the other Yukawa couplings and gauge couplings are small. The reason is that, simplifying, a loop is proportional to the coupling constant, following the example above, of one of the SU(2) groups. The divergences to the Higgs mass which remain are present only at the two-loop level and, therefore, the weak scale can be stabilized in an effective field theory which is valid up to ~ 10 TeV. Recall that in supersymmetry, the divergences to the Higgs mass are exactly cancelled at all orders.
At least two varieties of Little Higgs models have been shown to contain possible dark matter candidates [218−225]. One of these classes of models, called "theory space" Little Higgs models,

provide a possibly stable, scalar particle which can provide the measured density of dark matter: the detection prospects for such a candidate were found to be not dissimilar to WIMPs predicted in models of supersymmetry or universal extra dimensions. Cheng and Low have developed another variety of Little Higgs model, motivated by the problem of the hierarchy between the electroweak scale and the masses of new particles constrained by electroweak precision measurements. They solve this problem by introducing a new symmetry at the TeV scale which results in the existence of a stable WIMP candidate with a TeV mass. For a potential dark matter candidate from a Little Higgs model to be stable, it must be assumed that the discrete symmetry, called *T*-symmetry, which protects it from decay is fundamental and is not broken by the operators in the UV completion. The most modern candidate are vector bosons which emerge from latest theories spectra and are called A_H. They're a sort of *massive photons*.

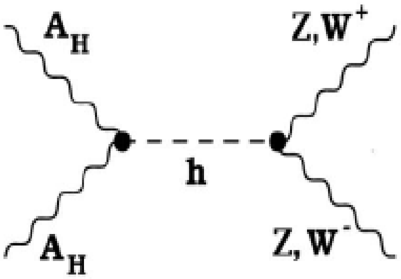

$$\begin{cases} W^\pm \to hadrons \to \pi^\pm \to \mu^\pm \to e^\pm \\ W^+ \to \mu^+\nu \to e^+\nu\bar{\nu}\nu \\ W^+ \to e^+\nu \end{cases}$$

Figure 36 – Positron enhancement due to a Little Higgs particle decay.

Due to kinematic reasons and properties of the theory, the hadronic annihilation for a LTP (Lightest T-symmetry Particle) is strongly suppressed. But the positron channel (in Fig. 36) is very promising. Also a photon-photon annihilation is a favored process.

AMS-02 can explore the parameters space of this theory, increasing our knowledge [219, 225]. Figure 37 illustrates how AMS covers a wide region of the parameters space, i.e. it can distinguish from background signal above the marked line.

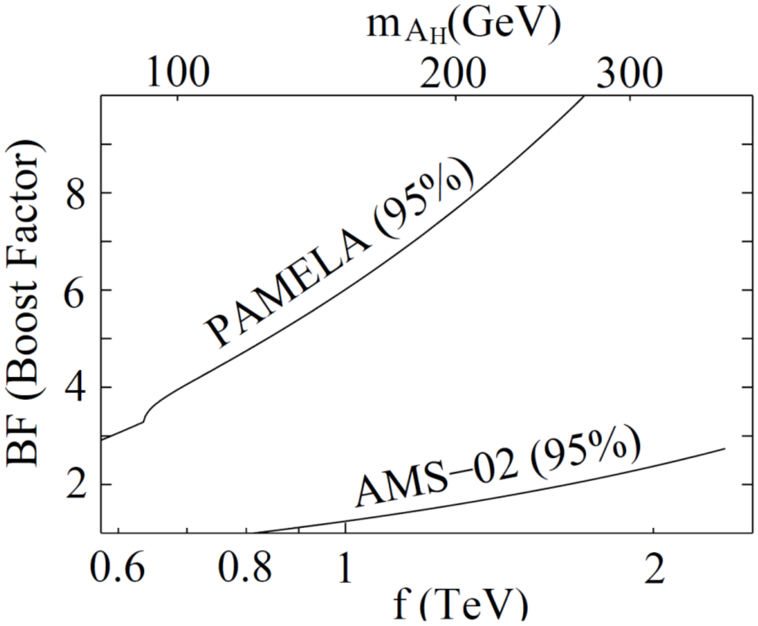

Figure 37 - 95% C. L. contour within WMAP constraint for Little Higgs Dark Matter parameters space. The plot is not uptodate for heavy candidate, but the principle is the same and can naively be extended to the TeV scale, without losing its meaning.

3.5.3 Scalar Singlet

One of the simplest extensions of the Standard Model that can explain the dark matter is the addition of a real scalar singlet and an unbroken Z_2 symmetry under which the singlet is odd while all other fields are even. Such a model, known as the singlet scalar model of dark matter, has been studied several times in the literature [226, 227]. Predictivity is undoubtedly its most salient feature. In contrast with other common scenarios that explain the dark matter, the singlet model contains only one additional field, the singlet scalar, and two new parameters: the singlet mass and the coupling between the singlet and the Higgs boson – the only Standard Model field that couples to it. The singlet relic density as well as its direct and indirect detections rates depend additionally on the Higgs mass. After imposing the dark matter constraint, the viable parameter space gets reduced simply to the singlet mass and the Higgs mass, now well-know. The singlet scalar model, therefore, provides a compelling and predictive scenario to explain the dark matter. It has a simple renormalizable Lagrangian:

$$\mathcal{L} = \mathcal{L}_{SM} + \frac{1}{2}\partial_\mu S \partial^\mu S - \frac{m_0^2}{2} S^2 - \frac{\lambda_S}{4} S^4 - \lambda S^2 H^\dagger H \,, \qquad (3.53)$$

where $\mathcal{L}_{SM}$ denotes the Standard Model Lagrangian, H is the Higgs doublet, and S is the singlet scalar field.

This is surely a promising model and several authors provide estimate for its detection and "advice" on how to explore the parameter space of the theory.

AMS-02, as it's show below in Fig. 38, could put some constraints on these theories in the antiproton channel.

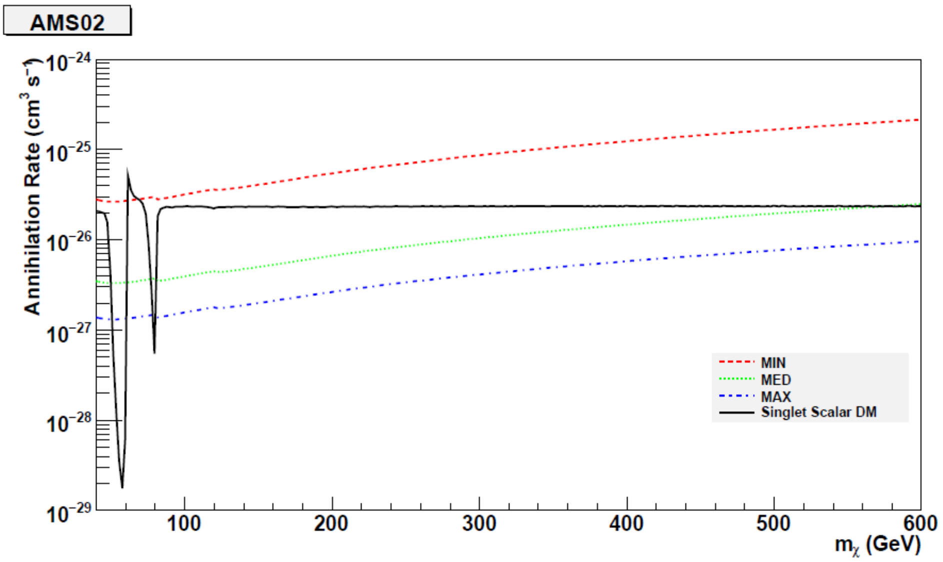

Figure 38 - Regions of the parameter space that are within the sensitivity of the AMS-2 experiment in the antiproton channel. The area above the MIN, MED, and MAX lines is detectable by AMS-02. The solid (black) line shows the prediction of the singlet model. Notice that for MED and MAX, essentially the whole parameter space is detectable [228].

Also **Scalar Multiplet** extensions have been explored (*Doublet*, *Triplet* and so on) [393]: these quite predictive theories produce scalar candidates with higher masses, from about 3 to 10 TeV, naturally include the Sommerfeld effect and they are successful in reproducing the correct DM relic density.

3.5.4 Primordial Black Holes

Micro black holes are predicted as tiny black holes, also called *quantum mechanical black holes* or *mini black holes*, for which quantum mechanical effects play an important role. It is possible that such quantum primordial black holes were created in the high-density environment of the Early Universe, or possibly through subsequent phase transitions. They might be observed by astrophysicists in the near future, through the particles they are expected to emit by Hawking radiation (Fig. 39).

Some theories involving additional space dimensions predict that micro black holes could be formed at an energy as low as the TeV range, which are available in particle accelerators such as the LHC. Such quantum black holes would instantly evaporate, either totally or leaving only a very weakly interacting residue.

In principle, a black hole can have any mass equal to or above the Planck mass (about 22 micrograms). To make a black hole, one must concentrate mass or energy sufficiently that the escape velocity from the region in which it is concentrated exceeds the speed of light. This condition gives the Schwarzschild radius, $R = 2GM/c^2$, where *G* is gravitational constant and *c* is the speed of light, of a black hole of mass *M*. On the other hand, the Compton wavelength, $\lambda = h/Mc$, where h is Planck's constant, represents a limit on the minimum size of the region in which a mass *M* at rest can be localized. For sufficiently small *M*, the reduced Compton wavelength ($\lambda = \hbar/Mc$) exceeds half the Schwarzschild radius, and no black hole description exists. This smallest mass for a black hole is thus approximately the Planck mass.

But in higher-dimensional space-time, the strength of gravity increases more rapidly with decreasing distance than in three dimensions. With certain special configurations of the extra dimensions, this effect can lower the Planck scale to the TeV scale, through the relation $M_P^2 = 8\pi M_*^2 R^2$, where M_* is the effective Planck scale and R the additional dimension lenght. Examples of such extensions include large extra dimensions, special cases of the *Randall-Sundrum model* [229], and string theory. In such scenarios, black hole production could possibly be an important and observable effect at the LHC. It would also be a common natural phenomenon induced by the cosmic rays [230–236].

All this assumes that the theory of General Relativity remains valid at these small distances. If it does not, then other, presently unknown effects, will limit the minimum size of a black hole.

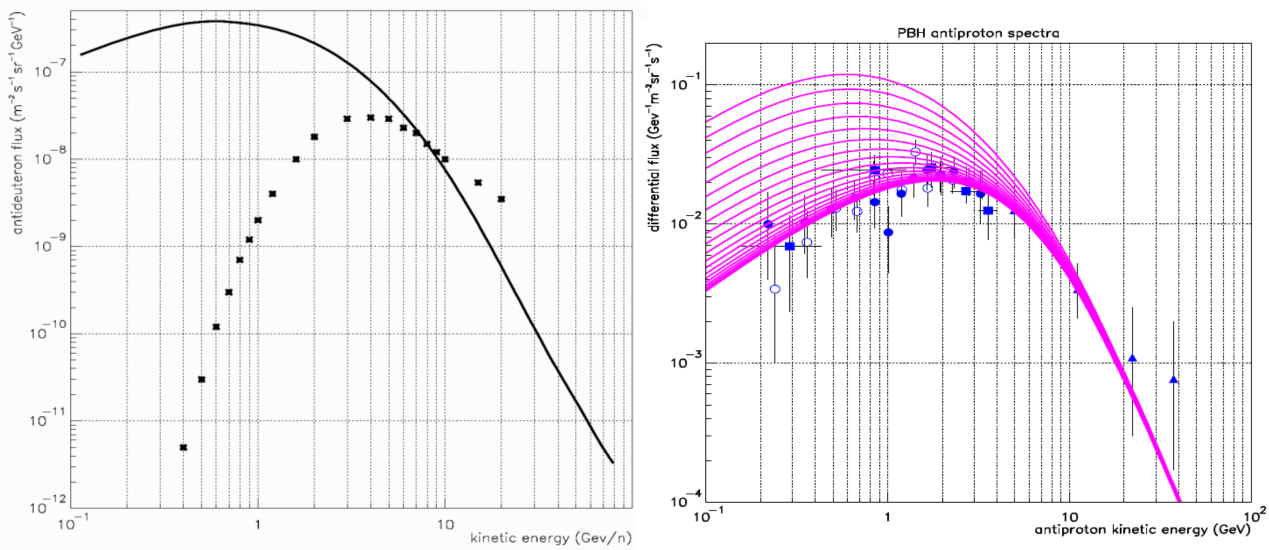

Figure 39 – Antideuterons (left) astrophysical spectrum (straight black line) from primordial quantum black holes. On the right, the antiprotons spectra (several parameterizations) [230–233].

About their detectability, there are many problems. They especially produce low energy hadrons. Antiprotons production is incompatible with PAMELA's data and the antideuterons one is at the border of AMS-02 sensitivity discussed in 3.4.2.

Furthermore CMS researches for PBH are still inconclusive. They put some high energy constraints: from CMS results at March 2012, PBH should have masses above 3.8 to 5.3 TeV, but they have seen no signal at all [CMS Website].

Finally, sometimes also **Holeums** are taken into account in dark matter theoretical searches [237, 238, 239], which are stable, quantized gravitational bound states of primordial or micro black holes.

3.5.5 Kaluza-Klein particle

An alternative possibility for new weak-scale physics is extra dimensions. The idea that there may be extra spatial dimensions is an old one, going back at least as far as the work of Kaluza and Klein in the 1920's. Their original idea is untenable, but it has many modern descendants, of which the closest living relative is universal extra dimensions (UED). In UED, all particles propagate in flat, compact extra dimensions of size 10^{-18} m or smaller. In the simplest UED model, minimal UED, there is one extra dimension of size R compactified on a circle, with points with *y* and *-y* identified, where *y* is the coordinate of the extra dimension. Every SM particle has an infinite number of partner particles, with one at every Kaluza-Klein (KK) level *n*, with mass $\sim nR^{-1}$. In contrast to supersymmetry, these partner particles have the same spin. As a result, UED models do not solve the gauge hierarchy problem; in fact, their couplings become large and non-perturbative at energies far below the Planck scale [3, 78]. The motivation to consider UED models is that they provide an interesting and qualitatively different alternative to supersymmetry, but it assumes that UED are a low-energy approximation to a more complete theory that resolves the gauge hierarchy problem and is well-defined up to the Planck scale. Minimal UED parameter space is extremely simple, as it is completely determined by only two parameters: the mass of the SM Higgs boson, today known, and R, the compactification radius.

The simplest UED models preserve a discrete parity known as KK-parity, which implies that the lightest KK particle (LKP) is stable and a possible dark matter candidate [240, 241, 242].

The lightest KK particle (LKP) is typically $B^{(1)}$, the level 1 partner of the hypercharge gauge boson. The regions of parameter space with the correct $B^{(1)}$ thermal relic density have been investigated in a series of increasingly sophisticated studies; the required LKP mass is 600 GeV < $m_{B^{(1)}}$ < 3 TeV, a heavier range than for traditional neutralinos. This is because LKPs annihilation is through S-wave processes, and so is not P-wave suppressed, in contrast to neutralinos.

KK particles are able to annihilate in all antiparticles, producing hypothetical enhancements both for antiprotons and positrons (Figs. 40, 41) [243, 244, 250].

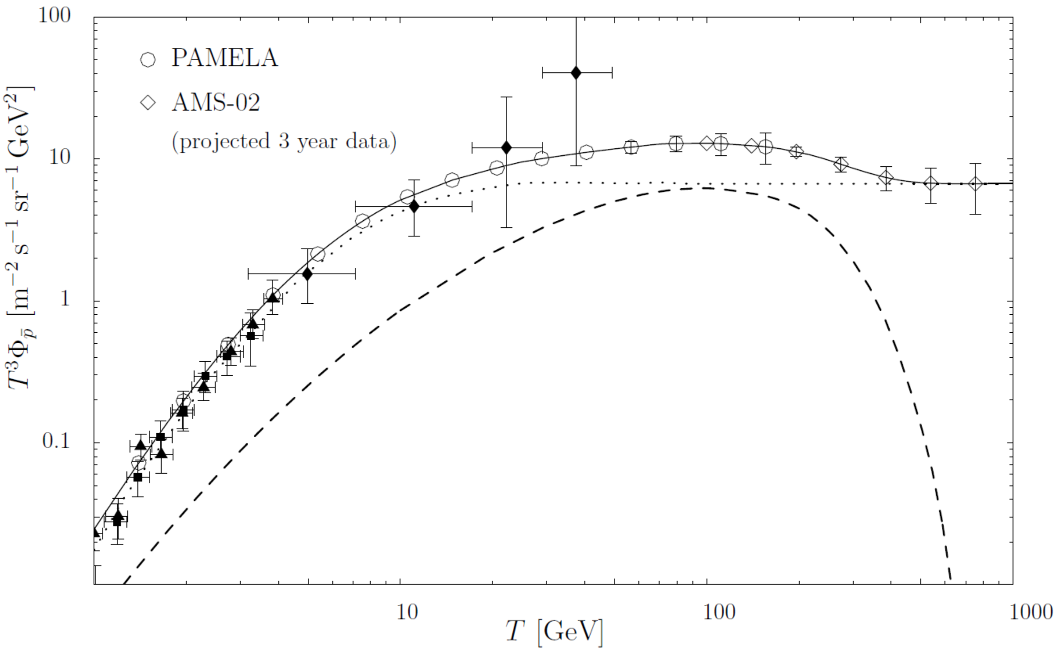

Figure 40 – The solid line shows the expected antiproton spectrum for the case of a clumpy NFW profile and a $m_{B^{(1)}}$ = 800 GeV; the dotted and dashed lines give, respectively, the background flux and the contribution from LKP annihilations alone. The data points are from BESS 1998 and CAPRICE 1998; the detectional prospects of PAMELA and AMS-02 are indicated by displaying their projected data after three years of operation (only statistical errors are included; error bars smaller than the symbol size are not shown). For AMS-02, only energies above 100 GeV are considered [245].

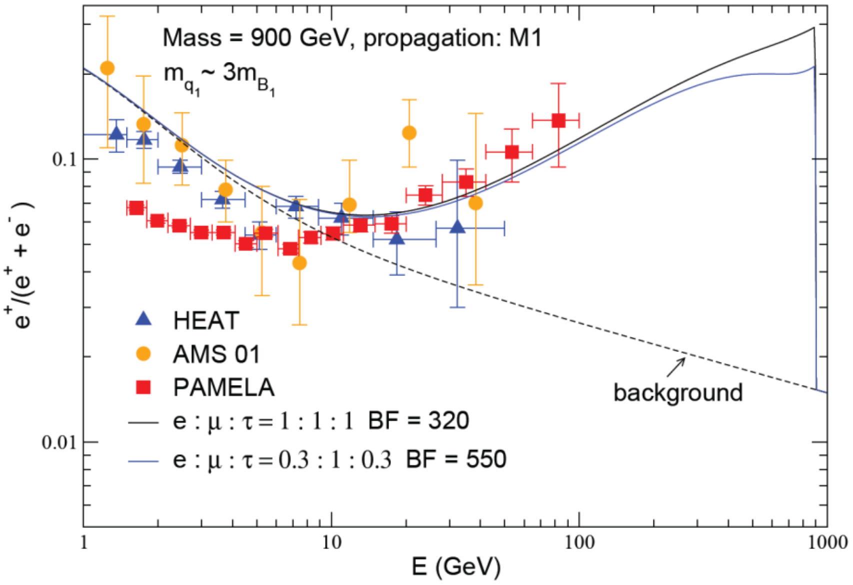

Figure 41 – The positron fraction produce d by a 900 GeV mass vector KK particle compared to PAMELA's data with a particular set of parameters. The two line represent two different privileged decay channels [246].

The stability of the LKP is also granted by a Z_3 symmetry, linear combination of the baryonic charge and the SU(3) color. If the baryonic number is a good conserved quantum number this transformation become a symmetry of the theory:

$$\phi \rightarrow e^{2i\pi\left(B-\frac{n_c-n_{\bar{c}}}{3}\right)}\phi \tag{3.54}$$

where B is the baryonic number of the field ϕ and n_c is the number of colors [3, 78].

Another particle produced by the KK theory spectrum is the LZP, i. e. a **right-handed neutrino** which also may account for the dark matter observations. In fact, while SM particles are clearly not charged under Z_3, exotic states such as colored grand unified gauge bosons and most KK fermions with no zero modes (different from the $B^{(1)}$ vector) are charged under Z_3, since they have the "wrong" combination of color and baryon number. As a consequence of this symmetry, the lightest Z_3 charged particle (LZP) cannot decay into SM particles and is stable, a neutrino-like state [252, 253, 254]. LZP has gauge quantum number of right-handed leptons indeed, it's colorless and electrically neutral and lighter than gauge KK states. In the Pati–Salam model (and Warped GUT) [247, 248], each Z_3 charged particle decays into the LZP ν_R' easily.

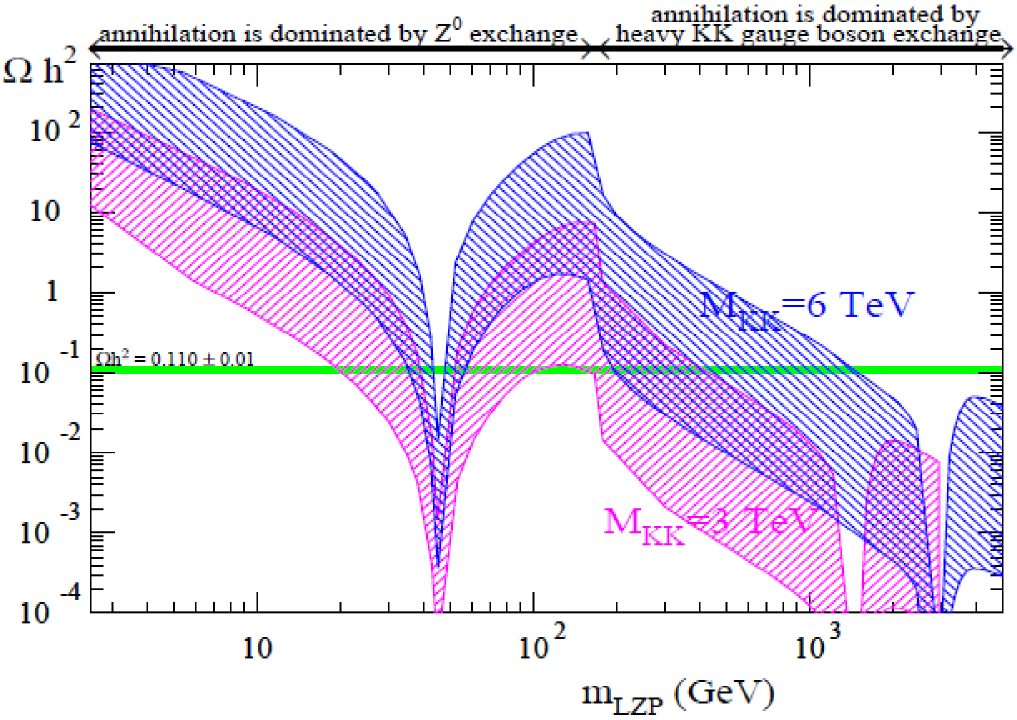

Figure 42 - Predictions for the relic density for two values of the gauge KK mass M_{KK}. The two bands are obtained by varying two parameters of the model. The kink at $m_{LZP} = m_t$ corresponds to the opening of the annihilation channel into top quarks [248].

It's clear from Fig. 42 it is possible to reach very heavy candidate for the KK boson ($\lesssim 10\ TeV$), and the TeV÷2 TeV scale for the LZP.

Both LKP and LZP can be detected by AMS-02 in all particle channels: positrons, antiprotons and antideuterons. Especially in the antiproton, there's the opportunity to see a sharp bump in the spectrum in the high energy range, which could grant an important clue of DM existence.

However, you have to accept a Universe with extra-dimensions and there isn't any evidence yet.

3.5.6 Axions and other particles

Axions

Introduced in an attempt to solve the problem of CP violation in particle physics, the *strong CP problem*, axions have also often been discussed as a dark matter candidate [1, 2, 3].

The CP violating term in the QCD Lagrangian is:

$$\mathcal{L}_{CP} = \Theta \frac{g^2}{32\pi^2} G^a_{\mu\nu} \widetilde{G}^{a\mu\nu} \ , \tag{3.55}$$

where $G^a_{\mu\nu}$ and $\tilde{G}^a_{\mu\nu}$ are the gluon field strength and its dual respectively, while Θ is a dimensionless parameter, whose value sets the magnitude of the effective term of the Lagrangian. The axion is a pseudo Nambu-Goldstone boson of the spontaneously broken Peccei-Quinn symmetry. When the symmetry breaks the axions acquire an effective coupling to gluons that cancels the Θ parameter of equation, thus solving the problem.

Laboratory searches, stellar cooling, the dynamics of supernova 1987A and cosmological observations constrain axions to be extremely light ($\sim 10^{-(5\div3)}$ eV). Furthermore, they are expected to be extremely weakly interacting with ordinary particles, which implies that they were not in thermal equilibrium in the Early Universe.

The calculation of the axion relic density is uncertain, and depends on the assumptions made regarding the production mechanism. Nevertheless, it is possible to find an acceptable range where axions satisfy all present-day constraints and represent a good dark matter candidate: in particular, if $m_a \sim 10$ μeV they could be the dominant component of DM.

They are not detectable with AMS-02 but they're quite good candidates, even if they can't justify the positron excess alone.

Sterile neutrinos

These hypothetical particles are similar to Standard Model neutrinos, but without Standard Model weak interactions, apart from mixing. They were proposed as dark matter candidates in 1993 by Dodelson and Widrow [255]. Stringent cosmological and astrophysical constraints on sterile neutrinos come from the analysis of their cosmological abundance and the study of their decay products. Light neutrinos, with masses below a few keV, would be ruled out as dark matter candidates. In fact, if the WMAP result for the reionization optical depth is correct, then dark matter structures were in place to form massive stars prior to redshift $z > 20$, which is simply not possible if the dark matter particle mass is smaller than ~ 10 keV. An alternative explanation for the WMAP optical depth is reionization by decaying particles such as sterile neutrinos [3, 78].

Sterile neutrinos could also be *cold* dark matter, if there is a very small lepton asymmetry, in which case they are produced resonantly with a non-thermal spectrum [256–264].

Also sterile neutrinos are not detectable with AMS-02.

Singlino

In particle physics, NMSSM is an acronym for *Next-to-Minimal Supersymmetric Standard Model*. It is a supersymmetric extension to the Standard Model that adds an additional singlet chiral superfield to the MSSM. For review articles about the NMSSM see [265].

The Minimal Supersymmetric Model does not explain why the μ parameter in the superpotential term $\mu H_u H_d$ is at the electroweak scale. The idea behind the Next to Minimal Supersymmetric Model is to promote the μ term to a gauge singlet, chiral superfield S. Note that the scalar superpartner of the singlino S is denoted by $\hat{S}$ and the spin-1/2 singlino superpartner by $\tilde{S}$. The superpotential for the NMSSM is given by

$$W_{\mathrm{NMSSM}} = W_{\mathrm{Yuk}} + \lambda S H_u H_d + \frac{\kappa}{3} S^3 \qquad (3.56)$$

where W_{Yuk} gives the Yukawa couplings for the Standard Model fermions. Since the superpotential has mass dimension three, the couplings λ and κ are dimensionless, hence the mu-problem of the MSSM is solved in the NMSSM; the superpotential of the NMSSM is scale invariant. The role of the λ term is to generate an effective μ term. This is done with the scalar component of the singlet $\hat{S}$ getting a vacuum-expectation value $\langle \hat{S} \rangle$, that is $\mu_{eff} = \lambda \langle \hat{S} \rangle$. Without the κ term the superpotential would have a U(1)' symmetry. This additional symmetry would alter the phenomenology completely. The role of the κ term is to break this U(1)' symmetry. However there remains a discrete Z_3 symmetry, which is moreover broken spontaneously. In principle this leads to the *domain wall problem*. Introducing additional but suppressed terms, the Z_3 symmetry can be broken without changing phenomenology at the electroweak scale. It is assumed that the domain wall problem is circumvented in this way without any modifications except far beyond the electroweak scale.

In practice, the spin-1/2 singlino $\tilde{S}$ gives a **fifth neutralino**, compared to the four neutralinos of the MSSM. The singlino does not couple to gauge bosons, gauginos (the superpartners of the gauge bosons), leptons, sleptons (the superpartners of the leptons), quarks or squarks (the superpartners of the quarks). Supposed that a supersymmetric partner particle is produced at a collider, for instance at the LHC, the singlino is omitted in cascade decays and therefore escapes detection. However, in case the singlino is the lightest supersymmetric particle (LSP) all supersymmetric partner particles eventually decay into the singlino. Due to *R* parity conservation this LSP is stable. In this way the singlino could be detected via missing transversal energy in the detector.

The “singlino-dominated” neutralino $\tilde{\chi}_S$ (in terms of mixing, for example 90% singlino and 10% Higgsino) is a light particle: in function of the parameter of the theory and of the now known Higgs mass, its mass is between 10 and 160 GeV [266–269]. Recent studies [270] performed to constrain the Singlino scenario with PAMELA and WMAP data favor a very light singlino-dominated neutralino, which could produce the cosmic antiproton spectrum measured by PAMELA (but not the positron one) and has the correct cosmological properties. This particle would be compatible with the circumstantial signals by CoGeNT and DAMA-LIBRA and would have a mass of 12 GeV.

This is in complete disagreement with all the reasoning performed and all the empirical evidences from the entire scientific community (see 3.8.1 for insights). So we will not dwell over with this candidate.

4th SM generation MDM

The Minimal Dark Matter (MDM) proposal pursues a different and somewhat opposite direction: focusing on the Dark Matter problem only, let’s add to the SM the minimal amount of new physics (just one extra EW multiplet X) and search for the minimal assignments of its quantum numbers (spin, isospin and hypercharge) that make it a good dark matter candidate without ruining the positive features of the SM [271]. No ad hoc extra features are introduced: the stability of the successful candidates is guaranteed by the SM gauge symmetry and by renormalizability. Moreover, due to its minimality, the theory is remarkably predictive: no free parameters are present and therefore the phenomenological signatures can be univocally calculated, e.g. at colliders and for direct/indirect detection, up to the astrophysical and cosmological uncertainties. Unfortunately, the current bounds on the masses of the 4th generation quarks within the SM4 are rather high- reaching up to 600 GeV, i.e. around the unitarity bounds on quark masses [272, 273, 274]. The implications of such a “super-heavy” 4th generation spectrum are far reaching. In fact, the SM4 as such is also strongly disfavored from searches at LEP (neutrino's three family bound), and from the LHC and Tevatron searches of the single Higgs particle of this model, essentially excluding the SM4 Higgs with masses up to 600 GeV and, thus, making it incompatible with the recent observation/evidence of a light Higgs with a mass of $\sim$ 125 GeV [275, 276].

So there's no evidence of a new family at LHC and, even if detectable by AMS-02 via its annihilation products, a fourth generation dark candidate seems to be rather improbable.

Tulin antibaryionic dark matter (a special Asymmetric Dark Matter theory)

Asymmetric DM theories take into account the possibility of a DM internal matter-antimatter asymmetry, introducing a DM sector with Standard Model-like violations [277−281].

The Tulin theory arise from the intent of explaining the dark matter problem and the matter-antimatter cosmic asymmetry at the same time, through a not perfectly conserved number which could generate on one side the visible world, and on the other the dark conjugate.

Asymmetric DM theories try to deal with a unique comprehensive theory; for example, in Tulin *antibaryonic scenario* [282] a X postreheating particle especially decays into visible material hadronic/leptonic world and dark antibaryonic antimatter (Φ and Y) . Then these "antibaryonic" dark matter candidates could induce a proton decay into positive charge mesons which, in turn, could decay into positrons (see Figure 43).

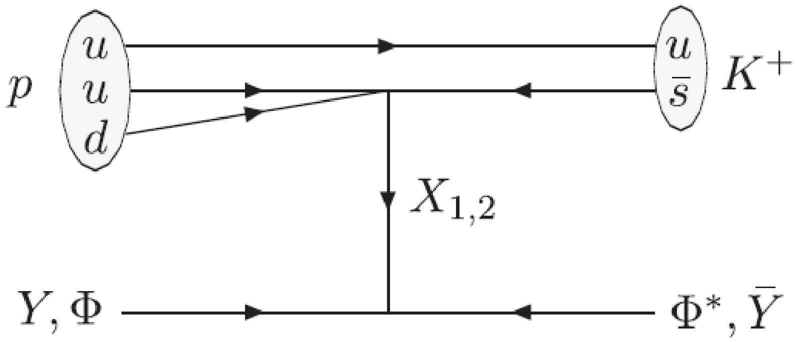

Figure 43 - Diagram for representative induced nucleon decay processes $pY \to K^+\Phi^*$ and p$\Phi \to K^+\bar{Y}$

This is only an example of new ambitious models that are going to be explored in these years. Moreover it represents a simple natural leptophilic scenario that produces a positron excess. The dark matter candidate from Tulin Theory and generic Asymmetric Dark Matter Models are usually very light, with masses of $\sim few\ GeV$.

But it's very difficult to prove such a theory and it needs more work and speculation before considering it (and Asymmetric DM theories in general) a viable dark matter theory.

3.5.7 AMS-02 fluxes estimates

To complete our understanding of the indirect detection of dark matter, let's compute the number of fundamental particles (and (anti)deuterons) that AMS-02 could detect per year, starting from the known species fluxes at low kinetic energies (< tens of GeV). This is easily done from the observed fluxes by calculating the relative abundances with respect to the proton one (Table 5).

	Absolute Flux $[GeV\ m^2\ s\ sr]^{-1}$	**Number of particles in one year w.r.t. *p***
protons	10^2	10^{10}
deuterons	10	10^9
helium	$10 \div 1$	$10^{8\div 9}$
electrons	$1 \div 10^{-1}$	$10^{7\div 8}$
positrons	$10^{-(2\div 1)}$	$10^{6\div 7}$
antiprotons	10^{-2}	10^6
Secondary antideuterons	$10^{-(8\div 7)}$	$1 \div 10$
***Primary* antideuterons for M = 1 TeV DM**	$10^{-(9\div 8)}$	$10^{-1} \div 1$

Table 5 – Absolute fluxes summary and particle average statistical relevances (order of magnitude) in the known kinetic energy range (0.1 GeV ÷ tens of GeV, less than 100 GeV), considering 10^{10} protons measured in one year with AMS-02. The fluxes are in descending order.

We expect 10 billion protons per year, tens million electrons (and positrons), one million antiprotons and only few antideuterons in low energy window. The total number of particle is about 12 billion per year. The fluxes are collected from several experimental data [283, 284, 285], some of them already discussed in this chapter. In Table 5 only the last row represents a predicted dark matter primary flux: the others are all secondary species. It can be noted, as already known, that is very difficult to distinguish a dark matter antideuteron signal from the background: the 0.1÷1 GeV range has to be zoomed and each source of uncertainty carefully considered.

Table 5 also shows the order of magnitude of the number of particles AMS-02 should have seen in one year data, once discriminated the particle species: this is a guide line to test the goodness of our preliminary observations. The low energy antiparticle-particle mean predicted ratios are reported in Table 6.

Fluxes Ratios at Low Energies	
e^+/e^-	10^{-1}
$\overline{p}/p$	10^{-4}
$\overline{d}/d$	$< 10^{-8}$

Table 6 – Antiparticle to particle predicted flux ratios at low energies. The reference value for the interesting antiproton to proton ratio is 10^{-4}. We expect to see an antiproton fraction enhancement at high energies if dark matter injects antiproton in the CRs through self-annihilation.

More interesting is the high energy range, from about 100 GeV to 2 TeV. Here there are only leptonic observed information from FERMI and PAMELA (Table 7, in green). The hadronic CR fluxes are predicted for secondary sources and primary sources, i. e. dark matter non-leptophilic candidates with multi-TeV masses (Table 7, in red).

	Absolute Flux $[GeV\ m^2\ s\ sr]^{-1}$	**Number of particles in 1 year w.r.t. *p***
protons (T>100 GeV)	10^{-2}	10^6
protons (T ≳ 1 TeV)	10^{-4}	10^4
Secondary antip (T>100 GeV)	$10^{-(8\div6)}$	$1 \div 10^2$
Primary DM antiprotons for M > 2 TeV (T>100 GeV)	$10^{-3}\Phi_p = 10^{-5}$	10^3
DM antiprotons for M > 2 TeV (T ≳ 1 TeV)	$10^{-2}\Phi_p = 10^{-6}$	10^2
electrons (T>100 GeV)	10^{-4}	10^4
Primary DM positrons for M > 2 TeV (T>100 GeV)	$10^{-1}\Phi_{e^-} = 10^{-5}$	10^3

Table 7 - Absolute fluxes summary and predicted particle average statistical relevances (order of magnitude) in the high kinetic energy range (100 GeV – 1 TeV). We expect to see about one thousand of total antiprotons per year in case of dark matter.

One sees from Table 7 that DM primary antiprotons overcome the secondary ones of 2÷3 order of magnitude, producing a clear detectable signal (data taken from [88, 125, 245]). The average number of primary antiprotons above 100 GeV is the same of primary positrons; the electrons are ten times them, so they represent a great background for antiprotons, if the analysis doesn't discriminate them and because of experimental charge confusion (see 5.1.2.4 and 5.1.2.5).

Fluxes Ratios at High Energies	
e^+/e^-	10^{-1}
$\bar{p}/p$ **with DM**	$10^{-(3\div2)}$
$\bar{p}/p$ **without hadronic DM**	$10^{-(5\div4)}$

Table 8 – Antiparticle to particle predicted flux ratios at high energies.

As shown in Table 8, in this energy range the positron to electron ratio remains about the same (the positron enhancement it's not so big, i.e. doesn't reach an order of magnitude), while the antiproton to proton ratio permits to distinguish two scenarios: a cosmic rays physics without non-leptophilic dark matter for decreasing ratio, and one with a heavy dark matter candidate for increasing ratio. The fraction amplification could be of two order of magnitude, so very difficult to be confused with the background. Moreover flux ratios aren't affected by experimental uncertainties, because every experimental acceptance or efficiency factor is erased with the algebraic ratio.

3.6 A synthetic scheme: the uptodate DM candidates landscape

Now one can ask to himself if there are some experimental hints capable to discriminate the several dark matter candidates and restrict these theories parameter space.
The astrophysical observations have already been discussed and here we turn to collider experiments.
They can give us important exclusion regions for dark matter mass and corroborate or disqualify the previous models.
In few words, LHC ATLAS and CMS experiments are showing a great particle desert up to 1 TeV, which grandly favors a heavy multi-TeV dark matter scenario. A detailed examination follows in sections 3.6.1 and 3.6.2..

3.6.1 LHC input

Below, the uptodate to winter 2012 results from ATLAS research for dark matter are presented. They are very discouraging and promising at the same time. In fact there's no evidence of new physics but, on the other hand, this is a good clue of high energy new phenomenology, compatible with space experiments results and with our hunt path. Nor DM missing signals nor particle different from dark matter (emerging from theories spectra) have been detected yet [286, 287, 288]. The landscape is summarized in Figs. 44 and 45.

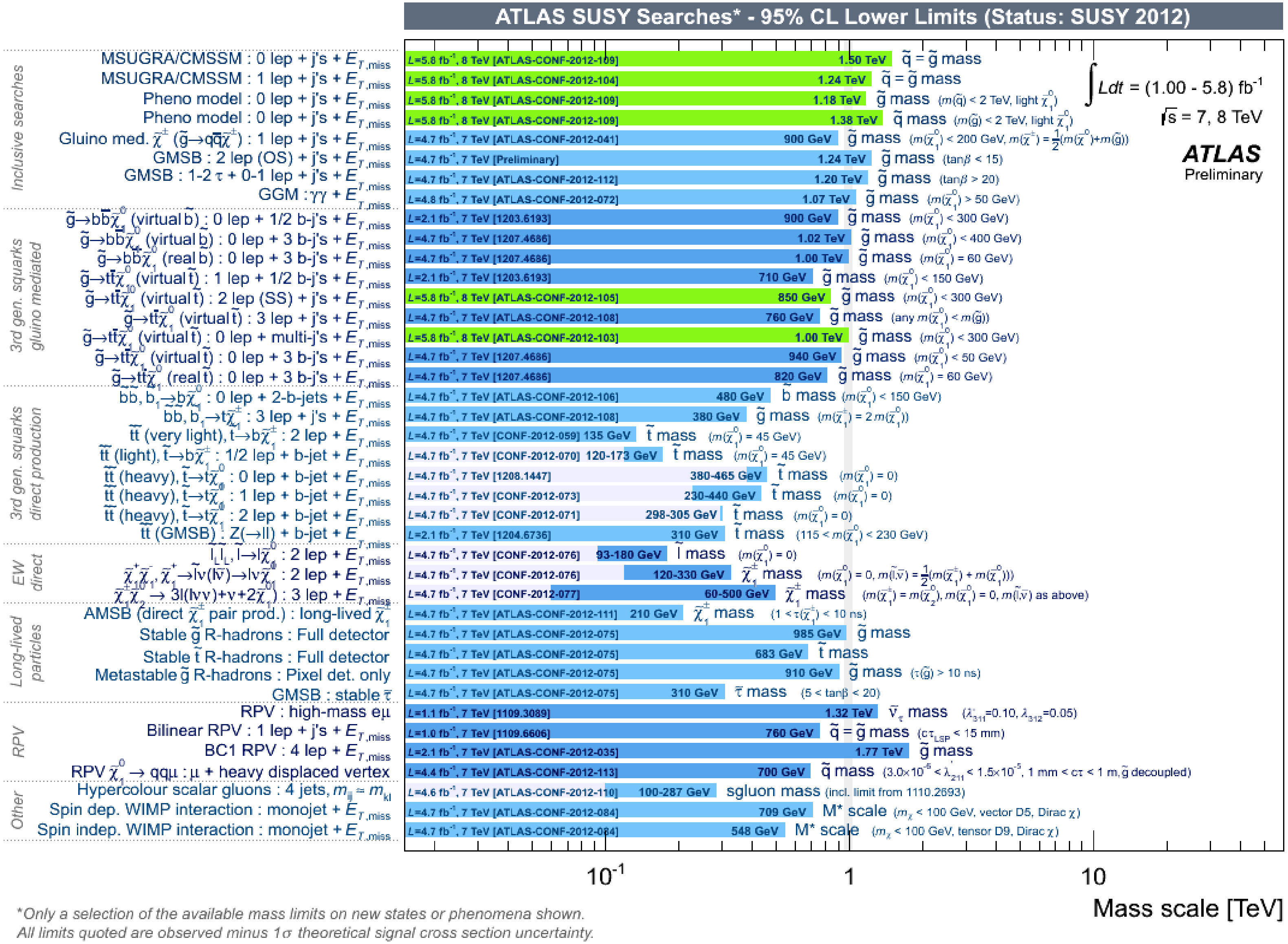

Figure 44 – ATLAS SUSY searches uptodate to autumn 2012: from MSUGRA/CMSSM (up) models to less minimal scenarios. Luminosity and energy are shown in figure [from ATLAS Website].

Figure 45 – ATLAS Exotic searches uptodate to autumn 2012: extra-dimensions theories (UED, Quantum Black Holes), new charged gauge bosons, lepto-quark theories, fourth generation, excited quarks and new exotic scalars (axigluon scalar octet and so on). Luminosity and energy are shown in figure [from ATLAS website].

From Figure 44, it's evident that squarks and gluinos are excluded up to 1 TeV, a fact which represents a big problem for minimal (and also non-minimal) SUSY theories: they don't allow so heavy supersymmetric partners. Also CMS measurements confirm this trend (Fig. 46).

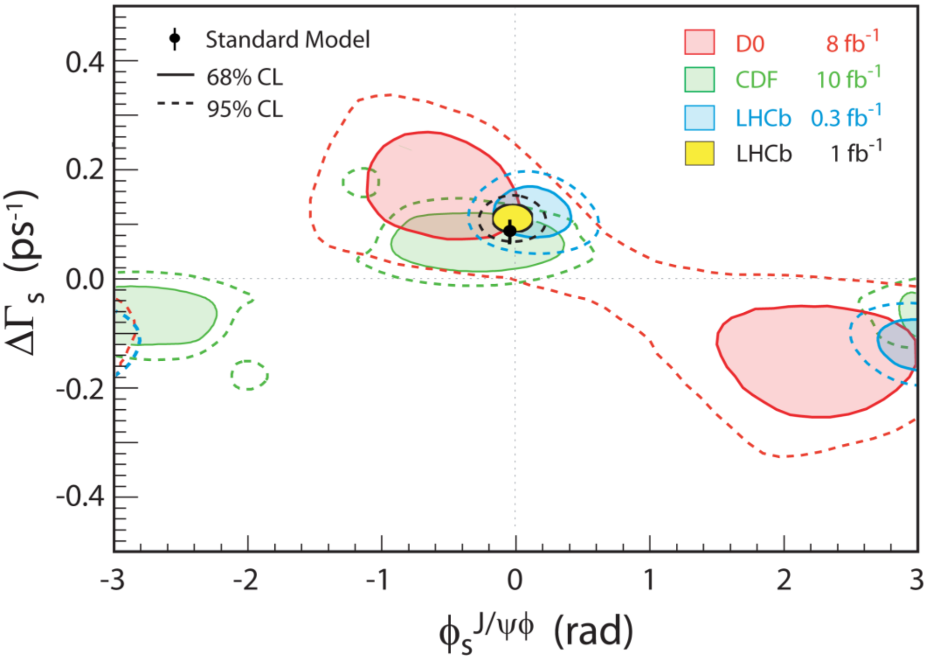

Figure 46 – The artist's view shows the result of the ϕ_s measurement in a plane together with the correlated measurement of another value $\Delta\Gamma_s$ which describe the oscillation properties of the strange-beauty meson B_S^0 [from LHCb website].

The measurement of the difference between properties of matter and antimatter for the strange-beauty B_S^0 mesons can give estimate of Standard Model goodness.

The size of this difference is controlled by the parameter ϕ_s, which is predicted to be small in the Standard Model. However, effects of new particles not predicted by the Standard Model can make the measured value much larger. The progress is depicted in the image: the remaining allowed region is shown in yellow and compared to the previous results from LHCb in blue, and from CDF and D0 experiments in green and red, respectively.

The decay of the strange-beauty particle B_S^0, composed of a beauty antiquark (b) bound with a strange quark (s), into a J/ψ meson and a ϕ meson was used for this measurement. The J/ψ meson decays in turn into a $\mu^+\mu^-$ pair, and the ϕ decays to K^+K^- pair.

The results of the measurement favor two regions, one of which is located around $\phi_s = -0.036 \pm 0.002$ rad, i. e. the exact Standard Model prediction (Fig. 46).

Also exotic theories have to run for recover. Figure 45 shows that graviton, KK particle and Quantum BH have not been seen up to the few-TeV scale. The same for 4th generation quarks and other exotic candidates.

Recently new searches update have been published by ATLAS collaboration [286]: they confirm there is no new physic evidence at all, not even a low sigma signal (Figs. 47, 48, 49).

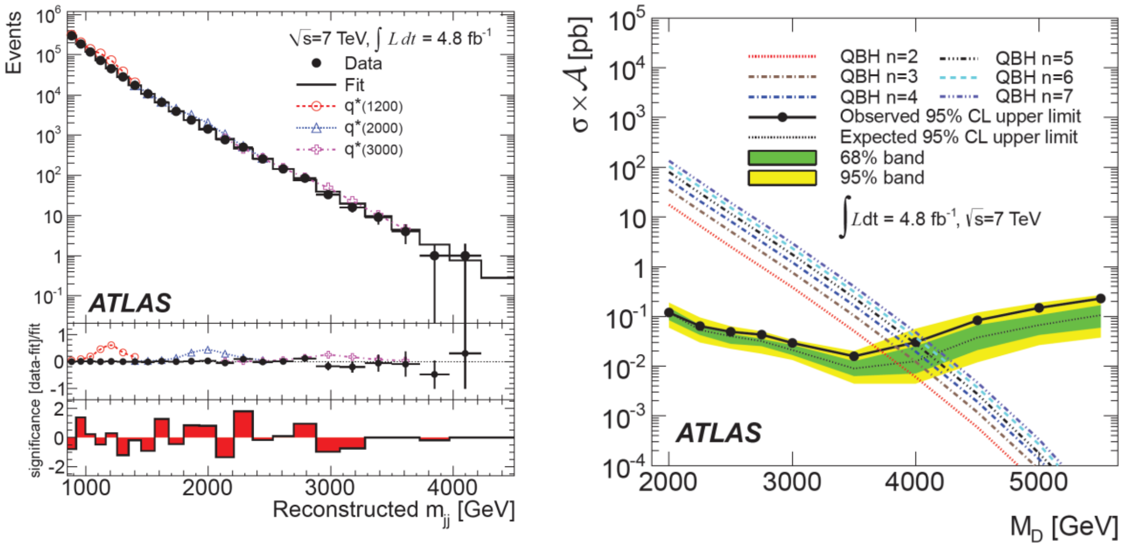

Figure 47 – On the left, the reconstructed dijet mass distribution m_{jj} (filled points) fitted with a smooth functional form (solid line). Mass distribution predictions for three q* masses are shown above the background. The middle part of figure shows the data minus the background fit, divided by the fit. The bin-by-bin significance of the data-background difference is shown in the lower panel.
On the right, the 95% CL upper limits on $\sigma \times \mathcal{A}$ as function of the reduced Planck mass MD of the QBH. The black dotted curve shows the 95% CL upper limit expected from MonteCarlo, and the green and yellow bands represent the 68% and 95% contours of the expected limit, respectively. Theoretical predictions of $\sigma \times \mathcal{A}$ are reported for various numbers of extra dimensions [286].

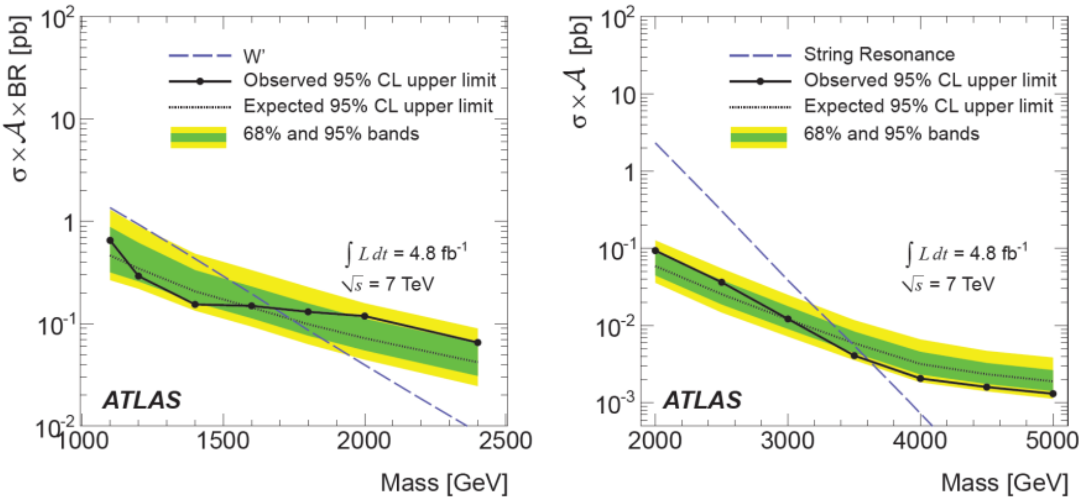

(a) Heavy charged gauge bosons, W'.

(b) String resonances, SR.

Figure 48 - In (a), 95% CL upper limits on $\sigma \times \mathcal{A} \times \mathrm{BR}$ as a function of particle mass (black filled circles) from m_{jj} jet analysis are shown for heavy gauge bosons, W'. The black dotted curve shows the 95% CL upper limit expected in the absence of any resonance signal, and the green and yellow bands represent the 68% and 95% contours of the expected limit, respectively. The observed (expected) limit occurs at the crossing of the dashed theoretical $\sigma \times \mathcal{A} \times \mathrm{BR}$ curve with the observed (expected) 95% CL upper limit curve. In (b), 95% CL upper limits on $\sigma \times \mathcal{A}$ are shown for

string resonances, SR, with the equivalent set of contours for this model, and the same method of limit determination [286].

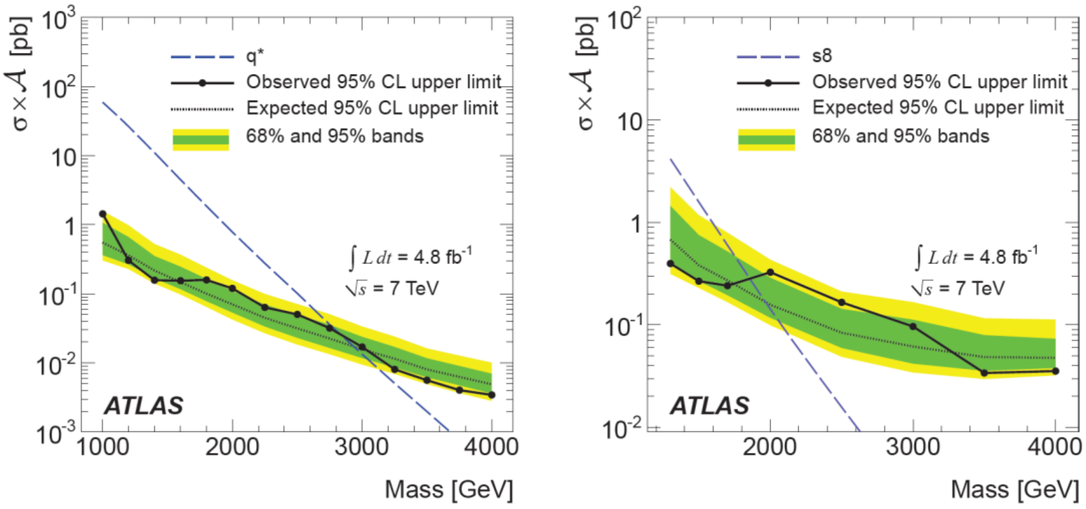

(a) Excited-quark model.

(b) Colour scalar octet model.

Figure 49 - The 95% CL upper limits on $\sigma \times \mathcal{A}$ as a function of particle mass (black filled circles) using m_{jj}. The black dotted curve shows the 95% CL upper limit expected in the absence of any resonance signal, and the green and yellow bands represent the 68% and 95% contours of the expected limit, respectively. Theoretical predictions of $\sigma \times \mathcal{A}$ are shown (dashed) in (a) for excited quarks, and in (b) for colour octet scalars. For a given NP model, the observed (expected) limit occurs at the crossing of the dashed $\sigma \times \mathcal{A}$ curve with the observed (expected) 95% CL upper limit curve [286].

3.6.2 Favored and ill-favored candidates

At this point one is able to review the entire landscape, showing the favored and ill-favored DM candidates and the detection opportunities with accelerator and space experiments such as AMS-02.

AMS-02 is also able to do a gamma astronomy, but its performance are not comparable with FERMI's ones, because it's a spectrometer and not a photon-dedicated experiment. But it's not excluded that in the future it could be corroborate FERMI's data, even if it's not its main purpose.

In Table 9 are summarized the properties of the analyzed DM models.

For what concern the **spin statistics**, dark matter could be a scalar boson, a vector boson, a Dirac fermion, a Majorana fermion, or a Rarita-Schwinger fermion: no constraints are posed. The only one criterion to discern these theories is that only few of these particle satisfy the annihilation physics described previously: S = 0,1 bosons and Majorana fermions are the most interesting candidates because they're their own antiparticle and so capable to self-annihilate. So right-handed LZP neutrinos, sterile neutrinos, gravitinos, MDM 4th generation DM and Tulin Antibaryonic/Asymmetric DM need more specific decay models.

The only two very light candidates are the axion and the sterile neutrino, while all the other candidates are in the multi-GeV/multi-TeV **mass** range. As said before, not Wino-like neutralinos, Little Higgs particles and LZPs tend to be not too heavy ($m_D < 1\,TeV$), and also NLSP singlinos, singlet scalars and gravitinos don't exceed few hundreds of GeV. The heaviest particles are the AMSB Wino, the LKP, 4th generation/Minimal DM particle and the Scalar Multiplet.

Some of them can’t reproduce the correct today **relic density**, i. e. quantum BHs, sterile neutrinos and gravitinos; for the incredibly light axion, a nonthermal quantum-field production (via a misalignment angle mechanism) must be added with which it’s possible to match the DM density parameter. Remember, moreover, that sterile neutrinos and gravitinos are Dirac fermions and they’re addressed as decaying dark matter with a possible EM dipole moment [338, 340]. These theories differ for the typical annihilation cross section of their candidate.

Regardless the Sommerfeld boost factor, high **self-annihilation cross section** are obviously privileged (for example the Wino one); in some cases it’s not possible to easily compute the annihilation cross section, because other processes take place: Hawking radiation for BHs, Primakoff effect for axions [2] or oscillation for sterile neutrinos.

Each model arises for a proper **physical reason**. The most relevant is the Gauge Hierarchy Problem, i. e. the stabilization of the quadratic divergence of the Higgs boson. But also the strong CP problem and the attempt to explain the matter-antimatter asymmetry are very important.

Most of the candidates can annihilate into neutrinos, gamma-rays, positrons, antiprotons and antideuterons at the same time, producing a **detectable signal** in each channel, except for the singlino, which especially produces antiprotons (and secondarily leptons), the axion (which only couples with photons) and antibaryonic DM, which is pure leptophilic. Also the Little Higgs LTP is leptophilic, due to kinematic suppression of the hadronic channel in astrophysical DM processes.

Extra-dimensional theories and SUSY could be leptophilic but, a priori, it’s not known any physical law capable to inhibit the hadron production. For SUSY models a possible **Hidden Sector** scenario must be also taken into account: Arkani-Hamed et al. [289, 290] propose that the peculiar properties of DM can be explained if dark matter is charged under a hidden sector gauge group that kinetically mixes with SM gauge symmetries and is broken at the GeV scale.

In other words, there could be a *dark partner* of the Standard Model, linked to it through a “Higgs portal”, and a full spectrum of dark particles, not only one, which could decay one into another, and only at last producing visible SM particles (the same idea is explored by the so-called **Dynamical DM theories** [291]). These are not-minimal DM models which are far to be tested.

Now the query is if these particles can be detected, directly or indirectly.

For example, from Table 10, it can be noted that the singlino favorite **detection** is the direct one, via nuclear scattering, because its annihilation products fluxes are too tiny to be measured by AMS-02 or other indirect search experiments. Also the LZP could be seen with direct detection facilities and certainly the light axion and sterile neutrino.

The axion is the only candidate which couldn’t be seen by both AMS-02 and LHC experiments. For the axion proper settlements have to be arranged: they are called “Light shining through walls experiments” and are based on the Primakoff effect shown in Fig. 50.

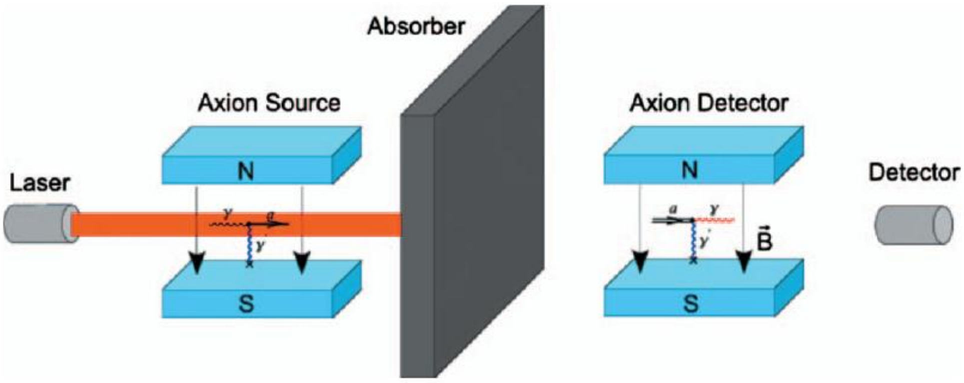

Figure 50 – A Light shining through walls experiment. A laser produces a monochromatic light beam, which passes through an EM cavity and can convert into an axion. An absorber stops the

light, letting the axion travel through it. Then the axion has a probability to convert into a photon again, in a second EM field, and to be detected by the detector on the right.

It has to be stressed that only few candidates produce **AMS detectable particles** in all channels: only Wino and LKP could produce notable e^+, $\bar{p}, \bar{d}$, γ fluxes. Some of them don't generate detectable antihadrons nor photons (light SUSY candidate, Little Higgs massive photon, gravitino and antibaryonic dark matter), others don't produce measurable leptons (singlino and PBH).

In the fourth and fifth column of Table 10, the **LHC and PAMELA/FERMI constraints**, largely discussed before, are summarized: there's no evidence of new physics and the astroparticle data depict a heavy DM scenario or a leptophilic one.

Despite the fact we consider the neutral boson discovered on the 4th of July to be the Higgs boson, one has to remember which theories are independent from Higgs and SUSY paradigms and do not rely on other apparatus: axions and extra-dimensional particles are good examples.

Let's try to act as a jinx shortly. Following the LHC guideline, it's necessary to take into account to discard SUSY theories. That produces a complex scenario in which, however, there are several candidates: LTP, KK particles, PBH, Singlet/Multiplet Scalar, Axion, Minimal Dark Matter (MDM), Sterile Neutrino, Antibaryonic DM. Here, a criterion for simplicity is applied (a quite realistic exclusion), refusing to live in the extra space-dimensions Universe of String Theory: only LTP, Singlet/Multiplet Scalar, Axion, MDM, Sterile Neutrino, Antibaryonic DM survive. Little Higgs particle, Singlet/Multiplet Scalar and 4th generation fermions are detectable by AMS-02, but only 4th generation DM and Singlet/Multiplet Scalar could be seen in both the leptonic and hadronic channels. Moreover, the first candidate is disfavored by LHC researches and by its spin; the Singlet Scalar is too light to reproduce the astrophysical cosmic rays data, instead; only Multiplet Scalars are viable candidates. This is a quite bad scenario.

Therefore, to conduct an effective hadronic high energy research, it's better to hope to preserve a heavy SUSY, non necessarily minimal, candidate or an exotic one, like an extra-dimensional boson.

Not claiming to detect an antiproton (antideuteron) flux, instead, the Scalar Singlet and the Little Higgs vector are very suitable DM particles.

So the landscape is incredibly knotty, many models could be refined and new theories could be implemented to fit the observations.

	Spin	Mass	Symmetry	Correct $\Omega_{DM}h^2 \approx 0.11$	Thermal $\langle\sigma v\rangle_{ann} \approx 1\,pb$	Motivation	Detectable Annihil. Products	Leptophilic (e,μ,τ especially)
SUSY χ - Wino AMSB LSP	½ *M*	300 GeV÷10 TeV	R	√	$\gtrsim$	Gauge Hierarchy Problem	$\boldsymbol{\nu}$, $\boldsymbol{\gamma}$ (Gamma), e^{+}, $\bar{p}, \bar{d}$	√ (perhaps:HS?)
SUSY χ – Bino/Higgsino LSP	½ *M*	100 GeV÷1 TeV	R	√	$\lesssim$	Gauge Hierarchy Problem	$\boldsymbol{\nu}$, $\boldsymbol{\gamma}$, e^{+}, $\bar{p}, \bar{d}$	√ (perhaps:HS?)
NMSSM $\tilde{S}$ NLSP	½ *M*	10÷160 GeV	Z_3 and R	√	$\lesssim$	Gauge Hierarchy Problem	$\bar{p}$, e^{+}	–
UED $B^{(1)}$ LKP	1	300 GeV÷6 TeV	KK	√	0.6	String Theory	$\boldsymbol{\nu}$, $\boldsymbol{\gamma}$ (Gamma), e^{+}, $\bar{p}, \bar{d}$	√ (perhaps)
KK ν_R LZP	1/2	30 GeV÷1 TeV	Z_3	√	1	String Theory	$\boldsymbol{\nu}$, $\boldsymbol{\gamma}$ (Gamma), e^{+}, $\bar{p}, \bar{d}$	–
Singlet Scalar S	0	60÷600 GeV	Z_2	$\lesssim$	1	Minimal	$\boldsymbol{\nu}$, $\boldsymbol{\gamma}$, e^{+}, $\bar{p}, \bar{d}$	–
Multiplet Scalar	0	3÷10 TeV	Z_2	√	1	Minimal	$\boldsymbol{\nu}$, $\boldsymbol{\gamma}$, e^{+}, $\bar{p}$	–
PBH (&Holeum)				X	– (Hawking Rad.)	Astrophysical	$\boldsymbol{\gamma}$, e^{+}, $\bar{p}, \bar{d}$	X
Little Higgs A_h LTP	1	600 GeV÷2.5 TeV	T	√	0.8	Gauge Hierarchy Problem	$\boldsymbol{\nu}$, $\boldsymbol{\gamma}$ (Gamma), e^{+}, $\bar{p}, \bar{d}$	√ (hadron inhibited)
Axion a	0	10^{-5}÷10^{-3} eV	PQ	√ (thermal+nonthermal)	– (Primakoff eff.)	Strong CP Problem	$\boldsymbol{\gamma}$	–
Sterile ν_S	1/2	1÷15 keV	Z_N	X	– (Oscillation)	ν Mass	X-Ray, $\boldsymbol{\nu}$	–
Gravitino $\tilde{G}$	3/2	200÷600 GeV	R	X	$\lesssim$	Gauge Hierarchy Problem	$\boldsymbol{\nu}$, $\boldsymbol{\gamma}$ (Gamma), e^{+}, $\bar{p}, \bar{d}$	–
MDM (4th generation)	1/2	1÷10 TeV	Y	√	≈	Only SM Extended Physics	$\boldsymbol{\nu}$, $\boldsymbol{\gamma}$ (Gamma), e^{+}, $\bar{p}, \bar{d}$	–
Tulin Antibaryonic/ Asymmetric DM Y,Φ	1/2	2÷3 GeV	B	√	– (INDirect)	Antimatter	**IND**: $mesons \rightarrow e^+$	√

Legenda: $^{(*)}$: ill-favored detection   X : NOT (correct, possible)   – : not defined   *M* : Majorana fermion   HS: Hidden sector

Table 9 – Synthetic view of Dark Matter candidates' properties: spin statistics, mass, symmetry, relic density, annihilation cross section, theory motivation, annihilation products, *leptophilicness* of the model. Their properties are achieved from a comparative literature study which took into account common features of similar models and mathematical constraints for each theory discussed and supplied with references.

	Favorite detection	**AMS-02 detection**	**LHC sensitivity**	**LHC constraints**	**PAMELA/FERMI constraints**	**SUSY dependence**	**Higgs dependence**
SUSY χ - Wino AMSB LSP	IND	$e^+, \bar{p}, \bar{d}, \boldsymbol{\gamma}$	√	No SUSY $\tilde{g}, \tilde{q}$ signal for M < 1 TeV, no missing-energy events	Wino with M > 2 TeV	Yes	Yes
SUSY χ – Bino/Higgsino LSP	IND	$e^+, (\bar{p}, \bar{d}, \boldsymbol{\gamma})^{(*)}$	√		ill-favored or barely leptophilic	Yes	Yes
NMSSM $\tilde{S}$ NLSP	DIR	$(\bar{p}, e^+)^{(*)}$	√		Disfavored	Yes	Yes
UED $\boldsymbol{B^{(1)}}$ LKP	IND	$e^+, \bar{p}, \bar{d}, \boldsymbol{\gamma}$	√	No signal for M < few TeV, *no yet* extra dimensions	Heavy, HE $\bar{p}, \bar{d}$	No	No
KK $\boldsymbol{\nu_R}$ LZP	DIR/IND	$e^+, \bar{p}, \bar{d}$	√		No constraint	No	No
Singlet/Multiplet Scalar S	IND	$e^+, \bar{p}$	√	No constraint	No constraint	No	Yes
PBH (&Holeum)	IND	$\bar{p}, \bar{d}, (\boldsymbol{\gamma}, e^+)^{(*)}$	√	No hard $\boldsymbol{\gamma}$, e±, no μQBH for M < 4 TeV	No LE $\bar{p}$ signal	No	No
Little Higgs $\boldsymbol{A_h}$ LTP	IND	$e^+, \boldsymbol{\gamma}^{(*)}$	√	No constraint	No constraint	No	Yes
Axion $\boldsymbol{a}$	DIR/LAB	X	X	X	No constraint	No	No
Sterile $\boldsymbol{\nu_S}$	DIR	X	√	No evidence	No constraint	No	No
SUSY Gravitino $\tilde{\boldsymbol{G}}$	IND	$e^+, \boldsymbol{\gamma}^{(*)}$	√	No SUSY signal, no graviton for M < 2 TeV	No constraint	Yes	Yes
MDM (4th generation)	IND	$e^+, \bar{p}, \bar{d}$	√	No 4th q generation for M < 500 GeV, Higgs mass problem	No LE $\bar{p}$ signal	No	Yes
Tulin Antibaryonic/ Asymmetric DM Υ,Φ	IND	$(e^+)^{(*)}$	X	X	No constraint	No	No

Legenda: $^{(*)}$: ill-favored detection X : NOT (correct, possible) – : not defined *M* : Majorana fermion HE: high energy LE: low energy

Table 10 – Synthetic view of Dark Matter candidates detection: the main experiment researches, the actual state of art, the constraints, SUSY and Higgs theories dependence.

3.7 Alternatives

Even if this is the standard scenario, there are some alternative theories which interpret the astroparticle data in completely different ways and some new astrophysical features which must be taken into account.

3.7.1 Modified Fluxes: IBEX and anisotropic propagation

One first objection to take into account is the **IBEX no-shock** discovery [292] (2012 spring), that demonstrates that there's no supersonic bow shock at the heliosphere edge, after the heliopause.
As mentioned, the heliosphere is a bubble of charged particles in the space surrounding the Solar System, "blown" into the interstellar medium by the solar wind. Although electrically neutral, atoms from interstellar volume can penetrate this bubble, virtually all of the material in the heliosphere emanates from the Sun itself.
For the first ten billion kilometers of its radius, the solar wind travels at over 1,600,000 km/hour. As it begins to interact with the interstellar medium, it slows down before finally ceasing altogether. The point where the solar wind begins to slow is called the *termination shock*; then the solar wind continues to slow as it passes through the *heliosheath* leading to a boundary where the interstellar medium and solar wind pressures balance called the *heliopause* (Fig. 51).
Beyond the *heliopause*, where the interstellar medium collides with the heliosphere, it was once thought there was a bow shock. However, data from the Interstellar Boundary Explorer suggest that the velocity of the Sun through the interstellar medium is too low for a bow shock to form. Also, Cassini data challenged the "heliotail" theory in 2009.

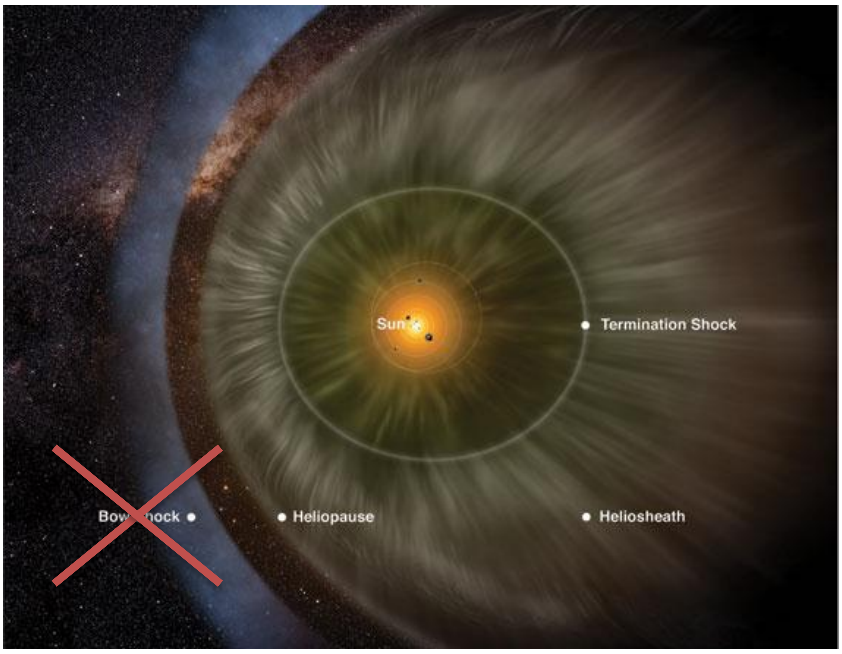

Figure 51 – Heliosphere pictorial view the solar system at the center. The bow shock assumption has fallen.

Does the absence of the bow shock region modify the interpretation of the CR spectra?
The IBEX results do not have direct implications for CR propagation codes as GALPROP or DRAGON. In fact, these codes model the propagation of cosmic rays up to the edge of the heliosphere and not through it.

The connection between external spectra (so-called LIS) and those observed at the top of the atmosphere is generally done in the force-field approximation that treats the solar modulation by means of a single parameter (see section 3.2.1), tuned on experimental data in the different periods of solar activity. In this approximation the details of the physics of the heliosphere are quite irrelevant. For high energy cosmic rays, from tens of GeV on, the absence of the bow shock has no repercussion. But, at lower energies, the drifting effects in the magnetic field of the heliosphere (depending on the charge) become significant and modulation must be treated in a more complex way. The parameters that become relevant are different: the diffusion coefficient, the speed of drift and, in particular, the *heliospheric current sheet* (HCS). This is the surface within the Solar System where the polarity of the Sun's magnetic field changes from north to south. This field extends throughout the Sun's equatorial plane in the heliosphere. The shape of the current sheet results from the influence of the Sun's rotating magnetic field on the plasma in the interplanetary medium. A small electrical current flows within the sheet, about 10^{-10} A/m² and the thickness of the current sheet is about 10000 km [293].

So, even if in a not yet understood way, the lack of this *shock wall* at the border of the heliosphere may modify or modulate the top-of the-atmosphere spectra for charged particle in the 0.1÷few GeV windows. That is relevant, for example, for antideuterons searches, but not for DM positrons and protons. Probably, this is yet another uncertainty source for CR antideuteron spectrum.

Another contrasting and disturbing study arises from **non-isotropic** magnetic field **propagation**.

The isotropic propagation picture is based on hydromagnetic wave theories, in which the random (small-scale) component of the magnetic fields dominates over or are of the same order of magnitude as the regular large scale components. From the isotropy of the CRs one assumes that the regular components of the magnetic fields can be neglected, so there is no preferred direction for Alfvén waves. The turbulent component is locally as large as 10 µG, while the regular field is only about 3 µG. However, even if the turbulent small scale and regular large scale components are of the same order of magnitude, the ratio of perpendicular/parallel diffusion is about 0.1, which implies that the CRs still preferentially follow the regular magnetic field lines [295].

In other words, the correct propagation model needs a diffusion tensor (see 3.2.1).

An additional effect concerning charged particles may be related to molecular clouds [124]: the gas density in the disk varies from 10^{-3}/cm^3 in the warm ionized medium to 10^2/cm^3-10^3/cm^3 in clumps of cold gas with a size of a few pc. In the center the density may be as high as 10^7/cm^3 in dense molecular clouds (MCs), where star formation occurs. Inside MCs, magnetic fields far above the random components have been observed, that seem to be correlated with the observed static magnetic fields outside the MCs. This can only be understood if the MCs remember the large scale magnetic fields in the interstellar medium, i.e. if during the contraction flux freezing occurs. In this case the magnetic field lines from the ISM will become highly concentrated near the MCs and the MCs will form a network of interconnected clouds, focusing the magnetic field lines towards them. CRs in the ISM following these field lines will be reflected by the concentration of the field lines. So MCs can act as magnetic mirrors for CRs, just like the concentration of magnetic field lines near the poles from the earth trap the CRs in the famous Van Allen radiation belts.

The large distances (pc scale) between the MCs allows to trap particles up to the TeV scale, thus increasing the grammage and the residence time. In such a setup particles acquire grammage and age in the low density regions in the disk (between MCs) and not in the halo as in the isotropic propagation model. Thus, the halo size is not a sensitive parameter anymore and particles, once in the halo, will be preferentially transported away from the disk by a combination of convection and fast diffusion along the regular poloidal field lines in the halo.

Once this propagation picture is implemented within GALPROP with a primary DM source, one obtains a particular result, shown below in Fig. 52.

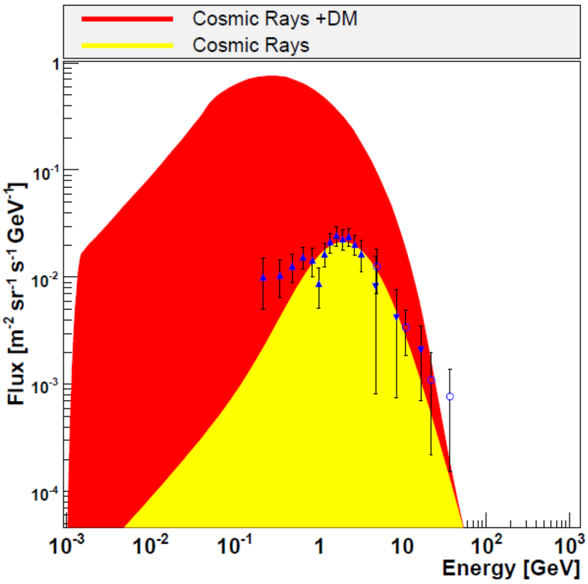

Figure 52 - Comparison of the antiproton low energy production including dark matter annihilation in a model with isotropic propagation (a-left) and a model with anisotropic propagation and trapping between molecular clouds (b-right) [124].

The anisotropic model shoots down the total antiproton flux with dark matter sources by two order of magnitude, mimicking the usual secondary spectrum. This means that dark matter antiprotons could have been already seen, without realizing the fact yet. The implications for positrons have not been explored yet, but it's easy to be convinced that this trapping could be more efficient for hadrons (antideuterons and antiprotons) than for positrons and that this scenario hardly reproduces the positron fraction enhancement.

Moreover, this model could be tested by AMS-02 with high-precision measurements of CR nuclei ratios (Fig. 53).

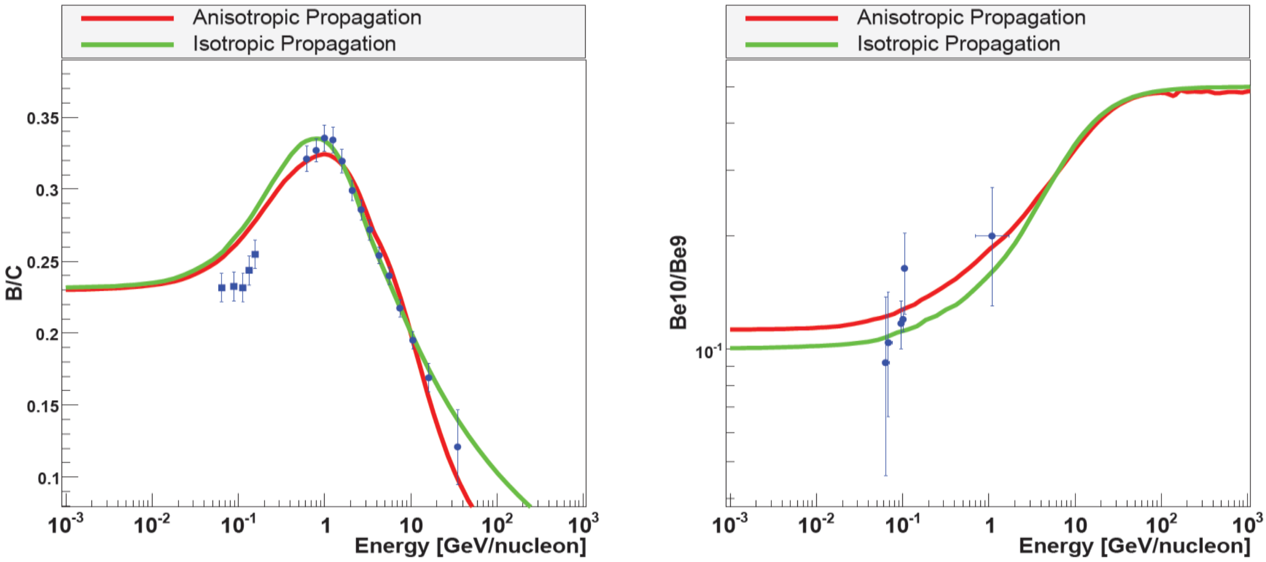

Figure 53 - The B/C ration (a-left) and the beryllium-fraction (b-right) for an anisotropic diffusion model with trapping between MCs (red) and for a model with isotropic diffusion (green) [124].

3.7.2 Astrophysical primary fluxes

Another fundamental alternative lies in the fact that the observed positron excess could be generated by astrophysical sources (compact stars, black holes and so on), i.e. unknown energetic primary leptonic fluxes could reach the Earth atmosphere from nearby objects or processes. Remember that most of the leptons with E < 100 GeV should come from sources within 1 kpc away from us [79].
This scenario has been explored in literature by many authors, in particular by Blasi and Serpico (Fig. 54). They have demonstrate that it's possible to reproduce the positron enhancement measured by PAMELA and FERMI adding to the secondary spectrum the contributions from two **nearby pulsars** [296].

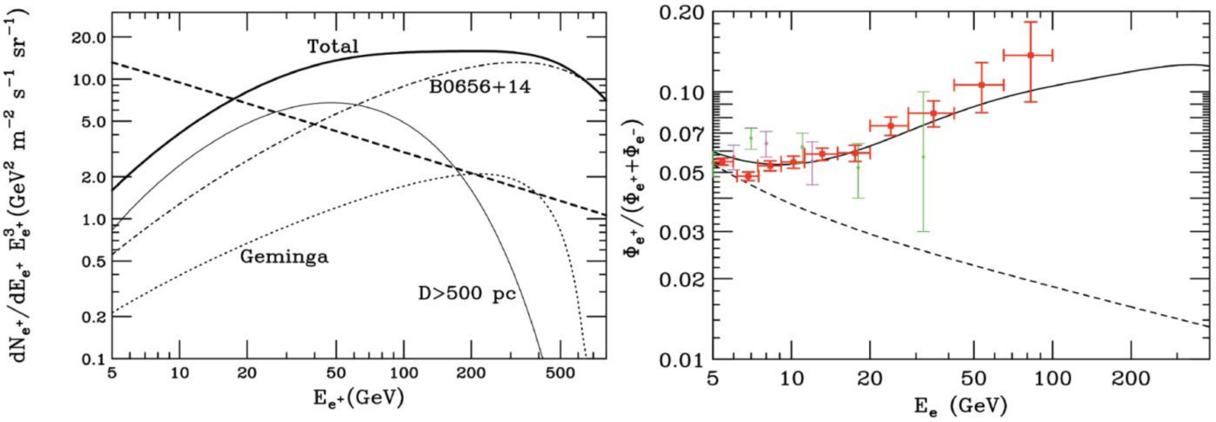

Figure 54 – Combination of Galactic contribution and two nearby pulsars, Geminga (157 pc) and B0656+14 (290 pc), can fit PAMELA excess (and perhaps also FERMI total electrons bump). On the left the positron flux, on the right the positron fraction [296].

But there are some differences between an isotropic halo-injected dark matter pool of positrons and localized sources. The signal from these nearby pulsars is expected to generate a detectable dipole anisotropy in the CR electron spectrum, providing a method by which FERMI would be capable of discriminating between pulsar and dark matter origins of the positron anomaly**:** for DM sources the anisotropy is in the direction of the Galactic Center, for pulsar it is in the opposite direction (Geminga & B0656+14).

How is this possible? The idea that pulsars might be associated with the production of cosmic ray electrons/positrons is quite old. The reason is that, being pulsars identified with fast rotating magnetized neutron stars, a large electric field is induced which can extract electrons from the star surface: in fact these effects are so strong that a pulsar rotating with angular velocity Ω is not living in vacuum, rather it is surrounded up to a distance known as light radius $r_L = c/\Omega$ by a comoving plasma configuration called "magnetosphere". In turn, the stripped electrons lose energy via curvature radiation (plus additional processes) while propagating far from the star along the magnetic field lines, and the emitted photons are so energetic that an electron-positron pair can be formed in the intense neutron star magnetic field. Numerous QED processes induce a multiplicative cascade which populates the magnetosphere of the pulsar with pairs. The pairs produced in the magnetosphere, together with the Poynting flux emanating from the pulsar, form a relativistic magnetized wind evolving in a rich environment: since the pulsar is born from the collapse of a massive star (core collapse supernova), it lies initially well within the ejecta of its

progenitor, in turn surrounded by the supernova blast wave propagating in the ISM. When the cold, magnetized relativistic wind launched by the star hits the non-relativistically expanding ejecta, a shock wave system forms in the impact: the outer one propagates in the ejecta, while a reverse shock propagates back towards the star. The latter is known as termination shock, where the wind is slowed down, its bulk energy dissipated and turned into that of a relativistically hot, magnetized fluid, which then shines as a Pulsar Wind Nebula (PWN). If we denote with B_s the surface magnetic field and with R_s the radius of the neutron star, from Faraday's law one can naively estimate a potential drop of up to $\varphi \simeq \omega B_s R^2_s \sim 10^{16}$ V available for accelerating $e^{\pm}$ in the magnetosphere. Those pairs suffer at least adiabatic energy losses while reaching the termination shock. Nonetheless, at the termination shock a relatively large fraction (a few tens of percent) of the wind bulk energy is converted into accelerated pairs, which then radiate a broad-band photon spectrum, extending from radio frequencies to multi-TeV gamma-rays, through synchrotron and Inverse Compton processes. The fraction of them escaping in the ISM depends probably on astrophysical details [296, 297].
Given this broad picture, can one attribute the signal inferred from the charged lepton data to the PWN contribution? Observationally, the spectrum of radiation from several PWNe requires a spectrum of electrons and positrons which has a broken power-law shape: the break happens at Lorentz factor of $10^5 \div 10^6$ — hence at the O(100) GeV scale — with a very hard power-law below the break, of the kind $\simeq E^{-1.5}$, while significantly softer (softer than E^{-2}) above the break. The hard spectral index matches what needed to fit the data, as explained in section 3.3.1. So, on general grounds, one can conclude that: i) pulsars have more than enough rotational energy to explain the cosmic ray lepton features ($\sim$ 40% of rotational energy must be released as energetic e^+); ii) a significant part of this energy is converted into kinetic energy of lepton pairs at the termination shock of the PWNe, with the right spectral properties to match the high energy positron fraction as well as $e^- + e^+$ energy spectra. Also, it is worth adding that observations from Fermi-LAT instrument show clearly that pulsars are the most abundant population of Galactic objects to shine in the GeV gamma-ray band. Including their contribution to any account of the leptonic CR sources is thus a requirement for any realistic description of Galactic CR sources [298–301].
It also has to be mentioned that other astrophysical mechanisms capable to produce high energy positrons are being studied, i.e. acceleration models for **white dwarf pulsars** [302, 303] and **galactic microquasars** [304, 305, 306], which may compete with neutron stars pulsars for producing and accelerating leptons up to the TeV scale. So DM is not necessary to describe leptonic anomalies.

There's an important ploy to disentangle stars contribution from DM one.
It is now crucial to consider the associated signals in the photon diffuse fluxes that necessarily accompany them, previously neglected. Starting from them, new constraints can be put on dark matter properties and, in particular, a possible method to distinguish primary astrophysical source from primary dark matter sources may be formulated. These photon fluxes can be produced in different ways, among which [30]:

i. **"Prompt" gamma-rays**: produced directly by DM annihilations themselves, mainly from the bremsstrahlung of charged particles and the fragmentation of hadrons, e.g. π^0 decay, produced in the annihilations. They peak therefore at energies close to the DM mass. Their spatial distribution of course follows closely the distribution of DM.
ii. **ICS gamma-rays**: produced by the Inverse Compton Scattering (ICS) of the energetic electrons and positrons, created in the DM annihilation, onto the low energy photons of

the CMB, the galactic star-light and the infrared-light, which are thus upscattered in energy. Typically, they cover a wider range of energies than prompt gamma rays, from energies of a fraction of the DM mass to almost up to the DM mass itself. Their spatial distribution traces the distribution of $e^{\pm}$, which originate from DM but then diffuse out in the whole galactic halo.

iii. **Synchrotron emission**: consisting in the radiation emitted in the magnetic field of the Galaxy by the $e^{\pm}$ produced by DM annihilations. For an intensity of the magnetic field of O(μGauss), like in the case of the Milky Way halo, and for leptons of GeV÷TeV energies, the synchrotron emission falls in the radio band.

Individuating the best targets to search for these annihilation signals is one of the main games in the field. Not very surprisingly, the preferred targets have to be regions with high DM densities and/or regions where the astrophysical "background" is reduced and therefore the signal/noise ratio is favorable. The distinction between the two types of regions is of course not clear-cut, and there are specific cases in which other environmental reasons make a region more suitable than another (such as in the case of synchrotron radiation which needs a region with a strong magnetic field). For the sake of schematizing, one can list the following targets at which the experiments look:

- The Milky Way Galactic Center (GC) and small regions around or just outside the GC.
- Wide regions of the Galactic Halo (GH) itself, from which a diffuse flux of gamma-rays is expected, including the one due to the DM ICS emission.
- Globular clusters (GloC), which are dense agglomerates of stars, embedded in the Milky Way galactic halo. They are a peculiar kind of target since they are not supposed to be DM dominated, quite the opposite, as they are rich of stars. The interest in them arises from two facts: that they may have formed inside a primordial DM subhalo and some of the DM may have remained trapped; that the density of baryonic matter may create by attraction a DM spike and thus enhance the annihilation flux.
- Subhalos of the galactic DM halo, the position of which, however, is of course not known a priori. In a similar class, Intermediate Mass Black Holes (IMBH) have recently attracted some attention because they could create around them spikes of DM.
- Satellite galaxies of the Milky Way, often of the dwarf spheroidal (dSph) class, such as Sagittarius, Segue1, Draco and several others, which are star-deprived and believed to be DM dominated, as explained in all chapter 2.1.
- Large scale structures in the relatively nearby Universe, such as galaxy clusters (e.g. the Virgo, Coma, Fornax, Perseus clusters and several others).
- The Universe at large, meaning looking at the isotropic flux of (redshifted) γ-rays that come to us from DM annihilation in all halos and all along the recent history of the Universe. Often this flux is called *extragalactic* or *cosmological*.

Besides these searches, many independent works have analyzed varying combinations of datasets (FERMI+MAGIC+HESS), considered different targets and studied different models. Without entering in the details of each single analysis, the overall common conclusions of almost all the studies is that no clear anomalous signals are individuated. And it's difficult to put neat constraints on dark matter properties. One exception is the recent constraint from satellite dwarf galaxies with FERMI data [307, 308, 310]: for some annihilation channels, thermal DM is excluded for masses below 30 GeV. Furthermore, FERMI has the challenging task to individuate the sources of half the diffuse emission yet.

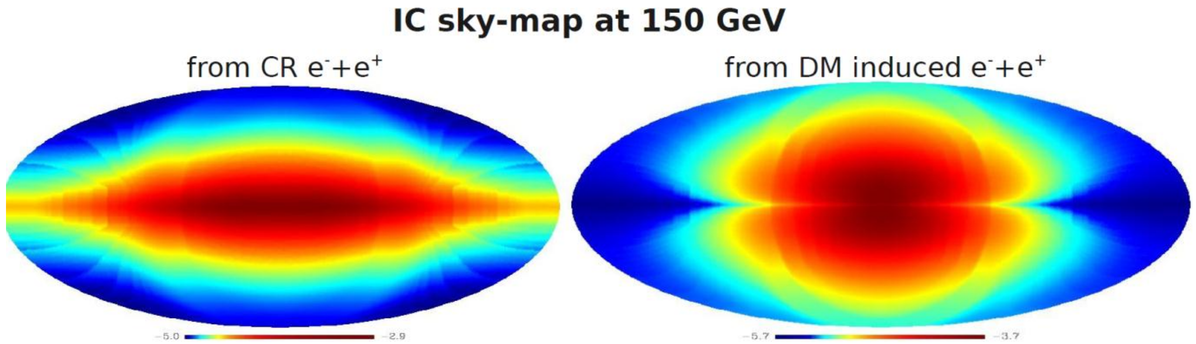

Figure 55 – Diffuse gamma sky at a given energy for Inverse Compton Scattering, simulated for a pure astrophysical scenario (left) and a dark matter leptons injection from the halo.

So, to discriminate astrophysical contributions from DM ones, the reasoning is quite simple: CR sources and astrophysical primary sources of positrons are confined to the Galactic Disc, while the DM component has a rather spherical distribution.

The ratio of DM signal vs CR/astrophysical signal in the diffuse emission is clear enhanced at mid-high latitudes if dark matter does exist: non-localized non-bilobed excess means no DM origin of the signal (Fig. 55). This will be a cute way to exclude – we hope – primary astrophysical sources.

Also AMS-02 will be able to give some indications about positron fraction galactic anisotropies.

A completely different explanation has been put forward in [90, 311, 312, 313]: the PAMELA-FERMI excess is interpreted as due to positrons created as byproducts of hadronic interactions inside old **supernova remnants** (SNRs), the standard source of the bulk of sub-TeV cosmic rays. It has long been believed that galactic CRs are generated by diffusive shock acceleration (DSA) in supernova remnants. Hadronic interactions of the accelerated protons will create $\pi^{\pm}$ (and π^0) which then decay to yield secondary $e^{\pm}$ and neutrinos (and γ rays). The crucial physical ingredient which leads to a natural explanation of the positron flux is the fact that the secondary production takes place in the same region where cosmic rays are being accelerated. The fraction of secondary $e^{\pm}$ which are accelerated increases with energy, so their final spectrum is harder than the injected spectrum.

A similar effect is then predicted at higher energies for both antiprotons (Fig. 56) and for secondary nuclei, such as boron.

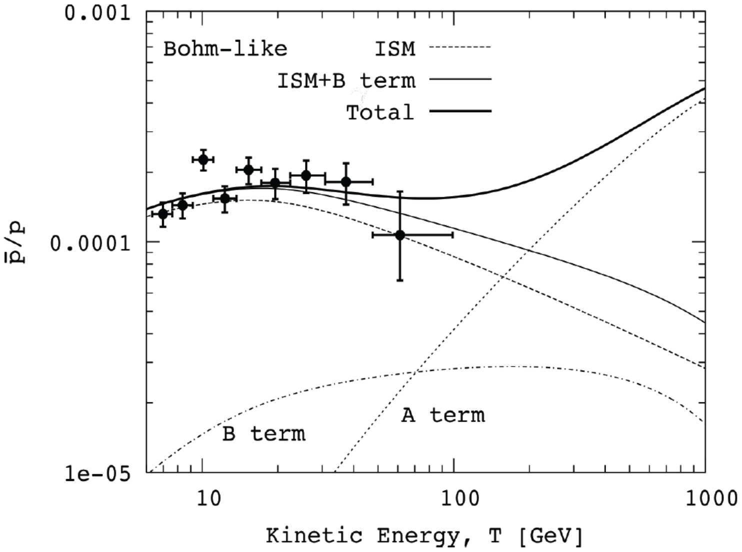

Figure 56 – The $\bar{p}/p$ ratio from the SNRs reacceleration, together with a simple model of secondary production in the ISM (dashed line), and with data from PAMELA. The dotted and dot-

dashed lines represent the contributions of two acceleration terms alone, respectively. The thick solid curve is the overall contribution due to ISM plus the new mechanism, while the thin solid curve only includes the ISM contribution plus the B term contribution. See text for details [296].

This sounds distressing, because there is also a possible astrophysical origin for “primary” antiproton, which could affect and tamper our hadronic research with AMS-02. But, as just said, a similar reacceleration changes the secondary nuclei spectra. So, if an increasing B/C ratio after ~ 100 GeV energies is not measured, this SNRs antiproton mechanism loses credibility. And CREAM balloon experiments measurements already disfavor this scenario (Fig. 57). The absence of a rise in the B/C ratio would prove that reacceleration does not lead to a change in the secondary to primary ratios. As result, a rise of the antiproton ratio could be used as signature for dark matter searches [312, 315, 316]. AMS-02 is going to confirm this result.

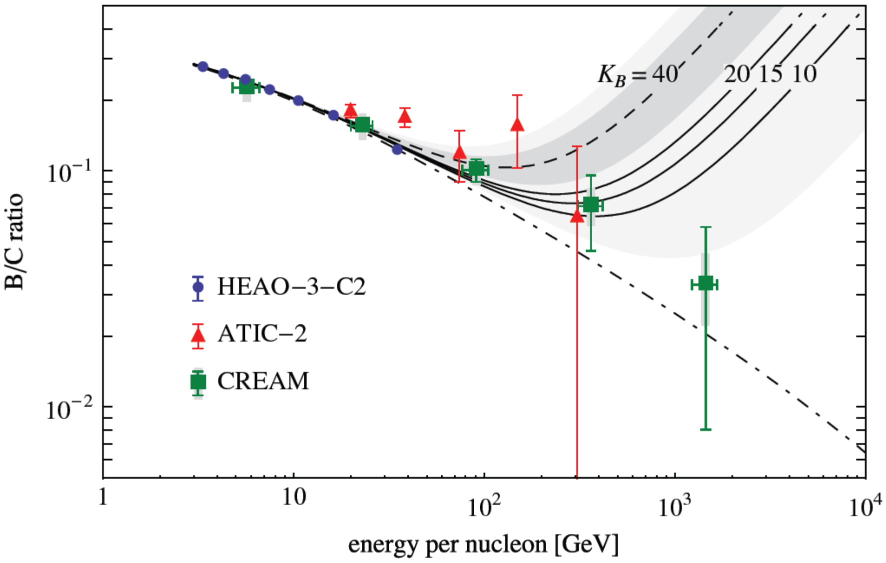

Figure 57 - The B/C ratio in cosmic rays along with propagation model predictions: production of secondaries during propagation only (dot-dashed line), and including production and acceleration of secondaries in a nearby SNR (solid lines) for values of the diffusion coefficient near the shock wave which best fit the $e^{\pm}$ spectrum. The dashed line corresponds to the value of the diffusion coefficient required to fit the ATIC-2 data on Ti/Fe, with the 1σ and 2σ bands. The data points are from HEAO-3-C2 (circles), ATIC-2 (triangles) and CREAM (squares) [312].

3.8 The Final Recipe: a DM search guideline

3.8.1 Scattering Cross Section

Let’s conclude with a little discussion of the “direct properties” of dark matter. Space experiments can’t measure them, but they’re very important to further constraint theories and examine the problematic more deeply.

The latest results come from the great XENON experiment from Laboratori Nazionali del Gran Sasso (LNGS) in Italy: it measures the dark matter spin-independent nucleon cross section.

A 15 kg liquid xenon detector was installed at Gran Sasso underground laboratory during March 2006, and searched for WIMP interactions until October 2007. No WIMP signatures were found, the limits on WIMP-nucleon cross sections extend down to below 10^{-43}cm^2 for a 30 GeV WIMP mass. The current phase, XENON100, for a total of 150 kg of liquid Xenon, is now running and has achieved a factor of 50 better sensitivity, compared to XENON10. It lowered the cross section value [318, 319] to 10^{-44}cm^2 (10^{-45}cm^2 with 2012 data [394]) for the DM mass range 20 ÷ 400 GeV and to 10^{-43}cm^2 (10^{-44}cm^2 with 2012 data [394]) for TeV-ish WIMP (see Figure 58). The next generation XENON detector will reach another order of magnitude sensitivity to cover SUSY parameter space down to 10^{-46}cm^2 in the next three years: the collaboration is currently designing Xenon1t, whose fiducial volume will contain 1 ton of ultra radio-pure liquid Xenon.

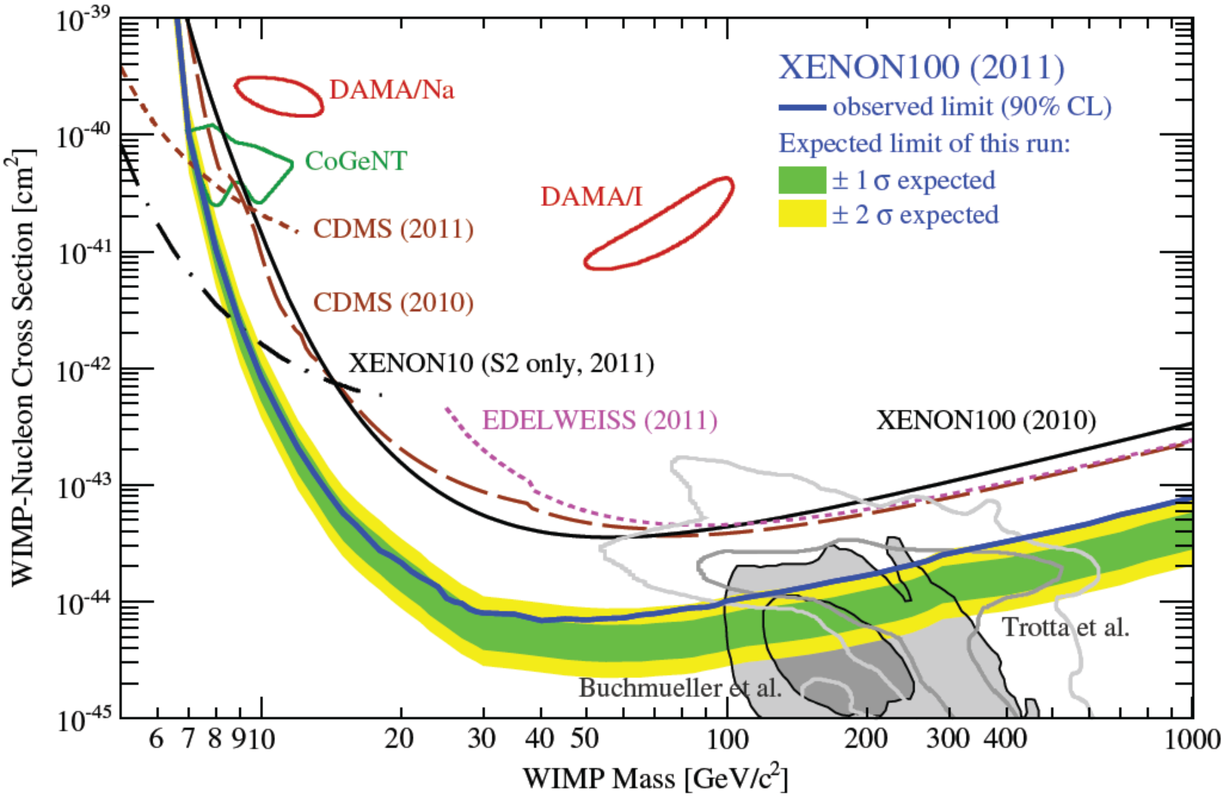

Figure 58 - Spin-independent elastic WIMP-nucleon cross section σ as a function of WIMP mass m_χ. The new XENON100 limit at 90% C.L., as derived with the profile likelihood method taking into account all relevant systematic uncertainties, is shown as the thick (blue) line together with the expected sensitivity of this run (green-yellow band) [318]. The limits from XENON100 (2010), EDELWEISS (2011), CDMS (2009) (recalculated with Galactic escape velocity v_{esc} = 544 km/s, and mean WIMP halo velocity v_0 = 220 km/s), CDMS (2011), and XENON10 (2011) are also shown. Expectations from CMSSM are indicated at 68% and 95% C.L. (shaded gray, gray contour), as well as the 90% C.L. areas favored by CoGeNT and DAMA.

The **spin-independent (SI) cross section** is measured using the simple relation

$$\langle \sigma v \rangle_{SI}^{scatt} = R\,\frac{m_{DM}}{\rho_\odot} \qquad (3.57)$$

where R is the interaction rate and $\rho_\odot$ is the local dark matter density.
This is an incredible goal which gives us an estimate of how much dark matter is elusive.
The low energy effective Lagrangian for WIMP-quark interaction that determines the dynamic of the scattering is:

$$L = f_q(\bar{\chi}\chi)\cdot(\bar{q}q) + d_q(\bar{\chi}\gamma^{\mu}\gamma^{5}\chi)\cdot(\bar{q}\gamma_{\mu}\gamma^{5}q) + ... \qquad (3.58)$$

where the first term is the scalar spin-independent interaction and the second a vector-axial spin-dependent interaction. The others are velocity-dependent contributions and can be neglected in the non-relativistic limit for direct detection. The scalar interaction scales with the atomic weight and almost always dominates for nuclei with A > 30, like Xenon [320, 321].

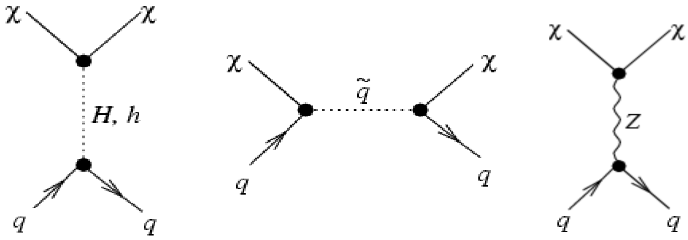

Figure 59 – Main Feynmann diagrams for WIMP nucleon elastic scattering, via Higgs boson, hypothetical squarks bosons and Z^0 electroweak boson.

The scattering is mediated principally by the Z^0 boson, then by the Higgs boson (and other hypothetical and real fermions or bosons [322] – Fig. 59). Table 11 is a scheme of possible interactions.

Dark Matter	Mediator	Process	Scattering
Scalar	Z, Z'		SI
	h	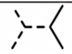	SI
	Q		SI
Dirac Fermion	Z,Z'		SI, SD†
	h	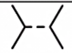	SI
	X	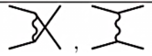	SI, SD
	Φ	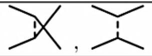	SI, SD
Majorana Fermion	Z,Z'		SD
	h	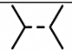	SI
	X	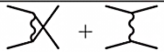	SD in chiral limit
	Φ	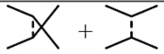	SD in chiral limit
Real Vector	h	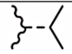	SI
	Q	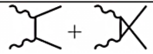	SD in chiral limit
Complex Vector	Z, Z'		SI
	h	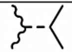	SI
	Q	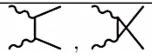	SI, SD

Table 11 - A summary of results for hypothetical WIMP-nucleon scattering, for each dark matter candidate type and mediator. SD stands for Spin-Dependent cross section. In the Feynman diagrams, scalars are represented by dashed lines, fermions by solid lines and vector bosons by wavy lines. Of the mediators, Φ, h, Z' and the SM Z are neutral under both electromagnetism and color, while X, and Q (quarks) transform as triplets under color and carry electric charge [334].

An experimental constraint for a very heavy 10 TeV dark matter is posed by the combined 2011 CDMS and EDELWEISS data [323], which explore the 1 TeV ÷ 10 TeV window, and is worth $\sigma_{SI} \leq 10^{-42}\ cm^2$, that it's still a great bound.

In Fig. 58 the strange signals of *DAMA and CoGeNT* are shown. They seem to imply very light DM candidate, starting from SI cross section and isothermal halo assumptions. It's to mention that also these *results could be overturned in favor of multi-TeV dark matter*, introducing the idea of a cylindrically symmetric **Dark Disk** (DD) density profile which shall be added to the halo profiles described in section 3.1. This type of DM disk could have the exponential form [324], in the cylindrical coordinates *(R, z)*,

$$\rho(R, z) = \rho_0 \exp\left[\frac{1.68\,(R_\odot - R)}{R_{1/2}}\right] \exp\left[-\frac{0.693\,|z|}{z_{1/2}}\right], \qquad (3.59)$$

where $R_{1/2}$ = 11.7 kpc and $z_{1/2}$ = 1.5 kpc are respectively the half mass scale lengths in the Galactic Plane and perpendicular to the Galactic Plane, with a usual local density of 0.3÷0.4 GeV·cm^{-3}. It does have important implications for the direct detection of dark matter, because of its low velocity with respect to the Earth. The mean relative velocity of dark matter in this DD, which penetrates the luminous one, should be just a fraction of the halo one, originating a corotating cold DM flux. The lower velocity dispersion of dark matter particles in the dark disk can naturally lead to higher annihilation rates through the Sommerfeld enhancement, which, it has been shown, scales as $1/v_{rel}$. If the dominant dark matter contribution to the local high energy $e^{\pm}$ flux comes from a dark disk rather than the spherical halo, it's possible to get good fits of Fermi and PAMELA's data [325], with a boost factor that is almost an order of magnitude smaller than what is needed for the fits when only the spherical halo profile is taken into account. Thus, the Sommerfeld enhancement for the spherical halo with a velocity dispersion of $v_0 = v_{rel}$= 220 km/s doesn't need to take the extremely large values previously thought [91, 105], once applied to a DD with $v_0 = 50 \div 70$ km/s (Fig. 60). These dark disks are provided by structure formation simulations of standard ΛCDM cosmology in presence of baryons.

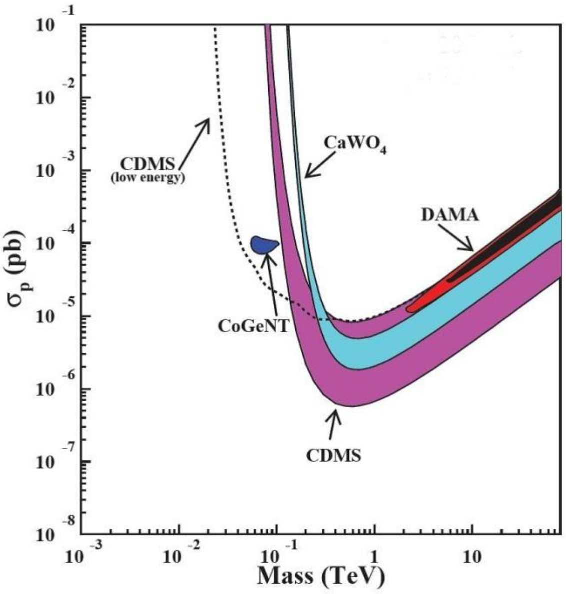

Figure 60 - Allowed configurations at 2σ C.L. obtained for a cold corotating halo with $v_0 \sim 50$ km/s The black filled area inside the DAMA region marks the configurations allowed at 1σ C.L. [326].

The dynamical friction analysis applied to direct search experiments results leads to intriguing aftermath, reversing the old perspective [326]: DAMA/LIBRA annual modulation data and CoGeNT and CDMS-II excesses of events over the expected background could be reanalyzed in terms of a very heavy dark matter particle signal of a corotating dark disk with $v_0 \sim 50$ km/s. It can be noted from Fig. 60 that, for a SI cross section of about 10^{-5} pb (10^{-41} cm^2), DAMA and CDMS excesses [327, 328] correspond to a dark matter with $3\,TeV \lesssim m_{DM} \lesssim 10\,TeV$.

Finally, if you want to test the **spin-dependent DM properties** you need another type of detector, low atomic weight dynamics and peculiar features.
As mentioned at the beginning of the dissertation (section 3.2.2), also neutrinos constitute a dark matter measurable annihilation product. A neutrino dark matter astronomy is possible only with dedicated cyclopean experiments such as the Antarctic IceCube (IC). This is the principle: WIMPs could be gravitationally captured by massive objects like the Sun and accumulate in the core of the Sun itself. With a high enough density of these particles, they would annihilate with each other at a significant rate. The decay products of this annihilation could decay into neutrinos, which could be observed by IceCube as an excess of neutrinos from the direction of the Sun. Therefore this technique is an indirect special one. Solar WIMP searches are more sensitive to spin-dependent models than many direct searches, because the Sun is made of lighter elements than direct search detectors (e.g. xenon or germanium). Not only solar neutrino could be detected, but also galactic sources and possible inner Earth one. IceCube has set better limits with the recent 40-string detector configuration than its predecessor AMANDA limits: stringent bounds from IceCube for the spin-dependent DM cross-section have been accomplished [329−332], shown in Fig. 61.

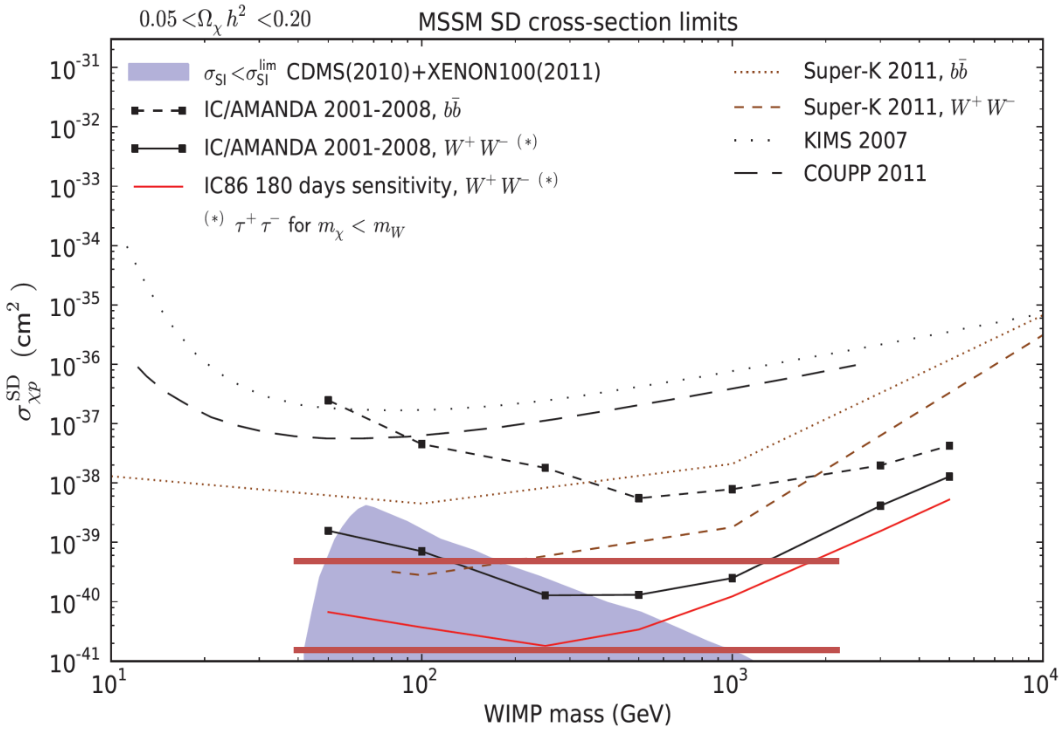

Figure 61 – Upper limits at 90% confidence level on the spin-dependent WIMP-proton cross section assuming that the neutrinos are produced by $\bar{b}b$ and WW annihilation [330]. The limits have been obtained with IceCube operated with 40 strings. Also shown is the reach of the completed detector. Limits from the Super-Kamiokande and direct detection experiments are reported for comparison. The shaded region represent supersymmetric models not ruled out by direct experiments.

The two red horizontal bars in Fig. 61 delimit the mass region (40 GeV ÷ 2 TeV) where the spin-dependent cross section is of the order of

$$\sigma_{SD} \lesssim 10^{-(41\div40)}\ cm^2 \tag{3.60}$$

This is another great bound, three order of magnitude less stringent than the one on spin-independent cross section by XENON. But the two researches are going on the same direction: no WIMP signal has been detected yet, and the DM interaction “ability” to interact with standard matter is going deeper and deeper.

To compare it with the neutrino’s one is very astonishing: it has been proved that for $m_\chi > 10$ GeV the dark matter SI nucleon-cross section should be less than $10^{-43}\ cm^2$, i. e. at least 3 orders of magnitude beneath the neutrino’s one [333], for a solar 10 MeV neutrino, using a typical cross section parameterization

$$\sigma(\nu N) = (0.677 \pm 0.014) \times 10^{-38}\ \mathrm{cm}^2 \times E_\nu/(\mathrm{GeV}) \tag{3.61}$$

and of the order of magnitude of the neutrino’s one for the SD process.

It’s to mention they also obtained a notable result from composite analysis: they have shown [332] that, when 500-1000 GeV dark matter annihilates into a large fraction of neutrinos, annihilation boost factors of the O(100) and above could be constrained and leptophilic models which favor primary neutrino production are disfavored by their results.

For $m_\chi \sim$ 10 TeV DM the SD cross section bound comes from Super-Kamiokande (Fig. 61) and it is $\sigma_{SD} \lesssim 10^{-36}\ cm^2$.

To conclude the topic, SI and SD cross sections can be related to the parameters space of different DM models, such as the UED, to create new constraints, and could also be correlated to each other [336]. This fact is helpful for the indirect searches. For example, SI cross section results by XENON100 suggest a heavier Scalar Singlet candidate which could reach the TeV scale (Fig. 62), while SI and SD data together push KK particle masses below the TeV scale. These are only preliminary study, but they open the doors to new constraints perspective, which could be very useful for space experiments (Figs. 62, 63).

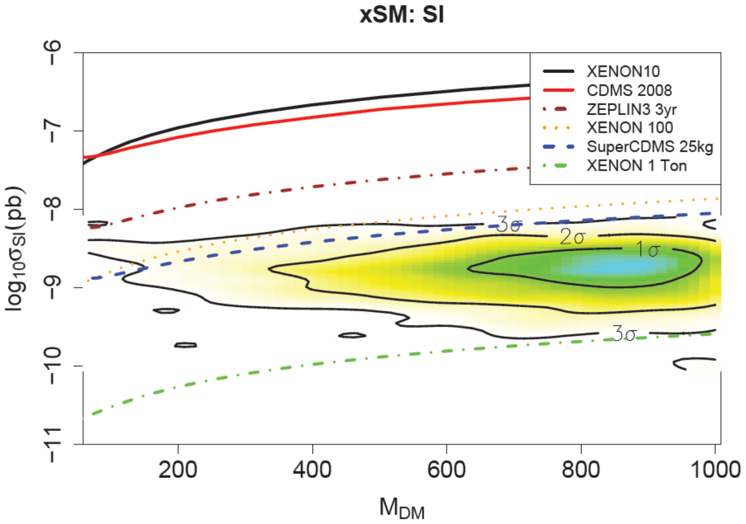

Figure 62 – Real Singlet Scalar extended SM posterior distribution of the SI cross section versus dark matter mass [336].

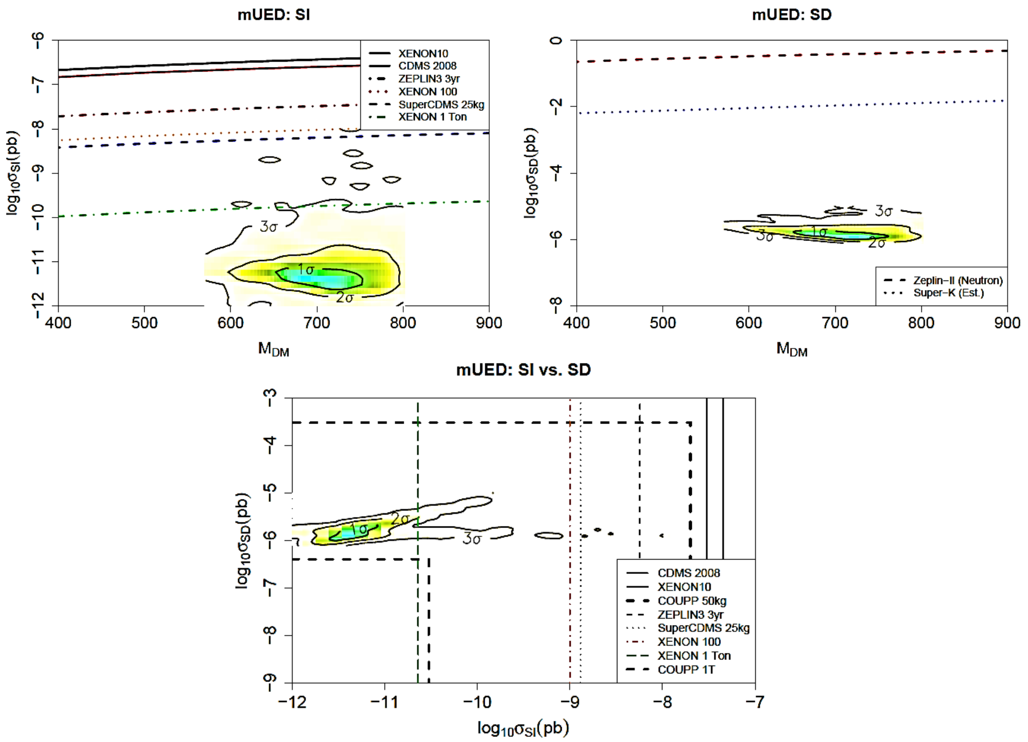

Figure 63 - mUED predictions of the SI and SD cross sections. The mUED predictions for the SD cross section may be probed with a one Ton detector if it has sufficient sensitivity at $m_{DM}\sim$ 700 GeV [336].

3.8.2 Particle Dark Matter ID: conclusions

Let's try to summarize the stakes and what has been learned from this phenomenological analysis, to put a guide line for AMS-02 and other indirect space-born experiments, and describe the opportunities of dark matter searches (especially in the non-leptophilic case).

- The CR fluxes are a function of the halo model, of the parameters set MIN-MED-MAX adopted for the CR propagation (and nuclear coalescence properties, in the case of antideuterons), of primary astrophysical high energy phenomena (pulsars, SNRs dynamics), and of the DM candidate physics: mass, decay channels, annihilation cross section. AMS Collaboration hopes to corroborate the MED or MAX set with AMS-02 nuclei ratio measurements, which could give the higher and detectable primary fluxes.
- Uncertainties are reflected almost exclusively on primary flux from dark matter. The greatest uncertainties are given by propagation models: about two orders of magnitude, one above one below the MED set. Also decay models greatly affect fluxes, especially because of electroweak NLO corrections. Radial distribution of the halo modulates spectra in a less significant ways, even if higher DM density regions could induce a greater annihilation cross section: clusters and spikes in the inner Galaxy, due to the dynamics of the supermassive BH, can significantly increase the flux or generate localized sources, detectable in gamma and neutrinos.
- The joined results of PAMELA and FERMI pose tight constraints on DM properties. The antiproton flux between 0.1 and about 120÷150 GeV is perfectly described by a secondary flux from spallation. The positron flux is discordant instead. The annihilation cross section must be very high, not purely thermal, to reproduce this positron enhancement and the positron-antiproton tension; the Sommerfeld mechanism could be a natural well-posed way to generate the enhancement, giving rise to a new ϕ boson force mediator.

- PAMELA results suggest that DM must be very massive ($\lesssim$ 10 TeV), with hadronic annihilation products shifted in the high energy range, or not too massive (600 GeV ÷ 1 TeV) but leptophilic. Heavy masses could be also granted by coannihilation processes in the Early Universe. So the “thermal low-mass” paradigm must be thrown away and substitute with a “DM TeV-ish age” one.
- From the absence of low energy antiprotons and the solid prediction of antiproton on antideuteron ratio, one can estimate an upper limits for low energy antideuteron flux. It can be said that the primary antideuteron events expected for AMS-02 in three years, from a “well-done” DM candidate, are about one.
- So, opportunities in antideuterons channel, in the low energy range 0.2 ÷ 3 GeV, are not null but disadvantaged, as AMS-02 can see some antideuterons especially from not too heavy candidates (< few TeV), probably excluded by PAMELA and FERMI results in antiprotons, electrons and positrons from non-leptophilic scenarios.
- Gamma rays and neutrino astronomy for DM search is a powerful comparison and constraint instrument for AMS-02 dark matter searches.
- The hadronic low energy region is realistically obsolete and should be replaced with a high energy research. Higher masses correspond to lower fluxes and less chances for AMS-02 to see a signal beyond the sensitivity of about $5 \cdot 10^{-7}$ at the GeV scale. It's probable that AMS-02 will see neither DM antiprotons nor antideuterons at this scale.
- In function of AMS-02 performances, an hadronic research related to very heavy DM particle can still be made between 100 and 2000 GeV, to restart from PAMELA data. This would be the most significant signal of new particle physics, even cleaner and clearer than the leptonic one, a strong evidence in favor of dark matter. In fact, while positron signal could have a primary astrophysical source, an antiproton anomaly would be very difficult be explained without dark matter, in particular after the future AMS-02 B/C ratio results. The puzzle can hardly be solved looking to leptons only.
- The positron signal, on the other hand, is of course a fundamental channel for DM study. In terms of intensity of annihilation products fluxes, AMS-02 can see a positron peak for all DM candidates capable of producing e^+ beyond 100 GeV, testing all DM theories.
- AMSB Wino-like neutralino, KK LKP particle, Scalar Multiplet and Little Higgs LTP are the most suitable candidates for a space experiment. The first three could be non-leptophilic theories capable to grant a very heavy candidate producing high energy substantial fluxes, i. e. good candidate for the hadronic dark matter research; but SUSY and KK theory are quite disfavored if a simplicity criterion is invoked and once taken into account LHC evidences.
- The parameters space for a non-leptophilic stable candidate obtained from the phenomenological analysis is the following:
    - $2\,TeV < M_{DM} \lesssim 10\,TeV$
    - $\tau_{DM} \approx 10^{26} s$
    - $\langle \sigma v \rangle_{ann} \sim a + bv^2 + c\frac{1}{v} \sim 10^{-(26\div23)} cm^3 s^{-1}$
    - $\sigma_{SI}^{\chi N} \lesssim 10^{-(43\div42)}\ cm^2$ *and* $\sigma_{SD}^{\chi N} \lesssim 10^{-(39\div36)}\ cm^2$
    - *Preferred first type annihilation final states: heavy quark-antiquark, gluon-gluon and WW, with subsequent decay channels*
    - *High AMS-02 well-detectable* $\bar{p}\ fluxes \sim 10^{-(5\div6)}[GeV\ m^2\ s\ sr]^{-1}$ *and* $\bar{p}/p$ *fluxes ratio* $\sim 10^{-(3\div2)}$ *for kinetic energy of* $100 \div 2000\ GeV/n$

- Introducing a Dark Disk with the proper rotational properties, even DAMA's discordant observations can be easily traced back to these paradigms.
- It seems that nature does some particular energy scale jumps in the fundamental constituents: we had to wait 66 years between the proton discovery (1917) – a GeV scale particle – and the electroweak bosons one (1983), i. e. 100 GeV scale particles. And other ten and thirty years to complete the 100 GeV scale landscape: with the quark top and the Higgs boson. It's probable and not surprising that nature conceals the new particle bestiary over another two order of magnitude barrier, i.e. the 10 TeV border.

3.8.3 Open Questions

Finally, it's important to conclude with some features and reasoning about our ignorance and our possible false beliefs. Chapter 2 begins with a brief discussion about our basis knowledge of dark matter problem and our paradigms. It has already been shown that the thermal paradigm, i. e. the low mass and low cross section assumptions, must be relaxed and reinterpreted, to allow heavy candidates with a probable Sommerfeld mechanism. But maybe all the assumptions must be questioned, without claiming to be exhaustive or to provide answers, trying to go further:

- Dark Matter is neutral, but in some theories it has an electric or magnetic dipole moment [337–340]. Moreover, it's known its cross section should be very tiny: maybe this non-interaction characteristic is only a human experimental limitation and not a physical interaction veto. Then, is DM really *dark* or only *shady* and what does this imply? Is it possible to study an electromagnetic DM cross section from CMB polarization, for example? Only a Dirac fermion could have an electric or magnetic dipole moment and, as already stressed, not-Dirac DM candidates are preferred: this would introduce a non-self-annihilating surely not minimal scenario.
- It could be possible to "see" Dark Matter at LHC in a *No missing-energy channel*? Could DM be produced in pp collisions without escaping, so that it's possible to see the same hadronic/leptonic cosmic signature (e. g. for a Dynamical Dark Matter particles spectrum [291])? Or can a collider result be compared to an AMS-02 cosmic rays analysis, if a mediator between dark and visible sectors exists?
- We usually imagine a stable self-annihilating Majorana particle, when talking about DM. But no one knows if Majorana particles, in terms of statistics, truly exist (only quasiparticle Majorana manifestation seems to be measured in a nanotechnology experiment [341], but not a fundamental particle) and, if not, uncommon and fine-tuned decaying channels have to be invoked. So, which is the real mechanism that triggers the DM weak process with which CR hadrons and leptons are produced? Can we guess new reasonable processes, such as a WIMP oscillation (a fundamental flavor ν-like oscillation or a neutral meson-like matter/antimatter oscillation – like in *asymmetric oscillating* DM theory [277, 279]) or an induced β-like decay (similar to $p + \bar{\nu} \rightarrow n + e^{+}$), without modifying to much the Standard Model [99, 211, 342]? Would they generate a correct amount of cosmic particles?
- *Furthermore*: i) if any substructure in the positron fraction will be seen by AMS-02 at low energies (i.e. for example a little bump around 10 GeV, as theorized and discussed in [343] but for a very light DM candidate), could this be a distinctive feature of a new annihilation process of a *Sommerfeld dark scalar* with a $\sim$ 10 GeV mass? ii) Is it possible to create a physical link between the different DM cross sections, i.e. nuclear, annihilation/decay cross section and an hypothetical EM one [347]?

These are the brand new conceptual challenges to be faced.

Chapter 4

The detector: AMS-02, the TOF and the Data Acquisition

In this chapter the main detector characteristics are reviewed, stressing their peculiar importance for the physical goals, dealing with apparatus performances, single detector capabilities and data taking features. In particular, the Time-of-Flight physics and performances will be deeply analyzed.

Let’s explain AMS-02 in a nutshell [403].

- The Alpha Magnetic Spectrometer is a state-of-the-art particle physics detector designed to operate as an external module on the International Space Station. It uses the unique environment of space to study the universe and its origin by searching for antimatter, dark matter while performing precision measurements of cosmic rays composition and flux at Low Earth Orbit (LEO), from few hundred MeV/n up to few TeV/n. It is an improved version of AMS-01 [351–355].
- AMS-02 is built, tested and operated by an international Collaboration of 56 institutions from 16 countries represented by the United States Department of Energy (DoE). The principal investigator is Nobel laureate particle physicist Samuel Ting. NASA is responsible for the installation of AMS-02 on the International Space Station (ISS), where AMS will operate for the lifetime of the ISS. AMS-02 is mounted on the upper Payload Attach Point (S3) on the main truss of the ISS.
- Orbiting the Earth on the ISS at an altitude of about 350 km, AMS-02 is studying with an unprecedented accuracy of one part in 10 billion the composition of primary cosmic rays, exploring a new frontier in the field of particle physics.
- AMS-02 will collect more than 100 billion of primary cosmic rays which, after being accelerated by strong magnetic fields, traveled for hundreds of millions of light years before reaching the experiment.
- The core of the AMS-02 spectrometer is a large magnet to measure the sign of the charge of each particle traversing the instrument: the experiment is collecting data continuously, producing a data stream of 7 Gigabits per seconds, which, after online processing, is reduced to a 2 Mbs average of downlink bandwidth.
- Its chronicle: after CERN final testing at ESA's European Space Research and Technology Centre (ESTEC) facility in the Netherlands, delivery to the Kennedy Space Center in Florida took place on 26 August 2010. The launch of Space Shuttle Endeavour flight STS-134 carrying AMS-02 took place on 16 May 2011, and the spectrometer was installed on 19 May 2011. In July 2012, AMS-02 had recorded over 18 billion cosmic ray events since its installation.

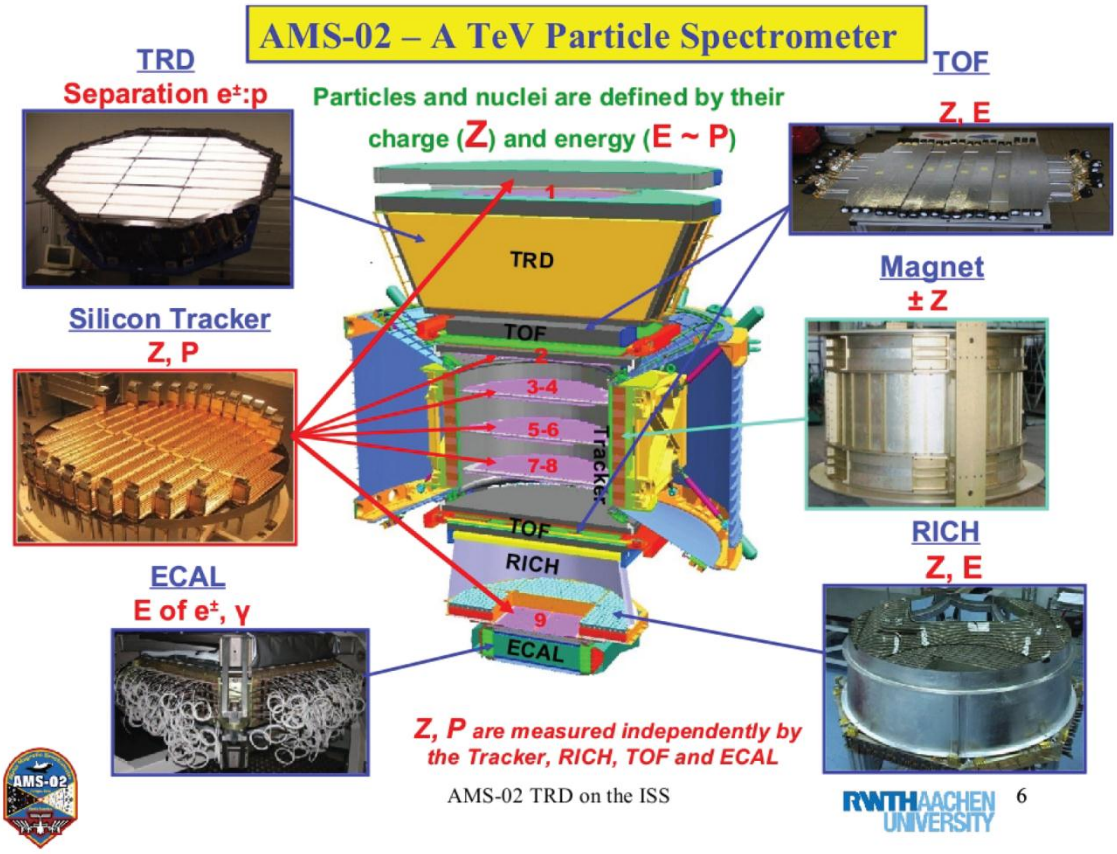

AMS-02 – A TeV Particle Spectrometer

Particles and nuclei are defined by their charge (Z) and energy (E ~ P)

Z, P are measured independently by the Tracker, RICH, TOF and ECAL

AMS-02 TRD on the ISS

Figure 1 – The AMS-02 Spectrometer. The detector components are: Transition Radiation Detector (TRD), Time Of Flight detector (TOF), silicon Tracker (Tracker), Ring Imaging CHerenkov detector (RICH), Electromagnetic CALorimeter (ECAL), AntiCoincidence Counters (ACC) the magnet. Here are illustrated the main physical quantities measured by each subdetector. Also ECAL contributes to the electron/proton separation [403].

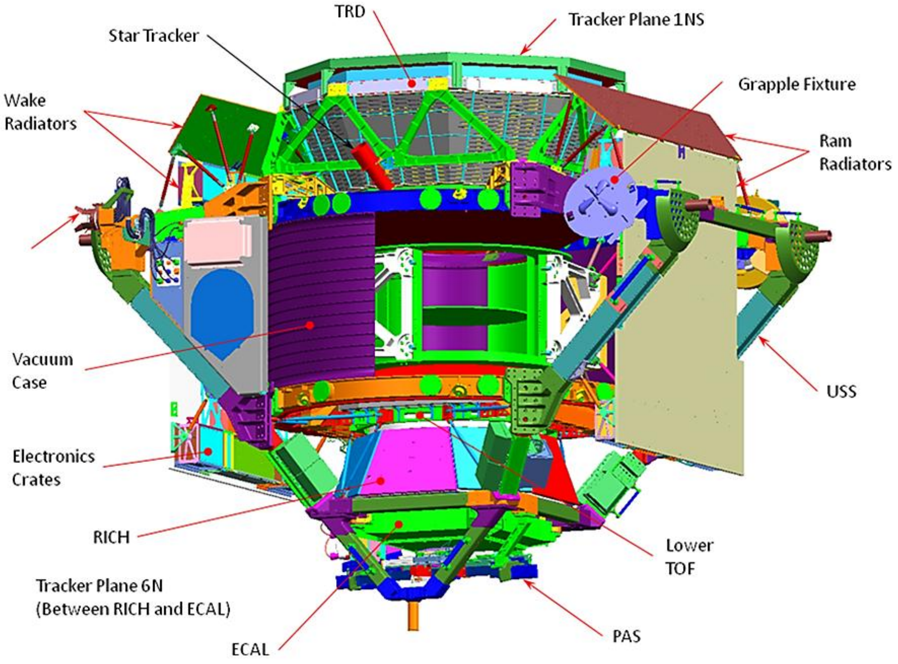

Figure 2 – Realistic view of AMS-02 with additional technical components [403].

- The main AMS-02 characteristics are the following [403]:

- Mass: 8500 kg
- Dimensions: 5x4x3 m^3
- Acceptance: 0.45 m^2 sr
- Power: 2500 watts
- Internal data rate: 10 Gbit/s
- Data rate to ground: 2 Mbit/s
- Magnetic field intensity: 0.15 Teslas produced by a 1,200 kg $Nd_2Fe_{14}B$ permanent magnet
- Original superconducting magnet: 2 coils of niobium-titanium at 1.8 K producing a central field of 0.87 Teslas. AMS-02 flight magnet changed to non-superconducting AMS-01 version to extend experiment life and to solve reliability problems in the operation of the superconducting system
- Subsystems: 15 among particle detectors and supporting subsystems
- Launch: 16th May 2011, 08:56 am EDT
- Mission duration: through the lifetime of the ISS, until 2020 or longer (it will not return back to Earth)
- Construction: 1999-2010
- Cost: 1.5 billion dollars

In Figs. 1 and 2 the AMS subdetectors are shown. Let's give a preliminary synthetic picture of the detectors [384, 403].

1. The Transition Radiation Detector (TRD) is designed to separate e^+/e^- from p^+/p^- up to 600 GeV. TRD consists of 20 layers of straw tubes, filled with a mixture of Xe/CO_2 , alternating with fleece radiators.

2. The Time of Flight detector (TOF) consists of four planes of plastic scintillators placed at both ends of the magnet. It provides a fast trigger to the experiment, velocity with a $\Delta\beta/\beta \approx 3\%$ for protons and a charge identification up to $Z = 15$.

3. The Anti-Coincidence Counter (ACC) ensures that only particles passing the magnet aperture and not being scattered in the tracker are accepted. The ACC system is composed by 16 plastic scintillator paddles, displaced in order to form a cylinder of an inner diameter of 109.1 cm.

4. The Tracker consists of eight layers of double side silicon microstrip detectors mounted on 5 carbon fiber planes for a total active area of about 6.4 m^2. In each layer, simultaneous measurements of position and energy loss in silicon are performed along the particle trajectory. With its high spatial resolution, 10 μm for singly charged particles (≈ 6 μm for $Z > 1$), the silicon tracker allows the determination of the rigidity (R) and the charge sign of particles up to several TVs, with a resolution $\sigma_R/R \approx 2.5\%$ up to $O(100)$ GV. The low noise and wide dynamic range of the silicon readout electronics allow exploiting the energy loss measurements to determine the particle absolute charge for nuclei up to Fe.

5. The Ring Imaging CHerenkov detector (RICH) provides Z measurement up to iron and a precision velocity measurement with $\Delta\beta/\beta \approx 0.1/Z$ % allowing for isotope separation in the kinetic energy range from 0.5 GeV/n to 10 GeV/n for $A = 10$.

6. The Electromagnetic CALorimeter detector (ECAL) has a total radiation depth of 17 X_0 for shower development. ECAL is designed to assure precise e^-, e^+ and γ spectra from 1 GeV to 1 TeV with dE/E < 5% and good e^+/p discrimination (below 500 GeV). For gamma ray studies, ECAL acts as an independent photon detector with an angular resolution of approximately 1° ($\sigma(\theta)$ of 2 arc-sec).

Let's mention in few words the constructive detector performances.
In Figs. 3 and 4 the overall performances of the subdetectors relevant for particle identification, as measured on test beams of protons at CERN, are shown [350].

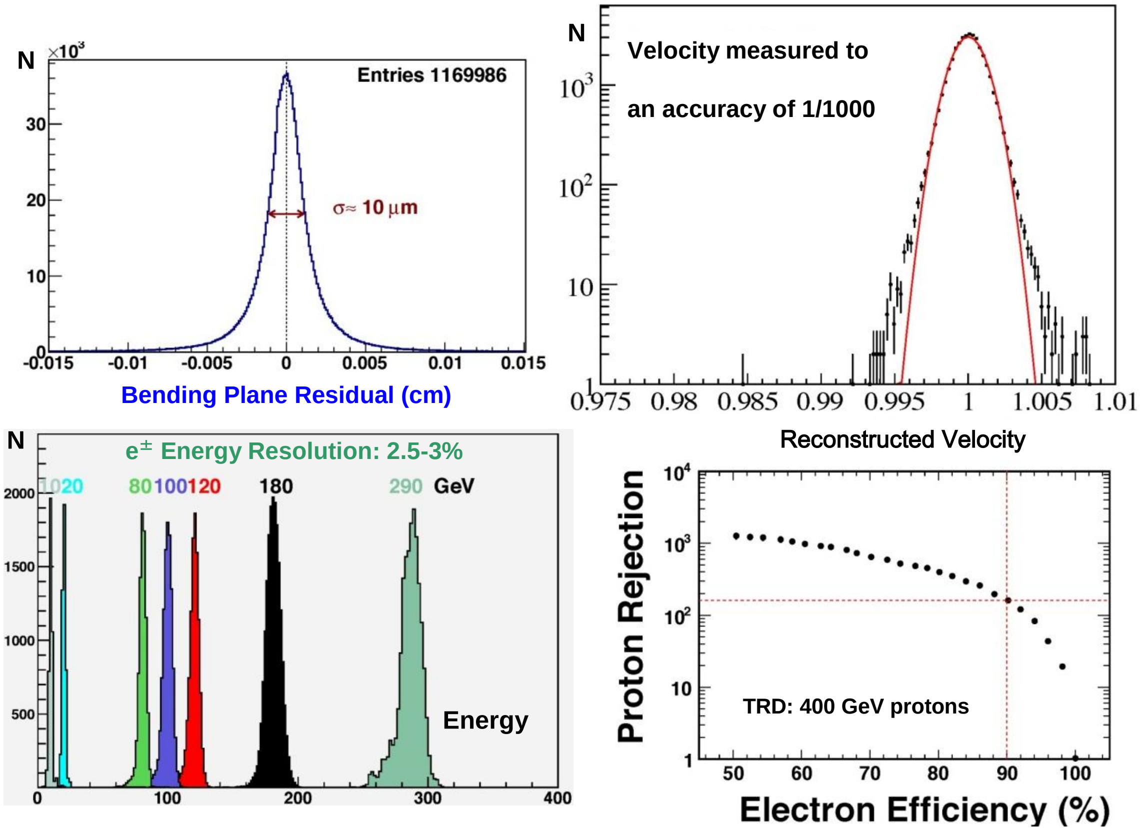

Figure 3 - Test Beam Results with permanent magnet – 8-20 Aug 2010. From left clockwise: the measured residuals of the TRACKER fitted tracks in the curvature plane of the magnet; the measured RICH velocity resolution, of the order of 0.1 %; the measured ECAL energy spectra of electrons from 10 to 290 GeV; the measured TRD separation between electrons and protons [350].

The performances of the AMS-02 spectrometer are also monitored periodically running a cosmic ray trigger on ground since the first assembly. All detectors are found to behave according to the design characteristics. No degradation of the detectors has been shown from CERN, where it was assembled first, to ESTEC in Holland, where underwent the space qualification tests, then at CERN to change from the superconducting magnet to the permanent magnet, and finally to the NASA laboratory KSC in Florida, where is undergoing integration in the Shuttle and the ISS.

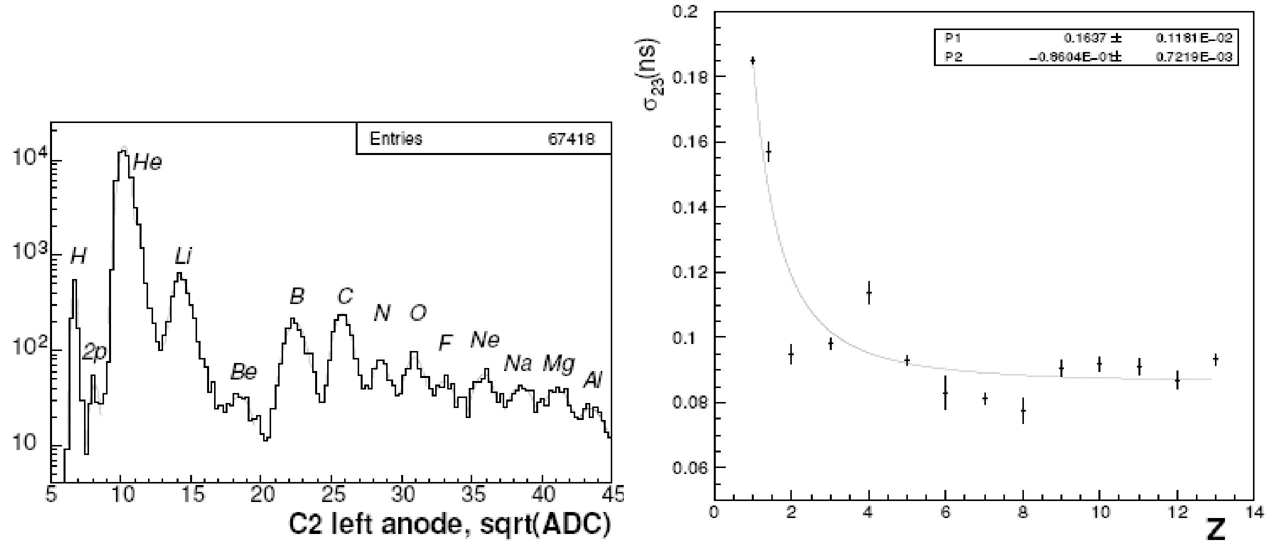

Figure 4 - Measured performances of the TOF detector on an Ions test beam. Left: charge resolution of beam Ions. Right: time of flight resolution as function of Ion charge [350].

Scientific goals

The AMS-02 will use the unique environment of space to advance knowledge of the Universe and lead to the understanding of its origin by searching for antimatter, dark matter and measuring cosmic rays.

- **Antimatter**: experimental evidence indicates that our galaxy is made of matter; however, astronomers estimate there are about 100–200 billion galaxies in the Universe and some versions of the Big Bang theory of the origin of the Universe require equal amounts of matter and antimatter. Baryogenic theories, based on Sakharov principia, that explain this apparent asymmetry, violate other measurements and, in general, are very difficult to be proved, because they're far from the energy scale accessible in nature and in our modern colliders. Whether or not there is significant antimatter is one of the fundamental questions of the origin and nature of the Universe. Any observations of an antihelium nucleus would provide evidence for the existence of antimatter in space, because there aren't any known astrophysical mechanisms capable to produce antinuclei, from antihelium on (i.e. the astrophysical cross section production for antihelium is zero). In 1999, AMS-01 established a new upper limit of 10^{-6} for the antihelium/helium flux ratio in the Universe. AMS-02 will search with a sensitivity of 10^{-9}, an improvement of three orders of magnitude over AMS-01 (Fig. 5), sufficient to reach the edge of the expanding Universe and resolve the issue definitively [356, 357].

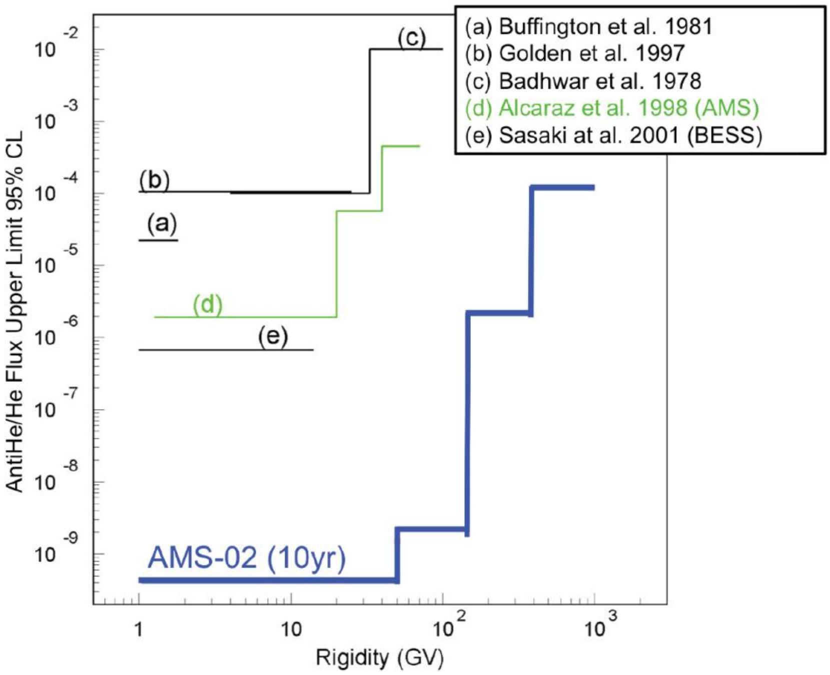

Figure 5 - The sensibility accessible to AMS-02 in the antiHe search. Here it is compared to the sensibilities reached by previous experiments.

- **Dark matter**: if WIMP particles do exist, as already explained in the previous chapter, they should be colliding with each other and giving off an excess of charged particles that can be detected by AMS-02. Any peaks in the background positron (Fig. 6), antiproton (antideuteron), or gamma ray flux could signal the presence of DM, but would need to be distinguished from poorly known confusing astrophysical signals [358–362].

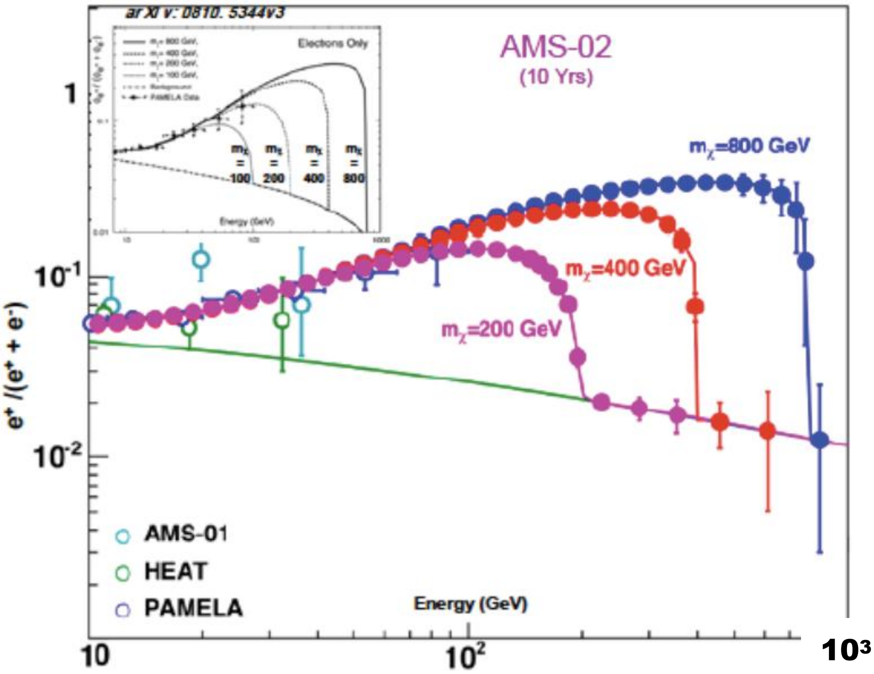

Figure 6 – Predicted sharp positron excess from a 200, 400, 800 GeV mass WIMP in ten years. For heavier candidates the spectrum fall is expected in the multi-TeV range.

- **Strangelets**: six types of quarks (up, down, strange, charm, bottom and top) have been found experimentally; however, the majority of matter on Earth is made up of only up and down quarks. It is a fundamental question whether there exists stable matter made up of strange quarks in combination with up and down quarks (Fig. 7). Particles of such matter are known as strangelets. Strangelets might have extremely large mass and very small charge-to-mass ratios, typically Z/A ~ 0.1. It would be a totally new form of matter: an hadronic, but not confined in hadrons, quark matter. This is the "strange matter hypothesis" of Bodmer and Witten (1984). The stability of this new matter would occur because of the Pauli Exclusion Principle; having three types of quarks, rather than two as in normal nuclear matter, allows more quarks to be placed in lower energy levels. Its size would be a minimum of a few femtometers across (with the mass of a light nucleus). Once the size becomes macroscopic (on the order of meters across), such an object is usually called a quark star or "strange star" rather than a strangelet. An equivalent description is that a strangelet is a small fragment of strange matter.
  AMS-02 may determine whether this extraordinary matter exists in our local environment (Fig. 8) [363].

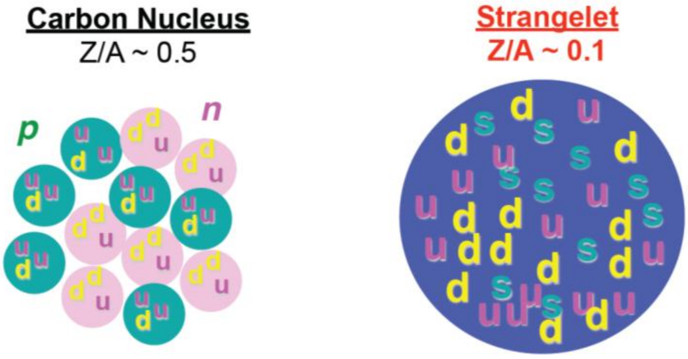

Figure 7 – Schematic picture of strangelet matter compared to a common nucleus.

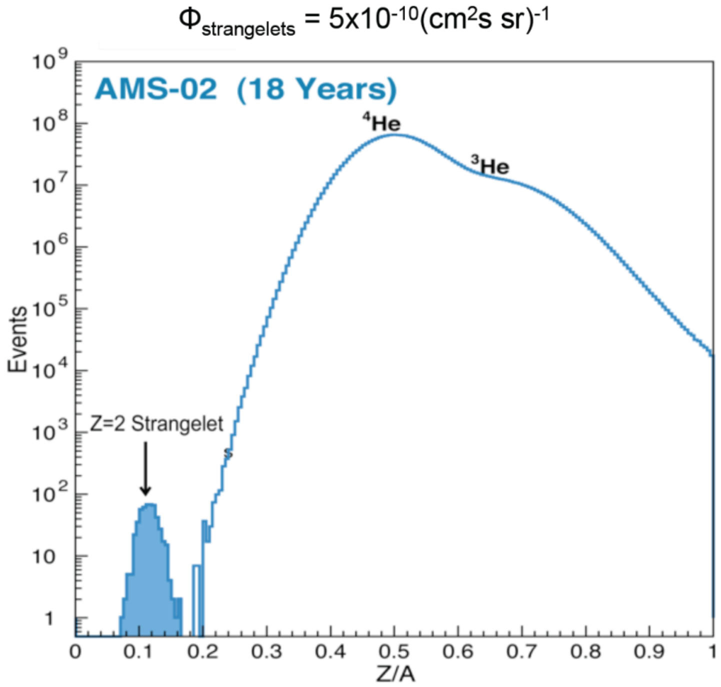

Figure 8 – Simulation for AMS-02 strangelet search. During its life AMS-02 could detect tens of strangelets.

- **Cosmic Rays astrophysics**: AMS-02 will be operative on the ISS for at least 10 years, gathering a huge amount of data and determining long term variations of the cosmic rays fluxes and composition, from protons to iron, and over a wide energy range (Figs. 9, 10). These data will improve our understanding of the interstellar propagation and of the mechanisms at the origins of cosmic rays [364−367].

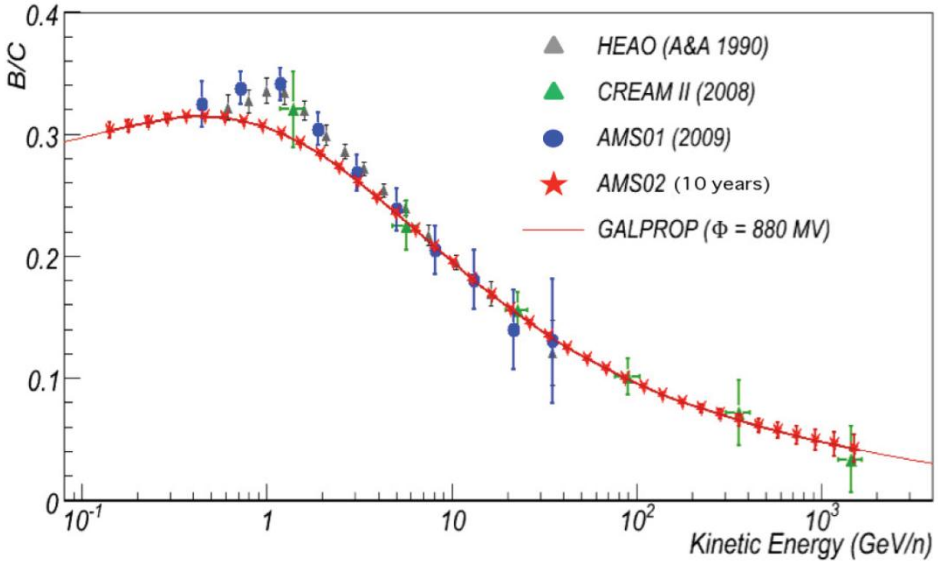

Figure 9 - The measurement capabilities on the B/C ratio. Some recent measurements and a GALPROP model are shown.

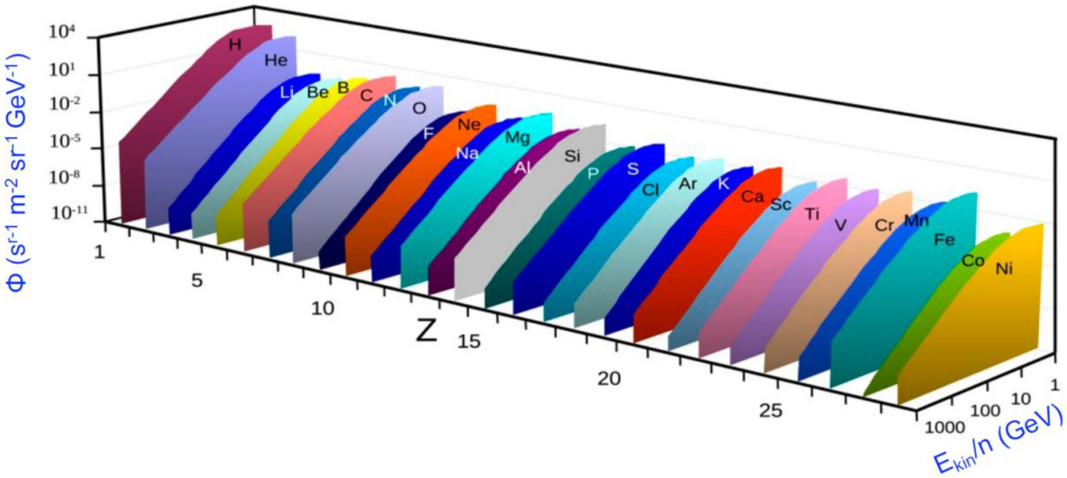

Figure 10 – AMS is measuring cosmic rays nuclei spectra, from 100 MeV to 2 TeV, with a 1 % accuracy, continuously over the solar cycle. The isotopic composition of the CR is correlated with their propagation mechanism.

- **Space radiation environment**: Cosmic radiation is a significant obstacle to a manned space flight to Mars. Accurate measurements of the cosmic ray environment are needed to plan appropriate countermeasures. Most cosmic ray studies are done by balloon-borne instruments with flight times that are measured in days; these studies have shown significant variations.

4.1 The magnet and the tracker

The magnet

A superconducting magnet (SM) was ideal for a three year stay on ISS, from 2005 to 2008, as originally planned for AMS. After the 2003 Shuttle accident the AMS program was slowing down while the ISS operation was scheduled to end in 2010. Last year the ISS scientific program has been strengthened and its lifetime has been extended to 2020 (2028). Shuttle flights, however, ended in 2011, thus eliminating any possibility of returning and refilling the SM.

A superconducting magnet was therefore no longer the ideal choice. Most importantly, the permanent magnet option will have 10(18) years time to collect data, providing much more sensitivity to search for new phenomena. The replacement of the SM with the old AMS-01 permanent magnet (PM) was performed in less than 5 months, thanks to the fact that the SM had been designed with the same aperture and the same tracker planes as those equipping the PM.

Another important challenge for the experiment was to loose not too much analyzing power at high particles momenta with a 5 times lower magnetic field. This was achieved, at least for high rigidities, with a modified set of tracker planes, exploiting a characteristic property of a magnetic spectrometer. In fact the analyzing power of a dipole field, i.e. the momentum resolution ($\Delta p/p$) is the sum of two contributions [350]:

1. Measurement inside the magnet with an effective length L

$$(Z/p)\cdot(\Delta p/p) \propto 1/BL^2 \qquad (4.1)$$

2. Measurement of the incident (θ_1) and exit (θ_2) angles which depends on the lever arm L_1

$$(Z/p)\cdot(\Delta p/p) \propto 1/BLL_1 \qquad (4.2)$$

where L_1 is the first-second and second last-last Tracker planes distance. For both magnets, $L \sim 80$ cm, but in the permanent magnet B is 5 times smaller. To maintain the same $\Delta p/p$ the lever arm L_1 has been increased from the old ~15 cm of the superconducting magnet to ~125 cm.

In Figure 11 the comparison of the resolution in rigidity for the SM and the PM is shown. The two lines refer to the calculated rigidity resolution, whereas the points show the results obtained in the 400 GeV proton test beam at CERN for the two configurations of the spectrometer. As one can see, above 1 TV the difference in the resolution is of the order of 12% and is decreasing as the rigidity becomes higher. This is of particular importance for the measurements of electron and positron spectra at high momenta.

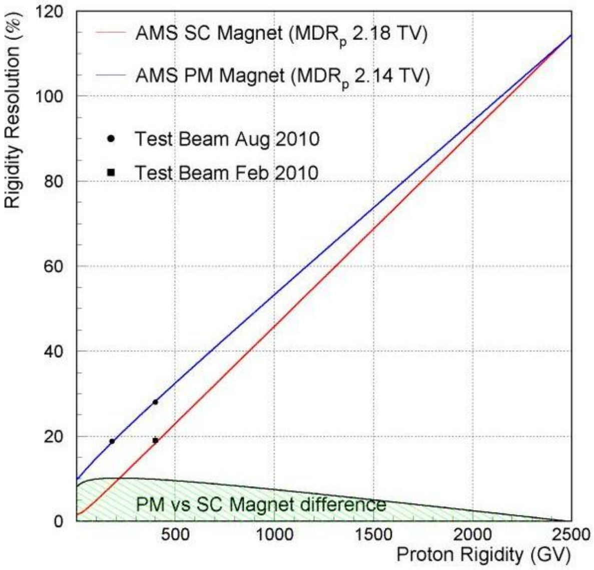

Figure 11 - Comparison of the rigidity per cent resolution of SM and PM [350].

The AMS-02 actual permanent magnet is designed to optimize the competing requirements of a large, powerful and uniform dipole magnetic field in a flight-qualified, relatively light-weighted system. The external field has been designed to be smaller than $2 \cdot 10^{-2}$ T to avoid torques on the Space Shuttle and on the International Space Station and to minimize unwanted interferences with the electronic devices.

The magnet is made of 6400 Nd-Fe-B blocks of sides 5×5×2.5 cm^3. The blocks are arrayed in 100 circle shaped 64 elements layers (one layer is depicted in Fig. 14), constituting a cylinder of length 800 mm, inner radius r_1 = 111.5 cm and outer radius r_2 = 129.9 cm. The blocks are arranged to form 64 segments with varying field directions in order to produce a 0.15 T field intensity in the magnet center.

The magnetization vector resulting in the cylindrical shell is constant in magnitude and oriented according to:

$$\alpha = 2\phi + \pi/2 \tag{4.3}$$

being ϕ the angular cylindrical coordinate. Such a distribution gives an internal field of:

$$B = B_r \ln(r_1/r_2) \tag{4.4}$$

where B_r is the residual magnetic flux density of the ring and r_1/r_2 is the inner/outer radii ratio. The magnet fulfills the strict space requirements, as demonstrated in its first space flight in 1998 as constituent of the AMS-01 detector. The orientation of the almost uniform magnetic field defines the whole reference frame of the AMS-02 experiment [368]. The center of the frame is at the center of the magnet. The AMS-02 *x* axis is oriented along the direction of the field lines (Fig. 12). The z axis is defined by the magnet cylinder symmetry axis, with positive values toward the top of the instruments. The last axis, y completes the Cartesian right-handed tern. All the curved motion of a charged particle in the AMS-02 magnetic field is contained in the z-y plane.

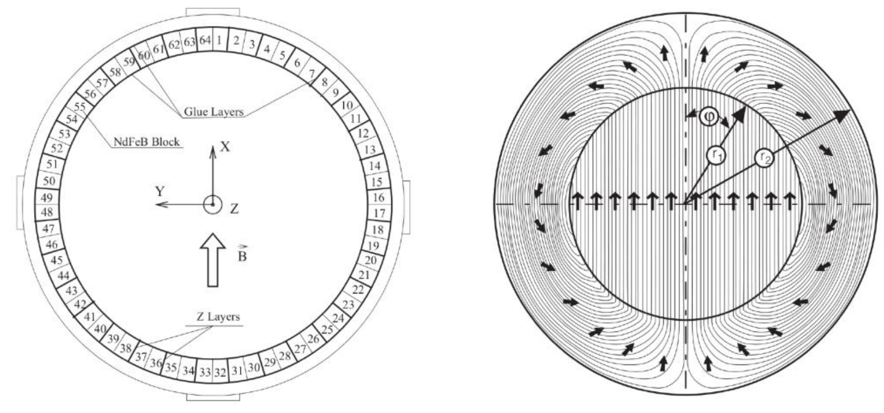

Figure 12 - The AMS-02 magnet field orientation [352]. The varying direction of the magnetic field in the material allowed the flux to be returned primarily within the material allowing for a negligible external field. A quite uniform field is generated in the inner part of the volume. The magnet blocks and the coordinate system are shown in the left picture. The arrows in the right exhibit the magnetization direction α.

Figure 13 - The AMS-02 permanent magnet that operated [352] on board of the Space Shuttle Discovery in 1998 (Mission STS-91 - Experiment AMS-01).

The Silicon Tracker

The core of the AMS-02 apparatus is a micro-strip silicon tracker [369, 370]. The tracker is composed by 9 layers arranged along the height of the AMS-02 detector, as shown in Fig. 14a). Layers 1 and 9 constitute the external tracker and are positioned at both ends of the AMS-02 detector, above the TRD (z=155 cm) and the ECAL (z=-135 cm) respectively, to maximize the lever arm in the trajectory determination. Layers 2 to 8 constitute the inner tracker and are arranged just above the magnet mechanical structure (layer 2, z=55 cm) and inside the magnet bore (layers 3-8). Three carbon fiber and aluminum honeycomb planes (see Figs. 14) support the layer pairs inside the magnet bore (3-4, 5-6,7-8), with a relative distance between layers belonging to the same plane of about 4 cm along the z axis. The most inner plane (layers 5-6) is placed at the magnet center (z=0) and the two neighbors symmetrically disposed at z=± 27 cm from the central one.

Each layer contains a variable number (around 20) of read-out units, called ladder. Each ladder has a variable number (from 7 to 15) of silicon sensors. The total active area of 6.4 m^2, for a total number of 2264 Silicon sensors arranged in 192 ladders, makes the AMS-02 Silicon Tracker the largest tracker for a magnetic spectrometer ever built for space applications.

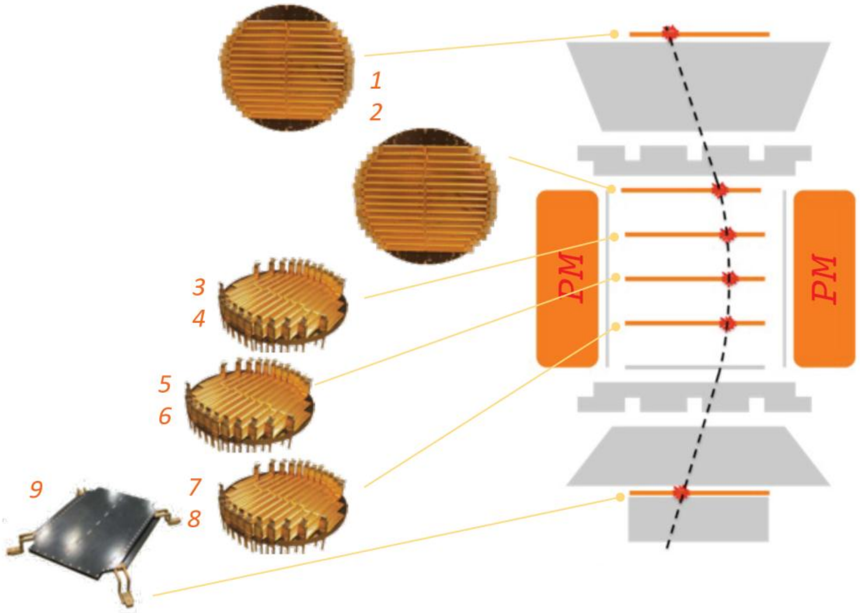

Figure 14 a) – Sketch of the AMS-02 tracker layers configuration.

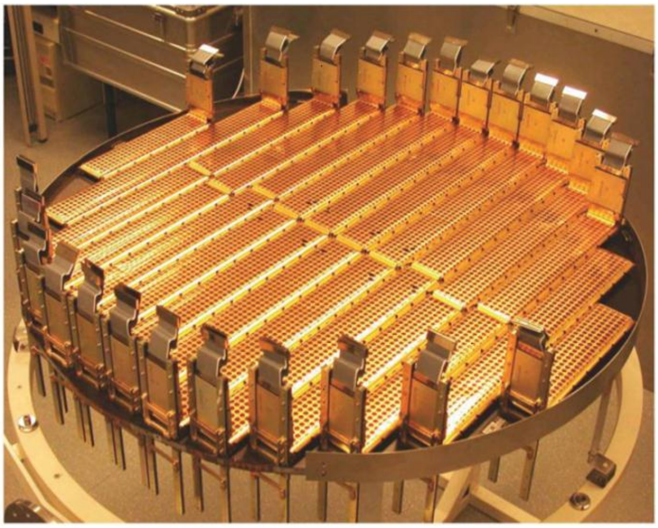

Figure 14 b) – One of the internal tracker planes. On one of the two sides are visible the shielded silicon detectors installed with the front-end electronics in vertical.

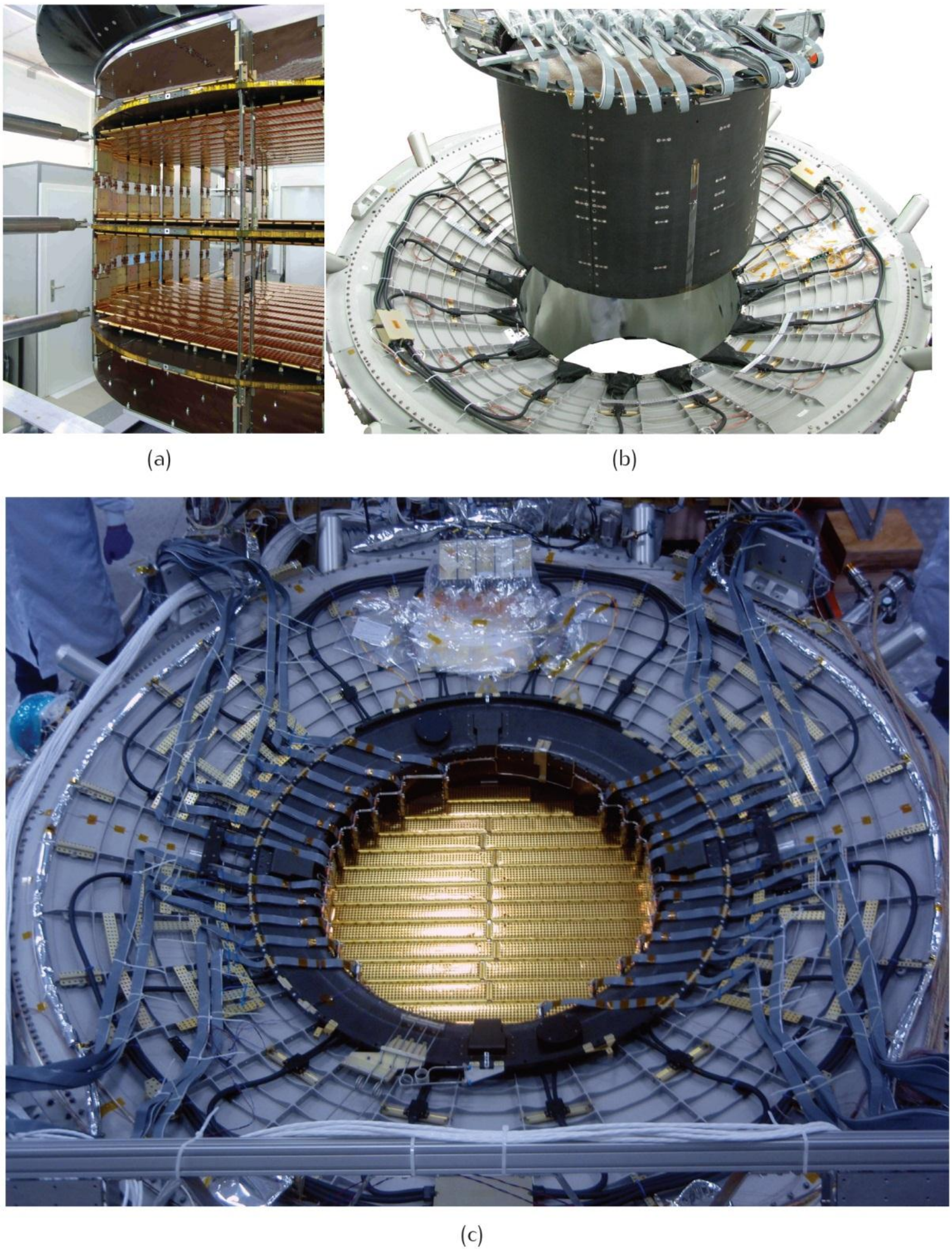

Figure 15 - The internal part of the AMS-02 Silicon Tracker. The three planes with coupled layers integrated together (a). The cylindrical carbon fiber support structure with the internal layers being lowered into the magnet case bore (b). The internal part of the tracker integrated and cabled (c).

The Silicon sensor

The basic element of the Silicon Tracker is a double-sided micro-strip sensor. Its size is 72.045 × 41.360 × 0.300 mm^3. The thickness of the silicon (300 µm) as well as the choice of a double-side detector is made to minimize the material budget along the particles path and so the consequent multiple scattering.

The substrate is high resistivity n-type Si sensor made with a dynamic resistive coupling, as punch through and surface-through techniques. The sensors are inverse biased with an operating voltage of 80 V. On the two surfaces are placed p+ strips, with a readout (implantation) pitch of 110 (27.5) µm, and n+ strips (orthogonal to the previous ones) with a pitch of 104 (208) µm. The capacitive coupling net between the implanted strips and the analog readout of the strip signals allows to apply a center-of-gravity technique to achieve a 10(30) µm position measurement resolution on the junction (ohmic) side of the sensor for single charged particles. The junction side strips are used in AMS to measure the y coordinate in the bending (yz) plane of the particle trajectory.

Tracker Alignment System (TAS)

Laser diodes are installed on the layer 2 support structure. Five laser beams permit to monitor the mechanical movements of the 7 layers of the internal tracker.

To minimize absorption and reflection of the laser beams, special windows have been implemented on the shielding of 20 ladders along their path, the corresponding sensors have been produced with a reduced strip metallization width and their surface treated with an anti-reflective coating.

4.2 The TRD

On the top of the instrument, just below the first layer of the Silicon Tracker, a Transition Radiation Detector is used to identify electrons and positrons within the overwhelming background of protons and nuclei [371].

The AMS TRD has truncated octagonal pyramidal shape (see Fig. 16) and is divided in 20 layers along the vertical (z) coordinate. Each layer is made by 20 mm irregular polypropylene/polyethylene 10 µm fiber fleece as radiator (0.06 g/cm^3) and Xe/CO_2 filled proportional wire straw tubes. The straws are made of double layer aluminized kapton foils with an inner diameter of 6 mm. A centered 30 µm gold plated tungsten wire is operated at $\sim$ 1300 V for a gas gain of 3000. The tubes are arranged in modules of 16 straws for a total of 328 units that cover an area of 2 × 2 m^2. Using a likelihood selection to combine the 20 measurements of the transition radiation emitted by the ultra-relativistic electron/positron component it possible to obtain a proton/electron rejection at the level of 10^4-10^5 with an efficiency for electrons at the level of 90% up to few hundred GVs. The energy deposition due to minimum ionizing nuclei can also be used to infer the magnitude of their charge up to iron.

The TRD has also tracking capabilities with a resolution at the mm level. The tubes in the 12 central TRD layers are oriented along the y axis to provide a coarse reconstruction of the particle trajectory in the non-bending plane and contribute to solve the ambiguity arising from the bonding scheme in the tracker.

The tubes in the first and last four layers of the detector are oriented along the x axis, sampling the particle trajectory in the bending direction between the inner tracker and the upmost layer of the external tracker.

To keep the detector filled with clean gas, AMS has a gas recirculation system; an extra amount of Xe and CO_2, stored in lightweight bottles, accompany the TRD. A network of valves and pressure sensors can whip up fresh Xe:CO_2 80:20, at a rate of 7 liters per day, in to the 300 liter detector volume. Within the TRD, the gas is flushed in a closed circuit and there are pumps, valves, and CO_2 analyzers to monitor its properties.

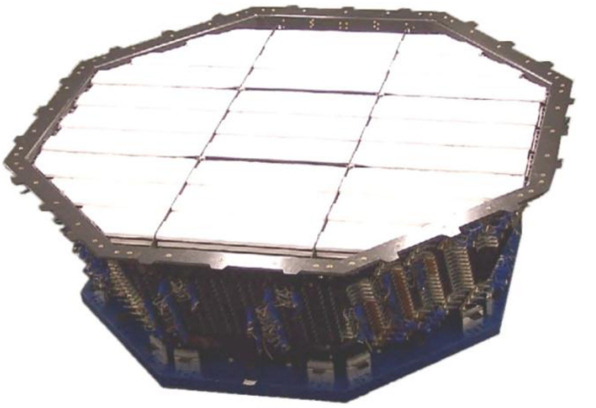

Figure 16 - The truncated octagonal pyramid shape TRD integrated and ready to be installed on the whole AMS-02 detector.

4.3 The ECAL and the Star Tracker

The ECAL, placed at the bottom of the AMS-02 detector, is a fine grained sampling calorimeter providing a tridimensional imaging of the longitudinal and lateral electromagnetic shower development. It has also tracking capabilities with an angular resolution of 1°.
Made of lead and scintillating fibers, the calorimeter is a square parallelepiped with a 65.8×65.8 cm^2 basis and a 16.5 cm height (see Fig. 17). It is divided into 9 superimposed superlayers. Each superlayer, 18.5mm thick, consists of 11 grooved lead foils, 1mm thick, interleaved with layers of 1mm diameter scintillating fibers. In each superlayer fibers run along the same direction: the 3-D imaging capability is obtained by stacking superlayers with fibers alternatively parallel to Y-axis (4 layers, X-view) and X-axis (5 layers, Y view). The resulting composite structure has a lead-fiber-glue volume composition of 1:0.57:0.15 and an average density of 6.8 g/cm^3. Total calorimeter thickness corresponds to almost 17 radiations lengths. The high granularity permits a high rejection power between electrons and hadrons: each square element (9 mm side) corresponds to half Molière radius in traverse dimensions and one radiations length in depth. The fibers bring the signal outside the calorimeter volume where is read by 324 four anodes PMTS. All measurement properties are put together in a software algorithm called Boosted Decision Tree (BDT) Classifier for showers, to discriminate leptons from hadrons with 90% of efficiency for deposited energy less than 200 GeV [372–376].

Figure 17 - The ECAL before the PMTs installation on the lateral slots (visible on the detector sides).

The resolution for vertical particles was measured with 6-250 GeV electron beams to be [374]:

$$\frac{\sigma(E)}{E} = \frac{9.9\%}{\sqrt{E(\mathrm{GeV})}} \oplus 1.5\%$$

In combinations with the TRD, the ECAL makes possible a $\sim 10^6$ electrons/hadrons discrimination. A fast recognition of possible showers is made by a dedicated board (ETRG) inserted in the Level-1 trigger logic. Being self-triggering, the ECAL can be used as a standalone detector (in particular for photons).

AMS measures high-energy γ-rays energy and arrival direction in two complementary ways.
1) *Single Photon Mode*: i.e., by the direct detection of ECAL. In this case, ECAL works like a standalone instrument. It can trigger and record the gamma ray event by itself. The ECAL position and energy resolution are very good up to 300 GeV or more.
2) *Conversion Mode*: i.e., by the photon pair conversion in the Tracker. When a high-energy photon converts into the electron/positron pair before or in the Tracker, the pair couple is produced in the forward direction and is then separated by the magnetic field. We can reconstruct the photon energy and its arrival direction from the electron/positron vertex production angle and from the two separate curvature measurements.
The photon direction with respect to fixed stars is finally derived using the Star Tracker orientation information.

The Star Tracker
AMS-02 has two different γ-rays measurement possibilities. By the direct measurement with the ECAL, with a $\sim$ 1° pointing precision, and by conversion (i.e. a photon produces a e^+e- pair on the upper part of AMS and the two charged particles are reconstructed by the tracker) with an angular expected resolution of $\sim$ µrad, at high energies.
To identify γ-rays sources, the AMS-02 orientation with respect to the fixed stars should be known with an angular resolution comparable to that achievable in the photon measurement in the detector [377]). AMS-02 has been equipped with a pair of CCD cameras which constitute the Star Tracker system. The 512 × 512 pixelized cameras are oriented at 40° (see Fig. 18) with respect the AMS-02 zenith and take pictures of the sky with a 10 Hz rate. From the pattern recognition of groups of stars in the sky and the comparison with stellar maps is possible to determine the detector orientation in the sidereal reference frame with the required accuracy.

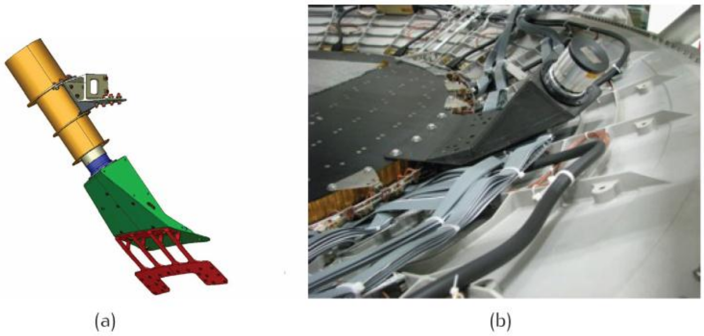
(a) (b)

Figure 18 – Star Tracker single camera: a CAD model (a) and a picture of the device installed on the conical flange of the magnet case (b).

4.4 The RICH

The AMS-02 RICH consists of a radiator plane, a conical mirror and a photon detection plane.
The radiator is the responsible for the Cherenkov radiation production. It consists of a dodecahedral polygon with a 118.5 cm internal tangent diameter. An array of 2.7 cm thick aerogel tiles with a refractive index between 1.03–1.05 surrounds a central 35×35 cm^2 region equipped with 5 mm thick Sodium Fluoride (NaF) radiator (n_{NaF} = 1.335). This radiators combination optimizes the overall counter acceptance since the Cherenkov photons radiated by the NaF in large cones will fall within the detection area. Indeed the detector plane has an empty 64×64 cm^2 area in its center, matching the active area of the electromagnetic calorimeter located below.
Outside the ECAL hole, 680 4×4-multi-anode PMTs (gain 10^6 at 800 V) are arranged to cover the circular 134 cm diameter surface at the basis of the conical mirror [378] (Fig. 19).
A 47 cm height conical reflector multi-layer structure on a Carbon fiber reinforced composite substrate encloses the radiator and the detection plane. The mirror increases the RICH acceptance reflecting high-inclination photons and provides the necessary photon drift ring expansion. RICH provides the β measurement with a resolution ~ 0.1% for Z=1 particles, and ~ 0.01% for nuclei. It also provides a particle charge measurement with a charge confusion of the order of 10%.

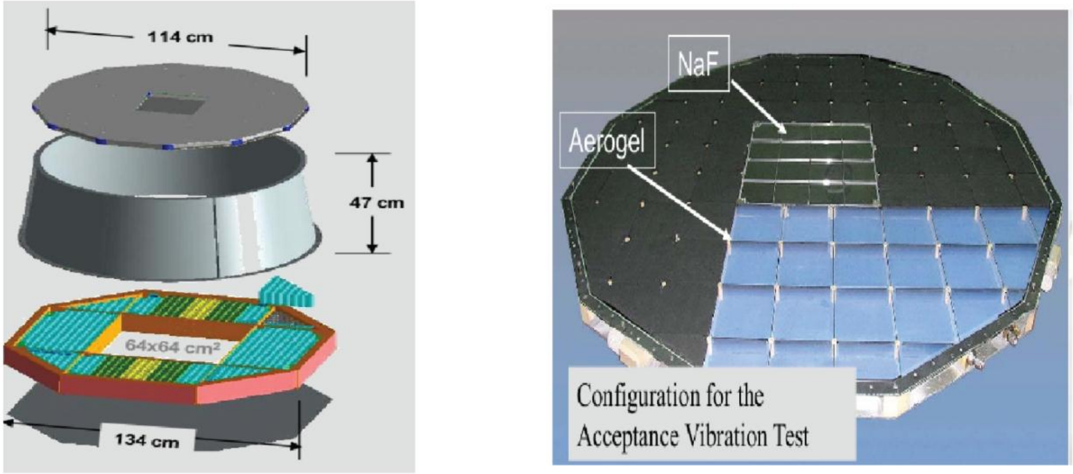

(a) (b)

Figure 19 – a) RICH detector exploded view; b) radiator structure, with 80 aerogel bricks and 16 sodium floride bricks.

4.5 The ACC, the DAQ and the Trigger

The Anti-Coincidence Counter (ACC)

The inner tracker is surrounded by 16 scintillators panels (dimensions: 220 × 830 × $8mm^3$) inserted in the internal bore of the magnet. The light coming from both ends of each scintillator is collected by wavelength shifter fibers of 1 mm diameter, embedded in grooves milled into the scintillation panels [379]. The fibers are arranged in bunches of 37 fibers and brought outside the magnet bore where are read by 16 PMTs (8 in the upper part of the magnet and 8 in the lower, to provide redundancy), similar to the ones used for TOF. The system is designed to have a very low inefficiency (below 1/300.000) and the high degree of homogeneity of the scintillating fibers ensures a reliable and fast signal for the high inclination particles with also some impact point determination capabilities. The signals from the 8 segments of the ACC system are inserted into the Level-1 trigger logic (see Fig. 20 for examples).

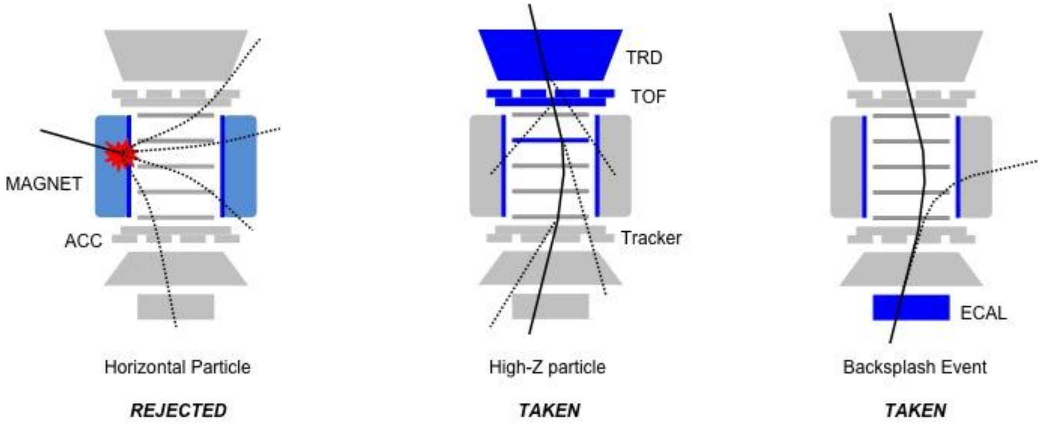

Horizontal Particle **REJECTED** | High-Z particle **TAKEN** | Backsplash Event **TAKEN**

Figure 20 - In such a geometry a vertical particle will give a signal in TOF and not on ACC. Conversely a horizontal particle may give a signal on ACC and not in TOF (left). Then an event should be recorded following the logic *TOF AND NOT ACC*. This restrictive condition can be released in 2 particular condition. The first is (central case) an incoming ion (high-Z particles): when an ion traverses matter it is accompanied by electron production, the so called δ-rays. These electrons can easily fire the ACC. In order to keep ion events the ACC veto is disabled. The second is an electron/positron converting on the ECAL (right): when an electron/positron passes through the ECAL backsplash particles are produced. These particles may exit from the calorimeter surface and hit the ACC. In this case the trigger condition should be TOF AND NOT MORE THAN 4 ACC PADDLES FIRED.

The DAQ chain

AMS-2 Data Acquisition System collects data from over 200K analog channels of the various AMS-2 sub-detectors: TRD (abbrev. U, from German word “übergangsstrahlungsdetektor”, i.e. transition radiation detector), TOF and Anti-Coincidence Counters (abbrev. S, from scintillators), Tracker (abbrev. T), RICH (abbrev. R), Electromagnetic Calorimeter (abbrev. E) and Level-1 Trigger module (abbrev. LV1). It consists of nearly 300 computational nodes based on ADSP-2187L Digital Signal Processors (DSP) and a Main DAQ Computer based on PPC750 processor (JMDC) [76, 403].
DAQ architecture has a tree-like structure (see Fig. 21):

- 264 xDR nodes (DR -Data Reduction, “x” specifies a sub-detector: T, U, R or E) collect data from analog electronics Front-Ends;
- 28 JINF nodes collect data from xDR nodes;
- 8 SDR2 nodes collect data from TOF/ACC and produce trigger signals;
- 2 JLV1 nodes collect analog and digital information to produce LV1 trigger;
- JINJ collect data from JINF+SDR2+JLV1 nodes.

All the nodes (electronics boards) are hosted in two radiators (vertical panels on the two sides of AMS-02) to allow the exchange of heat with the outer space. The nodes are interconnected with point-to-point LVDS serial links and a dedicate protocol (AMSWire) is used for communication. The data throughput per link is 100 Mbits/s. The software for the DSP is designed with a sub-detector independent framework where a set of detector dependent data processing routines are inserted. The general framework has the responsibility for:

- AMSWire protocol for communication between nodes;
- data protection based on CRC algorithm;
- event building routines for physics event assembly.

Beside the general framework common to all the nodes, specific procedures, to process the raw physics events and to monitor and configure the hardware status, are implemented in both xDR and JINF nodes. The raw physics events are digitized and a compression (zero-suppression) is performed by the xDR nodes. With its ~ 200k read-out channels the Silicon Tracker is the sub-detector where the more efficient compression is needed: the Tracker Data Reduction board (TDR) will be detailed below as xDR example.

The AMS experiment operates at input trigger rates up to 2 kHz with an average event size of about 2 KBytes. In order to minimize the dead time due to data processing, event buffering is used at every level of DAQ hierarchy (4 raw and 4 compressed for the xDRs, 4 for JINFs, 4 for JINJs and 2 in the JMDC) [404, 405].

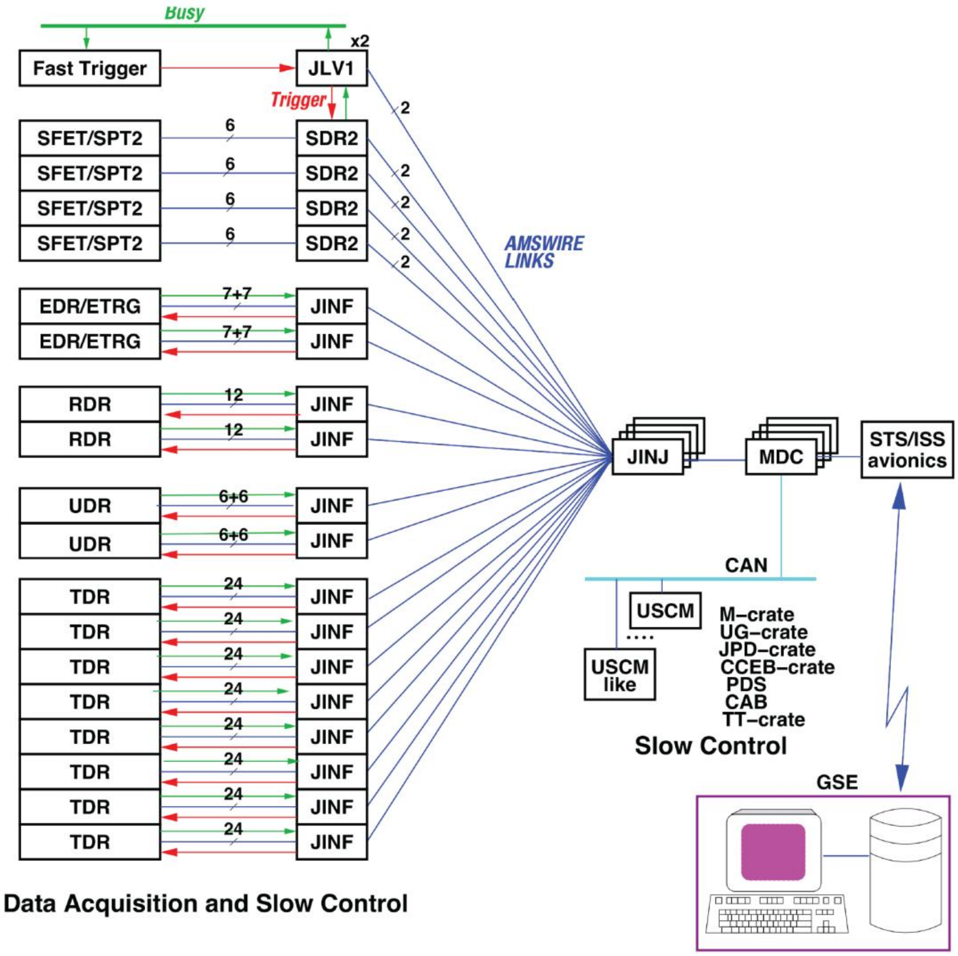

Figure 21 - The AMS-02 DAQ block diagram. The DAQ has a tree-like structure with full redundancy.

The Trigger

The trigger of the whole detector is built from signals coming from TOF, ACC and ECAL, inside a dedicated electronics board, the JLV1 [407]. To generate a trigger in the LVL1 logic is necessary to latch the various input signals to get rid of the differences in their arrival times. Moreover there are some signals which need some pre-processing, as ECAL-A signals, which inhibit the readout of the corresponding electronics (Fig. 22). The time needed to latch signals and to process them in the LVL1 logic results in a dead time of 1 μs. To minimize this dead time, a Fast Trigger (FT) technique is used: a loose trigger condition is first evaluated with a dedicated logic which does not introduce dead time in the system. Only if the Fast Trigger logic condition is satisfied, the LVL1 is activated and the acquisition inhibited during the 1 μs needed to take the trigger decision.

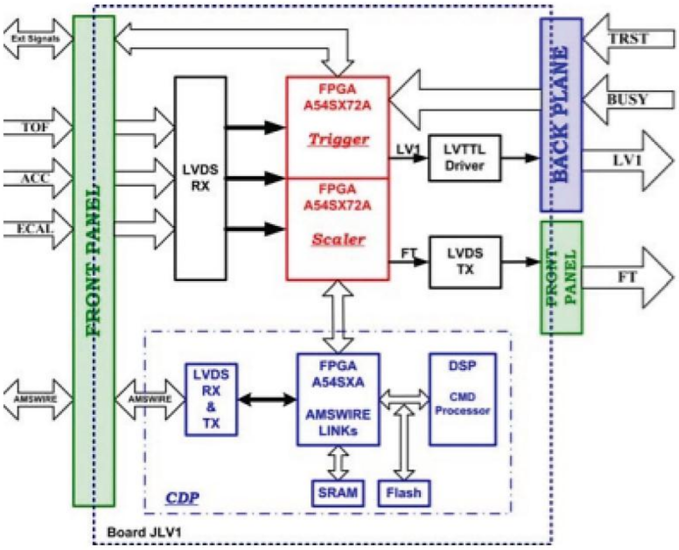

Figure 22 - The block diagram of the JVL1 (AMS-02 "trigger board"). In input TOF, ACC, ECAL and external signals. The first three are transferred to the register (LVDS) and then to the trigger unit. The external signals are directly transferred to the trigger unit. The unit produces the Fast Trigger (FT) and the Level1 trigger (LV1) [381, 407]. A protocol developed for the experiment (AMSWIRE) is used for communication with other electronic modules.

The Fast Trigger

Every 40 ns (25 MHz) the signals coming from TOF and ECAL are sampled and sent to fast and simple logics. The complete set of signals used in the Fast Trigger is detailed below [380, 408, 409] (see Fig. 23).

The TOF produces six signals for each plane:

- CP-(1...4)-p/n: Charged Particle signal from p/n-side (positive/negative side) of TOF plane (1...4). The signal is the OR of all the digital signals (i.e. above the HT) from the paddles (from 8 to 10) on one plane side. In normal conditions all TOF paddles are used in the OR, however specific configuration can be loaded in the logic for dedicated studies;
- CT-(1...4)-p/n: Charged particle in Tracker acceptance signal from p/n-side (positive/negative side) of TOF plane (1...4). Identical to the CP signal but only the paddles corresponding to the Tracker acceptance are normally used;
- BZ-TOF(1...4)-p/n: Big Z signal from p/n-side of TOF plane (1...4). As the CP but with the digital signals produced using the SHT;

The p and n signals are combined in OR to generate a CP, a CT and a BZ-TOF for each plane.

The ECAL, instead, produces two signals:

- ECAL-F-x: ECAL Fast signal from x superlayers: a given number (typically 3) of near cells in the x view of the ECAL have a signal over threshold;
- ECAL-F-y: ECAL Fast signal from y superlayers: as above.

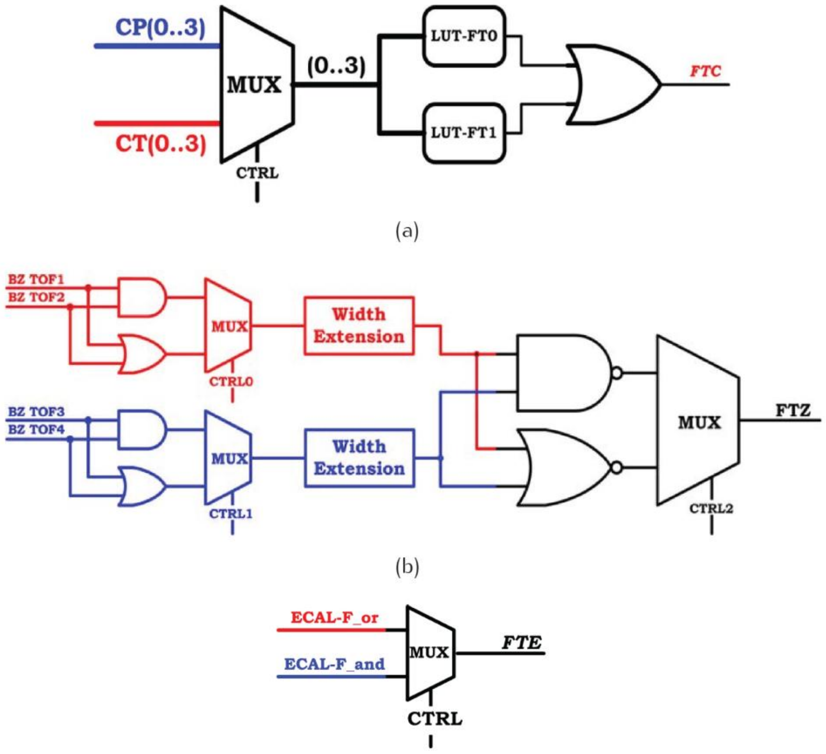

(a)

(b)

(c)

Figure 23 - Schematic to generate the three FTs. (a) FTC from charged particle signals from TOF, (b) FTZ from big Z particle signals from TOF, (c) FTE from ECAL-F signals from ECAL.

The signals from the two views are ORed and ANDed giving ECAL-F_or and ECAL-F_and signals. The signals described above are used to produce three different Fast Triggers:

- **FTC**: fast trigger for charged particle. CP and CT signals from the 4 planes are multiplexed and fed into two look-up tables (LUT-FT0 and LUT-FT1). If one of the 4 conditions is satisfied a Fast Trigger Charged (FTC) is generated (see Fig. 23(a));
- **FTZ**: this fast trigger is meant to alert the system to trigger strangelets. The BZ-TOF signals from the 2 top (bottom) planes are multiplexed. The two resulting signals, BZ-TOP and BZ-BOTTOM are extended up to 640 ns (slow particles) and multiplexed again. If the condition is satisfied a “strangelet” Fast Trigger (FTZ) signal is generated (see Fig. 23(b));
- **FTE**: ECAL-F_and and ECAL-F_or are multiplexed to generate a Fast Trigger ECAL (FTE) signal (see Fig. 23(c)).

The three FTs are ORed to produce a general Fast Trigger signal. Up to the generation of the FT signal all the multiplexing, ORing and ANDing are done continuously and no dead time is introduced. Every time a Fast Trigger is produced, it is delivered to all the interested sub detectors to allow the computation of specific quantities.

Level 1 Trigger

After the generation of FT the JLV1 starts the LVL1 evaluation. This will take exactly 1 μs, independently from the result of the LVL1 evaluation and during this time the system will be busy. The signals produced after a FT, used in the Level1 logic, are the following [404, 409]:

- **Charged particle signals**: these signals are used to build the charged particle trigger. After the FT a 240 ns gate is opened to latch charged particles signals, CP and CT. The latched signals are fed into look-up tables, LUT-FT0 and LUT-FT1, to produce signals, FTCP0, FTCP1, FTCT0 and FTCT1. The logic is similar to the one shown in Fig. 23(a). The same CP and CT signals used above are latched till the end of the gate. The coincidence for FTCP0, FTCP1, FTCT0 and FTCT1 is evaluated independently within the opened gate. For the flight the LUT-FT0 is set to accept events with 3 out of 4 TOF planes (meant for unbiased triggers) and LUT-FT1 to 4/4;
- **Big Z signals**: these signals are used to build the trigger for ions, allowing in the LVL1 logic to loose conditions on ACC with respect to the “standard” charged particle trigger. A 240 ns gate is opened to latch BZ-TOF signals. The latched signals are fed into a LUT, LUT-BZ, to produce a signal, BZ. For the flight the LUT-BZ is set to accept 4/4 events;
- **ACC signals**: these signals are used to veto triggers produced by particles passing out of the detector acceptance but inducing a trigger due to secondaries produced in the interactions with the materials. A 240 ns gate is opened to latch ACC signals. The latched signals are used to count number of ACC signals. This number is compared to two adjustable thresholds to produce signals, ACC0 and ACC1. For the flight the thresholds are set to 1 and 5. This gives a ACC0 signal when the number of ACC fired is 0, and ACC1 when is, at maximum, 4;
- **ECAL-F signals**: these signals are used to build the unbiased electromagnetic trigger. A 240 ns gate is opened to latch ECAL-F signals. The latched signals, ECAL-F_or and ECAL- F_and, are used in LV1 logic;
- **ECAL-A signals**: these are used to build ECAL standalone triggers dedicated to non converting photons. A 640 ns gate is opened to latch ECAL-A signals. The latched signals, ECAL-A_or and ECAL-A_and, are used in LV1 logic;
- **EXT-GATE signals**: A 240 ns gate is opened to latch external gate signals. The latched signals, EXT-GATE0 and EXT-GATE1, are used in LV1 logic. They are not used during flight.

The produced signals (plus FTE and FTZ), for a total of 15 signals, are multiplexed to evaluate 8 LVL1 sub-triggers under different conditions (see Fig. 24). Each sub-trigger can be pre-scaled (from 1:1 to 1:1024). The 8 sub-triggers are ORed to give the LVL1 trigger to the experiment.

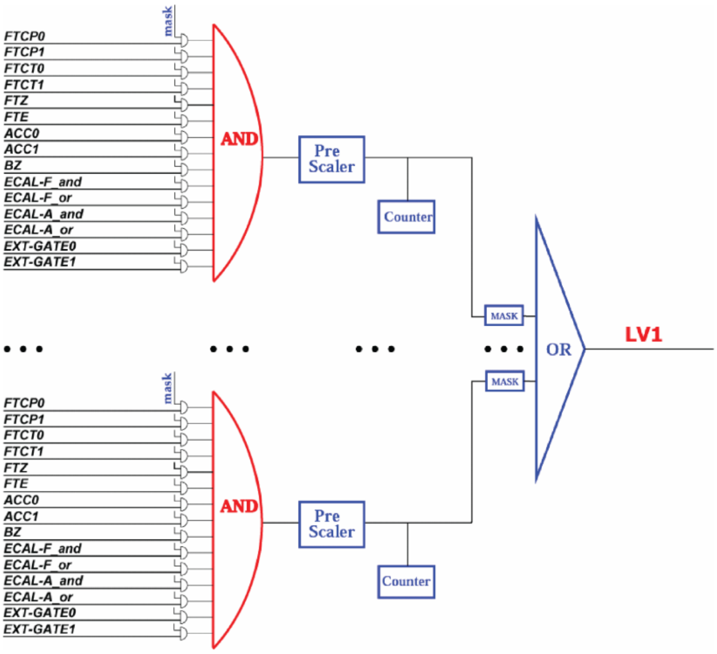

Figure 24 - Schematic of the LVL1 logic. 15 signals are multiplexed to evaluate 8 different LVL1 sub-triggers that are ORed to give the LVL1 to the experiment.

Flight trigger

For the flight, i. e. cosmic rays detection, 7 sub-triggers were designed and implemented [404]:

0) **Unbiased charged (protons)**: TOF 3/4 (HT), pre-scaling factor 128. Is produced by the FTCP0;
1) **Single charged (protons and helium)**: TOF 4/4 (HT), $N_{ACC}=0$. Is produced by the coincidence of FTCT1 and ACC0;
2) **Normal ions (above helium)**: TOF 4/4 (SHT), $N_{ACC}<5$. Is produced by the coincidence of BZ and ACC1;
3) **Slow ions (exotic matter like strangelets)**: TOF 4/4 (SHT), gate extended to 640 ns. Is produced by the FTZ;
4) **Electrons**: TOF 4/4 (HT), ECAL signal over threshold on both views. Is produced by the coincidence of FTCT1 and ECAL-F_and;
5) **Photons**: ECAL shower. Is produced by the ECAL-A_and;
6) **Unbiased EM**: ECAL signal over threshold, pre-scaling factor 1024. Is produced by the ECAL-F_or;

The Live-Time scaler

For an absolute flux measurement is necessary to know the exact time the detector is ready to accept events. This time, called exposure time, is the fraction of the nominal data taking time to be evaluated taking into account the dead time of the system [76].

Possible dead time sources in AMS-02 are the following:

- Every time a FT is produced the system is busy for 1 µs till the end of the LVL1 decision. This is a fixed amount of time.
- Every time a LVL1 is produced and delivered to the subdetectors a finite amount of time will be needed by the front-end electronics for the signal digitization. This operation is carried in parallel for all sub-systems and introduces 200µs of dead time, which includes the 90µs needed for the digitization of the tracker signals and an additional delay introduced to optimize the noise performances in the detector.

- The compression of the events by the DSP, in xDRs, takes a variable amount of time (~ 300 µs). To reduce the corresponding dead time, up to four "raw" events can be buffered in the xDRs: compression of a given event can be then carried in parallel to the digitization of the following event. Dead time will be introduced only when the xDRs buffer is full: this is a source of variable dead time, usually depending on the DAQ rate.

A 20 ns fine scaler continuously samples the status of the DAQ within a time window of 2 seconds and counts the number of times the system was found ready to accept new events. The system Live-Time is defined as the ratio between the accumulated number of counts and the maximal number (108) in the sampling window. The exposure time is then evaluated by multiplying the raw acquisition time by the corresponding Live-Time.

4.6 The Time of Flight in details

The TOF system provides:

- the fast trigger to the whole AMS;
- the measurement of the time of flight (Δt – better than 180 ps), for the determination of the particle velocity (β), with a resolution of few %;
- the distinction from upward and downward going particles at a level of 10^{-9} necessary to distinguish between matter and antimatter;
- the measurement of the absolute particle charge up to Z = 15.

The TOF consists of 4 plastic scintillator layers, in x and y direction, 2 above (Upper TOF) and 2 below (Lower TOF) the magnet¸ with an acceptance of 0.4 m^2 sr [385, 386]. The counters of adjacent planes are orthogonal (see Fig. 26); the upper TOF is situated at the entrance of the magnetic volume, the lower at the exit, at a distance of ±626 mm in the z direction, as defined in the reference frame of the experiment. Each layer contains 8 (10 for the third layer) scintillator paddles of different length, called counters, staggered and overlapped by 0.5 cm to avoid geometrical inefficiencies (34 scintillators).

Each counter of the TOF detector is made of a 1 cm thick and around 120 cm long scintillator paddle (Eljen-Technology type: Ej-200), optically coupled at both ends with two or three PhotoMultiplier Tubes (PMTs), 76 in total, connected with transparent light guides, in order to have a time resolution nearly independent from the position of the impact point of the measured particle (see Fig. 25).

The PMTs are R5946 Hamamatsu fine mesh, that provide a gain of about 10^6 when powered at 2000 V.

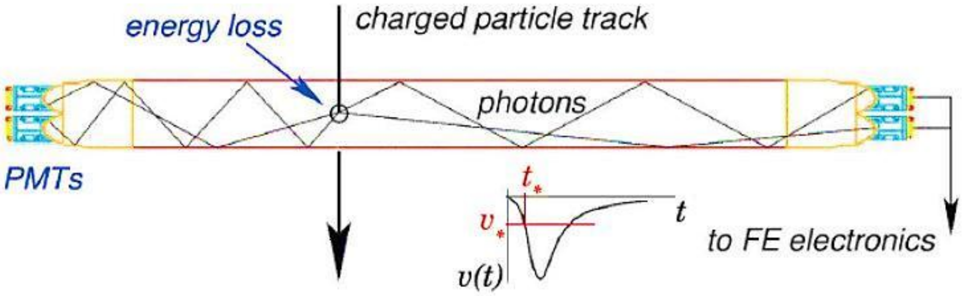

Figure 25 - Principle design of one TOF counter.

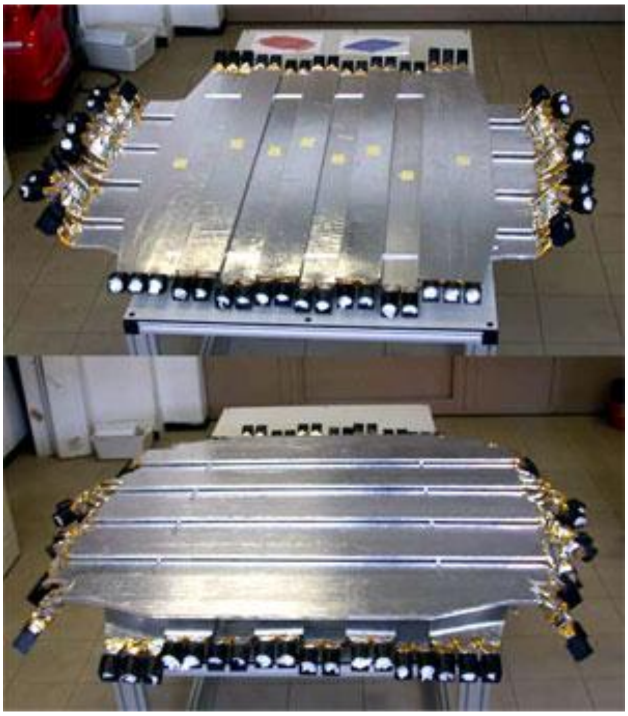

Figure 26 - The upper (a) and the lower (b) part of the TOF system. The PMT inclinations and directions are designed to minimize the effect of the magnetic field. The external detectors of each of the 4 floors of the TOF have trapezoidal shape, while the remaining 26 detectors have a rectangular shape. The two opposite ends of a counter are called *p* (positive with respect the TOF-AMS coordinate system) and *n* (negative) sides [388, 410].

The Fig. 27 below shows the voltage divider scheme of each PMT. Two signals are produced, the anode signal and the 3rd last dynode one [381].

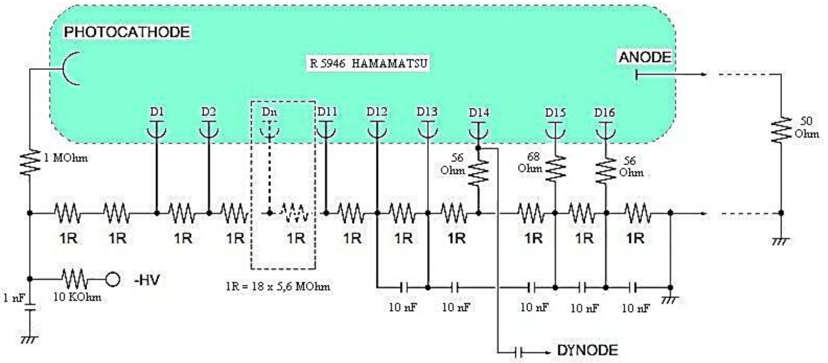

Figure 27 – PMT Voltage Divider.

The anode signals from the PMTs of the same side of each counter are passively summed together, by soldering 5 cm cables to the 50 Ω coaxial anode cable, that is connected to the front end board called SFET2. This signal sum does not degrade the nominal rise time of the signal (1.9 ns). The 3rd last dynode signal is picked up through a capacitor, and connected to a 50 Ω coaxial cable to the front-end board called SFEC. The SFEC and SFET2 boards will be described in the following. The anode sum signal from each side of a counter are used to measure the total light released in the counter by the traversing particle, and to produce a logical signal (low-threshold) for time measurement and two logical signals (high-threshold and super-high-threshold) for trigger purposes.

As said before, the TOF main tasks are three: fast trigger for charged particles, time measurements and charge measurements.

It has been stressed that when a particle cross the AMS-02 detector, the fast trigger and veto signals generated by the TOF and the ACC system, and the fast trigger generated by the ECAL, are processed inside the trigger board to generate the level 1 trigger. The level 1 trigger signal is used to start the AMS-02 data acquisition. The first task of the TOF scintillator system is to select charged particles crossing in the spectrometer. When a charged particle crosses at least 3 out of 4 TOF layers, a **fast trigger** is generated. Low charge and high charge particles generate two different kinds of fast trigger. Depending on the number of ACC scintillators fired by a particle, a veto signal can be also generated and used in the level 1 trigger generation.

When a particle crosses the TOF system, the crossing time in each plane is measured. The time difference between the upper and lower TOF planes define the **time of flight** of the particle and is used for particle identification. The time measurement is performed using a low-power, radiation-tolerant, multi-hit TDC chip, with a 25 ps time resolution, developed at CERN for the LHC experiments.

The AMS-02 spectrometer detects cosmic particles from minimum ionizing electrons and protons to highly ionizing nuclei with large nuclear charge Z. The **charge** measure (proportional to Z^2) is performed using a custom sample and hold chip (AICPPP chip), specially developed by the AMS-02 collaboration [387]. Both anode and dynode signals are used in the measurement of the charge, so different AICPPP chips have been produced for negative (anode) and positive (dynode) signals.

The anode signal is used to measure absolute charge at low Z, while the dynode signal is used to extend the dynamic range when the anode signal saturates. The charge measured by the anode ranges from a few photoelectrons to around 2000 photoelectrons. The dynode signal ranges from about 100 photoelectrons to above 5.000 photoelectrons.

4.6.1 TOF electronics

As you can see in Fig. 28, the TOF (-ACC) is composed by [383, 387]:

1. the SHV (Scintillator High Voltage) brick to supply the high voltage to the TOF PMTs;
2. the SFEC (Scintillator Front End Charge) board located inside the cover of the TOF detector to measure the charge from the dynode signals (Fig. 29);
3. the SFET (Scintillator Front End Time) boards to process the TOF anode signals;
4. the SFEA (Scintillator Front End Anticounter) board to process the ACC anode signals;
5. the SPT board to produce a local fast trigger;
6. the SDR board for the data acquisition;
7. the TSPD board to supply the low voltage to all the modules.

All SFETs, SFEAs, SPTs and SDRs are placed in 4 electronics *Scintillators crates* (S-crates). Each crate serves two TOF layer sides and one fourth of the ACC.

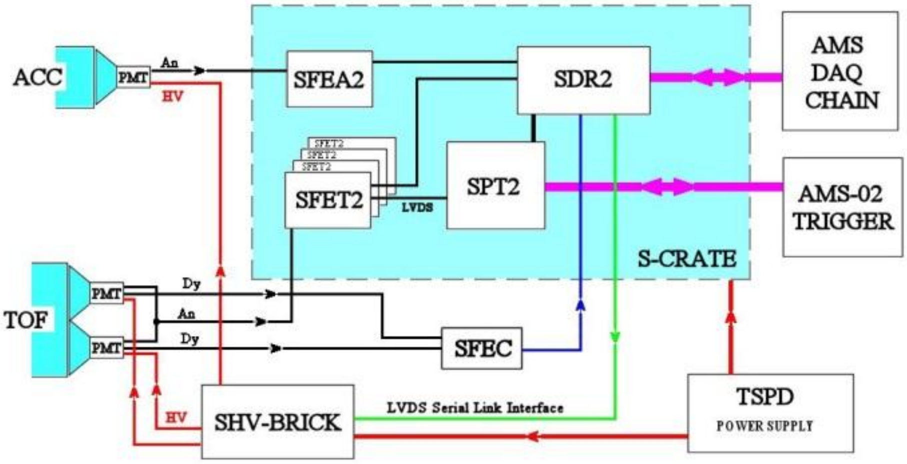

Figure 28 - Block diagram of the TOF-ACC electronics.

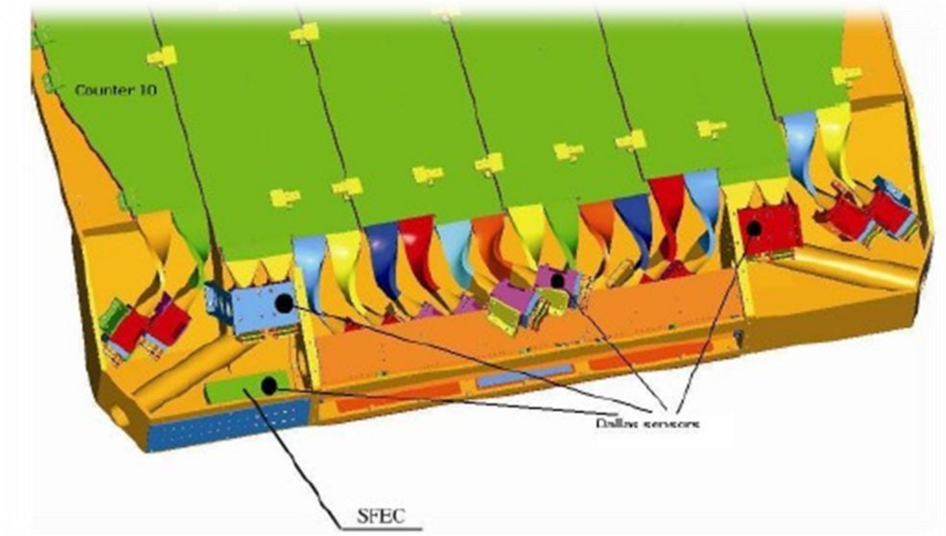

Figure 29 - The SFEC board located inside the cover of the TOF detector.

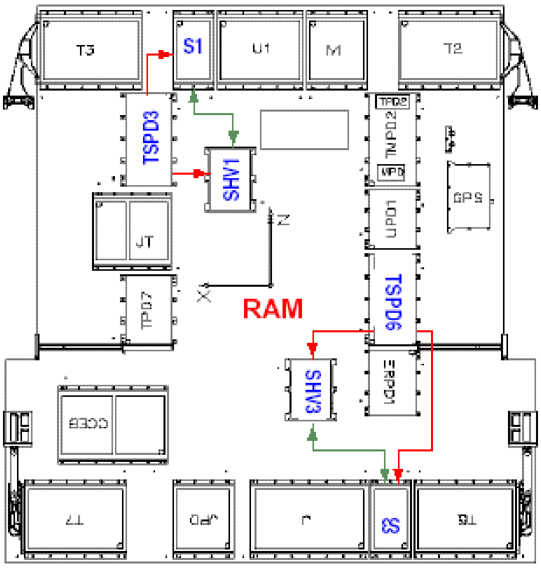

Figure 30 - The RAM radiator. The two S-Crates (S1, S3) and the two SHV-Bricks (SHV1, SHV3) are highlighted together with the two TSPDs (TSPD3, TSPD6) for low voltage power distribution.

The 4 TSPDs, 4 S-Crates and 4 SHV-Bricks modules, are located on the AMS-02 radiator panels (RAM and WAKE) as illustrated in the Figs 30 and 31 [381].
The electronics has been designed and built taking into account the following constraints:

- radiation tolerance;
- vacuum and thermal environment in space;
- redundancy;
- power and weight limitation.

Special radiation-tolerant chips and components developed for high-energy physics have been chosen. Space qualification tests on the custom devices have been performed.

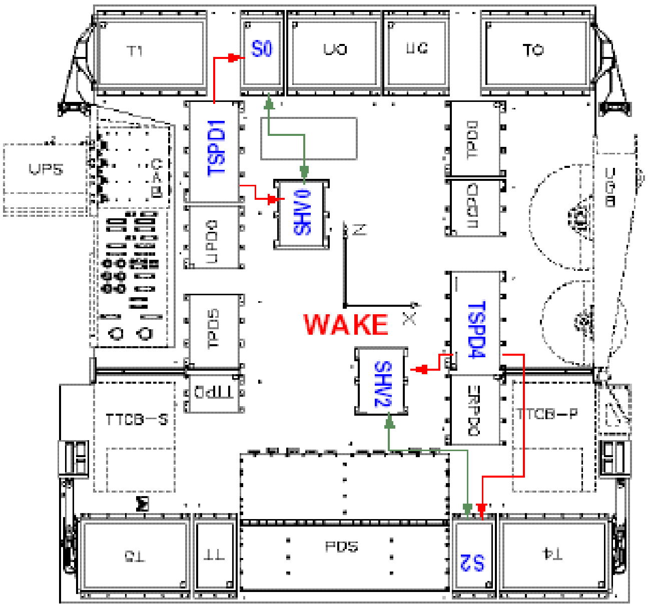

Figure 31 - The WAKE radiator. The two S-Crates (S0, S2) and the two SHV-Bricks (SH0, SH2) are highlighted together with the two TSPDs (TSPD1, TSPD4) for low voltage power distribution.

Operation in vacuum required the use of two special thermal radiator panels (Figs. 30 and 31) in order to dissipate the heat load generated from the electronics and to maintain the temperature of the electronics within the operating limits specified in Table 1.
Since no human intervention is foreseen in space in case of failure, all electronic boards (except for SFEC) and SHV-Bricks are built on double-face printed circuit boards, with exactly the same electronics mounted on both sides, called A and B. In case of failure of the electronics on one side, it is possible to switch to the redundant one (see Fig. 32). Together with the redundant PMTs on each side of a scintillator paddle, this system increase the overall fault tolerance of the experiment.
Because of power (150 Watts were allocated for TOF) and weight limitations, the number of SHV-bricks have been limited. Therefore, most of the channels supply the high voltage to two PMTs. To increase the fault tolerance of the system, the two PMTs powered by the same HV channel are located in two different TOF counters. Moreover, the SFEC boards have been installed close to the TOF detector to reduce the weight of the front- end cables.

Temp. in °C	Min Non op.	Min Oper.	Max Oper.	Max Non op.
SHV-Brick	-35	-20	+50	+65
S-Crate	-40	-20	+50	+80
SFEC	-55	-40	+80	+80
PMTs	-35	-30	+35	+42

Table 1 - Non operative and operative temperatures limits for the TOF electronics. Outside the operative range the electronics must be powered off, outside the non operative range the electronics could be damaged.

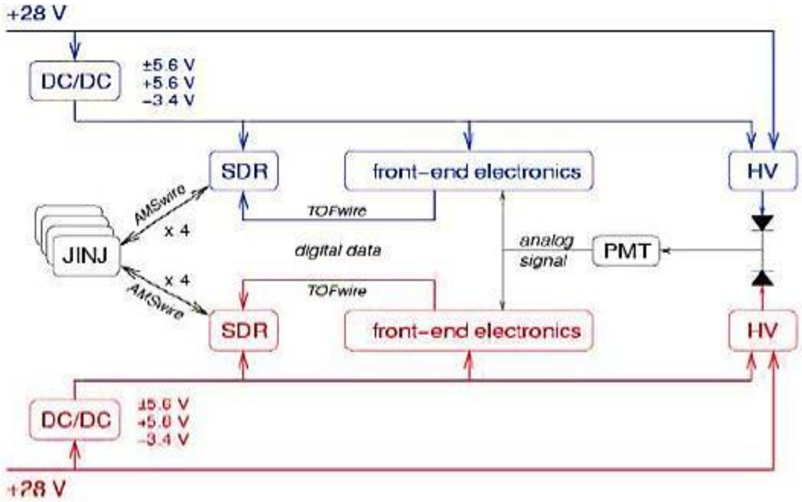

Figure 32 - Principle design of the built-in redundancy in AMS-02 electronics. The electronics normally used is shown in black and blue. The red part is the back-up which can be activate by software [381].

The SHV-Brick

The SHV Brick was designed and assembled by CAEN, Viareggio, Italy.

The SHV-Brick power supply is double redundant, and it consists of 1+1 DC/DC converters feeding 24+24 independent linear regulators. The DC/DC converters can be independently programmed to provide a maximum voltage from 0 to 2500 V, with 10 bit resolution. Each linear regulator can supply either one or two PMTs. The output voltage range depends on the load: for one PMT the range is between 1176 V and 2366 V, for two PMTs the range is between 952 V and 2310 V.

The linear regulator output voltage is controlled by a DAC and the overall system control takes place via a LVDS Serial Link.

The SFEC board

The SFEC board [387] provides the measurement of the charge from the dynode signals of the TOF PMTs. Each SFEC is made by two AICPPP chips, two analog to digital converter (ADC) and a FPGA (field programmable gate array) Actel A08.

The AICPPP chip consists of a preamplifier, an integrator and a sample-and-hold circuit which provides the maximum, proportional to the pulse charge, after roughly 1.7 µs from the pulse start. Each AICPPP chip collects the signals from 10 dynodes in parallel and serially sends the resulting sample and hold signals to the ADC. The Actel A08 acquires the digitized signals and transmits the

data to the master node (SDR). The SFEC receives the low voltage power and the clock through twisted pair cables and it transmits the data through a differential LVDS digital link.
The AICPPP chip provides a linear response up to 36 pC (corresponding to 3500 ADC channels).

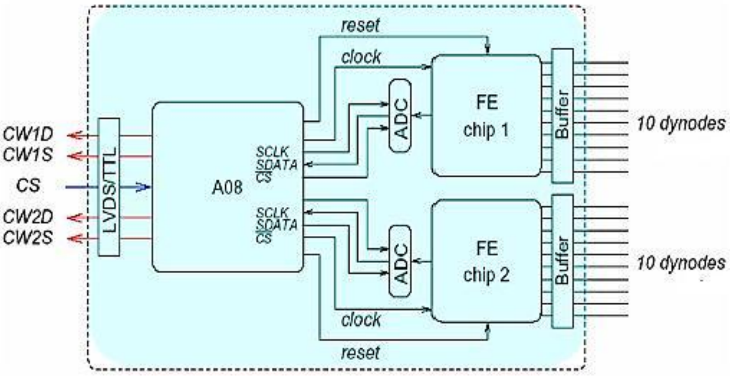

Figure 33 - Block diagram of the SFEC board (FE= AICPPP chips, A08=FPGA chips).

The S-Crate electronics
Each S-Crate (see Fig. 34) serves two TOF half-planes and four ACC sectors with:

- 4 SFET boards that process the TOF anode signals;
- 1 SFEA board that processes the ACC anode signals;
- 1 SPT board that processes the TOF signals for local trigger;
- 1 SDR board that acquires the data from the front- end boards, processes the physics event and performs the communication with the upper nodes in the AMS-02 DAQ chain.

The back plane of the S-Crate allows the communication among the boards and the SDR, and provides the lower voltages to the boards.

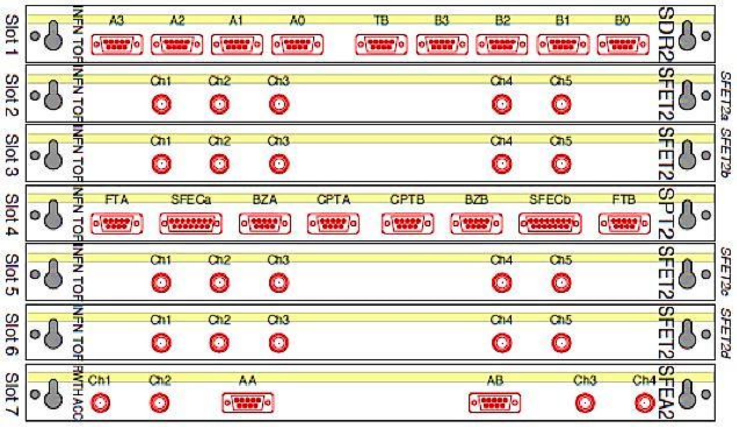

Figure 34 - Front view of an S-Crate.

The so-called S0 crate serves the layer 1 side n and the layer 2 side p; the S1 crate the layer 1 side p and the layer 2 side n; the S2 crate serves the layer 3 side p and the layer 4 side p; the S3 crate serves the layer 3 side n and the layer 3 side n.

The SFET board
The SFET and SFEA boards [387, 409]:

- provide the logical signals for event trigger/veto;

- measure with high resolution the arrival time of the hits in a window from -8.5 µs to +7.5 µs with respect to the fast trigger time;
- measure the analog pulse charge;

Each SFET module has 5 analog input lines. Each input line is split with a passive divider into two paths: the bigger fraction (95%) goes to the time measurement unit, whereas the smaller fraction (5%) goes to the charge measurement unit.

In each SFET 161 parameters are defined. Their nominal values were chosen during ground tests.

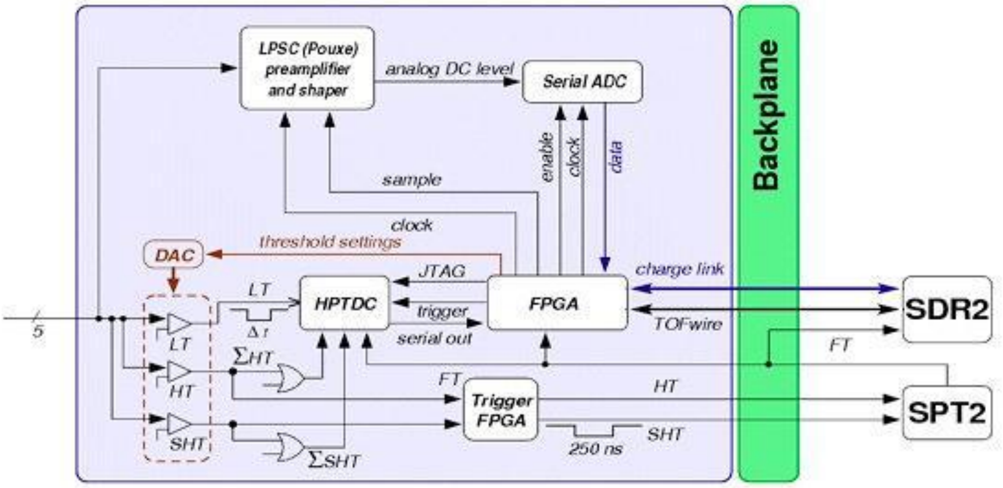

Figure 35 - Block diagram of the SFET (SFEA) boards.

The *charge measurement* unit consists of:

- one AICPPP chip for negative signals that processes the analog channels and produces a sample-and-hold signal proportional to the integrated charge;
- an ADC that serially digitize the signals from the AICPPP;
- a FPGA that provides the clock and sample signals to the AICPPP, acquires the data from the ADC and transmits the data to the SDR board.

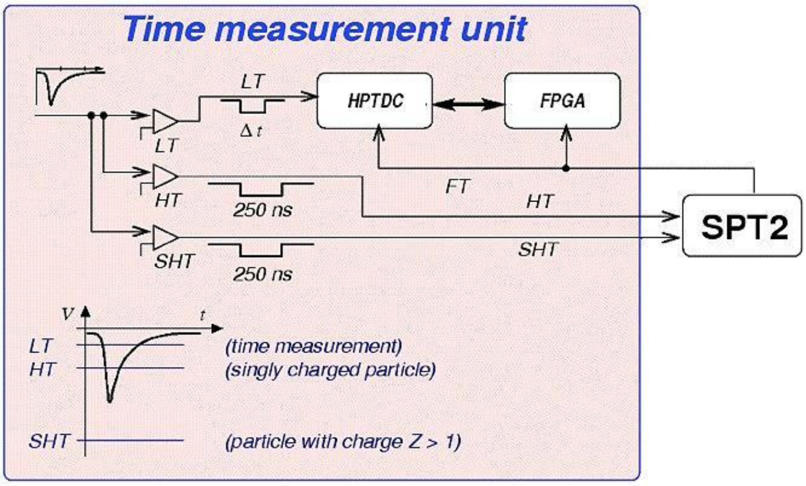

Figure 36 - The SFET time measurement unit.

In the *time measurement* unit of the SFET the signal from the anode is compared to three thresholds:

- the *Low Threshold* (LT), set at about 20% of a minimum ionizing particle (MIP) signal for ground-measured muons – typically 15 mV or a few photoelectrons) – to measure the time of the particle hitting the counter;
- the *High Threshold* (HT), set at 50% of the MIP peak (about 60 mV), used in the Z = 1 Fast Trigger;
- the *Super High Threshold* (SHT), set at about four times the MIP peak (about 350 mV), used in the high Z Fast Trigger.

The outputs of the discriminators are sent to the HPTDC for time measurement. The signals from the HT and SHT discriminators are ORed with the signals from the other input channels of the same SFET and sent to the HPTDC also for time measurement. The HPTDC has an external clock a 40 MHz clock which is used in a three-stage multiplication, finally providing 24.2 ps resolution for the time measurement. The HPTDC also registers the time of the Fast Trigger which is broadcasted to all SFET cards by the trigger board and serves as the reference for all the time measurements. Finally, an FPGA acquires the data from the HPTDC and transmits the data to the SDR board.

The SPT board and the TOF Fast Trigger

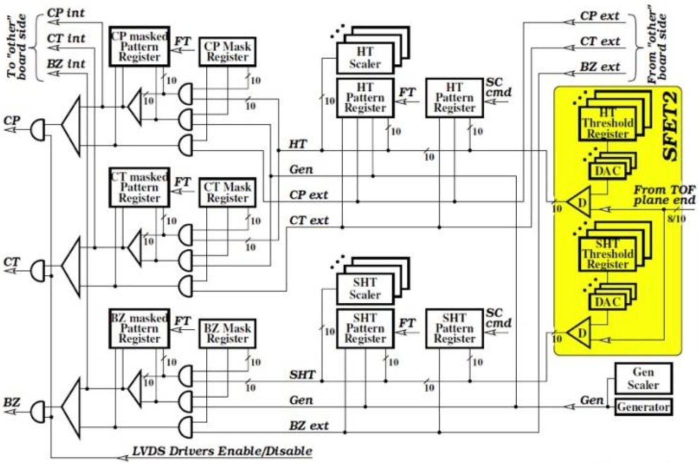

Figure 37 - The SPT2 pre trigger logic. It has 10 independent parameters, fixed during the first data taking week in space [381].

The SPT board implements a local trigger using all signals coming from the SFET boards of the same S-crate. It combines the digital HT and SHT signals to produce three independent trigger signals, as previously mentioned – CP, CT and BZ which are sent, using an LVDS connections, to the trigger board for the fast trigger (FT) and level 1 trigger (LV1) trigger generation.

The HT signals from one side of all the counters of one TOF layer are compared to two different *trigger masks*: CP and CT. Each bit of the masks represents one counter side in the layer, that can be included or masked in the pre-trigger combination. In normal data taking, the CP masks contain all TOF counters while the CT masks exclude the external counters of TOF layer 3 to decrease the data acquisition rate [381].

The masked outputs are ORed, generating signals that represent the logic OR of the HT signals from each TOF layer side. The SHT signals are compared to another trigger mask (BZ mask), and generate a BZ signal from each TOF layer side. The HT and SHT signals are also stored in a pattern register, and two scalers count how many HT and SHT signals are present in a time interval of up to 2 s.

The SPT can also generate an internal random trigger, used for specific calibration runs (e.g., pedestal measurement).

There are two types of TOF fast triggers: **FTC**s, generated from CP and CT signals (at least 3 out of 4 TOF layers with at least one anode signal above the HT), for Z = 1 particle trigger, and **FTZ**, generated from BZ signals (at least 3 out of 4 layers with at least one anode signal above the SHT), for ions.

The CP and CT signals coming from all SPTs are sampled by a 40 ns clock in the trigger board and then combined: the CP (or CT) signal from each TOF layer side is combined in a logic OR with the CP (CT) signal coming from the opposite side. The coincidence maximum time is 340 ns. The four signals that represent the four TOF layers, are combined in a logical AND with a trigger mask, to provide the FTC signals. There are up to two possible FTCs (FTCP0, FTCP1) generated from the combination of the CP signals and two FTs (FTCT0 and FTCT1) from the combinations of the CT.

The BZ signals, latched with a *trigger gate* of 340 ns, are used to generate FTZ for high Z. Signals from the two top TOF layers are combined in AND or in OR, depending on a programmable setting, and the same is done for the signals from two bottom TOF layers. The width of the combined signals, BZ top and BZ bottom, can be extended up to 640 ns. The BZ top signal and the BZ bottom signal are combined together by an AND or OR gate to generate the FTZ trigger signal. In normal running conditions, all signals are combined in AND (see Fig. 23).

The SDR board

As anticipated in the DAQ acquisition explanation, the AMS-02 Data Acquisition System collects data from over 200K analog channels of the different AMS-02 sub-detectors: TRD, TOF and Anti-Coincidence Counters, Tracker, RICH, Electromagnetic Calorimeter and Level-1 Trigger module. It consists of nearly 300 computational nodes based on ADSP2187L Digital Signal Processors (DSP) and four main DAQ Computers (for redundancy), with a tree-like structure. The nodes are interconnected with point-to-point LVDS serial links. The data throughput per link is 100 Mbits/s. Hierarchy in the system is defined by a master/slave communication protocol. The nodes linking the TOF-ACC electronics to the AMS-02 data acquisition system are the SDR boards. The main constituents of the framework software are the following [381]:

- ROM monitor program which allow for several boot options;
- FLASH update utility to store and retrieve information between power cycles;
- AMSWire protocol for communication between nodes;
- data protection based on CRC algorithm;
- slow control procedure to gather and keep up-to-date information on the node state;
- a set of test routines for node functional testing;
- framework routines for hardware initialization and configuration;
- a set of routines to perform calibration;
- event building routines for physics event assembly.

The typical sequence for an event processing by the SDR is:

1. During the level-1 trigger a sequencer is activated; it moves the digitalized data into a memory. The SDR data length is not fixed and its maxim acceptable value is 1024 16-bit words. The data processing can occurs in normal or compressed format,
2. The DSP reads and processes the data; the result, the event fragment, is stored in the output event buffer. In the normal event fragment format, the words are organized in this way: 1 word dedicated to the event length; 1 word for the event number; 90 words for

charge data from SFET, SFEC and SFEA; 4 words for trigger information about high and superhigh thresholds; a variable number of words for temperatures, times and errors of SFET, SFEA and TDC; 10 words for the validation of the data type.

3. The event fragment is transferred using the AMSWIRE protocol.

The SDR2 has 21 independent parameters whose reference values were chosen during ground tests and in the first week of data taking in space.

Radiation damage tests of the electronic components
Space radiation produces two classes of effects on microelectronic devices:

- long-term effects, due to the prolonged exposure to radiation, as measured by the Total Ionizing Dose (TID): caused by trapped protons and electrons (0.1−102 MeV) and by Solar protons (10 −102 MeV);
- events caused by the passage of a single, highly ionizing particle as Single Event Effects (SEE), Single Event Upsets (SEU) and Single Event Latch-ups (SEL): caused by trapped protons (100 eV − 10 keV), solar heavier ions, galactic cosmic rays (from 100 MeV up to ∼ 1021 eV), neutrons.

The AMS electronics components have been chosen among those typically used for space and military applications. In addition, extensive radiation tests were performed on critical components in the GSI (Germany) beam test facilities in 2001 and 2002.

The vibration tests for the SHV-Brick has been performed at Galileo Avionica (Firenze, Italy) in 2008. The random vibration was along the 3 axes for 2 minutes. The accelerometers, placed on the external SVH-Brick walls, did not detect any eigenfrequency below 50 Hz, as required by space qualification. The vibration test of the rest of the TOF-ACC electronics was performed in Taiwan.

The Thermal Vacuum Test (TVT) of the flight modules of the TOF electronics has been performed in the SERMS facilities in Terni (Italy) at a pressure below 10^{-5} mbar and following the temperature cycle shown in Fig. 39. The setup, was a subset of the DAQ chain of the AMS-02 system: three S-Crates and three SHV-Bricks, with loads to simulate the PMTs, were located inside the vacuum chamber together with the higher level AMS DAQ chain (JT-Crate).

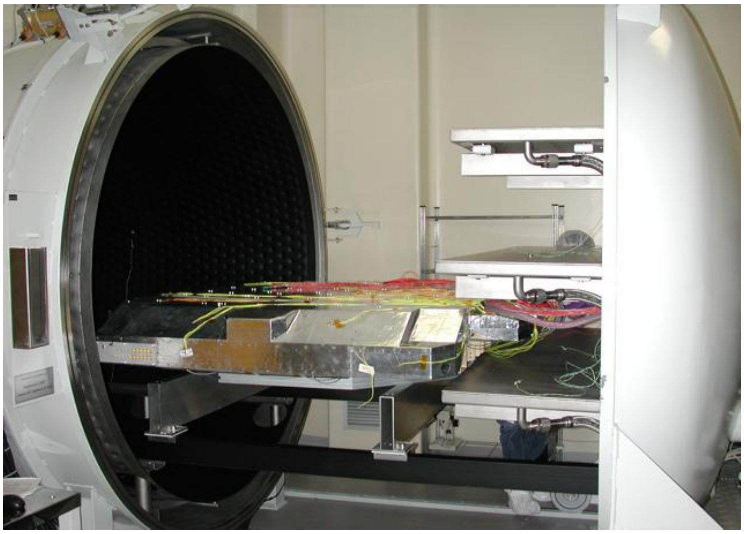

Figure 38 – The upper and lower TOF were located inside the vacuum chamber for the test.

The power supplies for the S-Crate and the SHV-Bricks, and two PCs to run the data monitor programs and the command interfaces were placed outside the vacuum chamber. Data was constantly monitored and commands were sent during the functional tests.

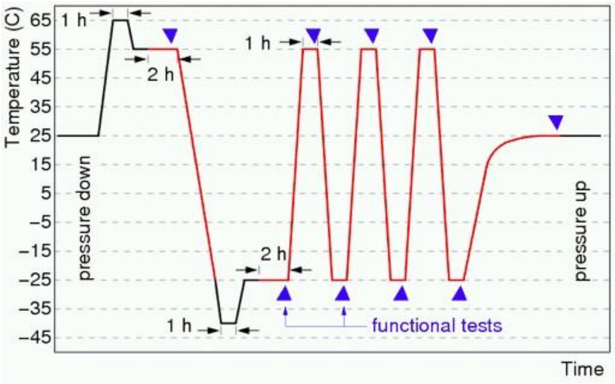

Figure 39 - The temperature cycle for the thermal vacuum test of the TOF-ACC electronics.

The performance of the S-Crate boards has been studied using calibrated signals from pulse generators. Particular emphasis in these studies was on the trigger rate and the temperature dependence of the charge and time measurements as well as on the amplitude and threshold linearity.

Figure 40 shows the temperature dependence of the pedestals of three SFEC channels over a wide temperature range [381]. Similar dependences are observed for charge measurements on SFET. Individual channels exhibit very different temperature behaviors, therefore an average correction (red dots in Fig.) is not applicable.

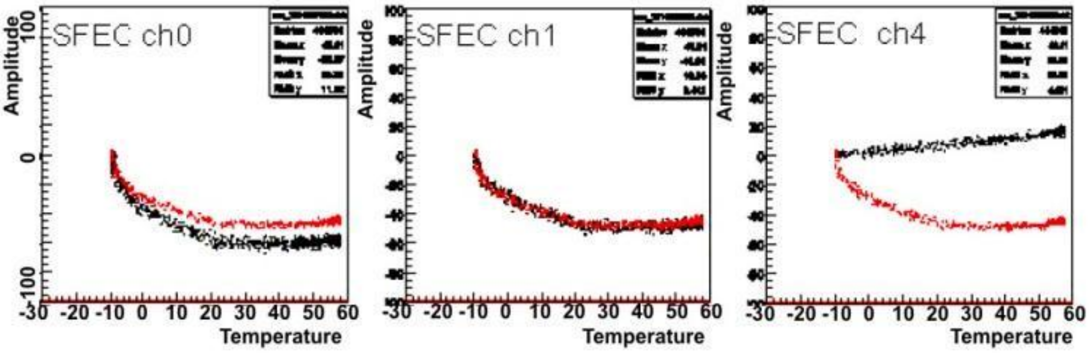

Figure 40 - Temperature dependence of pedestal amplitudes in three channels of the SFEC board. Red dots correspond to the average pedestal computed averaging 10 channels of the same board.

A dynamic pedestal correction procedure has been implemented in the DAQ program. It accounts for the temperature dependence and has negligible contribution to the pedestal width. Fig. 41 shows the temperature behavior of one SFEC channel when dynamic correction to the pedestal is applied.

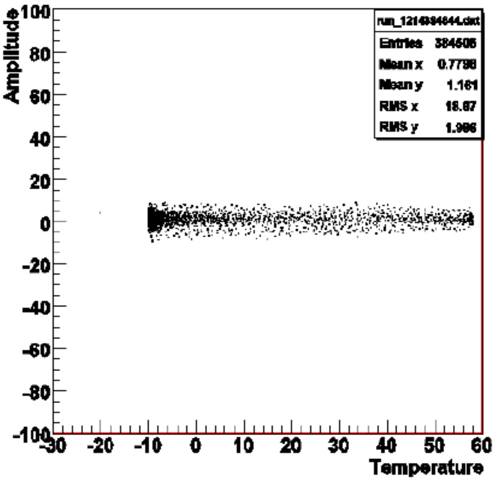

Figure 41 - Temperature dependence of the amplitudes from SFEC ch0 when dynamic pedestal correction is used.

A significant dependence of pedestal average value and dispersion at low trigger rates is present (see Fig. 42) for individual SFET channels. At very low rates the magnitude of the pedestal drift is comparable to the MIP value. In addition correlation between individual channels reaches 90% at rates around 1-2 Hz.

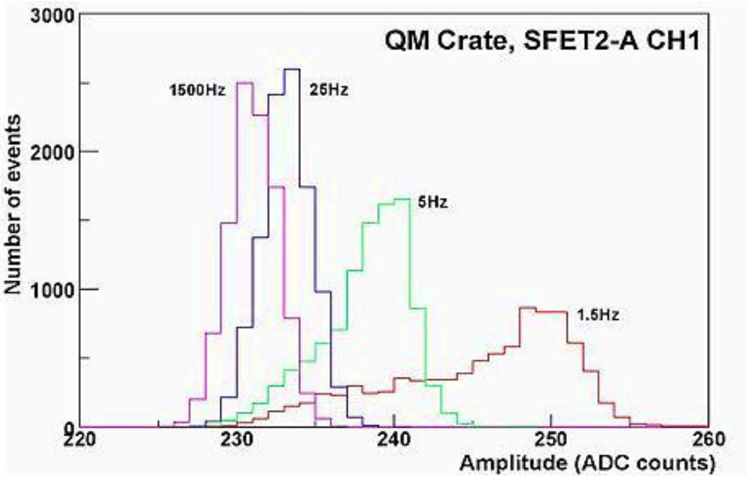

Figure 42 - Pedestal shapes of one SFET channel measured at different trigger rates.

Most of the deviation from the average value occurs at rates below 30Hz, as shown in Fig. 43. The variation of the average pedestal value can also be corrected for by the dynamic pedestal procedure. The pedestal initial value is calculated from a calibration usually performed at 400-500 Hz rate. The Fig. 44 shows the dynamic pedestal drift from the initial value (left plot). The spread of dynamic pedestal is negligible compared to the pedestal event-by-event variations (Fig. 44, right plot), therefore there are no significant effects on the measured charge amplitudes [381].

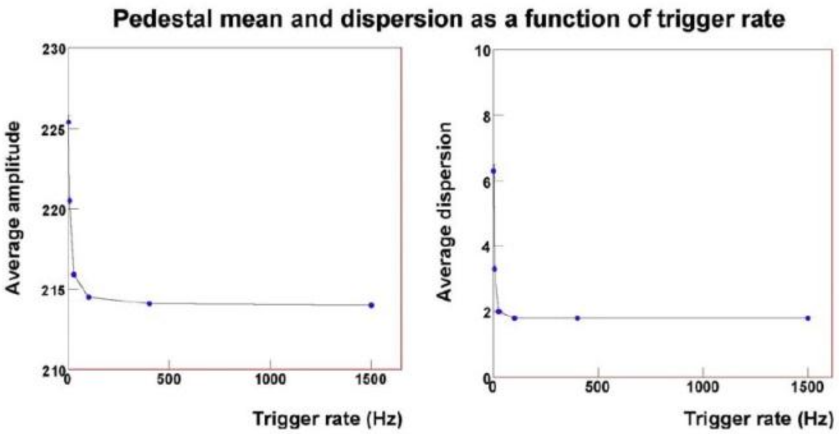

Figure 43 - Dependence of the average pedestal (left plot) and pedestal dispersion (right plot) on trigger rates.

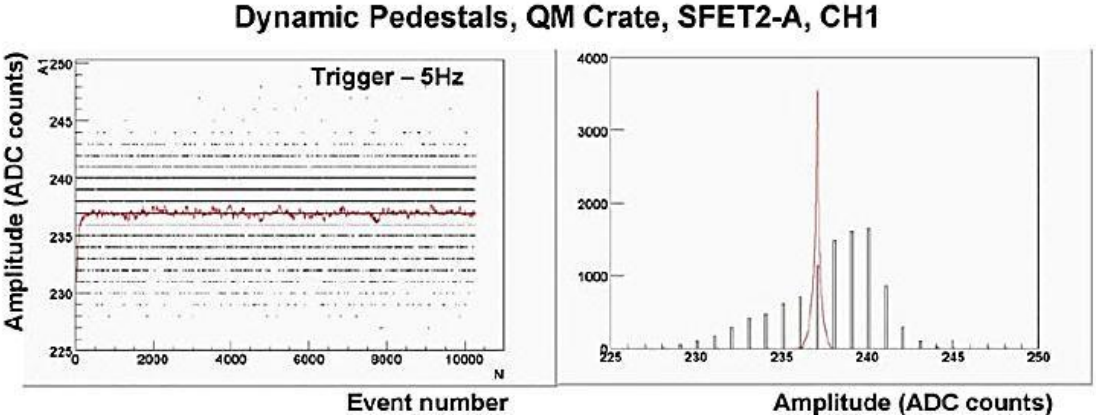

Figure 44 - Dynamic pedestal drift (red points, left plot) and shape (red line, right plot) compared to the distribution of the pedestal for the same channel (black points and line). Initial dynamic pedestal value is 231.

Once the temperature dependence of the pedestals is corrected for by using the dynamic pedestal procedure, the charge measurement in TOF electronics does not exhibit temperature dependence [381]. In Fig. 45, the measured charge amplitude in a SFET channel is shown as a function of the input signal. The measurements do not show a dependence on the temperature.

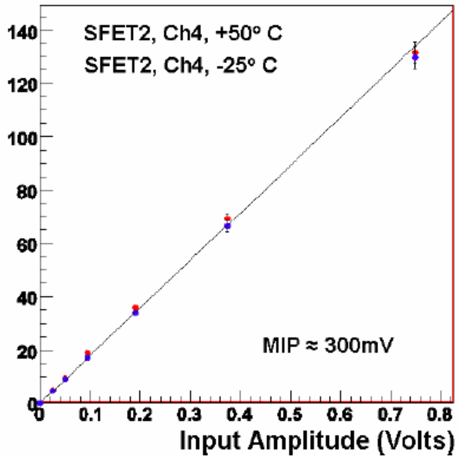

Figure 45 - Measured amplitude versus the amplitude of the input signal at the temperatures of +50° C (red) and -25° C (blue).

4.6.2 How it works

The scintillation detector is one of the most often and widely used particle detection devices. It makes use of the fact that certain materials when struck by a particle or radiation, emit a small flash of light, i.e. a scintillation. In general the scintillator signal is capable of providing a variety of information. Among is most outstanding features are:

- Sensitivity to energy lost by the crossing particle.
- Fast time response.
- Pulse shape discrimination.

Scintillator materials exhibit the property known as *luminescence*. Luminescent materials, when exposed to certain kinds of energy (light, heat, radiation, etc.) absorb and remit the energy like visible light. If the re-emission occurs immediately after absorption or more precisely within 10^{-8} s (being roughly the time taken for atomic transitions), the process is usually called fluorescence. However, if remission is delayed because the excited state is meta-stable, the process is called *phosphorescence* or afterglow. In such cases, the delay time between absorption and emission depends on the material. The time evolution of the emission process may be described as a simple exponential decay:

$$N = A \cdot e^{\frac{-t}{\tau_f}} + B \cdot e^{\frac{-t}{\tau_s}} \tag{4.5}$$

where *N* is the number of photons emitted at time *t*, τ_f and τ_s are the *fast* and *slow* decay constants, *A* and *B* are material constants depending on the importance of the two components. In most cases the fast component dominates.

In general, a good detector scintillator should satisfy the following requirements:

1. high efficiency for conversion of exciting energy to fluorescent radiation,
2. transparency to its fluorescent radiation so as to allow transmission of the light,
3. emission in a spectral range consistent with the spectral response of existing photomultipliers,
4. a short decay constant.

Birks in 1951, assuming the response of organic scintillators to be ideally linear, explained the deviations as being due to quenching interactions between the excited molecules created along the path of incident particle, i.e. interactions which drain energy which would otherwise go into luminescence. Since a higher ionizing power produces a higher density of excited molecules, more quenching interactions will take place for these particles. In this model, the light output per unit length, dL/dx, is related to the specific ionization by

$$\frac{dL}{dx} = \frac{A\frac{dE}{dx}}{1 + kB\frac{dE}{dx}}, \tag{4.6}$$

with *A* the absolute scintillation efficiency, *kB* a parameter relating the density of ionization centers to dE/dx. In practice, *kB* is obtained by fitting Birk's formula to experimental data. As observed experimentally, the formula is reduced to a linear relationship for small dE/dx

$$\frac{dL}{dx} \simeq \frac{dE}{dx}. \tag{4.7}$$

However, for large dE/dx, the formula differs in its predictions. Not all the organic scintillators are composed by a single material. Most of the organic scintillators, to increase the efficiency in a particular application, make use of wavelength shifters which absorb light of one frequency and emit it into another frequency. This can also be added to make the spectrum compatible with a photomultiplier cathode. Chou in 1952, taking into account a solution of two materials, with different probabilities of emissions and quenching and with a probability of photons transmission between themselves, suggested deviations at the second order on the Birks formula in order to better fit the experimental data

$$\frac{dL}{dx} = \frac{A(dE/dx)}{1 + kB(dE/dx) + C(dE/dx)^2}. \tag{4.8}$$

In our case the sensitive material is an organic plastic paddle (polyvinyl-toluene) whose scintillator light is internally reflected until it reaches the two edges, where plexiglas light guides bring it to the photomultipliers [387]. The light guides consist of two different parts: a straight extender that prolongs the scintillator paddle is connected to two bended and twisted pieces that end with conical junctions whose the PMTs are fixed to. All the conical parts are identical to match the rectangular shape of the counter and the light guide with the circular photocathode of the PMT.
Between the guide and the PMT window a soft transparent pad, in Dow Corning 93-500 material, is placed, that guarantees the needed optical couplings. The phototube is enclosing into a black plastic box (in Fig. 46), to be connected with the light guide. The scintillator, extenders and light guides are wrapped by thin Mylar foils, that improves reflectivity blocking external light and protects the surfaces from dust and small debris that may be produced by the enclosing carbon fiber 0.5 mm thick boxes, which provide the needed rigidity. Light tightness is provided by a large carbon fiber envelope 0.7 mm thick that encloses the couple of adjacent planes and their photomultipliers.

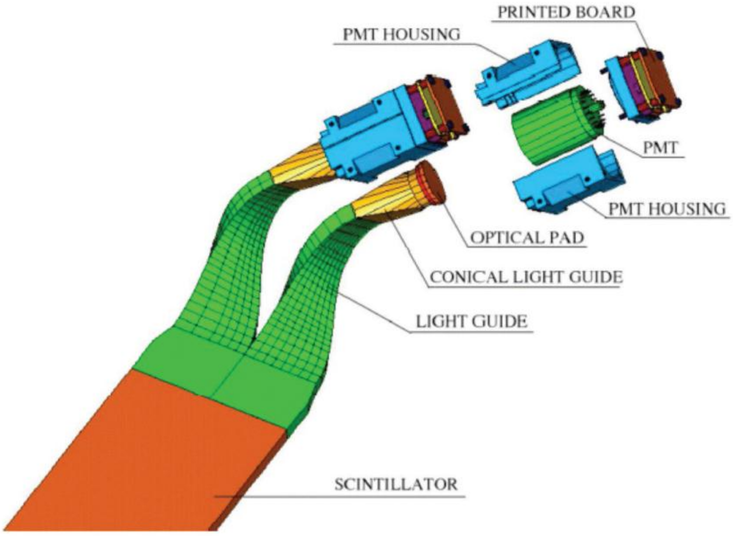

Figure 46 - The mechanical fixation of the PMT to the conical part of the light guide is realized through the PMT housing.

In Table 2 are displayed the main characteristics of TOF counters and PMTs.

TOF Counters	
Polymer	Polyvinyl-toluene
Luminous response	64 % Anthracene
Photons/1 MeV	10000 e^-
Rising time	0.9 ns
Falling time	2.1 ns
Density	$1.032 g/cm^3$
Refraction index	1.58
Attenuation length	3.80 m

TOF PMTs	
Dimension	38 mm
λ (max sensitivity)	375 nm
Gain	10^6
Dark current	5 nA
Rising time	1.9 ns
Transit time	7.2 ns
Spread transit time	0.35 ns
Number of dynodes	16

Table 2 – Main characteristics of TOF scintillators (left) and phototubes (right) [391].

Now let's try to visualize an event, a particle passing through the TOF, and describe the operating principle with which the detector measures the time of flight (Figs. 47, 48).

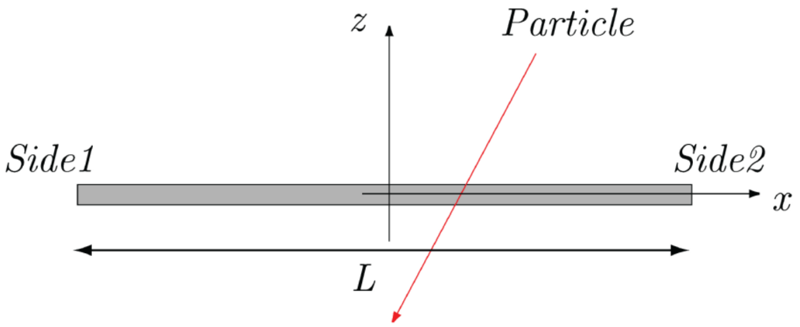

Figure 47 – Schematic view of a particle crossing a TOF counter. L is the counter length (120 cm), the two sides are called *p* (positive) and *n* (negative).

The true time of particle crossing must be computed taking into account each instrumental delay.

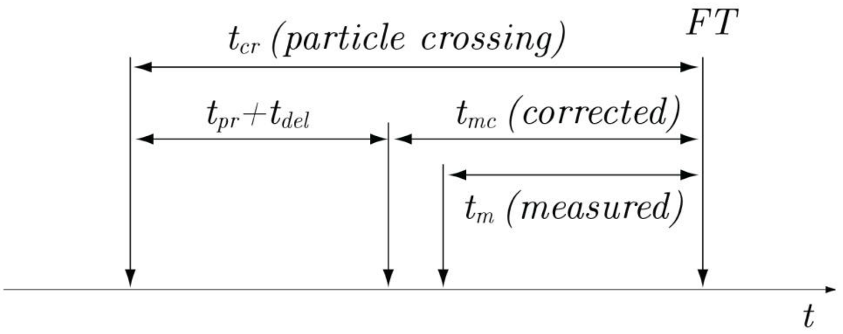

Figure 48 – Measurement scheme of the effective time of particle crossing in one TOF counter. $t_m$is the time measured with respect the Fast Trigger, t_{mc} is the time corrected for the "slewing", t_{pr} is the delay introduced by the propagation of light in the scintillator and t_{del} the delay due to electronic cables.

The particle induces the scintillation emission, which travels through the counter with a velocity V of about 15 cm/ns. The photons that arrive from the scintillator hit the photocathode of the photomultiplier where, through photoelectric effect, they are converted into electrons, with a quantum efficiency given by:

$$n(\lambda) = \frac{numero\ di\ fotoelettroni\ emessi}{numero\ di\ fotoni\ incidenti} \tag{4.9}$$

$n(\lambda)$ is generally less than 30% and has a maximum for values of wavelength around 400 nm (this value depends on the material of the photocathode).

Subsequently, the photoelectrons are focused in the multiplication region, which is composed of a series of dynodes, each at a higher potential than the previous one, so that the electrons undergo a continuous acceleration step by step. The electrons that hit dynodes transfer part of their energy to the dynodic material causing the emission of secondary electrons in a process very similar, from a theoretical point of view, to the photoelectric effect; the geometry of the dynodes is such that at each step the number of electrons increases. Then the electrons reach the anode, where the accumulation of charge determines the formation of a strong current pulse, which is measured by the front-end electronic.

All of the time signals are measured with respect to a common value, the Fast Trigger, which is defined by the coincidence of signals from at least one counter on each TOF layer. Every time a particle generates a Fast Trigger signal the time t_{m1} (t_{m2}) is stored, with respect to the Fast Trigger (Fig. 48), in which the side 1 (2) of the counter involved in the event has exceeded the preset threshold. These must be corrected for the slewing (Fig. 49), i. e. the time interval between the start of the signal and the actual exceeding of the threshold.

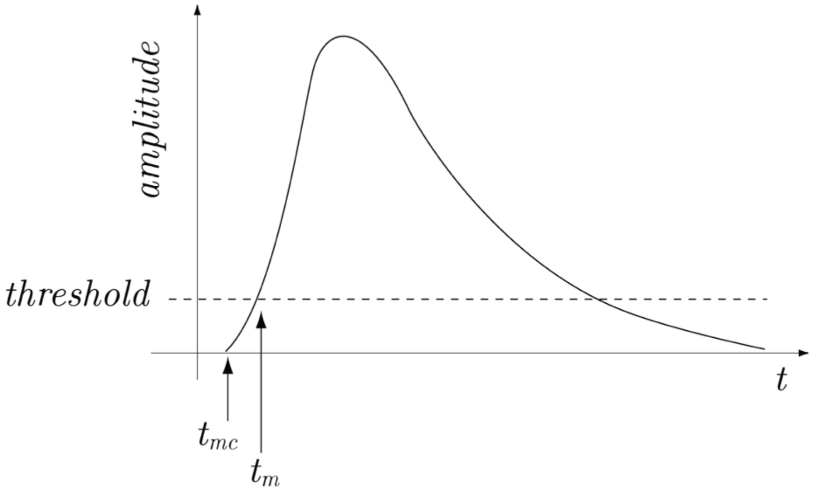

Figure 49 – Schematic view of the contribution of the slewing correction: the effective time of the signal start is t_{mc}, while the time measured by the detector is t_m. So, the real physical time is t_{mc}.

Finally, it is necessary to take into account the delay introduced both by the propagation of light from the point of impact to the ends of the counter (Fig. 48) and the electronic cables. As a result, the actual time of passage of a particle measured from each side of the counter is given by:

$$\begin{gathered} t_{cr_1} = t_{m_1} + \frac{s_1}{\sqrt{A_1}} + \frac{\frac{L}{2} + x}{V} + t_{del_1} \\ t_{cr_2} = t_{m_2} + \frac{s_2}{\sqrt{A_2}} + \frac{\frac{L}{2} - x}{V} + t_{del_2} \end{gathered} \tag{4.10}$$

where the only difference is the sign of the impact point due to the geometrical definition. t_{cr} is the actual time of particle crossing through the counter with respect to the Fast Trigger, t_m is the time measured with respect to the Fast Trigger, $\frac{s}{\sqrt{A}}$ represents the **slewing correction**, which depends on the slewing parameter *s* and on the amplitude of the signal *A*, $\frac{L/2\pm x}{V}$ is the delay introduced by the propagation of light, that depends on the impact point of the particle with respect to the half of the counter and on the speed of light in the scintillator counter, t_{del} the cable delay. Solving the system (4.10) for *x*, i. e. subtracting the two equations, the impact coordinate can be obtained

$$x = V\left(\frac{t_{m_2} + \frac{s_2}{\sqrt{A_2}} - t_{m_1} - \frac{s_1}{\sqrt{A_1}} + t_{del_2} - t_{del_1}}{2}\right) \tag{4.11}$$

while the crossing time, that is obviously independent from the crossing point, is computed adding the previous equations:

$$t_{cr_i} = \frac{t_{m_1} + \frac{s_1}{\sqrt{A_1}} + t_{m_2} + \frac{s_2}{\sqrt{A_2}} + \frac{L}{V} + t_{del_1} + t_{del_2}}{2} \tag{4.12}$$

where the subscript *i* stands for the *i*-th counter. In this way, both time and position information for the event are achieved from the detector signal.

To be very accurate, as anticipate by the previous formulas, all the slewing constants should be taken into account, one for each counter side. Without entering into too technical details [411, 412], it's easy to understand that there are two set of unknown parameters, the slewing and the electronic delay associated to each counter side. The t_{del1-2} linear combination are now called zero-time calibration constant C_i, one for each counter, i. e. 32.

The principle of the measurement of these two set of instrumental parameters is to take into account couple of layers and counters and compute the unknown constants starting from the measured TOF quantities, such as track length, paddle time and ADC signal. Track lengths between different layers are given by the track extrapolation into TOF planes.

So the computation starts from this formula:

$$-\frac{l_{ij}}{v} = \left(\frac{t_{m_1} + \frac{s}{\sqrt{A_1}} + t_{m_2} + \frac{s}{\sqrt{A_2}}}{2}\right)_i - \left(\frac{t_{m_1} + \frac{s}{\sqrt{A_1}} + t_{m_2} + \frac{s}{\sqrt{A_2}}}{2}\right)_j + C_i - C_j \tag{4.13}$$

where l_{ij} is the positive track length from plane *i* to plane *j*, *v* the particle velocity (note that the time difference on the left side of the equation is negative because times are measured relative to FT time).

The slewing/zero-time calibration must be done in two steps:

1. Compute the slewing parameters for each counter side with strict definition of the hit point in the counters, using all particles and with adequate statistics.
2. Compute the zero-times using the slewing corrections previously computed in point 1. All constants are determined at the same time with a global minimization procedure.

The characteristic plots are two. One is

$$[t_{m_s}]_{i,l1} - \left[\left(\frac{t_{m_1} + t_{m_2}}{2}\right)\right]_{4,l2} \quad \text{vs.} \quad \frac{1}{\sqrt{A_{i,s}}} \tag{4.14}$$

in Fig. 50, where *i* is the counter under measurement, *s* is the side under measurement, *l1* is the layer under measurement, *l2* is the reference layer (layer 1 for layer 4, layer 4 for layer 1, layer 2 for layer 3 and layer 3 for layer 2), and $A_{i,s}$ is the amplitude of the signal on side *s* of counter *i*. The linear fit of this plot gives the slewing correction.

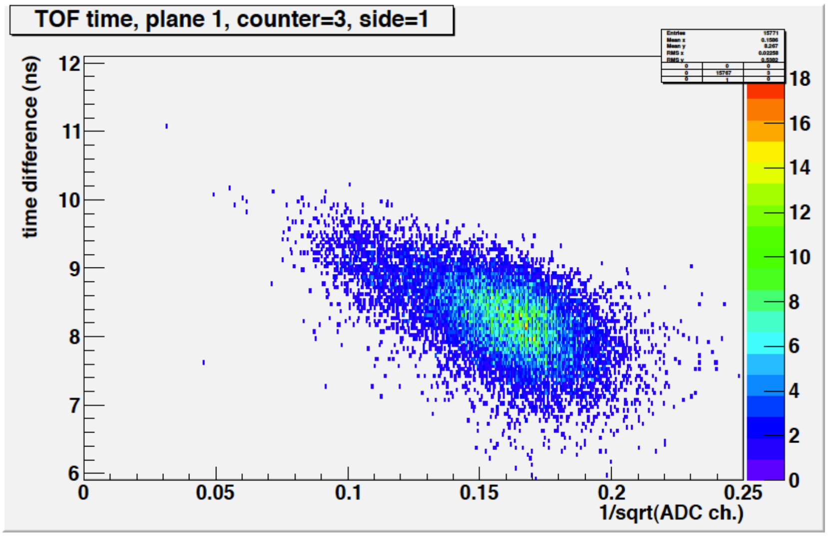

Figure 50 – Slewing correction dispersion relation between the reference time difference and the ADC signal of the 1031 counter.

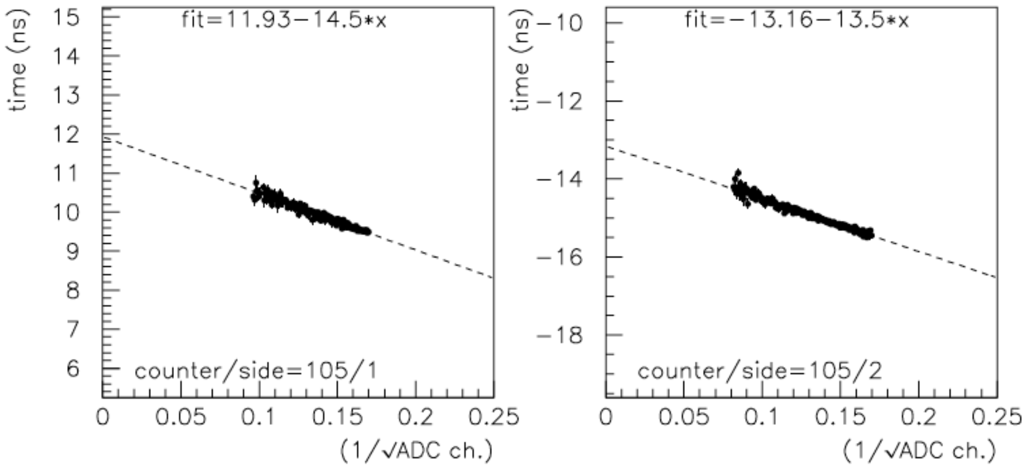

Figure 51 – Linear fit of the time-ADC relation to obtain the slewing constant for the two sides of the 105 (first layer, fifth counter) counter [412].

The other quantity, in Fig. 52, is

$$\left(\frac{t_{m_1}+\frac{s_{1i}}{\sqrt{A_1}}+t_{m_2}+\frac{s_{2i}}{\sqrt{A_2}}}{2}\right)_i-\left(\frac{t_{m_1}+\frac{s_{1j}}{\sqrt{A_1}}+t_{m_2}+\frac{s_{2j}}{\sqrt{A_2}}}{2}\right)_j+\frac{l_{ij}}{v} \tag{4.15}$$

where i and j are counters from different layers and $A_{1,2}$ is the amplitude of the signal on side 1 or 2.

A single slewing calibration needs a very long period of time (at least 2 months of data), but it is stable with time and running conditions. Zero time calibrations can be repeated every 2 million triggers. Slewing corrections should be calculated individually for each counter side and then zero-times have to be computed for all counters.

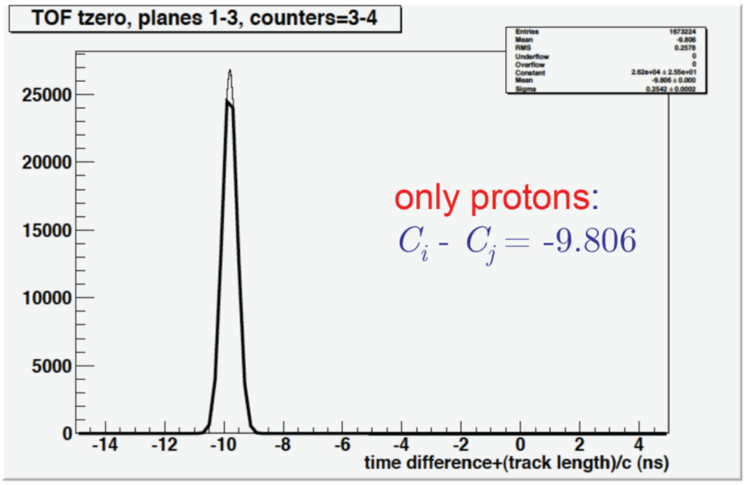

Figure 52 – The Gaussian fit of the distribution gives the difference between the zero time constants of the two counters involved: $C_i - C_j$. The single constants are obtained through a global fit, after 288 combinatorial measurements [412, 415].

Finally, to conclude this dissertation about Time of Flight principia and time measurements, some features of thresholds with respect to the TDC time window and the fast trigger are presented. TOF time signals and the Fast Trigger are registered on pipeline TDCs, constituted by 655360 channels at 25 ps/ch, i. e. on a 16384 ns wide time window.

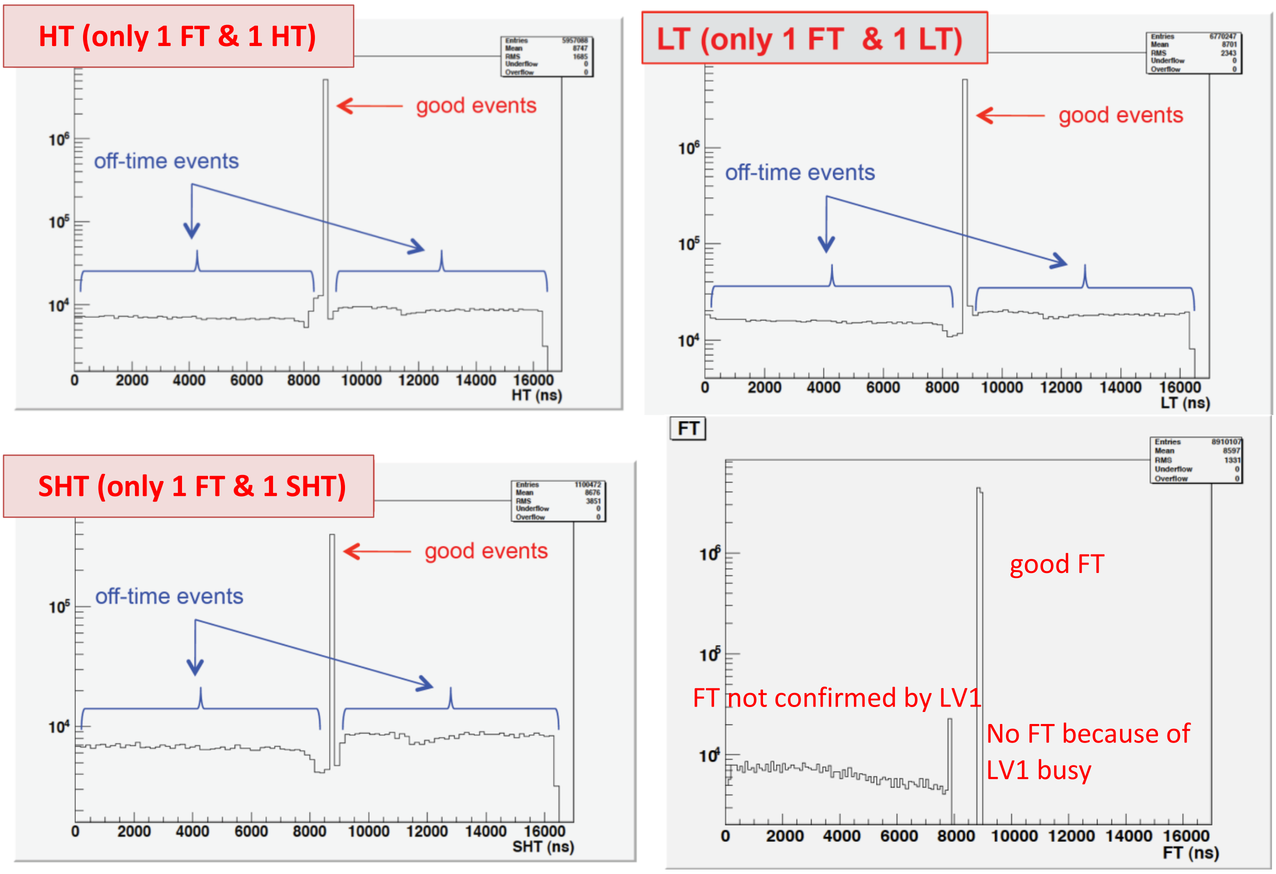

Figure 53 – High Threshold and Low Threshold events in the TDC 16 μs time window (upper row) associated with only one FT and only one LT/HT/SHT; SuperHigh Threshold with only one FT and only one LT/HT/SHT and Fast Trigger events without cuts.

Most of the events have one LT/HT/SHT/FT signal per counter side, but about a tenth of them has two LT/HT/SHT/FT, a hundredth three signals, and so on, and the correct signal for these multiple signals events has to be discriminated. The request of only one FT and only one LT/HT/SHT cleans up the distributions. In Fig. 53 it's shown that the good events with one FT and one LT/HT/SHT/FT are those which occur at about 8.9 μs of the TDC pipeline.
Therefore the assumption is that, when more than one LT/HT/SHT signal is present, the good ones follow the distributions depicted in Fig. 53, and in the expanded scale of Figure 54 below.

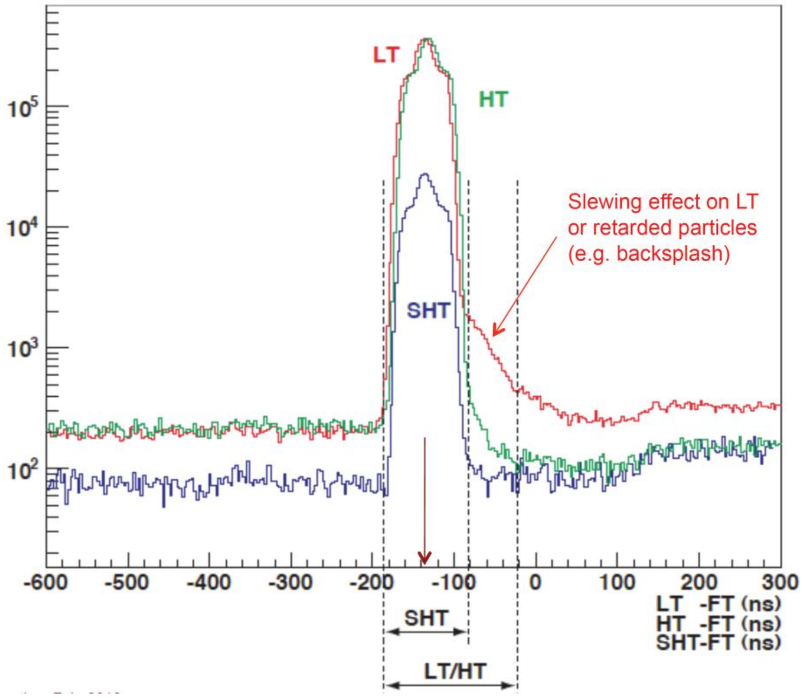

Figure 54 – Absolute time distribution of LT/HT/SHT respect to the FT. You can see the distorted shape of the LT events due to retarded particles, i. e. fake signals of particle backsplashed from the underlying ECAL [413].

From Fig. 53 FT distribution, it's deducible that, if there is more than one FT signal, the good one must be the last and, anyhow, the good FT signal must have a value between 8870 and 8930 ns (consistent with the 50 ns clock of the JLV1).
For LT, HT and SHT, instead, if there is more than one signal, the best guess for the good one is the signal nearest to -140 ns w.r.t. the FT time [413].

By combining off-time events on both sides of one counter, the absolute rate on that counter can be computed, and also the **live time** of the data, which can be defined as the number of analyzed events multiplied by the TDC interval considered.
So, another main task for the TOF detector could be to border the orbital regions of physical interest, in function of CR rates and live time. In fact not all AMS data can be used, because of the previously described in 3.2.1 South Atlantic Anomaly, which corrupts part of the events.
With the TOF counting rate an exclusion criterion for the SAA region can be determined, cutting the scientific data with a trigger rate greater than 2 kHz (Fig. 55, white region with red margins).

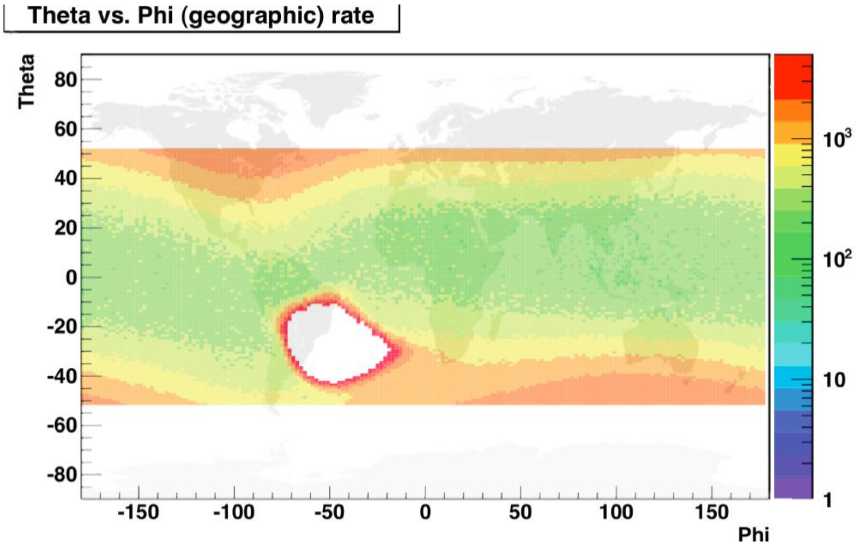

Figure 55 – Absolute TOF particle rate as a function of geographical position. AMS-02 operates at trigger rates up to 2 kHz with an average event size of about 2 Kbytes [382].

The absolute rates of one paddle in the first plane in different geographical location along the orbit of the ISS is shown in figure. Higher rates correspond to regions with lower values of the geomagnetic cutoff as in the polar regions, and in the South Atlantic Anomaly [382, 392, 417].

4.6.3 TOF performances and optimizations

Here some general features of the TOF detector in space are presented, to illustrate the uptodate performances and some optimization checks made in space to test the correct tuning of the detector. First of all, the TOF counters are working properly and show great trigger efficiencies (Figs. 56 and 57).

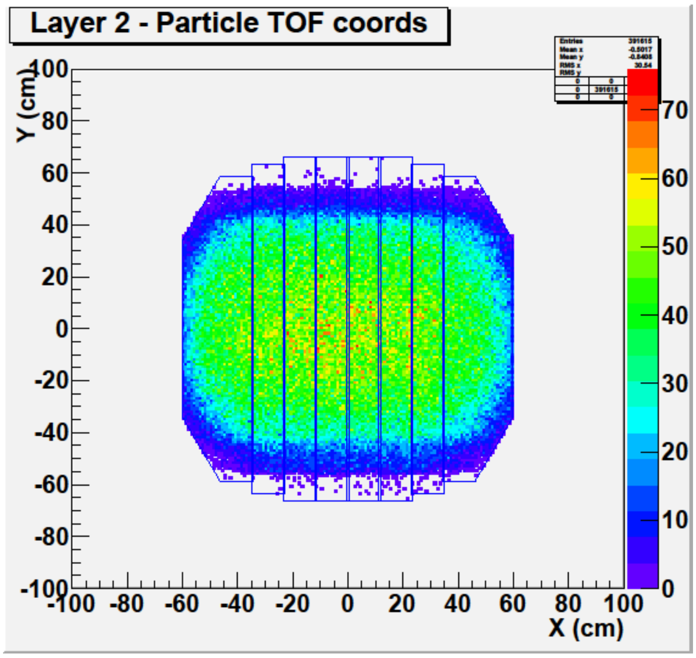

Figure 56 – The track hit points in X and Y coordinates on each of the four TOF planes are shown. The distributions agree with AMS acceptance [382, 416].

During this first year of operation in space, 15 billion physical events were acquired. TOF kept the nominal settings in terms of high voltages and thresholds. All TOF channels are working as expected.

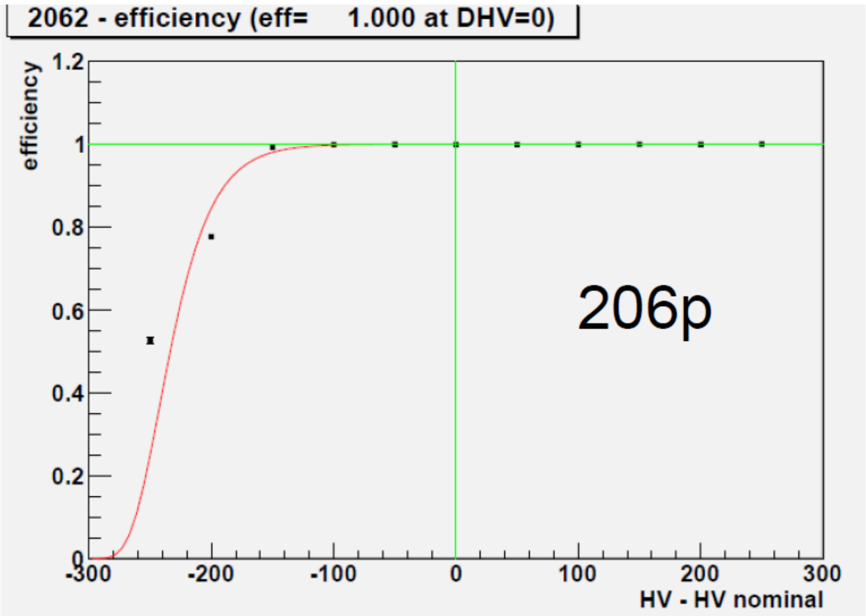

Figure 57 – Example of plateau for the trigger efficiency of one counter. On x axis there's the difference with respect to the nominal used value [418].

The previous plateau curve in Fig. 57 is determined varying the HV of the PMTs in the counter side under measurement, in 50 V steps with respect to the nominal value (± 250 V), using the other side as a trigger. Plateau curves for trigger efficiency have been determined for all TOF counters sides. All counters sides give trigger efficiency greater than 95%.

The HV scan for the TOF has been important to determine the most appropriate HV to apply at each PMT in order to:

- have a MIP signal corresponding to the 60 mV threshold (high threshold) at the counter center, to improve the trigger efficiency;
- equalize the signals from the two sides of each the counters to increase the time resolution;

The resulting calibration curve was then fitted with the function (Fig. 58):

$$Q = \left(\frac{\mathrm{HV}}{\mathrm{HV}_0}\right)^p \tag{4.16}$$

where Q is the charge peak in ADC channels, p is the gain factor of each PMT, HV is the applied voltage in Volts, and HV_0 is a parameter common to all PMTs.

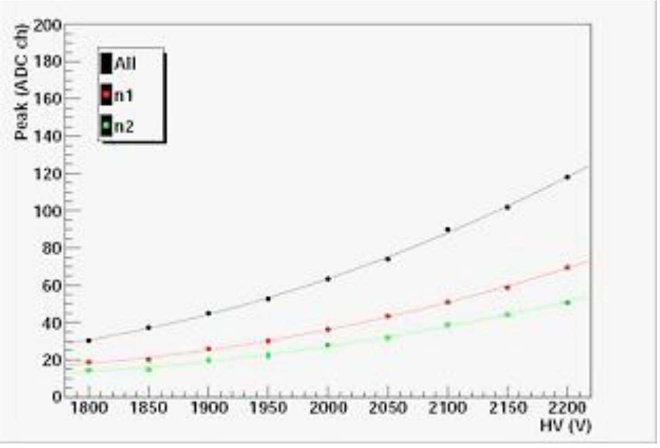

Figure 58 – Calibration curves for PMTs equalization [419].

HV was tuned to acceptable value for both PMTs connected to the same HV channel. In case a PMT required a HV higher than the paired one, both have been set to the higher HV value. The anode signal in function of the counter coordinate is shown below in Fig. 59.

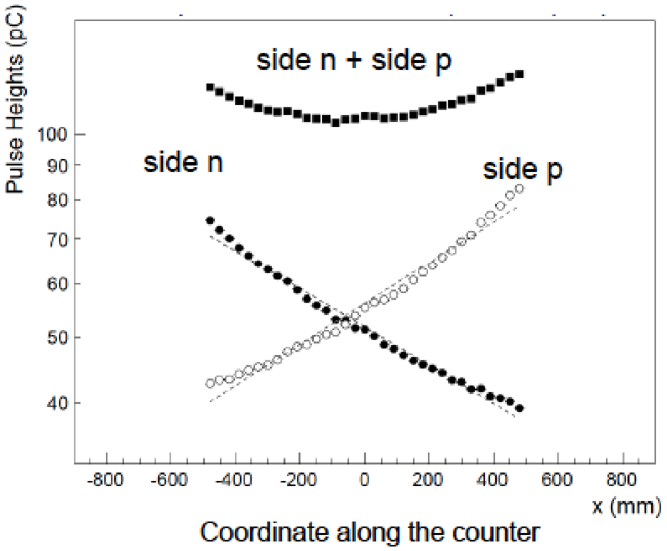

Figure 59 - Anode amplitude as a function of the particle impact point [419].

These space results are in complete agreement with the previous ones obtained with cosmic muons at CERN and at NASA KSC and during the test beam. The overall trigger efficiency obtained for each layer is optimal, with efficiency less than 0.5% (Fig. 60).

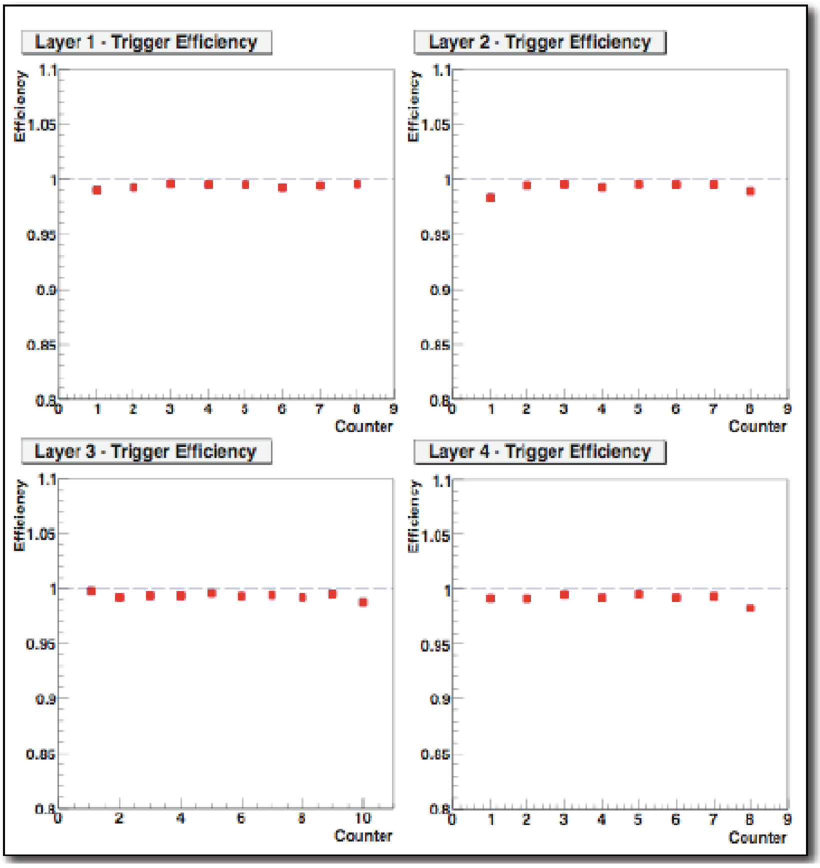

Figure 60 a) - The efficiency of the counter is computed as the ratio between the number of events with any High Threshold in the counter and the total number of events with a particle hitting the counter. Most of the inefficiency is due to the particles hitting the edges of the counters.

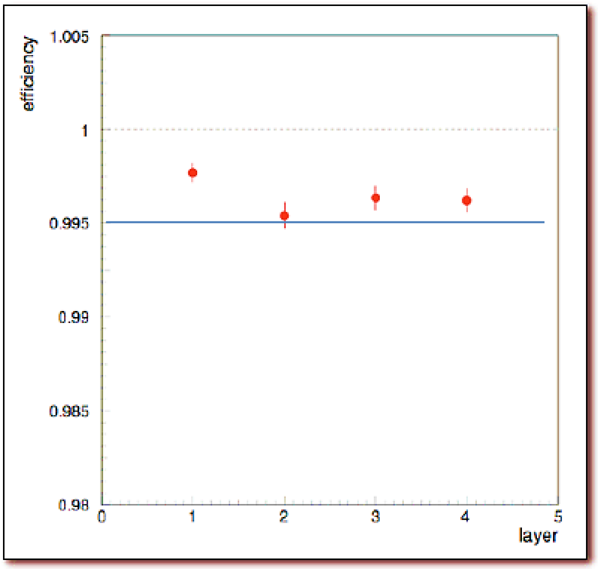

Figure 60 b) – Overall efficiency for each TOF layers. The efficiency of the plane is computed as the ratio between the number of events with any High Threshold in the plane and the total number of events with a particle hitting the plane. Efficiency is better than 0.995 in each plane [420].

Moreover, extraordinary particle beta and position resolution have been recently obtained, as it's clear from Figs. 61a) and 61b), respectively less than 60 ps and 1 cm for high charge nuclei.

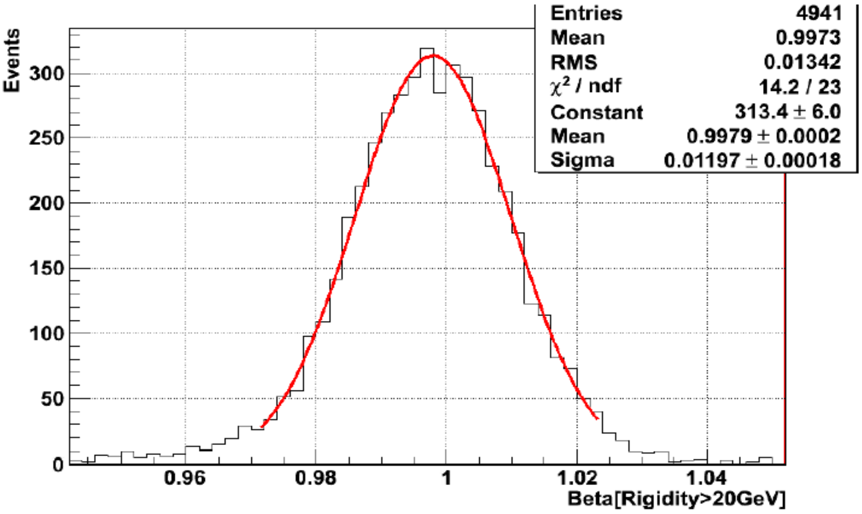

Figure 61 a) – Cosmic rays velocity (Beta) is measured by TOF using the time between the upper and lower planes and the trajectory length.

The resolution in velocity measurement is 4% for protons and increases for high Z nuclei. From the relation $p/c = m\beta\gamma$ it is possible to identify the particle mass. In Fig. 61a) case, Carbon beta resolution is 1.2 %, i. e. a time resolution of about 48 ps.

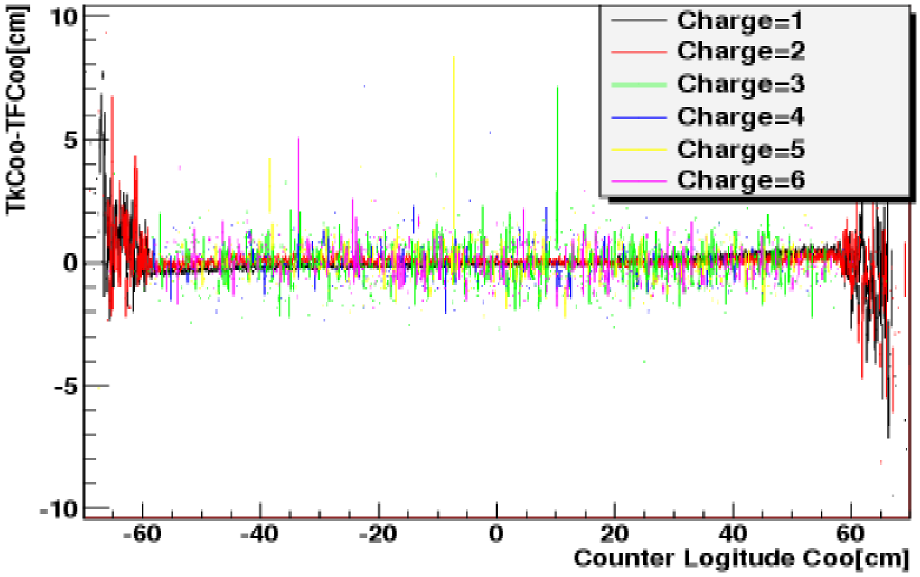

Figure 61 b) - Longitudinal TOF-Tracker coordinate alignment [421].

The alignment reported in Fig. 61b) is optimal, obviously except for the counters edges, i.e. ± 60 cm. This means a spatial resolution of 2.8 cm for proton, and 0.9 cm for Carbon.

Another fundamental physical measurement is the charge, that could be reconstructed both from anodic and dynodic signal of the PMTs (Fig. 62). Anode and dynode signals have different features and they’re used for different Z windows (Fig. 63).

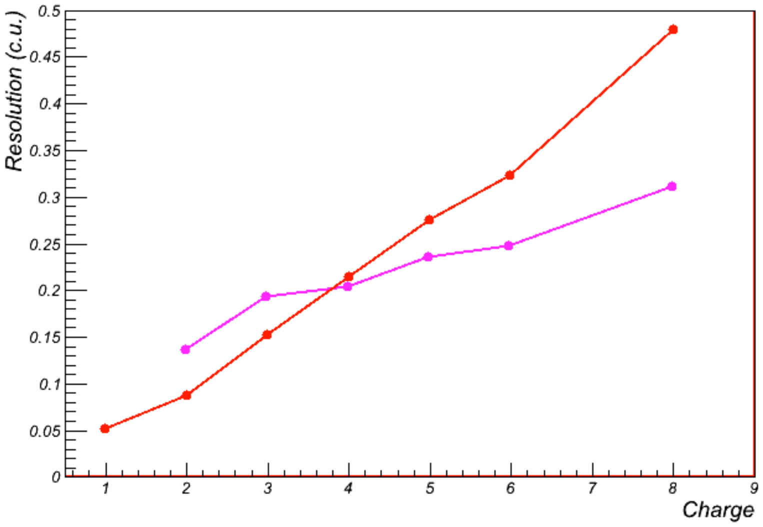

Figure 62 - In TOF both the sum of the anode signal (red) from each counter side and the last third dynode from each TOF photomultiplier (rose) are acquired and used in the measurement of the charge [382, 423].

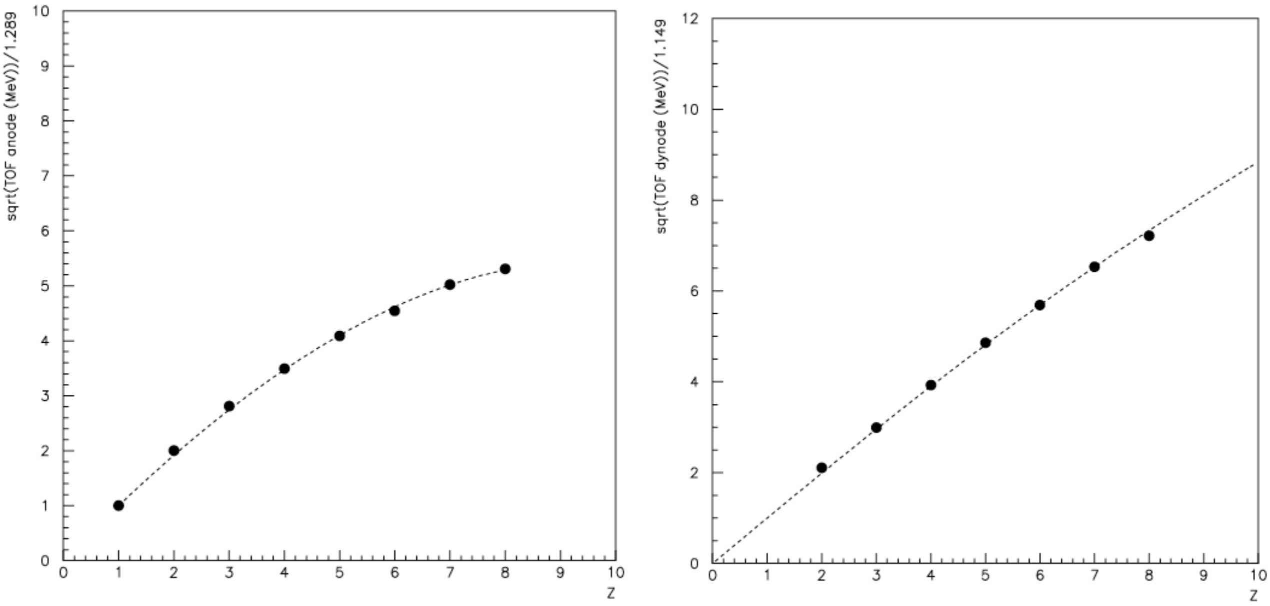

Figure 63 – Anodic (left) and dynodic (right) signals as a function of particle Z.

The anode signal heavily saturates for Z>2. The dashed line in Fig. 63 left is the fit function Z_{anode}:

$$(1-a-b)Z + aZ^2 + bZ^3 \tag{4.17}$$

with a = -0.039 and b = -0.001. The dashed line in Fig. 63 right is the Birks-Chou's law

$$Z_{\mathrm{dynode}} = \frac{Z}{\sqrt{1 + aZ^2 + bZ^4}} \tag{4.18}$$

with the parameters a = 3.3 x 10^{-3} and b = -5 x 10^{-6}, the same measured in the test beam [424]. These charges, in particular the anodic one, must be corrected for signal saturation and also with a supplementary linear correction from Bethe-Block, which could be used to estimate the charge from the energy loss and the particle β:

$$Z = \sqrt{\frac{dE/_{dx}}{\frac{P_1}{\beta^2}\left(\ln(P_2\gamma^2\beta^2) - \beta^2\right)}} \tag{4.19}$$

where P_1 and P_2 are two materials constant. So TOF anodes saturates for charge Z>2 and they can be used mainly for Z=1 and Z=2. Most of TOF dynodes give good signals for Z≥3.The corrected TOF charge follows the correct trend in Fig. 64a).

This is another example of recent tuning and optimization done by the TOF group in order to maximize the detector performances.

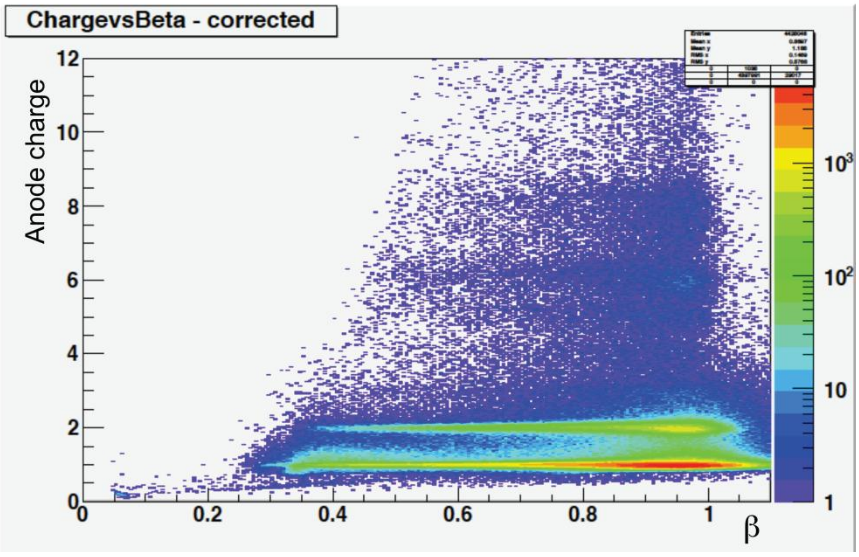

Figure 64 a) – Corrected anode charge versus particle beta. The two Z=1 and Z=2 curves are shown.

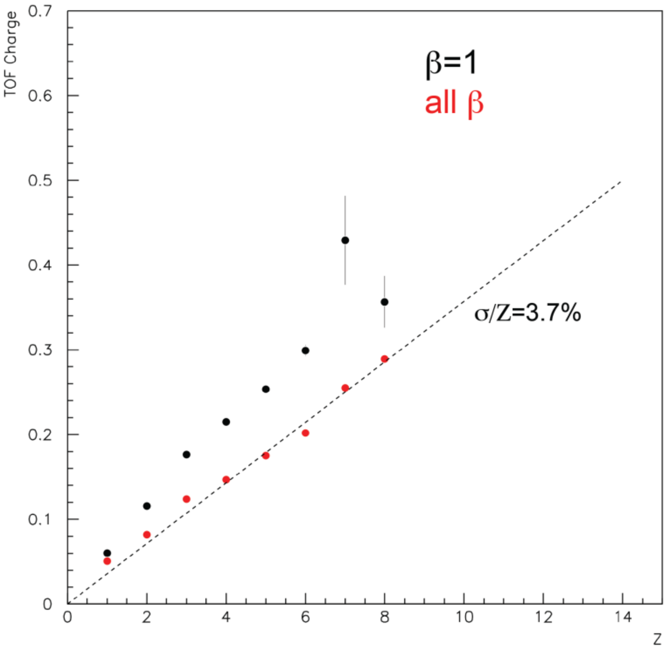

Figure 64 b) - TOF Charge (Dynodes, or Anodes if dynodes not all present) resolution for two set of data. The difference is probably due to the different tracker charge selection [424].

With this arrangement and resolution the TOF can compete with the Tracker in particle and nuclei identification, with accurate measurements of the CR abundances (Fig. 65), and of particle beta and beta resolution as a function of the TOF charge (Figs. 66).

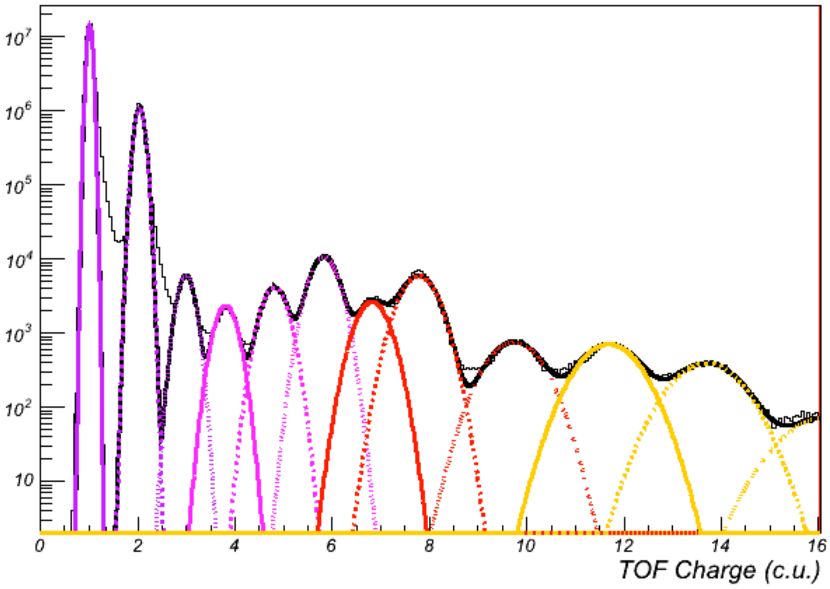

Figure 65 – The anode signals distinguish the charged particles with low Z, and when anode signal starts to saturate, the dynode signals are used to enlarge the dynamical range for the charge measurement. TOF is able to measure the charge released by the particle in the scintillator up to at least charge Z=15 [382].

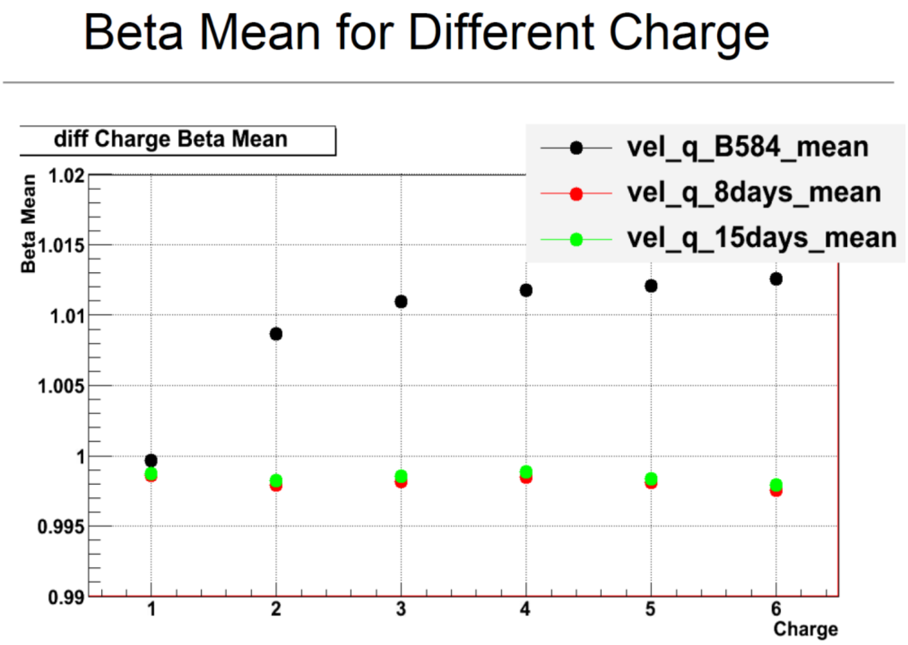

Figure 66 a) – Particles' beta as a function of charge for three data samples [421].

Not only technical, but also "physical" targets have been achieved, such as the measurement of particles' beta as a function of charge. The three sets of points in Fig. 66a) correspond to different set of data. Black points exceed 1 because of the beta variable implemented in the particular B584 data repository.

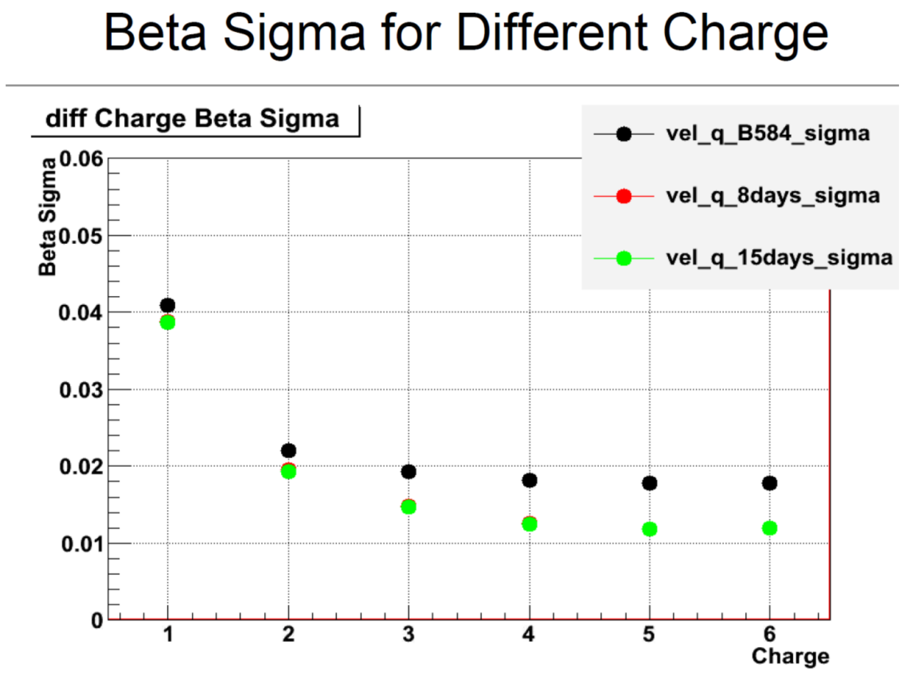

Figure 66 b) – Beta standard deviation as a function of TOF charge, for the same data sets of Fig. 66a) [421].

As said before, in Fig. 66b) the resolution increases with Z, reaching, after Z = 2, the expected plateau of 1 ÷ 2 %, corresponding to a resolution in time better than 60 ps. The three set of points are the same of the previous figure. The beta resolution can be fit with a $\sqrt{p_0^2 + \frac{p_1^2}{Z^2}}$ function.

4.7 AMS-02 Chronology

An AMS prototype designated AMS-01, a simplified version of the detector, was built by the international consortium under Ting's direction and flown into space aboard the Space Shuttle Discovery on STS-91 in June 1998. By not detecting any antihelium the AMS-01 established an upper limit of 1.1×10^{-6} for the antihelium to helium flux ratio and proved that the detector concept worked in space. This shuttle mission was the last shuttle flight to the Mir Space Station.

After the flight of the prototype, Ting began the development of a full research system designated AMS-02. This development effort involved the work of 500 scientists from 56 institutions and 16 countries organized under United States Department of Energy (DOE) sponsorship [403].

The instrument which eventually resulted from a long evolutionary process is "the most sophisticated particle detector ever sent into space", rivaling very large detectors used at major particle accelerators, and it has cost four times as much as any of its ground-based counterparts. Its goals have also evolved and been refined over time. As built it is a more comprehensive detector, which has a better chance of discovering evidence of dark matter.

The power requirements for AMS-02 were thought to be too great for a practical independent spacecraft. So AMS-02 was designed to be installed as an external module on the International Space Station and use power from the ISS. The post-Space Shuttle Columbia plan was to deliver AMS-02 to the ISS by space shuttle in 2005 on station assembly mission UF4.1, but technical difficulties and shuttle scheduling issues added more delays.

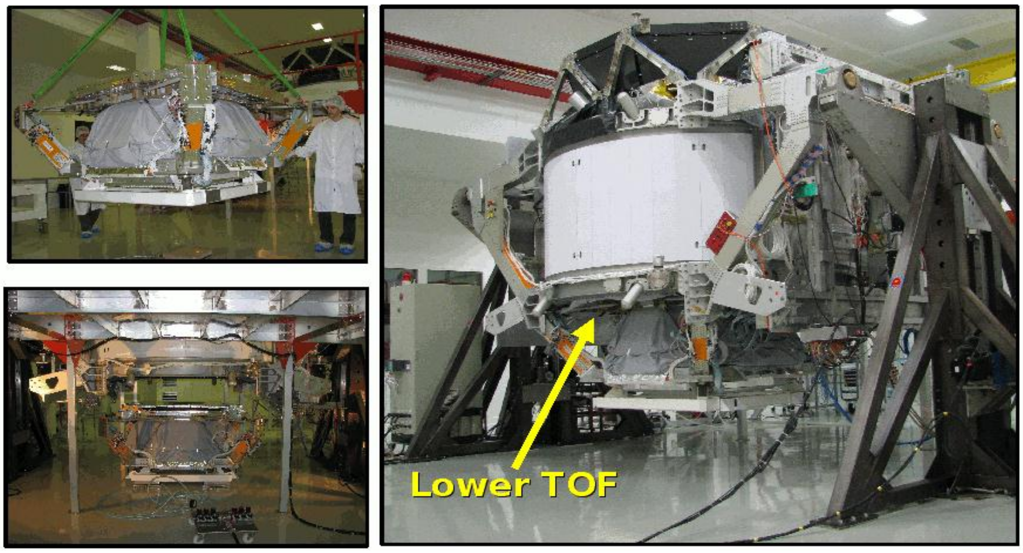

Figure 67 – Integration of AMS in the CERN Prevessin clean room; lower TOF is tagged.

The detector has been integrated in its final configuration between the May and July 2010 in a dedicated clean room at CERN. In August 2010 a beam test with up to 400 GeV/c momentum protons, positrons, electrons and pions was performed in the SPS H8 beam line. The purposes of the test were:

- to check the alignment of the Silicon Tracker. AMS was moved and inclined on the 400 GeV/c momentum protons beam in more than 500 positions, allowing the study of alignment for all the combinations of ladders in the 9 layers;
- inter-calibrate the various sub-detectors with known rigidity beams. The performances of the various subdetectors have been verified and in particular the electrons/hadrons rejection power has been investigated.

Then AMS-02 was then shipped to ESA's European Space Research and Technology Centre (ESTEC) facility in the Netherlands where it arrived 16 February 2010. Here it underwent thermal vacuum, electromagnetic compatibility and electromagnetic interference testing.

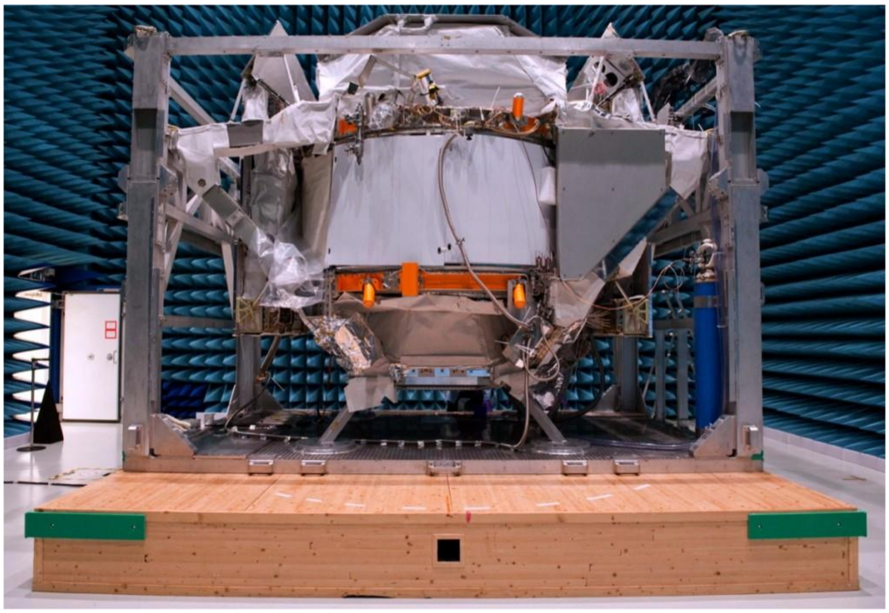

Figure 68 – AMS in the thermal vacuum chamber in ESTEC.

AMS-02 was scheduled for delivery to the Kennedy Space Center in Florida, U.S.A. in late May 2010. This was however postponed to August 26, as AMS-02 underwent final alignment beam testing at CERN.

A cryogenic, superconducting magnet system was developed for the AMS-02. This was a critical technology, enabling a high sensitivity needed to achieve mission objectives. Late in its development, poorly understood anomalous heating in the cryogenic magnet system was discovered. The anomalous heating would place additional demand on the cryogenic cooling. This characteristic significantly reduced the original system design lifetime and contributed to a decision to abandon the cryogenic system in favor of a previously developed but less capable permanent magnet system.

With Obama administration plans to extend International Space Station operations beyond 2015, the decision has been made by AMS management to exchange the original AMS-02 superconducting magnet for the non-superconducting magnet previously flown on AMS-01, with its magnetic configuration remained unchanged by 1% [368]. Although the non-superconducting magnet has a weaker field strength, its on-orbit operational time at ISS is expected to be 10 to 18 years versus only 3 years for the superconducting version. This additional data gathering time has been deemed more important than higher experiment sensitivity.

Activities relating to payload integration, launch, and deployment of AMS-02 are managed by the Alpha Magnetic Spectrometer Project Office at NASA's Johnson Space Center in Houston, Texas, U.S.A. [403].

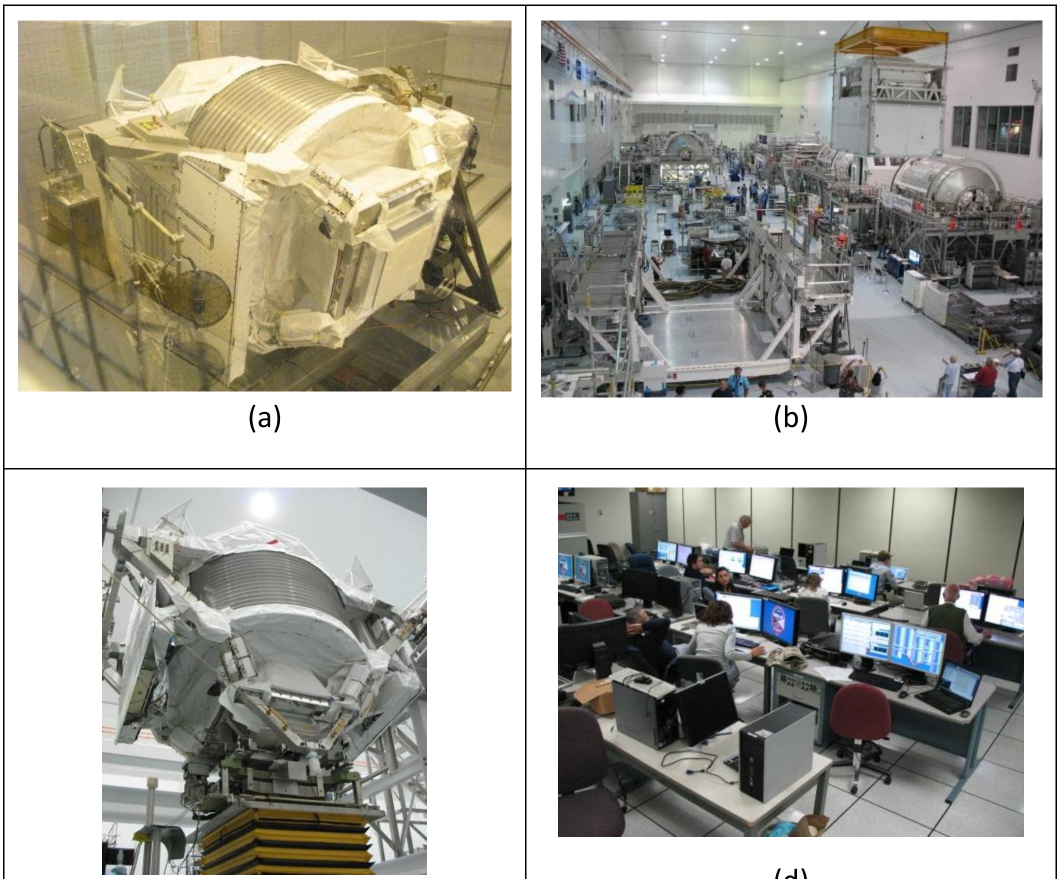

(a) (b) (c) (d)

Figure 69 - Preparation of the AMS-02 Payload for the ISS (a) Calibration of AMS in Test Beam with permanent magnet – 8-20 Aug 2010. (b) AMS being installed in Space Station Processing Facility –

26 Aug 2010. (c) AMS mated with a Payload Attach System simulator - 22 October 2010. (d) Since 28 August, AMS has been undergoing tests at KSC control POCC [350].

For several years it was uncertain if AMS-02 would ever be launched because it was not manifested to fly on any of the remaining Space Shuttle flights. After the 2003 Columbia disaster NASA decided to reduce shuttle flights and retire the remaining shuttles by 2010. A number of flights were removed from the remaining manifest including the flight for AMS-02. In 2006 NASA studied alternative ways of delivering AMS-02 to the space station, but they all proved to be too expensive.

Figure 70 – AMS-02 arrival at Kennedy Space Center after its oceanic flight in the USA military C5 airplane.

In May 2008 a bill was proposed to launch AMS-02 to ISS on an additional shuttle flight in 2010 or 2011. The bill was passed by the full House of Representatives on 11 June 2008. The bill then went before the Senate Commerce, Science and Transportation Committee where it also passed. It was then amended and passed by the full Senate on 25 September 2008, and was passed again by the House on 27 September 2008. It was signed by President George W. Bush on 15 October 2008. The bill authorized NASA to add another space shuttle flight to the schedule before the space shuttle program is discontinued. In January 2009 NASA restored AMS-02 to the shuttle manifest. On 26 August 2010, AMS-02 was delivered from CERN to the Kennedy Space Center by a Lockheed C-5 Galaxy, and it was launched into space on STS-134 on 16 May 2011.

4.8 On the ISS: Data Acquisition

AMS-02 has been activated on the first day of flight (May 16 2011), few hours after the launch, to verify data transmission and subdetectors temperatures behavior. Three days after it has been successfully installed: AMS-02 was delivered to the International Space Station on May 19, 2011 as part of station assembly flight ULF6 on shuttle flight STS-134, commanded by Mark Kelly. It was removed from the shuttle cargo bay using the shuttle's robotic arm and handed off to the station's robotic arm for installation. AMS-02 is mounted on top of the Integrated Truss Structure, on USS-02, the zenith side of the S3-element of the truss.

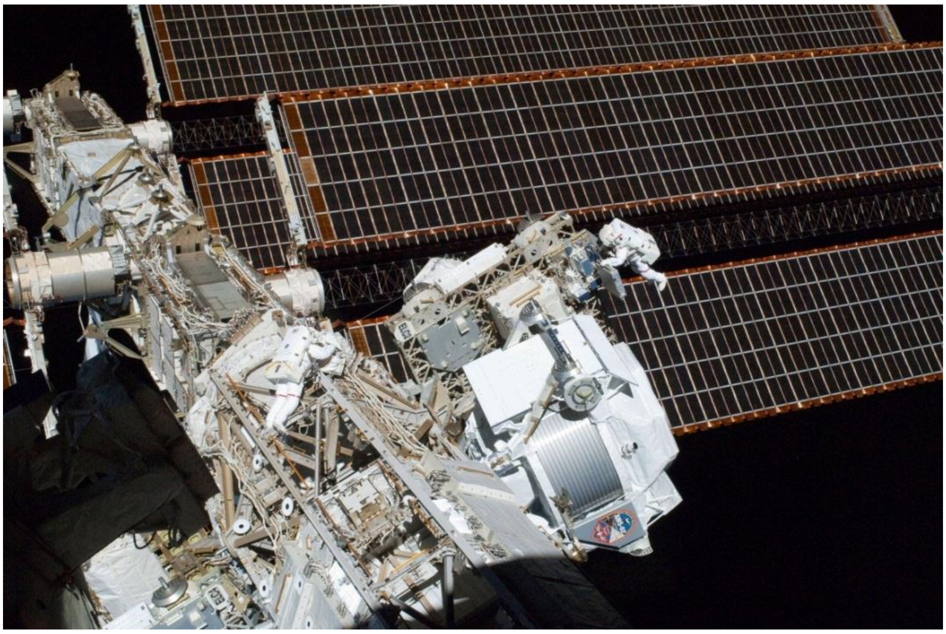

Figure 71 a) – AMS has just been installed. Two astronauts do their spacewalk. On the background, the ISS solar wings. The solar ISS wings represent a fundamental issue for AMS-02, because they periodically overshadow the detector, limiting its acceptance and changing its temperature.

Figure 71 b) – "Postcard" picture of AMS in space.

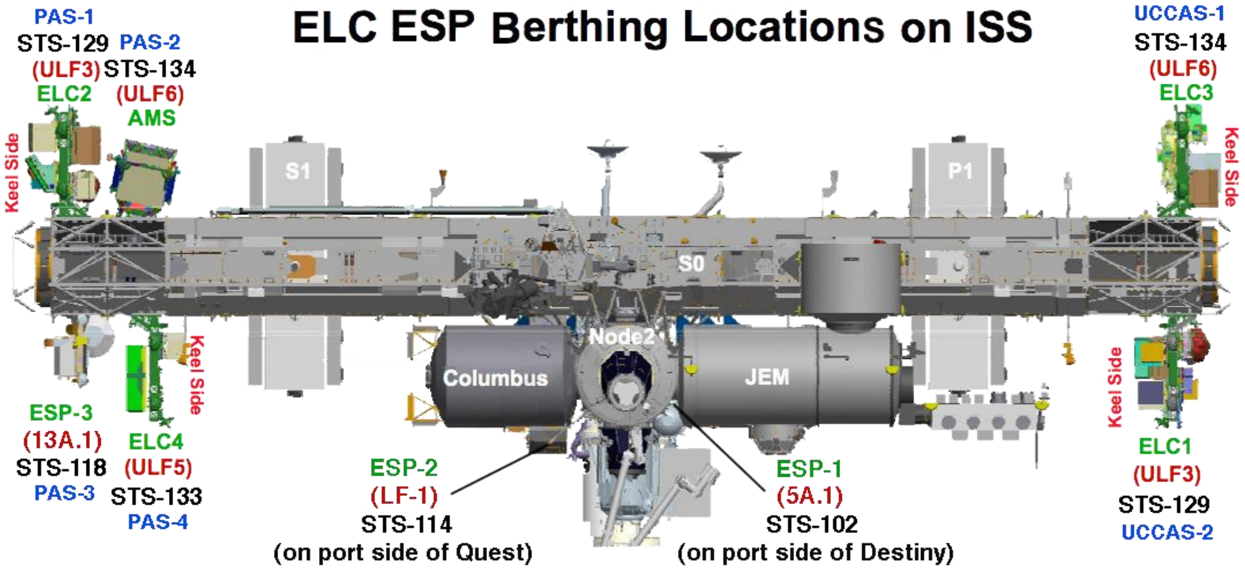

Figure 72 - After the docking to the ISS, the Shuttle arm, after removing another payload, the ExPRESS Logistics Carrier 3 (ELC3), picked AMS up out of the bay and brought it near the station, where the ISS Canadarm 2 (SSRMS) grabbed it, rolled out to the truss and plopped AMS down on its mount point in figure.

The reference system of AMS-02 is shown in Figure 73 and described below: the x-axis points to the so-called sides “PORT “and “STAR” of AMS, with the positive direction oriented from the center of AMS toward the center of the ISS; the y-axis intercepts sides “WAKE” and “RAM” with the positive direction oriented from the center towards the side of “WAKE”; the z axis is perpendicular to the axes x and y, with the positive direction oriented from the center of the AMS towards the Transition Radiation Detector (TRD), i.e. upwards; the origin is at the center of AMS and the magnetic field oriented along the x axis. The reference system of the ISS is, instead, rotated by 180 ° with respect to the z axis.

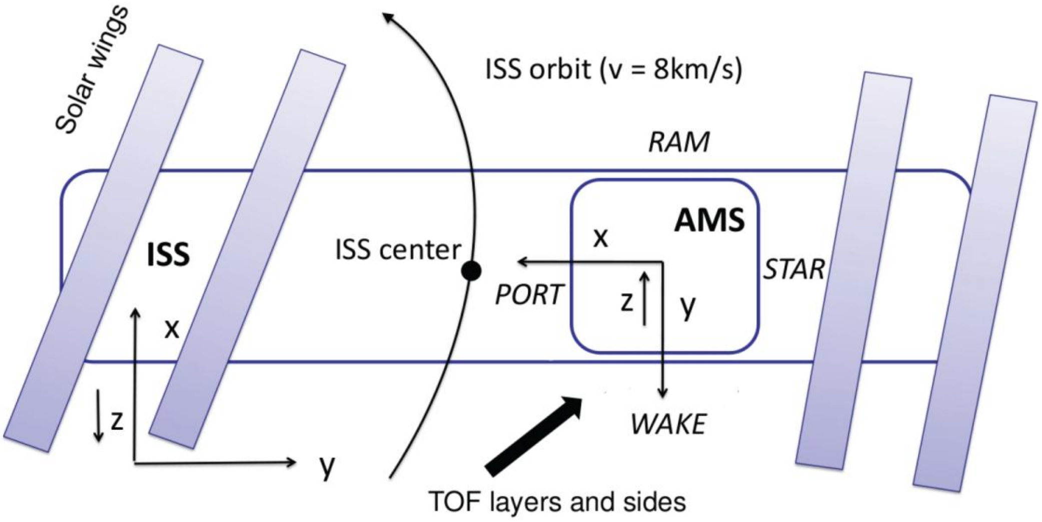

Figure 73 – Schematic view of reference frame of AMS in space on the ISS.

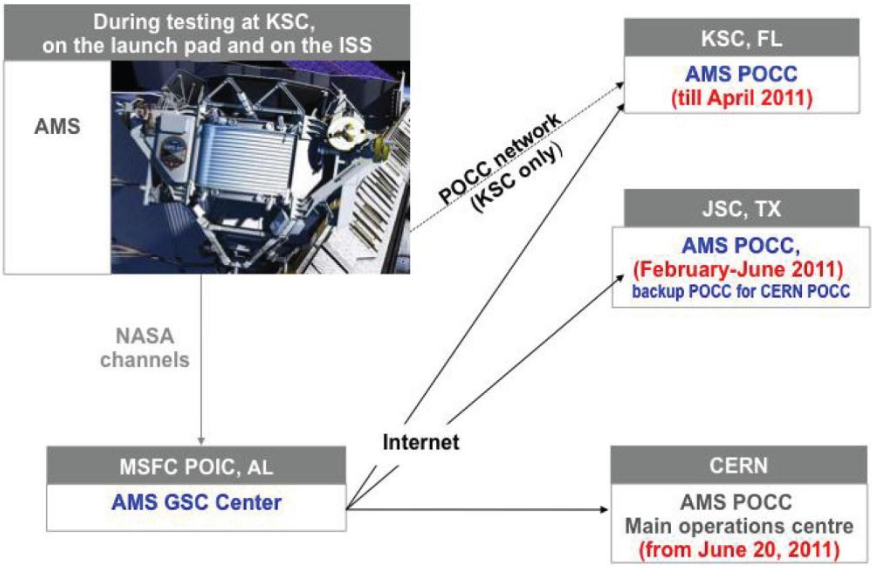

Figure 74 – The data flow of AMS-02: the data are downloaded by using the NASA "KU-Band" or the "S-band" and then transferred to the POCC. The POCC is currently located at CERN, while in the past was placed before at the Kennedy Space Center in Florida and then at the Johnson Space Center in Houston.

Let's explain the data flow (Fig. 74). AMS-02 data flow [403] allows for data recording on the AMS Laptop right on board the International Space Station (ISS) as well as for a direct transmission, by means of satellites, to Marshall Space Flight Center (MSFC) in Alabama. From MSFC, via internet, the bulk of the data flow to the Payload Operation Control Center (POCC), while critical health data (CHD) are directly transmitted from AMS-02 to the POCC in order to have a quick overview of the detector status. At POCC, beside the control activity during flight operations, online data monitoring is performed to verify the correct subdetectors operation. Then, the data are sent to the Science Operation Center (SOC) where they are processed and analyzed. Subsequently, data are distributed from SOC to Regional Sites, which will store AMS-02 data and are Monte Carlo production facilities as well. The Milano-Bicocca Data Transfer (DT) system overviews the overall data transfer from/to CERN, where the final POCC and SOC are located, to/from Regional Sites [425].

The Italian Ground Segment Data Storage (IGSDS), located at CNAF in Bologna (Italy), hosts a master copy of the whole AMS-02 data sample: raw frames, reconstructed and simulated data. The corresponding data volume is around 150 TB per year. The IGSDS acts as a "distribution center", in order to allow fast data access to the AMS collaborators, meanwhile avoiding interfering with SOC activities. IGSDS will also provide computing power for Monte Carlo production and analysis facility, as a part of the network of AMS Regional Sites. Data Transfer software was developed and is maintained by INFN Milano-Bicocca since 2004. Its core is a Multi-threaded finite state automa plus state transition jobs. It uses a database (Mysql/Oracle) for book-keeping and can work in GRID and non-GRID environments. AMS-02 Milano-Bicocca DT system's aim is to move data efficiently from SOC to IGSDS, without interfering with SOC activities and keeping track of what successfully or unsuccessfully has been moved. The minimum throughput required is 36 Mb/s, being three times the data rate foreseen: this makes possible, in case of DT malfunction, a fast recovery of data sets alignment (at CERN and at CNAF). The DT is also capable of moving data from remote locations to SOC, which can be useful for example in case of Monte Carlo production taking place in regional sites. Thanks to its flexibility and implementation easiness, the data transfer system has been installed on the following locations: IGSDS at CNAF (Bologna) ASI Science Data Center, Beijing Univ. Aeronautics and Astronautics (BUAA/NLAA), South East University (SEU).

4.9 The Payload Operation Control Center

Since Monday June 27th 2011 at 5:00 am GMT, AMS-02 is controlled from the newly built POCC (Payload Operation Control Center) at CERN (Prevessin Side). Continuous shifts are organized to monitor AMS-02 operation and the continuous flow of data to ground.

The transition started on Wednesday June 22nd, and took place smoothly, initially with two shifts overlapping between JSC and CERN. The average experiment downlink rate is about 10 Mbps, with peaks at higher rate to cope with the periods when the downlink channel is not available.

On June 26th the POCC has been inaugurated in the presence of two exceptional guests, Charlie Bolden, NASA Administrator and Rolf Heuer, CERN DG.

Through the summer AMS-02 will collect several billion of Cosmic Rays events (with a rate of about 50 million events per day), which, after reception at CERN, will be deframed and reconstructed at the CERN Science Operation Centers, before being sent to the various regional centers for calibration and analysis.

Figure 75 – The Payload Operation Control Center at CERN (Prevessin).

The experiment is controlled by the POCC 24 hours a day, 7 days on 7, and each subdetector of AMS-02 has a dedicated workstation to check the correct operation in space and the data quality. Daily AMS-02 team gets together for a meeting where data taking and any problems occurred the day before are discussed. I have actively participated in data taking, monitoring and calibration in each phase of the experiment, from KSC, through JSC to CERN. In this chapter I will illustrate the organization of data taking, some examples of troubles at the POCC and the main procedures for the data quality control developed from Bologna TOF-group, with my contribution.

As already said, the AMS space data are grouped in packages by the main experiment computer on the ISS and organized in *scientific*, *calibration* and *housekeeping* data. These packages are transmitted to a NASA computer at Marshall via satellites, with two bands of communication: the KU-Band, through which events are transferred with a rate of 10 Mbit/s, and the S-Band, through which events are transferred with a rate of 30 Kbit/s. The S-band also allows you to send commands to AMS-02 with a rate of 1 kbit/s and to have real-time *housekeeping data*, which contain information on temperatures and on the configuration parameters of main computers and all subdetectors' electronic boards. Then they're transferred to the POCC and the SOC at CERN, where they are checked and saved in dedicated computers (Fig. 75). If there are problems or errors in data transmission, on the ISS there's the *AMS ISS Laptop*, which allows you to store data with a two months capacity. The data stored in this primary computer are then transferred to the ground as soon as one of the two bands is available. From the AMS ISS laptop is also possible to send commands to AMS-02. POCC people and computers have to handle all activities related to the operation, control and monitoring of AMS-02 detector [426].

Hereinafter the data quality check and the electronic sensors monitoring are described, subdetector by subdetector.
In the TRD 30 on-board computer are used, which measure 482 temperatures, 5284 electronic signals and control valves and radiators in such a way as to maintain a uniform signal within 1%. In tracker the data control takes place thanks to 212 on-board computers, which measure 196608 electronic signals, the 20 positions of the alignment lasers, 142 temperatures and control the radiators. In the calorimeter the computers are 32 and manage around 2916 electronic signals. Six computers are used to control 492 temperature sensors 492 and 242 global radiators. Inside the POCC each subdetector has a specific location, three computers are dedicated to data quality monitoring, and a "LEAD" (the shift leader) coordinates operations, monitors the data taking, manages communications with NASA and sends commands to AMS-02 in space. The main operations of the POCC can be summarized as follows [425]:

1. To monitor daily operations and discuss with NASA USA control centers through voice loop.
2. To monitor all ISS on-board computers of the experiment to ensure that everything is working properly and coordinate activities between the ISS and AMS.
3. Send commands to AMS detector in case of problems.
4. Monitoring the correct functioning of the main data acquisition computer and the AMS level 1 trigger.
5. To receive and store data from POIC (Payload Operations and Integration Center at NASA's Marshall Center, managing the AMS laptop computer and the data stream between AMS and the POCC.
6. To process about 10% of data in "real-time" mode to provide fast information to the shift taker.
7. To display the ISS video distribution (in Fig. 75).
8. To check all subdetector temperatures.
9. To check the calibration of each subdetector, to monitor performances and report anomalies.
10. To check the ISS temperature, enable or disable the radiators and evaluate the possible relocation of the ISS radiators solar panel wings.

During the first and half year of operations all subdetectors have correctly functioned, with the overall expected performances. The acquisition rate varies between approximately 200 Hz and 1600 Hz (Fig. 76), with a live time between 65% and 98%.

At the POCC are usually present five people, that control five stations: *LEAD*, *DATA*, which controls the data transfer from NASA to CERN, *THERMAL*, which controls all subdetectors, *TEE*, which monitors TRD and Tracker, and *PM* (that stands for "PhotoMultiplier"-based detectors), which controls RICH, ECAL and TOF. Before and after the Shuttle launch I managed the PM station as a shifter before and then as the TOF position expert on-call, who is allowed to send commands to the TOF in space, reboot programs, do calibrations, reload and modify TOF electronic board parameters through the configuration files (Fig. 84).

Here, some procedural examples will be given, to highlight the complexity of the operations required for the maintenance of the experiment and the scientific data monitoring. Inside the POCC, the PM position is responsible for the control of TOF, RICH and ECAL detectors. Its main task is the data quality monitoring for the three detectors and to send commands to AMS to correct problems.

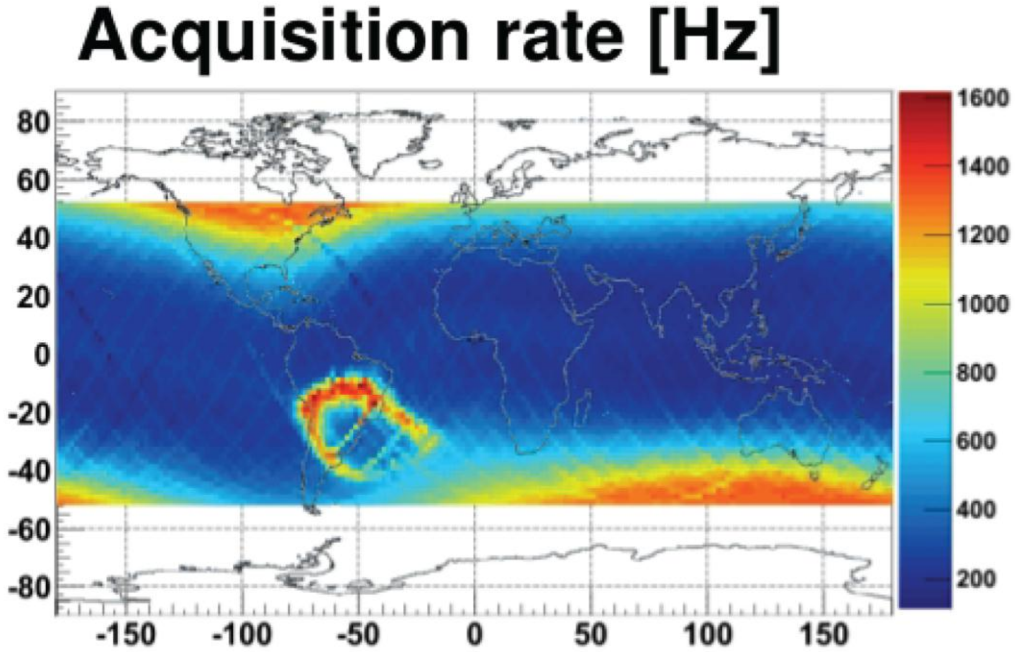

Figure 76 - Rate of acquisition as a function of geographical position, latitude on the abscissa and longitude on the ordinate. The rate, codified market the scale of the figure yet colored, varies between 200 and 1600 Hz.

ECAL and RICH location

Two computers of the PM station are dedicated to the electromagnetic calorimeter and several programs are available to monitor data quality and temperatures. The shifter must essentially act on three occasions [426]:

- Eventual noise in the trigger channels of the calorimeter, which could cause an increase in the dead time of AMS-02.
- Increase in temperature above the critical limits.
- Decrease of the temperature below the critical limits.

Regarding the first point, through the aid of a program that reconstructs a subset of data, it's possible to monitor all the cells in each plane of the calorimeter and verify signal values in ADC channels. A cell which gives a zero value indicates a dead one, whereas a cell whose value is an order of magnitude higher than the others represents a “hot” cell. With only one dead cell data acquisition can continue, but if a group of dead cell occurs and the problem persists for more than an hour it becomes necessary to restart some electronic boards using appropriate commands. For hot cells, if they produce a significant increase in the trigger rate, they must be removed from the trigger logic. Regarding the last two points, a specific monitoring tool for temperatures is available. If the temperatures are out of critical limits critics, you have to agree with the LEAD a procedure for switching on the radiators or switching off the detector. For the RICH, a unique monitoring program exists, which allows the shifter to control five eventualities:

- RICH desynchronization during the data taking. If the desynchronization is longer than an hour, the data taking must be restarted, in coordination with LEAD.
- Bad calibrations.
- Different PMTs tensions from the nominal value.
- PMTs whose signal is too low or too high.

In each of these cases, the LEAD must make a series of agreed procedures with RICH experts.

TOF position: Online monitoring

TOF is configured and monitored using several software. For commanding/configuration there are:

- BBtool - a software used to communicate and send commands to S-crates.
- SDR2, SPT2, SFET2, Brick command interfaces - used to send direct commands to TOF boards and SHV bricks.
- AMSTOF_configuration - used to generate TOF configuration file in a format compatible with the DSP program.

For pure monitoring, the following programs are used:

- *Slow control* PDS-M, JLV1-M, SPT2-M and TOF-DTS-M are used to monitor TOF input currents, trigger signals and temperatures.
- DAQ software

TOF online monitor is used during data acquisition to verify TOF configuration and data quality [427].

During the first and half year of operations in space the Time of Flight System had no particular problems in data acquisition. During the first few days of operation, as anticipated, several tests were made to verify the correct functioning of the Time of Flight:

1. A check of the supply voltages for each photomultiplier (PMT), to measure the gain curves in space (20-22/05/2011).
2. A check of the thresholds (LT, HT and SHT), for each counter.
3. A check of the trigger efficiency and of the tension curves for each PMT.

Through these tests it has been shown that the values set on the ground did not need modifications and the TOF performances were coherent with those measured before the flight.
Also anode-dynode charge ratio analysis has been performed to verify the power law (linear in bilogarithmic scale) relation measured on ground.

During these 18 months of activity several routine procedures have been standardized. The most remarkable, to be run once every 30 minutes, are [427]:

1. To verify that each TOF counter is operative, controlling the trigger signal behavior in the last 2-3 minutes (Fig. 77).
2. To check the event size for each S-Crate (Fig. 78).
3. To control the number of times the signal exceeds the LT threshold each counter. This number should not be zero (Fig. 79) and not too high.
4. To control the number of times the signal exceeds the HT threshold HT for each counter. This number should not be zero (Fig. 80) and not too high.
5. To check the calibrations stability, i. e. the noise trend (Fig. 82).
6. To check in the housekeeping data the stability of the parameters written in the TOF boards and of the temperatures (Fig. 83).

All monitoring TOF software has been tested and developed with a common effort by the group of Bologna.

Sometimes, some errors, due to “bit flips” occur, i. e. unexpected and random changes in some bits of the electronic boards, which led to the random change of TOF parameters (Fig. 83). These errors are mainly due to interactions of cosmic rays with the electronic boards. So two different programs have been developed and tested, to allow you to automatically resolve such errors, easily reloading the nominal configurations files.

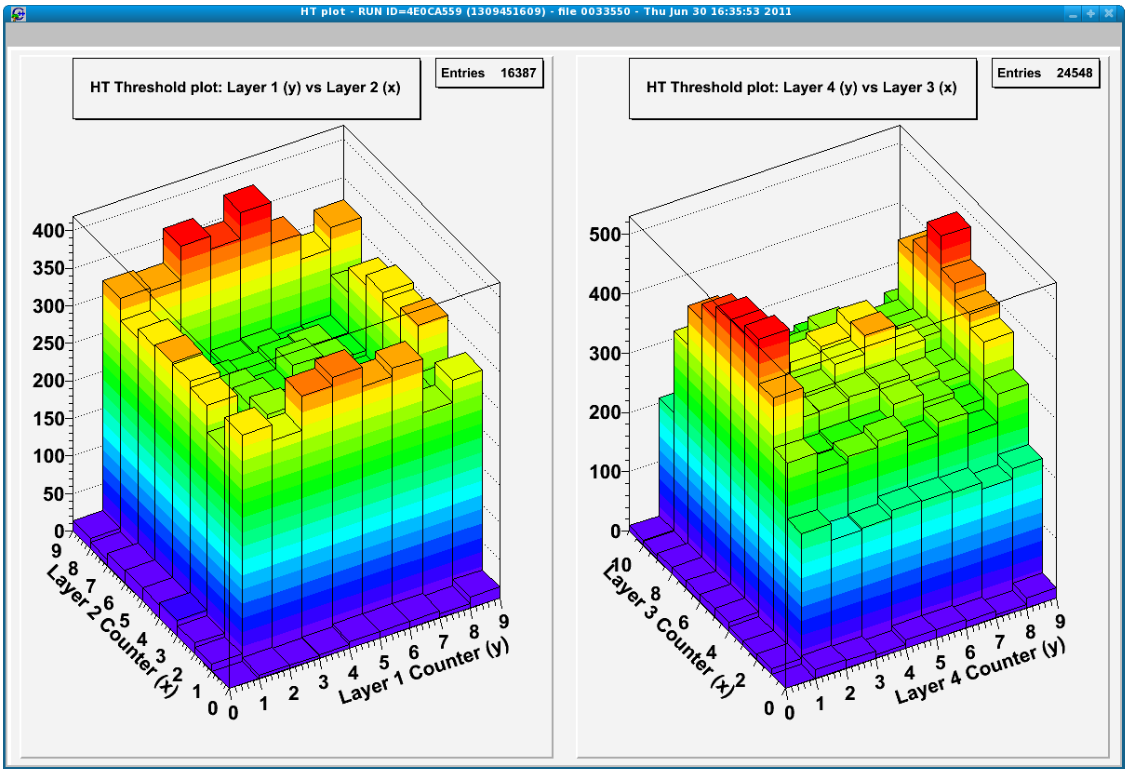

Figure 77 – These two histograms give a global view that the TOF is triggering, in particular they show the number of times each TOF counter gave a trigger in the last 2-3 minutes. On the left the Upper TOF (layer 1 on y, layer 2 on x) – the z-axis shows the number of triggers for each detector - on the right the Lower TOF. The shifter should check that these histograms are not empty [427].

During the first week of data taking, the TOF had problems with a photomultiplier (Fig. 81), and it was necessary to lower the supply voltage from 2150 V to 1750 V for avoid discharges, which could result in data corruption and damages for the contiguous PMTs. After two weeks the tension has been set again to the nominal value (2150 V) and the PMT returned to work properly. Other major operations have been the raising of the low threshold of the counter 8 of the layer 4, in order to reduce the noise, and the decision to exclude from the Z=1 trigger the two external counters of the layer 3, following a common statement of the collaboration for conformance to the Tracker acceptance.

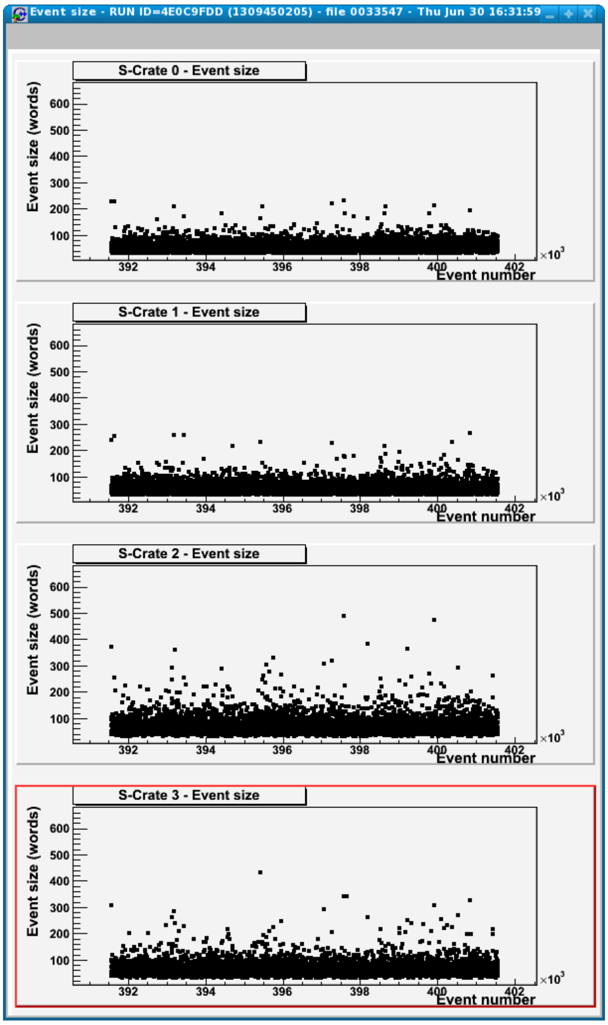

Figure 78 - *Events Size* in number of words as a function of the event number. The four figures refer to the four TOF S-Crates. The number of words for each S-Crate must be around 100÷200 [427]. In the SAA the crates event size increase and could become a series of sharp peaks.

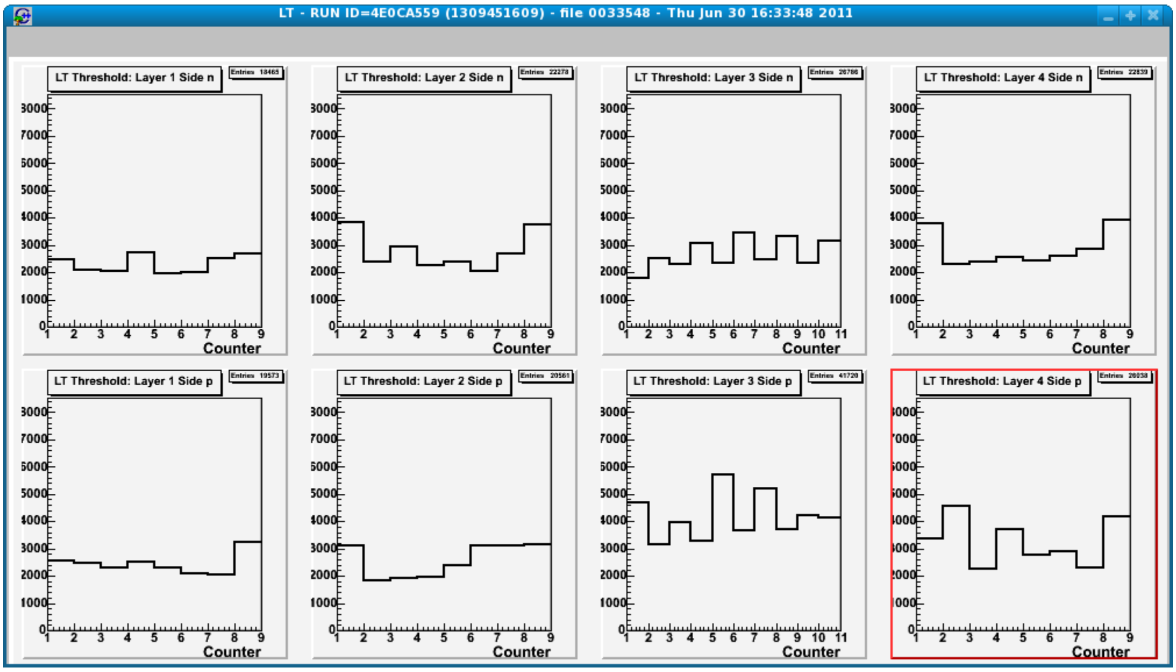

Figure 79 - Screenshot of the program for data quality control. These histograms show the number of times that the signal cross the low thresholds used for the time measurements (number of hits in the TDC). From left to right each couple of histograms (top for side n counters and bottom for positive ones) represent respectively the first, the second, the third and the fourth TOF layer.
In each histogram the number of hits measured in each TOF counter is shown. The shifter has to check that all the counters are giving some hits (no holes should be presents), considering that layers 3 side p and 4 side p, linked to SCrate 2, are usually noisier [427].

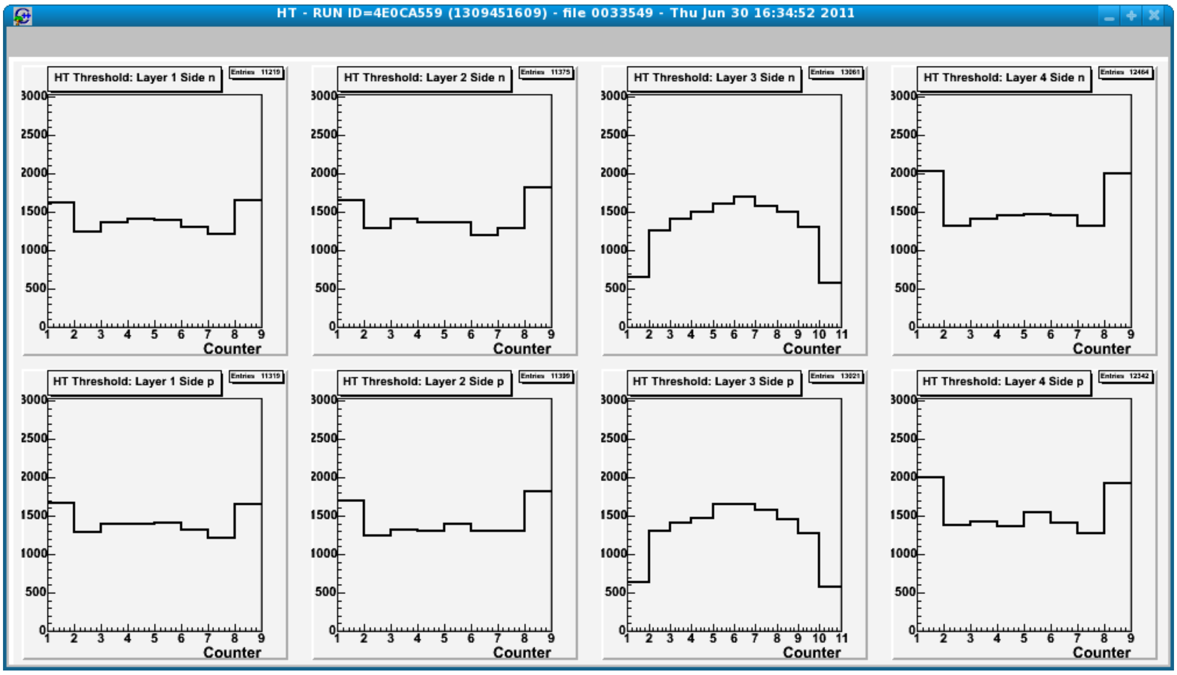

Figure 80 – The same of the previous figure, for the HT thresholds. The first and last counter of each plot give always more counts because of geometrical reasons (their trapezoidal, with a larger surface), except for layer 3, which has 10 counters, because counters 1 and 10 are removed from the physical trigger. This was done to have an acceptance conform to the Tracker [427].

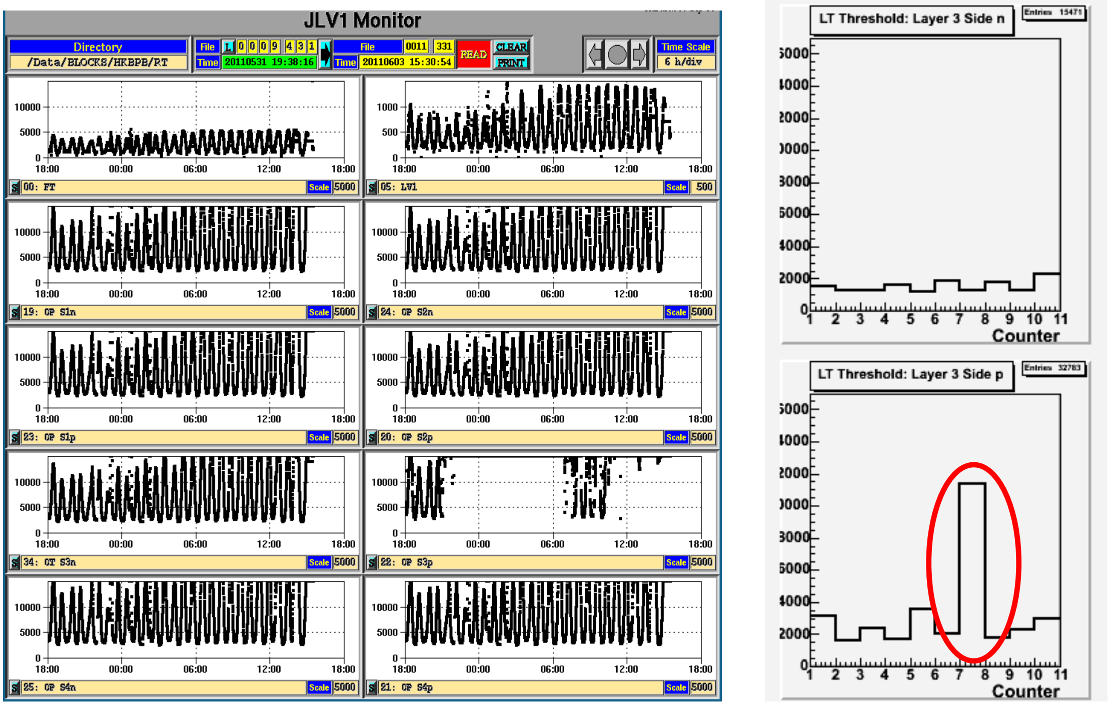

Figure 81 – The JLV1 monitor shows the FT, the LV1 (upper panel) and the TOF CP inputs to the trigger box for each layer and side. JLV1 monitor shows anomalous peaks, due to an unknown noise (left) and the corresponding LT high count for the layer 3, counter 7, side p associated with the S2 crate: a broken phototube which was producing a discharge, altering the counts. This is an example of problems occurred at the end of May-first of June 2011 [428].

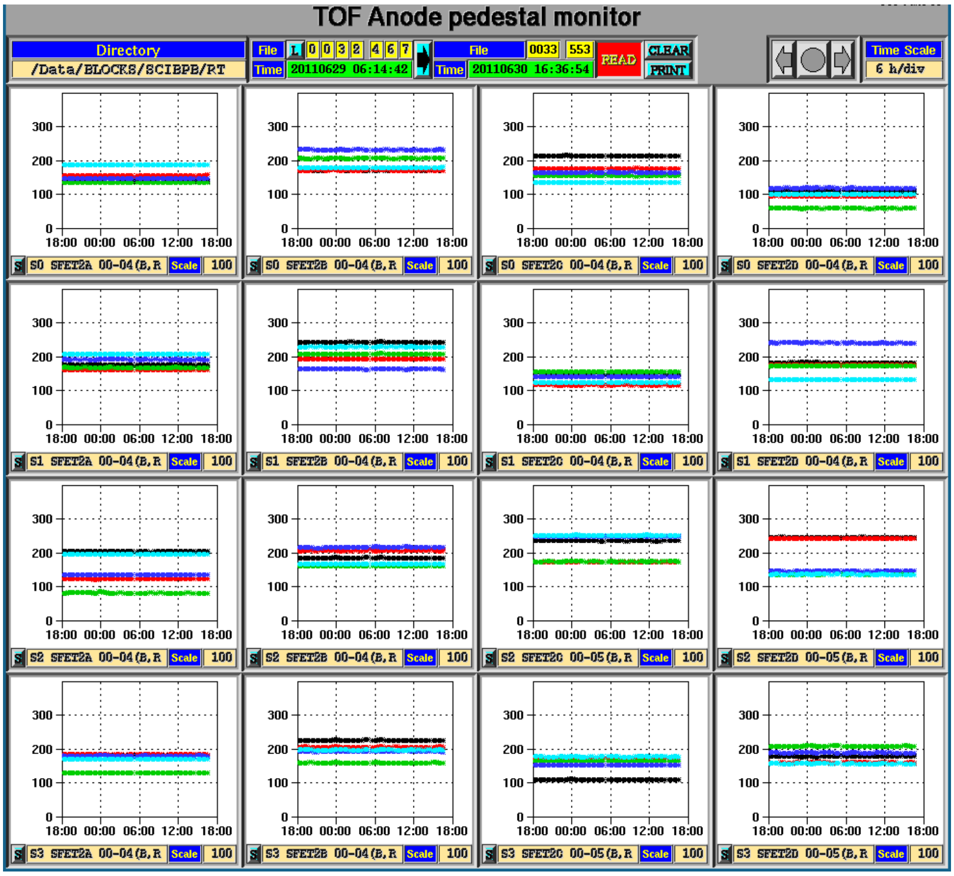

Figure 82 - Anodic Pedestal signals (in ADC channels) for SFETs boards as a function of time. The pedestal must be stable over the time [427].

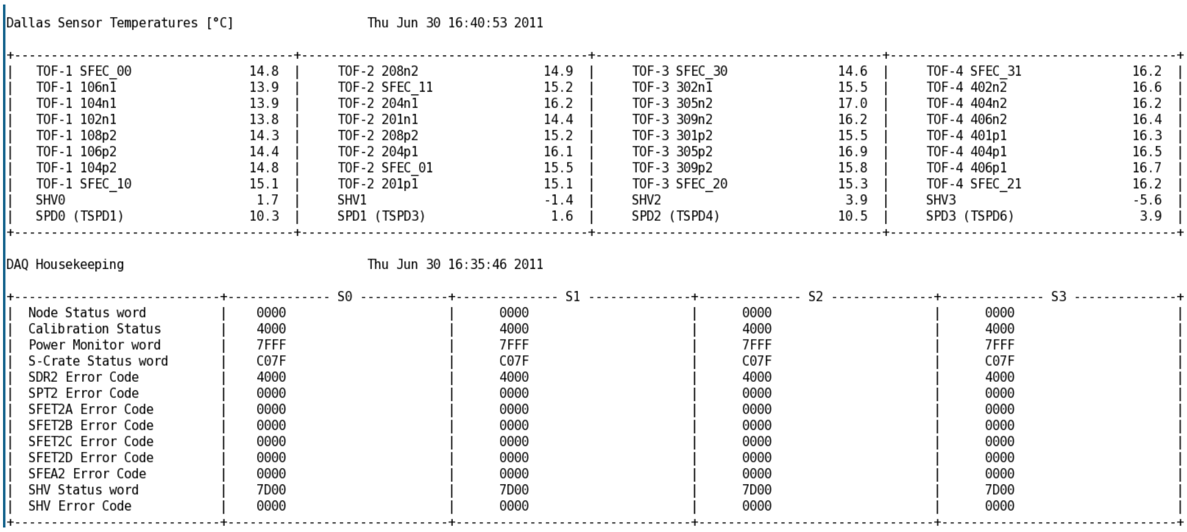

```
Dallas Sensor Temperatures [°C]                   Thu Jun 30 16:40:53 2011

+---------------------------------------+---------------------------------------+---------------------------------------+---------------------------------------+
|   TOF-1 SFEC_00              14.8  |     TOF-2 208n2                 14.9  |     TOF-3 SFEC_30               14.6  |     TOF-4 SFEC_31               16.2  |
|   TOF-1 106n1                13.9  |     TOF-2 SFEC_11               15.2  |     TOF-3 302n1                 15.5  |     TOF-4 402n2                 16.6  |
|   TOF-1 104n1                13.9  |     TOF-2 204n1                 16.2  |     TOF-3 305n2                 17.0  |     TOF-4 404n2                 16.2  |
|   TOF-1 102n1                13.8  |     TOF-2 201n1                 14.4  |     TOF-3 309n2                 16.2  |     TOF-4 406n2                 16.4  |
|   TOF-1 108p2                14.3  |     TOF-2 208p2                 15.2  |     TOF-3 301p2                 15.5  |     TOF-4 401p1                 16.3  |
|   TOF-1 106p2                14.4  |     TOF-2 204p1                 16.1  |     TOF-3 305p2                 16.9  |     TOF-4 404p1                 16.5  |
|   TOF-1 104p2                14.8  |     TOF-2 SFEC_01               15.5  |     TOF-3 309p2                 15.8  |     TOF-4 406p1                 16.7  |
|   TOF-1 SFEC_10              15.1  |     TOF-2 201p1                 15.1  |     TOF-3 SFEC_20               15.3  |     TOF-4 SFEC_21               16.2  |
|   SHV0                        1.7  |     SHV1                        -1.4  |     SHV2                         3.9  |     SHV3                        -5.6  |
|   SPD0 (TSPD1)               10.3  |     SPD1 (TSPD3)                 1.6  |     SPD2 (TSPD4)                10.5  |     SPD3 (TSPD6)                 3.9  |
+---------------------------------------+---------------------------------------+---------------------------------------+---------------------------------------+

DAQ Housekeeping                                  Thu Jun 30 16:35:46 2011

+-----------------------------+-------------- S0 ------------+-------------- S1 --------------+-------------- S2 --------------+-------------- S3 --------------+
|  Node Status word           |    0000                      |     0000                       |     0000                       |     0000                       |
|  Calibration Status         |    4000                      |     4000                       |     4000                       |     4000                       |
|  Power Monitor word         |    7FFF                      |     7FFF                       |     7FFF                       |     7FFF                       |
|  S-Crate Status word        |    C07F                      |     C07F                       |     C07F                       |     C07F                       |
|  SDR2 Error Code            |    4000                      |     4000                       |     4000                       |     4000                       |
|  SPT2 Error Code            |    0000                      |     0000                       |     0000                       |     0000                       |
|  SFET2A Error Code          |    0000                      |     0000                       |     0000                       |     0000                       |
|  SFET2B Error Code          |    0000                      |     0000                       |     0000                       |     0000                       |
|  SFET2C Error Code          |    0000                      |     0000                       |     0000                       |     0000                       |
|  SFET2D Error Code          |    0000                      |     0000                       |     0000                       |     0000                       |
|  SFEA2 Error Code           |    0000                      |     0000                       |     0000                       |     0000                       |
|  SHV Status word            |    7D00                      |     7D00                       |     7D00                       |     7D00                       |
|  SHV Error Code             |    0000                      |     0000                       |     0000                       |     0000                       |
+-----------------------------+------------------------------+--------------------------------+--------------------------------+--------------------------------+
```

Figure 83 – "Housekeeping" Data Monitor. The first table shows the temperatures for each TOF board, while the second shows error code or status words for each electronics component of each TOF counter (see chapter). Words with different values from those of reference are shown in red and indicate an error board. In this case, as usual, no errors occurred [427].

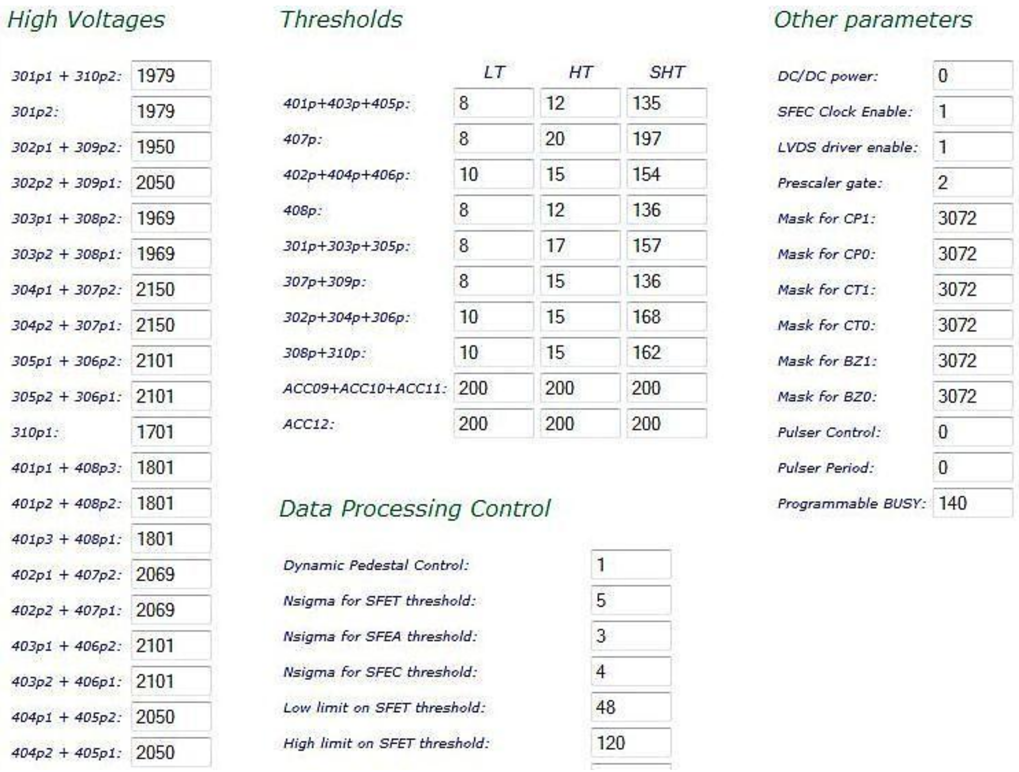

High Voltages

301p1 + 310p2: 1979
301p2: 1979
302p1 + 309p2: 1950
302p2 + 309p1: 2050
303p1 + 308p2: 1969
303p2 + 308p1: 1969
304p1 + 307p2: 2150
304p2 + 307p1: 2150
305p1 + 306p2: 2101
305p2 + 306p1: 2101
310p1: 1701
401p1 + 408p3: 1801
401p2 + 408p2: 1801
401p3 + 408p1: 1801
402p1 + 407p2: 2069
402p2 + 407p1: 2069
403p1 + 406p2: 2101
403p2 + 406p1: 2101
404p1 + 405p2: 2050
404p2 + 405p1: 2050

Thresholds

	LT	HT	SHT
401p+403p+405p:	8	12	135
407p:	8	20	197
402p+404p+406p:	10	15	154
408p:	8	12	136
301p+303p+305p:	8	17	157
307p+309p:	8	15	136
302p+304p+306p:	10	15	168
308p+310p:	10	15	162
ACC09+ACC10+ACC11:	200	200	200
ACC12:	200	200	200

Data Processing Control

Dynamic Pedestal Control: 1
Nsigma for SFET threshold: 5
Nsigma for SFEA threshold: 3
Nsigma for SFEC threshold: 4
Low limit on SFET threshold: 48
High limit on SFET threshold: 120

Other parameters

DC/DC power: 0
SFEC Clock Enable: 1
LVDS driver enable: 1
Prescaler gate: 2
Mask for CP1: 3072
Mask for CP0: 3072
Mask for CT1: 3072
Mask for CT0: 3072
Mask for BZ1: 3072
Mask for BZ0: 3072
Pulser Control: 0
Pulser Period: 0
Programmable BUSY: 140

Figure 84 – TOF configuration program. (http://g5.ambra.unibo.it/AMSTOF_configuration/index.php). Parameters table for the S2 crate.

This program is an example of expert on-call responsibility and it is used to generate TOF and ACC configuration files in the DSP format containing all the parameters for the TOF electronics. This software, written in *php*, is installed in a web server and accessible through internet from any sites (username and password are required).

A user friendly interface allows changing the key parameters described before for the tuning of the detector. All the generated configuration files are stored in the disc so they can be reused in a second moment to reconfigure the detector or to check the used configuration of the detector in a specific date.

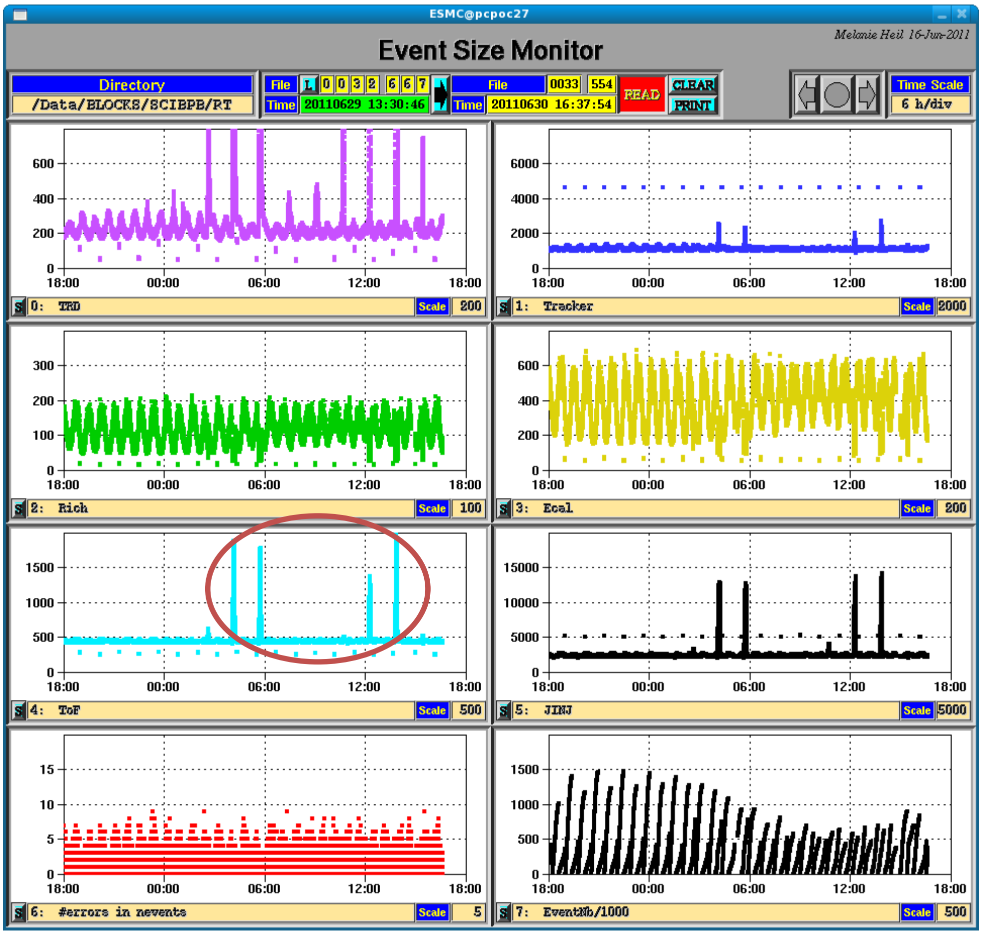

Directory /Data/BLOCKS/SCIBPB/RT

File L 0 0 3 2 6 6 7 Time 20110629 13:30:46

File 0033 554 Time 20110630 16:37:54

Time Scale 6 h/div

Figure 85 – The *Event Size Monitor* is a general monitor, also used by the lead, to control the size of the events for each subdetector. In the TOF one, you can see (circled) the known periodic peaks due to the South Atlantic Anomaly [427].

Solar Beta angle

A photomultiplier (layer 3, counter 9), for five days in January 2012, has reached a temperature of “warning” (30° C, Fig. 87). Temperature increasing is due to the “Solar Beta Angle” cycles.

The beta angle (β) is a measurement that is used most notably in spaceflight. The beta angle determines the percentage of time an object such as a spacecraft in Low Earth Orbit (LEO) spends in direct sunlight, absorbing solar energy. Beta angle is defined as the angle between the orbit plane and the vector from the sun (which direction the sun is shining from, Fig. 86). The beta angle is the smaller angle (there are two angles) between the sun vector (where the sun is shining from in the sky) and the plane of the object's orbit. Note that the beta angle does not define a unique orbit plane; all satellites in orbit with a given beta angle at a given altitude have the same exposure to the sun, even though they may be orbiting in completely different planes around the Earth. The beta angle varies between +90° and −90°, and the direction the satellite revolves around the body it orbits determines whether the beta angle sign is positive or negative. An imaginary observer standing on the sun defines a beta angle as positive if the satellite in question orbits in a counter clockwise direction and negative if it revolves clockwise.

The complicated simulations and temperature measurements of the various subdetectors have been studied by experts in function of the Solar Beta Angle. For the Lower TOF, a decrease in the

Solar Beta Angle results in a temperature increase of the counters. During the month of January, the temperature has exceeded the warning when the Solar Beta Angle has reached its minimum from the month of May (Fig. 87). The warning is disappeared as soon as the Solar Beta Angle has decreased and there were no other thermal problems.

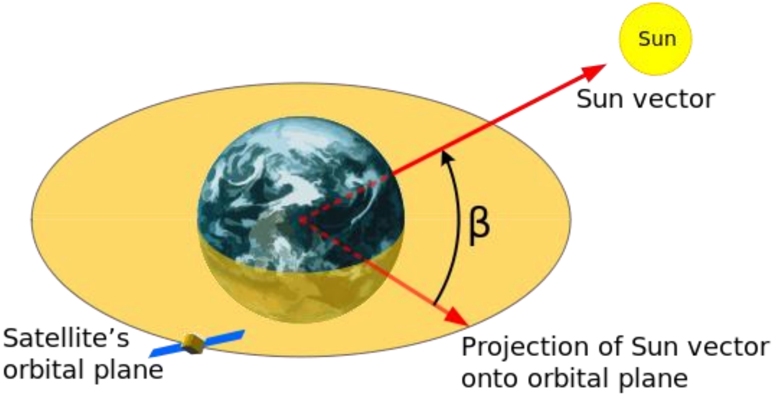

Figure 86 – Solar Beta Angle representation.

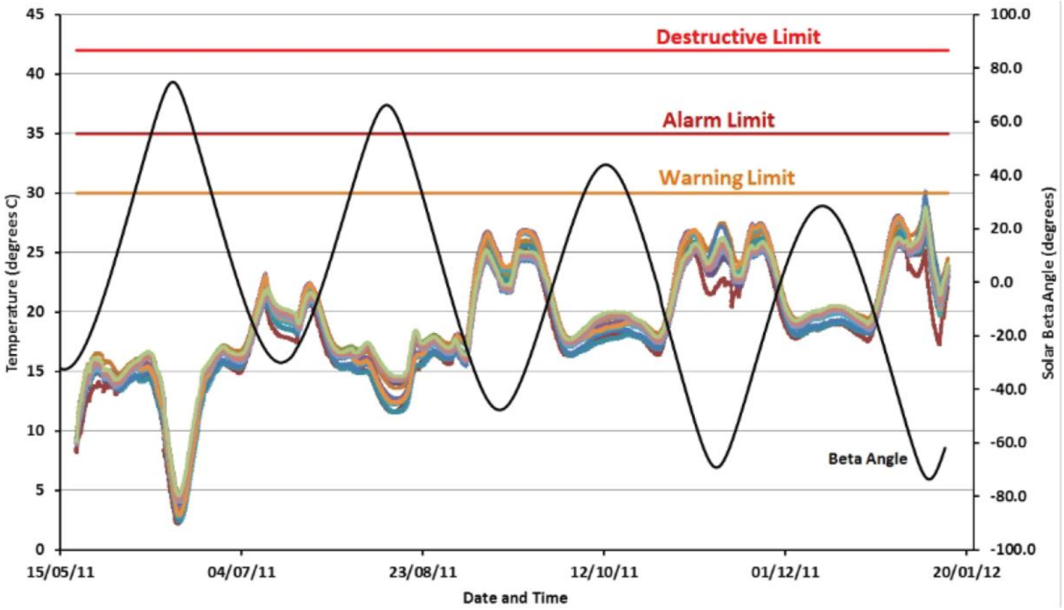

Figure 87 - Temperature sensitivity of photomultiplier tubes (colored curves), expressed in Celsius degrees, from 22 May 2011 up to 15 January 2012. The three “Warning” (30° C), “Alarm” (35° C), and Destruction (42° C) temperatures are drawn (straight lines). Is also shown the trend of the “Solar beta angle” (in degrees) in the period before mentioned (black curve). In this period only a photomultiplier has exceeded the limit of Warning [429].

TOF position: Offline Monitoring

The tools described so far are on-line monitoring tools. To check specific properties of the TOF detector using the just collected data, such as TDC/ADC signals, efficiencies, alignment, threshold behaviors (Figs. 88-91) and also particle properties (mass, momentum, TOF charge and beta), I developed a proper offline monitor, running on POCC data. This is a performance monitor for expert which gives you some peculiar information about the TOF physical response and represents a sort of pre-analysis tool.

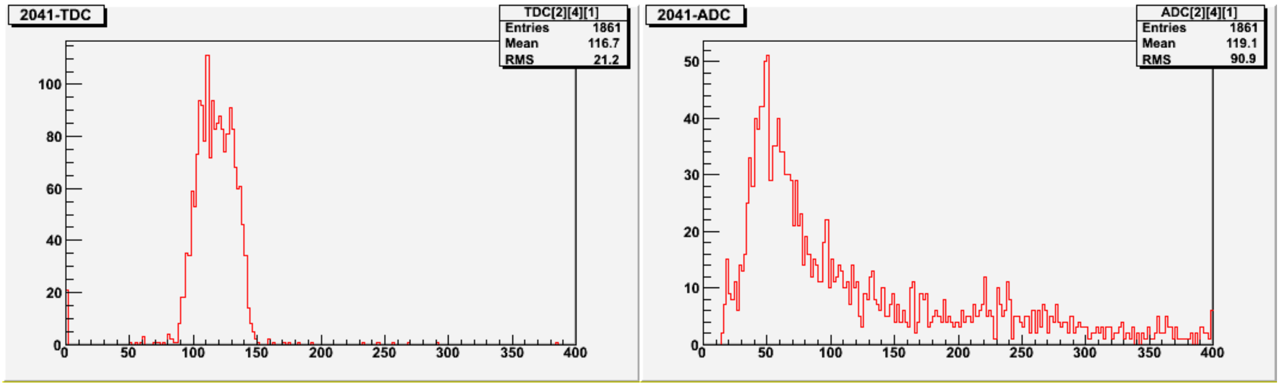

Figure 88 – TDC and ADC channel signals in pC. On the y axis the number of events.

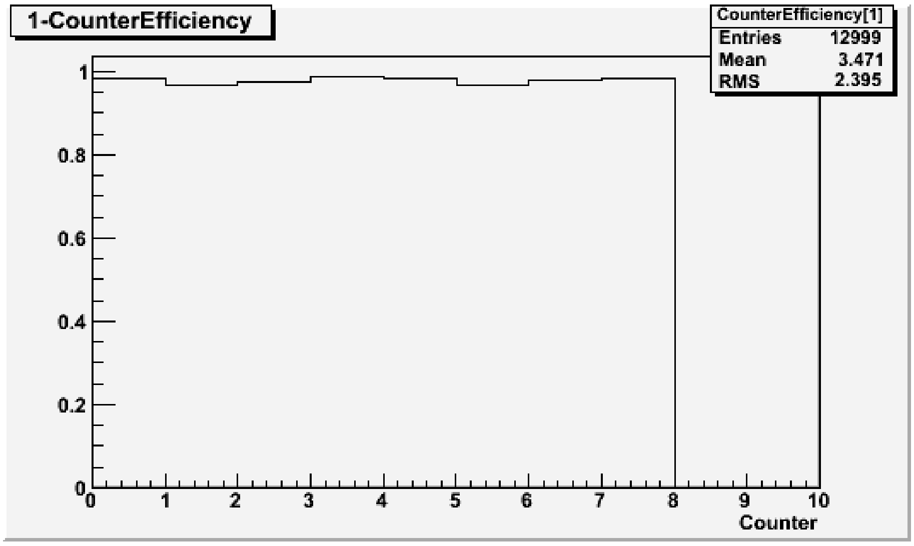

Figure 89 – Example of counter efficiency monitoring for a TOF counter in the first layer.

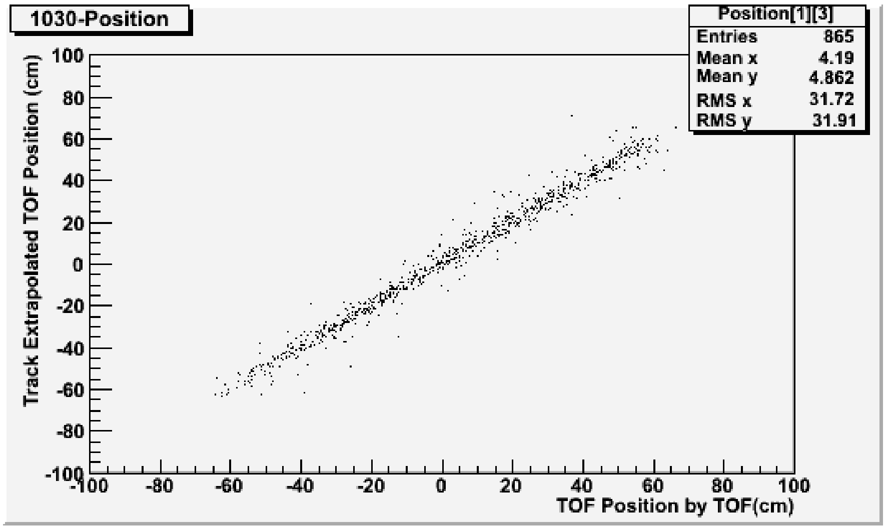

Figure 90 – TOF x position alignment with respect Tracker coordinate for the layer 1, counter 3, side n (marked with 1, 03, 0).

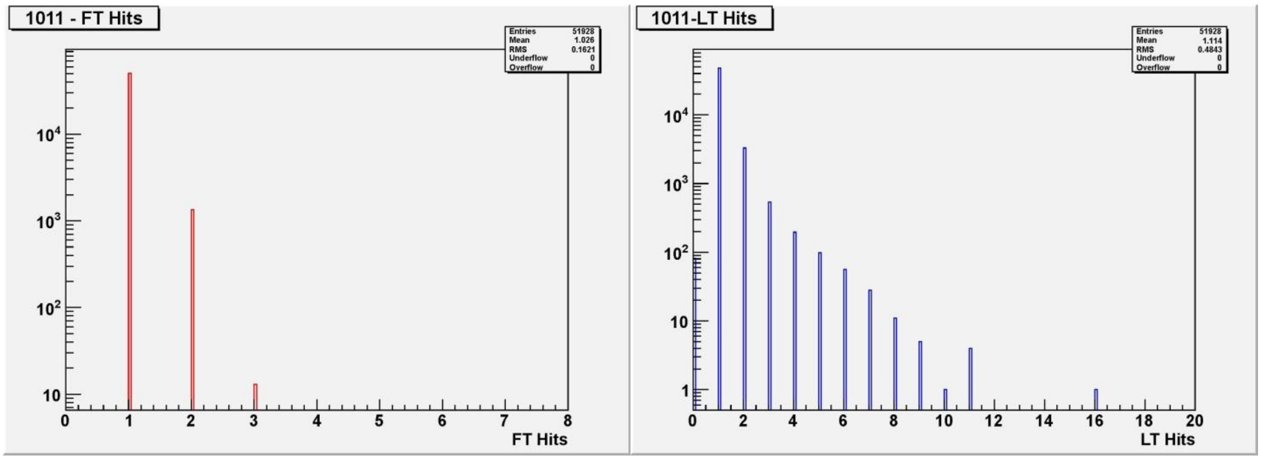

Figure 91 – Fast Trigger (left) and Low Threshold (right) hits time history in a randomly selected sample of data for the layer 1, counter 1, side p (1011). On the y axis the number of events.

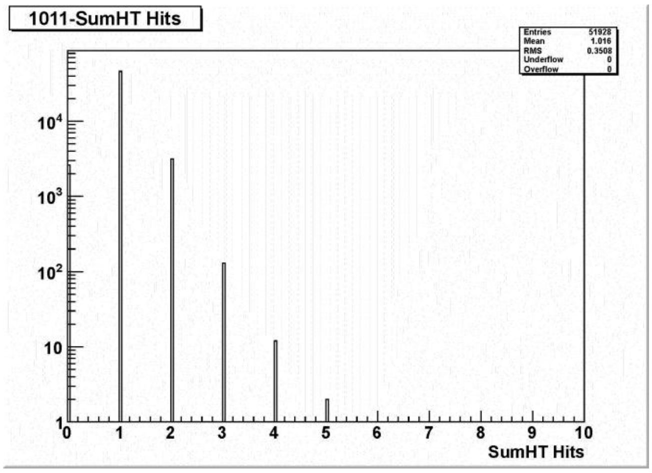

Figure 92 – High Threshold hits time history in a randomly selected sample of data for the layer 1, counter 1, side p.

Chapter 5

The Analysis: Event Selection and Cut Stability

5.1 Events Selection

The first AMS-02 Collaboration paper, expected to be published in the coming months, will concern the positron fraction (i.e. the ratio of positrons to all electrons) as a function of energy.
The data selection presented in this chapter is not meant to maximize the signal efficiency, nor to be the final analysis of the positron fraction. Its purpose is to assess the stability of AMS-02 physical measurements in time so as to verify AMS-02 capability to discover the dark matter signals discussed in chapter 3.
In this chapter the main analysis cuts are illustrated, including the fundamental background for the lepton analysis together with subdetectors lepton-hadron discrimination, and results are presented.

5.1.1 Background description

The basic aim of the analysis and of the cut chain is to increase the signal quality, rejecting background and bad reconstructions. A good selection should have the following properties:

1. maximum efficiency for signal: events of the species under study should survive the cut;
2. maximum rejection of badly reconstructed events: events without the required quality on detection and off-line reconstruction should be rejected. These events are potentially dangerous. They can be due to background or, even if due to signal, they can contaminate the measurement;
3. maximum rejection of background: the events of different species should be rejected by the cuts.

In real cases, each single cut is meant to satisfy, as much efficiently as possible, point 2 or point 3. Moreover, to reach optimized cut efficiencies is not the purpose of the present analysis, which is focused on the temporal stability of the selection and on the particle species discrimination.

Badly reconstructed events
To select a good analysis sample, against badly reconstructed events, it’s necessary to define what a “well detected” event corresponds to. Sources of badly reconstructed events can be:
Wrong Charge (WC): events reconstructed with the wrong sign of the charge. These events can be due to spillover or to anomalous deflection in the detector. The “Wrong Charge” particles are mainly at high rigidities because of the spillover effect;
Low Reconstructed Rigidity (LR): events with a low measured rigidity (few GV) but high energy release in the calorimeter (tens of GeV). These events are generally due to interactions in the detector, such as δ rays production, pair production and multiple scattering. In our sample this is not an important contamination.
More important are **Bremsstrahlung photons conversion and ECAL-backsplash particles**, which can also produce multiple tracks and signals in TOF and ACC.

The main **instrumental background** is represented by events without an associated Tracker track, events with several ACC signals, probably due to particles entering the side of the detector, events with less than three TOF planes signals registered, events in the South Atlantic Anomaly region, particle passing through or produced in the ISS solar arrays panels, upgoing particles, which may come from interactions with the ISS structure.

Main **physical particle background** contamination for positrons is obviously constituted by protons, which have the same charge and whose flux is almost 4 orders of magnitude more intense. TRD and ECAL allow for an electron/proton rejection at the needed level. In addition, electrons could appear as positively charged due to Wrong Charge reconstruction.
Charged pions are a source of background only at very low energies.

5.1.2 Variables definition

The following variables are used in the analysis:

- *Geographical and Geomagnetic longitude and latitude coordinates*: through GPS, ISS coordinate localization and the IGRF simulation (which takes into account the periodic variation of the Earth magnetic dipole axis), the geographical and geomagnetic AMS position is continuously traced with a per mill precision.
- *TOF scalers rate and livetime*: the trigger rate measured by the upper TOF can be used as a definition of the SAA, as explained in section 4.6.2. In the same way, a livetime > 0.65 cut can be used to separate poor exposure times from good data taking.
- *Geomagnetic Cutoff*: this is the physical rigidity value which separates the region where AMS data are *geomagnetic and solar-wind*-free. It is a function of geomagnetic latitude.
- *DAQ status words*: as discussed in chapter 4.5, there are several DAQ electronic words, which describe the accuracy of the data acquisition chain. Many types of error may occur.
- *Status words for subdetectors*: these are specific electronic sensors responses to verify the efficiency of each subdetector data taking, allowing to identify peculiar errors or event misalignments. A bad runs list, which contains every known data taking error has been validated.
- *Run tag*: the AMS runs (packages of data) must be “science-like” and not calibration or housekeeping ones. Each science run lasts for about thirty minutes.
- *ISS configuration*: AMS-02 is attached to the ISS, so it follows ISS altitude and orbit. The position of the Station influences AMS subdetectors temperatures; moreover the solar wings may represent an important obstruction for data taking because they can shadow a portion of AMS solid angle acceptance. Finally, GPS Antenna and other AMS electronic instrumentation could be affected by ISS hardware in proximity.
- *Data period selection*: the data period has to be chosen as a function of the analysis but, primarily, the bad runs periods must be rejected.
- *Number of ACC*: the number of ACC counters that have fired for a specific event is very important because it separates good downgoing events from transverse ones. A too severe choice of the maximum number of anticoincidence may lower the statistics, taking into account that multiple ACCs could derive from electronic delta rays or backsplash particles from the calorimeter.
- *Number of TOF layers*: to validate an event, the number of TOF layers (and clusters) which have given a signal must be checked.
- *Number of TRD segments*: this is the number of track segments in the TRD. The proper number of X and Y has to be present.

- *Number of particles*: a “particle” is defined as a set of subdetectors giving correlated signals.
- *Number of Tracks*: events may have multiple Tracker tracks, due to Bremsstrahlung effects and interactions in the whole detector.
- *Geometrical X-Y-Z variables*: the detector has a 3D system of coordinates with respect to which each subdetector element has a specific position. The travel of the particle through AMS is reconstructed in the three dimensions, matching trajectories for each subdetector.
- *ECAL acceptance*: for a proper electron/positron identification, the particle must pass through the ECAL, i. e. it has to fall into its X-Y geometrical acceptance.
- *Chi-square for Tracker tracks*: the goodness of the Tracker track is checked with a χ^2 method.
- *TOF and Tracker Charge*: the absolute charge is measured by TOF and Tracker. The Tracker is especially important for low charge measurements, the TOF for high charges. The sign of the charge is determined by the curvature and by the particle direction (upward or downward).
- *Beta (TOF)*: this the particle velocity. Only positive betas (i.e. downgoing particles) are used for the analysis.
- *Energy deposited (ECAL)*: this is the shower reconstructed energy (GeV). Through the deposited energy, the total particle energy is computed. For ultrarelativistic electrons and positrons energy and rigidity should be equal, but resolution of the Tracker, losses in the calorimeter and rigidity migration, due to interaction in the detector, can make them different.
- *Tracker Configuration*: as explained in chapter 4.1, two external silicon layers have been added to the original inner Tracker. So each event has several independent measurements of rigidity: inner planes only, inner plus L1 plane, inner and L9 plane and full span configuration (inner+L1+L9), which represents the most accurate measurement.
- *Rigidity (Tracker)*: the Tracker measures the event rigidity with an algorithm which is a function of the Tracker planes configuration and of the fitting algorithm chosen.
- *BDT (ECAL)*: this value is obtained by a *Boosted Decision Tree Classifier*, in which ECAL showers variables are combined to describe the morphology of the event and discriminate leptonic showers from hadronic ones. The BDT has been trained on different energy intervals, for space and MonteCarlo data: 0.5-2, 2-5, 5-10, 10-20, 20-40, 40-70, 70-120, 120-200 GeV.
- *Likelihood (TRD)*: this is a TRD algorithm of track segments and Lorentz gamma elaboration, to define a lepton-hadron discriminator for a particle that has just entered the detector volume.

The “**preselection**” sample for the analysis is defined as follows: to avoid rates oscillation and complex low energy physics, which is affected by geomagnetic cutoff and solar wind modulation (see Fig. 1), a conservative 20÷100 GeV energy range is chosen, together with an over-cutoff condition. This latter condition is $R > 1.3\ R_{\text{Cutoff}}$, where R_{Cutoff} is the geomagnetic cutoff (as a function of magnetic angle theta), and the proportionality factor comes from primary *cosmic rays backtracing analysis*, done by the Milano group [430] using uptodate Earth shifted and tilted magnetic dipole models by Tsyganenko et al. (1996, 2005). A |Q|=1 constraint (both for TOF and Tracker charge measurements) is also applied.

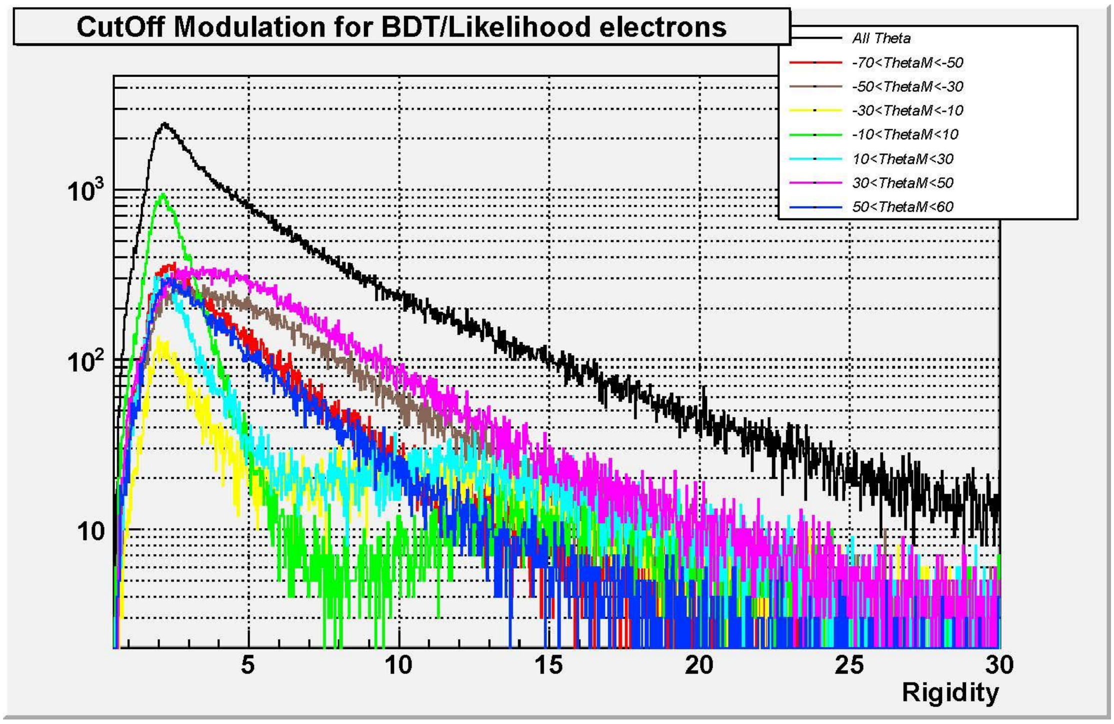

Figure 1 – Electrons rates for different ranges of Earth magnetic latitude, between -70 and +60 degrees. Electrons are selected through ECAL BDT and TRD Likelihood methods (see section 5.1.2). The great modulation due to Earth magnetic field physics is evident up to a rigidity of 15÷20 GV, i. e. the geomagnetic cutoff used to identify a clean sample of leptons.

5.1.2 Integrity, Cleaning and Physical Cuts on Events Variables

The analysis has been performed on **B610 – 2ecal** data, from May 2011 to October 2012. “B610” is the tag of the uptodate set of data: the reconstruction software applied to ISS *raw data* is continually upgraded from one repository to the next one. “2ecal” means that events have been preselected with at least one ECAL shower with total reconstructed energy greater than 2 GeV.

The cuts are summarized in Tables 1, 3 and 8. They give a specific understanding of each selection criteria and present the applied cuts chain, or cascade, with respect to which relative data reduction is defined. The fundamental cuts are divided into “data integrity” (which refers to data taking quality) and “subdetectors cleanness”, i. e. instrumental cuts related to subdetectors aimed at a good full-detector definition of particle events. Then “particle identification” cuts (electron/proton rejection and particle/antiparticle separation) are discussed.

5.1.2.1 Data Integrity Cuts

1. *AMSEventR existing:* this is the basic condition for the existence of the event.
2. *Level1R existing*: in some events the LVL1 part of the event is missing. This can be related to an error in the JINJ.
3. *DaqEventR existing, 4. HeaderR existing, 5. Not Status(30)*: they are DSP errors (coming from JINJs, JINFs, SDRs, JLV1s), assembly errors (in xDR nodes – see Fig. 2), desyncronization errors (i.e. subdetector event misalignments), at whatever level (between JINJ and JMDC), decoding errors (problems of coherence of the event data). Not Status(30) are particular event reconstruction errors.

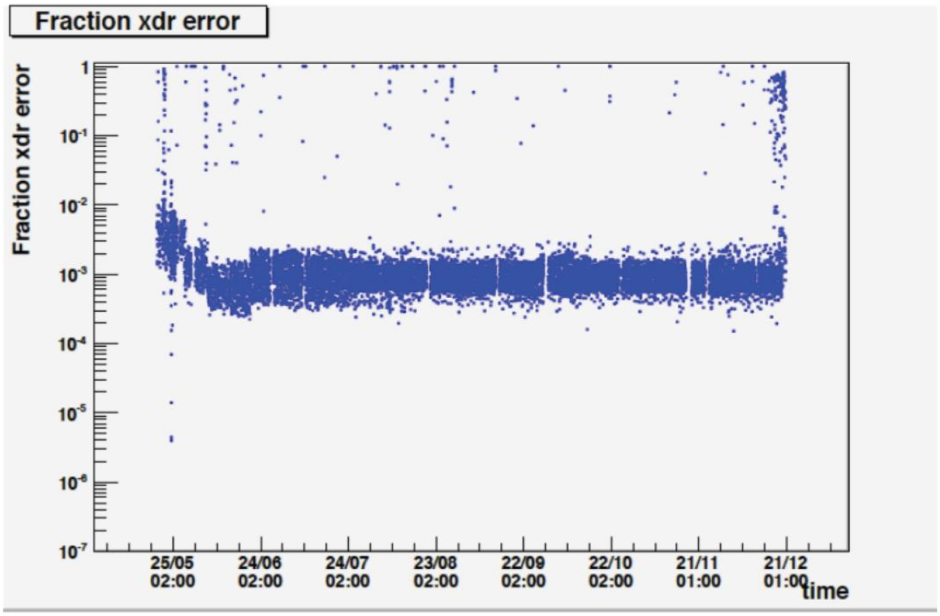

Figure 2 – Events fraction with electronics errors as a function of time. Each dot represents a physical run.

As explained in chapter 4.5, the triggered event mustn’t show a xDR node error, which is produced by a too large event size or by a bit flip. The error fraction per run shown in Fig. 2 is tiny, of the order of per mil. This represents a great success for the space instrumentation built by the Collaboration.

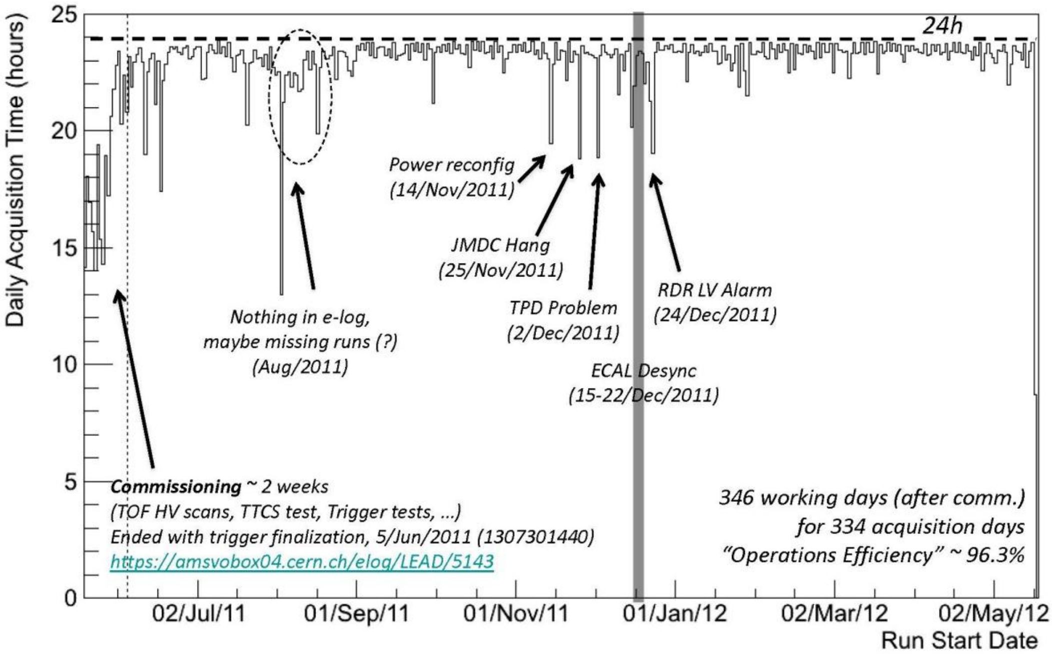

Figure 3 – A synthetic view of main operations done at the POCC during the first year of data taking. Ordinate shows the daily acquisition time [431].

The first two weeks of data taking have been characterized by calibrations, tests and scans (Fig. 3). Other “poor” acquisition periods are due to DAQ problems, power reconfigurations from electronics side A to side B or vice versa, and subdetectors desynchronization. The last one caused a corruption of data around the week of 15-22 December 2011. This gap will be visible in the data reduction plots vs time in section 5.2. The overall *operation efficiency* is about 96.3%. During the second half of 2012, AMS-02 has showed a stable acquisition time of almost 24 hours per day.

6. *Science Run*: each run must have the correct hexadecimal tag which differentiates scientific data from calibration and housekeeping.
7. *Not h/w error:* with hardware errors especially JINJ's errors are addressed. In general they're errors in data acquisition chain subsets (Fig. 4).

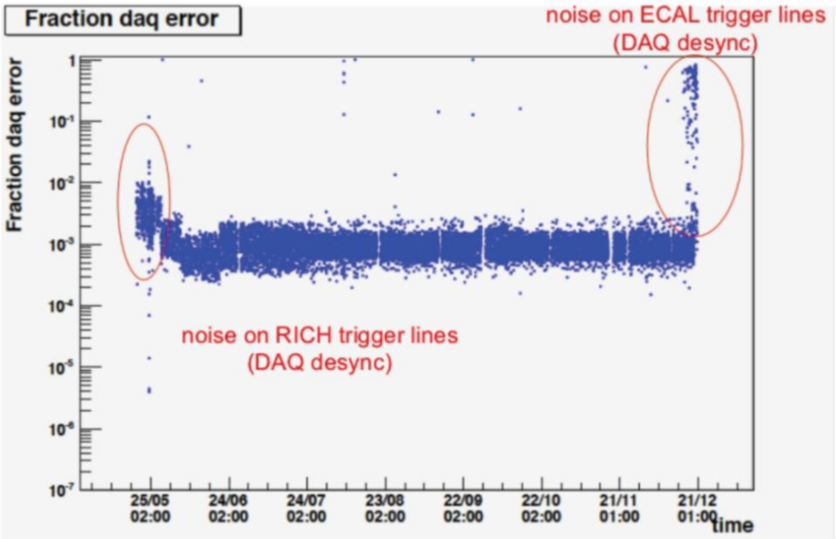

Figure 4 - Events fraction per run with acquisition errors as a function of time, for 2011. Each dot represents a physical run.

As shown in Fig. 4, a first period of data taking has been characterized by a RICH noise with an error fraction of some per mil. Another great peak appears during the week before Christmas, due to the ECAL desynchronization illustrated in Fig. 3. This error fraction reaches the unit. So these data are tagged as "bad runs" and not used for analysis.

8. *Not SAA:* the data which come from the South Atlantic Anomaly region, definable in terms of geographical/magnetic coordinates and livetime/TOF rates, are excluded (Fig. 5).

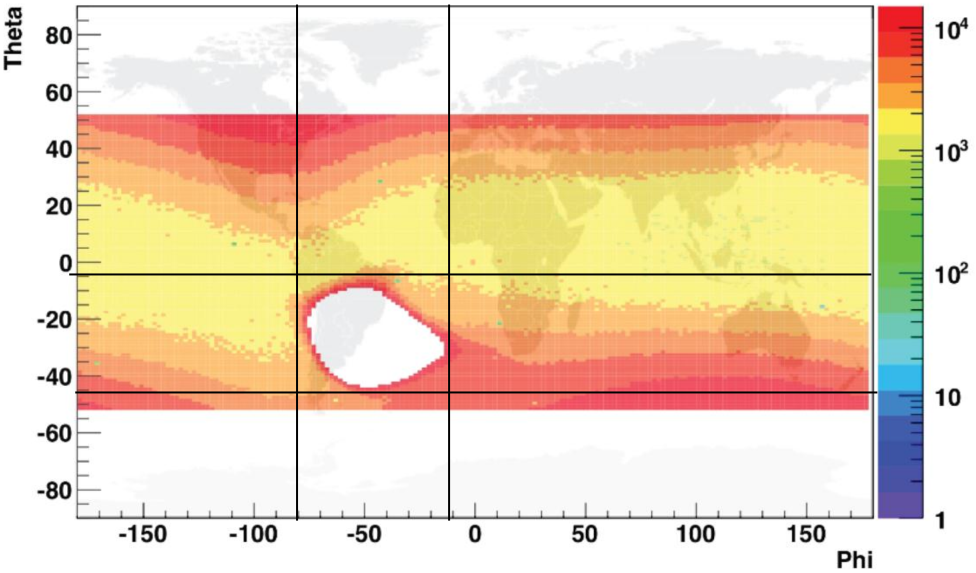

Figure 5 – Particle Rates in the Upper TOF in Hz unit on the Earth geographic map. The white cut region is the South Atlantic Anomaly.

As explained in chapter 3.2.1, the events that are triggered inside the SAA, which could be described as the orbital region where the rate measured by the Upper TOF exceeds $2 \cdot 10^4$ Hz (Fig. 5), must be excluded from the physical analysis. This is an *event selection* and not a *run selection*, like the previous ones (cuts 1-7).

Data reduction summary for data integrity cuts is presented in Table 1.

Data Reduction: Integrity	Detector	%	Reference Cut
Integrity Cuts			
1. AMSEventR existing	AMS-02	100	w.r.t. total
2. Level1R existing		100	w.r.t. previous
3. DaqEventR existing		100	w.r.t. previous
4. HeaderR existing		100	w.r.t. previous
5. Not Status(30)		99,97	w.r.t. previous
6. Science Run		96,20	w.r.t. previous
7. Not h/w error		99,87	w.r.t. previous
8. Not SAA		92,02	w.r.t. previous

Table 1 - Data reduction of integrity cascade cuts, as defined in this section. On the second column the cuts type, on the third the percentage of data reduction, on the fourth the reference cut.

The only two notable cuts are *Science Run* and *Not SAA*. The *Science Run* selection cuts the 4% of AMS-02 data and the *SAA* 8% of the scientific runs. The other integrity cuts are quite negligible: this is a sign of the correct behavior of the detector.

The two cuts together throw away about 9% of total data. The Science Run cut reflects the AMS data organization and storage, whereas the SAA one is a physical cut.

5.1.2.2 Cleaning Cuts

9. *ACC<5:* the number of ACC counters which have fired has to be zero (an ideal event), or less or equal four. This has been calculated not to exclude complex physically useful events characterized by internal interactions. In Fig. 6 the distribution of the number of ACC for the events selected after SAA exclusion is shown.

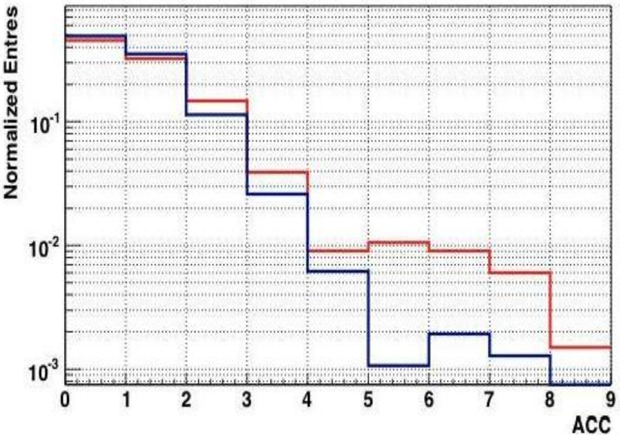

Figure 6 – Number of ACC which have fired for R>0 proton events (red) and R<0 electron events (blue), using BDT and TRD lepton-hadron discriminators.

From Fig. 6 it's clear that a ACC<5 cut is a good choice, especially for electrons, which doesn't diminish the statistics and excludes problematic transverse events [442].

Tracker cuts

10. *NTrTrack()>0:* the event must have at least one reconstructed Tracker track, to exclude fake triggered events.
11. *NTrTrack()<=4:* the event mustn't have more than four tracks associated. In Fig. 7 the histogram for the number of tracks is shown. A good event not necessarily has a unique track. For example, as anticipated, a 2-tracks event could mean a good particle which produces a Bremsstrahlung photon which converts into leptons with an associated track. So an inefficiency is expected for a too stringent one-track cut.

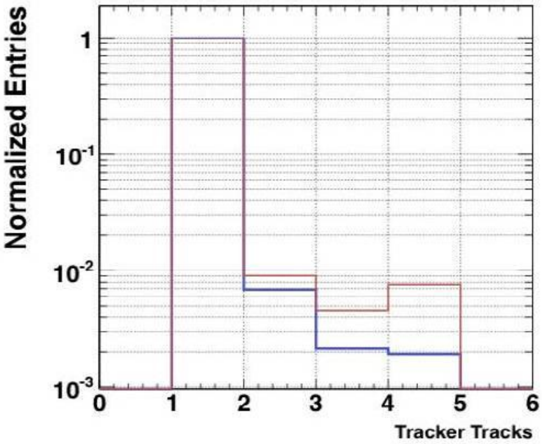

Figure 7 - Number of Tracker tracks for positive charged (red) and for negative charged events (blue), using BDT and TRD lepton-hadron discriminators.

Most of the events have just one reconstructed track. Only few percent of events have two, three or four tracks. There are almost no events with five or more tracks.

12. *Existing (for TrTrack 1,2,3,4):* after applying the ACC and the Number of Tracker tracks cuts, a further check of correct reconstruction of tracks is applied.
    The events with second, third and fourth track, together, are less than quarter of the first track existing ones alone (see Table 2).

Data reduction Cut	**w.r.t. Existing TrTrack1 (%)**
Existing for TrTrack 2	12,3
Existing for TrTrack 3	6,4
Existing for TrTrack 4	4,3

Table 2 – Percentages of second, third and fourth track events w.r.t. first track existing condition.

13. *Good:* a good Tracker track must satisfy some quality criteria [432], such as chi-square cuts, as illustrated in Fig. 8.

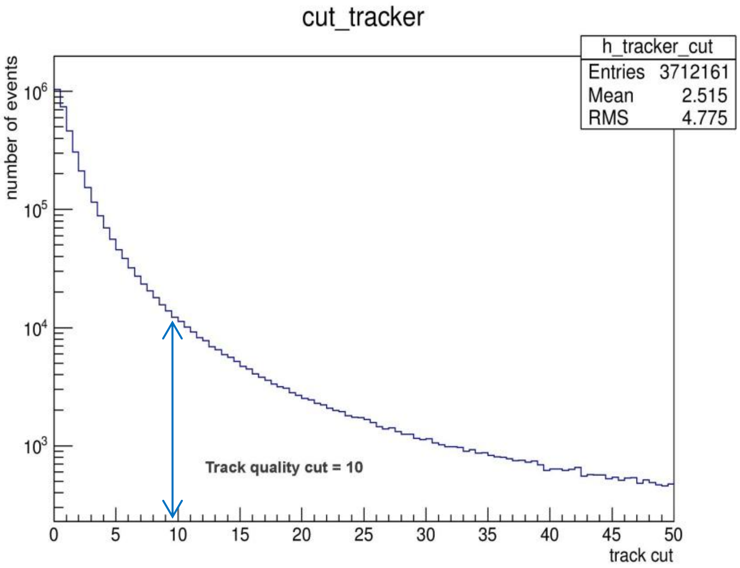

Figure 8 – Quality Tracker track cut in the $\tilde{\chi}^2$ for Y coordinate. The cut value is 10.

TOF and beta cuts

14. *Match with TOF:* the geometrical match between the Tracker track and TOF clusters is required (see Figs. 9 and 10).

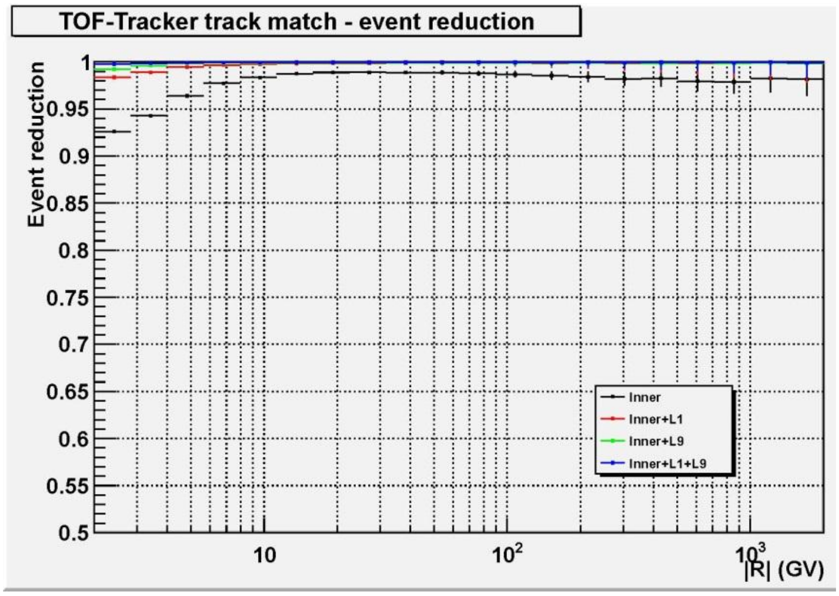

Figure 9 – Event reduction for TOF-Tracker track match as a function of rigidity.

For the Inner Tracker+L1, the Inner Tracker+L9 and Full Span configuration the event reduction remains constant at 1, up to TeV scale, except for tiny fluctuations in the region under the geomagnetic cutoff (Fig. 9) [439].

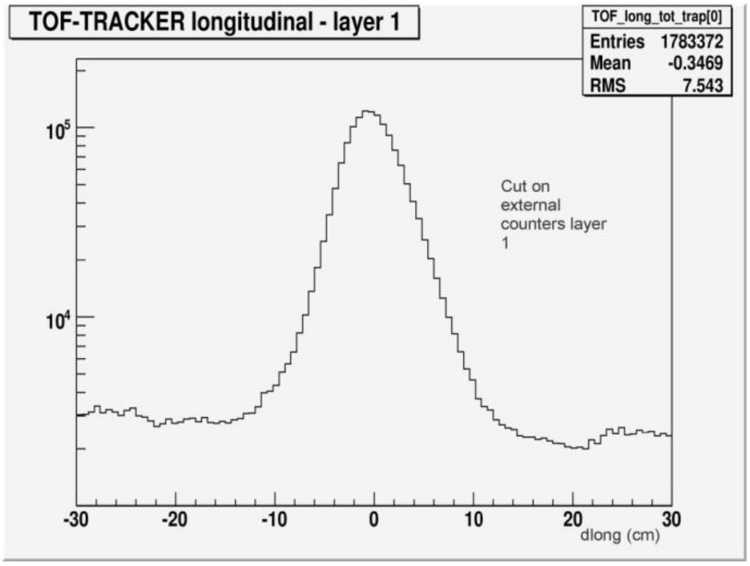

Figure 10 – TOF-Tracker longitudinal match for TOF layer 1, counter 1. The plot is relative to all good tracks (cut 13).

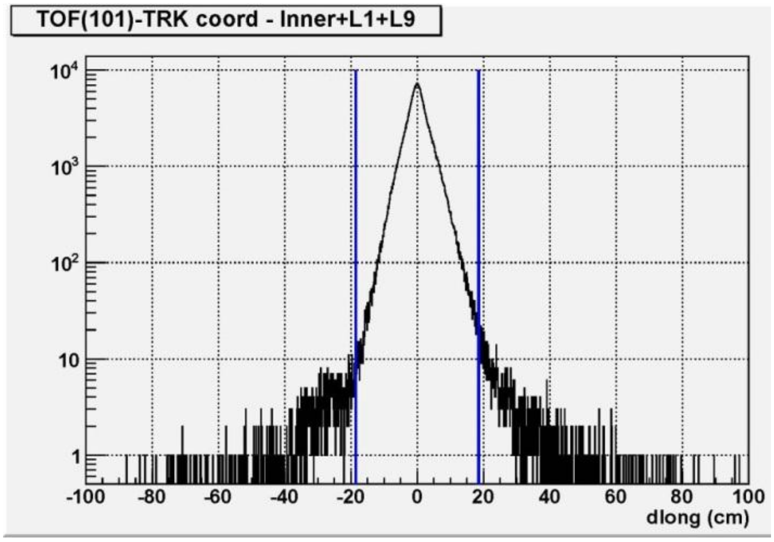

Figure 11 – TOF-Tracker longitudinal match for TOF layer 1, counter 1, after applying all other cuts of Tables 1 and 3.

Figure 10 shows the difference between the longitudinal coordinate of the track and the coordinate computed by TOF timings. The background, which is present if all tracks are used, disappears when all other cuts are applied.
The ±20 cm cut shown in the figure is highly efficient (the actual longitudinal cut varies from ±10 cm to about ±20 cm depending on the counter) but still useful to eliminate background.

15. *<u>At least one BetaH</u>*: BetaH is one of the several AMS algorithms to compute betas. This is the most precise one. The cut is done to ensure that the event has at least one physical velocity.
16. *<u>Good BetaH match</u>*: after checked its existence, the beta value has to be associated with the Tracker tracks. If more than one beta is present, the first is chosen. Fig. 12 illustrates the BetaH distribution as a function of logarithm of rigidity for downgoing particles.

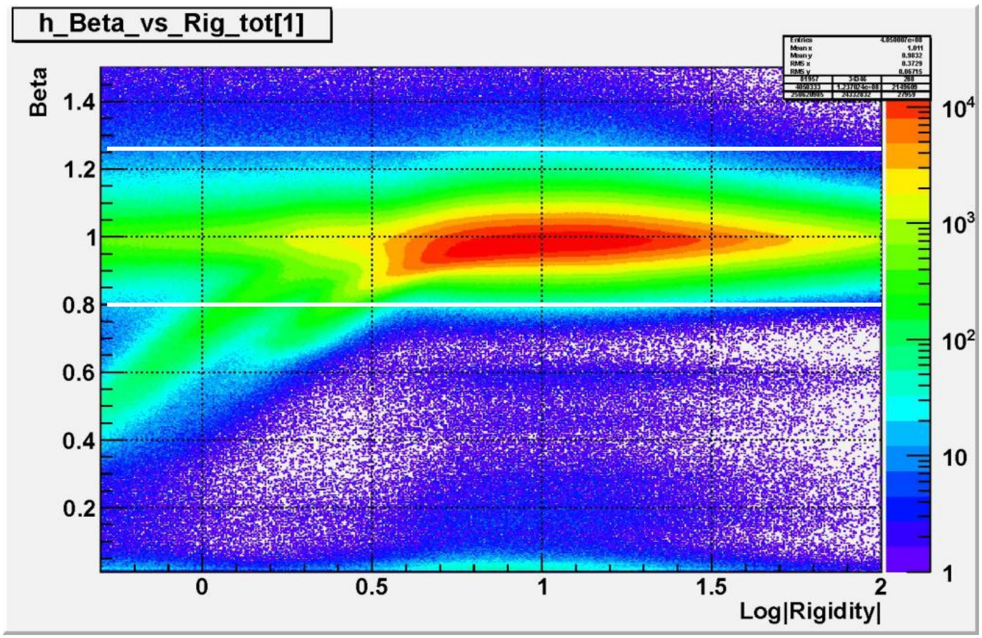

Figure 12 – Color map of particle beta as a function of the rigidity in the 0.5÷100 GV range.

The two white lines in Fig. 12 anticipate the good beta range that is going to be chosen for Cut 17. Zooming into the 0.5÷5 GeV range, it's possible to see the population of charged pions, Helia (the little tail in Fig. 12, which starts at about 0.2 Log|R|), and deuterons. It's already evident that almost all betas lie in the 0.8÷1.25 range (cut 17).

17. *<u>0.8<Beta<1.25</u>*: this is a conservative value for high energy particles, which grants good efficiency for both leptons (see Fig. 13) and hadrons.

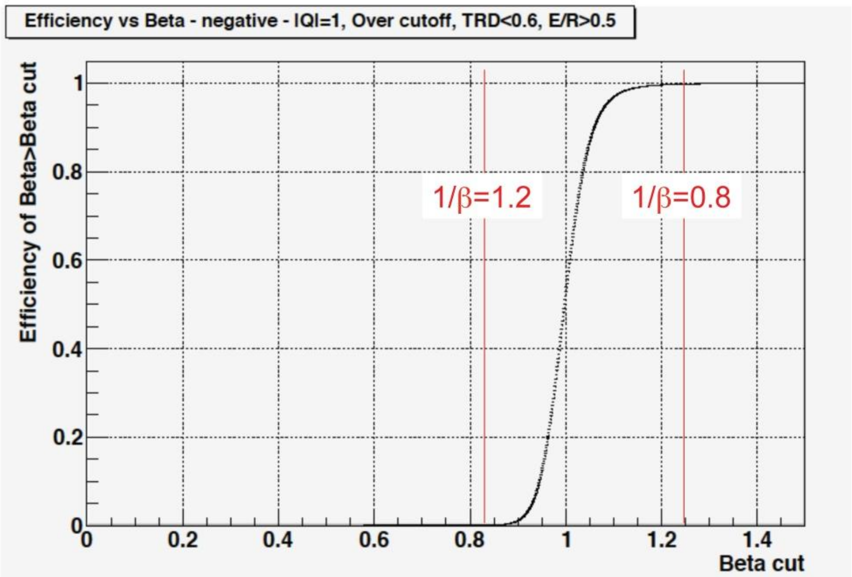

Figure 13 – Efficiency of the beta cut for TRD-Likelihood and E/p selected electrons (R<0, |Q|=1, over cutoff, TRD lepton, |E/R|>0.5), with the corresponding cut values for the inverse of beta. For the definitions of TRD Likelihood and E/p discriminators see section 5.1.2.4.

TRD Cuts

18. <u>At least one TrdTrack</u>, 19. <u>At least one good TRD track</u>, 20. <u>Match with good TRD track</u>: these are cuts to define a good TRD track pattern, which will be used for Likelihood computation. The event must satisfy a proper number of TRD segments, a correct hit pattern (at least 12 ÷ 15 hits on at least 6 layers) and χ^2 criteria. The 20 measurements from the 20 transition radiation layers are then combined.

21. *Likelihood (S) existing:* this a previous version of the uptodate algorithm that has been casted off, after verifying that it is much less efficient than K-algorithm.
22. *Likelihood (K) existing:* the TRD K-Likelihood must exist for the particle, in order to operate e/p rejection. This is the proper Likelihood algorithm, for which calibrations have been done for all the data sample.

ECAL Cuts

23. *Track in ECAL acceptance*: the particle track must fall into the calorimeter geometrical acceptance. To have an idea of the order of magnitude of this demand, in Table 5 it can be noted that the absolute data reduction for this cut is 18.5%; comparing composite subdetectors acceptances, the AMS with ECAL one is the smallest [434, 435]:

$$A_0(TOF\ trigger) \approx 0.785\ m^2 \cdot sr$$
$$A_1(inner\ Tracker) \approx 0.480\ m^2 \cdot sr$$
$$A_2(TRD + TOF + InnTRK) \approx 0.141\ m^2 \cdot sr$$
$$A_3(TRD + TOF + FullTRK) \approx 0.040\ m^2 \cdot sr$$
$$A_4(TRD + TOF + ECAL + FullTRK) \approx 0.026\ m^2 \cdot sr$$

The last A_4 (with ECAL) acceptance is only 18.4% of the A_2 (TRD + TOF + Inner Tracker) acceptance.

24. *At least one ECAL shower:* the event must have at least one reconstructed shower to which a reconstructed energy can be associated.
25. *Match with ECAL*: there must be a match between the Tracker track and the shower trajectory reconstructed in the calorimeter [432]. This match is tested checking the discrepancy between the Tracker extrapolated track at the ECAL upper surface and the center of gravity of the shower (see Figs. 14 and 15).

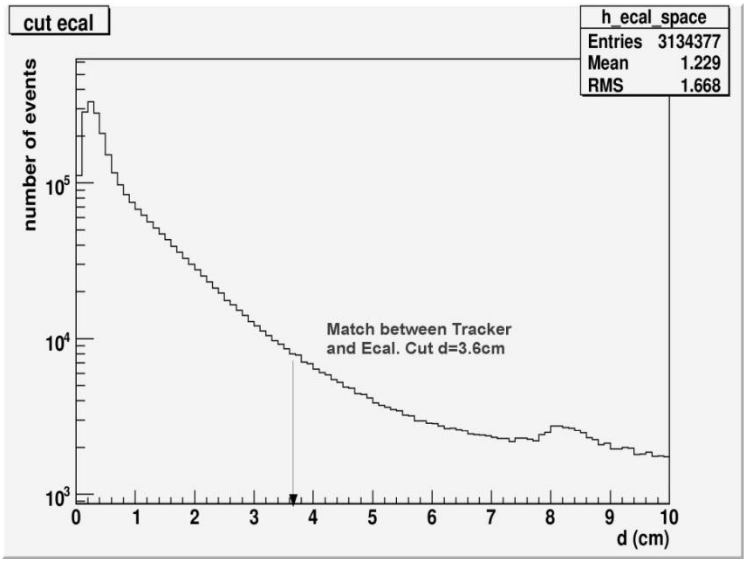

Figure 14 – Geometrical match between Tracker track and ECAL.

The center of gravity of the ECAL shower (i.e. the ECAL cell characterized by the maximum release of energy) must coincide with the shower axis extrapolated by the Tracker, within a specific tested value that is 3.6 cm in the x direction (Fig. 14).

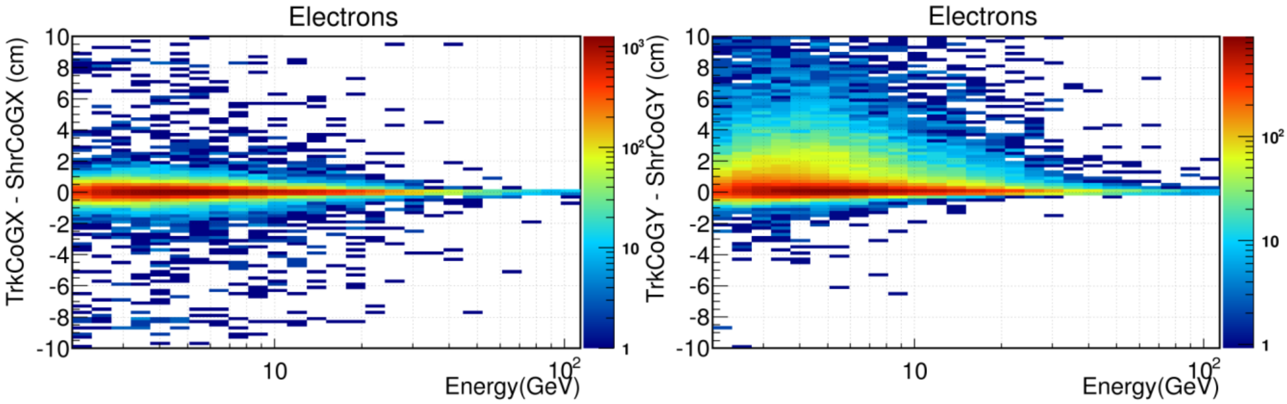

Figure 15 – Distribution of Tracker-ECAL shower position difference in the x (left plot) and y (right plot) coordinates [436].

The difference in x (Fig. 15 - left) is uniformly distributed around zero. A cut at a Tracker-ECAL shower distance less than 3.6 cm (the same value of Fig. 14, which represents one ECAL PMT length), gives an inefficiency of 1%. The difference in y (Fig. 15 - right) is asymmetric because of the Bremsstrahlung effect (and the consequent magnetic field deflection of the produced particles along the y direction), determining a larger cut: about 7.2 cm, i. e. less than 2 PMTs lengths.

Final Cleanness Cuts

26. *At least one Particle*: the number of particles associated to the event must be greater or equal to one.
27. *Match with Particle*: the defined particle must be correlated to the Tracker track.
28. *Not in Solar Arrays*: the AMS field of view mustn't be shadowed by ISS solar wings. A specific software variable takes into account solar panels movements and calculates their interference with AMS data acquisition.
29. *Good Tracks>0*, *30. Good Tracks=1*: this two final cuts are applied to cut 11 (NTrTrack()<=4), to calculate, at this cascade selection level, how many good particles we have. *Good particles* are events which satisfy at the same time "good Tracker track", "good TRD track", "ECAL acceptance" and "TRD-Tracker, TOF-Tracker and ECAL-Tracker tracks matches" cuts.

The summary of cleanness cuts data reduction is shown in Tables 3 and 4.

Data Reduction: Cleanness Cuts	**Detector**	**%**	**Reference Cut**
Cleanness Cuts			
9. ACC<5	TRACKER	97,06	w.r.t. previous
10. NTrTrack()>0		73,13	w.r.t. previous
11. NTrTrack()<=4		100	w.r.t. previous
12. Existing		100	w.r.t. previous
13. Good		81,66	w.r.t. previous
14. Match with TOF	TOF	85,86	w.r.t. previous
15. At least one BetaH		99,97	w.r.t. previous
16. Good BetaH match		99,99	w.r.t. previous
17. 0.8<Beta<1.25		71,91	w.r.t. previous
18. At least one TrdTrack	TRD	100	w.r.t. previous
19. At least one good TRD track		77,35	w.r.t. previous
20. Match with good TRD track		87,27	w.r.t. previous
21. Likelihood (S) existing		73,20	w.r.t. 20
22. Likelihood (K) existing		93,58	w.r.t. 20
23. Track in ECAL acceptance	ECAL	92,50	w.r.t. previous
24. At least one ECAL shower		100	w.r.t. previous
25. Match with ECAL		97,22	w.r.t. previous
26. At least one Particle	General	100	w.r.t. 25
27. Match with Particle		99,75	w.r.t. previous
28. Not in Solar Arrays		99,99	w.r.t. previous
29. Good Tracks>0		12,35	w.r.t. 11
30. Good Tracks=1		79,82	w.r.t. previous 32

Table 3 – Data reduction of cleanness cascade cuts. On the second column the cuts type, on the third the percentage of data reduction, on the fourth the reference cut.

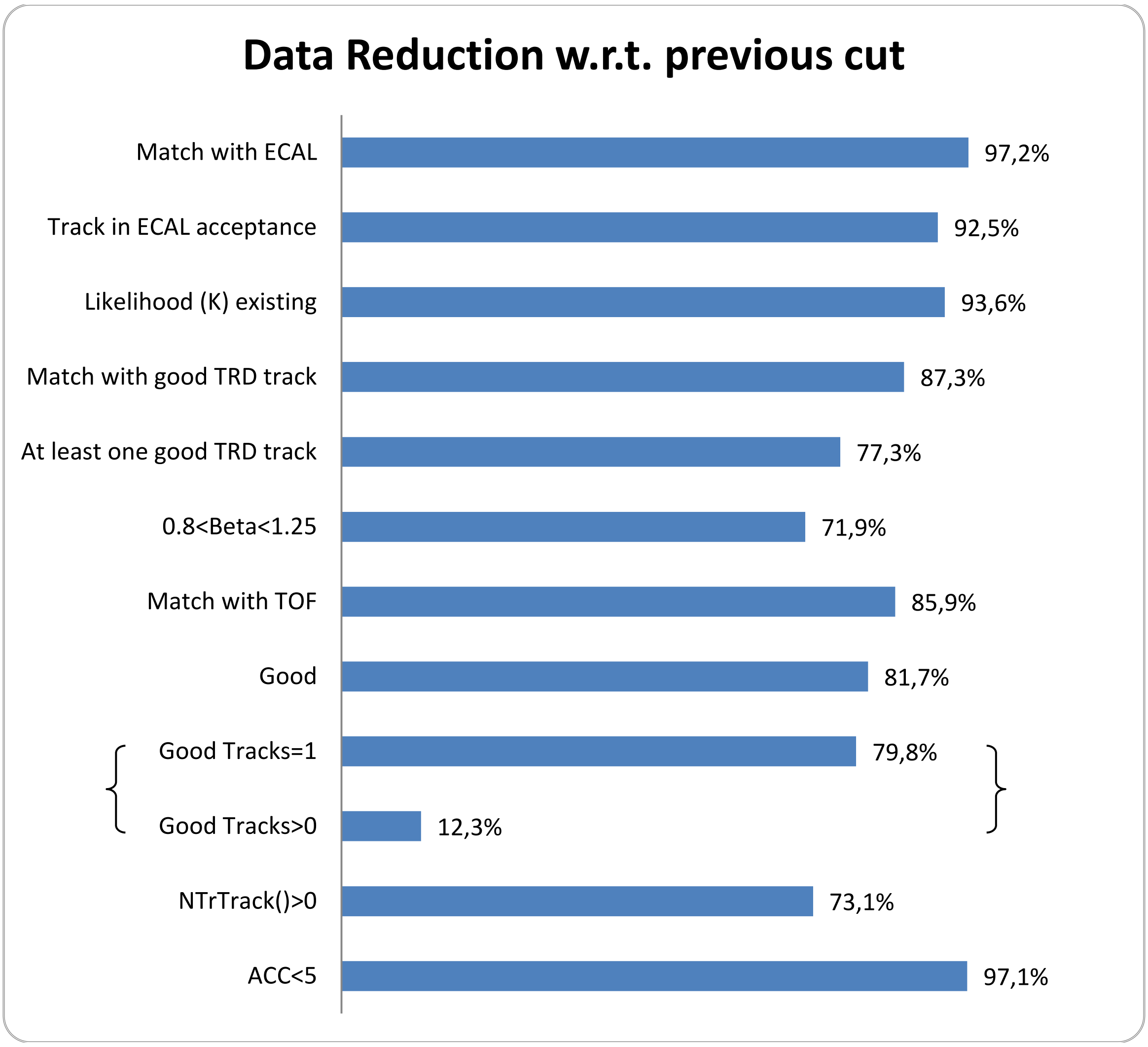

Table 4 – Histogram of "cascade" data reduction cuts for cleanness cuts, from bottom to top. Cuts which produce no data reduction do not appear.

As said, the *ACC* cut is really conservative.
The *K-Likelihood* cut (the S-Likelihood is not reported in Table 4) shows a great data reduction percentage w.r.t. previous TRD tracks cuts, highlighting the goodness of the current discriminator algorithm.
The *beta value* cut eliminates slow hadron-like particles, or events with bad beta association.
In general, all the cascade data reductions don't lower the statistics too much, except for the *Good Tracks>0* cut w.r.t. *NTrTrack>0*, which shows the importance of the Tracker track finding and of the multiple subdetectors matches in the complete definition of the event. *Good Tracks>0* and *Good Tracks=1* are between brace brackets because they're the last applied cuts.

Finally, in Table 5 the absolute data reduction w.r.t. all events, for all integrity and cleanness cuts, is presented.

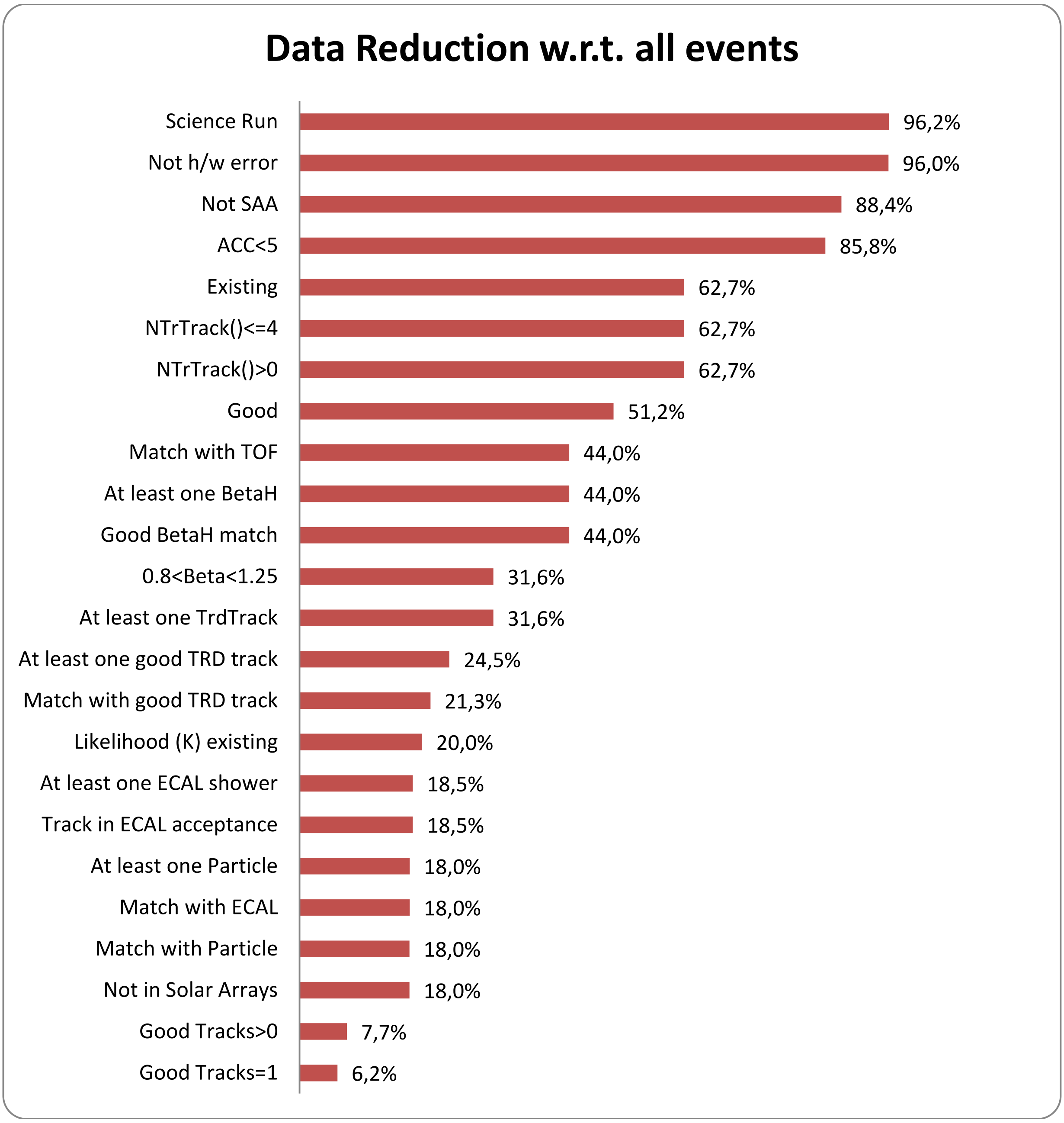

Table 5 - Histogram of “absolute” data reduction cuts for integrity and cleanness cuts. The completely efficient cuts are removed. They start from *Science Run* Cut.

In the absolute data reduction histogram it can be noted that the full SAA effect is to eliminate 12% of the total data.

Some groups of cuts are comparable. For example, the *track existing* cut and the correct number of *Tracker tracks* one select 63% of the statistics. Less than half the total statistics survive after TOF and good beta cuts. The TRD cuts kill about 80% of all events and ECAL and particle matches cuts amounted to 18%; also the *Solar arrays* reduction is at the same level.

After *Good Tracks=1* cut (6.2% of all events), a good sample for physical analysis has been identified: it is free from instrumental errors and contains events which have been reconstructed step by step by the whole detector.

5.1.2.3 Particle Identification Cuts

Before defining other analysis cuts, it has to be stressed that from now on all data selections follow the *"preselection"* criterion defined in section 5.1.2, to create a good sample for the stability analysis which satisfies the energy range condition 20÷100 GeV and the over-cutoff condition. Helia (and Z > 1 nuclei in general) are rejected.

The "particle identification" cuts are the physical cuts used to define samples of protons, electrons, positrons and antiprotons, in order to study the stability of the detector and of the positron fraction measurement as a function of time.
Here it must be stressed again that the present cuts aim is to isolate a pure enough lepton sample and not to optimize efficiencies.

Charge

1. *At least 1 Q negative, match with ECAL*, 2. *At least 1 Q positive, match with ECAL:* the events are separated with R<0 and R>0 prescriptions respectively, with the additional request of |Q|=1, both for Tracker and TOF measurements, rigidity over cutoff and match with the calorimeter. This ensemble of conditions might exist for at least one track of a multi-tracks event (i. e. an OR condition for the tracks). In Fig. 16 the Tracker charge distribution is shown.
3. *Q=-1, match with ECAL:* same as previous cut 1, but the cut must be satisfied for each of the tracks of the event.

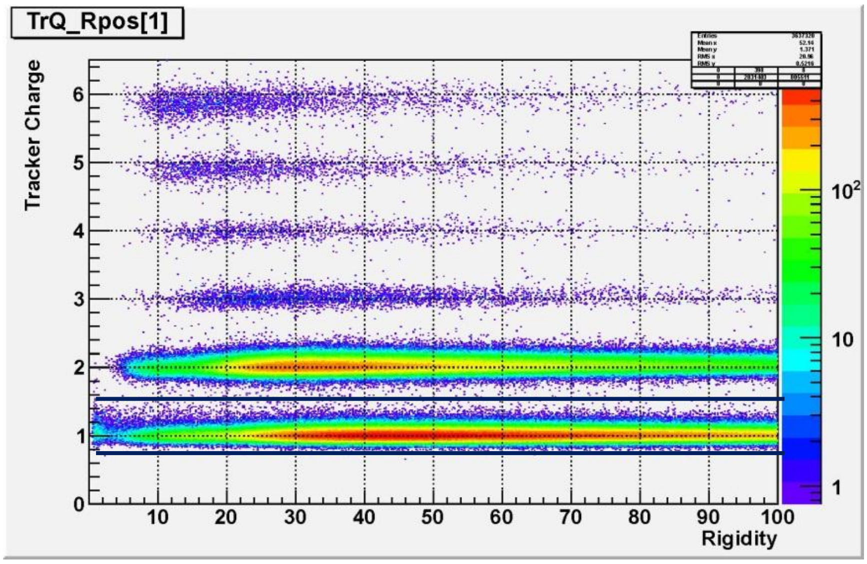

Figure 16 – Tracker Charge distribution as a function of rigidity for positive particles.

The two black lines in Fig. 16 show the limits defined for Tracker Q=1 particles: 0.7<Q<1.5. For TOF charge the limits are 0.6<Q<1.6.

After choosing the desired sample of fundamental particles, lepton-hadron discrimination is needed. This is possible using three main particle species separators: the ECAL BDT, the TRD Likelihood and the ratio of energy and rigidity.

BDT

4. *Good BDT electron*: in Fig. 17 the BDT distribution for positive (R>0) and negative (R<0) charged particles is shown. Positive particles are mainly protons and the negative ones electrons, because of the non influential backgrounds of positrons and antiprotons, respectively. The two confidence conditions for 95% efficiency separation are BDT <-0.8 for hadrons and BDT>0.6 for leptons.

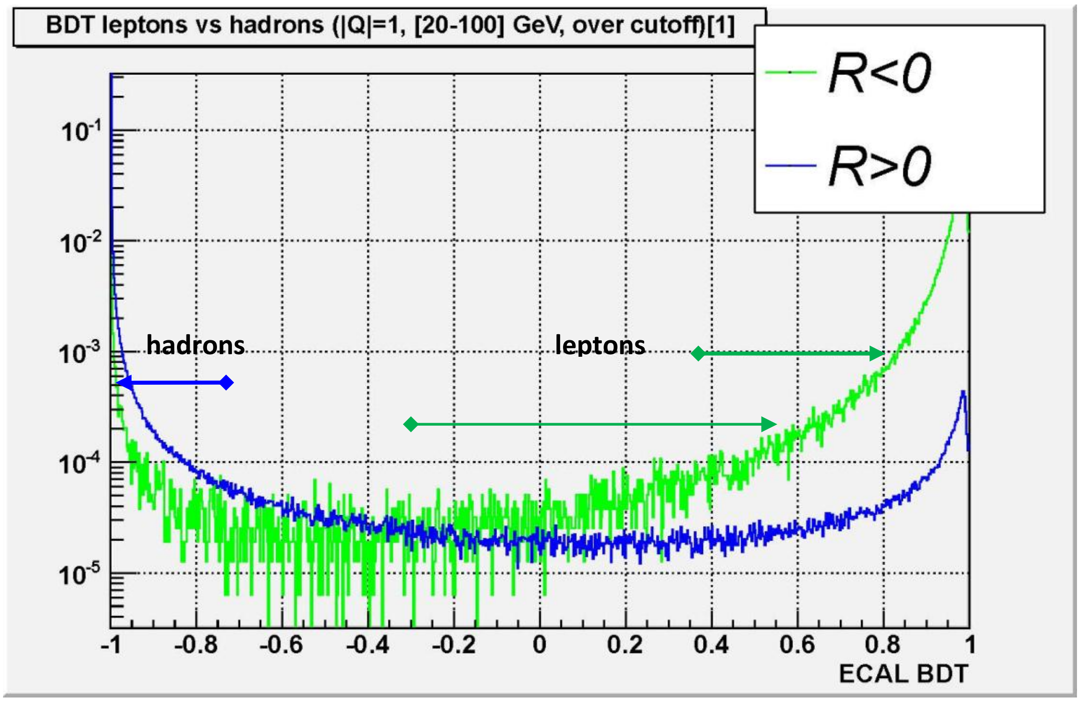

Figure 17 – ECAL BDT distributions for *preselected* negative particles (mostly electrons) in green and positive particles (mainly protons) in blue.

The two arrows in Fig. 17 depart from the BDT values where one curve overcomes the other, i.e. -0.7 for hadrons (blue arrow) and -0.3÷0.4 for leptons (green arrows). For the analysis more stringent values will be used.

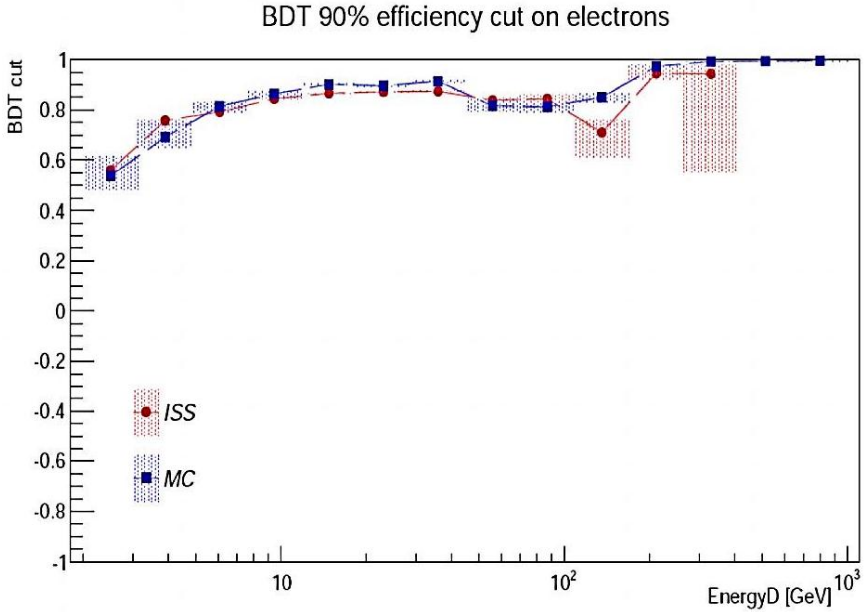

Figure 18 – BDT discriminators efficiency compared to the MonteCarlo one as a function of energy deposited in the calorimeter [436].

The setting of the cut corresponding to 90% electron efficiency on ISS data is quite compatible with the one obtained with MonteCarlo (Fig. 18). The real data BDT efficiency starts to be unstable from 300 GV on. MonteCarlo setting of the cuts will be used for the whole energy range between 0.5 and 1000 GeV.

TRD Likelihood

5. *Good electron S*: this is the S-Likelihood cut. As said, this cut gives a larger data reduction than K-Likelihood and is not used in the following.
6. *Good electron K*: in Fig. 19 the Likelihoods for positive and negative charged particles are shown. The two confidence limits for 95% efficiency separation are Likelihood < 0.6 for leptons and Likelihood > 0.8 for hadrons. The plot is done before the BDT selection; the relative data reduction is calculated on the BDT selected sample.

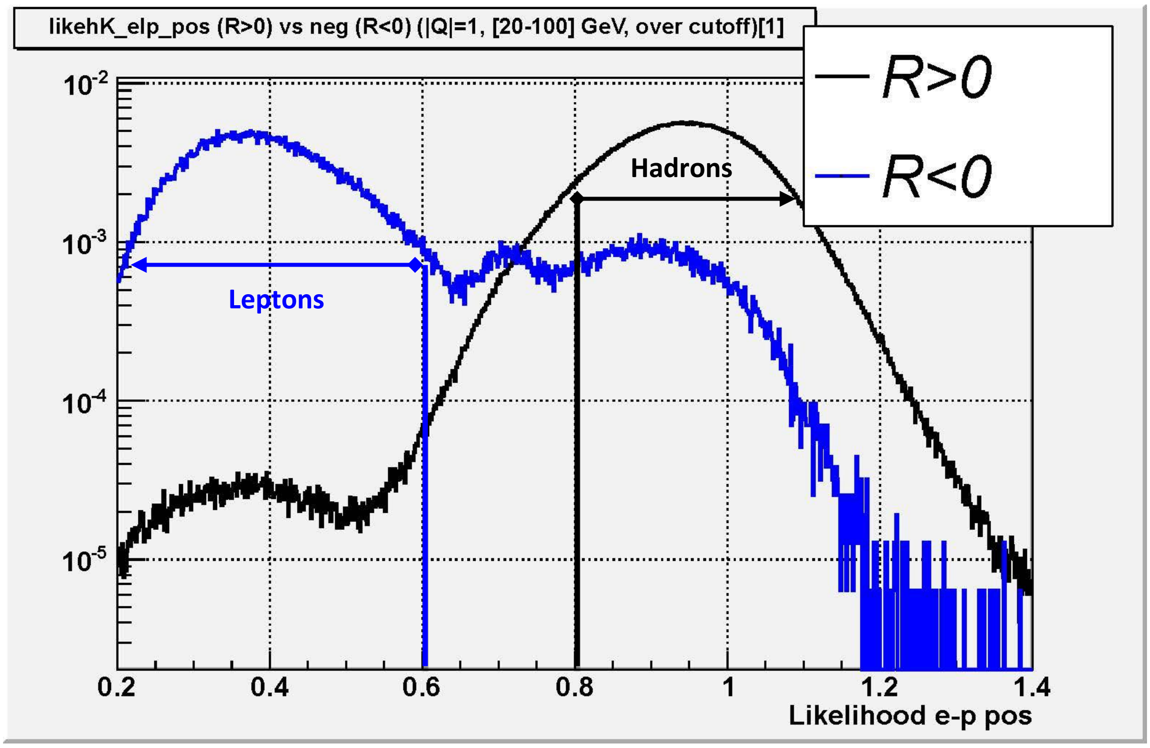

Figure 19 – TRD e/p K-Likelihood normalized distributions for negative (blue) and positive (black) particles.

The two arrows in Fig. 19 depart from the Likelihood values where one curve intersects the other, i.e. about 0.6 for leptons and 0.8 for hadrons. The curves are for *preselected* particles, without any other cut.

7. *Good electron K 20<E<100*: the 20<E<100 GeV energy range prescription is added to the previous selection, discarding 97% of events.

The K-Likelihood discriminator has been trained on space and MonteCarlo data for energies less than half TeV.

From Fig. 19 it's clear K-Likelihood is a very neat and clean discriminator, the best AMS-02 hadron-lepton selector, much more powerful than ECAL BDT shown in Fig. 17, which doesn't present a definite separation of the two curves.

The electron-like population isolated with the TRD K-Likelihood is of the order of 5%, whereas the proton statistics of the order of 85% and the “probably protons”, from the mixed zone between 0.6 and 0.8, is about 10% (see Table 6).

Population	w.r.t. total preselected events %
K-Likelihood electrons with R<0	4.7
K-Likelihood protons with R>0	84.4
Mix	10.2

Table 6 – Percent population of the three regions defined by the K-Likelihood of Fig. 19, w.r.t. total preselected events: the electron-like one, the proton-like one and the mixed.

The same cuts are symmetrically applied to the positive particle sample (R > 0) to select positrons: *8. Q=+1, match with ECAL, 9. Good BDT positron, 10. Good positron S, 11. Good positron K, 12.* Good *positron K 20<E<100*.

13. *Electron or positron (K) 20<E<100 GeV*: this is an OR condition of the next two cuts, to select a high purity leptonic sample.
14. *Electron (K) 20<E<100 GeV*: this is the fundamental cut with which the electrons used in the positron fraction are defined.
15. *Positron (K) 20<E<100 GeV*: this the fundamental cut with which the positrons used in the positron fraction are defined.

Energy over Rigidity

E/R is the third particle species selector. It can be used to distinguish not only between hadrons and leptons but also between particle and antiparticle. Moreover, with the energy-rigidity ratio it is possible to distinguish Wrong Charge events (section 5.1.2.5).

The constraints for leptons are $|E/p| > 0.5$. In fact, from Fig. 20 it can be noted that negative charged particles have a peak at -1.1 which rises from -0.5, suggesting an $E/p < -0.5$ selection cut. The antiproton component is negligible and is not a background for electrons, so these negative charged particles are electrons indeed. Therefore, a symmetric cut is chosen to increase the number of positrons within positive charged particles. Obviously the positive cut $E/p > 0.5$ doesn’t separate protons from positrons in a neat way, leaving a background for the latter. For higher energies this cut should be specialized with more stringent values, for example $E/p > 0.6$ for positrons.

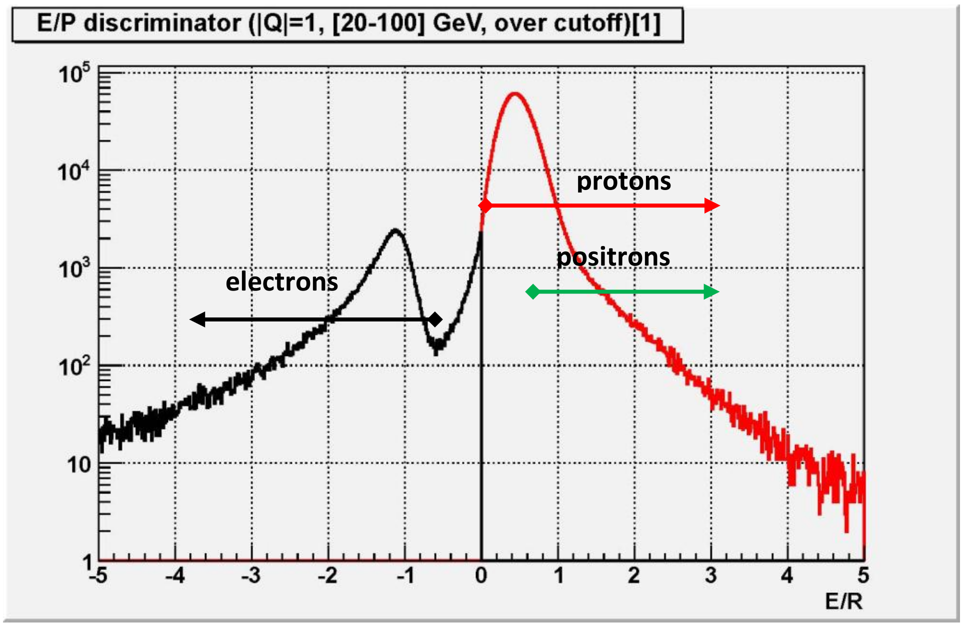

Figure 20 –E/p distribution for negative charged particles (black curve) and for positive charged particles (red curve). Each particle interval is evidences by colored arrows.

Looking at Fig. 20, it can be noted that for $|E/p| > 0.5$ leptons are selected: $E/p < -0.5$ for electrons (black arrow) and $E/p > 0.5$ for positrons (green arrow). While the negative peak is purely electronic, the positive red curve contains both protons and positrons. The intervals are depicted by the arrows.

The selection criteria for particle species are summarized in the last three cuts, depicted in Table 7.

		BDT	e/p K-Likelihood	E/p	Log|E/p|	p/He K-Likelihood
16.	*Total Protons (K)*	< -0.8	> 0.8			< 0.2
17.	*Total Electrons (EoP)*	> 0.6	< 0.6	< -0.5	> 0.3	
18.	*Total Positrons (EoP)*	> 0.6	< 0.6	> 0.5	> 0.3	

Table 7 – Cuts 16, 17, 18, definitions. Particle species discrimination through main classifiers. *EoP* stands for the "Energy over Momentum" additional cut.

Also an electron/Helium K-Likelihood could be added to the criteria, but this would be quite useless for leptons with energies lower than 100 GeV, according to TRD tracks combining algorithm, and the charge cut and the rigidity one offer a sufficient discrimination for electrons. The Log|E/p| discriminator will be used later.
The protons data reduction and the antiprotons fraction are computed only to check the goodness of the discrimination.

For completeness, it must be also added that ECAL BDT and e/p TRD-K-Likelihood values slightly depend on the particle energy. To optimize the rejection power, they have been calibrated in energy bins between 2 and 100 GeV. In particular, for BDT leptons the cut value runs from 0.77 at

25 GeV to 0.44 at 100 GeV, with full span Tracker configuration; for e/p TRD-K-Likelihood leptons the cut value runs from 0.51 at 25 GeV to 0.57 at 100 GeV.

The particle identification cuts data reduction synthesis is shown in Tables 8 and 9.

Data Reduction Particle Identification Cuts	**%**	**Reference Cut**
1. At least 1 Q negative, match with ECAL	9,14	w.r.t. 30 (Good Tracks=1)
2. At least 1 Q positive, match with ECAL	17,78	w.r.t. 11 (NTrTrack()<=4)
For TrTrack 1		
3. Q=-1, match with ECAL	95,08	w.r.t. 1 (1 Q <0 + ECAL)
4. Good BDT electron	83,60	w.r.t. previous
6. Good electron K	78,46	w.r.t. 4 (Good BDT e-)
7. Good electron K 20<E<100	6,94	w.r.t. previous
8. Q=+1, match with ECAL	99,88	w.r.t. 2 (1 Q >0 + ECAL)
9. Good BDT positron	0,93	w.r.t. previous
11. Good positron K	20,05	w.r.t. 9 (Good BDT e+)
12. Good positron K 20<E<100	9,63	w.r.t. previous
13. Electron or positron (K) 20<E<100 GeV	0,45	w.r.t. 30 (Good Tracks=1)
14. Electron (K) 20<E<100 GeV	0,42	w.r.t. 30 (Good Tracks=1)
15. Positron (K) 20<E<100 GeV	8,17	w.r.t. 13 (e- + e+ (K))
16. Total Protons (K) 20<E<100 GeV	85,21	w.r.t. 30 (Good Tracks=1)
17. Total Electrons (EoP) 20<E<100 GeV	59,34	w.r.t. 14 (electron)
18. Total Positrons (EoP) 20<E<100 GeV	64,33	w.r.t. 15 (positron)

Table 8 – Data reduction of particle identification cuts. On the second column the percentage of data reduction, on the third the reference cut. Cuts 5 and 10 for S-Likelihood are omitted. From cut 3 to 18 the data reductions are presented for TrTrack 1 (see cleaning cut 12), which represents 99.6% of total events.

The particle identification cut 3 (Q=-1, match with ECAL), which is similar to cut 1 (data reduction of 95%), selects 9% of the events with *one good AMS track* (cut 33), while the symmetric cut for positive charge selects 18% of the events.
The *Good electron(positron) K 20<E<100* are only 7%(10%) of the total *Good electron(positron) K*, (the latter are selected for $R>R_{cut\text{-}off}$), and the number of selected leptons (cut 13) is 5 per mil of the total events with *one good track*. The mean positron fraction (cut 15) is about 0.08.
Both electrons and positrons computed with the additional request of a proper E/p, i. e. cuts 17 and 18, are about 60% of the previous selection without E/p constraint (*Electron/Positron (K) 20<E<100 GeV*, cut 7-12-13). So, in order to have more statistics for the stability study of the positron fraction, the selection without the E/p cut will be used.
The total number of protons, selected with the e-p K-Likelihood cut, the p-He K-Likelihood < 0.2 condition and the BDT, is about 85% of the number of *one good track events*. Furthermore, if the ECAL match condition is added for *Total Protons 20<E<100 GeV*, the data reduction reaches 18%. The ECAL match condition doesn't appreciably affect *Total Electrons and Positrons (EoP)* data reduction.
From Table 8 it can be qualitatively argued that BDT and K-Likelihood selectors are efficient enough (84% and 79%) to set up a basis for particles rates and spectra computation.

In Table 9 the absolute data reductions for particle identification cuts are shown. The conditions *At least 1 Q positive, match with ECAL* and *Q=+1, match with ECAL* (particle identification cuts 2 and 8 in Table 8) worth about one tenth of total events, whereas the *Total protons* condition leaves about 77% of the whole *preselected* statistics: positive particle are dominant because of the high rate of CR protons.

BDT and Likelihood produce for electrons an absolute reduction of the order of few per mil; this value is very close to the reduction for negative particles (cut 3): this is another evidence of the fact that discriminators don't significantly lower the statistics.

As expected, the surviving good electrons are of the order of 10^{-4} whilst positrons of the order of 10^{-5}, which are the physical reciprocal orders of magnitude of CR rates discussed in section 3.5.7.

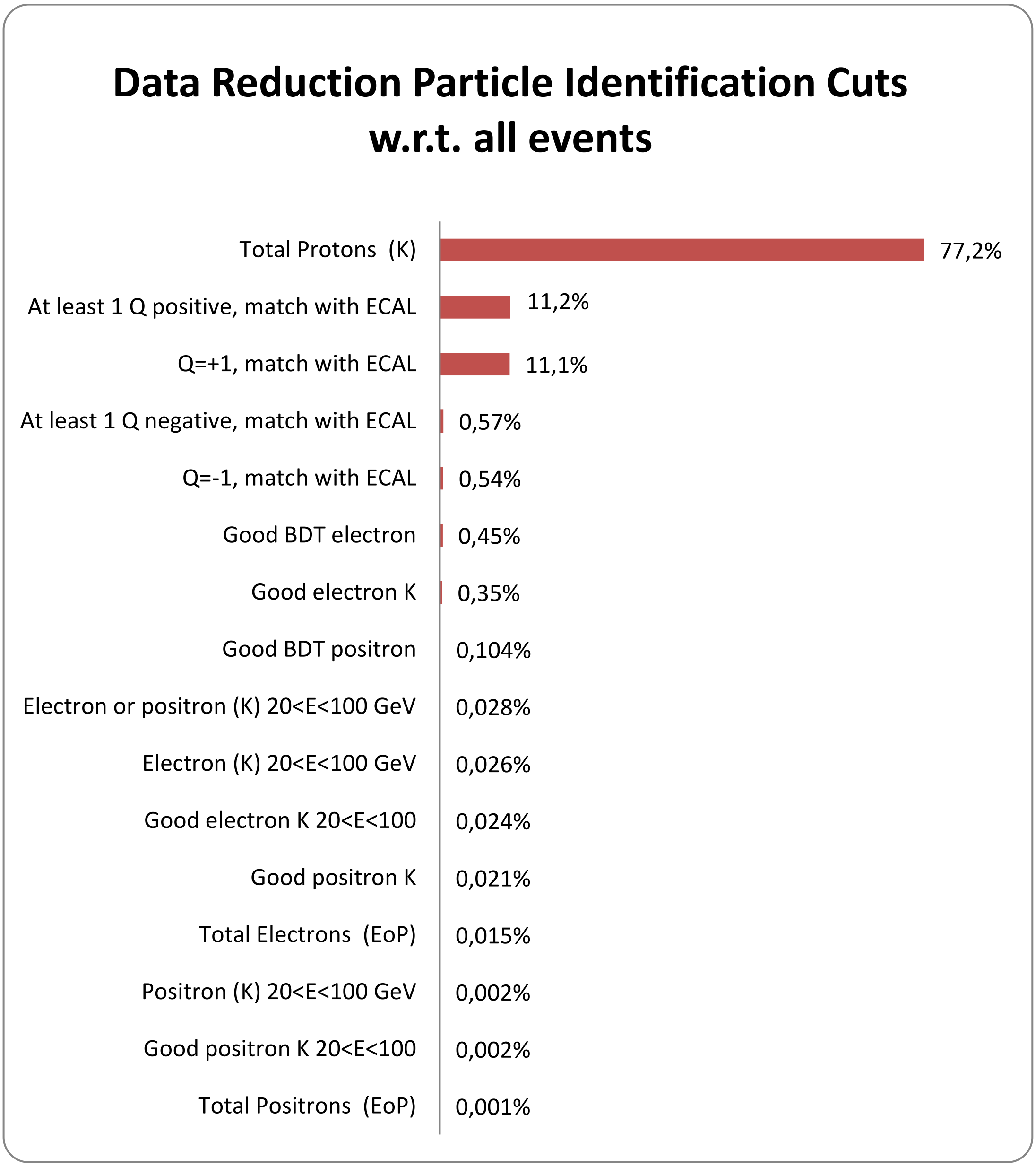

Table 9 - Histogram of "cascade" data reduction cuts for particle identification cuts. The completely efficient cuts are removed.

As anticipated in Fig. 9, it must be stressed that the data reduction study is stable in rigidity, making the selection itself stable and well-posed, without the necessity of cut modulation as a function of particle energy: the data reduction for positive particles is almost constant in the 20÷100 GV window (see Fig. 21).

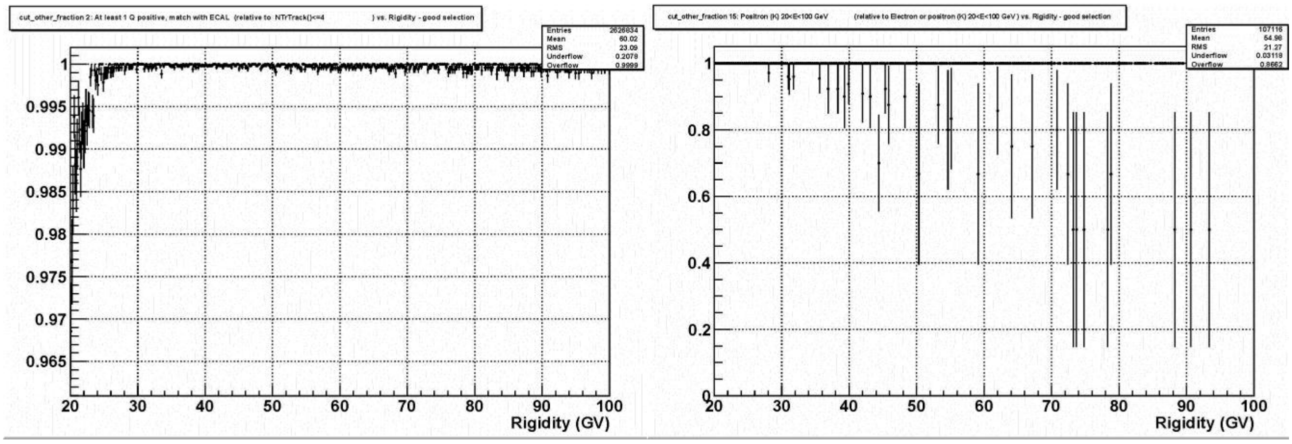

Figure 21 – Examples of cut dependence on rigidity over geomagnetic cutoff. On the left the "*At least 1 Q positive, match with ECAL*" relative data reduction; on the right the "*Positron (K) 20<E<100 GeV*", i. e. the positron fraction.

5.1.2.4 Discriminators Maps

In this section the composite behaviors of the three particles species selectors are presented. The aim is to understand in detail the overall capability of discrimination, plotting each discriminator as a function of the other and using the third to isolate the species population. Each plot slice is integrated to compute the effective data reduction and the rejection power with respect to the total preselected events before the cut.

Fig. 22 shows E/p versus ECAL BDT discriminators.

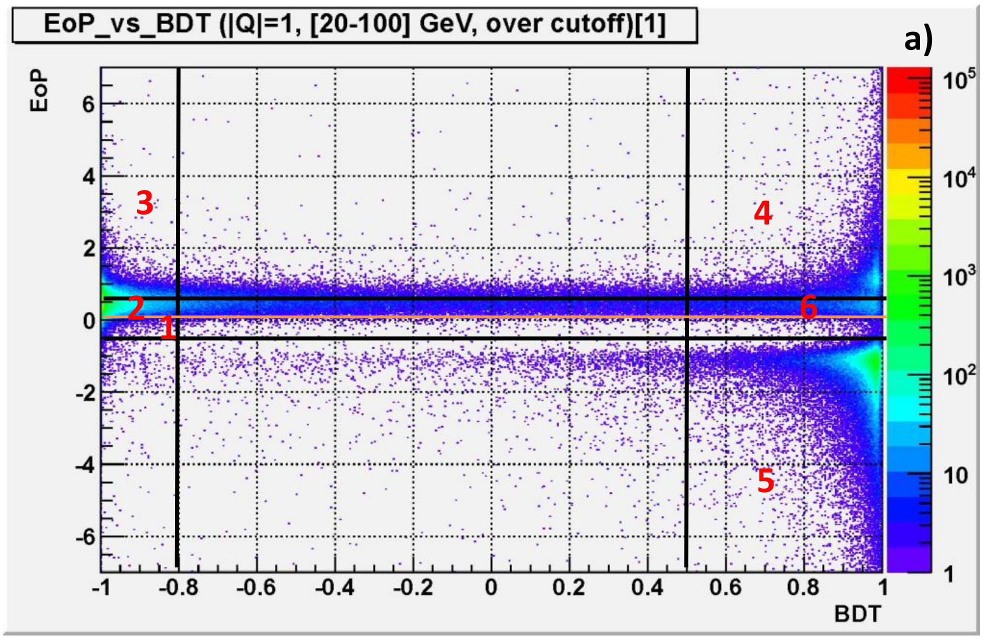

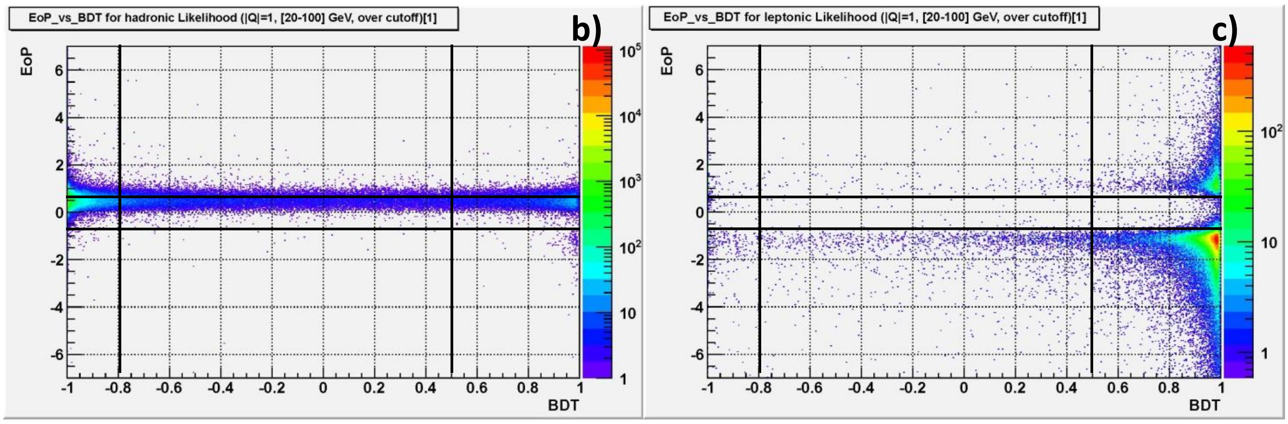

Figure 22 – E/p versus ECAL BDT. a) All *preselected* events. The black lines and the orange one at zero delimit the two purely proton-like and electron-like regions. The other ones must be studied to understand their populations. All the regions are numerically tagged; b) *preselected* K-Likelihood hadrons; c) *preselected* K-Likelihood leptons.

In Table 10 the results of slices counts are shown, before and after the Likelihood cuts for hadrons and leptons. The second-last column shows the per cent populations of each region with respect to all events of Fig. 22a), whereas the last one shows the per cent population after the Likelihood cut, with respect to the events of that region before the cut. This is done to understand how much a discriminator is able to individuate leptons and hadrons already selected by the other two discriminators.

Discriminator		**Region**	**X Range**	**Y Range**	**Population**	**w.r.t. total events %**	**w.r.t. region total after cut %**
E/p vs ECAL BDT	No cut (Fig. 22a)	**1**	[-1, -0.6]	[-0.5, 0]	mix	1,2	
		2	[-1, -0.6]	[0, 0.51]	proton-like	57,1	
		3	[-1, -0.6]	[0.52, 1.5]	mixed protons	38,4	
		4	[0.6, 1]	[-0.3, 2.2]	mix	1,0	
		5	[0.5 1]	[-4, -0.5]	electron-like	4,6	
		6	[0.5, 1]	[-0.5, -0.28]	mixed electrons	1,5E-02	
	Likelihood cut for hadrons (Fig. 22b)	1			mix	0,7	55,4
		2			proton-like	50,0	87,6
		3			mixed protons	34,3	89,4
		4			mix	0,6	59,8
		5			electron-like	7,2E-03	0,2
		6			mixed electrons	1,9E-03	12,4
	Likelihood cut For leptons (Fig. 22c)	1			mix	4,6E-03	0,4
		2			proton-like	5,0E-02	0,1
		3			mixed protons	0,1	0,1
		4			mix	0,3	27,3
		5			electron-like	4,0	86,6
		6			mixed electrons	1,1E-02	74,2

Table 10 - Integral population of the six regions defined in Fig. 22: the electron-like one, the proton-like one, the mixed zones and the mixed protons (good BDT but not E/p) and mixed electrons (good BDT but not E/p) ones. In the second-last column, the percent populations of the three Fig. 22 plots w.r.t. total *preselected* events is shown; in the last column the per cent population after the Likelihood cut, with respect to the events of that region before the cut, is presented. The total percentage of the six regions slightly exceeds 100% because of the overlapping of some regions.

Some map regions satisfy one discriminator but not the other (see Table 10). For example, the third region is occupied by here-called “mixed protons”, i.e. BDT protons which don’t satisfy the E/p<0.5 constraint: they constitute 38% of all events. Once the Likelihood cut is applied, the mixed protons are recognized as protons. Also pure protons and electrons received a ~ 90% cut by the Likelihood. So, the total percentage of protons after the Likelihood cut is about 91%. The fully mixed regions, which do not satisfy any selectors, represent 2% of the statistics.
The Likelihood cut in Table 10 shows a great selection power: it reduces of three order of magnitude the “wrong” populations (electrons after hadron cut and vice versa), both for hadrons and leptons.

The second selectors map is Likelihood versus BDT (Fig. 23).

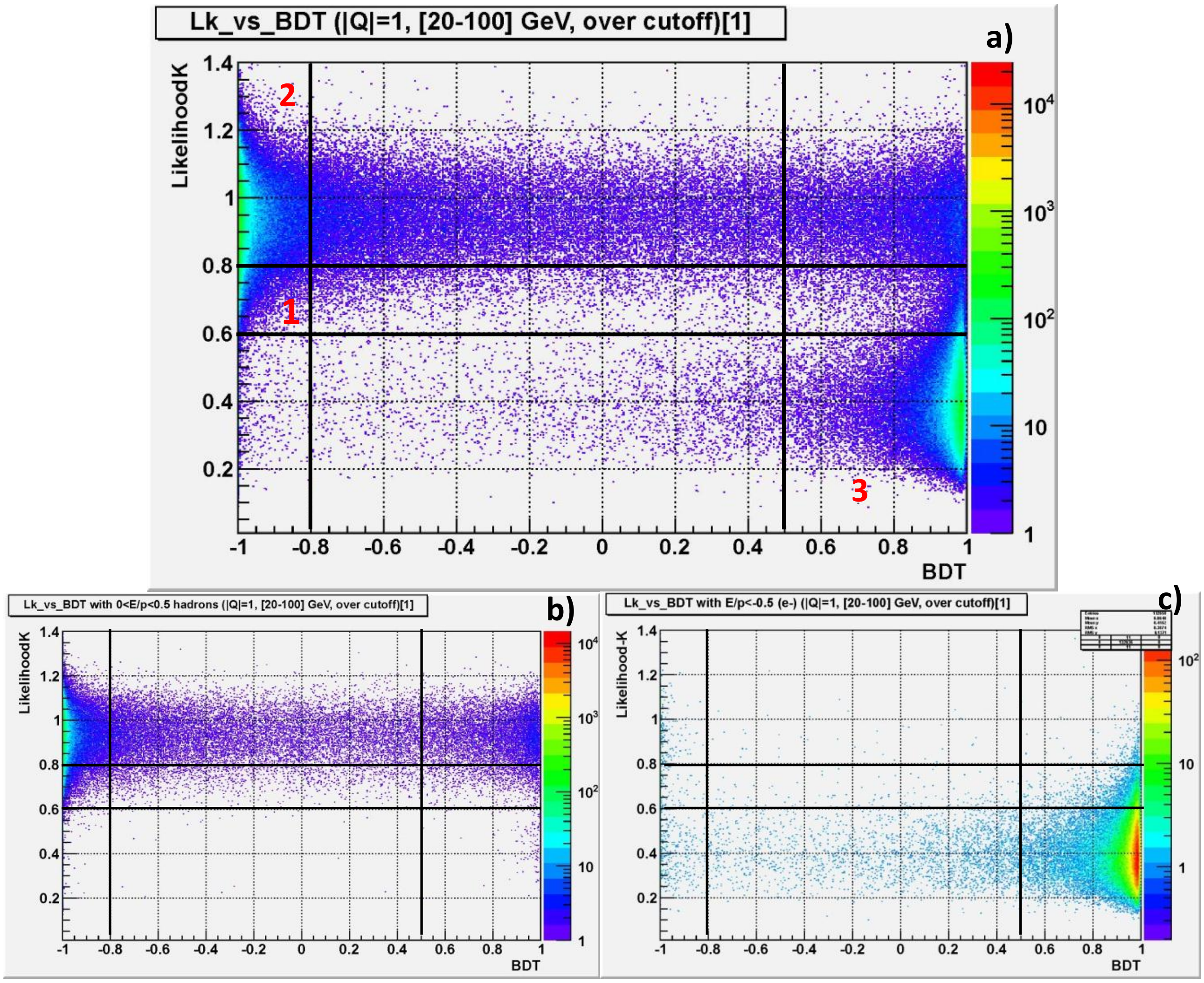

Figure 23 – TRD K-Likelihood versus ECAL BDT. a) All *preselected* events. The black lines delimit the two purely proton-like and electron-like regions. The other regions must be studied to understand their populations. All the regions are numerically tagged; b) *preselected* E/p hadrons; c) *preselected* E/p leptons. The upper right region is composed by good likelihood protons.

Discriminator		Region	X Range	Y Range	Population	w.r.t. total events %	w.r.t. region total after cut %
TRD Likelihood vs ECAL BDT	No cut Fig. 23a	**1**	[-1, -0.75]	[0.5, 0.8]	mixed protons	10,2	
		2	[-1, -0.75]	[0.8, 1.2]	proton-like	82,1	
		3	[0.5, 1]	[0.15, 0.6]	electron-like	0,3	
	E/p cut hadrons (Fig. 23b)	1			mixed protons	6,1	60,2
		2			proton-like	45,6	55,6
		3			electron-like	5,0E-02	15,1
	E/p cut leptons (Fig. 23c)	2			proton-like	0,1	0,1
		3			electron-like	0,2	66,3

Table 11 – Integral population of the three regions defined in Fig. 23: the electron-like one, the proton-like one and the mixed protons (good BDT but not K-Likelihood). In the second-last column, the percent populations of the three Fig. 23 plots w.r.t. total *preselected* events is shown; in the last column the per cent population after the E/p cut, with respect to the events of that region before the cut, is presented. The total percentage of the three regions is less than 100% because the upper left region of Fig. 23a) is not computed.

It's clear from Fig. 23 and Table 11 that the two main particle discriminators work perfectly together, isolating 82% of neat protons and 10% of the Likelihood "mixed protons" (0.5<Likelihood<0.8) of region 1. The total number of protons obtained summing the protons and the mixed protons which survive the E/p cut constitutes 88% of total events. On the other hand the cut in E/p is quite strong: it kills 44% of good protons and 33% of good electrons, respectively.

If the positron selection E/p>0.5 cut is applied to Fig. 23a), the positron population alone can be highlighted (Fig. 24, lower right corner), together with the remaining protons of the E/p positive peak described in Fig. 20.

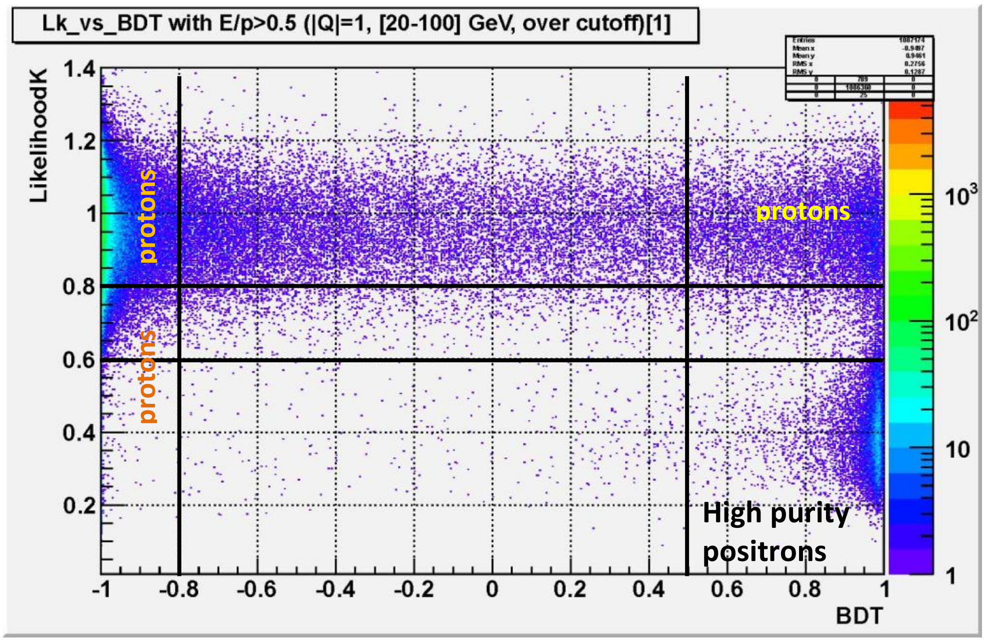

Figure 24 – TRD K-Likelihood versus ECAL BDT for E/p>0.5 positrons. Only 0.14% of the total entries for E/p>0.5 are high purity positrons (lower right corner), i. e. 0.056% of the total *preselected* analyzed events.

Positrons still represent only 0.1% of the events selected with the E/p>0.5 cut but, since protons rate is four order of magnitude larger than positron one in our energy window, this means that the E/p>0.5 reduces the proton background by a factor 10.

The third selectors map is Likelihood versus E/p (Fig. 25).

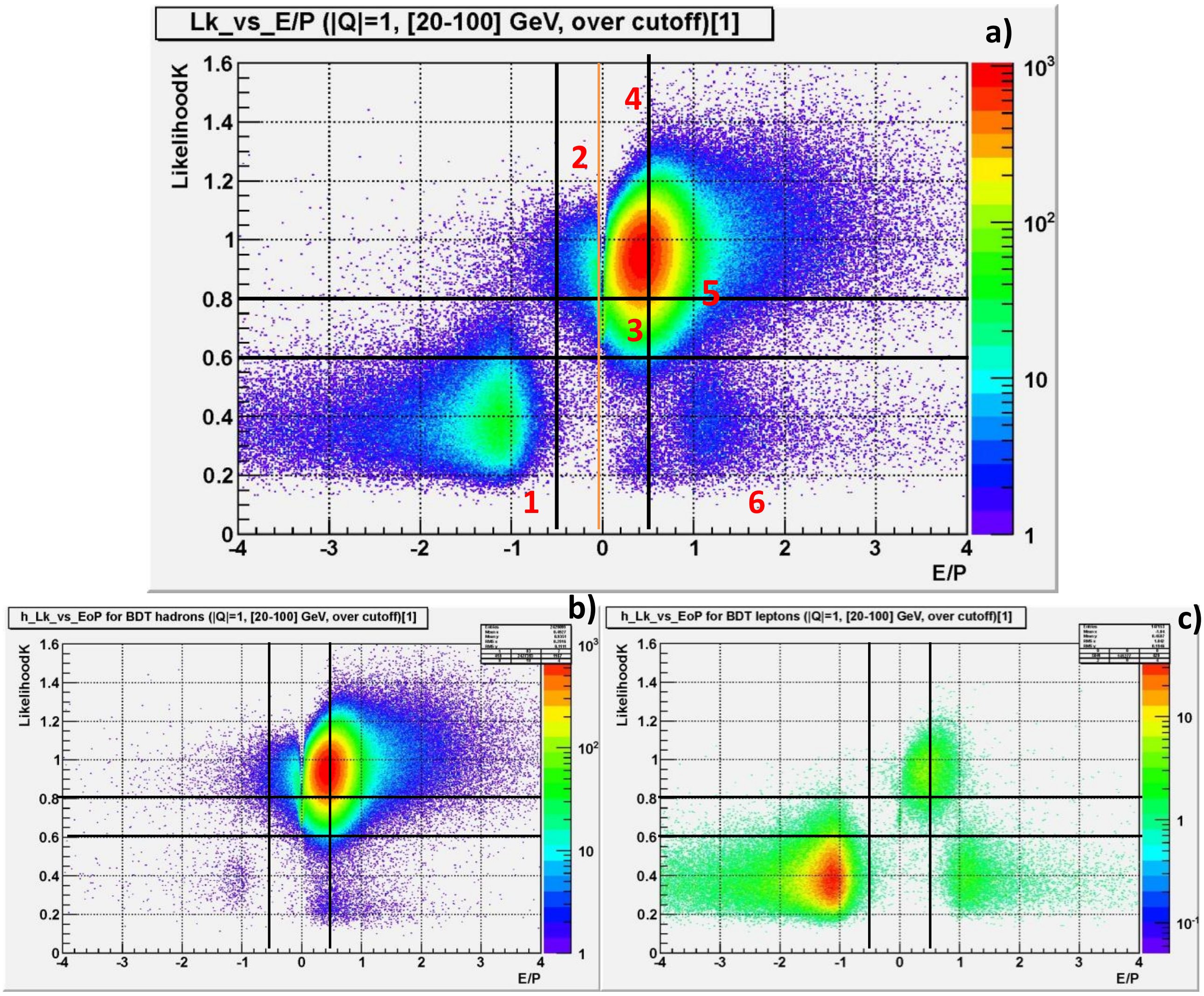

Figure 25 – TRD K-Likelihood versus E/p. a) All *preselected* events. The black lines and the orange one at zero delimit the two purely proton-like and electron-like regions. The other quadrants must be studied to determine their populations. All the regions are numerically tagged; b) *preselected* BDT hadrons. c) *preselected* BDT leptons.

In the Likelihood-E/p map of Fig. 25 many different regions can be delimited. Only two of them are clearly identified: the others are fully mixed zones or “mixed protons”. The mixed contribution is still at 2% level (see Table 12). After the hadron selection BDT cut, the two mixed protons regions shows a proton contents of 97÷98%; so the total percentage of protons becomes 98%.

Moreover, after the hadron selection BDT cut, the mix region 2 (-0.75<E/p<0) manifests an hadronic nature, i.e. antiprotonic, because of the negative charge; on the other hand, after the leptonic BDT cut the mix region 6 (0.7<E/p<3.5) shows a leptonic behavior, i. e. positronic. The mixed/antiproton-like region 2 has a so high statistics (the usual antiproton/proton ratio is 10^{-4}), because of charge confused protons.

It must be noted that, at this analysis level, the BDT cut is very refine, because it discards only 2% of good protons and 5% of good electrons.

Discriminator		Region	X Range	Y Range	Population	w.r.t. total events %	w.r.t. region total after cut %
TRD Likelihood vs E/p	No cut (Fig. 25a)	**1**	[-0.4, -0.35]	[0.13, 0.6]	electron-like	4,5	
		2	[-0.75, 0]	[0.65, 1.2]	mix	1,3	
		3	[0, 0.5]	[0.5, 0.8]	mixed protons	6,4	
		4	[0, 0.5]	[0.8, 1.4]	proton-like	47,2	
		5	[0.5, 3]	[0.55, 1.4]	mixed protons	45,1	
		6	[0.7, 3.5]	[0.15, 0.6]	mix	0,4	
	BDT cut for hadrons (Fig. 25b)	1			electron-like	2,8E-02	0,6
		2			mix	1,2	97,0
		3			mixed protons	6,2	97,9
		4			proton-like	46,3	98,0
		5			mixed protons	43,8	97,2
		6			mix	0,1	18,0
	BDT cut for leptons (Fig. 25c)	1			electron-like	4,3	95,0
		2			mix	1,4E-02	1,1
		3			mixed protons	3,9E-02	0,6
		4			proton-like	0,3	0,5
		5			mixed protons	0,3	0,7
		6			mix	0,3	77,8

Table 12 - Integral population of the six regions defined in Fig. 25: the electron-like one, the proton-like one, the mixed, the mixed protons ones (good E/p but not K-Likelihood and vice versa). In the second-last column, the percent populations of the three Fig. 25 plots w.r.t. total *preselected* events is shown; in the last column the per cent population after the BDT cut, with respect to the events of that region before the cut, is presented. The total percentage of the six regions slightly exceeds 100% because of the overlapping of some regions.

Composite discriminator

Other convenient discriminators can be set up in order to arrange more handy selectors. Two examples are illustrated in Figs. 26 and 27.

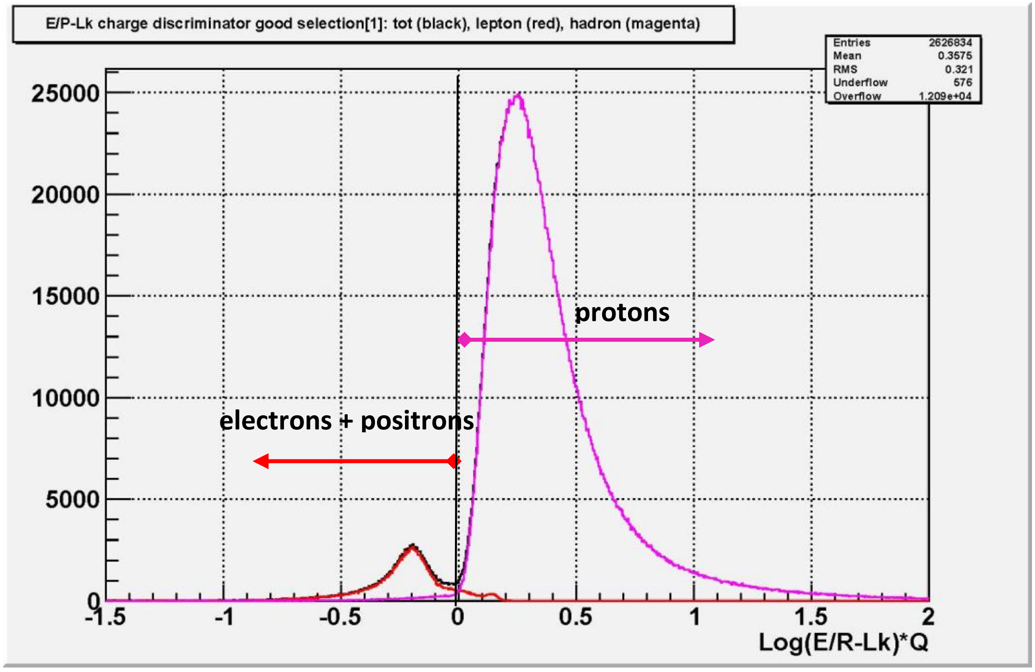

Figure 26 – E/p-Likelihood composite discriminator. It's possible to combine the discriminators to obtain more suitable selection criteria. With this function, leptons and hadrons are discriminated

by a > 0 or < 0 cut: the red line represents the leptonic shape, while protons one completely overlaps the total positive distribution. The two arrows depart from the $Log(E/p - Lk) * Q_{Tracker}$ values where one curve separates from the other, i.e. at the origin [437].

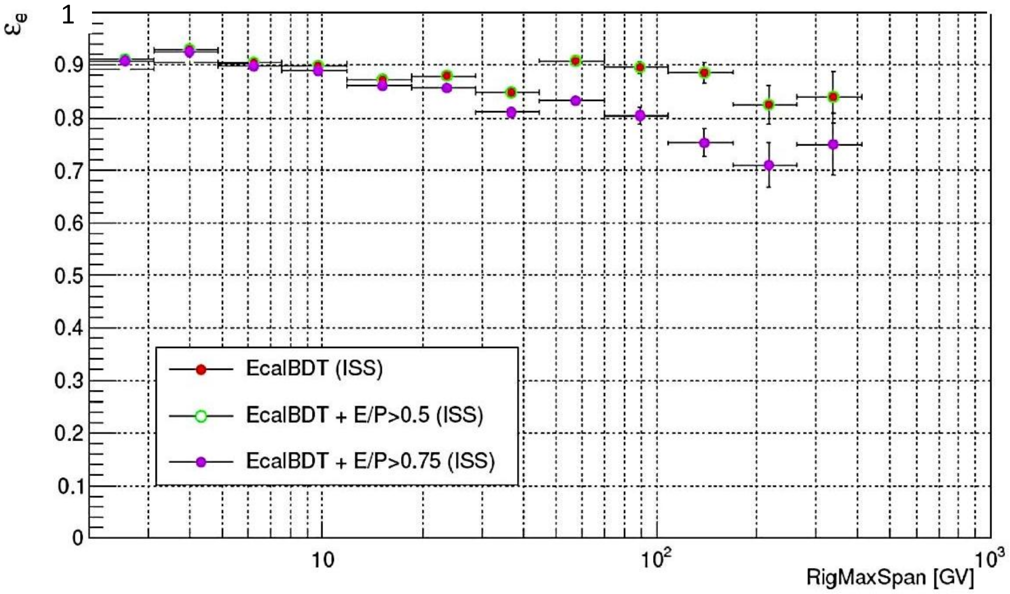

Figure 27 – Overall BDT+E/p efficiency on selected electrons [436].

In Fig. 27, BDT plus $|E/p| > 0.5$ has a 100% efficiency on leptons, whereas BDT plus $|E/p| > 0.75$ efficiency considerably decreases with rigidity. This is an example of cut instability in rigidity for a not well-tuned selector.

Discriminators analysis demonstrates that AMS is largely capable to separate particle species in the 20-100 GeV energy range, at few % level of e/p rejection; proton background is well understood, allowing us to define particles ratios, such as the positron fraction, in a strong and self-confident way.

5.1.2.5 Charge confusion

As explained in the first paragraph, a source of background are the so-called *Wrong Charge* events, mainly due to high rigidity spillover, i. e. reconstruction errors of the event curvature in the Tracker. In general, rigidity-migrations of events must be taken into account.

A first method to estimate the Charge Confusion (CC) is to compare the discrepancy between the rigidity calculated with the inner Tracker alone and with the full span configuration, assuming that the error derives from L1 and L9 wrong interpolation with inner Tracker layers. In Fig. 28 the inverses of the two rigidities are plotted. The charge confused particles lie in a discordant quadrant, with correct positive R_{inner} (positive charge) and incorrect negative $R_{full\ span}$ (negative charge) for hadrons and vice versa for leptons.

From Fig. 28b) it is evident that the amount of events lying in the discordant quadrant is very small.

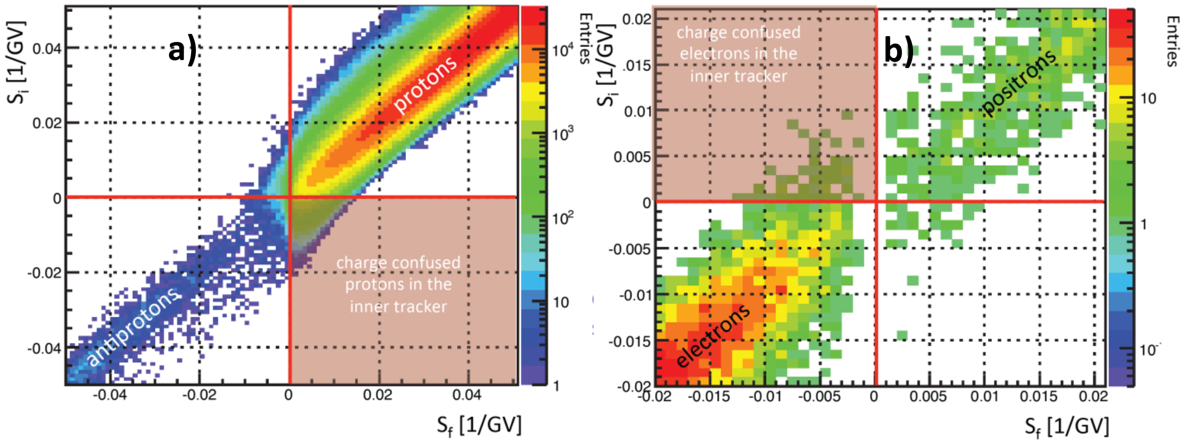

Figure 28 – *Sagitta method* for CC computation: $S_i = 1/R_{inner}$ versus $S_f = 1/R_{full\ span}$ [438]. The comparison between the two measured rigidities gives an idea of the Tracker CC due to effective MDR. a) The colored lines delimit the region of Charge Confused protons in the inner Tracker, selected with the three discriminators; b) Charge Confused electrons region (over cutoff), after BDT, Likelihood and E/p leptons selection.

Doing a comparison between detected rigidity in Tracker and reconstructed energy in ECAL, three fundamental regimes can be individuated: for energy almost equal to rigidity, for big energies and small rigidities and vice versa. The three regions are shown below in Fig. 29.
If the rigidity is much smaller than the reconstructed energy, a rigidity-migration and a wrong charge association probably have occurred.

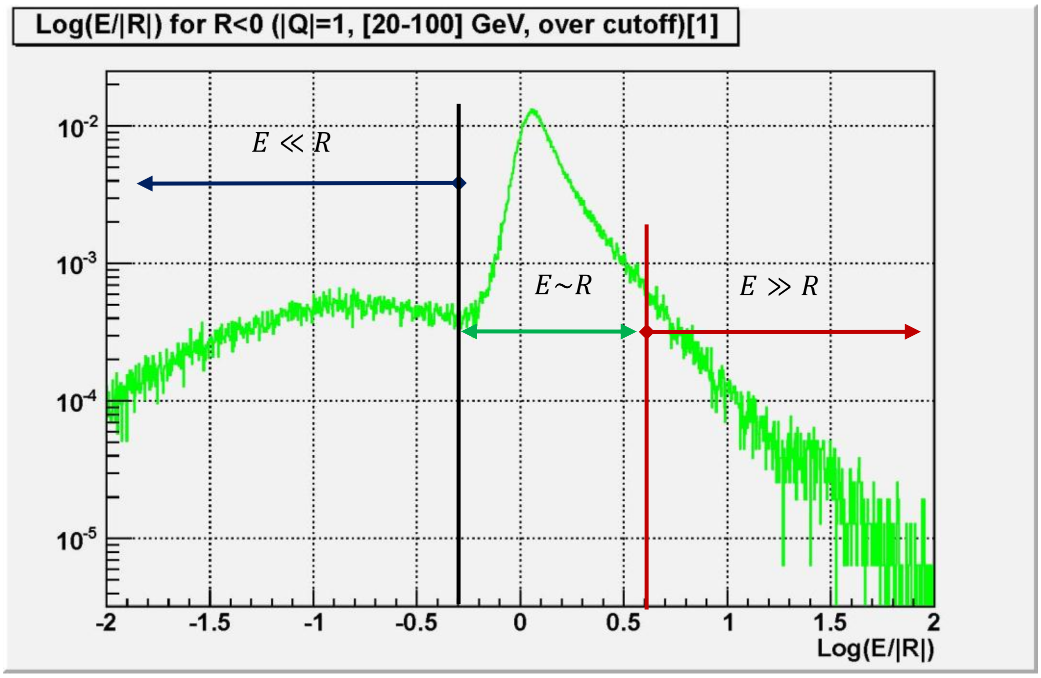

Figure 29 – $Log(E/|R|)$ *Charge Confusion discriminator* distribution for negative charged particles (R<0). This combined use of absolute rigidity, measured by the Tracker, and deposited energy, measured by the calorimeter, allows to define three measurement regimes, highlighted by the colored arrows and characteristics for electrons (green), protons (black) and charge confusion (red).

In principle, we would expect an electron curve symmetric w.r.t. zero, but this is not the case (Fig. 29): it reaches a local minimum from one side and decreases broadening on the other, instead. This is due to Charge Confusion.

In Fig. 29 the three regimes are defined as follow: for $Log(E/|R|) < -0.3$, where $E \ll R$, typical of protons, for $-0.3 < Log(E/|R|) < 0.6$, where the two physical quantities are almost equal (the electron region), and for $Log(E/|R|) > 0.6$, where $E \gg R$ (the CC region – red arrow). The electron ($E \sim R$) peak is clearly visible at 0.1. The third part of the plot, when the electron curve starts to oscillate, is the charge confused one: $Log\left(\frac{E}{|R|}\right) > 0.6$ is the limit for the CC range, which corresponds to $|R| \approx {}^{E}/_{4}$.

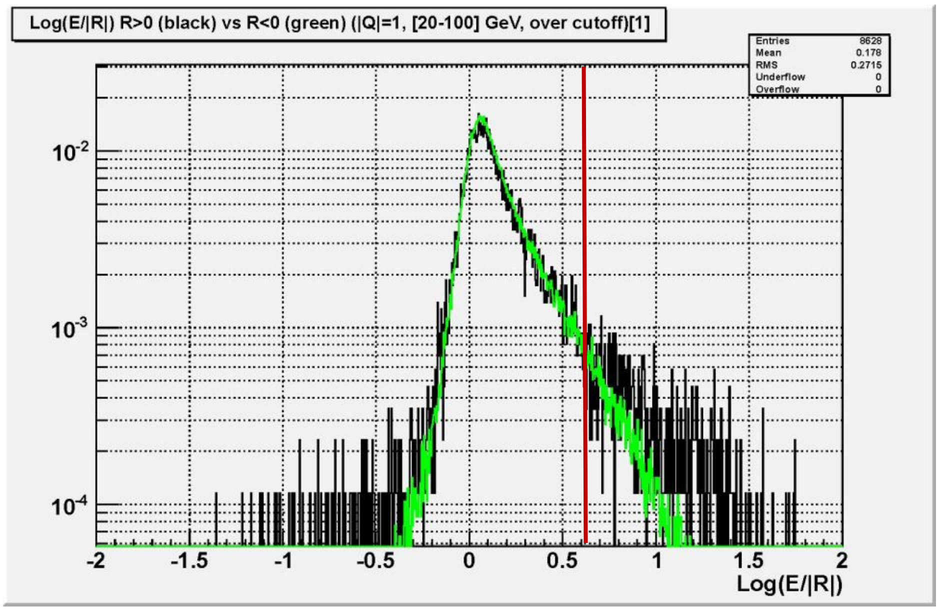

Figure 30 - $Log(E/|R|)$ for leptons selected with BDT and K-Likelihood. Green curve corresponds to R<0 particle and black curves to R>0 particles.

The Fig. 30 plot is complementary to the colored discordant quadrant of Fig. 28b): after selecting leptons via BDT and Likelihood discriminators, the two $Log(E/|R|)$ functions are quite similar and the R>0 electronic curve, beyond $Log(E/|R|) = 0.6$ (red straight line), subtends a little area, i. e. a very small CC population which is $\lesssim 1.5\%$.

Another way to deal with Charge Confusion and analyze its nature and origin, with the joint assistance of the MonteCarlo, is to study the charge distribution of the Time-of-Flight as a function of the same discriminator Log|E/p|, analyzing the populations with large Q (i. e. Q > 1.6), which may be due to multiple particles hitting the same TOF paddle and inducing a wrong hit association (WHA) [440]. This phenomenon is mainly due to Bremsstrahlung effects**.** This a possible source of charge confused events not due to MDR (Maximum Detectable Rigidity), i. e. not bad computed curvature in the Tracker.
The electrons which “live” in the charge confusion window are of the order of 1÷2%, considering both MDR charge confusion and WHA due to interactions in the detector.
So, it can be argued that, for the sake of events selection and cuts stability study, CC is almost of no interest.

5.2 Data analysis as a function of time

After computing the mean data reduction for integrity, cleanness and particle identification cuts, proving they're well-defined, efficient, stable in rigidity and capable to discriminate particle species, to complete the understanding of the experiment and check the reliability of its results, an analysis as a function of data taking time has been developed.
In principle, many effects of physical and instrumental origins could affect the temporal stability of the AMS-02 detector. For example, anisotropies could occur following the Sun activity, the Earth position in the Solar system (w.r.t. Sun, planets and galactic sky), or due to the Moon, which periodically shadows the sky viewed by the ISS, if high energy leptons sources are localized and not too distant. Also human operation could interfere with AMS data acquisition, i. e. Soyuz and other low orbit space vehicles docking and undocking from the ISS, satellites communications and scientific operations on the Station itself. Moreover, the detector has been subjected to several refinements: the TRD gas refilling procedure has been fixed, the Tracker alignment procedure has been developed, the trigger evolved, through different thresholds configurations and subdetectors elements powering. Some features were corrected by new reconstruction software, but others cannot be corrected and the raw data cannot be "fixed".

In the following, a review of each data selection cut is presented as a function of time and geomagnetic latitude $\theta_{M.}$ Cuts which does not produce a data reduction are omitted.
The analysis of the data reduction as a function of the geomagnetic latitude is an important issue because, before applying the rigidity range cut (R>20 GV and over-cutoff) [392], appreciable dependences are expected, due to the Earth magnetic field. The dependence from geomagnetic latitude of the cuts is averaged on the entire data taking period (May 2011 – September 2012).
The positron fraction dependency versus time is discussed in section 5.3.
As a general comment, all plots show a break in December 2011 caused by the DAQ/ECAL desyncronization explained in 5.1.2, whereas the first period of data taking (till August 2011) shows a less stable behavior due to the setting up of the apparatus [431].

It should also be taken into account that the integrity and cleanness cuts (numbered 1 to 30 in section 5.1) concern the full statistics, including nuclei and particles with under-cutoff energies.

The first relevant cut is cut 6 (Science Run - Fig. 31), which shows the reduction corresponding to calibration and other non-science runs; the second is cut 8 (SAA exclusion) shown in Fig. 33.

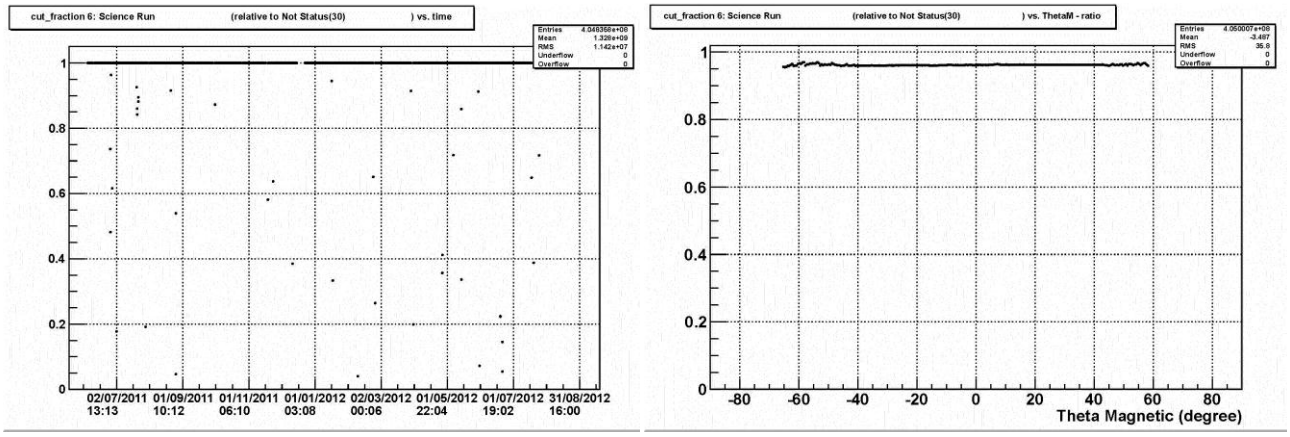

Figure 31 – Cut 6 stability: *Science Run*. Left: data reduction as a function of time, from May 2011 to September 2012. Each point represents one hour. Right: Data reduction as a function of the geomagnetic latitude.

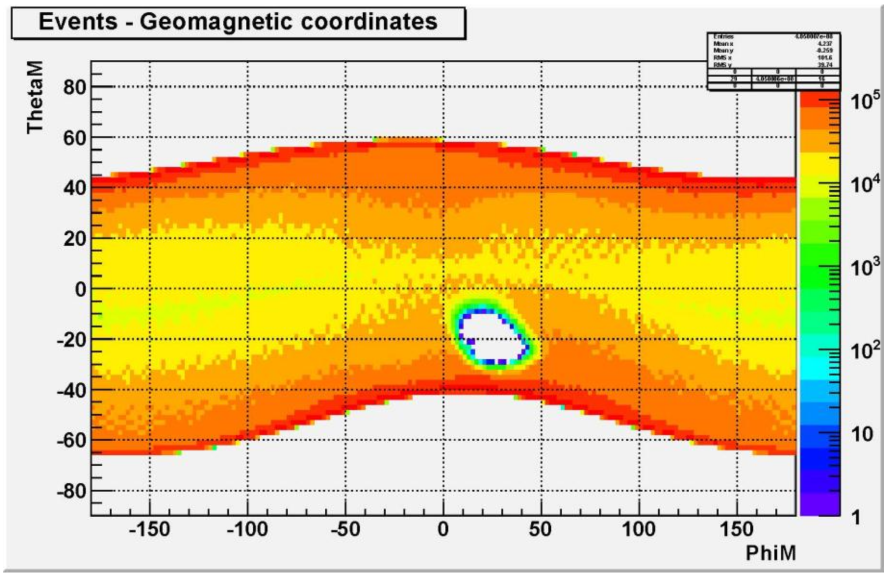

Figure 32 – Geomagnetic map of the AMS-02 data taking. The color code represents the number of collected events.

Along its orbital path, AMS-02 sweeps geomagnetic longitudes Φ_M from -180° to +180° and geomagnetic latitudes θ_M from -70° to +60°. Fig. 32 shows the number of reconstructed events with a good track. The white region is the SAA, where the very high rate results in the AMS-02 data acquisition system to be nearly blind; it lies approximately in the quadrant between 0° and 50° for Φ_M and between 0° and -40° for θ_M. The rate increases towards the magnetic poles, where the geomagnetic field configuration allows more particles to penetrate down to the AMS-02 altitude.

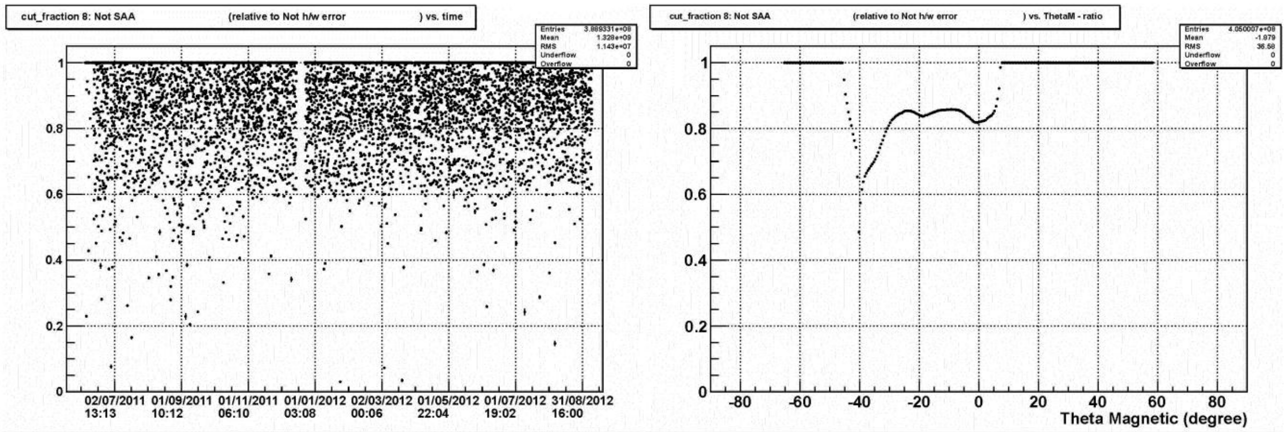

Figure 33 - Cut 8 stability: *Not SAA*. Left: data reduction as a function of time, from May 2011 to September 2012. Each point represents one hour. Right: data reduction as a function of the geomagnetic latitude.

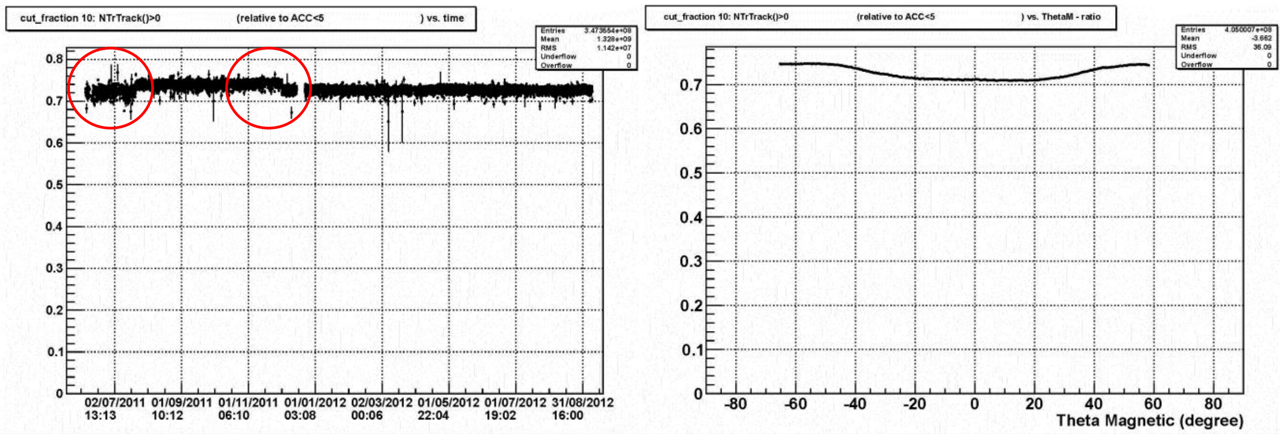

Figure 34 - Cut 10 stability: *NTrTrack()>0*. Left: data reduction as a function of time, from May 2011 to September 2012. The red circles indicate the main changes in data reduction, discussed in the text. Each point represents one hour. Right: data reduction as a function of the geomagnetic latitude.

Cut 10 (NTrTrack()>0) is shown in Fig. 34. During the setting-up period the track reconstruction efficiency has been slightly lower. In December 2011, a power supply failed, reducing the number of active tracker strips by about 3%.

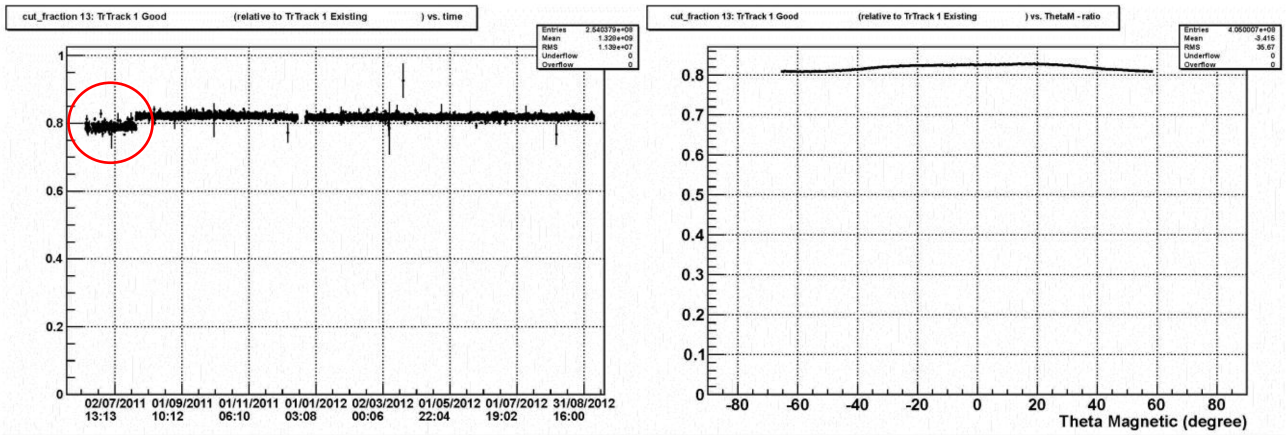

Figure 35 - Cut 13 stability: *Good Track*. Left: data reduction as a function of time, from May 2011 to September 2012. Each point represents one hour. Right: data reduction as a function of the geomagnetic latitude.

Cut 13 (Good Track) behavior, illustrated in Fig. 35, is similar to cut 10. Data selection is quite stable in geomagnetic latitude, with less effect at low latitudes, where the particle rate is lower and the data taking much cleaner.

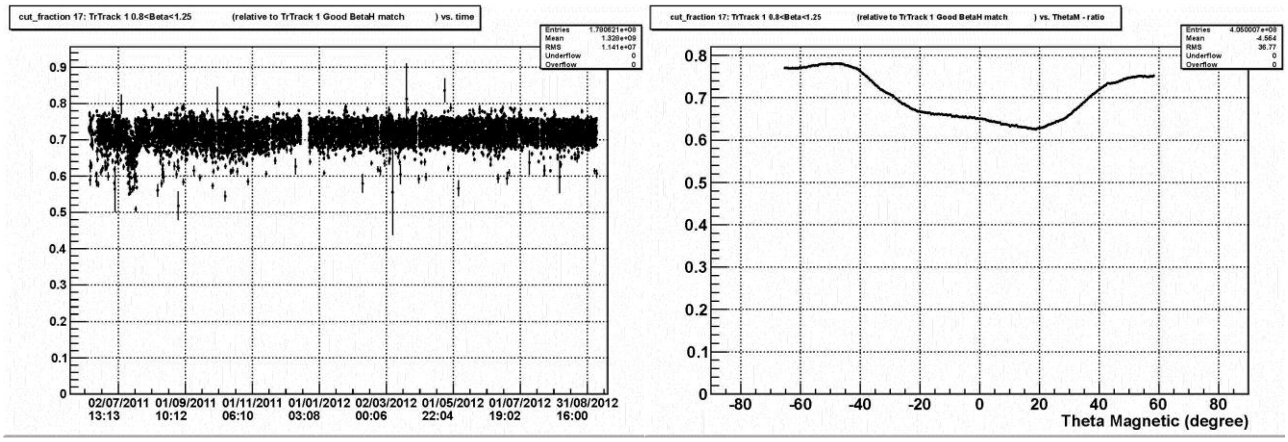

Figure 36 - Cut 17 stability: *0.8<Beta<1.25*. Left: data reduction as a function of time, from May 2011 to September 2012. Each point represents one hour. Right: data reduction as a function of the geomagnetic latitude.

Cut 17 (0.8<Beta<1.25) data taking in Fig. 36 is broader than the previous ones, with an oscillation of ±3%. The data reduction due to this cut depends on the geomagnetic latitude: towards equator, more low-energy trapped particles are detected by AMS02.

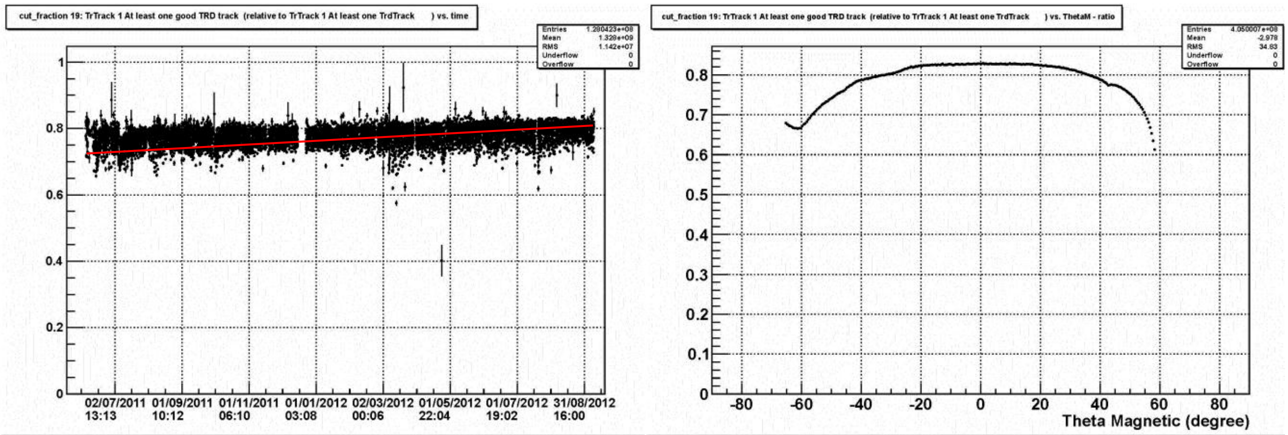

Figure 37 - Cut 19 stability: *At least one good TRD track*. Left: data reduction as a function of time, from May 2011 to September 2012. Each point represents one hour. The red line is a linear fit to the data points. Right: data reduction as a function of the geomagnetic latitude.

Cut 19 (At least one good TRD track) is shown in Fig. 37. It must be noted that the data reduction decreases with time (red line), thanks to better calibration and refilling procedure and software development. The TRD performances are worse (about a factor ten) at high geomagnetic latitudes, i. e. near the magnetic Poles, because of the larger particle rate.

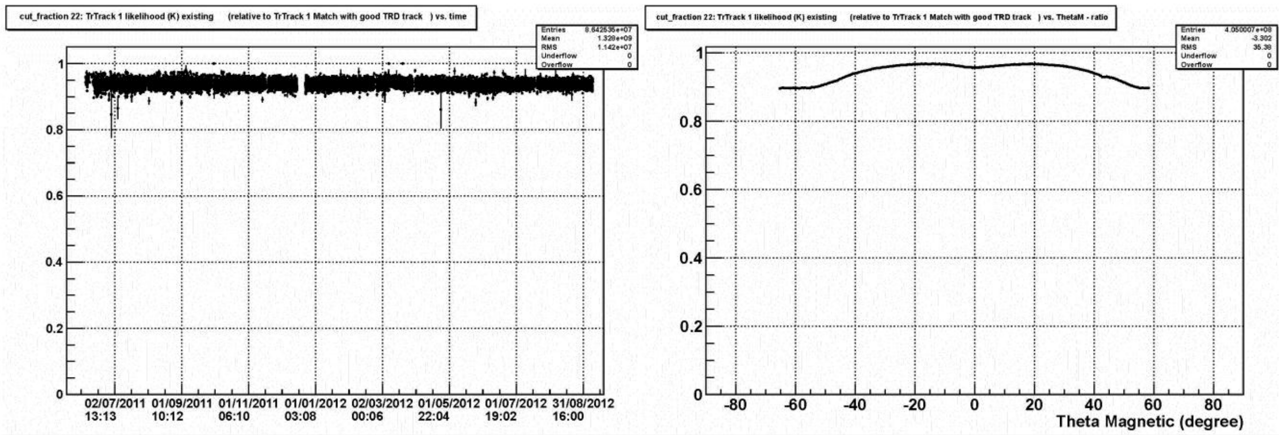

Figure 38 - Cut 22 stability: *Likelihood (K) existing*. Left: data reduction as a function of time, from May 2011 to September 2012. Each point represents one hour. Right: data reduction as a function of the geomagnetic latitude.

Cut 22 (K-Likelihood), shown in Fig. 38, is quite stable, with slightly larger data reduction towards the geomagnetic poles as for cut 19.

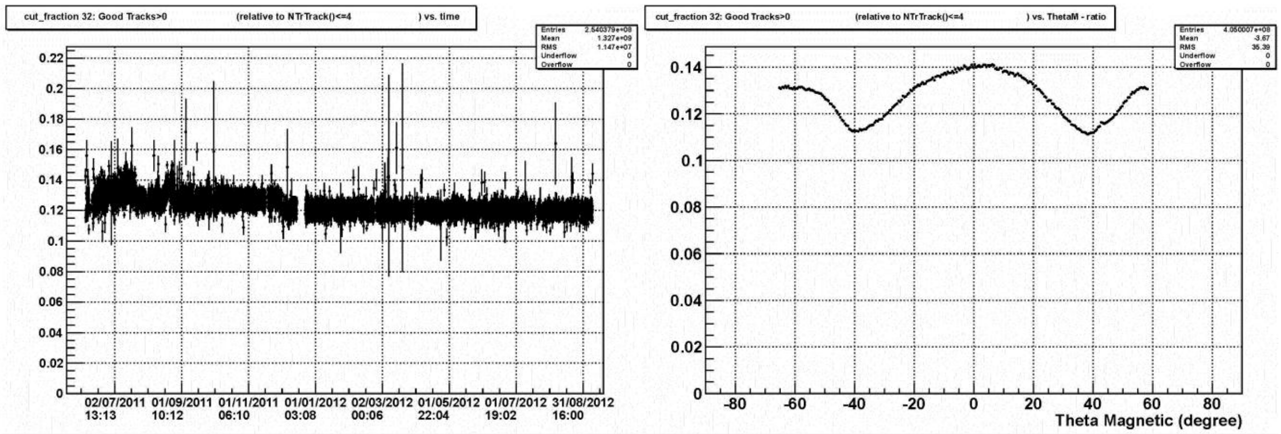

Figure 39 - Cut 29 stability: *Good Tracks>0*. Left: data reduction as a function of time, from May 2011 to September 2012. Each point represents one hour. Right: data reduction as a function of the geomagnetic latitude.

Cut 29 (Good tracks>0) in Fig. 39 manifests the same behavior as cut 10.

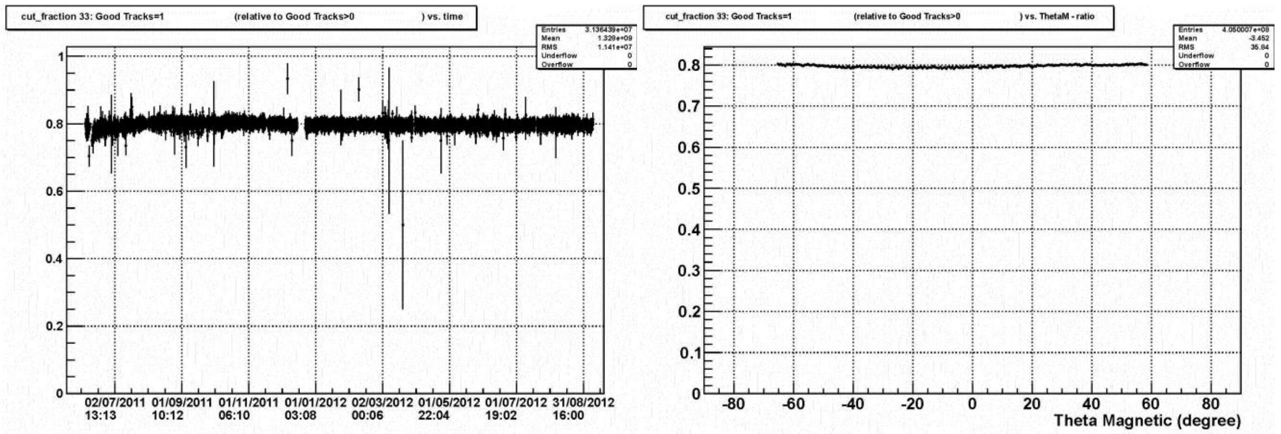

Figure 40 - Cut 30 stability: *Good Tracks=1*. Left: data reduction as a function of time, from May 2011 to September 2012. Each point represents one hour. Right: data reduction as a function of the geomagnetic latitude.

Fig. 40 shows cut 30 (Good Tracks=1), which is the reference cut for particle identification analysis: it is stable and geomagnetic latitude independent.

Unlike fundamental integrity and cleanness detectors cuts, the **particle identification selections** are more delicate and produce small statistical samples, with greater fluctuations and largest dependence on geomagnetic latitude.

Figures 41, 42, 43, 44 and 45 show particle identification cuts 1 (At least 1 Q negative, match with ECAL), 4 (Good BDT electron), 6 (Good electron K), 7 (Good electron K 20<E<100 GeV) and 13 (Electron or positron (K) 20<E<100 GeV), respectively.

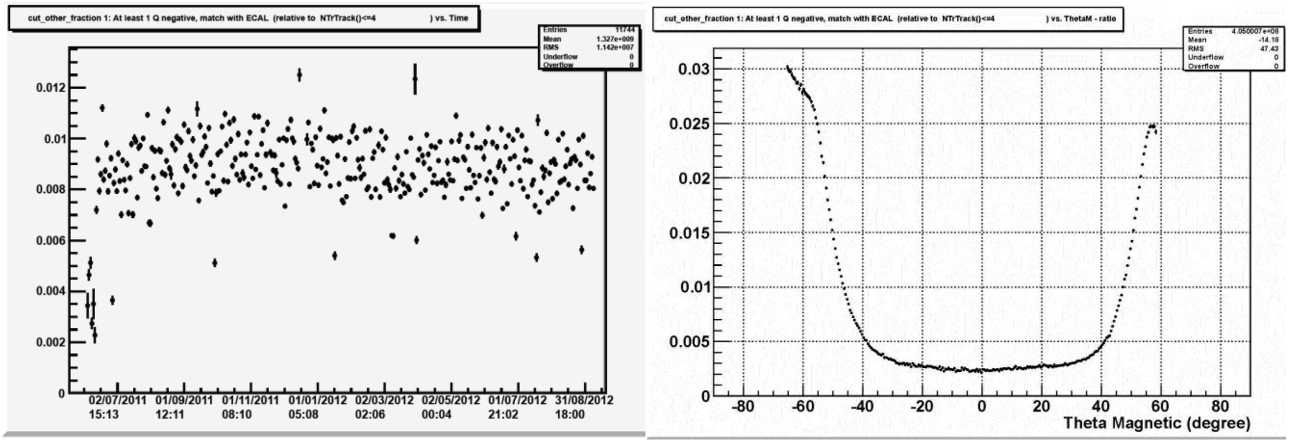

Figure 41 – Particle identification Cut 1 stability: *At least 1 Q negative, match with ECAL*. Left: data reduction as a function of time, from May 2011 to September 2012. Each point represents eight hours. Right: data reduction as a function of the geomagnetic latitude.

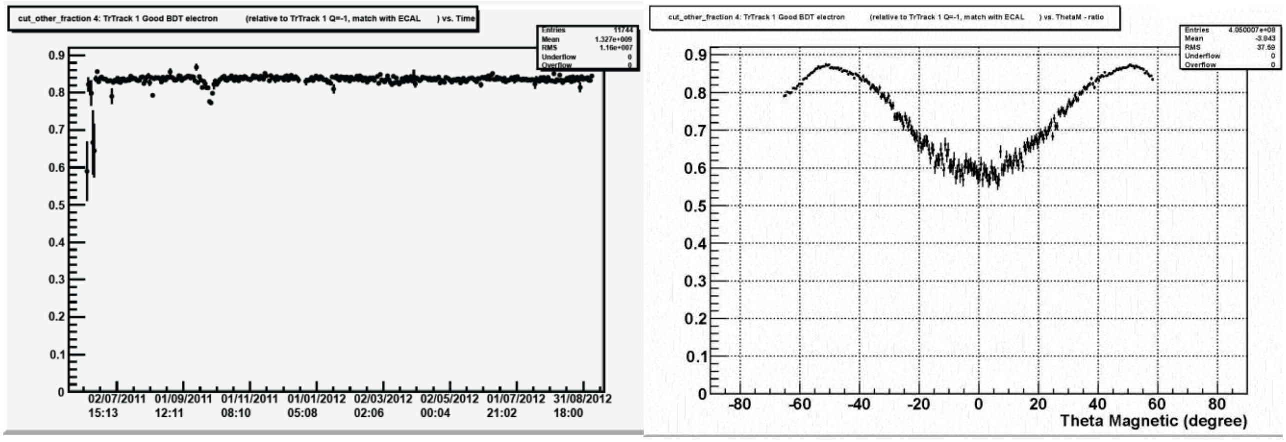

Figure 42 – Particle identification Cut 4 stability: *Good BDT electron*. Left: data reduction as a function of time, from May 2011 to September 2012. Each point represents eight hours. Right: data reduction as a function of the geomagnetic latitude.

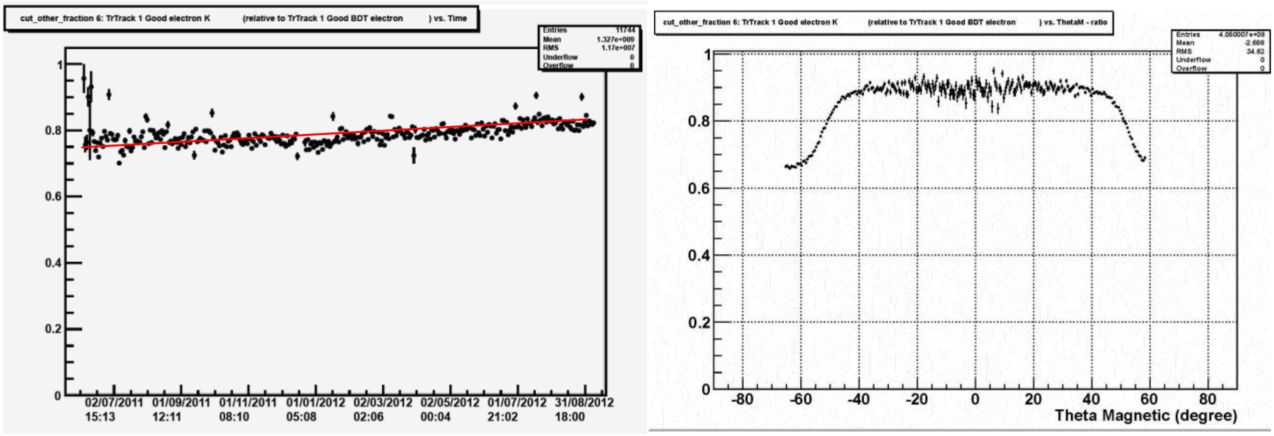

Figure 43 - Particle identification Cut 6 stability: *Good electron K*. Data reduction as a function of time, from May 2011 to September 2012. Each point represents eight hours. Right: data reduction as a function of the geomagnetic latitude.

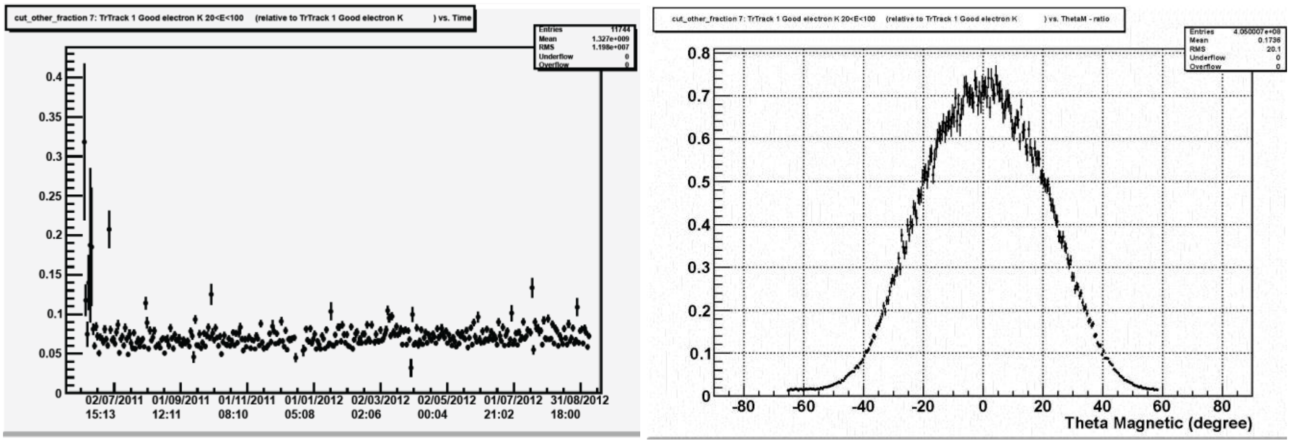

Figure 44 - Particle identification Cut 7 stability: *Good electron K 20<E<100*. Data reduction as a function of time, from May 2011 to September 2012. Each point represents eight hours. Right: data reduction as a function of the geomagnetic latitude.

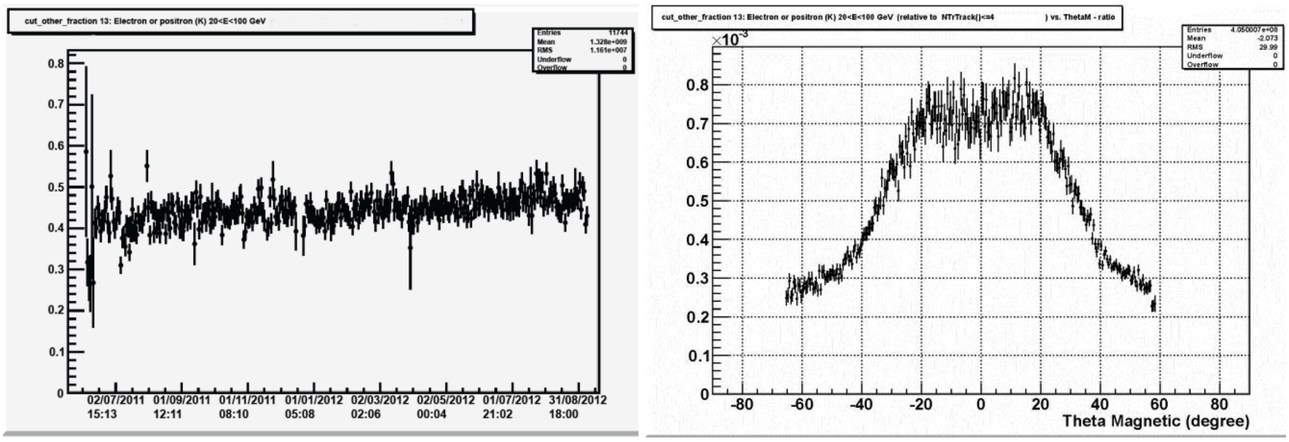

Figure 45 - Particle identification Cut 13 stability: *Electron or positron (K) 20<E<100 GeV*. Data reduction as a function of time, from May 2011 to September 2012. Each point represents eight hours. Right: data reduction as a function of the geomagnetic latitude.

In several plots the initial period shows a higher data reduction due to trigger and data acquisition set up and calibrations.

Also, in Fig. 43 an increasing trend in time can be noted, which is linked to the improvement in the TRD performances already explained in relation to Fig. 37.

The behavior of the data reduction as a function of the geomagnetic latitude reflects the cut under examination and the reference cut. In particular, the energy range selection (cut 7, 13 in Figs. 44, 45) is less important around the geomagnetic equator, where the natural rigidity cutoff is higher (with the maximum at 0° and the minimum at the Poles). The energy range excludes the high rate complicated region where CR energy is less than 20 GeV, circumscribing a good clean sample of leptons and hadrons which come from mid-low geomagnetic latitudes.

5.3 Positron fraction stability

In this section the positron fraction, between 20 and 100 GeV of energy, as a function of time and geomagnetic latitude is presented.

The data reduction as a function of time of several cuts has shown that the apparatus and the analysis are not completely stable. These fluctuations must be taken into account when computing absolute particle fluxes. However, if the fluctuations are charge-symmetric, they cancel in fluxes ratios and, in particular, in the positron fraction. This is demonstrated in the following.

Figs. 46, 47 and 48 present the positron fraction with different time binnings, to highlight the stability of the physical measurement: 8, 24, 96, 192 and 720 hours (1 month), respectively.

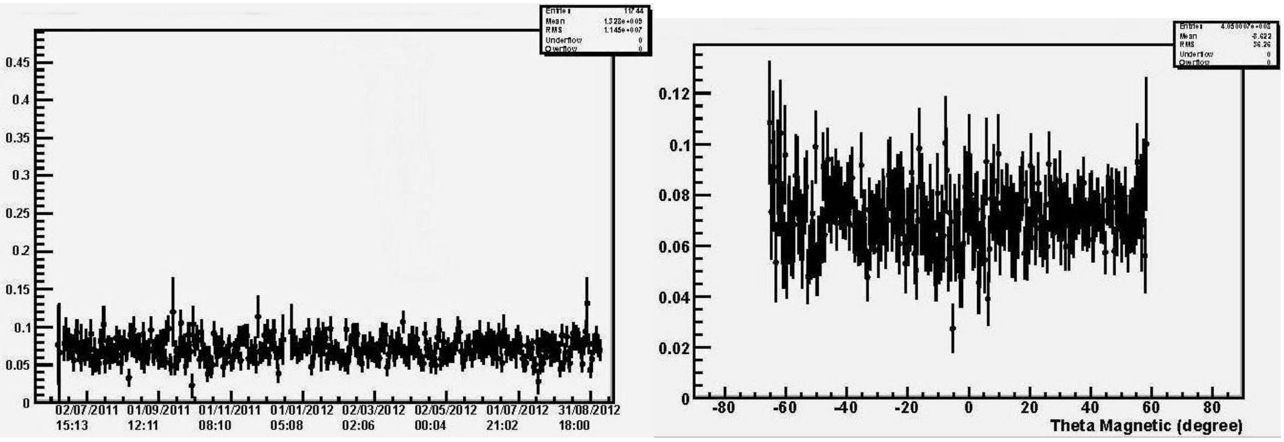

Figure 46 – Positron fraction stability with 8 hours per bin. Left: as a function of time, from May 2011 to September 2012. Right: as a function of the geomagnetic latitude.

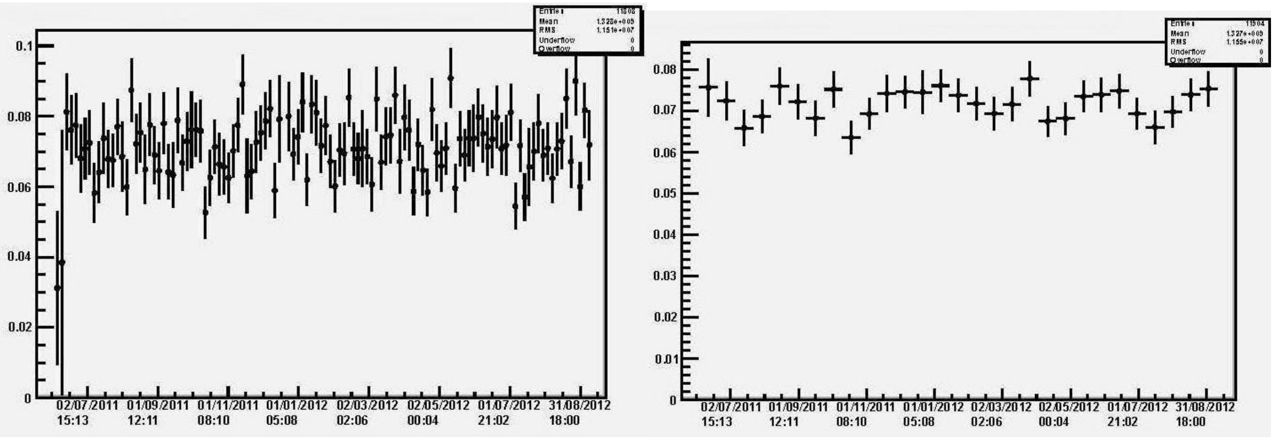

Figure 47 – Positron fraction stability. Data reduction as a function of time with 24 hours (1 day) per bin (left), and 96 hours (4 days) per bin (right).

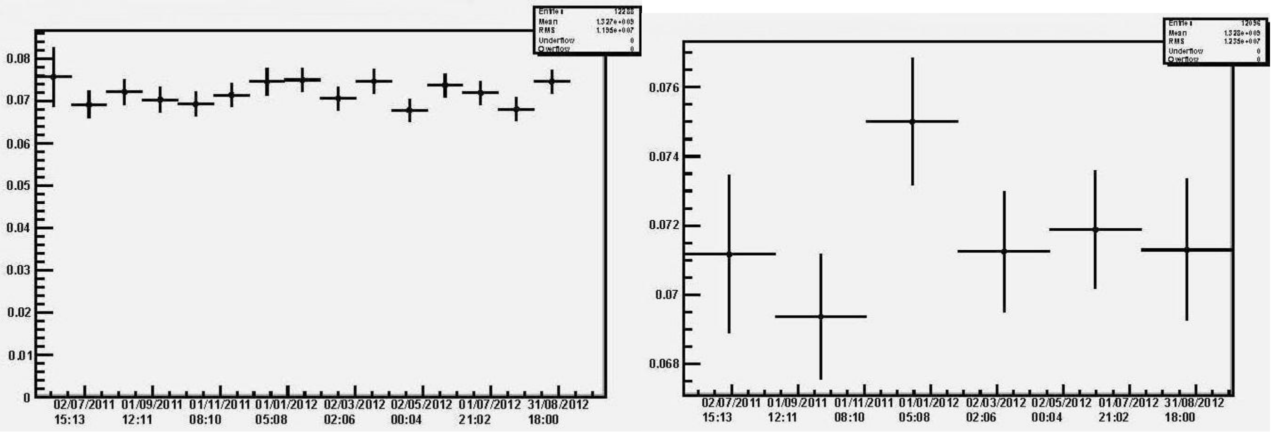

Figure 48 - Positron fraction stability. Data reduction as a function of time with 192 hours (8 days) per bin (left), and 720 hours (1 month) per bin (right).

For each plot (and further not presented binnings) the distribution of values has been histogrammed and fitted with a gaussian function. As an example, Figures 49 shows the time distribution of the positron fraction in 12 hours bins.

The distribution of the values for each bin is presented in Fig. 50. The average is 0.085, with a standard deviation of 0.022.

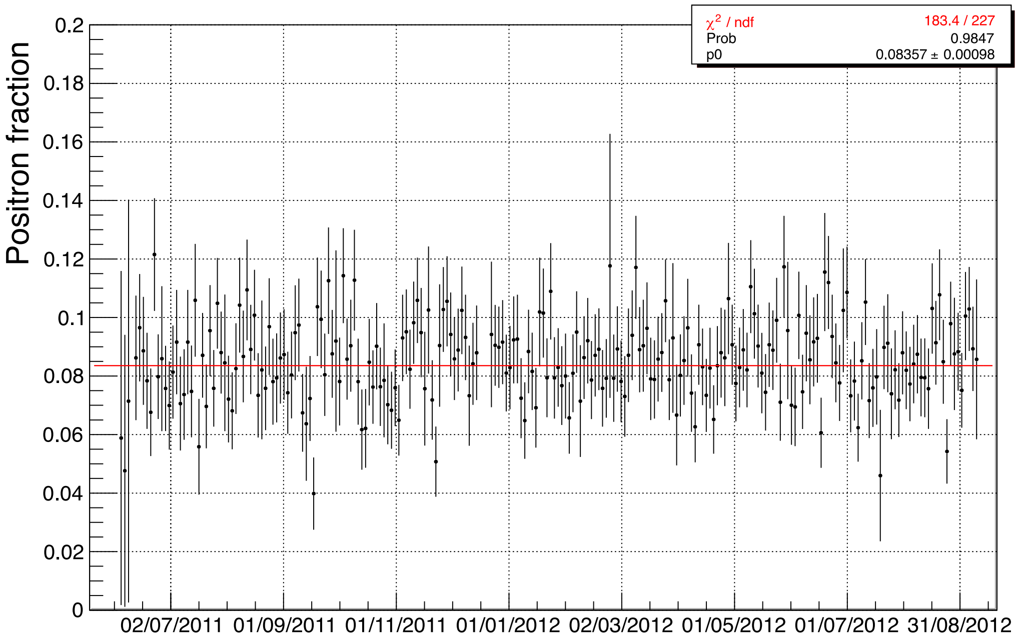

Figure 49 – Positron fraction as a function of time from May 2011 to September 2012, with 12 h/bin binning. The straight red line is the global linear fit.

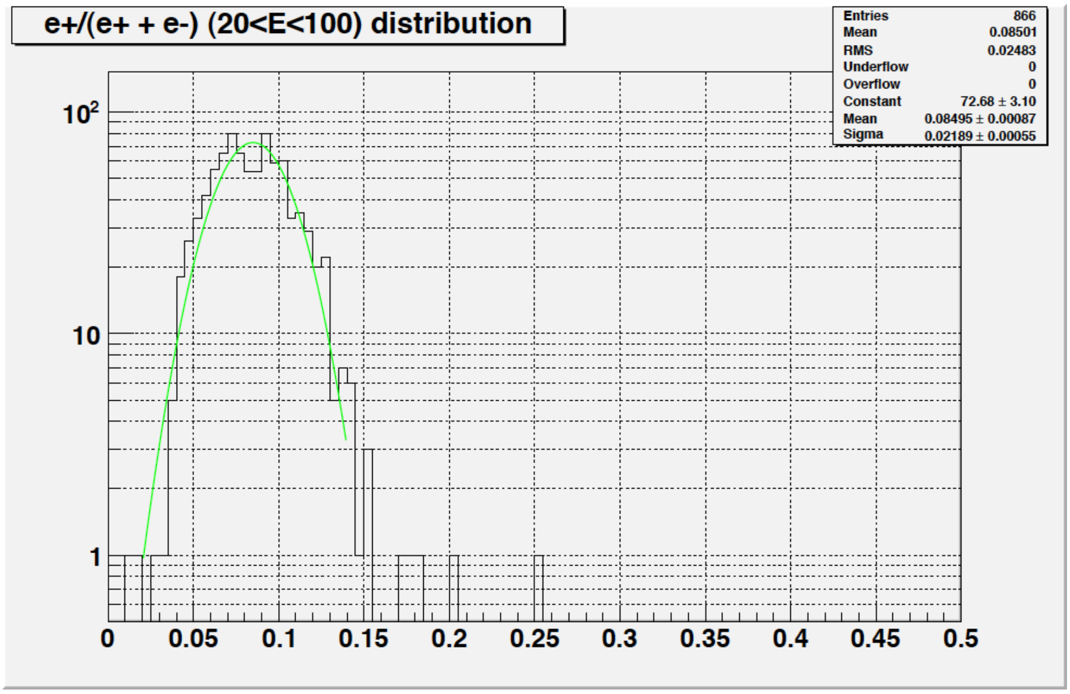

Figure 50 – Positron fraction temporal means distribution in the energy range under study for 12 h/bin binning. The green curve is a Gaussian fit to the data.

Then the overall mean values of the temporal means for nine different binnings have been compared to understand the oscillation of the measurement as a function of the selected binning.

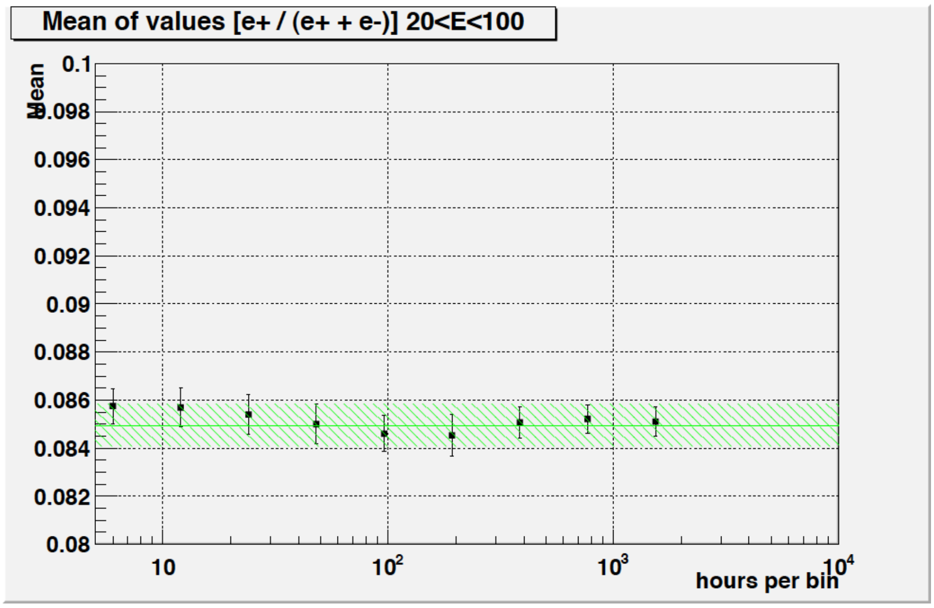

Figure 51 – Mean values of the positron fraction as a function of hours per bin, from few hours binning to more than one thousand hours binning.

The average positron fraction is very stable, irrespective of the bin size, as illustrated in Fig. 51 (the oscillation is less than 0.001).

The associated standard deviations have been plotted and fitted, to estimate the total temporal error which accompanies the positron fraction obtained with the discussed cuts ensemble: the standard deviation of the distributions decreases with increasing time per bin, as expected due to the increase in statistics, as shown in Fig. 52.

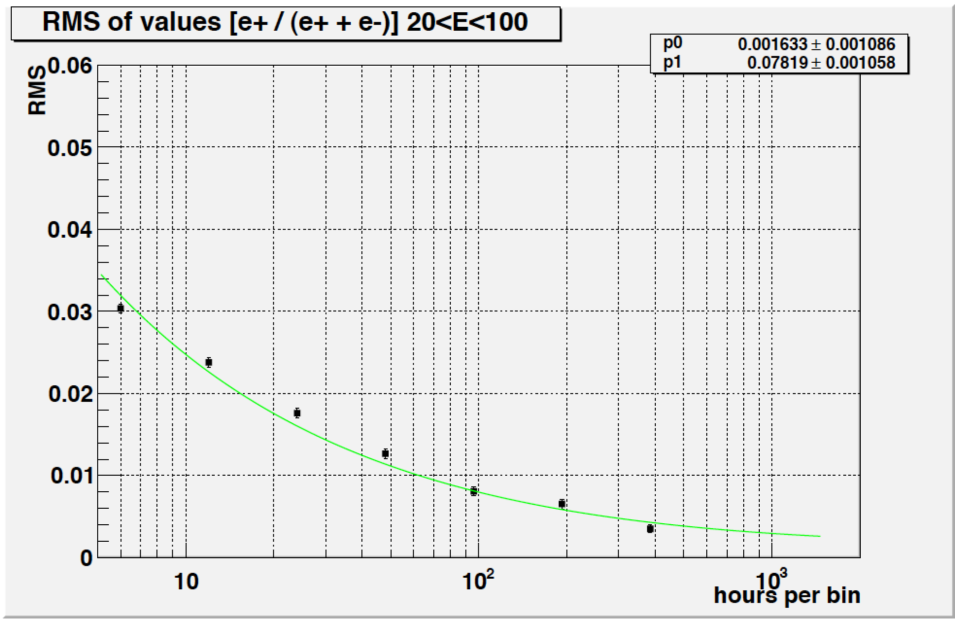

Figure 52 – Global fit of the RMS, associated to positron fraction means of Fig.51, as a function of hours per bin. The two fit parameter are shown in the legend. The systematic error achieved from the analysis is essentially compatible with zero.

The data points in Fig. 52 have been fitted with a quadratic sum of a constant term p_0 plus a term linked to statistics, proportional to the inverse square root of the number of hour per bin (i.e of the number of events, because $1/\sqrt{h} \propto 1/\sqrt{N}$):

$$\text{fit} = \sqrt{(p_0)^2 + \left(\frac{p_1}{\sqrt{h}}\right)^2} \tag{5.1}$$

The resulting constant term is (0.0016±0.0011)/0.0850 = (1.9 ± 1.2)%, essentially compatible with zero.

As an alternative method, the time distribution of Fig. 49 can be fitted with a straight line with constant ordinate value. The reduced $\tilde{\chi}^2$ of the fit is 0.81, confirming that there is no structure in the time distribution of the positron fraction measured by AMS-02.

The result is really impressive and confirms the stability of the whole apparatus and of the analysis, and the measure potentiality of AMS-02.

Chapter 6

Conclusions

AMS-02 is running after great scientific goals since one year and a half: a final setting up for dark matter searches has been achieved, allowing to study the so important antiparticle to particle ratios, which will probably be the first dark matter signals ever corroborated.

In chapter 2 it has been largely debated the necessity of dark matter, which is strongly demanded by all astrophysical and cosmological observations and that is, by far, the best and cleverest way to explain our Universe content.

Even if primary cosmic rays fluxes are subjected to a lot of uncertainties sources, from the propagation model to the physical characteristics of the dark matter particle, passing through the hard disentanglement of a DM signal from an astrophysical primary one, some statements can be done and have been written down in chapter 3 about dark matter properties: DM should be a heavy Majorana fermion or Spin 0 or 1 boson, with a mass from about 1 TeV to 10 TeV - unveiling a new TeV-ish search age - which could be able to originate antiparticle fluxes enhancements at high energies, both for positrons and antiprotons. These enhancements perfectly fall into the research window of AMS-02 (100 GeV ÷ 2.14 TeV, i. e. the MDR of the Tracker), allowing the experiment to attack each today credible theory: the AMSB SUSY, the UED KK theory, the Little Higgs theory and the minimal Scalar Singlet/Multiplet Model. Also an investigation of the Sommerfeld effect-associated dark boson will be possible, in terms of antiparticle to particle ratios substructures.

Moreover, it has been phenomenologically demonstrated that all the observations, direct and indirect, point to these new paradigms or can be traced back to them quite easily.

AMS is going to put several indirect constraints on dark matter parameters space (such as the annihilation cross section and the preferred annihilation channels, the mass range and the spin-statistics) from the fluxes fine structure measurements and from the CR nuclei ratios, with unprecedented resolution and binning; these constraints can be used to tune up or falsify DM models and to inaugurate brand new speculative frontiers.

The first great AMS-02 measurement is the positron fraction: an official paper is going to be submitted in few months. In this paper the correct behavior of the apparatus will be reviewed and the full positron fraction rate will be analyzed up to 350 GeV.

The study leaded in chapter 5 will flow into this collaboration publication to demonstrate the stability of the experiment for what concerns the cosmic rays fluxes ratios. Here it has not been possible to deal with an examination of the positron fraction value nor to extend the stability study beyond the physically known kinetic energy threshold (100 GeV) because of internal policies of the Collaboration.

One of the objectives of this work was to test the AMS-02 capability and versatility in doing these dark matter researches, thanks to an orbital temporal (and geomagnetic) stability; particle species can be easily separated through the composite effort of TRD and ECAL, and TOF offers a unique time resolution and charge measure. So, in this concern the goal has been accomplished: the experiment is very stable in time, so that the temporal error associated to the positron fraction measurement is compatible with zero, offering a beyond belief opportunity to measure CR antiparticle to particle ratios. AMS-02 perfectly lives and works in the space environment continuously producing high quality data and represents an efficient DM indirect search laboratory.

Appendix

In this appendix the remaining plots relative to the stability of the cuts (chapter 5.2) are collected.

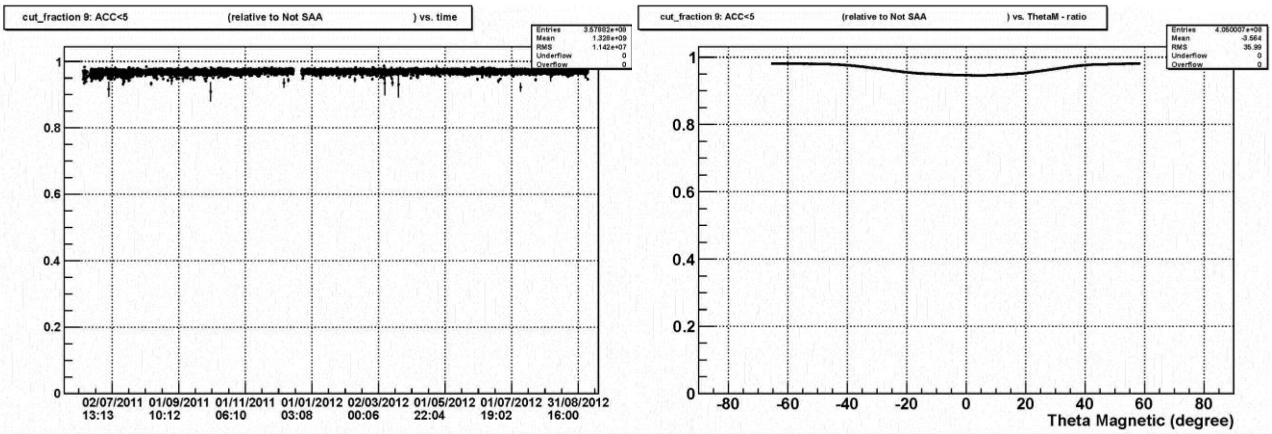

Figure 1 - Cut 9 stability: *ACC<5*. Left: data reduction as a function of time, from May 2011 to September 2012. Each point represents one hour. Right: data reduction as a function of the geomagnetic latitude.

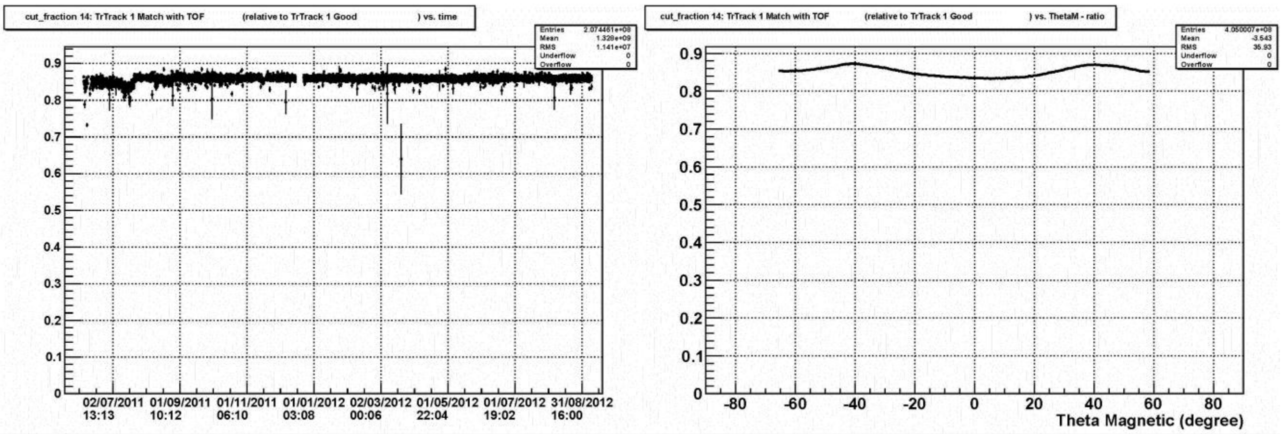

Figure 2 - Cut 14 stability: *Match with TOF*. Left: data reduction as a function of time, from May 2011 to September 2012. Each point represents one hour. Right: data reduction as a function of the geomagnetic latitude.

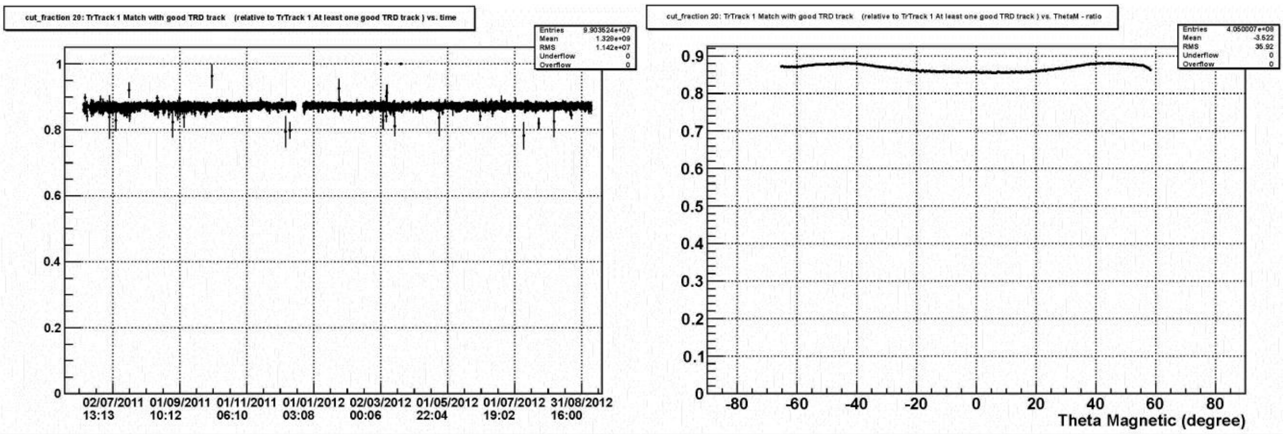

Figure 3 - Cut 20 stability: *Match with good TRD track*. Left: data reduction as a function of time, from May 2011 to September 2012. Each point represents one hour. Right: data reduction as a function of the geomagnetic latitude.

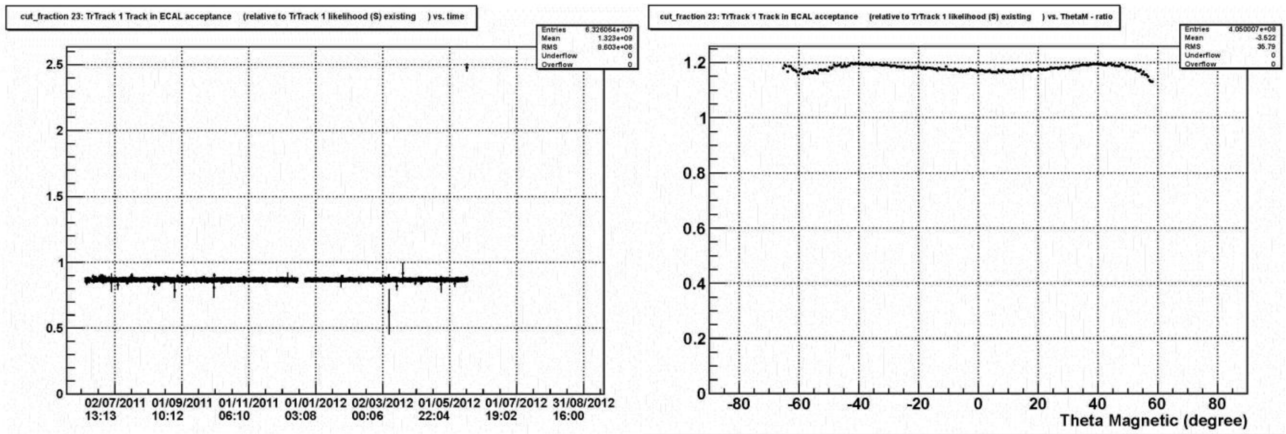

Figure 4 - Cut 23 stability: *Track in ECAL acceptance*. Left: data reduction as a function of time, from May 2011 to September 2012. Each point represents one hour. Right: data reduction as a function of the geomagnetic latitude. The interruption is due to the reference S-Likelihood cut.
The interruption is due to the reference S-Likelihood cut.

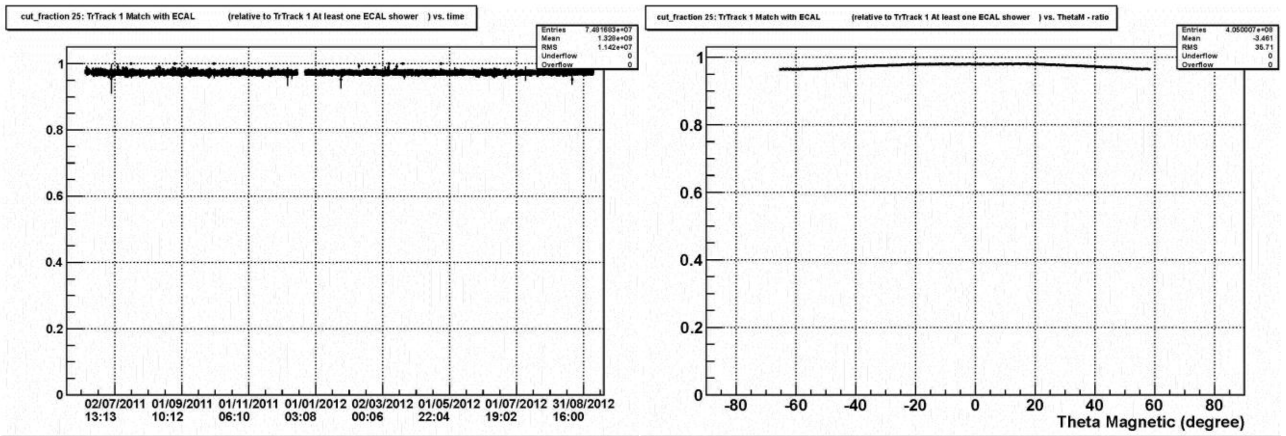

Figure 5 – Cut 25 stability: *Match with ECAL*. Left: data reduction as a function of time, from May 2011 to September 2012. Each point represents one hour. Right: data reduction as a function of the geomagnetic latitude.

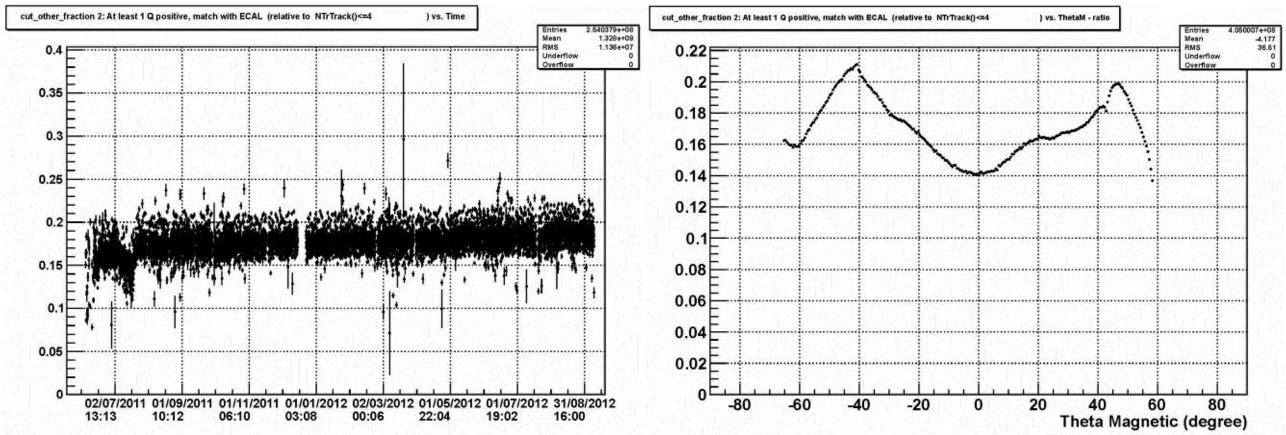

Figure 6 - Particle identification Cut 2 stability: *At least 1 Q positive, match with ECAL*. Left: data reduction as a function of time, from May 2011 to September 2012. Each point represents one hour. Right: data reduction as a function of the geomagnetic latitude.

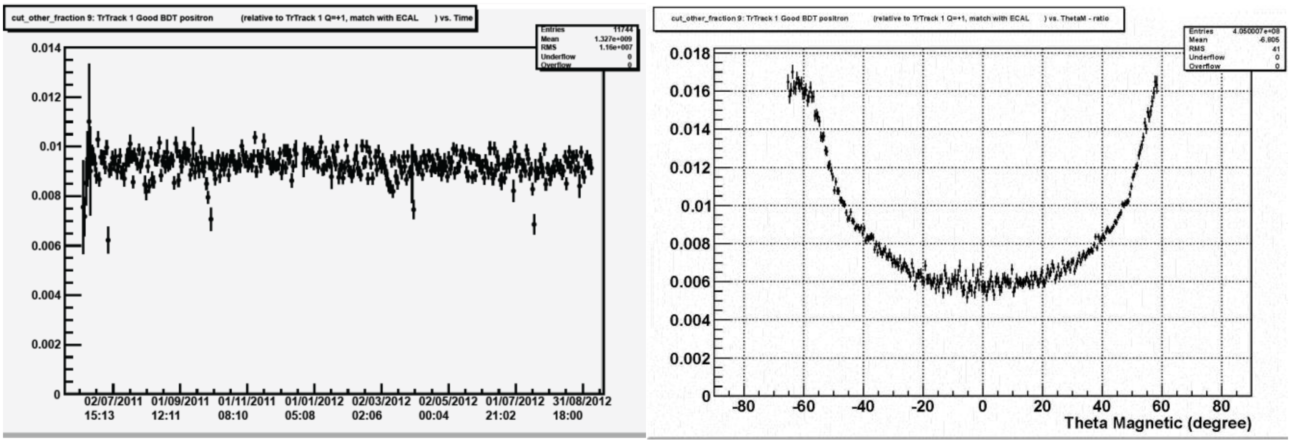

Figure 7 - Particle identification Cut 9 stability: *Good BDT positron*. Data reduction as a function of time with 8h/bin (left), from May 2011 to September 2012. Each point represents one hour. Right: data reduction as a function of the geomagnetic latitude.

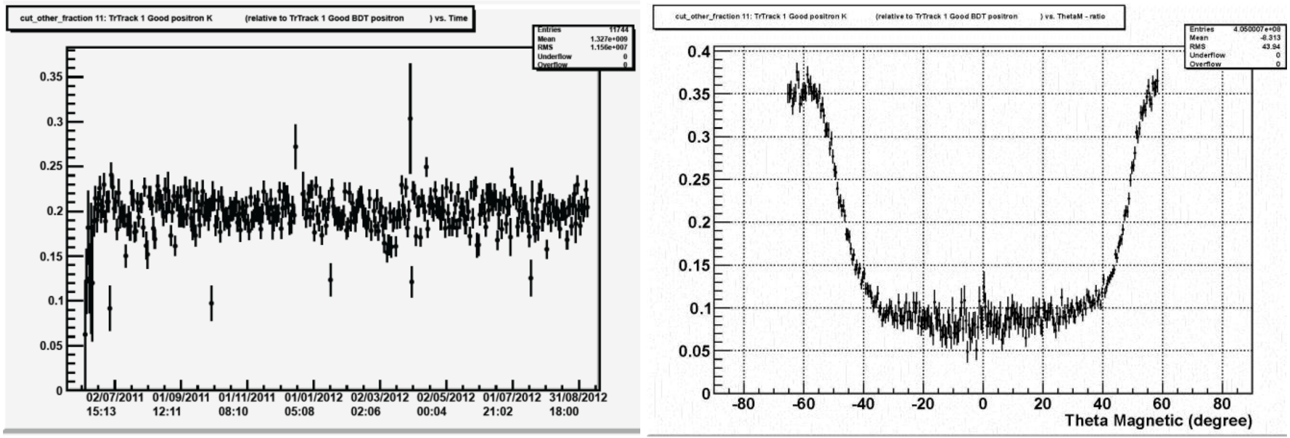

Figure 8 - Particle identification Cut 11 stability: *Good positron K*. Data reduction as a function of time with 8h/bin (left), from May 2011 to September 2012. Each point represents one hour. Right: data reduction as a function of the geomagnetic latitude.

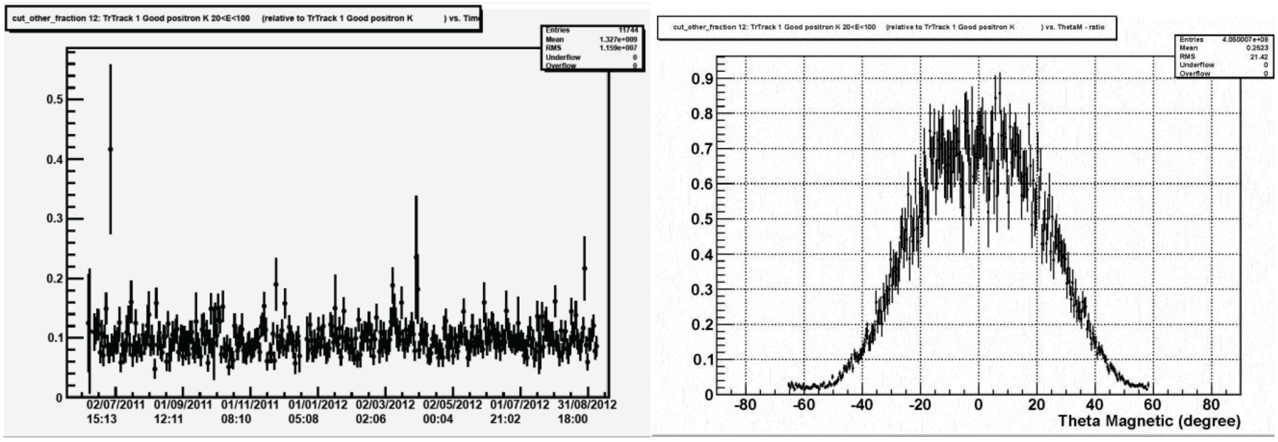

Figure 9 - Particle identification Cut 12 stability: *Good positron K 20<E<100*. Data reduction as a function of time with 8h/bin (left), from May 2011 to September 2012. Each point represents one hour. Right: data reduction as a function of the geomagnetic latitude.

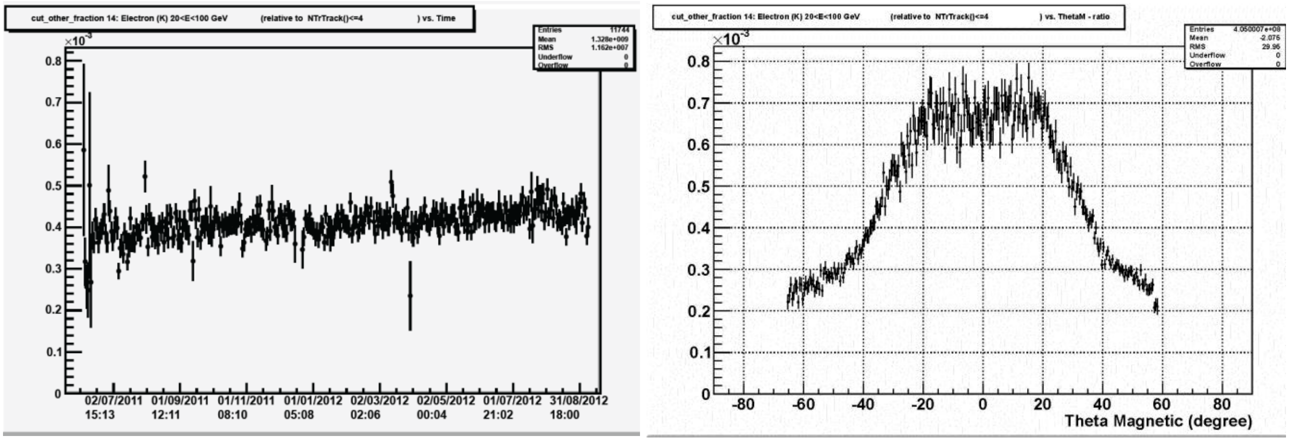

Figure 10 - Particle identification Cut 14 stability: *Electron (K) 20<E<100 GeV*. Data reduction as a function of time with 8h/bin (left), from May 2011 to September 2012. Each point represents one hour. Right: data reduction as a function of the geomagnetic latitude.

Bibliography

[1] E. W. Kolb, M. S. Turner, *The early universe*, Addison-Wesley, 1988

[2] M. Kuster, G. Raffelt, B. Beltrán, *Axions– Theory, Cosmology, and Experimental Searches*, Springer 2008

[3] G. Bertone et al., *Particle Dark Matter Evidence, Candidates and Constraints*, [arXiv:hep-ph/0404175v2], 2008

[4] K. Griest, M. Kamionkowski, *Unitary Limits on the Mass and Radius of Dark-Matter Particles*, Phys. Rev. Lett. Vol. **64** No. 6, 1990

[5] Y. Sofue et al., *Unified Rotation Curve of the Galaxy — Decomposition into de Vaucouleurs Bulge, Disk, Dark Halo, and the 9-kpc Rotation Dip*, [arXiv:0811.0859v2], 2008

[6] R. Catena et al., *A novel determination of the local dark matter density*, [arXiv:0907.0018v2], 2009

[7] M. Roos, Dark Matter: *The evidence from astronomy, astrophysics and cosmology*, [arXiv:1001.0316v2], 2010

[8] A. Boyarsky et al., *New evidence for dark matter*, [arXiv:0911.1774], 2009

[9] M. Mateo, *Dwarf galaxies of the local group*, [arXiv:astro-ph/9810070v1], 1998

[10] M. G. Walker, M. Mateo et al., *Velocity dispersion profiles of seven dwarf spheroidal galaxies*, [arXiv:0708.0010v1], 2007

[11] E. L. Lokas, *Velocity dispersions of dwarf spheroidal galaxies: dark matter versus MOND*, [arXiv:astro-ph/0107479v2], 2001

[12] E. S. Levine et al., *The vertical structure of the outer Milky Way HI disk*, The Astrophysical Journal Vol. **643**, No. 2, 33-36, 2006

[13] M. D. Weinberg, *A magellanic origin for the warp of the galaxy*, The Astrophysical Journal Vol. **641**, No. 1, 881-896, 2006

[14] S. Chakrabarti, L. Blitz, *Tidal imprints of a dark sub-halo on the outskirts of the Milky Way. II. Perturber azimuth*, The Astrophysical Journal **731** (2011) 40

[15] S. Chakrabarti et al., *Finding dwarf galaxies from their tidal imprints*, [arXiv:1101.0815v2], 2011

[16] M. Bonamente et al., *Swift XRT Observations of the Possible Dark Galaxy VIRGO HI 21*, [arXiv:0805.1665v2], 2008

[17] R. F. Minchin, *A Dark Galaxy in the Virgo Cluster Imaged at 21-cm*, [arXiv:astro-ph/0508153v1], 2005

[18] PLANCK Collaboration, *Planck intermediate results. IX. Detection of the Galactic haze with Planck*, [arXiv:1208.5483v1], 2012

[19] G. Cupani et al., *Cluster mass estimation through Fair galaxies*, [arXiv:0910.2882v3], 2010

[20] A. D. Chernin et al., *Dark energy and the mass of the Local Group*, [arXiv:0902.3871v1], 2009

[21] B. Fuchs et al., *The amount of Dark Matter in galaxies*, [arXiv:0010358], 2000

[22] D. Clowe et al., *A direct empirical proof of the existence of dark matter*, Astro. J. **648**, L109 (2006)

[23] M. Bradač et al., *Revealing the properties of dark matter in the merging cluster MACSJ0025.4-1222*, Astrophys. J., **687**, 959 (2008)

[24] R. J. Smith et al., *Discovery of Strong Lensing by an Elliptical Galaxy at z=0.0345*, Astro. J., **625**, L103 (2005)

[25] R. Ellis et al., *Dark matter maps reveal cosmic scaffolding*, [arXiv:astro-ph/0701594v1], 2007

[26] J. Richard et al., *Abell 370 revisited: refurbished Hubble imaging of the first strong lensing cluster*, [arXiv:0910.5553], 2009

[27] J. P. Dietrich et al., A filament of dark matter between two clusters of galaxies, Nature **487**, 202-204, July 2012

[28] G. Bertone, *Particle Dark Matter*, Cambridge University Press, 2010

[29] L. Papantonopoulos, *The Invisible Universe Dark Matter and Dark Energy*, Springer 2007

[30] L. Dorman, *Cosmic ray interactions, propagation and acceleration in space plasmas*, Springer, 2006

[31] J. Terning, *Modern Supersymmetry; Dynamics and Duality*, Oxford University Press, 2006

[32] W. J. Percival et al., *Measuring the Baryon Acoustic Oscillation scale using the SDSS and 2dFGRS*, Mon. Not. Roy. Astr. Soc., **381**, 1053 (2007)

[33] V. Springel al., *The Aquarius Project: the subhalos of galactic halos, Mon. Not. Roy. Astr. Soc.*, **391**, 1685 (2008)

[34] T. A. Porte et al., *Dark Matter Searches with Astroparticle Data*, [arXiv:1104.2836v1], 2011

[35] M. Azzaro et al., *Motion properties of satellites around external spiral galaxies*, [arXiv:astro-ph/0310487v1], 2003

[36] P. Salucci, *The mass distribution in Spiral galaxies*, [arXiv:0707.4370v2], 2007

[37] C. Deffayet et al., *Nonlocal metric formulations of MOND with sufficient lensing*, [arXiv:1106.4984v2], 2011

[38] J. D. Bekenstein, *The modified Newtonian dynamics—MOND and its implications for new physics*, [arXiv:astro-ph/0701848v2], 2007

[39] R. Wojtak et al., *Gravitational redshift of galaxies in clusters as predicted by general relativity*, Nature **477**, 567-569 (September 2011)

[40] J. W. Moffat, *Gravitational Theory, Galaxy Rotation Curves and Cosmology without Dark Matter*, [arXiv:astro-ph/0412195v3], 2004

[41] J. W. Moffat et al., *Modified Gravity: Cosmology without dark matter or Einstein's cosmological constant*, [arXiv:0710.0364v6], 2007

[42] J. W. Moffat et al., *Testing modified gravity with globular cluster velocity dispersions*, [arXiv:0708.1935v5], 2007

[43] C. Skordis, *The Tensor-Vector-Scalar theory and its cosmology*, [arXiv:0903.3602v1], 2009

[44] E. S. Fradkin, A. A. Tseytlin, *Conformal Supergravity*, Phys. Rept. **119** (4–5): 233–362, 1985

[45] A. O. Barvinsky, *Cosmological constant problem and long-distance modifications of Einstein theory*, [arXiv:hep-th/0409144v1], 2004

[46] D. Espriu et al., *Gravity as an effective theory*, Acta Phys. Pol B **40** (2009) 12

[47] T. Clifton et al., *Modified Gravity and Cosmology*, [arXiv:1106.2476v3], 2011

[48] A. S. Koshelev, *Modified non-local gravity*, [arXiv:1112.6410v2], 2012

[49] D. H. Perkins, *Particle Astrophysics*, Oxford Universiy Press, 2009

[50] A. Borriello, P. Salucci, *The dark matter distribution in disk galaxies*, Mon. Not. R. Astron. Soc. **323**, 285-292 (2001)

[51] D. Merritt et al., *Empirical Models for Dark Matter Halos*, [arXiv:astro-ph/0509417v2], 2005

[52] N. Bernal et al., *Constraining the Milky Way Dark Matter Density Profile with Gamma-Rays with Fermi-LAT*, [arXiv:1103.2377v1], 2011

[53] J. F. Navarro, C. S. Frenk, S. D. M. White*, Structure of Dark Matter Halos*, Astro. J. **462**:563-575, 1996

[54] J. F. Navarro, J. E. Taylor, *The Phase-Space Density Profiles of Cold Dark Matter Halos*, The Astrophysical Journal, **563**:483-488, December 2001

[55] F. Prada et al., *Halo concentrations in the standard Λ cold dark matter cosmology*, Monthly Notices of the Royal Astronomical Society, Vol. **423**, Is. 4, 3018–3030, July 2012

[56] E. Retana-Montenegro et al., *Analytical properties of Einasto dark matter haloes*, [arXiv:1202.5242v1], 2012

[57] A. Boyarsky et al., *Constraints on decaying Dark Matter from XMM-Newton observations of M31*, [arXiv:0709.2301v2], 2007

[58] J. Diemand et al., *Dark matter substructure and gamma-ray annihilation in the milky way halo*, [arXiv:astro-ph/0611370v1], 2006

[59] A. Dekel et al., *Lost & found dark matter in elliptical galaxies*, [arXiv:astro-ph/0501622v3], 2005

[60] T. Stanev, *High Energy Cosmic Rays*, Springer, 2010

[61] L. Dorman, *Cosmic Rays in Magnetospheres of the Earth and other Planets*, Springer, 2009

[62] M. Hillas, *Cosmic Rays: Recent Progress and some Current Questions*, [arXiv:0607109v2], 2006

[63] M. Ave et al., *Composition of primary cosmic-ray nuclei at high energies*, Astro. J. **678**:262-273, 2008

[64] F. Donato et al., *Cosmic rays below Z=30 in a diffusion model: new constraints on propagation parameters*, Astro. J. **555**:585-596, 2001

[65] F. Donato et al., *Galactic Cosmic Ray Nuclei as a Tool for Astroparticle Physics*, [arXiv:astro-ph/0212111v1], 2002

[66] F. Donato et al., *Antiproton fluxes from light neutralinos*, Phys. Rev. D **72**, 083518 (2005)

[67] F. Donato et al., *Antiprotons from spallations of cosmic rays on interstellar matter*, Astro. J. **563**:172-184, 2001

[68] F. Donato et al., *Antiprotons in cosmic rays from neutralino annihilation*, Phys. Rev. D **69**, 063501 (2004)

[69] N. Tommasetti, F. Donato, *Secondary Cosmic Ray Nuclei from Supernova Remnants and Constraints to the Propagation Parameters*, [arXiv:1203.6094v1], 2012

[70] S. N. Ganguli et al., *Fluxes of γ-rays, antiprotons and deuterons in cosmic rays*, J. Phys. A: Math. Vol. **9**, No. 2, 1976

[71] S. N. Ganguli et al., *Propagation of cosmic-ray nucleons in the galaxy*, J. Phys. A: Math. Gen. **9** 311 (1976)

[72] J. W. Mitchell et al., *Precise measurements of the cosmic ray antiproton spectrum with BESS including the effects of solar modulation*, Advances in Space Research **35**1 (2005) 135-141

[73] M. Boezio et al., *The cosmic-ray antiproton flux between 0.62 and 3.19 GeV measured near solar minimum activity*, Astro. J. **487**:415-423, 1997

[74] P. Bobik et al., *Proton and antiproton modulation in the heliosphere for different solar conditions and AMS-02 Measurements Prediction*, [arXiv:1012.3086v4], 2010

[75] D. Grandi, *A tracing model for the Earth magnetosphere: the effect on Cosmic Ray access to a space detector*, Thesis

[76] M. Duranti, *Measurement of the Atmospheric Muon Flux on Ground with the AMS-02 Detector*, Thesis

[77] N. F. Bell et al., *Gamma-ray Constraints on Dark Matter Annihilation into Charged Particles*, [arXiv:0811.0821v2], 2008

[78] J. L. Feng, *Dark Matter Candidates from Particle Physics and Methods of Detection*, [arXiv:1003.0904v2], 2010

[79] W. de Boer, *Indirect Dark Matter Signals*, [arXiv:0810.1472v3], 2008

[80] J. Lavalle et al., *Antimatter cosmic rays from dark matter annihilation: First results from an N-body experiment*, [arXiv:0808.0332v2], 2008

[81] P. Picozza et al., *PAMELA – A payload for antimatter matter exploration and light-nuclei astrophysics*, Astro. Phys. **27** (2007) 296–315

[82] FERMI Collaboration, The Large Area Telescope on the FERMI Gamma-Ray Space Telescope Mission, Astro. J., **697**:1071-1102, June 2009

[83] O. Adriani et al., *PAMELA Measurements of Cosmic-ray Proton and Helium Spectra*, [arXiv:1103.4055v1], 2011

[84] O. Adriani et al., *PAMELA Results on the Cosmic-Ray Antiproton Flux from 60MeV to 180 GeV in Kinetic Energy*, PRL **105**, 121101 (2010)

[85] O. Adriani et al., *The high-energy antiproton-to-proton flux ratio with the PAMELA experiment*, PROCEEDINGS OF THE 31st ICRC, ŁODZ 2009

[86] O. Adriani, *The cosmic-ray electron flux measured by the PAMELA experiment between 1 and 625 GeV*, [arXiv:1103.2880v1], 2011

[87] O. Adriani et al., *The cosmic-ray electron flux measured by the PAMELA*, [arXiv:1103.2880v1], 2011

[88] M. Cirelli, *Indirect Searches for Dark Matter: a status review*, [arXiv:1202.1454v2], 2012

[89] G. Sau et al., *Understanding the New High Energy Data-sets Measured by BESS, CAPRICE and PAMELA on antiproton flux and* $\bar{p}/p$ *ratios*, [arXiv:0906.3866v3], 2009

[90] P. D. Serpico, *Astrophysical models for the origin of the positron "excess"*, [arXiv:1108.4827v2], 2011

[91] F. Donato et al., *Constraints on WIMP Dark Matter from the High Energy PAMELA* $\bar{p}/p$ *Data*, PRL **102**, 071301 (2009)

[92] A. A. Abdo, *Measurement of the Cosmic Ray* $e^+ + e^-$ *Spectrum from 20 GeV to 1 TeV*, PRL **102**, 181101 (2009)

[93] M. Ackermann et al., *Measurement of separate cosmic-ray electron and positron spectra with the Fermi Large Area Telescope*, [arXiv:1109.0521v1, 2011]

[94] D. Grasso et al., *Cosmic ray models compared to Fermi-LAT positron and electron separate spectra*, [arXiv:1110.2591v1], 2011

[95] Sannino et al., *Decaying Dark Matter can explain* $e^{\pm}$ *excess*, [arXiv:0811.4153v1], 2008

[96] C. Barbot, *Ultra-high energy cosmic rays from super-heavy X particle decay*, [arXiv:hep-ph/0210280v1], 2002

[97] S. Chang et al., *Charge asymmetric cosmic ray signals from dark matter decay*, Phys. Rev. D **84**, 023524 (2011)

[98] I. Cholis, *New Constraints from PAMELA anti-proton data on Annihilating and Decaying Dark Matter*, [arXiv:1007.1160v1], 2010

[99] S. Profumo et al., *Constraints on Decaying Dark Matter from Fermi Observations of Nearby Galaxies and Clusters*, [arXiv:1009.5988v2], 2010

[100] A. Ibarra, C. Weniger et al., *Cosmic Rays from Leptophilic Dark Matter Decay via Kinetic Mixing*, J. HEP 0408:061, 2004

[101] T. Cohen et al., *Leptophilic Dark Matter from the Lepton Asymmetry*, [arXiv:0909.2035v1], 2009

[102] P. J. Fox et al., *Leptophilic dark matter*, Phys. Rev. D **79**, 083528 (2009)

[103] L. Pieri, J. Lavalle, G. Bertone, E. Branchini, *Implications of High-Resolution Simulations on Indirect Dark Matter Searches*, Phys. Rev. D **83** (2011) 023518

[104] W.-L. Guo, Y.-L. Wu, *Enhancement of Dark Matter Annihilation via Breit-Wigner Resonance*, [arXiv:0901.1450v2], 2009

[105] T. R. Slatyer, *The Sommerfeld enhancement for dark matter*, [arXiv:0910.5713v2], 2009

[106] J. Bovy, *Substructure Boosts to Dark Matter Annihilation from Sommerfeld Enhancement*, [arXiv:0903.0413v2], 2009

[107] S. Mohanty et al., *Reconciling heavy wino dark matter model with the relic density and PAMELA data using Sommerfeld effect*, [arXiv:1009.5058v1], 2010

[108] C. Arina et al., *Constraining Sommerfeld Enhanced Annihilation Cross-sections of Dark Matter via Direct Searches*, [arXiv:1004.0645v2], 2010

[109] J. L. Feng et al., *Sommerfeld Enhancements for Thermal Relic Dark Matter*, [arXiv:1005.4678v3], 2010

[110] G. Bertone et al., *Gamma-ray and radio tests of the* $e^{\pm}$ *excess from DM annihilations*, JCAP **0903** (2009) 009

[111] A. A. Abdo et al., *Constraints on Cosmological Dark Matter Annihilation from the Fermi-LAT Isotropic Diffuse Gamma-Ray Measurement*, [arXiv:1002.4415v1], 2010

[112] S. Ando et al., *Fermi-LAT constraints on dark matter annihilation cross section from observations of the Fornax cluster*, [arXiv:1201.0753v2], 2012

[113] G. Bertone, S. Galli et al., *Updated CMB constraints on Dark Matter annihilation cross-sections*, Phys. Rev. D **84**, 027302 (2011)

[114] G. Bertone, S. Galli et al., *CMB constraints on Dark Matter models with large annihilation cross-section*, Phys. Rev. D **80**, 023505 (2009)

[115] P. Meade et al., *Dark Matter Interpretations of the* $e^{\pm}$ *Excesses after FERMI*, [arXiv:0905.0480v2], 2009

[116] O. Adriani et al., *A new measurement of the antiproton-to-proton flux ratio up to 100 GeV in the cosmic radiation*, [arXiv:0810.4994v2], 2008

[117] J. W. Mitchell et al., *Measurement of 0.25-3.2 GeV Antiprotons in the Cosmic Radiation*, PRL **76**, No. 17, April 1996

[118] F. Donato et al., *Which fraction of the measured cosmic ray antiprotons might be due to neutralino annihilation in the galactic halo?,* [arXiv:astro-ph/9804137v1], 1998

[119] I. V. Moskalenko et al., *Antiprotons below 200 MeV in the interstellar medium perspectives for observing exotic matter signatures*, [arXiv:astro-ph/0102207v1], 2001

[120] S. Orito et al., *Precision Measurement of Cosmic-Ray Antiproton Spectrum*, PRL **84**, Vo. 6, February 2000

[121] M. Boezio et al., *The cosmic-ray antiproton flux between 3 and 49 GeV*, Astro. J. **561**:787-799, 2001

[122] O. Adriani et al., *The discovery of geomagnetically trapped cosmic ray antiprotons*, [arXiv:1107.4882v1], 2011

[123] D. Maurin, *Transport of exotic anti-nuclei - Fast formulae for* $\bar{p}$ *fluxes*, [arXiv:astro-ph/0609522v3], 2006

[124] I. Gebauer, *Uncertainties of the antiproton flux from Dark Matter annihilation in comparison to the EGRET excess of diffuse gamma rays*, [arXiv:0710.4966v2], 2007

[125] M. Cirelli et al., *Model-independent implications of the* $e^{\pm}, \bar{p}$ *cosmic ray spectra on properties of Dark Matter*, Nucl. Phys. B **813** (2009) 1–21

[126] T. Bringmann, *Antiproton and Radio Constraints on the Dark Matter Interpretation of the Fermi Gamma Ray Observations of the Galactic Center*, [arXiv:0911.1124v1], 2009

[127] K. Abe, *Measurement of the cosmic-ray low-energy antiproton spectrum with the first BESS-Polar Antarctic flight*, [arXiv:0805.1754v2], 2008

[128] A. Ibarra et al., *Antiproton constraints on dark matter annihilations from internal electroweak bremsstrahlung*, J.C.A.P. **07** (2011) 028

[129] C. Evoli et al., *Antiprotons from dark matter annihilation in the Galaxy astrophysical uncertainties*, [arXiv:1108.0664v1], 2011

[130] K. Cheung et al., *Cosmic Antiproton constraints on effective Interactions of Dark Matter*, [arXiv:1011.2310v1], 2010

[131] L. Bergström et al., *Cosmic antiprotons as a probe for supersymmetric dark matter*, Astro. J. **526**:215-235, 1999

[132] S. Torii et al., *High-energy electron observations by PPB-BETS flight in Antarctica*, [arXiv:0809.0760v1], 2008

[133] P. Brun, G. Bertone et al., *Antiproton and Positron Signal Enhancement in Dark Matter Mini-Spikes Scenarios*, [arXiv:0704.2543v3], 2007

[134] M. Perelstein et al., *Antiprotons from dark matter Effects of a position-dependent diffusion coefficient*, Phys. Rev. D **83**, 123508 (2011)

[135] R. Essig et al., *Bounds on cross sections and lifetimes for dark matter annihilation and decay into charged leptons from gamma-ray observations of dwarf galaxies*, Phys. Rev. D **80**, 023506 (2009)

[136] N. Jarosik et al., *Seven-Year Wilkinson Microwave Anisotropy Probe (WMAP) Observations: Cosmological Interpretation*, [arXiv:1001.4538v3], 2010

[137] F. Aharonian et al., *Energy Spectrum of Cosmic-Ray Electrons at TeV Energies*, PRL **101**, 261104 (2008)

[138] P. Salucci, a. Borriello, *The Intriguing Distribution of Dark Matter in Galaxies*, [arXiv:astro-ph/0203457v1], 2002

[139] A. Ibarra, C. Weniger et al., *Decaying Dark Matter in Light of the PAMELA and Fermi LAT Data*, [arXiv:0906.1571v3], 2009

[140] C. Combet et al., *Decaying dark matter a stacking analysis of galaxy clusters to improve on current limits*, [arXiv:1203.1164v1], 2012

[141] D. Grasso et al., *CR electrons and positrons: what we have learned in the latest three years and future perspectives*, [arXiv:1110.6626v2], 2011

[142] M. Perelstein et al., *Remarks on calculation of positron flux from galactic dark matter*, Phys. Rev. D **82**, 043505 (2010)

[143] A. W. Strong et al., *Galprop explanatory supplement*, 2012

[144] Lisa Randall et al., *General Analysis of Antideuteron Searches for Dark Matter*, [arXiv:1006.0983v1], 2010

[145] M. Kadastik, *Enhanced anti-deuteron Dark Matter signal and the implications of PAMELA*, arXiv:0908.1578v2, 2009

[146] S. Profumo et al., *Low energy antideuterons shedding light on dark matter*, J.C.A.P. **12** (2005) 008

[147] F. Donato et al., *Antideuteron fluxes from dark matter annihilation in diffusion models*, Phys. Rev. D **78**, 043506 (2008)

[148] F. Donato et al., *Antideuterons as a signature of supersymmetric dark matter*, Phys. Rev. D **62**, 043003

[149] F. Donato et al., *Antideuterons from supersymmetric dark matter*, [arXiv:0709.2098v1], 2007

[150] T. Aramaki, *Antideuterons as an indirect dark matter signature Si(Li) detector development and a GAPS balloon mission*, Advances in Space Research **46** (2010) 1349–1353

[151] Z. D. Myers, *Cosmic ray ^{1}H and ^{2}H spectra from BESS 98,* Adv. Space Res. Vol. **25**, No. 1 (2005) 151-155

[152] M. Cirelli et al., *Anti-deuterons from heavy Dark Matter*, [arXiv:0904.1165v1], 2009

[153] J. E. Koglin, *Indirect Dark Matter Search with Antideuterons: Progress and Future Prospects for General Antiparticle Spectrometer (GAPS)*, Nuclear Physics B (Proc. Suppl.) **173** (2007) 75–78

[154] C. J. Hailey, *An indirect search for dark matter using antideuterons the GAPS experiment*, New Journal of Physics **11** (2009) 105022

[155] J. E. Koglin, *Antideuterons as an Indirect Dark Matter Signature Design and Preparation for a Balloon-born GAPS Experiment*, Nucl. Phys. B (Proc. Suppl.) **173** (2007) 75–78

[156] A. Ibarra et al., *Antideuterons from Dark Matter Decay*, [arXiv:0904.1410v2], 2009

[157] A. Ibarra et al., *Prospects of antideuteron detection from dark matter annihilations or decays at AMS-02 and GAPS*, [arXiv:1209.5539v1], 2012

[158] L. A. Dal, *Antideuterons as Signature for Dark Matter*, Thesis

[159] F. Giovacchini, *Cosmic Rays Anti-Deuteron Flux Sensitivity of the AMS-02 Detector*, Thesis

[160] G. A. De Nolfo et al., *A Measurement of Cosmic Ray Deuterium from 0.5-2.9 GeV/nucleon*, ACE 2000 Symposium. AIP Conference Proceedings, Vol. **528**, pp. 425-428 (2000)

[161] D. A. Lubovich, *Deuterium Nucleosynthesis in AGN: Is D Cosmological?*, Nucl. Phys. A **758** (2005) 795c–798c

[162] H. Fuke et al*., Search for Cosmic-Ray Antideuterons*, PRL **95**, 081101 (2005)

[163] T. Aramaki et al., *The General Antiparticle Spectrometer (GAPS) - Hunt for dark matter using low-energy antideuterons*, [arXiv:1012.0273v1], 2010

[164] A. Riotto et al., *Electroweak bremsstrahlung for wino-like Dark Matter annihilations*, [arXiv:1202.0692v1], 2012

[165] A. De Simone, *Electroweak lights from Dark Matter annihilations*, [arXiv:1201.1443v1], 2012

[166] M. Cirelli, A. Riotto et al., *Initial State Radiation in Majorana Dark Matter annihilations,* [arXiv:1107.4453v1], 2011

[167] M. Cirelli, A. Riotto et al., *On the Importance of Electroweak Corrections for Majorana Dark Matter Indirect Detection*, [arXiv:1104.2996v2], 2011

[168] X. Chen, *Particle decays during the cosmic dark ages*, Phys. Rev. D **70**, 043502 (2004)

[169] F. Donato, P. D. Serpico, *''Discrepant hardenings'' in cosmic ray spectra: A first estimate of the effects on secondary antiproton and diffuse gamma-ray yields*, Phys. Rev. D **83**, 023014 (2011)

[170] A. D. Panov et al., *The results of ATIC-2 experiment for elemental spectra of cosmic rays*, [arXiv:astro-ph/0612377v1], 2006

[171] F. Sannino et al., *Technicolor dark matter*, Phys. Rev. D **80**, 037702 (2009)

[172] F. Sannino et al., *Ultra Minimal Technicolor and its Dark Matter TIMP*, [arXiv:0809.0713v1], 2008

[173] F. Sannino et al., *Dark Matter from new Technicolor Theories*, [arXiv:hep-ph/0608055v1], 2006

[174] C. P. Burgess, G. D. Moore, *The Standard Model: A Primer*, Cambridge University Press, 2007

[175] N. Fornengo, *Status and perspectives of indirect and direct dark matter searches*, Advances in Space Research **41** (2008) 2010–2018

[176] G. Bertone, D. Merritt, *Dark matter dynamics and indirect detection*, [arXiv:astro-ph/0504422v1], 2005

[177] V. Trimble, *Existence and nature of dark matter in the universe*, Ann. Rev. Astron. Astrophys. 1987, **25**: 425-472

[178] D. J. Phalen, *Searches for Dark Matter*, Thesis

[179] B. S. Acharya et al., *Non-thermal dark matter and the moduli problem in string frameworks*, J. HEP. **06**(2008)064

[180] D. Caraffini, *Anti-proton Flux Detection and Indirect Search for Dark Matter with the AMS-02 Experiment*, Thesis

[181] J. Hisano et al., *Heavy wino-like neutralino dark matter annihilation into antiparticles*, Phys. Rev. D **73**, 055004 (2006)

[182] H. Baer et al., *Mixed Wino Dark Matter: consequences for direct, indirect and collider detection*, J. HEP. **07**(2005)046

[183] H. Baer et al., *Mixed Higgsino Dark Matter*, J. Hep. **04** (2006) 041

[184] S. P. Martin, *A Supersymmetry Primer*, [arXiv:hep-ph/9709356v6], 2011

[185] A. Masiero et al., *Neutralino Dark Matter Detection in Split Supersymmetry Scenarios*, [arXiv:hep-ph/0412058v2], 2004

[186] A. Arbey et al., *Implications of a 125 GeV Higgs for supersymmetric models*, [arXiv:1112.3028v3], 2011

[187] L. Roszkowski et al., *Bayesian Implications of Current LHC Supersymmetry and Dark Matter Detection Searches for the Constrained MSSM*, [arXiv:1202.1503v2], 2012

[188] J. Cao et al., *A SM-like Higgs near 125 GeV in low energy SUSY: a comparative study for MSSM and NMSSM*, [arXiv:1202.5821v2], 2012

[189] D. Curtin et al., *Excluding Electroweak Baryogenesis in the MSSM*, [arXiv:1203.2932v2], 2012

[190] I. Maor, *Annihilating dark matter and the galactic positron excess*, [arXiv:astro-ph/0602440v1], 2006

[191] A. Canepa, *Associated production of neutralino and chargino*, [arXiv:hep-ex/0603032v1], 2006

[192] H. Baer et al., *Mixed axion-neutralino cold dark matter in supersymmetric models*, [arXiv:1103.5413v1], 2011

[193] S. Y. Choi et al., *Analysis of the neutralino system in supersymmetric theories*, [arXiv:hep-ph/0108117v1], 2001

[194] B. Mura, *Determination of Neutralino Masses with the CMS Experiment*, Thesis, 2006

[195] F. Donato, *Antimatter from supersymmetric dark matter*, [arXiv:hep-ph/0006188v1], 2000

[196] P. Gondolo et al., *CP-violating effects in neutralino scattering and annihilation*, J. Hep. **07** (2002) 052

[197] P. Gondolo et al., *Stellar Orbit Constraints on Neutralino Annihilation at the Galactic Center*, [arXiv:astro-ph/0602400v2], 2006

[198] O. Kittel, *How light can the lightest neutralino be?*, J. Phys.: Conf. Ser. **259** 012058, 2010

[199] X. Chen et al., *Kinetic decoupling of neutralino dark matter*, Phys. Rev. D **64** (2001) 021302

[200] G. F. Giudice, F. Strumia, *Probing High-Scale and Split Supersymmetry with Higgs Mass Measurements*, [arXiv:1108.6077v2], 2011

[201] D. Cumberbatch et al., *Local dark matter clumps and the positron excess*, [arXiv:astro-ph/0602320v3], 2006

[202] G. Bélanger et al., *Lower limit on the neutralino mass in the general MSSM*, LAPTH-1001/03, 2003

[203] V. Mandic et al., *Minimal Supersymmetry, Supersymmetric Frameworks, and the Expected Neutralino-Quark Scattering Cross-Section*, Berkeley, 1999

[204] P. Salati, *Neutralino clumps and cosmic rays*, [arXiv:astro-ph/0701530v1], 2007

[205] M. Lemoine et al., *Neutralino Dark Matter and the Curvaton*, [arXiv:astro-ph/0611948v2], 2006

[206] S. Profumo, P. Ullio, *The Role of Antimatter Searches in the Hunt for Supersymmetric Dark Matter*, [arXiv:hep-ph/0406018v2], 2004

[207] N. Fornengo, *Neutrino oscillation effect on the indirect signal of neutralino dark matter from the Earth core*, [arXiv:hep-ph/9904351v1], 1999

[208] J. H. An et al., *Simple Models for the Distribution of Dark Matter*, [arXiv:astro-ph/0508419v3], 2005

[209] J. Moortgat-Pick et al., *Spin effects in neutralino production in $e^+ e^-$ annihilation with polarized beams*, Acta Phys. Pol. B **29** (1998) 5

[210] D. Hooper et al., *The PAMELA and ATIC Excesses From a Nearby Clump of Neutralino Dark Matter*, [arXiv:0812.3202v1], 2008

[211] S. Poddar, *Top squark and neutralino decays*, Pramana (Indian Academy of Science Journal), Vol. **69**, No. 5, 2007

[212] N. Fornengo, *Susy Dark Matter with gaugino non-universality*, International Workshop on Astroparticle and High Energy Physics, 2003

[213] L. Roszkowski, R. Trotta, *On prospects for dark matter indirect detection in the Constrained MSSM*, [arXiv:0707.0622v2], 2008

[214] G. P. Carosi, *A search for signatures of dark matter in the AMS-01 electron and antiproton spectrum*, Thesis

[215] J. Olzem, *Signatures of SUSY Dark Matter at the LHC and in the Spectra of Cosmic Rays*, Thesis

[216] M. Perelstein, *Little Higgs Models and their Phenomenology*, [arXiv:hep-ph/0512128v1], 2005

[217] M. Schmaltz, D. Tucker-Smith, *Little Higgs review*, [arXiv:hep-ph/0502182v1], 2005

[218] D. Tseliakhovich, *Dark Matter in the Little Higgs Models*, Thesis

[219] M. Perelstein et al., *Indirect Detection of Little Higgs Dark Matter*, [arXiv:hep-ph/0610357v1], 2006

[220] A. Birkedal et al., *Little Higgs Dark Matter*, [arXiv:hep-ph/0603077v3], 2012

[221] H.-C. Cheng et al., *TeV Symmetry and the Little Hierarchy Problem*, J. HEP **03**09:051, 2003

[222] H.-C. Cheng et al., *Little Hierarchy, Little Higgses, and a Little Symmetry*, J. HEP **04**08:061, 2004

[223] A. Birkedal et al., *Little Higgs dark matter*, Phys. Rev. D **74**, 035002 (2006)

[224] C.-S. Chen et al., *Novel Collider Signatures for Little Higgs Dark Matter Models*, [arXiv:hep-ph/0605314v2], 2006

[225] M. Asano, *Cosmic Positron Signature from Dark Matter in the Littlest Higgs Model with T-parity*, hep-ph/0602157, 2006

[226] W.-L. Guo, Y.-L. Wu, *The real singlet scalar dark matter model*, [arXiv:1006.2518v3], 2010

[227] S. Profumo et al., *Singlet Scalar Dark Matter: monochromatic gamma rays and metastable vacua*, [arXiv:1009.5377v2], 2010

[228] A. Goudelis et al., *Antimatter signals of singlet scalar dark matter*, [arXiv:0909.2799v2], 2009

[229] Y. Sendouda et al., *Sub-GeV galactic cosmic-ray antiprotons from primordial black holes in the Randall-Sundrum braneworld*, Phys. Rev. D **71**, 063512 (2005)

[230] A. Barrau et al., *Antideuterons as a probe of primordial BH*, [arXiv:astro-ph/0207395v3], 2002

[231] A. Barrau, *Antimatter from primordial black holes*, [arXiv:astro-ph/0208182v1], 2002

[232] A. Barrau et al., *Galactic cosmic rays from pbhs and primordial spectra with a scale*, [arXiv:astro-ph/0210149v2], 2002

[233] A. Barrau et al., *Some aspects of primordial black hole physics*, [arXiv:astro-ph/0212225v1], 2002

[234] J. D. Wells et al., *Illuminating dark matter and primordial black holes with interstellar antiprotons*, hep-ph/9811325, 1998

[235] J. F. Ormes et al., *Interstellar Low Energy Antiprotons as a Probe of Dark Matter and Primordial Black Holes*, [arXiv:9912140], 1999

[236] P. H. Frampton, *Looking for Intermediate-Mass Black Holes*, [arXiv:0907.1646v1], 2009

[237] A. L. Chavda, L. K. Chavda, *Ultra High Energy Cosmic Rays from decay of Holeums in Galactic Halos*, [arXiv:0806.0454v1], 2008

[238] L. K. Chavda, A. L. Chavda, *Dark matter and stable bound states of primordial black holes*, [arXiv:gr-qc/0308054v1], 2003

[239] L. K. Chavda, A. L. Chavda, *Black hole immunity theorem and dark matter*, [arXiv:0406159], 2004

[240] H. C. Cheng, *Kaluza-Klein Dark Matter*, Phys. Rev. Lett. Vol. **89**, No. 21, 2002

[241] G. Bertone et al., *Indirect detection of Kaluza-Klein dark matter*, Phys. Rev. D **68**, 044008 (2003)

[242] G. Servant et al., *Is the lightest Kaluza-Klein particle a viable dark matter candidate?* Nuclear Physics B **650** (2003) 391–419

[243] D. Hooper et al., *Kaluza-Klein dark matter and the positron excess*, Phys. Rev. D **70**, 115004 (2004)

[244] K. Cheung et al., *Cosmic positron and antiproton constraints on the gauge-Higgs Dark Matter*, [arXiv:1007.0282v1], 2010

[245] T. Bringmann, *High-energetic Cosmic Antiprotons from Kaluza-Klein Dark Matter*, [arXiv:astro-ph/0506219v2], 2005

[246] C.-R. Chen et al., *Kaluza-Klein Dark Matter After Fermi*, [arXiv:0908.4317v1], 2009

[247] K. Agashe et al., *Warped Unification, Proton Stability and Dark Matter*, [arXiv:hep-ph/0403143v3], 2004

[248] G. Servant et al., *Baryon Number in Warped GUTs*, [arXiv:hep-ph/0411254v3], 2004

[249] E. A. Baltz et al., *Kaluza-Klein Dark Matter, Electrons and Gamma Ray Telescopes*, [hep-ph/0411053], 2004

[250] D. Hooper et al., *The PAMELA and ATIC Signals From Kaluza-Klein Dark Matter*, [arXiv:0902.0593v1], 2009

[251] M. Kakizaki et al., *Significant effects of second Kaluza-Klein particles on dark matter physics*, Phys. Rev. D **71**, 123522 (2005)

[252] E. Elfgren et al., *Analysis of heavy neutrinos as a dark matter candidate*, [arXiv:0710.3893v1], 2007

[253] G. Belanger et al., *Dirac Neutrino Dark Matter*, [arXiv:0706.0526v2], 2007

[254] K. Kadota et al., *Heavy Right-Handed Neutrinos and Dark Matter in the νCMSSM*, [arXiv:0909.3075v2], 2009

[255] S. Dodelson et al., *Sterile Neutrinos as Dark Matter*, [arXiv:hep-ph/9303287v1], 1993

[256] K. Abazajian, *Production and Evolution of Perturbations of Sterile Neutrino Dark Matter*, [arXiv:astro-ph/0511630v4], 2005

[257] U. Seljak et al., *Can sterile neutrinos be the dark matter?*, [arXiv:astro-ph/0602430v1], 2006

[258] A. Boyarsky et al., *Restrictions on parameters of sterile neutrino dark matter from observations of galaxy clusters*, [arXiv:astro-ph/0603368v1], 2006

[259] K. Abazajian, *Constraints on Sterile Neutrino Dark Matter*, [arXiv:astro-ph/0605271v2], 2006

[260] G. Barenboim et al., *Neutrino Coannihilation on Dark-Matter Relics*, [arXiv:astro-ph/0604215v1], 2006

[261] H. Yüksel et al., *Strong Upper Limits on Sterile Neutrino Warm Dark Matter*, [arXiv:0706.4084v2], 2007

[262] A. Merle et al., *Deriving Models for keV sterile Neutrino Dark Matter with the Froggatt-Nielsen mechanism*, [arXiv:1105.5136v2], 2011

[263] J. Sayre et al., *Sterile neutrinos and global symmetries*, Phys. Rev. D **72**, 015001 (2005)

[264] R. Viollier et al., *Sterile neutrino dark matter at the center and in the halo of the Galaxy*, [arXiv:astro-ph/0310294v1], 2003

[265] M. Maniatis, *The Next-to-Minimal Supersymmetric extension of the Standard Model reviewed*, [arXiv:0906.0777v2], 2010

[266] J. T. Ruderman et al., *General Neutralino NLSP*, [arXiv:1103.6083v1], 2011

[267] D. Suematsu, *Singlino-dominated lightest supersymmetric particle as a CDM candidate*, Phys. Rev. D **73**, 035010 (2006)

[268] S. Hesselbach, F. Franke, *Singlino-dominated Neutralinos in Extended Supersymmetric Models*, [arXiv:hep-ph/0210363v1], 2002

[269] T. Han et al., *Higgs sector in a U(1) extension of the minimal supersymmetric standard model*, Phys Rev. D **70**, 115006 (2004)

[270] T. Delahaye et al., *Cosmic-ray antiproton constraints on light singlino-like dark matter candidates*, [arXiv:1106.2096v1], 2011

[271] M. Cirelli, A. Strumia, *Minimal Dark Matter: model and results*, [arXiv:0903.3381v3], 2009

[272] E. J. Chun, *Minimal dark matter in type III seesaw*, [arXiv:0909.3408v3], 2009

[273] K. Matchev, *Particle Dark Matter from Physics Beyond the Standard Model*, [arXiv:hep-ph/0402088v1], 2004

[274] S. Sultansoy, *The fourth generation, linac-ring type colliders, preons and so on*, [arXiv: 1208.3127], 2012

[275] S. Bar-Shalom et al., *Two Higgs doublets, a 4th generation and a 125 GeV Higgs*, [arXiv:1208.3195v1], 2012

[276] O. Eberhardt et al., *Impact of a Higgs boson at a mass of 126 GeV on the standard model with three and four fermion generations*, [arXiv:1209.1101v1], 2012

[277] D. E. Kaplan et al., *Asymmetric Dark Matter*, [arXiv:0901.4117v1], 2009

[278] A. Falkowski et al., *Asymmetric Dark Matter from Leptogenesis*, [arXiv:1101.4936v2], 2011

[279] M. L. Graesser et al., *Asymmetric WIMP dark matter*, [arXiv:1103.2771v3], 2011

[280] K. Ishiwata et al., *Cosmic-ray positron from superparticle dark matter and the PAMELA anomaly*, Physics Letters B **675** (2009) 446–449

[281] Lisa Randall, M. R. Buckley, *Xogenesis*, [arXiv:1009.0270v2], 2010

[282] S. Tulin et al., *Unified Origin for Baryonic Visible Matter and Antibaryonic Dark Matter*, PRL **105**, 211304 (2010)

[283] R. Sina et al., *The Flux of Cosmic-ray Deuterons*, 28th International Cosmic Ray Conference, 1973

[284] D. C. Kennedy, *Cosmic ray antiprotons*, [arXiv:astro-ph/0003485v2], 2000

[285] M. Boezio et al., *The Cosmic Ray Proton and Helium Spectra*, arXiv:astro-ph/0212253v1, 2002

[286] ATLAS Collaboration, *ATLAS search for new phenomena in dijet mass and angular distributions using pp collisions at* $\sqrt{s}$ *= 7 TeV*, [arXiv:1210.1718v1], 2012

[287] ATLAS Collaboration, *Search for direct production of charginos and neutralinos in events with three leptons and missing transverse momentum in* $\sqrt{s}$ *=7 TeV pp collisions with the ATLAS detector*, [arXiv:1208.3144v1], 2012

[288] G. Kane, S. Watson, *Dark Matter and LHC What is the Connection?*, [arXiv:0807.2244v1], 2008

[289] N. Arkani-Hamed et al., *A Theory of Dark Matter*, [arXiv:0810.0713v3], 2009

[290] J. T. Ruderman, *Light Hidden Sectors: Dark Matter and Lepton Jets*, Theis, 2011

[291] K. R. Dienes et al., *Distinguishing Dynamical Dark Matter at the LHC*, [arXiv:1204.4183v1], 2012

[292] D. J. McComas et al., *The Heliosphere's Interstellar Interaction: No Bow Shock*, Science June 2012, Vol. **336,** No. 6086, pp. 1291-1293

[293] P. Riley et al., *Modeling the heliospheric current sheet: Solar cycle variations*, J. Geophys. Res., Vol. **107**, No. A7, 10.1029, 2002

[294] D. F. Smart, *A review of geomagnetic cutoff rigidities for earth-orbiting spacecraft*, Adv. in Space Res. **36** (2005) 2012-2020

[295] E. Orazi, *Cosmic Rays Propagation in Galaxy*, Thesis

[296] P. Blasi, P. D. Serpico, *High-Energy Antiprotons from Old Supernova Remnants*, PRL **103**, 081103 (2009)

[297] P. D. Serpico et al., *Pulsars as the Sources of High Energy Cosmic Ray Positrons*, [arXiv:0810.1527v2], 2008

[298] P. D. Serpico, *High energy rise of the cosmic ray positron fraction: Possible causes*, Nuclear Physics B (Proc. Suppl.) **194** (2009) 145–150

[299] J. Chang et al., *An excess of cosmic ray electrons at energies of 300-800 GeV*, Nature **456**, 362-365

[300] P. Blasi, *Origin of the Positron Excess in Cosmic Rays*, PRL **103**, 051104 (2009)

[301] R.-Z. Yang et al., *Dark Matter Mini-halo around the Compact Objects: the Formation, Evolution and Possible Contribution to the Cosmic Ray Electrons/Positrons*, [arXiv:1112.3681v2], 2011

[302] G. Bertone et al., *Compact Stars as Dark Matter Probes*, [arXiv:0709.1485v2], 2007

[303] K. Kashiyama et al., *White Dwarf Pulsars as Possible Cosmic Ray Electron-Positron Factories*, [arXiv:1009.1141v3], 2010

[304] R. Sunyaev et al., *Cosmic Rays from Microquasars: a Narrow Component to the CR Spectrum?*, [arXiv:astro-ph/0204183v2], 2002

[305] N. Guessoum et al., *Microquasars' contribution to the galactic positron annihilation radiation*, The Obscured Universe: Proceedings of the VI INTEGRAL Workshop July 2006, Moscow

[306] N. Guessoum et al., *Microquasars as sources of positron annihilation radiation*, [arXiv:astro-ph/0607296v1], 2006

[307] V. Vitale et al., *Indirect Search for Dark Matter from the center of the Milky Way with the Fermi-Large Area Telescope*, [arXiv:0912.3828v1], 2009

[308] C. Weniger, *A Tentative Gamma-Ray Line from DM at FERMI-LAT*, [arXiv:1204.2797v1], 2012

[309] P. Gondolo et al., *Dark Matter Annihilation at the Galactic Center*, Phys. Rev. Lett. Vol. **83**, No. 9, 1999

[310] D. Hooper et al., *Dark Matter Annihilation in the Galactic Center As Seen by the FERMI Gamma Ray Space Telescope*, [arXiv:1010.2752v3], 2011

[311] M. Ahlers et al., *Cosmic ray acceleration in supernova remnants and the FERMI/PAMELA data*, Phys. Rev. D **80**, 123017 (2009)

[312] P. Mertsch, *The PAMELA anomaly indicates a nearby cosmic ray accelerator*, [arXiv:1108.1753v1], 2011

[313] Y. Fujita et al., *Is the PAMELA anomaly caused by supernova explosions near the Earth?*, Phys. Rev. D **80**, 063003 (2009)

[314] K. Auchettl, C. Balázs, *Extracting the size of the cosmic electron-positron anomaly*, [arXiv:1106.4138v1], 2011

[315] S. Ostapchenko et al., *B/C ratio and the PAMELA positron excess*, [arXiv:1211.1033v1], 2012

[316] P. Mertsch et al., *Testing Astrophysical Models for the PAMELA Positron Excess with Cosmic Ray Nuclei*, PRL **103**, 081104 (2009)

[317] M. T. Frandsen et al., *Direct detection of dark matter in models with a light Z'*, [arXiv:1107.2118v2], 2011

[318] E. Aprile et al., *Dark Matter Results from 100 Live Days of XENON100 Data*, PRL **107**, 131302 (2011)

[319] M. Farina et al., *Implications of Xenon100 and LHC results for Dark Matter models*, [arXiv:1104.3572v3], 2011

[320] G. Servant et al., *Elastic Scattering and Direct Detection of Kaluza-Klein Dark Matter*, [arXiv:hep-ph/0209262v4], 2002

[321] P. C. Divari*, Cross-sections for neutral-current neutrino scattering off 82Se isotope*, Acta Phys. Pol. B Vol. **41**, No. 6, 2010

[322] J.-M. Zheng, *Constraining the interaction strength between dark matter and visible matter: I. fermionic dark matter*, [arXiv:1012.2022v2], 2010

[323] Z. Ahmed et al., *Combined Limits on WIMPs from the CDMS and EDELWEISS Experiments*, [arXiv:1105.3377v2], 2011

[324] J. I. Read et al., *Thin, thick and dark discs in ΛCDM*, [arXiv:0803.2714v2], 2008

[325] I. Cholis et al., *Consequences of a Dark Disk for the Fermi and PAMELA Signals in Theories with a Sommerfeld Enhancement*, [arXiv:1006.2089v2], 2010

[326] F. Nozzoli, *TeV dark matter in the disk*, [arXiv:1103.6091v1], 2011

[327] R. Bernabei et al., *Technical aspects and dark matter searches*, [arXiv:0912.4200v1], 2009

[328] D. Hooper, *The Empirical Case For 10 GeV Dark Matter*, [arXiv:1201.1303v1], 2012

[329] F. Halzen, D. Hooper, *The indirect search for dark matter with IceCube*, New Journal of Physics **11** (2009) 105019

[330] R. Abbasi et al., *Multi-year search for dark matter annihilations in the Sun with the AMANDA-II and IceCube detectors*, [arXiv:1112.1840v2], 2011

[331] D. S. Akerib et al., *Limits on spin-dependent WIMP-nucleon interactions from the Cryogenic Dark Matter Search*, Phys. Rev. D **73**, 011102(R) (2006)

[332] I. F. M. Albuquerque et al., *Constraints on Enhanced Dark Matter Annihilation from IceCube Results*, [arXiv:1107.2408v3], 2011

[333] K. Zuber, *Neutrino Physics*, Taylor & Francis Group, 2004

[334] P. Agrawal et al., *A Classification of Dark Matter Candidates with Primarily Spin-Dependent Interactions with Matter*, [arXiv:1003.1912v2], 2010

[335] H. Yüksel et al., *Neutrino Constraints on the Dark Matter Total Annihilation Cross Section*, [arXiv:0707.0196v3], 2007

[336] V. Barger, *Spin Dependence of Dark Matter Scattering*, [arXiv:0806.1962v1], 2008

[337] Y. K. Semertzidis, *Electric Dipole Moments of Fundamental Particles*, [arXiv:hep-ex/0401016v1], 2004

[338] T. Banks et al., *Direct Detection of Dark Matter with electromagnetic dipole moment*, [arXiv:1007.5515v1], 2010

[339] W. S. Cho et al., *Constraining WIMP magnetic moment from CDMS II experiment*, [arXiv:1001.0579v3], 2010

[340] V. Barger et al., *Electromagnetic properties of dark matter: dipole moments and charge form factor*, [arXiv:1007.4345v2], 2010

[341] V. Mourik et al., *Signatures of Majorana fermions in superconductive nanowires device*, [arXiv:1204.2792v1], 2012

[342] C.-H. Chen et al., *ATIC/PAMELA anomaly from fermionic decaying dark matter*, Physics Letters B **675** (2009) 77–79

[343] D. Hooper, W. Xue, *Testing The Light Dark Matter Hypothesis With AMS*, [arXiv:1210.1220v1], 2012

[344] J. J. Beatty et al., *New Measurement of the Cosmic-Ray Positron Fraction from 5 to 15 GeV*, PRL **93**, 241102 (2004)

[345] E. J. Chun et al., *Non-perturbative Effect and PAMELA Limit on Electro-Weak Dark Matter*, [arXiv:1210.6104v1], 2012

[346] I.-Q Gu, *Nonlinear Spinors as the Candidate of Dark Matter*, [arXiv:0806.4649v2], 2008

[347] D. P. Finkbeiner et al., *Search for DM in the CMB: A Compact Parameterization of Energy Injection from New Physics*, [arXiv:1109.6322v1], 2011

[348] C. Destri et al., *Fermionic warm dark matter produces galaxy cores in the observed scales*, [arXiv:1204.3090v1], 2012

[349] A. L. Serra et al., *Measuring the dark matter equation of state*, [arXiv:1103.5465v2], 2011

[350] F. Palmonari, V. Bindi, A. Contin, N. Masi, L. Quadrani, *Search for dark matter in cosmic rays with the AMS-02 space spectrometer*, 2011 J. Phys.: Conf. Ser. **335** 012066

[351] J. Alcaraz et al., *Protons in near earth orbit*, Phys. Let. B **472** (2000) 215–226

[352] M. Agiular et al., *The alpha magnetic spectrometer on the international space station Part I - results from the test flight on the space shuttle*, Phys. Rep. **366** (2002) 331–405

[353] M. Aguilar et al., *Cosmic-ray positron fraction measurement from 1 to 30-GeV with AMS-01*, Phys. Lett. B **646**, 145-154, 2007

[354] P. Brun, *Indirect Searches for Dark Matter with AMS-02*, Lapp-Exp-2007

[355] J. Casaus, *The AMS-02 experiment on the ISS*, J. Phys.: Conf. Ser. **171** (2009) 012045

[356] F. Palmonari, *The search for Cosmic Antimatter*, Il Nuovo Saggiatore, Vol **25**, n. 1-2, pp. 13-23, 2009.

[357] C. Sbarra, *Astroparticle physicswith AMS-02: the quest of antimatter*, Frascati Physics Series, Vol. XXIV pp.297-302

[358] P. Bobik et al., *Electron Positron modulation for AMS-02*, [arXiv:1011.4843v3], 2010

[359] M. Pato, *Discriminating the source of high-energy positrons with AMS-02*, [arXiv:10105236v2], 2010

[360] A. G. Malinin, *Astroparticle Physics with AMS-02*, PHYSICS OF ATOMIC NUCLEI Vol. **67** No. 11, 2004

[361] J. Pochon, *Pulsar electrons detection in AMS-02 experiment*, [arXiv:1002.4213v1], 2010

[362] P. Brun, *Indirect Searches for Dark Matter with AMS-02*, Acta Phys. Pol. B Vol.**1** No. 2, 2008

[363] J. Sandweiss, *Overview of strangelet searches and Alpha Magnetic Spectrometer: when will we stop searching?*, J. Phys. G: Nucl. Part. Phys. **30** (1): S51–S59

[364] M. Sapinski, *Cosmic ray astrophysics with AMS-02 experiment*, International Cosmic Ray Conference Pune **00** (2005) 101–106

[365] M. Pato, *Pinpointing Cosmic Ray Propagation With The AMS-02 Experiment*, [arXiv:1002.3341v2], 2010

[366] M. Pato, *Propagation of galactic cosmic rays and the AMS-02 experiment*, icatpp proceeding, 2010

[367] F. Spada, *Antimatter and Dark Matter search in space with AMS-02*, [arXiv:0810.3831v1], 2008

[368] K. Lübelsmeyer et al., *Upgrade of the Alpha Magnetic Spectrometer (AMS-02) for long term operation on the International Space Station (ISS)*, Nuclear Instruments and Methods in Physics Research A **654** (2011) 639–648

[369] J. Alcaraz et al., *The alpha magnetic spectrometer silicon tracker: Performance results with protons and helium nuclei*, NIM A **593**, 376-398, 2008

[370] B. Alpat et al., *The internal alignment and position resolution of the AMS-02 silicon tracker determined with cosmic-ray muons*. NIM P.R.S. A: Accelerators, Spectrometers, Detectors and Associated Equipment, **613** (2), 207 – 217, 2010

[371] P. Von Doetinchem et al., *Performance of the AMS-02 transition radiation detector*, NIM A **558** (2), 526 – 535, 2006

[372] S. di Falco, *Indirect dark matter search with AMS-02*, [arXiv:astro-ph/0607100v1], 2006

[373] F. Cadoux et al., *The AMS-02 electromagnetic calorimeter*, Nucl. Phys. B, **113** (1-3), 159, 2002

[374] S. Di Falco, *Results of 2007 test beam of AMS-02 Electromagnetic Calorimeter,* Advances in Space Research, **45** (1), 112 – 122, 2010

[375] V. Vagelli, *Identification of positrons and electrons in the cosmic radiation with the electromagnetic calorimeter ECAL for the AMS-02 experiment*, Thesis

[376] C. Corti, *Measurement of the positrons fraction in cosmic rays with AMS-02*, Thesis

[377] A. Monfardini, R. Battiston et al., *AMICA, an astro-mapper for AMS*, [arXiv:0506377], 2005

[378] L. Arruda et al., *Particle identification with the AMS-02 RICH detector search for dark matter with antideuterons*, [arXiv:0710.0993v1], 2007

[379] T. Bruch et al., *The Anti-Coincidence Counter shield of the AMS tracker*, NIM A **572** (1), 505 – 507, 2007

[380] V. Bindi et al., *The scintillator detector for the fast trigger and time-of-flight (TOF) measurement of the space experiment AMS-02*, NIM, A **623**: 968 - 981, 2010.

[381] V. Bindi et al., *The tof-acc flight electronics for the fast trigger and the time of flight of AMS-02*, preprint submitted to NIM

[382] V. Bindi, N. Masi et al., *The time of flight detector of the AMS-02 experiment on the international space station*, NIM A (in press), 2012

[383] V. Bindi et al., *Time of flight readout system of the AMS-02 experiment*, 29th International Cosmic Ray Conference Pune (2005) **00**, 101-104

[384] V. Bindi, *The Alpha Magnetic Spectrometer AMS-02 soon in Space*, NIM A Vol. **617**, No. 1-3, 462-463, 2010

[385] J. D. Sullivan, *Geometrical factor and directional response of single and multi-element particle telescopes*, Nucl. Ins. Meth. **95** (1971) 5-11

[386] A. Tiseni, *Misura del rate di protoni con AMS-02*, Thesis

[387] V. Bindi, *Development and performances of the SFEC card for the TOF apparatus*, Thesis

[388] L. Quadrani, *Assembly and space qualification of the scintillator detector LTOF for the AMS-02 spectrometer*, Thesis

[389] L. Quadrani et al., *Optimization of time of flight of the AMS-02 experiment*, 29th International Cosmic Ray Conference Pune (2005) **00**, 101–106

[390] P. Bobik et al., *Antiproton modulation in the Heliosphere and AMS-02 antiproton over proton ratio prediction*, [arXiv:1102.0215v1], 2011

[391] R. Martelli, *Studio e simulazione delle caratteristiche dei fotomoltiplicatori "fine-mesh" per l'esperimento spaziale AMS-02*, Thesis

[392] M. A. Abdu et al., *South Atlantic magnetic anomaly ionization: A review and a new focus on electrodynamic effects in the equatorial ionosphere*, Journal of Atmospheric and Solar-Terrestrial Physics **67** (2005) 1643–1657

[393] T. Hambye et al., *Scalar Multiplet Dark Matter*, [arXiv:0903.4010v1], 2009

[394] M. Perelstein et al., *XENON100 Implications for Naturalness in the MSSM, NMSSM and λ-SUSY*, [arXiv:1208.0833v1], 2012

[395] J. Bovy et al., *Connection between a possible fifth force and the direct detection of Dark Matter*, [arXiv:0807.3060v3], 2008

[396] G. D'Agostini et al., *Uncertainties due to imperfect knowledge of systematic effects: general considerations and approximate formulae*, [arXiv:hep-ex/0002056v1], 2000

[397] A. László, *A Linear Iterative Unfolding Method*, [arXiv:1111.3387v1], 2011

[398] G. D'Agostini, *A multidimensional unfolding method based on Bayes' theorem*, Nucl. Ins. Meth. Phys. Res. A **362** (1995) 487-498

[399] G. D'Agostini, *Bayesian Inference in Processing Experimental Data*, [arXiv:physics/0304102v1], 2003

[400] AA. VV., *Proceedings of the PHYSTAT 2011 Workshop on Statistical Issues Related to Discovery Claims in Search Experiments and Unfolding*, CERN-2011-006

[401] G. Choudalakis, *Fully Bayesian Unfolding*, [arXiv:1201.4612v1], 2012

[402] G. D'Agostini, *Improved iterative Bayesian unfolding*, [arXiv:1010.0632v1], 2010

AMS-02 Collaboration Internal Sources

[403] AMS-02 Official WebSites, http://www.ams02.org/, http://ams02bologna.weebly.com/, http://ams.nasa.gov/

[404] A. Kounine, V. Koutsenko, *Flight Software for xDR and JINx nodes in AMS-02*, 2011

[405] A Kounine, *LV1 Trigger Studies*, May 2011

[406] A. Kounine, *Data processing in SDR*, November 2010

[407] V. Bindi, *AMS-02 Trigger System*, October 2011

[408] V. Bindi et al., *The TOF-ACC flight electronics for the fast trigger and time of flight of the AMS-02 Cosmic Ray Spectrometer*, 2012

[409] V. Bindi, *TOF Lectures*, 2011

[410] V. Bindi et al., *AMS-02 Scintillator Numbering Scheme*, 2010

[411] A. Contin, *TOF event selection*, June 2011

[412] A. Contin, *TOF Beta Resolution*, September 2011

[413] A. Contin, *TOF: TDC signal selection*, October 2012

[414] A. Contin, *TOF Status*, November 2011

[415] L. Quadrani, *TOF Calibration*, March 2012

[416] A. Contin, *TOF Alignment*, July 2011

[417] A. Contin, *TOF Absolute Rate*, October 2012

[418] F. Palmonari, V. Bindi, N. Masi, L. Quadrani*, TOF Status Report at JSC*, June 2011

[419] A. Contin, *TOF HV Setting*, May 2011

[420] A. Contin, *TOF Efficiency*, July 2011

[421] Q. Yan, *TOF Calibration and Development*, 2012

[422] Q. Yan, *TOF MC Status*, April 2012

[423] A. Contin, *TOF dynode calibration*, July 2011

[424] A. Contin, *TOF Charge Measurement*, October 2011

[425] M. Capell et al., *AMS-02 POCC and SOCC Implementation Plan*, 2010

[426] AMS Collaboration, *Handbook of AMS operations on ISS*, 2011

[427] V. Bindi, N. Masi, L. Quadrani, *TOF Shifter Guide*, July 2011

[428] N. Masi, *JLV1 Monitor Noise*, June 2011

[429] L. Quadrani, *TOF data taking*, February 2012

[430] D. Grandi, *Back Tracing*, November 2012

[431] A. Oliva, *Bad Runs*, July 2012

[432] N. Masi, A. Tiseni, *Antiprotons and Protons Selection*, November 2011

[433] M. Incagli, *Events Preselection for Ecal+Trd positron fraction*, November 2012

[434] S. Schael, *AMS Acceptance*, 2012

[435] N. Masi, *MC, Acceptance and Efficiency*, April 2012

[436] M. Incagli, C. Corti, *Status report on ECAL electron-proton rejection using a MultiVariate approach (BDT = Boosted Decision Tree)*, July 2012

[437] A. Obermeier, *The Positron Fraction from Template Fits to the TRD Likelihood*, November 2012

[438] A. Bachlechner et al., *Approach to quantify charge confusion for the inner tracker of AMS-02*, November 2012

[439] L. Quadrani, *TOF GoodMatch cut for event preselection*, October 2012

[440] F. Nozzoli, *Charge confusion for e+, e estimation and possible reduction*, November 2012

[441] M. Duranti, *Counting Ratio*, November 2012

[442] B. Bertucci, M. Duranti, *Positron fraction measurement*, November 2012

[443] V. Vagelli, *E/P purity fit analysis update*, November 2012